Wave run-up on beaches and coastal structures

by

Alejandro Hammeken Arana

Submitted to the Department of Civil, Environmental and Geomatic Engineering in partial fulfilment of the requirements for the degree of

Doctor of Philosophy in Coastal Engineering

at

University College London

March 2017

TO MY MUM AND DAD

Abstract

Wave run-up is an important design criterion for coastal structures and beach nourishment projects. Coastal engineers commonly use empirical formulae to predict this parameter. These formulae generally include the effect of berms, roughness and angle of wave attack, but neglect the influence of parameters such as hydraulic conductivity and beach groundwater levels. This thesis presents a laboratory and numerical study aimed to improve the predictive capability of existing formulae as well as to enhance our understanding of the swash hydrodynamics and their interaction with permeable beaches. In particular, it investigates the influence of hydraulic conductivity, roughness and beach groundwater on wave run-up and swash flows.

Most of the data presented in this study were obtained from wave flume experiments performed on smooth-impermeable, rough-impermeable and rough-permeable slopes. The influence of hydraulic conductivity on swash hydrodynamics was quantified by means of a novel experimental setup consisting of non-deformable permeable structures, in which the influence of the surface roughness was isolated. A procedure based on the development of time-stack images provided accurate measurement of run-up and swash depths, while pressure transducers were used to measure the water table elevations inside the permeable structures. Laser Doppler velocimetry, a technique that does not disturb the flow, was used to measure the velocity profile of the uprush and backwash flows. In addition to the laboratory experiments, simulations using a Volume-Averaged Reynolds-Averaged Navier-Stokes (VARANS) model, validated against experimental results, were used to investigate the influence of hydraulic conductivity on the near-bed flow velocities and to obtain larger datasets of run-up on impermeable slopes.

Analysis indicated that existing formulae adequately predict run-up from breaking waves on impermeable slopes. However, no previous formulae gave reliable predictions of run-up from non-breaking waves. Therefore, new empirical formulae were derived for non-breaking waves on impermeable slopes. These give good predictions when compared with the present data and data available in literature.

The beach groundwater levels were found to have negligible influence on wave run-up. In contrast, hydraulic conductivity was shown to have a significant effect on wave-structure interaction parameters such as wave run-up, wave-induced water table elevation, swash depths, and swash flow velocities. As a result, new prediction formulae for breaking and non-breaking waves on permeable slopes were developed; these formulae include the

influence of surface roughness and hydraulic conductivity through a new non-dimensional parameter.

Moreover, flow velocity measurements in the swash zone showed that infiltration enhances onshore flow and time asymmetries. This is expected to promote onshore sediment transport inside the swash zone. The near-bed velocity measurements were also used to estimate bed shear stresses using the log-law method. The results showed that infiltration directly increases the bed shear stresses during the uprush phase, mainly due to the change in the boundary layer thickness. However, infiltration was also shown to indirectly reduce the bed shear stresses during the backwash phase by significantly reducing the backwash flow depths and velocities (continuity effect).

Video observations of the breaking processes showed that hydraulic conductivity alters the shape of waves breaking on the slope. However, the change in shape is small and in all cases, the breaker type remained the same. Hydraulic conductivity was also shown to decrease the breaking point distance of plunging waves. The video analysis was also used to validate a new criterion presented in this study to determine whether or not waves will break on the slope; this criterion was shown to give better predictions of the transition between breaking and non-breaking waves than existing breaking criteria.

This is one of the first studies to include the influence of hydraulic conductivity on run-up prediction formulae. If the porosity or hydraulic conductivity of a coastal structure or beach is known, these formulae in combination with the reduction factors suggested by EurOtop (2007) can lead to more accurate predictions of wave run-up and wave overtopping on permeable slopes. The improved understanding of the influence of hydraulic conductivity on the wave-induced water table elevation and on the swash hydrodynamic processes will benefit the modelling and management of coastal aquifers as well as the prediction of sediment transport in the swash zone.

Acknowledgements

I would like to express my most sincere gratitude to my supervisor Professor Richard R. Simons for his advice, guidance and constant support throughout the course of study. I also would like to thank Dr Eugeny Buldakov for his feedback as second supervisor of my PhD. My sincere thanks also go to Leslie Ansdell and Keith Harvey, without their excellent technical support it would not be possible to conduct this research. Special thanks to Natalie Quinn for her continuous support and friendship. I would also like to thank Dr Deborah Ann Villarroel-Lamb and her students Anton Ali and Carol Ali for their collaborations and Dr Alan Brampton for his helpful advice at the beginning of my PhD. Thanks also go to my colleagues at the Civil, Environmental, and Geomatic Engineering Department, in particular my friends at GM 16. I would also like to thank CONACYT, SEP and UCL for their Scholarships awarded, which provided the means to carry out this work. Last but not the least, I would like to thank my family for supporting me throughout this thesis and in my life in general.

Contents

List of Figures

List of Tables

List of Symbols

η	Water table over-height
η^+	Maximum water table over-height
η_w^+	Wave-induced maximum water table over-height
MSL	Mean sea level
SWL	Still water level
MWL	Mean water level
H	Wave height
H_o	Deepwater wave height
H_{mo}	Zeroth-moment wave height
H_{rms}	Root-mean-squared wave height
H_s or $H_{1/3}$	Significant wave height
T_p	Spectral peak wave period
T_m	Mean wave period
T	Wave period
L	Wavelength
L_o	Deepwater wavelength
L_p	Wavelength associated with T_p
L_m	Wavelength associated with T_m
L_{op}	Deepwater wavelength associated with T_p
L_{om}	Deepwater wavelength associated with T_m
h	Water depth
C	Wave celerity
a	Wave amplitude
f	Wave frequency

ω	Angular frequency
k	Wavenumber
u	Horizontal particle velocity
$\bar{u}$	Ensemble-averaged flow velocity
w	Vertical particle velocity
α	Slope angle
k	Permeability
K	Hydraulic conductivity
n	Porosity
g	Gravitational acceleration
μ	Dynamic viscosity
ν	Kinematic viscosity
ρ	Density
$\boldsymbol{\sigma}$	Surface tension
ξ	Iribarren number or surf similarity parameter ($\tan\alpha/\sqrt{H/L}$)
ξ_m	Iribarren number based on the mean wave period
$\xi_{m-1,0}$	Iribarren number based on the spectral wave period
ξ_{op}	Iribarren number based on the deepwater wavelength
R	Wave Run-up height above SWL
$R_{u2\%}$	Run-up level exceeded by 2% of the run-up values in the distribution
R_s	Significant run-up
$\bar{R}$	Mean run-up level
R/H	Dimensionless wave run-up
R/h	Relative wave run-up

H/L	Wave steepness
h/L	Relative water depth
H/h	Relative wave height
U_R	Ursell number (L^2H/h^3)
p_{d}	Instantaneous wave dynamic pressure at a specified position
m_{f}	Momentum flux
M_{F}	Maximum depth-integrated wave momentum flux
$M_F/\rho g h^2$	Wave momentum flux parameter
A_0	Empirical coefficient
A_1	Empirical coefficient
K_p	Reduction factor to account for slope porosity
K_{M}	Constant of proportionality
a	Empirical coefficient
b	Empirical coefficient
η	Elevation of the wave crest above SWL
C_0, C_1 and C_2	Empirical coefficients
γ_b	Influence factor for a berm
r_B	Reduction of the average slope
r_{d_B}	Reduction of the influence of a berm caused by the berm depth
d_B	Berm depth
B	Berm width
L_{berm}	Characteristic berm length
γ_f	Influence factor for surface roughness
γ_β	Influence factor for oblique wave attack
B	Angle of wave attack

$\gamma_{f\ surging}$	Influence factor for surging waves
γ_h	Influence factor for shallow water
γ_K	Influence factor for hydraulic conductivity
γ_p	Influence factor for porosity
P	Notional permeability coefficient
C_r	Reflection coefficient (C_r=H_r/H_i)
H_i	Incident wave height
H_r	Reflected wave height
I	Hydraulic gradient
c_A	Added mass coefficient for porous media flow
α	Linear resistance coefficient for porous media flow
β	Non-linear resistance coefficient for porous media flow
d	Particle diameter
d_{50}	Mean nominal particle diameter
q_w	Discharge per unit width
Re_d	Reynolds number based on particle diameter
Re_p	Reynolds number based on pore size
MAE	Mean Absolute Error
f_i	Predicted value
y_i	Measured value
e_i	Absolute error
σ	Standard deviation
u_*	Friction velocity
τ_0	Bed shear stress
z_0	Vertical displacement of the origin of the mean velocity profile

κ	Karman constant
C_D	Drag coefficient, also known as friction factor
t'	Dimensionless time
t	Time
t_{swash}	Total duration of the swash cycle
h_{max}	Maximum water depth
h'	Dimensionless water depth
u'	Dimensionless velocity
v_0	Vertical velocity at the surface (infiltration velocity)
T_u	Uprush period
T_b	Backwash period
T_u/T_b	Time asymmetry
u_u	Maximum uprush velocity
u_b	Maximum backwash velocity
u_u/u_b	Velocity asymmetry
b_h	Thickness of half-width in a flow reversal velocity profile
U_m	Maximum negative velocity in a flow reversal velocity profile
b_m	Height of maximum negative velocity
δ	Boundary layer thickness
u_∞	Free-stream velocity

1 Introduction

The coastal regions are one of the world's most fragile, changing and vulnerable areas continuously exposed to the impact of waves, currents, tides and storm surges which can cause erosion and flooding. These risks are expected to increase with the threat posed by sea-level rise. Although the coastal region occupies less than 15% of the Earth's land surface, about 44% of the world's population is concentrated within 150km of the coast and, by 2025, this percentage is expected to increase to around 75% (UN Atlas of the Oceans, 2010 (2010)). According to the World Ocean Review (2016) more than 200 million people worldwide live along coastlines less than 5 metres above sea level. For this reason, coastal defence schemes are necessary to minimise the continuous risk of coastal erosion and flooding. The most common approaches adopted are the construction of coastal structures and beach nourishment projects. Their design depends on the accurate prediction of parameters such as wave run-up, *R*, which can be defined as the maximum vertical distance of wave uprush on a coastal structure or on a beach above the still water level (SWL) (Figure 1).

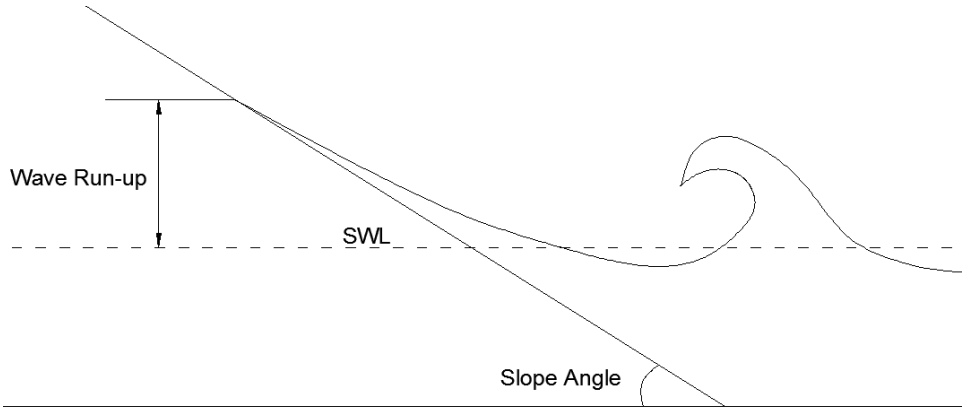

Figure 1 Definition of wave run-up

Wave run-up can be highly influenced by the hydraulic conductivity, surface roughness and beach groundwater levels. Yet very little has been done to investigate and include the influence of these parameters on prediction run-up formulae.

This study is a fundamental investigation on the interaction between waves and beaches/coastal structures. Its overall objective is to provide reliable wave run-up data from breaking and non-breaking waves over different types of slopes with the aim of analysing these data and improve our understanding of the influence that these parameters (mainly hydraulic conductivity) have on the swash and beach groundwater hydrodynamics. Particular focus is placed on improving the prediction of run-up formulae over impermeable and permeable slopes.

Importance of Wave Run-up. Until quite recently, the crest height of coastal structures was traditionally designed to be higher than the predicted values of maximum wave run-up, to prevent overtopping. However, in recent years, their crest height has been estimated based on tolerable overtopping discharges or on peak overtopping volumes rather than on the maximum wave run-up. Nevertheless, an accurate prediction of wave run-up on coastal structures is still necessary, as it is a key parameter for predicting the number or percentage of overtopping waves, and for estimating overtopping volumes, run-up velocities and run-up flow depths. Therefore, an overestimation of run-up can considerable increase their construction cost.

The prediction of wave run-up is also important in the management of beaches. As it delineates the area affected by waves, it is commonly used in the design of beach nourishment projects, for coastal risk mapping and monitoring, as well as for the prediction of beach/dune erosion and overtopping.

Predictions of wave run-up are commonly based on empirical formulae derived from data obtained mainly from field studies or laboratory experiments. However, the development of numerical models in recent years, capable of simulating the wave breaking processes and wave interaction with sloping structures, have made them a viable alternative to predict and obtain run-up data.

1.1 Research Methodology

The general research methodology followed in this study is described in the flow chart shown in Figure 2. As can be seen, the research data were obtained from run-up tests over permeable and impermeable slopes. These were carried out on both laboratory experiments and numerical simulations, and were planned according to the specific aims and objectives defined after the literature review.

This project is mainly focused on wave run-up and the influence that some parameters (mainly hydraulic conductivity) have on it. However, it also covers the influence of hydraulic conductivity on other nearshore parameters and processes such as wave breaking, water table over-height and swash hydrodynamics.

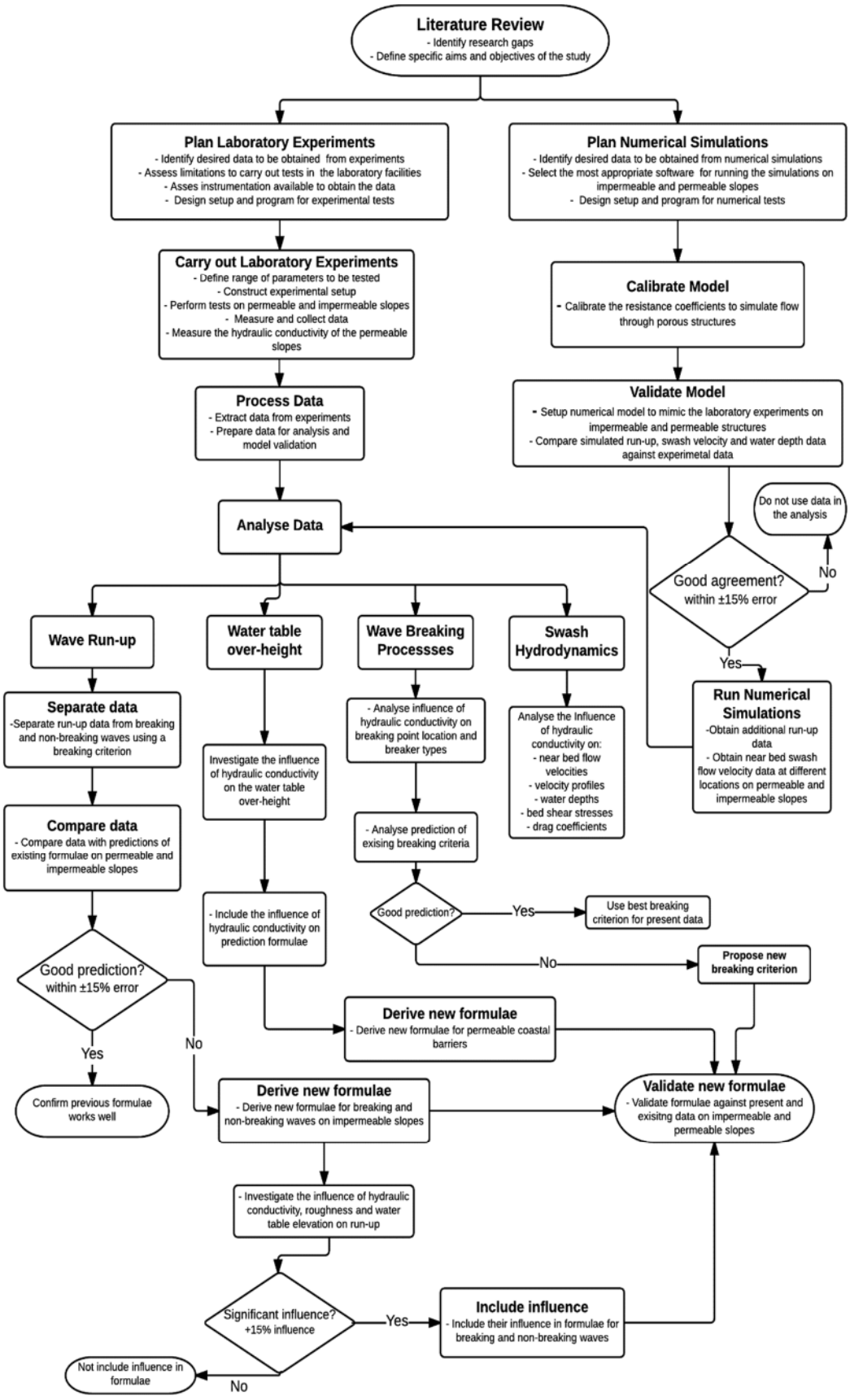

Figure 2 Research Methodology

1.2 Thesis Outline

Following the introductory chapter, the thesis covers a description of the relevant theory, a literature review, details of the laboratory experiments and numerical simulations carried out, an analysis and discussion of the results, and the main conclusions and future recommendations that are drawn from the study. The main body of the thesis is divided into seven chapters, the contents of which are summarised in the following paragraphs.

Chapter 2 defines and reviews the main processes and parameters relevant to this study.

Chapter 3 reviews past research and identifies the main research gaps. It reviews previous studies on wave run-up and on the main parameters that can influence its height. The chapter discusses previous formulae attempting to predict wave run-up for breaking and non-breaking waves on impermeable and permeable slopes, as well as the attempts to include the parameters that influence run-up in predictive formulae. It also reviews previous efforts in predicting the maximum water table over-height inside a beach and previous studies investigating the influence of hydraulic conductivity on the swash zone boundary layer dynamics are also reviewed. Following the literature review, the specific aims and objectives of the present study are defined.

Chapter 4 describes the wave flume laboratory experiments carried out. It details the experimental setup, test conditions and parameters used for each of these experiments. The chapter also describes the instrumentation and data processing procedures used.

Chapter 5 describes the numerical simulations performed using a 2D Reynolds-Averaged Navier-Stokes (RANS) model to simulate run-up over permeable and impermeable slopes. The chapter describes calibration performed to estimate values for the resistance coefficients needed to simulate flow through porous media. It also presents comparisons between the experimental and simulated data with the aim of validating the model, as well as a sensitivity analysis on the porous media parameters.

Chapters 6 and 7 present the analysis and discussion of the data obtained from the experimental tests and numerical simulations performed on smooth-impermeable and permeable slopes, respectively. Chapter 6 presents a dimensional analysis to investigate the influence of wave height, wave period and slope angle on wave run-up, followed by a non-dimensional analysis on data from regular and irregular waves on smooth-impermeable slopes. The chapter presents new formulae for predicting wave run-up as well as a new breaking criterion to predict the transition between breaking and non-breaking waves at the slope.

Chapter 7 presents the analysis on the influence of hydraulic conductivity, surface roughness and water table elevations on run-up, where their influence is included in the new run-up formulae through influence factors. The chapter also presents the analysis on the influence of hydraulic conductivity on the maximum water table over-height, as well as an analysis of the influence of infiltration on the swash flows and bed shear stresses.

Finally, Chapter 8 summarises the work conducted and the shows the main outcomes and conclusions that were drawn from the study, as well as the recommendations for future work.

2 Relevant Theory

This chapter briefly reviews and defines the main processes and parameters relevant to this study. The chapter is divided into four sections:

Section 2.1 describes the processes involved in the interaction between waves and beaches by defining the main concepts involved in the swash zone and in the beach groundwater system. This section includes a description of the beach groundwater fluctuations due to tides and waves.

Section 2.2 describes the main parameters and dimensionless parameters used to describe the interactions between waves and beaches/coastal structures, such as wave run-up. Special emphasis is made on two dimensionless parameters commonly used in prediction formulae to estimate wave run-up: the Iribarren number and the wave momentum flux parameter. These are described in Sections 2.3 and 2.4, respectively.

2.1 Interaction between Waves and Beaches

2.1.1 Swash Zone

The nearshore zone of a beach is generally divided into three zones of wave action: *breaker zone*, *surf zone* and the *swash zone* (Figure 3). The breaker zone is where the waves become unstable due to water depth and break. This leads to the surf zone where shallower broken waves migrate to the shore until they reach the swash zone, where waves can reform to break again. This is where wave run-up takes place (Figure 3).

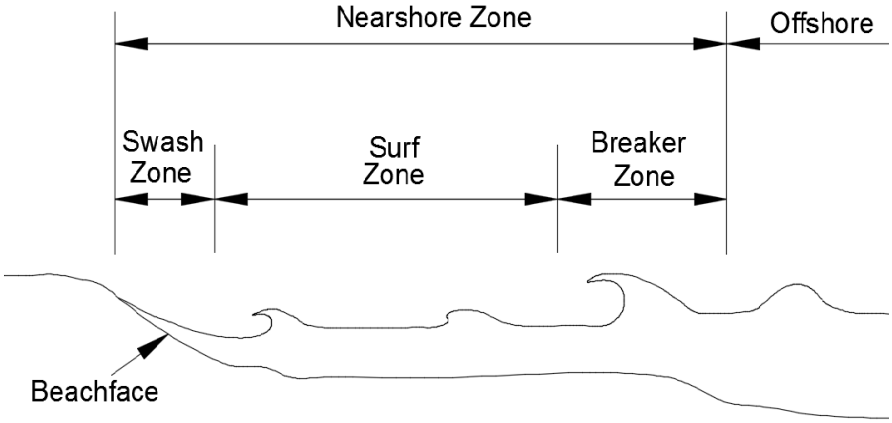

Figure 3 Beach nearshore zones defined by wave activity

Surface flows in the swash zone take place on the beachface and consist mainly of two phases: wave *uprush* and *backwash*. Wave *uprush* is the water motion moving up the slope of the beachface, while wave *backwash* is the downslope movement of the water after the maximum wave run-up. The initial boundary conditions between the uprush and

backwash motions are significantly different. During the uprush, the remaining kinetic energy after wave breaking is transformed into potential energy as it travels up the slope with gradually decelerating speed until it reaches a maximum height (wave run-up), where the velocity is zero. The uprush is mainly driven by the momentum of the incident wave and is moderated by the angle, roughness and hydraulic conductivity of the slope. In contrast, backwash is driven mainly by gravity and the volume of water remaining after uprush. During the backwash the potential energy is transformed back into kinetic energy as the wave travels seawards down the slope. Its lowest height is called *wave run-down*. Although for coastal design wave run-down is not as important as wave run-up, it is often considered to determine the lower extent of main armour protection in a coastal structure and it is also used to define the level for a toe berm.

Beaches have traditionally been classified according to the Wentworth scale. This scale defines sand beaches to have sediments with diameters between 0.0625 to 2mm, while beaches with larger sizes than this are classified as gravel beaches. Gravel beaches are subdivided into granular (2 to 4mm), pebble (4 to 64mm), cobble (64 to 256mm) and boulder (>256mm). Rounded gravel beaches, typical in UK coasts, are referred as *shingle* beaches and consist of pebbles and medium-sized cobbles stones.

2.1.2 Beach Groundwater System

In beach hydrology, the term *groundwater* is commonly used to mean any water held in the sand or gravel below the beach surface. The *beach groundwater system* can be considered to be an unconfined aquifer, highly dynamic, and a shallow system in which water flows through saturated and unsaturated sediments by tides, waves and swash, and to a minor extent by evaporation, and exchanges with deeper aquifers (Horn, 2002).

Horn (2002, 2006) presented comprehensive summaries of the main concepts involved in the swash zone and in the beach groundwater system. Some of these concepts are shown in Figure 4 and defined below.

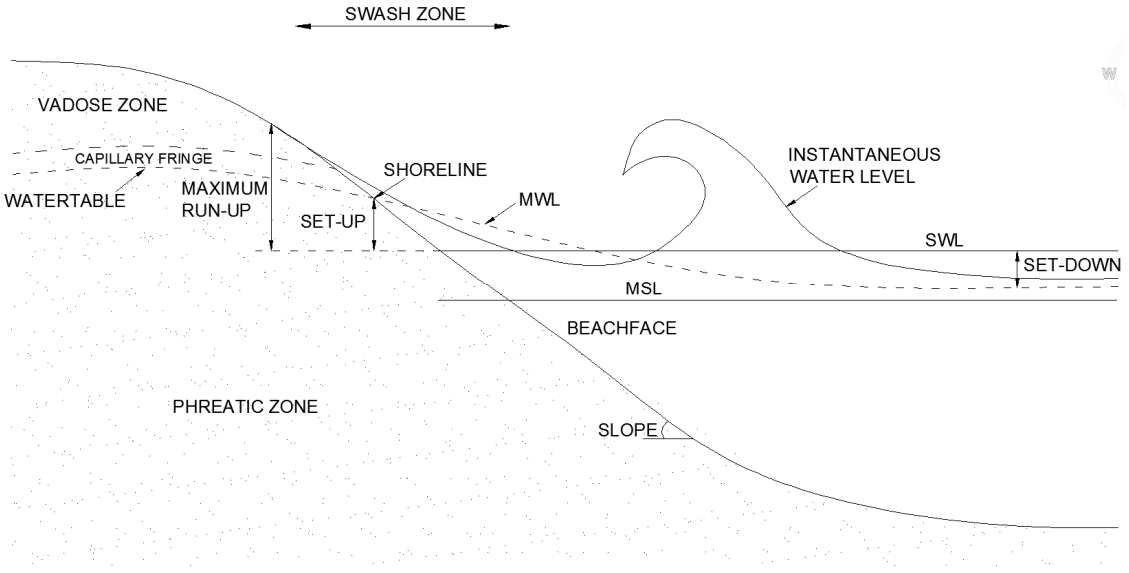

Figure 4 Relevant parameters in the swash zone and beach groundwater system (adapted from Horn, 2006)

The *water table* is the surface of the groundwater where the water pressure head is equal to the atmospheric pressure and in some cases it is considered to be the continuation of the mean water level, *MWL*, inside the beach (Figure 4). The *MWL* is the average level of the water surface over a period for which the level is determined.

The *phreatic zone* is the fully saturated zone below the water table, while the *vadose zone* (also called the aeration or the unsaturated zone) is the region that extends from the water table up to the beach surface (Figure 4). In the phreatic zone, pore spaces are filled with water and pore water pressures are greater than the atmospheric pressure. In contrast, in the vadose zone, pores are filled with water and air and pore water pressures are less than the atmospheric pressure. One of the most influential aquifer characteristics is the presence of moisture above the water table due to capillary action (Cartwright, 2004). This zone is called the *capillary fringe* and differs from the phreatic zone because pore water pressures are negative. According to Horn (2002), this is why beach groundwater zones are better defined by water pressure distributions rather than by saturation levels.

The mean sea level, *MSL*, is the long term average level of the ocean surface outside the surf zone. The still water level, *SWL*, is the average water surface elevation at any instant, excluding variation due to waves and wave set-up, but including the effects of tides, storm surges and long period seiches. Wave set-up is defined as an increase of the MWL due to the presence of waves; similarly, wave set-down is a wave-induced decrease of the MWL due to the presence of waves. Finally, the *shoreline* is the position where the MWL intersects the beachface (Figure 4).

2.1.3 Beach Groundwater Fluctuations due to Waves and Tides

As shown in Figure 4, near the beachface, the water table elevation generally stands considerably higher than the MSL. This super-elevation of the water table above the elevation of the tide is commonly called the *water table over-height*, η. It is partly governed by prevailing hydraulic conditions, such as wave run-up, setup, tide range and rainfall recharge, and partly by the hydraulic conductivity of the beach material (Gourlay, 1992). In coastal barriers, the influence of rainfall recharge on η is small compared to the influence from waves and tides, which can produce a *maximum water table over-height*, η^+, of several metres (Nielsen, 1999).

Beach Groundwater Fluctuations due to Tides. The response of beach groundwater to tides have been studied by many authors (e.g. Nielsen, 1988,1990; Turner et al., 1997; Gourlay, 1992). These studies have shown that tide-induced water table fluctuations are asymmetrical: the water table elevation rises quickly and drops off slowly compared to the tide which drives it. This asymmetry is due mainly to the hydraulic conductivity of the beach (Nielsen, 1990).

An interesting phenomenon relevant to this study occurs when the tidal elevation drops. As the water table elevation drops at a slower rate, *decoupling* occurs, with the water table elevation at a higher position than the shoreline elevation (Figure 5). When decoupling occurs, the *exit point* is said to be the position on the beach profile where the decoupled water table intersects the beachface. Below the exit point and above the shoreline point, a *seepage face* develops (Figure 5). On the seepage face, the water table coincides with the beachface causing exfiltration. The seepage face can be easily identified in the field as a beach surface with a glassy-shiny appearance (Cartwright, 2004; Cartwright et al., 2005). The extent of the seepage face varies between beaches as it is determined by the tidal regime, the hydraulic properties of the beach, and the geometry of the beachface (Horn, 2002).

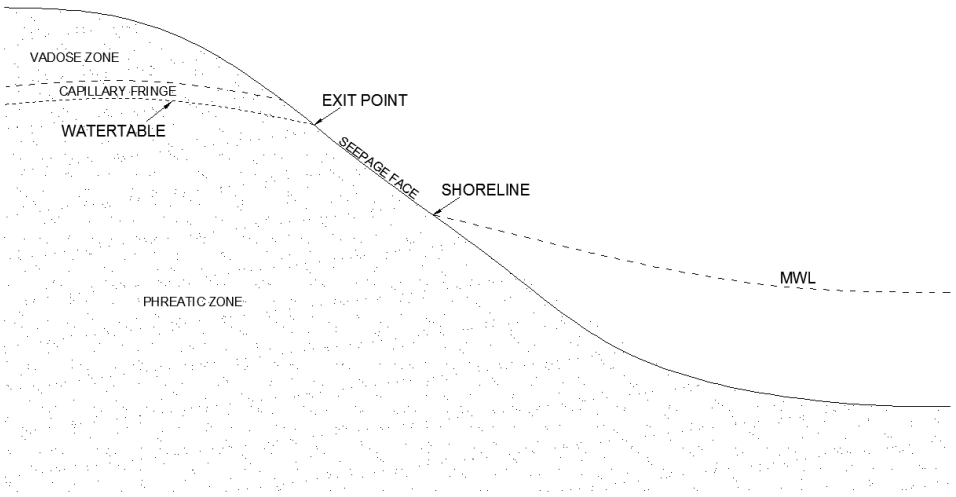

Figure 5 Sketch showing the exit point of the water table and seepage face when the tidal elevation drops and decoupling occurs

Beach Groundwater Fluctuations due to Waves. Waves can contribute to water table fluctuations mainly through two mechanisms: 1) by run-up of individual waves generating high-frequency water table and pore pressure fluctuations; and 2) by time-averaged wave effects contributing to a maximum water table over-height, η_w^+ , both by set-up raising the mean water surface at the shoreline and by run-up increasing the mean water surface. This project focuses only on time-averaged wave-induced fluctuations on the water table over-height.

Studies have shown that the time-averaged maximum wave-induced water table over-height, η_w^+, in a coastal barrier may cause a net groundwater flow to the landward direction (Figure 6) (e.g. Nielsen, 1999, 2009; Masselink and Turner, 2012). This groundwater flow can have a number of significant environmental consequences such as: 1) any wastewater released into the aquifer will flow towards the continent rather than towards the ocean; 2) any pollutants that land on the beachface will probably enter the aquifer under the barrier; and 3) the vegetation may be subject to salt poisoning under extreme conditions of large waves (Nielsen, 2009). Therefore, a good prediction of η_w^+ is essential for managing and modelling coastal aquifers.

The hydraulic conductivity of coastal barriers influences the magnitude of wave run-up and studies have shown that η_w^+ has a linear relationship with wave run-up. Therefore, it is expected that hydraulic conductivity will also the influence the magnitude of η_w^+. Yet, its influence on η_w^+ is still not clear as studies have shown mixed; these studies are discussed in the Literature Review chapter.

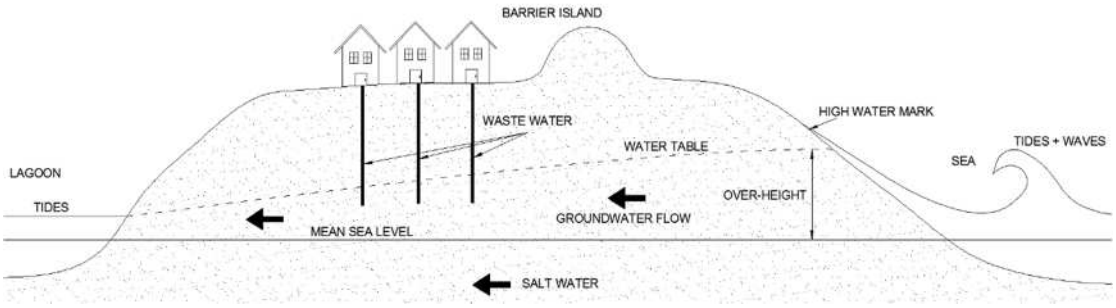

Figure 6 Net groundwater flow towards the continent as a consequence of the high water table caused by waves and tides in a coastal barrier (adopted from Nielsen (1999))

2.2 Relevant Parameters for Wave Run-up

The interaction processes between waves and coastal barriers/beaches coastal structures or coastal structures can be visible in front of (reflection), on top of (run-up), over (overtopping) and behind (transmission) of the structure/barrier. These interactions, called *hydraulic responses*, depend mainly on wave, structural and fluid parameters. These parameters are described and defined below.

Wave Parameters. The wave parameters are commonly derived for either *regular* or *irregular* waves. Regular waves assume a constant wave height and wave period, while irregular waves may have varying wave periods and heights and are commonly used to describe waves seen in nature.

Regular waves. Analysis using regular waves can provide a detailed understanding of the parameters involved in wave mechanics. These types of waves assume a constant wave height and wave period. The main wave parameters for regular waves are shown in Table 1 and sketched in Figure 7. These are generally derived from *linear* or *small amplitude wave theory,* also known as *Stokes I wave theory*, which assumes sinusoidal fluctuations of the surface elevation.

For linear waves, *wave amplitude*, a, is defined as the height of the crest above the still water level (SWL) and is equal to the vertical distance from the SWL to the trough. Therefore:

$$a = \frac{1}{2}H \tag{1}$$

RELEVANT REGULAR WAVE PARAMETERS		
H - wave height	a – wave amplitude	H_o - deepwater wave height
L – wavelength	f – wave frequency	L_o - deepwater wavelength
T – wave period	k - wavenumber	ω – angular frequency
C – wave celerity	u – horizontal particle velocity	w – vertical particle velocity

Table 1 Relevant regular wave parameters

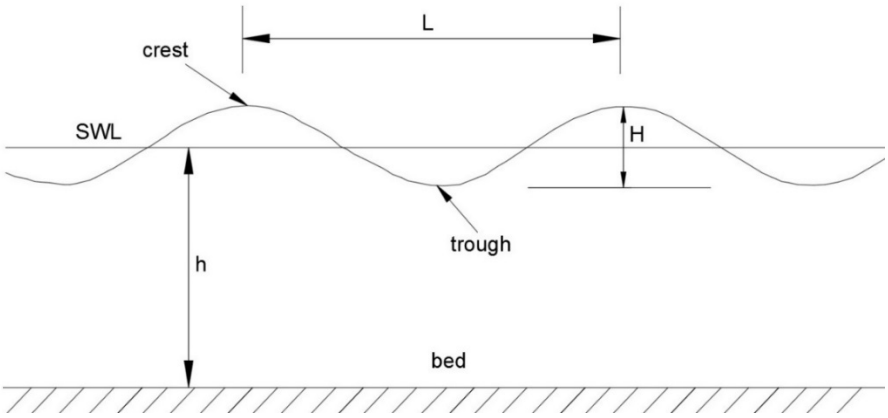

Figure 7 Wave Parameters

Waves propagate with a velocity called *wave celerity*, C, and the time that is required for a wave to pass a particular location is called *wave period*, T. The inverse of the wave period is the *wave frequency*, f, while *wavelength*, L, is defined the horizontal distance over which the wave pattern repeats itself. The *water depth*, h, is the vertical distance between the SWL and the bed, while the *angular wavenumber*, k, and *angular frequency*, ω, are related to wavelength and wave period by:

$$k = 2\pi/L \tag{2}$$

$$\omega = 2\pi/T \tag{3}$$

A numerical solution can be used to calculate the wavelength, L from the following expression derived from linear wave theory:

$$L = \frac{gT^2}{2\pi}\tanh\left(2\pi\frac{h}{L}\right) \tag{4}$$

The wavelength can also be estimated from solutions presented in tabular forms in the Shore Protection Manual (1984). For deepwater waves ($h/L > 1/2$), the wavelength can be estimated as:

$$L_o = \frac{gT^2}{2\pi} \tag{5}$$

where L_o is the deepwater wavelength.

Irregular waves. The term *irregular waves* is commonly used to represent natural sea states which is often a combination of different types of waves such as swell and sea waves. These waves are expected to have a statistical variability, so statistical and probabilistic methods are often employed to estimate characteristic wave parameters from irregular waves that could represent the randomness of ocean waves. The two most important parameters for quantifying a given sea state are a characteristic wave height

(such as *mean height, root-mean square height* and *significant wave height*) and a characteristic wave period (such as *mean period* and *spectral peak period*). Other important irregular wave parameters, such as characteristic wavelengths, can be derived from characteristic wave periods. The symbols representing these parameters are summarised in Table 2.

H_{mo} – zeroth-moment wave height	T_p – spectral peak wave period	L_m – wavelength associated with T_m
H_{rms} – root-mean-squared wave height	T_m – mean wave period	L_{op} – deepwater wavelength associated with T_p
H_s or $H_{1/3}$ – significant wave height	L_p – wavelength associated with T_p	L_{om} – deepwater wavelength associated with T_m

Table 2 Common irregular wave parameters

Structural and fluid parameters. Other relevant structural and fluid parameters that can influence wave run-up and the other hydraulic responses are summarised in Table 3.

RELEVANT STRUCTURAL PARAMETERS		
α – slope angle	slope roughness	K - slope hydraulic conductivity
k – slope permeability	n – slope porosity	η – water table over-height
RELEVANT FLUID AND OTHER PARAMETERS		
ρ - density	μ – dynamic viscosity	ν – kinematic viscosity
$\boldsymbol{\sigma}$ – surface tension	h – water depth	g – gravitational acceleration

Table 3 Relevant structural and fluid parameters for wave run-up

Dimensionless parameters. Wave run-up is commonly estimated with empirical or semi-empirical formulae based on dimensionless parameters and empirical coefficients. These dimensionless parameters are commonly formed combining the parameters shown in Tables 1, 2 and 3. The most relevant dimensionless parameters used to describe coastal processes are shown in Table 4.

Dimensionless Parameters	Value
Wave steepness	H/L; H/L_o; H/gT^2
Relative water depth	h/L; h/gT^2; kh
Relative wave height	H/h
Iribarren number, ξ	$\tan\alpha/\sqrt{H/L}$
Wave momentum flux parameter	$M_F/\rho g h^2$
Ursell number, U_R	$L^2 H/h^3$

Table 4 Relevant coastal dimensionless parameters

For wave run-up, the most relevant dimensionless parameters are the *Iribarren number* and the *wave momentum flux parameter.* These parameters have traditionally been used to characterise wave run-up data and are described below.

2.3 Iribarren Number

The Iribarren number, also known as the *surf similarity parameter*, is defined by the relationship between the slope and the square root of the wave steepness:

$$\xi = \frac{\tan \alpha}{\sqrt{H/L_o}} \tag{6}$$

This parameter was first introduced by Iribarren and Nogales (1949) as a *breaking criterion* to determine whether or not waves break at the slope. Around 25 years later, Battjes (1974) showed that this parameter was also useful to describe other processes of periodic waves on a slope such as: wave reflection, wave set-up, wave run-up and run-down, as well as to separate between the different breaker types. After Battjes (1974) work, this parameter has appeared in numerous empirical formulae related to the design of coastal structures and beach processes.

2.3.1 Iribarren Number for Identifying Breaker Types

Wave run-up depends on how the wave breaks, commonly known as the *breaker type*. The breakers types are traditionally divided into: *spilling*, *plunging*, *collapsing* and *surging* (Figure 8).

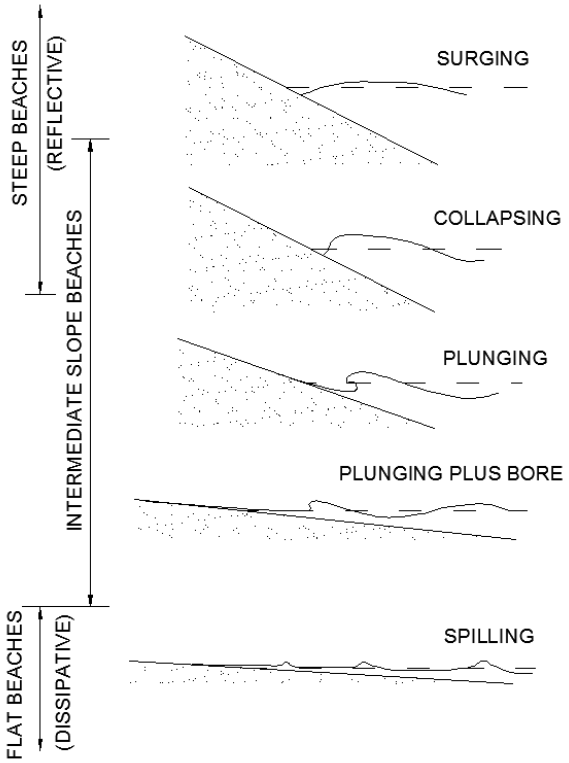

Figure 8 Beach and breaker types on impermeable plane beaches ((Gourlay, 1992))

These breaker types are briefly described below:

Spilling breakers. On a relatively gentle slope or if the wave is steep and short, the wave will steepen until the crest becomes unstable and starts to gently break. This results in turbulent white water spilling down the face of the wave which slowly dissipates the wave energy. This gentle breaking continues for a longer time and longer distance than other

breaking types, thus several wave crests may be breaking simultaneously. These waves are typical of dissipative beaches.

Plunging breakers. On steeper slopes and/or with slightly longer waves than spilling breakers; waves become much steeper than a spilling wave and the wave crest curls over, runs ahead and drops onto the through of the wave. Most of the energy is dissipated at once on the violent breaking impact.

Collapsing breakers. These types of waves occur on steep slopes and have a crest that never fully breaks. They tend to be a cross between plunging and surging breakers.

Surging breakers. These breakers are produced either from long waves, low steepness waves, and/or very steep slopes. Surging waves have almost no breaking and wave crest remains relatively smooth with little foam. As almost no energy is dissipated in their breaking processes, most of their energy is reflected back to the ocean. These waves are typical of reflective beaches.

Battjes (1974) suggested that the Iribarren number can be used to distinguish between the different breaker types and proposed the values shown in Table 5 to delimit the range values for each breaker type.

Breaker Type	ξ range
spilling	ξ <0.5
plunging	0.5< ξ <3.3
surging or collapsing	ξ >3.3

Table 5 Breaking Wave types according to their Iribarren number

2.3.2 Iribarren Number as Breaking Criterion

The Iribarren number has also traditionally been used as a breaking criterion to determine whether a wave will break or not at the slope. When waves break on impermeable slopes (*breaking waves*), most of the energy is dissipated by the heat generated by the turbulence of the breaking processes. On the other hand, when waves do not break and surge up the slope (*non-breaking waves*) most of the energy is reflected back to the sea. Therefore, run-up heights from breaking and non-breaking are generally entirely different. For this reason, most prediction run-up formulae have been developed for either breaking or non-breaking waves, so it is crucial to predict correctly which waves will break at the slope and which will not.

2.3.3 Wave run-up as a function of the Iribarren Number

Hunt (1959) investigated laboratory run-up data from previous studies and noticed that the non-dimensional run-up, R/H, from breaking waves was proportional to the slope and

a function of the square-root of the wave steepness, and thus, a function of the Iribarren number:

$$\frac{R}{H} = \frac{\tan\alpha}{\sqrt{H/L_o}} = \xi \tag{7}$$

This equation is commonly known as *Hunt's formula*. Several studies have shown evidence to support the successfulness of this and other formulae based on the Iribarren number to predict waves from breaking waves (plunging or spilling breakers). These studies are reviewed in Chapter 3. However, Ahrens et al. (1993) showed that the wave kinematics and water depth at the front of the structure play an important role for surging and collapsing waves. Therefore, the Iribarren number might not be the best parameter to describe the run-up of non-breaking waves as it does not consider water depth. This poor correlation between the non-dimensional run-up R/H of non-breaking waves and ξ has been shown in several studies, which are also discussed in Chapter 3.

2.4 Wave Momentum Flux Parameter

Hughes (2004b) suggested that the *wave momentum flux* is the ideal parameter to characterise waves in the nearshore region as it is the property of progressive waves most closely related to force loads on coastal structures. The momentum flux is defined as the rate of change of horizontal momentum which is moving across a unit area, equal to force per unit area. The instantaneous horizontal momentum flux, m_f, across a unit area of a vertical plane parallel to the wave crests is given by:

$$m_f(x,z,t) = p_d + \rho u^2 \tag{8}$$

where p_d is the instantaneous wave dynamic pressure at a specified position, ρ is the water density and u is the instantaneous horizontal water velocity at the same specified position. The integration of (8) over a uniform periodic wave results in the radiation stress, S_{xx}, introduced by Longuet-Higgins and Stewart (1964), who defined the radiation stress as the wave momentum flux integrated over the water depth and averaged over the wave:

$$S_{xx} = \frac{1}{L}\int_0^L \int_{-h}^{\eta(x)} (p_d + \rho u^2)\,\mathrm{d}z\mathrm{d}x \tag{9}$$

where L is the local wavelength, x is the horizontal coordinate positive in the direction of wave propagation, z is the vertical coordinate directed positive upward with origin at the SWL, h the water depth and $\eta(x)$ is the sea surface elevation at location x. The values of the depth-integrated wave momentum flux vary from large positive values in the wave crest

to large negative values in the trough. This means that the integrated value of S_{xx} is generally very small in comparison to its maximum flux values in the wave crest. For this reason, Hughes (2004b) suggested that a parameter representing the maximum depth-integrated wave momentum flux that occurs during passage of a wave, $M_F(x,t)$, would have better correlations with force loading on coastal structures than a parameter representing the integration over the entire wavelength. This parameter can be expressed as:

$$M_F(x,t) = \int_{-h}^{\eta(x)} (p_d + \rho u^2)\, dz \tag{10}$$

Hughes (2004b) derived empirical formulae to estimate dimensionless parameters of $M_F(x,t)$ for periodic and solitary waves. The derivation of the dimensionless M_F for non-linear periodic waves is described below.

2.4.1 Wave momentum flux parameter for non-linear periodic waves

For non-linear waves, Hughes (2004b) used Fourier approximation wave theory for regular steady waves over a horizontal bottom to derive an empirical equation to estimate a dimensionless M_F. This equation is expressed as a function of relative wave height (H/h) and relative depth (h/gT^2) and is given by:

$$\left(\frac{M_F}{\rho g h^2}\right) = A_0 \left(\frac{h}{gT^2}\right)^{-A_1} \tag{11}$$

where $\left(\frac{M_F}{\rho g h^2}\right)$ is the dimensionless M_F that for simplicity Hughes referred to as the "*wave momentum flux parameter*" and A_0 and A_1 are empirical coefficients expressed as:

$$A_0 = 0.64 \left(\frac{H}{h}\right)^{2.03} \tag{12}$$

$$A_1 = 0.18 \left(\frac{H}{h}\right)^{0.39} \tag{13}$$

2.4.2 Wave run-up as function of the wave momentum flux parameter

Archetti and Brocchini (2002) showed a strong correlation between depth-integrated mass flux and wave run-up. Following their observations, Hughes (2004a) derived a general run-up equation based on an assumption of a simplified geometry of the wave at the instant of maximum run-up on an impermeable slope (Figure 9):

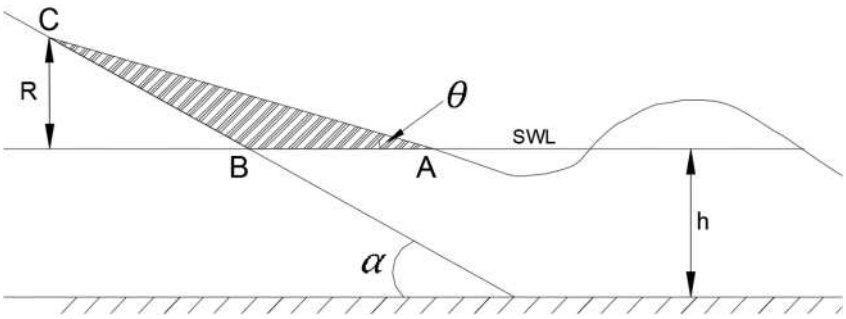

Figure 9 Maximum wave run-up on a smooth-impermeable plane slope (adapted from Hughes 2004 S. Hughes (2004a))

At the instance of maximum run-up, the water has almost no motion, so the weight of the water contained in the hatched triangular wedge ABC, $W_{(ABC)}$, (shown in Figure 9) can be given by:

$$W_{(ABC)} = \frac{\rho g}{2}\frac{R^2}{\tan\alpha}\left(\frac{\tan\alpha}{\tan\theta} - 1\right) \tag{14}$$

where R is the vertical run-up, α is the slope angle of the structure, and θ is an unknown angle between the still water level and the run-up water surface. As the water contained in the triangular wedge ABC, was pushed up the slope by the force of the incident wave, Hughes (2004a) suggested that at this instance, $W_{(ABC)}$ is proportional to the M_F of the wave before reaching the toe of the slope:

$$K_p(M_F)_{max} = K_M W_{(ABC)} \tag{15}$$

where K_p is a reduction factor to account for slope porosity (for impermeable slopes K_p=1) and K_M is a constant of proportionality. By replacing (14) in (15), rearranging, and dividing both sides by h^2, he derived the following formula for relative run-up, R/h:

$$\frac{R}{h} = \left(\frac{2K_p\tan\alpha}{K_M\left(\frac{\tan\alpha}{\tan\theta} - 1\right)}\right)^{1/2}\left(\frac{M_F}{\rho g h^2}\right)^{1/2} \tag{16}$$

which in a simplified form can be expressed as:

$$\frac{R}{h} = CF(\alpha)\left(\frac{M_F}{\rho g h^2}\right)^{1/2} \tag{17}$$

where C is an unknown constant and $F(\alpha)$ is a function of slope angle to be determined empirically. Hughes (2004a) fitted (17) to existing laboratory test measurements from regular, irregular and solitary waves and derived run-up formulae for breaking and non-breaking waves. These are discussed in more detail in Chapter 3. His results showed that

this new dimensionless parameter provided better descriptions of non-breaking and non-linear wave processes than existing wave parameters such as H/L_o and ξ.

3 Literature Review

This chapter discusses previous studies on wave run-up and on the main parameters that influence it. It also covers previous research on the influence of hydraulic conductivity on the wave breaking processes, water table over-height and swash hydrodynamics. The chapter is divided in 7 sections, which are briefly described below:

Sections 3.1, 3.2 and 3.3 review relevant studies investigating wave run-up and parameters that influence it. Section 3.1 reviews previous formulae attempting to predict wave run-up from breaking and non-breaking waves on smooth-impermeable plane slopes from normal incident waves. In that idealised scenario, the main parameters that influence wave run-up are the wave parameters (wave height and wave length) and the slope angle. However, studies have shown that parameters such as the slope's hydraulic conductivity, roughness, wave approach angle, shallow water and front berms can influence the magnitude of wave run-up. Relevant studies that have investigated the influence of these parameters are reviewed in Sections 3.2 and 3.3. As this project is mainly concerned with the influence of hydraulic conductivity on run-up, special emphasis is made on studies that have investigated its influence in Section 3.2, while Section 3.3 reviews studies that have investigated other key parameters influencing run-up.

Section 3.4 reviews studies investigating the influence of the hydraulic conductivity of the slope on the wave breaking processes, in particular on the breaker type and breaking point location. This section also discusses the most common breaking criteria used to differentiate between waves that will break upon a structure or beach and which will not. This differentiation is necessary when attempting to predict wave run-up from breaking and non-breaking waves.

Section 3.5 discusses previous attempts to predict the maximum water table over-height inside a coastal barrier. Here, the relationship between wave run-up and the water table over-height is discussed, as well as the influence that hydraulic conductivity has on this parameter.

Section 3.6 reviews previous works which have investigated the swash hydrodynamics by measuring flow velocities and flow depths in the swash zone. Special attention is made on the studies that have investigated the influence of hydraulic conductivity have on the swash zone boundary layer dynamics.

Finally, after identifying a number of key research gaps each of these sections, Section 3.7 presents the specific aims and objectives of the present study intended to fill these gaps.

3.1 Wave Run-up on Smooth-Impermeable Plane Slopes

In an idealised scenario with normally incident waves breaking on a smooth, impermeable and plane slope, the main parameters that influence wave run-up height are the incident wave parameters (wave height and wave length) and the slope angle. These parameters are often combined to form dimensionless parameters that are included in theoretical and empirical design formulae attempting to predict wave run-up. This section reviews previous formulae designed to predict run-up from breaking and non-breaking waves on smooth-impermeable plane slopes, from both regular and irregular wave trains.

3.1.1 Regular Waves

Several parametric formulae have been proposed attempting to predict the wave run-up on smooth-impermeable slopes from regular waves. These formulae have been used as the main method to predict wave run-up since the 1940s, and hence have been used for designing coastal structures. Although some theoretical attempts have been made to derive a run-up formula, most of these have been based on data from laboratory experiments. A summary of the most relevant formulae to estimate run-up of regular waves is shown in Table 6, giving the formula along with the type of wave breaking they are aimed to predict wave run-up from.

One of the first attempts to derive a theoretical run-up formula was shown by Miche (1944) and was aimed to predict wave run-up from non-breaking waves. Miche's equation was based on the linear Lagrangian equation of motion for shallow water and was given as:

$$\frac{R}{H} = \sqrt{\pi/2\alpha} \tag{18}$$

where R is the maximum run-up height above SWL; H is the wave height; and α is the slope angle. Equation (18) was later modified by Takada (1970) based on experimental data, where a shoaling coefficient, $K_{s,}$ was introduced (Table 6).

Other studies have attempted to derive theoretical expressions to predict run-up (e.g. Pocklington, 1921; Isaacson, 1950; Rundgren, 1958; Méhauté et al., 1968; Keller and Keller, 1964). However, due to the complex hydrodynamics in the swash zone and their incomplete understanding, most researchers have fitted empirical expressions for run-up levels to the results of experimental tests, instead of attempting to derive theoretical expressions to predict the run-up (Allsop et al. , 1985).

In 1959, Hunt proposed practical formulae based on previous laboratory experiments for smooth and rough plane and composite slopes. He proposed two different formulae for

breaking and non-breaking waves. For non-breaking (surging) waves on plane, impermeable slopes he suggested that:

$$\frac{R}{H} = 3 \tag{19}$$

where H is the wave height. For breaking waves, he suggested that the non-dimensional run-up R/H was proportional to the Iribarren number, ξ. This equation is commonly known as Hunt's formula:

$$\frac{R}{H} = \xi \tag{20}$$

Authors	Formulae	Breaking type
Miche (1944)	$\frac{R}{H_0} = \sqrt{\pi/2\alpha}$	non-breaking
Hunt (1959)	$\frac{R}{H} = 3$	non-breaking
	$\frac{R}{H} = \xi$	breaking
Takada (1970)	$\frac{R}{H} = \left(\sqrt{\frac{\pi}{2\alpha}} + \frac{h_0}{H}\right) K_s$, for $\frac{H}{L_0} \leq \sqrt{\frac{\pi}{2\alpha}\frac{\sin\alpha^2}{\pi}}$ $\frac{R}{H} = \left(\sqrt{\frac{\pi}{2\alpha}} + \frac{h_0}{H}\right) K_s \left(\frac{\cos\alpha_c}{\cos\alpha}\right)^{2/3}$, for $\frac{H}{L_0} > \sqrt{\frac{\pi}{2\alpha}\frac{\sin\alpha^2}{\pi}}$	non-breaking $\tan\alpha \leq 1/8$
Chue (1980)	$\frac{R}{H} = 1.8\left(1 - 3.11\frac{H}{L_o}\right)\xi\left(1 - exp\left(-\frac{\pi}{2\alpha}\right)^{1/2}\frac{1}{\xi}\right)$	breaking and non-breaking
Losada and Giménez-Curto (1980)	$\frac{R}{H} = \xi$, for $0 < \xi < 2.5$ $\frac{R}{H} = 2.5 - \frac{(2.5-\xi)}{3}$, for $2.5 < \xi < 4$ $\frac{R}{H} = 2$, for $4 < \xi$	breaking breaking non-breaking
Ahrens and Titus (1985)	$\frac{R}{H} = C_0\left(\frac{\pi}{2\alpha}\right)^{C_1} \exp\left(C_2\left(\frac{\eta}{H} - 0.5\right)^2\right)$	non-breaking
Schüttrumpf (2001)	$\frac{R}{H} = 2.25 * \tanh(0.5 * \xi)$	breaking and non-breaking
Hughes (2004a)	$\frac{R}{h} = 3.84\tan\alpha\left(\frac{M_F}{\rho g h^2}\right)^{1/2}$	breaking and non-breaking
Hsu et al. (2012)	$\frac{R}{H} = \xi$, for $\xi \leq 2$ and $\tan\alpha \leq 1/5$ $\frac{R}{H} = 2\left(\frac{\xi}{2}\right)^{0.04/tan^2\alpha}$, for $\xi > 2$ and $\tan\alpha > 1/5$	breaking and non-breaking

Table 6 Formulae predicting wave run-up from regular waves on smooth-impermeable slopes.

Several authors have confirmed the utility of (20) to predict regular wave run-up for mild slopes that produce low ξ values, indicating plunging or spilling waves breaking at the slope (e.g. Losada and Giménez-Curto, 1980; Hughes, 2004a; Hsu et al., 2012). This formula has also been shown to work well for many natural sand beaches, which are relatively smooth and generally have values of $\xi < 2.5$.

However, as slopes get steeper and ξ > 2 (region where the transition from breaking to non-breaking waves started to occur), several authors have noticed that Hunt's formula (20) does not predict accurately the run-up and scatter is increased (e.g. Gunbak, 1979; Sawaragi et al. , 1982; Losada and Giménez-Curto, 1980).

In an attempt to predict run-up for breaking and non-breaking waves, Schüttrumpf (2001) proposed the following hyperbolic formula, which describes a smoother transition between both types of waves:

$$\frac{R}{H} = a * \tanh(b * \xi) \tag{21}$$

where a and b are empirical coefficients. He suggested values of a=2.25 and b=0.5. Losada and Giménez-Curto (1980) proposed three formulae to cover run-up on smooth-slopes over a wider range of ξ values, including steeper slopes with non-breaking waves.

$$\frac{R}{H} = \xi, \quad \text{for } 0 < \xi < 2.5 \tag{22}$$

$$\frac{R}{H} = 2.5 - \frac{(2.5 - \xi)}{3}, \quad \text{for } 2.5 < \xi < 4 \tag{23}$$

$$\frac{R}{H} = 2, \quad \text{for } 4 < \xi \tag{24}$$

Chue (1980) attempted to produce a single formula for breaking and non-breaking waves by unifying previous theoretical and experimental formulae:

$$\frac{R}{H} = 1.8\left(1 - 3.11\frac{H}{L_o}\right)\xi\left(1 - exp\left(-\frac{\pi}{2\alpha}\right)^{1/2}\frac{1}{\xi}\right) \tag{25}$$

where:

$$\xi = \frac{\tan\alpha}{\left(H/L_0\right)^{0.4}} \tag{26}$$

Chue (1980) proposed the exponent 0.4 to be used in (26) as it was "found to fit remarkably well", but no supporting reference or data were given. In (25), the relative run-up R/H decreases with increasing wave steepness, H/L_0. However, Ahrens and Titus (1985) showed that the predictions of (25) did not match the data presented by Savage (1958) and Le Méhauté et al. (1968).

Ahrens and Titus (1985) followed Chue's (1980) approach in combining theoretical and experimental formulae, and proposed the following expression for non-breaking waves (ξ > 3.5):

$$\frac{R}{H} = C_0 \left(\frac{\pi}{2\alpha}\right)^{C_1} \exp\left(C_2 \left(\frac{\eta}{H} - 0.5\right)^2\right) \quad (27)$$

where η is the elevation of the wave crest above still water level, and C_0, C_1 and C_2 are dimensionless coefficients. Ahrens and Titus (1985) calculated values for these coefficients for non-breaking waves and suggested that the crest elevation η may be calculated using stream function wave theory. However, this calculation process may be complex and time-consuming (Allsop et al., 1985).

A recent attempt to predict run-ups on steeper slopes, Hsu et al. (2012) conducted a series of laboratory experiments and numerical simulations with regular waves breaking over ten impermeable sloping structures. They concluded that (20) was only correctly applicable for $\xi < 2$ and tan $\alpha < 1/5$. Equation (20) suggests that if the angle of the slope increases, the wave run-up will increase. However, they observed that this premise was not valid in the case of steeper slopes. For values of $\xi > 2$ and tan $\alpha > 1/5$, they noticed that as the slope increases, the run-up decreased and proposed the following formula:

$$R/H = 2\left(\frac{\xi}{2}\right)^{0.04/tan^2\alpha} \quad (28)$$

Hsu et al. (2012) suggested that the influence of slope on wave run-up increases due to the increase in the backwash force from the fluid weight component $\rho g \sin\alpha$, where ρ is the density of the water and g the gravitational acceleration. This backwash force opposes the water rushing upwards, resulting in lower run-up heights. Although (28) matched well their simulated data, it did not predict accurately the datasets of Grantham (1953) with steep slopes.

Hughes (2004a) presented a new approach for predicting the run-up from non-breaking waves. He proposed a run-up formula which was not based on ξ. Instead, his formula was given in terms of the wave momentum flux parameter ($M_F/\rho g h^2$), described in the previous chapter. As mentioned previously, this parameter represents the maximum depth-integrated wave momentum flux before reaching a slope. Hughes (2004a) re-examined the run-up data presented in Grantham (1953) and Saville (1955) from regular waves over smooth-impermeable slopes and derived the following equation:

$$\frac{R}{h} = 3.84 \tan\alpha \left(\frac{M_F}{\rho g h^2}\right)^{1/2} \quad (29)$$

However, this formula also did not predict accurately the run-up on the steeper slopes ($30^\circ \leq \alpha$) measured in Grantham's experiments, where surging breakers or non-breaking waves were present. Hughes (2004a) suggested that this was because these non-breaking waves did not conform to the straight line in the triangular wedge assumed in deriving

(29). However, the inaccurate prediction of (29) for the steeper slopes might also be explained by the importance of the slope of the structure on wave run-up in the case of the steeper slopes observed by Hsu et al. (2012). In (29), the relative run-up R/h is a function of the slope, $\tan\alpha$, meaning that if the slope of the structure increases, the run-up will also increase, which is counter to the observations of Hsu et al. (2012).

3.1.2 Irregular Waves

Two main methods have been used to derive run-up formulae for irregular waves (Allsop et al. 1985). The first method is based on the theory of equivalence, which means considering irregular wave run-up as the result of many, independent, regular waves. In this method, a typical run-up level for irregular waves, for example the significant run-up, R_s, is determined using a run-up formula for regular waves, and other run-up levels such as the $R_{u2\%}$ are then estimated using a Rayleigh distribution of run-up levels. The $R_{u2\%}$ parameter is defined as the vertical run-up elevation exceeded by 2% of the incoming waves at the toe of the structure. $R_{u2\%}$ is said to be a representative parameter of the wave run-up distribution of irregular wave trains and has been commonly used in existing formulae proposed to predict wave run-up.

However, formulae following this method might not be entirely realistic due to the character of natural sea states. The random nature of the incoming waves causes each wave to have a different run-up level. Unlike the case of regular waves that result in a single value of maximum wave run-up, irregular waves produce a run-up distribution. For this reason, a second method has been used to derive run-up formulae for irregular waves. This method is based on the measurements and description of the probability distribution of wave run-up under irregular or random wave conditions. This approach consists of fitting standard probability distributions to measured random wave run-up results.

A summary of some of the most relevant formulae for predicting wave run-up from irregular waves and the types of wave breaking they are aimed at is shown in Table 7.

One of the first formulae attempting to estimate irregular wave run-up was proposed by Wassing (1957), which was valid for milder slopes ($\tan\alpha \leq 1/3$), and was given by:

$$R_{u2\%} = 8H_{1/3}\tan\alpha \tag{30}$$

where $H_{1/3}$ is the significant wave height (average of the highest 1/3 waves) at the toe of the structure slope.

Battjes (1974) showed the applicability of (20) for irregular waves breaking as plungers, and included reduction factors to account for various rough slopes such as rock and concrete armour. After this, most formulae proposed to predict wave run-up from

irregular waves have also been based on the Iribarren number ξ (e.g. Ahrens, 1981; Mase, 1989; Van der Meer, 1992; Burcharth and Hughes, 2002; EurOtop, 2007).

Authors	Formulae	Breaking Type
Wassing (1957)	$R_{u2\%} = 8H_{1/3}\tan\alpha$	breaking
Ahrens (1981)	$\frac{R_{u2\%}}{H_{mo}} = 1.6\xi_{op}$	breaking
	$\frac{R_x}{H_{mo}} = C_1 + C_2\left(H_{mo}/gT_p{}^2\right) + C_3\left(H_{mo}/gT_p{}^2\right)^2$	non-breaking
Mase (1989)	$\frac{R_{u2\%}}{H_{mo}} = 1.86\xi_{op}{}^{0.71}$	breaking
Van der Meer (1992)	$\frac{R_{u2\%}}{H_s} = 1.5\gamma\xi_p$, with a maximum of 3.0	breaking and non-breaking
Burcharth and Hughes (2002) Coastal Engineering Manual	$\frac{R_{u2\%}}{H_{mo}} = 1.6\xi_{op}$	breaking
	$\frac{R_{u2\%}}{H_{mo}} = 4.5 - 0.2\xi_{op}$	non-breaking
Hughes (2004a)	$\frac{R_{u2\%}}{h} = 4.4\,(\tan\alpha)^{0.7}\left(\frac{M_F}{\rho g h^2}\right)^{1/2}$ any value of H_{mo}/L_p, and $1/30 \le \tan\alpha \le 1/5$	breaking
	$\frac{R_{u2\%}}{h} = 4.4\,(\tan\alpha)^{0.7}\left(\frac{M_F}{\rho g h^2}\right)^{1/2}$ $H_{mo}/L_p > 0.0225$, and $1/5 \le \tan\alpha \le 2/3$	breaking
	$\frac{R_{u2\%}}{h} = 1.75\left(1 - e^{-(1.3\cot\alpha)}\right)\left(\frac{M_F}{\rho g h^2}\right)^{1/2}$ $H_{mo}/L_p < 0.0225$, and $1/4 \le \tan\alpha \le 1/1$	non-breaking
EurOtop (2007)	$\frac{R_{u2\%}}{H_{mo}} = 1.65\xi_{m-1,0}$	breaking
	$\frac{R_{u2\%}}{H_{mo}} = 4.0 - \frac{1.5}{\sqrt{\xi_{m-1,0}}}$	non-breaking

Table 7 Formulae predicting wave run-up from irregular waves on smooth-impermeable slopes

Ahrens (1981) analysed previous studies which had reported measurements of irregular wave run-up on smooth-impermeable slopes with slope angles ranging from $\tan\alpha = 1/4$ to $\tan\alpha = 1/1$. For breaking waves on a slope of $\tan\alpha = 1/4$ he suggested that the elevation exceeded by 2% of the run-ups could be estimated by a slightly modified Hunt formula:

$$\frac{R_{u2\%}}{H_{mo}} = 1.6\xi_{op} \tag{31}$$

where

$$\xi_{op} = \frac{\tan\alpha}{\sqrt{H_{mo}/L_{op}}} \tag{32}$$

where H_{mo} is the energy-based zeroth-moment wave height and L_{op} is the deepwater wavelength, which is calculated with the peak spectral wave period T_p. This formula was valid for $\xi_{op} \leq 2.5$. This same equation was also adopted by Burcharth and Hughes (2002) in the Coastal Engineering Manual (CEM) to be used for breaking waves. For steeper slopes and non-breaking waves, Ahrens (1981) proposed to use the following formula:

$$\frac{R_x}{H_{mo}} = C_1 + C_2\left(H_{mo}/gT_p{}^2\right) + C_3\left(H_{mo}/gT_p{}^2\right)^2 \tag{33}$$

where C_1, C_2 and C_3 are empirical coefficients, and R_x represents either R_s, $R_{u2\%}$, or $\bar{R}$, R_s being the significant run-up, $R_{u2\%}$ the run-up level exceeded by 2% of the run-up values in the distribution, and $\bar{R}$ the mean run-up level.

Using the same data analysed by Ahrens (1981), Burcharth and Hughes (2002) proposed an equation for non-breaking waves with Iribarren numbers varying between $2.5 \leq \xi_{op} \leq 9$ which was given by:

$$\frac{R_{u2\%}}{H_{mo}} = 4.5 - 0.2\xi_{op} \tag{34}$$

In 1989, Mase published run-up data obtained from laboratory experiments performed on mild slopes ranging between 2° and 11.4°, and proposed the following expression to estimate run-up from breaking waves:

$$\frac{R_{u2\%}}{H_{mo}} = a\xi_{op}{}^b \tag{35}$$

where a and b are empirical coefficients. He proposed values of a = 1.86 and b = 0.71 to best-fit the $R_{u2\%}/H_{mo}$ of his presented data. The formulae showed good fit to his data, except for the steepest slopes with larger Iribarren numbers.

Van der Meer (1992) proposed the following general run-up formula for smooth slopes:

$$\frac{R_{u2\%}}{H_s} = 1.5\gamma\xi_p, \text{ with a maximum of 3.0} \tag{36}$$

where H_s is the significant wave height, ξ_p is the Iribarren number based on the peak period, and γ is a total reduction factor for various influences such as berms, roughness, shallow water, and oblique wave attack. These reduction factors are shown in de Waal and van der Meer (2012) and are described in Section 3.3.

The EurOtop (2007) manual recommended two formulae for breaking and non-breaking waves based on a large international dataset; these are also based on ξ. For breaking waves:

$$\frac{R_{u2\%}}{H_{mo}} = 1.65 \cdot \gamma_b \cdot \gamma_f \cdot \gamma_\beta \cdot \xi_{m-1,0} \tag{37}$$

While for non-breaking waves:

$$\frac{R_{u2\%}}{H_{mo}} = \gamma_f \cdot \gamma_\beta \left(4.0 - \frac{1.5}{\sqrt{\xi_{m-1,0}}}\right) \tag{38}$$

where,

$$\xi_{m-1,0} = \frac{\tan\alpha}{\sqrt{H_{mo}/L_o}} \tag{39}$$

where: $\gamma_b$is the influence factor for a berm, $\gamma_f$is the influence factor for roughness elements on the slope, γ_β is the influence factor for oblique wave attack, and L_o is the is the wavelength calculated with the spectral wave period $T_{m-1,0}$. Logically, in the case of a smooth-impermeable slope, these influence factors take a value of 1. This formula is valid for $0.5 < \xi_{m-1,0} < 8$ to 10. The influence of these factors is discussed in Section 3.3.

Hughes (2004a) proposed empirical equations to estimate irregular waves based on the momentum flux parameter. He used Ahrens (1981) and Mase (1989) data to derive his formulae and observed that Ahrens' data exhibited two distinct trends corresponding to non-breaking waves with $H_{mo}/L_p < 0.0225$, and for breaking waves with $H_{mo}/L_p > 0.0225$. Following these observations, he proposed the following empirical equations:

For non-breaking waves with $H_{mo}/L_p < 0.0225$, and $1/4 \leq \tan\alpha \leq 1/1$:

$$\frac{R}{h} = 1.75\left(1 - e^{-(1.3\cot\alpha)}\right)\left(\frac{M_F}{\rho g h^2}\right)^{1/2} \tag{40}$$

For breaking waves with $H_{mo}/L_p > 0.0225$, and $1/5 \leq \tan\alpha \leq 2/3$:

$$\frac{R}{h} = 4.4\,(\tan\alpha)^{0.7}\left(\frac{M_F}{\rho g h^2}\right)^{1/2} \tag{41}$$

For breaking waves with any value of H_{mo}/L_p, and $1/30 \leq \tan\alpha \leq 1/5$:

$$\frac{R}{h} = 4.4\,(\tan\alpha)^{0.7}\left(\frac{M_F}{\rho g h^2}\right)^{1/2} \tag{42}$$

These formulae had a better agreement with most of Ahrens's data than (31) and (34) recommended by Burcharth and Hughes (2002) in the Coastal Engineering Manual, which were derived using the same data set. However, Ahrens' data on steep slopes with $30° \leq \alpha$ and $H_{mo}/L_p > 0.0225$ were not accurately predicted by any of these formulae, and no new formula was proposed to describe the run-up for these tests.

3.1.3 Summary and Conclusions

From the previous literature review of wave run-up on smooth-impermeable slopes, the following major conclusions can be drawn:

- Most studies have fitted empirical expressions to run-up data from laboratory experiments, rather than deriving theoretical formulae to predict the run-up.
- For breaking waves, the run-up has been shown to be accurately predicted using the Iribarren number ξ.
- For non-breaking waves, formulae based on the wave momentum flux parameter $(M_F/\rho g h^2)$ have shown better predictions than those based on ξ. Yet, still no formulae predict accurately run-up from non-breaking waves in steep slopes.

The following two sections discuss previous studies that have investigated the effects of parameters such as hydraulic conductivity, roughness, wave approach angle, shallow water and front berms have on wave run-up, and their attempts to include them in predictive wave run-up formulae. The influence of these parameters has been commonly included in run-up formulae as reduction factors. Additionally, the water table elevation inside permeable beaches is also expected to influence the wave run-up height. However, the influences of this parameter on wave run-up has not been investigated so is also discussed below.

3.2 Influence of Hydraulic Conductivity on Wave Run-up

As coastal structures are generally steeper, rougher and more permeable than beaches, most run-up studies on permeable slopes have been carried out on coastal structures. For this reason, most run-up prediction formulae for permeable slopes have been designed for such structures, rather than for beaches. Van der Meer (1992) showed that the most significant parameters influencing run-up on permeable structures are the hydraulic conductivity of the structure and ξ (wave height, wave period and slope angle). So is it essential to include the influence of hydraulic conductivity on wave run-up formulae for its accurate prediction. However, including its influence on a prediction run-up formula has been proven to be challenging and different methods have been proposed. As it is difficult to have any degree of hydraulic conductivity in a structure or beach without some roughness, the reduction in wave run-up on a permeable slope is almost always attributed to both the roughness and the hydraulic conductivity of the slope. Therefore, the formulae predicting wave run-up on permeable slopes include both the influence of roughness and hydraulic conductivity.

The influence of the surface roughness on wave run-up has traditionally been taken into account by the inclusion of reduction factors in prediction formulae for smooth-impermeable slopes. In terms of predicting the wave run-up on permeable slopes, two main methods have commonly been used.

The first method follows the same approach used with the rough-impermeable slopes. It consists of including a reduction factor in the prediction formula for smooth-impermeable slopes. In this case, this reduction factor includes the total effect of both the hydraulic conductivity and the roughness of the slope. The second method uses prediction curves or formulae with empirical coefficients which are fitted to laboratory data for a particular type of permeable structure.

This section reviews the most relevant laboratory experiments carried out on permeable slopes for regular and irregular waves, as well as the predictive methods and formulae proposed to estimate their run-up.

3.2.1 Regular Waves on Permeable Slopes

Early experiments of wave run-up from regular waves on permeable armoured rubble slopes were reported by Saville (1955), Hudson (1958) and Savage (1958). However, one of the first attempts to predict run-up using the method of reduction factors to include the influence of the hydraulic conductivity of a structure was shown by Hunt (1959). He suggested that the reduction caused by the roughness and the hydraulic conductivity of the structure could be combined into a single reduction factor. This factor was added into a general formula for predicting wave run-up on a porous, rough continuous slope. Hunt (1959) suggested several values for these reduction factor based on data given by the Beach Erosion Board (1954) on permeable and impermeable slopes.

Other publications such as the Shore Protection Manual (1984), Technical Advisory Committee on Protection against Inundation (1974), Stoa (1978) and Ahrens (1981) have also recommended the use of reduction factors to account for the influence of both the hydraulic conductivity and the roughness of the structure.

However, several studies have shown that the behaviour of waves on permeable slopes is very different from those on impermeable slopes (e.g. Losada and Gimenez-Curto, 1980; Allsop et al., 1985; Van der Meer, 1992). Therefore, it is likely that the run-up magnitude on a permeable slope will not be well predicted by simply including a reduction factor to a smooth slope equation. For this reason, most studies have used the method of fitting curves or formulae to laboratory data.

The Shore Protection Manual (1984) provides a series of prediction curves for rough-impermeable slopes, and for rough-permeable slopes (including riprap, rock and dolos armoured breakwaters). These curves are based on the experiments performed by Saville (1955) and Hudson (1958) on roughened permeable slopes.

Gunbak (1979) proposed prediction formulae for breaking waves based on measurements on both smooth and rough porous slopes. For the rough permeable slopes he proposed:

$$\frac{R}{H} = \frac{a\xi}{\xi + b} \tag{43}$$

where a and b are empirical coefficients.

Losada and Gimenez-Curto (1980) developed an exponential model to predict wave run-up for breaking waves on rough-permeable slopes under regular waves and proposed the following expression:

$$\frac{R}{H} = a(1 - \exp(b)) \tag{44}$$

where A and B are empirical coefficients. Losada and Gimenez-Curto (1981) fitted (44) to previous experiment results carried out on structures with different armour types and different values for A and B were presented. They also observed that the run-up on smooth, impermeable slopes did not followed the trend described by (44) and concluded that it is not correct to apply a reduction factor depending on the type of armour. Although a good fit was shown by Losada and Gimenez-Curto (1980) between their predictions and the experimental data used, Allsop et al. (1985) suggested that the values proposed by Losada and Gimenez-Curto (1980) should be used with caution as their run-up measurements were made by a variety of different researchers and are quoted at second or third hand.

3.2.2 **Irregular Waves on Permeable Slopes**

A summary of the most relevant formulae proposed for different types of rough permeable slopes under irregular waves is shown in Table 8. These are discussed below.

Before 1985, as far as the author knows, there were no data available on wave run-up from irregular waves over rough-permeable slopes. Previous prediction methods were based either upon the results of regular wave tests on permeable slopes, or upon results on smooth-impermeable slopes with irregular waves. Ahrens (1981) suggested that the run-up on rough-permeable slopes from irregular waves could be predicted by applying the same roughness coefficients presented in the Shore Protection Manual (1984) and by

Stoa (1979) for regular waves to his prediction formula (33) for smooth-impermeable slopes from irregular waves.

Authors	Formulae	Slope type	Breaking type
Allsop et al. (1985)	$\frac{R}{H} = \frac{a\xi}{\xi + b}$	Rock armoured	breaking
	$\frac{R}{H} = a(1 - \exp(b\xi))$	Tetrapod quadripod dolos rip-rap	breaking
Ahrens and Heimbaugh (1988b)	$\frac{R}{H_{mo}} = \frac{a\xi}{1 + b\xi}$	Rip-rap revetments	breaking
Van der Meer (1992)	$\frac{R_{2\%}}{H_s} = 0.96\xi_m$, for $1.0 < \xi_m \leq 1.5$ $\frac{R_{2\%}}{H_s} = 0.96\xi_m$, for $1.0 < \xi_m \leq 1.5$ $\frac{R_{2\%}}{H_s} = 1.97$, for $3.1 < \xi_m \leq 7.5$	Rock armoured with permeable cores	Breaking Breaking Non-breaking
EurOtop (2007)	$\frac{R_{2\%}}{H_{mo}} = 1.65\gamma_b\gamma_f\gamma_\beta\xi_{m-1,0}$ with a maximum of: $\frac{R_{2\%}}{H_{mo}} = 1.0\gamma_p\gamma_{f\ surging}\gamma_\beta \cdot \left(4.0 - \frac{1.5}{\sqrt{\xi_{m-1,0}}}\right)$	Rock armoured with permeable cores	Breaking Non-breaking
Muttray et al. (2006)	$\frac{R}{H_i} = a(1 + C_r)$	Rubble mound	breaking
Calabrese et al. (2010)	$\frac{R_{2\%}}{h} = 1.804 \cdot {M_F}^{0.79}$	Rubble mound	breaking
Schimmels et al. (2012)	$\frac{R_{2\%}}{H_{mo}} = \gamma_p(1.65 \cdot \xi_{m-1,0})$ for $\xi_{m-1,0} \leq 2.7$ $\frac{R_{2\%}}{H_{mo}} = A \cdot \gamma_p\left(4.0 - \frac{1.5}{\sqrt{\xi_{m-1,0}}}\right)$ for $\xi_{m-1,0} > 2.7$	PBA revetment	Breaking Non-breaking

Table 8 Wave run-up formulae for permeable slopes from irregular waves

Allsop et al. (1985) presented probably the first run-up experiments on permeable slopes (armoured slopes) under irregular waves. Their tests were carried out on steep smooth slopes and on different types of armoured slopes such as: tetrapods, antifer cubes, stabits, diodes and SHEDs. Several interesting and useful observations were reported in this study. In their tests, both JONSWAP and Moskowitz spectral shapes were used and no significant differences between run-up values were observed. They showed that (43) proposed by Gunbak (1979) described well the run-up on rock armoured slopes, while (44) proposed by Losada and Gimenez-Curto (1981) predicted accurately their run-up measurements for tetrapod, quadripod, dolos and rip-rap armoured slopes. Several values for the coefficients *A* and *B* were estimated for both equations for the different types of permeable armoured slopes tested.

It was also noted that no single probability density function provided a good description for all cases tested. However, as most run-up formulae under irregular waves have been commonly expressed using $R_{u2\%,}$ they suggested that for design purposes, the most practical procedure was to estimate the significant run-up level, R_s, and then to estimate the extreme levels such as $R_{u2\%}$ using a Rayleigh distribution.

Although limited comparisons were shown, Allsop et al. (1985) observed that there was a good agreement between their measurements of significant run-up heights, $R_{s,}$ from irregular waves and the run-up heights R from regular waves analysed previously. These observations suggest that the results and prediction formulae from regular wave tests could be used to estimate significant run-up heights from irregular waves.

Allsop et al. (1985) concluded there was a need for significantly more run-up data to allow the derivation of more reliable empirical expressions to predict run-up on permeable slopes. So they recommended that model tests on a number of different armoured rubble slopes (with different hydraulic conductivity) and on smooth-impermeable slopes should be performed to measure wave run-up under a number of incident wave conditions.

Ahrens and Heimbaugh (1988a) reported the results of two laboratory studies conducted on rip-rap revetments. Later that year, Ahrens and Heimbaugh (1988b) proposed the following equation derived from the results from those two laboratory experiments:

$$\frac{R}{H_{mo}} = \frac{a\xi}{1 + b\xi} \tag{45}$$

where H_{mo} is the energy-based, zero-moment wave height, and a and b are empirical coefficients. Equation (45) was later used by Melito and Melby (2002) who carried out experiments on a breakwater with a CORE-LOC armour layer and proposed values for the coefficients a and b.

Kobayashi et al. (1990) analysed the hydraulic conductivity effects on irregular wave run-up by carrying out six tests on permeable and impermeable slopes. They observed that the reduction of wave run-up caused by the hydraulic conductivity effects was more pronounced for larger values of ξ. Their results showed similar trends to the predictions from (44) proposed by Losada and Gimenez-Curto (1980), while the predictions from (43) proposed by Gunbak (1979) lay between the results of the permeable and impermeable slopes.

Van der Meer (1988) presented an extensive series of model tests aimed primarily at assessing the stability of rock slopes under wave attack. During these tests, the run-up was also measured using a capacitance wire stretched along the slope. Three different structures were tested: 1) a structure with an armour layer over an impermeable core; 2)

a structure with an armour layer over a permeable core; and 3) a structure made of homogeneous permeable armour. He presented stability formulae for each of the different structures which included a power coefficient *P* on the Iribarren number ξ. For each of the three structures a different value of *P* was fitted: *P*=0.1 for the impermeable core structure, *P*=0.5 for the permeable core structure, and *P*=0.6 for the homogeneous structure.

The coefficient *P* is commonly known as the "notional permeability coefficients". However, this coefficient no physical meaning and does not describe the actual permeability or hydraulic conductivity of the structure. Instead it represent the specific configuration of the breakwaters

Van der Meer (1988) only used the notional permeability coefficient in stability formulae and was not included in any of his proposed run-up formulae based on the same set of experiments. Van der Meer and Stam (1992) suggested three formulae to estimate run-up on permeable structures with permeable cores depending on their ξ value. The formulae were derived using regression methods based on Van der Meer's (1988) tests.

$$\frac{R_{2\%}}{H_s} = 0.96\xi_m, \quad \text{for } 1.0 < \xi_m \leq 1.5 \tag{46}$$

$$\frac{R_{2\%}}{H_s} = 1.17{\xi_m}^{0.46}, \quad \text{for } 1.5 < \xi_m \leq 3.1 \tag{47}$$

$$\frac{R_{2\%}}{H_s} = 1.97, \quad \text{for } 3.1 < \xi_m \leq 7.5 \tag{48}$$

where $\xi_m$is the Iribarren number based on the mean wave period.

Van der Meer and Stam (1992) observed that the core permeability of the structure only had influence on run-up in the high ξ values, where surging waves are present. For ξ > 3.1, it was seen that a maximum value of the normalised run-up *R/H* of 1.97 was reached in the structures with permeable cores, whereas in the structures with impermeable cores, *R/H* kept increasing. EurOtop (2007) gives a physical explanation for this: on a very steep structure (large ξ values) with an impermeable core, the non-breaking or surging waves run up and down the slope with water remaining in the armour layer, which leads to high run-up values. In this scenario, the surging wave does not "feel" the roughness and behaves as a wave on a very steep smooth slope. In contrast, for a permeable core, the water can penetrate into the core and this will decrease the actual run-up.

Kingston and Murphy (1996) reported run-up results from irregular wave tests at a small-scale based on a model of the Zeebrugge rubble mound breakwater located in Belgium. As done by Ahrens et al. (1985), they also used the expression (44) proposed by Losada and

Gimenez-Curto (1980) and estimated coefficient values of A and B for the rubble mound breakwater.

De Rouck et al. (2007) showed the results from full-scale wave run-up measurements carried out on the Zeebrugge rubble mound breakwater. They compared their results with the model tests carried out by Kingston and Murphy (1996) and showed that their full-scale measurements resulted in slightly higher run-up values. However, this difference was mainly attributed to the measuring technique using a traditional wire gauge. In small-scale experiments, Schimmels et al. (2012) and Van Broekhoven (2011) showed that the run-up measurements recorded from wave gauges give lower run-up values than those measured from video recordings. The advantages and disadvantages of using wire gauges instead of video cameras to measure run-up in small-scale experiments is discussed in more detail in Chapter 4.

De Rouck et al. (2007) also compared their results with the measurements and run-up predictions on riprap revetments reported by Van der Meer and Stam (1992) and by Ahrens and Heimbaugh (1988a, 1988b). Their measurements were shown to be in the same region as those from Van der Meer and Stam (1992), although Van der Meer and Stam's prediction formulae slightly overestimated their measurements. Their measurements also showed similar results to those of Ahrens and Heimbaugh (1988a, 1988b), although Ahrens' and Heimbaugh's prediction formula slightly underestimated their measurements.

EurOtop (2007) used the same data from Van der Meer's (1988) tests and suggests the following formulae to predict the run-up in rubble mound slopes:

$$\frac{R_{2\%}}{H_{mo}} = 1.65 \cdot \gamma_b \cdot \gamma_f \cdot \gamma_\beta \cdot \xi_{m-1,0} \quad \text{with a maximum of:} \tag{49}$$

$$\frac{R_{2\%}}{H_{mo}} = 1.00 \cdot \gamma_p \cdot \gamma_{f\ surging} \cdot \gamma_\beta \cdot \left(4.0 - \frac{1.5}{\sqrt{\xi_{m-1,0}}}\right) \tag{50}$$

where:

$$\gamma_{f\ surging} = \gamma_f + \left(\xi_{m-1,0} + 1.8\right) \cdot \frac{1 - \gamma_f}{8.2} \quad \text{for } 1.8 < \xi_{m-1,0} < 10 \tag{51}$$

$$\gamma_{f\ surging} = 1.0 \quad \text{for } \xi_{m-1,0} > 10 \tag{52}$$

where $\gamma_{f\ surging}$ is the roughness factor for surging waves, $\gamma_b$is the influence factor for a berm, $\gamma_f$is the influence factor for roughness elements on the slope, and γ_β is the influence factor for oblique wave attack and $\xi_{m-1,0}$ is the Iribarren number calculated from the spectral wave period. For rubble mound slopes with two layers of rock on an impermeable

slope, EurOtop (2007) suggests a roughness factor of $\gamma_f = 0.55$, while for two layers of rock on a permeable core a roughness factor of $\gamma_f = 0.40$ is suggested. These roughness factors are used for values of $\xi_{m-1,0} < 1.8$. The roughness factor then increases linearly up to 1 from values of $1.8 < \xi_{m-1,0} < 10$. For rubble mound permeable slope, a maximum value of $R_{2\%}/H_{mo} = 1.97$ is also suggested.

Muttray et al. (2006) proposed an empirical run-up formula for rubble mound breakwaters that includes the reflection coefficient from porous structures. This formula was based on large scale tests with regular and irregular waves carried out in the Large Wave flume (GWK) in Hanover, Germany and is given by:

$$\frac{R}{H_i} = a(1 + C_r) \tag{53}$$

where H_i is the incident wave height, a is an empirical coefficient, and C_r is the reflection coefficient (C_r=H_r/H_i), H_r being the reflected wave height.

In 2010, Calabrese et al. showed the results from a series of wave run-up experiments performed on rubble mound breakwaters with a 2:3 slope. They compared their measurements against the predictions from the formulae of Van der Meer and Stam (1992), Melito and Melby (2002) and the EurOtop (2007). None of the formulae gave accurate predictions. They suggested that ξ might not be the ideal parameter to be used to predict wave run-up on rubble mound breakwaters. So they analysed the data against the wave momentum flux parameter (Hughes, 2004b). The results showed a significant reduction of scatter compared to the case when ξ was adopted as the variable. A curve fitting was carried out and the following formulae was proposed using the wave momentum flux parameter:

$$\frac{R_{2\%}}{h} = 1.804 \cdot {M_F}^{0.79} \tag{54}$$

Van Broekhoven (2011) reported a series of small scale experiments aimed to investigate the influence of roughness and permeability in the reduction of wave run-up in an armour layer breakwater. Four different 1:2 slopes were investigated: a smooth-impermeable slope, a rough-impermeable slope, and a rough-permeable top (armour layer) on an impermeable core and permeable core. All the rough slopes were constructed with the same stone diameter and regular and irregular wave tests were carried out. Their results showed that the surface roughness had a small influence on the reduction of wave run-up. In contrast, the permeable armour layer showed a big influence on the reduction of wave run-up. This can be attributed to the dissipated energy due to the turbulence in the pores

of the armour layer. The influence of the permeability of the armour layer on the reduction of wave run-up was quantified by a linear fit.

The influence of the core's permeability on the run-up was also analysed by Van Broekhoven (2011) for $\xi < 5$. As most of the energy was dissipated in the top permeable armour layer, it was found that the infiltration of water into the core did not have a significant influence on the run-up height for small ξ values. These findings support Van der Meer's (1992) results; he observed that the core permeability of the structure only had an influence on run-up for high ξ values, where surging waves are present.

The large influence of a permeable armour layer (top layer) on the reduction of the run-up magnitude and the small influence of the core permeability was also shown by Oumeraci et al. (2010). They reported the results of large-scale laboratory experiments carried out at the Large Wave Flume in Hannover, Germany, where the wave run-up on different permeable revetments was measured. The tests were carried out over three different permeable revetments, all of which contained three layers: an armour layer, a filter layer and a sand core. The top layer consisted of a 15cm bonded armour (with a mean grain size of d_{50}=.04m). This armour was bonded with a highly porous polyurethane aggregate (PBA) called *Elastocoast* and was placed over an unbonded filter layer, which laid over a sand core (d_{50}=.34mm). The difference between the three set-ups was the thickness of the unbonded filter layer. Regular and irregular wave tests were performed and all the run-ups were measured by resistive wave gauges and video cameras. However, only the results of the wave gauges were shown. Although all the revetments had different filter layers, they all had the same permeable armour layer, so their results showed almost no difference between run-up heights on the three revetments. These findings also support Van der Meer's (1992) and Van Broekhoven's (2011) observations, by showing that the run-up in a permeable breakwater is mainly reduced by the top armour layer and not by the layers underneath, or by the core's permeability.

Oumeraci et al. (2010) used (37) and (38) recommended by the EurOtop (2007) for dikes and coastal structures and proposed different roughness factors by curve fitting through the data for the regular and irregular waves. These roughness factors included the effect of both, the permeability and the roughness of the armour layer.

As far as the author is aware, Schimmels et al. (2012) is the only study in which the authors attempted to include a coefficient in a run-up formula to account for the influence of the hydraulic conductivity. By re-analysing the run-up data from Oumeraci (2010), they presented modified versions of (37) and (38) recommended by EurOtop (2007). As described above, (37) and (38) consider the effect of berms, roughness and angle of wave attack by adding reduction factors, but these formulae do not consider the effect of

hydraulic conductivity or porosity. Therefore, Schimmels et al. (2012) proposed a new empirical reduction porosity coefficient, $\gamma_{p,}$ to be included in the EurOtop (2007) formulae. Additionally, a second parameter A, was also introduced to avoid modifying the empirical coefficients c_1, c_2 and c_3 previously recommended in EurOtop (2007). In their study, the revetments were considered to be relatively smooth and the slope had no berm, so all the reduction parameters in (37) and (38) were assigned with a value of 1. The modified EurOtop (2007) formulae were presented by Schimmels et al. (2012) as:

$$\frac{R_{2\%}}{H_{mo}} = \gamma_p(1.65 \cdot \xi_{m-1,0}) \quad \text{for } \xi_{m-1,0} \leq 2.7 \tag{55}$$

$$\frac{R_{2\%}}{H_{mo}} = A \cdot \gamma_p \left(4.0 - \frac{1.5}{\sqrt{\xi_{m-1,0}}}\right) \quad \text{for } \xi_{m-1,0} > 2.7 \tag{56}$$

where H_{mo} is the spectral wave height and $\xi_{m-1,0}$ is the Iribarren number calculated from the spectral period. Best fit regressions were carried out and values for γ_p and A were proposed for each revetment. The relative run-up $R_{2\%}/H_{mo}$was observed to be reduced by between 20% and 45% when compared to the run-up of the EurOtop (2007) formula for a smooth-impermeable slope. However, the porosity coefficient γ_p does not represent the actual porosity, permeability nor hydraulic conductivity of the slope as it is simply a coefficient which was estimated to fit their data.

3.2.3 **Summary and Conclusions**

Several key conclusions can be drawn from the studies reviewed in this section concerned with the influence of roughness and hydraulic conductivity on wave run-up:

- The influence of roughness on wave run-up formulae has been traditionally included as a reduction factor defined as the ratio between the run-up on a rough-impermeable slope and that on a smooth-impermeable slope (under identical conditions)
- Wave run-up on permeable slopes has generally been studied in laboratories and relates to the design of coastal structures
- Factors such as roughness and hydraulic conductivity are generally considered in wave run-up formulae for natural beaches (mainly sand beaches)
- Two methods have been commonly used to predict run-up on permeable slopes: 1) by adding a reduction roughness factor; and 2) by fitting prediction curves or formulae with empirical coefficients to laboratory data for a particular type of structure

- Studies have shown that run-up on permeable slopes follows different trends to those on impermeable slopes, so reduction factors are not appropriate. Instead formulae should be fitted to specific run-up data observed on permeable slopes
- Allsop et al., 1985 showed similar results for significant run-up heights from irregular waves R_s and run-up heights R from regular tests. These observations suggest that regular run-up tests could be used to estimate the run-ups from irregular waves
- Several formulae have been proposed for permeable slopes, all of which include empirical coefficients chosen to fit and describe the run-up of specific types of permeable structures
- The armour layer (top layer) in a breakwater was shown to have a significant effect on the reduction of the wave run-up, while the permeability of the lower layers and of the core of the structure show an influence only for large ξ values (Van der Meer, 1992; Van Broekhoven; 2011; and Oumeraci et al. 2010)
- Calabrese et al. (2010) showed that the wave momentum flux parameter is a better parameter than the Iribarren number for predicting the run-up on permeable slopes
- A permeability parameter (P) called the "notional permeability coefficient" was presented by Van der Meer (1988) to take into account the permeability of various structures in his stability formulae for breakwaters. However, this coefficient does not represent the actual permeability of the structure and has not been used in run-up formulae.
- Schimmels et al. (2012) proposed a reduction porosity coefficient to be included in the EurOtop (2007) run-up formulae. This empirical coefficient also does not represent the porosity or hydraulic conductivity of the slope.

As can be seen from this literature review on run-up over permeable slopes, most studies have combined the influence of roughness and hydraulic conductivity together, and have proposed formulae to predict their run-up based on curve fitting of laboratory data for specific types of permeable structures. However, the influence of hydraulic conductivity alone on wave run-up is still unknown. As far as the author is concerned, there have been no studies carried out to investigate or quantify the actual influence of hydraulic conductivity on wave run-up and a hydraulic conductivity parameter has not been included in any run-up formulae.

To investigate and quantify the influence of hydraulic conductivity, it is necessary to carry out tests over several slopes with similar roughness surfaces and different hydraulic conductivities. Additionally, the hydraulic conductivity of the structures has to be known.

So far, no tests have been carried out in which the hydraulic conductivity of the structure or beach is known and varied.

If the influence of the hydraulic conductivity of the structure is to be quantified, a hydraulic conductivity parameter has to be considered, instead of a porosity parameter. The porosity is defined as the volume of voids in a sediment or rock divided by the total volume of the sediment or rock, and it is reported as a fraction or percent. However, the voids in a rock or sediment might not be interconnected, so a porous structure might not allow water to flow through. A better porosity parameter would be the *effective porosity*, as it represents the porosity available for fluid flow. The effective porosity is defined as the amount of interconnected pore space in a soil or rock through which fluids can pass, and it is expressed as a percent of bulk volume. However, the effective porosity also does not describe the ease with which a liquid can flow through a porous medium. For this reason, a permeability or a hydraulic conductivity parameter should be used. The hydraulic conductivity *K,* which is defined as the specific discharge per unit hydraulic gradient. It reflects the ease with which a liquid flows and the ease with which a porous medium permits the liquid to pass through it. The hydraulic conductivity considers both the characteristics of the porous medium and the characteristics of the fluid that flows through it. On the other hand, the permeability, *k*, is another parameter that describes the ability of a rock or soil to transmit fluids. The difference between the hydraulic conductivity and permeability parameter is that permeability only considers the characteristics of the porous medium and not the fluid which passes through it.

3.3 Other Key Parameters Influencing Wave Run-up

3.3.1 Influence of the Slope Roughness on Wave Run-up

The influence slope roughness on wave run-up has been extensively investigated for several types of coastal structures. On an impermeable slope, studies have shown that when the roughness is varied, the normalised wave run-up, *R/H,* follows a similar trend as that on smooth-impermeable slopes when plotted against ξ, but with lower values,. For this reason, the influence of the roughness of the slope on wave run-up has traditionally been included as a reduction factor to be added to formulae predicting run-up on smooth, impermeable slopes. The roughness factor, γ_f, values have been commonly determined by comparing run-up data between smooth and rough slopes.

The values of the roughness factor depend on the type of structure. Several artificial roughness elements (such as blocks or ribs) have been commonly used to increase the surface roughness in order to reduce the wave run-up height and the wave overtopping.

These roughness elements can be used to influence either the wave uprush or the backwash. The efficiency of these artificial roughness elements depends on their form and the distance between them.

A significant number of studies and manuals have recommended specific values for γ_f for various types of rough-impermeable surfaces; the most relevant being: the Technical Advisory Committee on Protection against Inundation (1974); the Shore Protection Manual (1984); and EurOtop (2007). It is worth mentioning that EurOtop (2007) manual considers sea dikes and embankment seawalls covered either by grass, by asphalt or by concrete to be smooth slopes and suggests a roughness factor of $\gamma_f = 1$ for them. Other studies that have investigated wave run-up on different types of rough-impermeable slopes and proposed roughness factors, although most of these have been aimed at coastal structures, rather than for beaches (e.g. Wassing, 1957; Battjes, 1974; Stoa, 1978; Szmytkiewicz et al., 1994; Shankar and Jayaratne, 2003; Capel, 2015).

The wave run-up on beaches has generally been studied using field measurements and several formulae have been proposed (e.g. Holman, 1986; Mase, 1989; Nielsen, 1988; Ruggiero et al., 2001; Stockdon et al., 2006; Vousdoukas et al., 2012). As most of these formulae are designed for sandy beaches (0.0625mm to 2mm), factors such as roughness and hydraulic conductivity are generally not considered. However, roughness and hydraulic conductivity might have a large influence on the run-up on gravel beaches.

Channell et al. (1985) performed tests with regular waves on shingle beaches with different slopes. He compared the results with Hunt's formula (20) for smooth impermeable slopes and suggested a reduction factor of 0.35 should be added to (20) to include the influence of the roughness and hydraulic conductivity of the shingle beach.

Hughes (2005) also followed the reduction factor approach to estimate the wave run-up on rip-rap rough-impermeable slopes. Based on the data from Van der Meer and Stam (1992) and Ahrens and Heimbaugh (1998), he estimated a reduction factor of 0.505 to be added to (42) for smooth-impermeable slopes based on the wave momentum flux parameter. His formula with the reduction factor was shown to have a good agreement with the run-up from the breaking waves. However, scatter increased in the case of non-breaking waves.

3.3.2 Influence of the Geometrical Shape of the Slope

Composite slopes. Most run-up formulae have been designed for uniform plane slopes. However, many structures and beaches do not have a straight slope from the toe to the crest. Some coastal structures consist of sections with varying slopes, a berm or multiple

berms which will influence the wave run-up height. These structures are commonly known as composite slopes. To calculate wave run-up for a composite slope, one approach is to estimate the average slope of the structure, $\tan\alpha$. This average slope then used in the Iribarren number ξ. Iterative solutions (e.g. Saville, 1957; EurOtop, 2007) have been suggested to estimate the average slope on a composite slope. However, these iterative solutions can be time consuming and require some calculation effort since the wave run-up height is unknown.

Influence of berms on wave run-up. A berm is a part in the profile of a structure or beach in which the slope varies between horizontal and 1:15. The Technical Advisory Committee on Protection against Inundation (1974) mentions that the influence of the berm width, B, and berm depth, d_B, (with respect to SWL) in the reduction of run-up was insufficiently known at that time. A better understanding the influence of the berm on run-up was provided by de Waal and Van der Meer (1992), who performed tests for berms of different widths and depths (Figure 10).

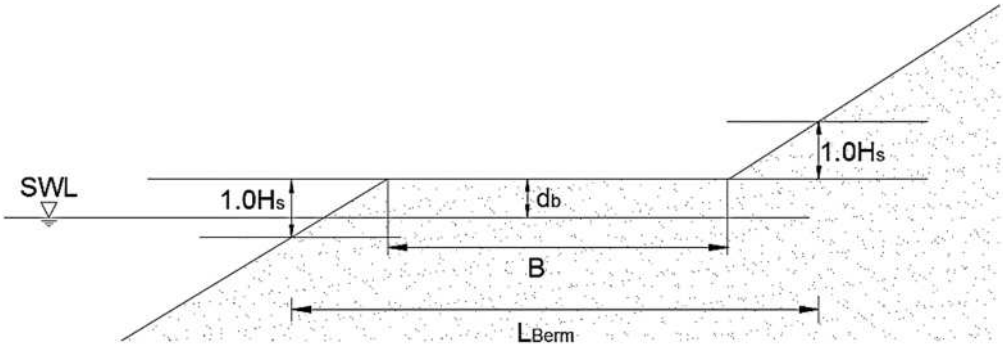

Figure 10 Berm Parameters

From their results, de Waal and van der Meer (2012) proposed a formula for a reduction factor to account for the influence of the berm on a run-up, γ_b. This was expressed as:

$$\gamma_b = 1 - r_B(1 - r_{d_B}) \tag{57}$$

where r_B is the reduction of the average slope ($\tan\alpha$) caused by the berm width B and r_{dB} is the reduction of the influence of a berm caused by the berm depth d_B. de Waal and van der Meer (2012) suggested the following formulae to estimate r_B and r_{dB}:

$$r_{B=}\frac{B/H_s}{2\cot\alpha + B/H_s} \tag{58}$$

$$r_{d_B=}\frac{1}{2}\left(\frac{d_B}{H_s}\right)^2 \tag{59}$$

EurOtop (2007) also adopted (57) to estimate the influence of berms on wave run-up. However, they recommend the following expressions to estimate r_B and r_{dB}:

$$r_{B=}\frac{B}{L_{berm}} \tag{60}$$

$$r_{B=}0.5-0.5\cos\left(\pi\frac{d_B}{R_{2\%}}\right), \text{for a berm above SWL} \tag{61}$$

$$r_{B=}0.5-0.5\cos\left(\pi\frac{d_B}{2\cdot R_{2\%}}\right), \text{for a berm below SWL} \tag{62}$$

where L_{berm} is the characteristic berm length defined in Figure 10.

Concave Shape Slopes. As previously mentioned, most run-up formulae have been developed and validated for uniform straight slopes. However, beaches generally have a concave shape, which will have an influence on wave run-up. An attempt to predict run-up in concave profiles was made by Mayer and Kriebel (1994). They integrated Hunt's formula (20) with Saville's (1957) iterative solution for composite slopes and provided an analytical solution to estimate wave run-up in complex concave beach topographies. For a bi-linear and a concave profile, their predictions showed a better agreement with their experimental results than Hunt's formula (20). However, this iterative method is complicated and requires a priori determination of the breakpoint.

3.3.3 Influence of the Angle of Wave Attack on Wave Run-up

The angle of wave attack, β, also influences the run-up height. The definition of β is shown in Figure 11.

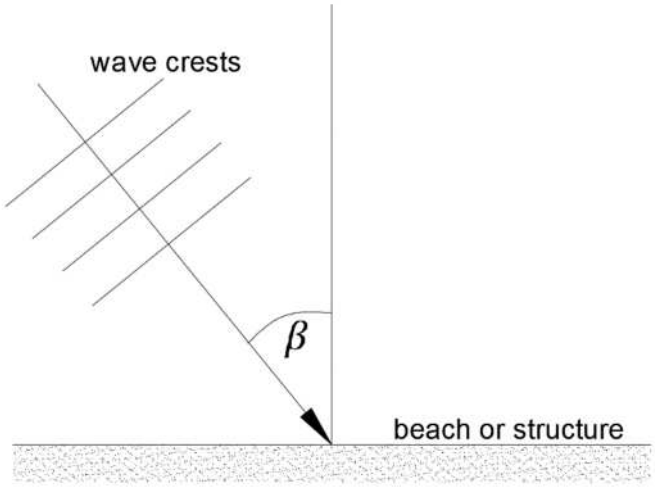

Figure 11 Angle of wave attack

Studies performed to investigate the influence of oblique attack on wave run-up are generally carried out in wave basins, which can be expensive. For this reason, few studies

have looked at run-up for oblique wave attack. One such study was performed by Tautenhain et al. (1982). Their results showed that the run-up for small angles of wave attack β of between 10-30˚ had larger run-up values than those from normal waves (β = 0). However, these findings were not observed by de de Waal and van der Meer (2012) and Schüttrumpf (2001), who found no increase of the run-up for small angles of wave attack. For short crested waves, de Waal and van der Meer (2012) suggested the following formula to estimate the reduction influence factor for oblique wave attack, γ_β:

$$\gamma_\beta = 1 - 0.0022\beta \tag{63}$$

This formula is also recommended by the EurOtop (2007). However, Schüttrumpf (2001) observed that this formula slightly overestimates the reduction of wave run-up for small angles of incidence and suggested that the influence of wave direction on wave run-up can be neglected for $\beta < 20^\circ$.

3.3.4 Influence of Shallow Water at the toe on Wave Run-up

The influence of shallow water at the toe of the structure on wave run-up was also investigated by de Waal and van der Meer (2012), who reported 40 small scale tests in which the water depth at the toe of the structure was varied. They noticed that the water depth at the toe of the structure only had an effect when the relative water depth, h/H_s, was smaller than 4. The following formula was proposed to estimate the influence factor of shallow water, γ_h:

$$\gamma_h = 1 - 0.03\left(4 - \frac{h}{H_s}\right)^2, \quad \text{for } 1 < \frac{h}{H_s} < 4 \tag{64}$$

3.3.5 Influence of Water Table Elevation on Wave Run-up

The rates of infiltration and exfiltration across the swash zone, which are mainly controlled by the water table elevation and the hydraulic conductivity of the beach, affect wave run-up heights.

A high water table elevation may occur when decoupling occurs and a seepage face develops between the exit point and the shoreline point (explained in Section 2.1.3). On the seepage face, the saturated part of the beach will cause exfiltration and will reduce the infiltration rates from the uprush and backwash motions into the beach. Therefore, the seepage face due to tidal elevation drop is expected to increase the run-up on permeable beaches.

In contrast, if the water table elevation is lower than the MWL, the unsaturated area of the beach will be increased and water from the uprush and backwash processes will be able to

infiltrate into the beach. As a consequence, the run-up is expected to be decreased. This scenario might occur if beach drainage system is installed Figure 12.

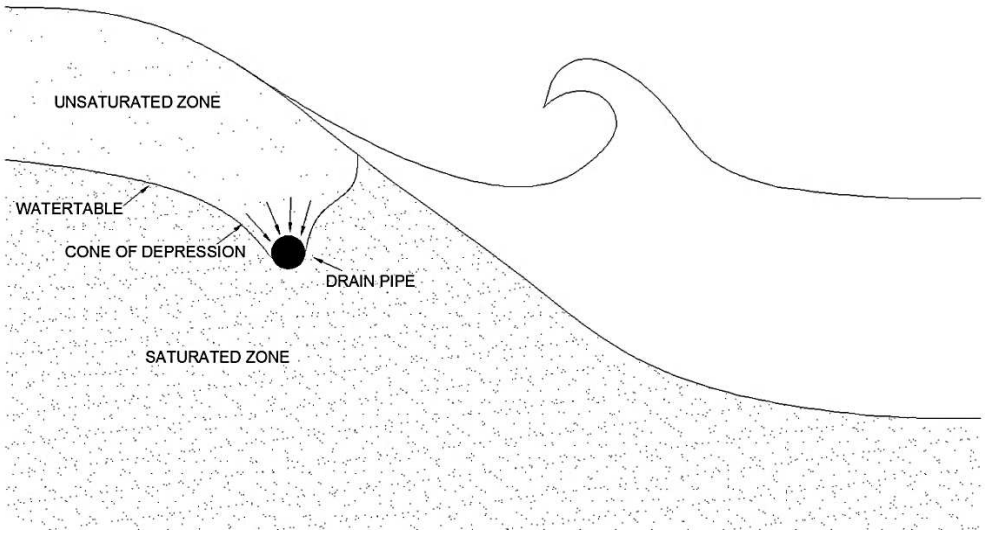

Figure 12 Sketch of a typical beach drainage system

Most studies involving the manipulation of beach groundwater levels have focused on the efficiency of different beach drainage techniques to lower the groundwater levels, and their influence on the sediment transport and the beach profile evolution. A summary of the most relevant of these field and laboratory studies, as well as their findings, is shown in Table 9. Yet, none of these studies have focused on measuring the effects of the seepage face with a high water table elevation after a tidal drop or an unsaturated beach with a low water table caused by a beach drainage system on wave run-up.

Author	Type of Study	Drainage Method	Results
Machemehl et al. (1975)	Small-scale laboratory, regular waves	Sub-sand filter system	Lower groundwater levels accelerated accretion at the foreshore and promoted the growth of a previously eroded berm.
Chappell et al. (1979)	Field, Duras Beach, Australia	Pumping water through an array of wells	Accretion in the first part of the experiment. In the second part, no morphological changes were observed
Kawata and Tsuchiya (1986)	Small-scale laboratory, solitary and regular waves	Sub-sand filter system	Offshore sediment transport was reduced under all wave conditions tested with a lowered groundwater level.
Sato (1990)	Small-scale laboratory, monochromatic waves	Coastal Drain System	No significant difference was observed with a lowered groundwater level
Ogden and Weisman (1991) and Weisman et al. (1995)	Small-scale laboratory, irregular waves	Beach Drainage System	Low groundwater levels showed no effect on erosion or accretion, but induced a berm at the top of the beach.
Oh and Dean (1992) and (1994)	Small-scale laboratory, regular waves, sand	Beach groundwater was drained out of an excavated hole in the beach berm	Low groundwater levels resulted in a more stable beach than with high groundwater levels
Davis et al. (1992)	Field, Why Beach, Australia	Gravity Drainage System, shore-normal coastal drains spaced between 5 to 15m intervals	No changes due to lower groundwater levels, nevertheless the technology showed efficiency in lowering the groundwater levels
Herrington (1993)	Large Scale Laboratory, regular and irregular waves	STABEACH (drains are connected by underground piping to a pumping well)	Tests with a drained beach showed greater stability than the non-drained tests.
Katoh and Yanagishima (1996)	Field, Japan	Gravity Drainage System, a permeable layer with a drainage pipe connecting the permeable layer with the surf zone	The permeable layer was able to drain water off the beach even in a storm, and the eroded foreshore recovered quickly after a storm.
Kanazawa et al. (1996)	Small-scale laboratory, regular waves	Gravity Drainage System, 3 different permeable layers were tested (gravel, gravel with a drainage pipe, and a permeable pipe with a drainage pipe)	The permeable pipe with a drainage pipe showed to be the most effective method to drain water. Erosion near the shoreline was mitigated with the permeable layers.
Lee et al. (2007)	Small-scale laboratory, regular waves	Groundwater levels were manipulated with a water control tank using pumps	As the groundwater levels were lowered, the beach surface became steeper, and a berm formed at the upper portion of the shoreline.
Ang et al. (2004) and Horn et al. (2007)	Small-scale laboratory, regular waves, coarse and fine sand	Groundwater levels were manipulated by an adjustable pipe connected through a back wall behind the beach	With coarse sand, accretion was observed with all groundwater levels, but a bigger berm developed under a lowered groundwater level. With fine sand, accretion was observed only with a lowered groundwater level and under low energy conditions.
Chiaia et al. (2005) and Damiani et al. (2009)	Small-scale laboratory, regular waves	Beach Drainage System	Lowered groundwater levels showed efficiency under erosive wave conditions.
Ciavola et al. (2011) and Contestabile et al. (2012)	Large Scale Laboratory, irregular waves, D=0.33 mm,	Beach Drainage System (4 corrugated drains)	Only under low energy wave conditions a positive effect was observed
Williams et al. (2010), Williams et al. (2012) and Masselink and Turner (2012)	Large Scale Laboratory, irregular waves, D=11 mm, Delta Flume	Barrier island with back-barrier lagoon levels varied	Low lagoon levels enhanced onshore sediment transport, beach accretion, and berm build up. High lagoon levels induced offshore sediment transport and erosion.

Table 9 Studies concerned with the manipulation of beach groundwater levels

3.3.6 Summary and Conclusions

This section has considered previous studies which have investigated parameters other than hydraulic conductivity that can influence wave run-up. There is already a good understanding of the influence on run-up of parameters such as the geometry of the slope, the angle of wave attack and shallow water at the toe of the structure. However, the influence of water table elevations on run-up has not yet been studied.

3.4 Influence of Hydraulic Conductivity on the Wave Breaking Processes

A significant number of studies have been focused in understanding the wave breaking processes over impermeable beaches (e.g. Stive, 1980; Mizuguchi, 1986; Pedersen et al.,1993; Ting and Kirby, 1996; Longo et al., 2002). However, little attention has been made to investigate the influence of the slope's hydraulic conductivity on the wave breaking processes (e.g. Cox and Kobayashi, 2000; Lara et al., 2002, 2006).

3.4.1 Influence of Hydraulic Conductivity on the Breaker Type and Breaking Point Location

As far as the author is concerned, the only study that has analysed the influence of the hydraulic conductivity of the slope on the breaker types and their breaking point locations was reported in Lara et al. (2006). The breaking point location for a plunging breaking is where the front face of the wave becomes nearly vertical (Bonmarin, 1989). In their study, the wave breaking processes of two different gravel sizes slopes were compared. They observed that under identical incident wave conditions, the breaking point on the larger grain size slope generally occurred closer to the slope than on the smaller grain size slope. The presence of a permeable slope causes additional energy dissipation before the waves reach the breaking point, and thus, reducing the breaking wave height. In addition, a permeable slope is expected to affect the undertow, which can influence the breaking point location. Lara et al. (2006) also reported that in some cases, the breaker types changed from plunging to spilling between both types of gravel.

3.4.2 Breaking Criteria

The mechanics of breaking and non-breaking waves are entirely different, so it is not surprising that when run-up data from both types of waves are plotted together, both show different trends. This is why most run-up formulae are specifically applicable either to breaking or to

non-breaking waves. Therefore, when attempting to predict the run-up, it is crucial to be able to predict first which waves will break at the slope and which will not. For this reason, *breaking criteria* have been commonly used to determine the transition between breaking and non-breaking waves, the most common ones being based on either ξ or H/L.

When the normalised run-up, R/H, is plotted against ξ, the data with small ξ values tend to follow different trends than those with large ξ values. Therefore, studies have traditionally used these plots to determine a ξ value representing the transition between breaking and non-breaking waves (e.g., Burcharth and Hughes (2002) recommends a value of ξ =2.5, while EurOtop (2007) suggests a value of ξ = 1.65 for this transition).

Another parameter commonly used as a breaking criterion is the wave steepness, H/L. Hughes (2004a) observed that a value of H/L = 0.0225 appeared to represent the transition between breaking and non-breaking waves, regardless of the slope of the structure. He came to this conclusion by re-analysing Ahrens' (1981) run-up data, where he plotted the relative run-up R/h against the wave momentum flux parameter and noticed two different trends depending on their H/L values. According to Hughes, the data of the first trend with values of $H/L < 0.0225$ appeared to represent the non-breaking waves, while the second trend corresponded to data with values of $H/L > 0.0225$, representing the breaking waves.

The main problem with these criteria is that they have been derived from run-up data plotted against dimensionless parameters and not from observations of the breaking processes. Moreover, as far as the author knows, the predictions from these breaking criteria have not been compared or validated against any experimental observations.

3.5 Influence of Wave Run-up and Hydraulic Conductivity on the Water table Over-height in Coastal Barriers

Section 3.2 and 3.3 reviewed studies concerned with the prediction of wave run-up and the main parameters that influence its magnitude. One of the parameters reviewed was the groundwater levels inside the beach, which tend to rise due to the action of waves, tides and rainfall recharge. The maximum time-averaged wave-induced groundwater level rise above the mean sea level, (maximum water table over-height, η_w^+) can produce a net groundwater flow towards the back-barrier lagoon. The importance of an accurate prediction of η_w^+ was discussed in Section 2.1.3.

The magnitude of η_w^+ is expected to vary depending on the hydraulic conductivity of the beach. However, previous studies have shown mixed conclusions on the influence of hydraulic conductivity on its magnitude. These studies are reviewed below.

Kang et al. (1994) and Kang and Nielsen (1996) reported the results of a series of wave flume experiments carried out to investigate the water table response due to wave run-up without tidal effects. The tests were performed with two sand beaches (d_{50}=0.18mm and 0.78mm) and with 10 different wave conditions. They observed that the ratio between η_w^+ and the run-up height R remained constant regardless of the sediment size of the beaches, hence independent of its hydraulic conductivity:

$$\eta_w^+/R \approx 0.62 \tag{65}$$

Based on this constant ratio Kang et al. (1994) and Nielsen (2009) concluded η_w^+ is independent of the hydraulic conductivity or the sediment size of the beach, so they suggested the use of Hunt's (1959) formula (20) for impermeable slopes to predict the maximum water table over-height in coastal barriers. Combining (20) and (65), Kang et al. (1994) proposed the following formula to predict the maximum water table over-height due to regular waves:

$$\frac{\eta_w^+}{H} = 0.62\xi \tag{66}$$

Kang et al. (1994) and Nielsen (2009) conclusion was further supported by Turner and Masselink (2012) who presented a subset of the results from the BARDEX (Barrier Dynamics Experiment) large-scale laboratory experiment conducted in the 250m long Delta flume in Netherlands. A 4m high and 50m long gravel barrier (d_{50}=11mm and K=0.16m/s) was constructed in the flume. This hydraulic conductivity was estimated in-situ by applying Darcy's law and measuring the groundwater flow through the barrier when the sea and lagoon water levels were manipulated. The grain size used in the BARDEX tests was 1-2 orders of magnitude larger than the two sand sizes used in Kang et al. (1994) tests, and according to Turner and Masselink, its hydraulic conductivities was around 4-5 orders of magnitude greater than Kang's tests. Nevertheless, the η_w^+ results of the three tests they presented showed a good agreement with the predictions of (66).

However, recent results shown by Turner et al. (2013) as part of the BARDEX II experiments do not support these findings. A medium-sized sand (d_{50}=0.42mm and K=0.0001m/s) coastal barrier was built in the same 250m long Delta flume used for the BARDEX experiments described above. Although only two different wave conditions were tested, their η_w^+ results showed to be substantially greater than those obtained with a gravel barrier, and therefore, were not properly predicted by (66). These results showed that the hydraulic conditions

(sediment size and thus the hydraulic conductivity) of the coastal barrier do influence the magnitude of the maximum water table over-height and cannot be neglected when trying to predict it, as is implied in (66). However, due to the limited data shown by Turner et al. (2013), they did not derive any new prediction formula to estimate η_w^+.

3.5.1 Summary and Conclusions

The study carried out by Kang et al. (1994) showed that the ratio between η_w^+ and run-up remains constant regardless the hydraulic conductivity of the beach, which suggests that a run-up formula can be used to predict η_w^+. However, this constant ratio does not mean that η_w^+ is independent of *K*, as concluded by them. In gravel barriers, where wave run-up is clearly influenced by *K*, it is expected that η^+ will also be influenced by *K*. Therefore, equation (66) might only be useful on sandy barriers, where *K* does not play an important role.

Another problem of predicting η^+using (66) might lie in the inappropriate way that it predicts wave run-up. Equation (66) is based on Hunt's (1959) run-up formula (20) which has been shown to work properly only for breaking waves on smooth-impermeable slopes. Therefore, it is anticipated that a more accurate prediction of wave run-up on permeable beaches (for both, breaking and non-breaking waves) will enable a better prediction of the maximum water table over-height.

3.6 Influence of Hydraulic Conductivity on the Swash Hydrodynamics

The fourth part of this research project focuses on the influence of hydraulic conductivity on the swash hydrodynamics. Interest in this topic has increased significantly over the last couple of decades. However, the complex hydrodynamic processes in the swash zone, which are influenced by wave breaking, turbulence, shear stresses and bottom friction, are still not fully understood, (Bakhtyar et al., 2009). Nevertheless, considerable advances have been made in the understanding of the complex processes involved in the swash zone. Most of these studies have been carried out either in the field or in laboratory facilities, although some numerical studies have also been carried out.

Bed shear stresses, roughness lengths and drag coefficients in the swash zone are commonly obtained from velocity measurements, although some attempts to measure direct bed shear stresses have been made (e.g. Barnes and Baldock, 2007; Barnes et al., 2009). A summary of the most relevant field studies carried out to measure flow velocities and water depths in the swash zone is shown in Table 10. This shows the main research areas of each field study, as well as the

site characteristics (beach slope, type, and sediment size) and the instrumentation used to measure the flow velocities and water depth.

Field studies have provided important insights into the swash zone hydrodynamics, the sediment transport processes and the beach profile evolution. However, as the bed is mobile and the wave parameters and slope characteristics cannot be controlled in the field, the swash hydrodynamics might be best studied in laboratory facilities or with numerical models on non-deformable slopes, where the tests can be identically replicated and repeated. This ability to control the parameters of the tests, helps in deriving ensemble-averaged velocity profiles, which can provide more detailed and precise estimations boundary layer measurements, and thus, bed shear stresses and drag coefficients. The most relevant laboratory studies analysing the swash zone hydrodynamics on deformable and non-deformable beds are summarised in Table 11.

Some numerical studies have investigated the evolution of the swash boundary layer with models based on the non-linear shallow water (NLSW) equations (e.g. Hughes and Baldock, 2004; Barnes and Baldock, 2010; Briganti et al., 2011). However, as these type of models assume hydrostatic pressure and depth uniformity of the velocity profile, the wave boundary layer modelling cannot be resolved directly with this approach (Pintado-Patiño et al., 2015). To overcome such limitations some studies have used either Lagrangian (Barnes and Baldock, 2010) or Eulerian (Briganti et al., 2011) boundary layer models forced by depth-averaged velocities from the NLSW models. Nevertheless, these studies assume that the log law prevails inside the boundary layer and uniform above it throughout the entire swash event. This assumption has also been employed in field studies based on single point measurements such as Raubenheimer et al. (2004) and Masselink et al. (2005), which have led to consistent estimates of bed shear stresses and friction coefficients (Pintado-Patiño et al., 2015). However, laboratory studies, where swash flow velocities have been measured on non-deformable slopes, have shown that the log law does not predict adequately the near bed flow velocities during the entire swash event. In particular during flow reversal, where log law fit is unable to represent the velocities with opposing directions near the bed and at the surface. On the other hand, recent studies using numerical models based on the Reynolds-Averaged Navier-Stokes (RANS) equations have shown significant improvements overcoming the limitations of the NLSW models (e.g. Zhang and Liu, 2008; Torres-Freyermuth et al., 2010; Torres-Freyermuth et al., 2013; Pintado-Patiño et al., 2015). Although computationally more expensive than the NLSW models, the RANS models have shown to be a good alternative to investigate the swash boundary layer dynamics.

Authors	Slope (tan β)	Beach Type	Sediment Size (D_{50})	Velocity Measuring Method	Water Depth Measuring Method	Researched Areas
Puleo et al. (2000)	0.083	Sand	0.44 mm	Impeller CM	Pressure transducers	Swash hydrodynamics Sediment transport
Butt et al. (2004)	0.108	Sand	-	Electromagnetic CM ADV	Pressure transducers	Swash hydrodynamics Sediment transport
Aagaard and Hughes (2006)	0.031 0.037	Sand	0.24mm 0.26mm	Electromagnetic CM ADV	Pressure transducers	Swash hydrodynamics Sediment transport
Blenkinsopp et al. (2011)	0.067	Sand	0.4mm	Electromagnetic CM	Pressure transducers	Swash hydrodynamics Sediment transport Beach profile evolution
Raubenheimer (2002)	0.019	Sand	0.2mm	ADV	-	Swash hydrodynamics
Conley and Griffin (2004)	-	Sand	-	Video camera	Pressure transducers	Swash hydrodynamics
Baldock and Hughes (2006)	0.028-0.11	Sand	0.22-0.53mm	Video camera	Optically (video camera)	Swash hydrodynamics
Masselink and Hughes (1998)	0.14	Sand	0.5mm	Ducted impeller CM meter	Not measured	Swash hydrodynamics Sediment transport
Hughes et al. (1997)	0.12	Sand	0.3mm	Ducted impeller CM	Wave gauges	Swash hydrodynamics Sediment transport Beach profile evolution
Masselink and Russell (2006)	0.016-0.049 0.077-0.11	Sand	0.3mm 0.55mm	Electromagnetic CM	Pressure transducers	Swash hydrodynamics Sediment transport Beach profile evolution
Masselink et al. (2010)	≈0.125	Gravel	2-10mm	Electromagnetic CM	Pressure transducers	Swash hydrodynamics Sediment transport Beach profile evolution
Austin and Masselink (2006)	0.15	Gravel	6mm	ADV	Pressure transducers	Swash hydrodynamics Sediment transport Beach profile evolution
Puleo et al. (2013) Lanckriet Lanckriet et al. (2013)	0.022	Sand	0.33mm	Electromagnetic CM ADV	Pressure transducers	Swash hydrodynamics Sediment transport Beach profile evolution

Table 10 Field studies carried out to investigate the swash hydrodynamics

Authors	Slope (tan β)	Slope types	Sed. Size (D_{50})	Wave generation method	Waves type	Velocity Meas. Method	Water Depth Meas. Method	Researched Areas
D. Cox and Kobayashi (2000)	0.028-0.1	Non-deformable, Rough, impermeable	6.3mm	Wave paddle	Irregular waves	LDV	Wave gauges	Swash hydrodynamics
Petti and Longo (2001)	0.1	Non-deformable, Rough, impermeable	0.03mm	Wave paddle	Regular waves	LDV	Wave gauges	Swash hydrodynamics
Shin and Cox (2006)	0.028-0.1	Non-deformable, Rough, impermeable	2.2mm	Wave paddle	Regular waves	LDV	Wave gauges	Swash hydrodynamics
Sou and Yeh (2011)	0.05	Non-deformable, Smooth, impermeable	-	Wave paddle	Regular waves	PIV	Optically (LIF)	Swash hydrodynamics
Yeh (1991)	0.13	Non-deformable, Smooth, impermeable	-	Dam-break	Solitary waves	Wave gauges	Optically (LIF)	Swash hydrodynamics
Barnes et al. (2009)	0.1	Non-deformable, Smooth and Rough, impermeable	6mm	Dam-break	Solitary waves	PIV	Acoustic sensors	Swash hydrodynamics
O'Donoghue et al. (2010)	0.1	Non-deformable, Smooth and Rough, impermeable	6mm	Dam-break	Solitary waves	PIV	Wave gauges	Swash hydrodynamics
Kikkert et al. (2012)	0.1	Non-deformable, Rough, impermeable	1.3mm 5.4mm 8.4mm	Dam-break	Solitary waves	PIV	Optically (LIF)	Swash hydrodynamics
Kikkert et al. (2013)	0.1	Non-deformable, Rough, permeable	1.3mm 8.4mm	Dam-break	Solitary waves	PIV	Optically (LIF)	Swash hydrodynamics
Lara et al. (2006)	0.05	Deformable, Rough, permeable	19mm 39mm	Wave paddle	Regular waves	LDV	Wave gauges	Surf zone hydrodynamics Beach profile evolution

Table 11 Laboratory studies carried out to investigate the swash hydrodynamics

Authors	Slope ($\tan\beta$)	Slope types	Sed. Size (D_{50})	Wave generation method	Waves type	Velocity Meas. Method	Water Depth Meas. Method	Researched Areas
Pedrozo-Acuña et al. (2006)	0.125	Deformable, Rough, permeable	21mm	Wave paddle	Irregular waves	-	-	Sediment transport Beach profile evolution
Williams et al. (2012) Bardex I	0.125	Deformable, Rough, permeable	11mm	Wave paddle	Irregular and Regular waves	ADV	Pressure sensors	Swash hydrodynamics Sediment transport Beach profile evolution
G. Pedersen et al. (2013)	0.175	Non-deformable, Smooth, impermeable	-	Wave paddle	Solitary waves	PIV	Optically	Boundary layer evolution
C. Lin et al. (2014)	0.1	Non-deformable, Smooth, impermeable	-	Wave paddle	Solitary waves	PIV	Optically	Boundary layer evolution
Masselink et al. (2016) Bardex II	0.067	Deformable, Rough, permeable	0.51mm	Wave paddle	Irregular and Regular waves	ADV	Pressure sensors	Swash hydrodynamics Sediment transport Beach profile evolution

cont. Table 11 Laboratory studies carried out to investigate the swash hydrodynamics

Few studies have reported swash measurements on permeable beaches (e.g., Pedrozo-Acuña et al., 2006; Williams et al., 2012; Masselink et al., 2016). In order to investigate exclusively the influence of beach roughness and hydraulic conductivity on swash hydrodynamics, sediment transport has to be avoided, hence a non-deformable permeable slope has to be used. To the author's knowledge, only one laboratory study (Kikkert et al., 2012, 2013) and two numerical studies (Masselink and Li, 2001; Pintado-Patiño et al., 2015) have investigated the influence of hydraulic conductivity on swash hydrodynamics using non-deformable slopes. However, only Kikkert et al. (2012, 2013) and Pintado-Patiño et al. (2015) have investigated the effects of hydraulic conductivity on the boundary layer dynamics, and hence on the bed shear stresses and drag coefficients.

Masselink and Li (2001) used a NLSW numerical model to investigate the uprush and backwash asymmetry induced by infiltration in a series of regular waves on plane slopes with different permeabilities. However, they did not investigate the near bed velocity profile distributions in a swash event. In their study, they observed that the majority of the infiltration loss occurs during the wave uprush, which reduced the backwash flow depths and velocities, and its duration.

By constructing permeable and impermeable slopes with identical roughnesses, Kikkert et al. (2012, 2013) analysed the effect of roughness and hydraulic conductivity independently on the boundary layer and swash hydrodynamics. A solitary wave was produced by the collapse of a dam-break, which was repeated 50 times in order to obtain ensemble-averaged flow velocities. The swash depth and flow velocities were measured using Laser-induced fluorescence (LIF) and Particle Image Velocimetry (PIV), respectively. Both roughness and hydraulic conductivity were shown to decrease the maximum run-up and the backwash velocities. However, roughness appeared to cause thickening of boundary layer, while infiltration into the permeable beach caused a slight thinning of boundary layer. The bed shear stress and drag coefficients (also known as friction factors) were observed to be enhanced by the hydraulic conductivity of the beaches compared to their impermeable counterparts.

Pintado-Patiño et al. (2015) reported the effects of infiltration and exfiltration in the swash zone boundary layer dynamics from a solitary wave using a 2D numerical model that solves the Volume-Averaged Reynolds-Averaged Navier-Stokes equations (VARANS) and validated their model using Kikkert et al. (2012 and 2013) results. Their results showed that infiltration thinned the boundary layer, enhancing the bed shear stress during the uprush phase.

3.6.1 **Summary and Conclusions**

Although significant advances have been made in the last 15 years in understanding the swash zone boundary layer dynamics during the uprush and backwash phases, very little work has

been done to investigate the influence of hydraulic conductivity. Furthermore, the only studies investigating this were performed with solitary waves. No studies have been reported analysing the influence of hydraulic conductivity on bed shear stresses and drag coefficients from periodic waves, where the reduction of uprush and backwash flows due to infiltration play an important role in swash-swash interaction.

3.7 Aims and Objectives of the Present Study

A number of important research gaps have been identified from the preceding literature review. Based on these gaps, the specific aims of the project were established. These are given as follows:

- Obtain reliable data from run-up tests over permeable and impermeable slopes
- Derive more accurate run-up formulae for breaking and non-breaking waves on smooth-impermeable slopes for both regular and irregular waves
- Investigate the effects of the following parameters on wave run-up and if considered necessary include their influence in prediction formulae for breaking and non-breaking waves:
    - Hydraulic conductivity
    - Surface Roughness
    - High and low water table elevations
- Analyse the influence of hydraulic conductivity on:
    - Breaking criteria, breaker type and breaking point location
    - Uprush and backwash flow velocities, water depths, bed shear stresses, boundary layer thickness, drag coefficients, swash duration and swash asymmetries
    - Water table over-height

To achieve this aims, the thesis was divided into four topics: wave run-up, wave breaking processes, water table over-height, and swash hydrodynamics. The research data for each of these topics was obtained from two main sources: wave flume laboratory experiments and CFD numerical simulations. These are described in Chapters 4 and 5, respectively, and the obtained data are analysed in Chapter 6. Table 12 summarises each of these topics, the tests performed of each topic and their objectives.

#	Topic	Setup	Source	Parameters	Objectives
1	**Wave Run-up**	Smooth-impermeable slopes	- 2D wave flume laboratory experiments	- wave run-up - water level changes	- Obtain run-up data from breaking and non-breaking waves on impermeable slopes to derive new run-up prediction formulae - Use run–up data to validate model
			- 2D CFD numerical simulations	- wave run-up - water level changes	- Set up a numerical model capable of simulating run-up on impermeable slopes - Validate the model with the experimental data - Obtain additional run-up data from steeper slopes and from irregular waves
		Permeable slopes	- 2D wave flume laboratory experiments	- wave run-up - water level changes	-Obtain run-up data from breaking and non-breaking waves on permeable slopes with different known hydraulic conductivities - Use run-up data to validate model
			-Constant head tests	-hydraulic conductivity	- Measure the hydraulic conductivity of the permeable slopes using a permeameter
			- 2D CFD numerical simulations	- wave run-up - water table elevations	- Set up a numerical model capable of simulating flow through porous structures, and thus, capable of simulating run-up on permeable slopes - Validate the model with the experimental run-up data
		Rough-impermeable slopes	- 2D wave flume laboratory experiments	- wave run-up - water level changes	- Obtain run-up data from impermeable slopes but with the same surface roughness as the permeable slopes
		Permeable slopes with varying water table elevations	- 2D wave flume laboratory experiments	- wave run-up - water level changes	- Obtain run-up data on different permeable beaches with high and low water table elevations

Table 12 Topics, methods and objectives to achieve the aims of the project (continues in the next page)

#	Topic	Setup	Method	Parameters	Objectives
2	**Wave Breaking Processes**	Permeable slopes	- 2D laboratory experiments	- wave breaking sequence	- Record the breaking sequence all the tests performed on permeable slopes - Classify the breaker type of each test - Identify the location of the breaking point from video images - Compare the prediction of previous breaking criteria against the experimental observations
3	**Water table Over-height**	Permeable slopes	- 2D laboratory experiments	- wave run-up - water table elevation	- Measure water table profiles inside the permeable beaches with different hydraulic conductivities - Estimate the maximum wave-induced water table over-heights
4	**Swash hydro-dynamics**	Impermeable Slope	- 2D laboratory experiments	- swash flow velocities -swash depths	- Measure swash depth and swash flow velocities - Derive the ensemble-average velocity profiles - Estimate bed shear stresses and friction factors - Use data to validate model
			- 2D CFD numerical simulations	- swash flow velocities -swash depths	- Validate the model with experimental data - Obtain flow velocity and swash depth data at different locations in the slope - Derive the ensemble-average velocity profiles and estimate their corresponding bed shear stresses and friction factors - Analyse swash duration and estimate swash asymmetries - Analyse the evolution of the velocity profiles in a swash event at different locations in the slope
		Permeable Slope	- 2D laboratory experiments	- swash flow velocities -swash depths	- Measure swash depth and swash flow velocities - Derive the ensemble-average velocity profiles - Estimate bed shear stresses and friction factors - Use data to validate model
			- 2D CFD numerical simulations	- swash flow velocities -swash depths	- Validate the model with experimental data - Obtain flow velocity and swash depth data at different locations in the slope to derive the ensemble-average velocity profiles and estimate their corresponding bed shear stresses and friction factors - Analyse the evolution of the velocity profiles in a swash event at different locations in the slope - Investigate the influence of hydraulic conductivity on the swash hydrodynamics and bed shear stresses

cont. Table 12 Topics, methods and objectives to achieve the aims of the project

4 Wave Run-up Laboratory Experiments

The laboratory experiments are an essential part of this study as they provided most of the data required for the analysis and were necessary to validate the numerical simulations. In total, 6 different wave run-up experiments were carried out on either smooth-impermeable, rough-impermeable or rough-permeable slopes. Each of these experiments had different objectives and are described in Table 13. This table shows the different variables, wave flume, number of setups and tests performed, as well as the parameters measured and the instrumentation used to record these parameters. In total, 43 different experimental setups were used and 982 tests were performed.

This chapter starts with a brief description of the two wave flumes used in Section 4.1, followed by a description of the instrumentation used to record the different parameters shown in Table 13. Then, the experimental setup and test conditions in each experiments are detailed in Section 4.4. The complete data sets of results from all the experiments used in the analysis are shown Appendix D. Finally, in Section 4.5 describes the data acquisition and post-processing procedures performed to obtain the data measured in the experiments.

#	EXPERIMENT	DESCRIPTION	VARIABLES	WAVE FLUME USED	PARAMETERS MEASURED	INSTRUMENTATION USED	NUMBER OF SETUPS	NUMBER OF TESTS
1	Preliminary wave run-up experiments	Effect of hydraulic cond. and roughness on wave run-up	- 1 slope roughness - 4 slope hydraulic cond. - 4 slope angles - 1 water depth - 20 regular wave conditions	- 20m long flume	- wave run-up - free surface elevation	- video cameras - wave gauges	16	320
2	Wave run-up tests on rough-permeable slopes	Effect of hydraulic cond. on wave run-up and wave-induced water table over-height	- 4 slope hydraulic cond. - 3 slope angles - 1 water depth - 25 regular wave conditions	- 13.7m long flume	- wave run-up - water table elevations - free surface elevation - breaking point location	- video cameras - wave gauges - digital pressure transducers	12	300
3	Wave run-up on smooth-impermeable slopes	Breaking and non-breaking waves on, flat, plane, impermeable slopes	- 1 smooth surface - 5 slope angles - 2 water depths - 25 regular wave conditions	- 20m long flume - 13.7m long flume	- wave run-up - free surface elevation	- video cameras - wave gauges	5	160
4	Wave run-up on rough-impermeable slopes	Effect of surface roughness on wave run-up	- 4 surface roughnesses - 1 slope angle - 1 water depth - 25 regular wave conditions	- 13.7m long flume	- wave run-up - free surface elevation	- video cameras - wave gauges	4	100
5	Wave run-up on rough-permeable slopes with varying water table elevations	Effect of beach groundwater levels on wave run-up	- 2 slope hydraulic cond. - 2 water table elevations - 1 slope angle - 1 water depth - 25 regular wave conditions	- 13.7m long flume	- wave run-up - free surface elevation - flow rates	- video cameras - wave gauges	4	100
6	Swash flow depths and velocity measurements on smooth-impermeable and rough-permeable slopes	Effect of slope hydraulic cond. and roughness on swash hydrodynamics	- 2 slope surfaces - 1 slope angle - 1 water depth - 1 regular wave condition	- 13.7m long flume	- swash flow depths - swash flow velocities	- Laser Doppler Velocimetry - video cameras - wave gauges	2	2
						TOTAL	**43**	**982**

Table 13 Summary of laboratory experiments

4.1 Experimental Facilities

4.1.1 Wave Flumes

The wave run-up experiments of this project were conducted in two wave-currents flumes located at UCL. The first of these flumes is located in the Mechanical Engineering Department and has dimensions of 20m long, 1.2m width, and 1m height, while the second flume is located in the Fluids laboratory of the Civil, Environmental and Geomatic Engineering Department. This flume is 13.7m long, 0.45m wide and 0.75m high. The side and bottom walls of both flumes are constructed with clear transparent glass plates. Both flumes are equipped with two wave paddles located at each end of the flume allowing waves to be generated at one end and absorbed at the other end.

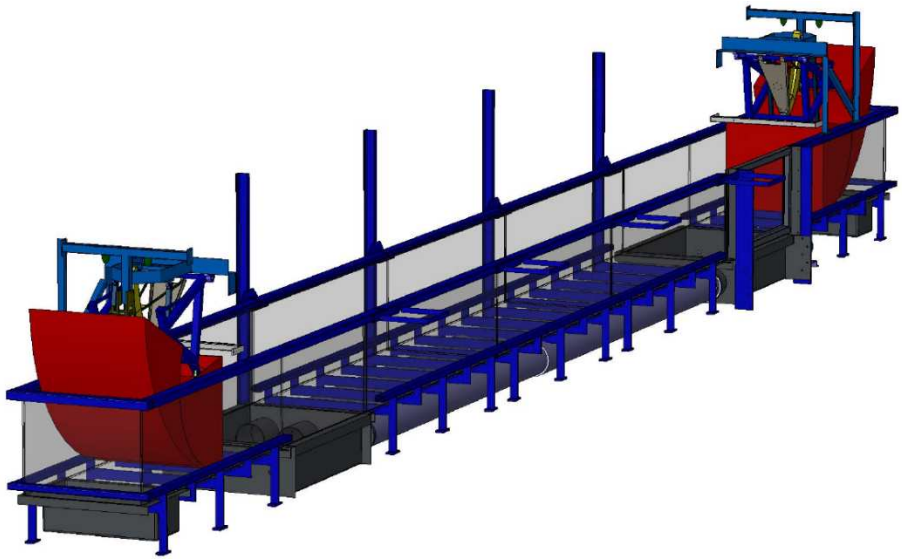

Figure 13 Sketch of 20m flume located at the Mechanical Engineering Department (Edinburgh Designs Ltd, 2010)

4.1.2 Wave Paddles

The wave paddles in the flumes are *piston type* wave makers, capable of generating shallow water waves, which are ideal for analysing near-shore processes (Figure 15 and Figure 16). Their flat surface displacement technique (back and forth movement) generates waves where the horizontal water particle motion is almost constant at all depths. This type of paddle differs from *flap type* paddles, as the latter typically are used to produce deep water waves, where the orbital particle motion decays with depth (Figure 14).

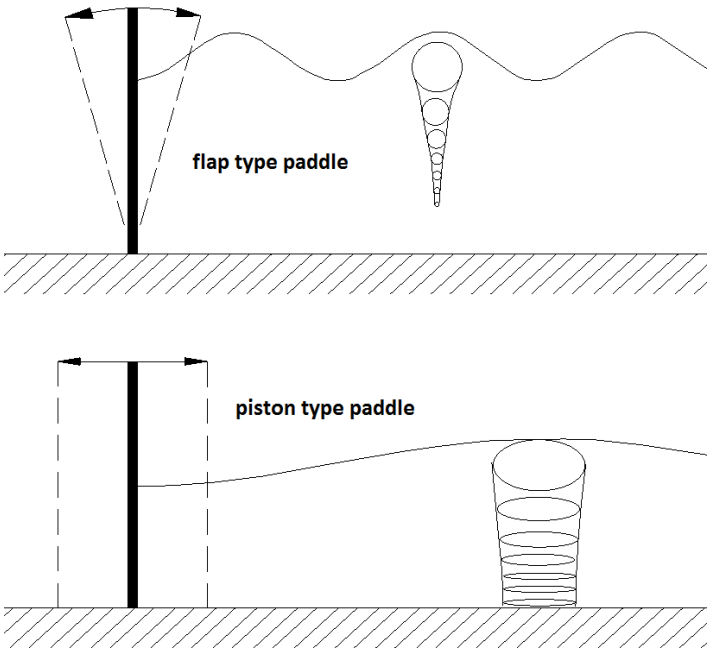

Figure 14 Flap and piston type wave paddles (adapted from Edinburgh Designs Ltd, 2010)

The piston type wave paddles were designed by Edinburgh Designs Ltd and consist of two interconnected shapes that rotate relative to each other (Figure 15). The combination of these two rotations produces a piston motion with a vertical front face, which prevents a back wave to form when the shapes rotate (shown in Figure 14).

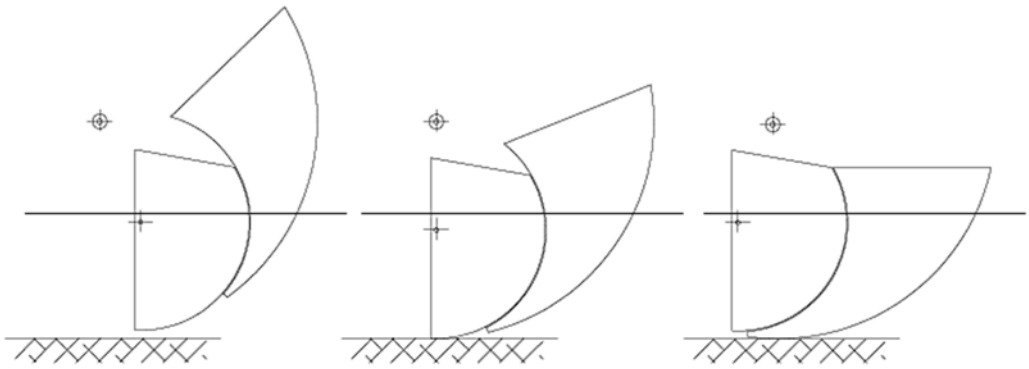

Figure 15 Sketch illustrating how the piston motion is achieved by the Edinburgh Designs Ltd wave paddles

The wave generator paddles in both flumes are capable of acting as wave generators and *active wave absorbers* at the same time. This is useful to reduce the waves reflected from the beaches that reach the wave generator, preventing them being re-reflected into the flume, an thereby allowing tests to run for longer periods of time without the build up of spurious waves.

Figure 16 Piston wave paddle in the 13.4m wave flume

4.2 Instrumentation

Six main parameters were measured during the tests presented in this research: wave run-up, free surface elevations, breaking point location, swash flow depths, swash flow velocities and water table elevations.

Four different instruments were used to measure these parameters. The free surface elevations were measured using *resistance wave gauges*, while *digital pressure transducers* were used to measure the water table elevations inside the permeable slopes. A *Laser Doppler Velocimeter* (LDV) system was used to measure the swash flow velocities and finally, wave run-up, the breaking point location and swash flow depths were measured using commercial *digital video cameras*. These instruments are described below, while the setup of these instrumentation is described in Section 4.4.

4.2.1 Resistance Wave Gauges

The free surface changes in the run-up experiments #1 to #5 shown in Table 13 were measured using resistance wave gauges. This type of wave gauge consists of two parallel wires separated by a fixed distance, which are aligned perpendicular to the direction of the wave travel. A high frequency voltage passes through the wires and the conductance between the wires is recorded. This conductance is proportional to the length of wire beneath the water surface and the conductivity of the water. This way, the changes in free surface elevations are recorded as changes in conductance.

Figure 17 Resistance Wave Gauges

The voltage output of the wave gauges was analysed through a wave monitor (WMPSU1) and a corresponding varying voltage signal fed to a data translation board, DT 9800-BNC (Figure 18). This data acquisition board has a voltage input range of -10 to +10 Volts and was connected to a computer. The QuickDAQ 2014 software was used to visualise and record the output signals of the wave gauges in the computer.

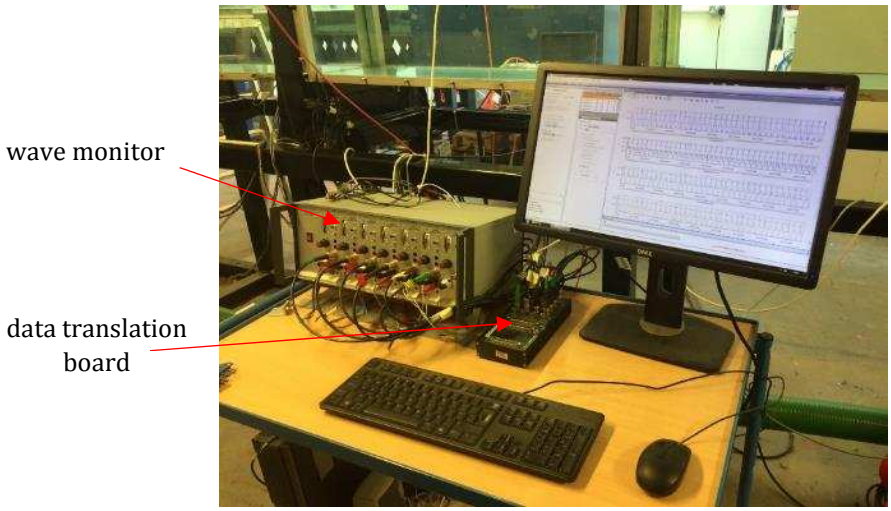

Figure 18 Wave monitor and data translation board used

Calibration of wave gauges. A static calibration was carried out at the beginning of each test to provide a calibration between the voltage outputs from the wave gauges and the depth of immersion of the probes in water. The voltage output from the resistance wave gauges have a linear relationship to the free surface elevation in metres, so the calibrations were performed by raising and lowering the wave gauges (vertically) at known distances. In this case, the known distance was 1cm, which is the distance between the holes observed on the rods holding the wave gauges in Figure 17.

To perform the calibration, the outputs of seven heights from each wave gauge were recorded for 20 seconds: -3, -2, -1, 0, +1, +2 and +3cm (relative to the SWL). The averages of the recorded outputs of each wave gauge at each height were plotted against their corresponding elevations in metres. Finally, conversion equations for each wave gauge were obtained by performing least-squares linear regressions in each graph. Figure 19 shows an example of a calibration graph where the x-axis represent the voltage readings and the y-axis the free surface elevation. This calibration procedure was performed for all the run-up experiments presented in this study.

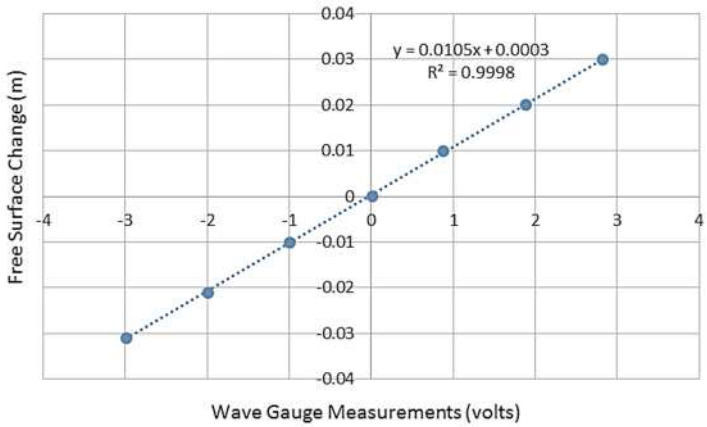

Figure 19 Example of calibration chart for resistance wave gauges

4.2.2 **Digital Video Cameras**

Several measuring techniques can be used to record measurements of the swash hydrodynamics such as wave run-up and swash flow depths. Some of the most common ones are resistance wire gauges, analogue camcorder and geographical information systems (GIS) technology (e.g. Foote and Horn, 1999; Larson and Sunamura, 1982). However, in recent years, digital video recording has become a popular and accepted method for taking measurements of the swash hydrodynamics. This technique was chosen in this project to measure wave run-up, swash flow depths and to record the breaking sequence of the run-up tests.

Three different commercial video cameras were used at the different stages of the test programme. These cameras (shown in Figure 20 and described in Table 14) are part of the laboratory equipment pool and were used depending on their availability.

Figure 20 Video cameras used for run-up and swash flow depths measurements

Video Camera	Specifications
Canon PowerShot S3 IS	1920 x 1080 pixels 65x zoom lens
Sanyo Xacti FH1	448 x 336 pixels 16x zoom lens
Olympus SP-610UZ	1280 x 720 pixels 22x zoom lens

Table 14 Specifications of video cameras

The methods used to measure wave run-up, the breaking point location and swash flow depths using video recordings are discussed below.

Wave Run-up Measurements. The advantages of using digital video imaging of the two-dimensional, cross-shore water surface over conventional analogue video techniques were reviewed by Foote and Horn (2002). Some of these include the removal of the post-capture analogue digital conversion stage and an improved image quality.

Van Broekhoven (2011) and Schimmels et al. (2012) showed comparisons between wave run-up measurements taken with an overhead video camera and with wire gauges placed along the slope for the same set of wave flume experiments. In both studies, the measurements recorded with the video cameras showed higher run-up values than those measured using the gauges. In Schimmels et al (2012) study, the run-up values recorded with the cameras were are 20-35% larger than those recorded with gauges.

The underestimation of the wire gauges might be because the wire gauges require a certain amount of water around the wire to give a good signal. Moreover, the wire itself was placed above the bed surface, so when the uprush water layer became very thin, the run-up gauge could not record a good signal. As a consequence, the wave run-up value was underestimated. An alternative would be to embed the wire gauges into the slope instead of placing it above the slope as performed by Van Broekhoven (2011) and Schimmels et al (2012). However, in small scale experiments, the uprush and backwash water layers are too thin for a wire gauge to record a good signal. As all the tests performed in this study were small-scale, it was decided to measure wave run-up using digital video cameras.

The video technique used in this study to extract the wave run-up values from the recorded videos is the *time-stack* method. This method has been previously used in field studies (e.g. Holland and Puleo, 2001; Vousdoukas et al., 2012) and in laboratory experiments (e.g. Schimmels et al., 2012). The post-processing procedure performed in this study to create the time-stack images and to extract the run-up values is described in Section 4.5.1.

Two camera view options were used in this study to record wave run-up: an overhead and a lateral view. For the overhead view, the video camera is set above the wave flume and the uprush and backwash motions are recorded from on top of the slope. This overhead view, used by Van Broekhoven (2011) and Schimmels et al (2012), has the advantage of visualising the entire swash edge across the width of the wave flume, which can sometimes follow an irregular shape. However, the swash edge might be difficult to visualise from this view, so editing of the time-stack image might be necessary to enhance the contrast.

For the lateral view, the camera is set at one side of the flume and the swash motions are recorded through the side glass walls of the flume. This view, used by Foote and Horn (2002), has the advantage of a clearer visualisation of the swash water surface.

For the experiments carried out in the 20m wave flume, it was not possible to take video recordings from the side of the flume as a concrete column of the laboratory is located just beside the slope of the beaches. For this reason, the only option was to take the measurements using an overhead camera held by a special metal support attached to the cross beams that held the slopes. In order to calibrate the images and extract the data from the recorded overhead videos, a grid was drawn on top of the slope and was used as control markers (Figure 21).

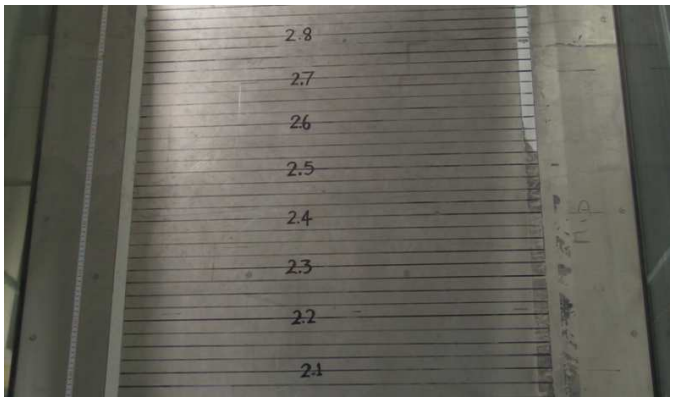

Figure 21 View from the overhead camera showing the grid drawn as control markers

For the tests carried out in the 13.4m long wave flume, the lateral view was achieved by setting the camera on a tripod at one side of the flume and recording the swash lens

through the side walls (Figure 22a). Control markers were drawn on the side wall along the bed slope to calibrate and extract the data from the videos. For clearer visualisation and higher contrast of the water surface, 0.2cm thick white opaque plastic sheets were placed in the background (behind the opposite side wall of the flume). These plastic sheets were illuminated using a series of 30Watt strip lights (Figure 22c, d).

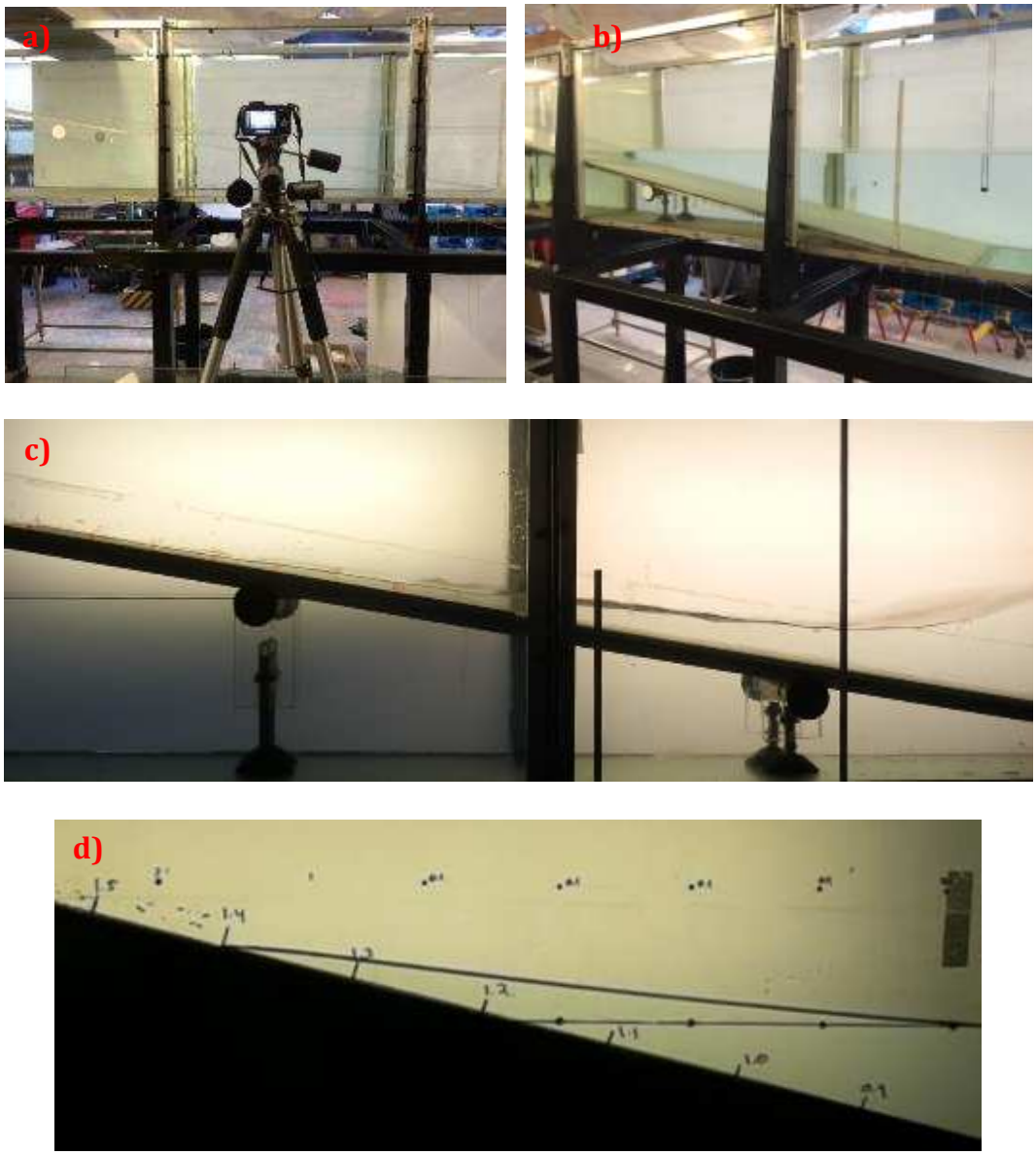

Figure 22 Images showing the lateral video camera, white opaque panels and control markings drawn on the side glass walls of the flume

This same technique of recording the swash motions from one side of the flume was also used to record the sequence of the wave breaking in run-up tests performed in experiment #2 listed in Table 13, as well as to measure the swash depth flows in experiment #6.

Wave Breaking Observations. Video recordings showing waves breaking from one side of the flume were used to assess how the hydraulic conductivity of the slope affects the breaking point location, as well as their breaker types and the breaking criterion. To

analyse these parameters, images were extracted at regular intervals from the side video recordings of the breaking process of a single wave from each test.

Swash Flow Depth Measurements. Experiment #6 listed in Table 13 involved the measurement of swash flow velocities and swash flow depths. The flow depths were measured at the same location where the velocity measurements were taken. As the wave uprush and backwash water depths were very thin, it was not possible to introduce a wave gauge to measure depth. Moreover, if a wave gauge were to be introduced, the velocity measurements would have been affected. For this reason, it was decided to record the swash flow depths using the same method used to measure wave run-up by creating time-stack images from videos recorded from the side of the flume. This measuring and post-processing procedure is described in Section 4.5.2.

4.2.3 Laser Doppler Velocimetry

The clear side glass walls of the 13.4m long wave flume allowed the swash flow velocity measurements to be recorded with a Laser Doppler Velocimetry (LDV) system. These measurements were part of experiment #6 listed in Table 13.

The LDV system is a non-intrusive instrument as it measures flow velocities by focusing laser beam lights at a point in the flow inside the flume, while the laser head remains outside the flume. This is one of the main advantages over other flow velocity measuring instruments such as acoustic probes, pressure probes, or propeller metres. Another advantage over other measuring techniques is the accuracy of its measurements, allowing detailed measurements in the boundary layer. However, it also has some disadvantages when compared to other laser systems such as Particle Image Velocimetry (PIV). The LDV system can only take measurements at a single point, while the PIV system can produce two-dimensional or even three-dimensional vector fields.

LDV Theory. LDV, also known as Laser Doppler Anemometer (LDA), is a laser-based technique that detects the frequency shift of laser light that has been scattered by particles moving in the flow. The motion of the particles in the flow causes a frequency shift (called Doppler frequency shift) in the scattered light relative to the incident light frequency. In other words, the Doppler frequency shift is the difference between the frequency of the incident laser beams and the scattered light frequencies.

The LDV system consists of a laser, an optical system, a photodetector, and a signal processor. The optical arrangement used by the LDV system is the dual-beam approach. This means that light produced by the laser is split into two beams by the optical system and focused by a lens to a point in the flow. The point where the beams intersect is called the *control volume* or *sampling volume* of the velocity (Figure 23).

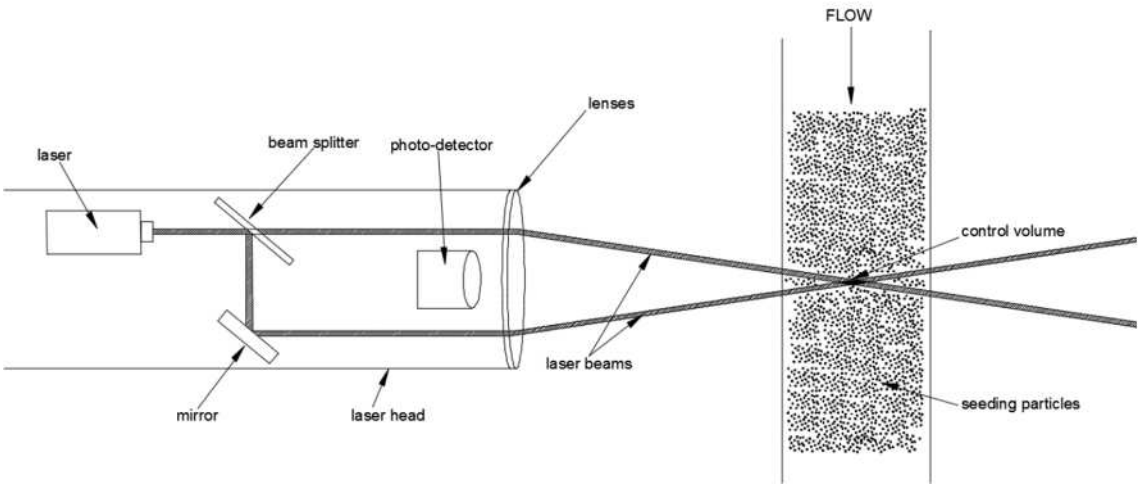

Figure 23 Principle components of a dual-beam LDV system

The intersection of the beams in the control volume creates a fixed pattern of equally-spaced straight fringes (Figure 24).

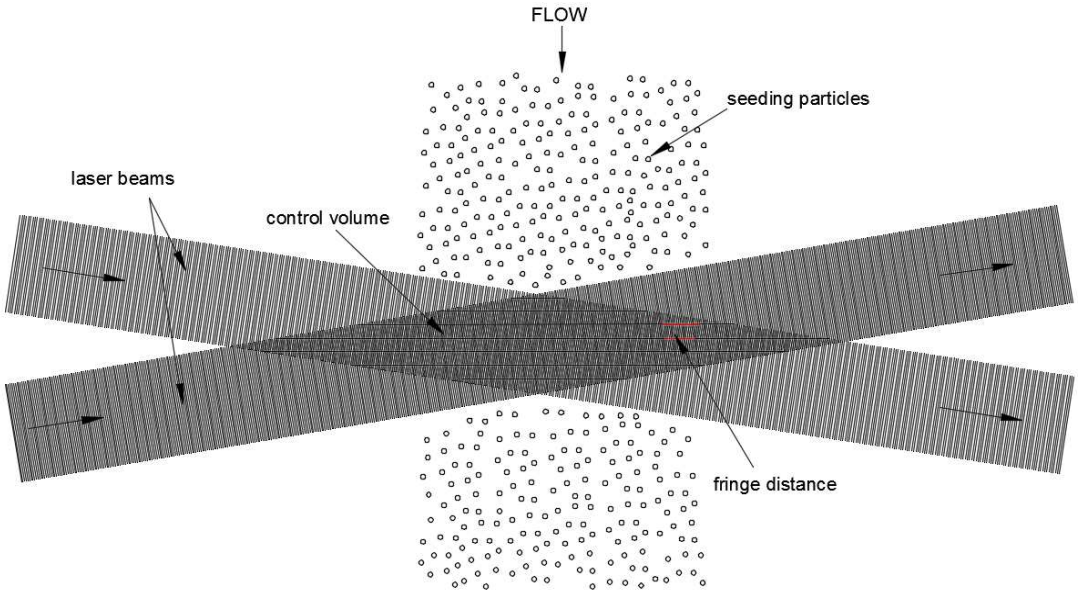

Figure 24 Flow particles passing through the control volume with fixed fringe spacing

As the particles in the flow move through the fringes of the control volume, they illuminate and scatter light, which is detected by the receiving optics and converted into an electrical signal by the photodetector. This electrical signal has a frequency proportional to the particle velocity. The signal processor then converts the variations in signal frequency into voltages, which are then converted to digital form. A more detailed analysis of the LDV theory can be found in Durst et al. (1981).

The LDV system used in these experiments is an INNOVA 70C 5-Watt Argon-ion laser and a two-component TSI laser anemometer. This two-colour (blue and green) dual-beam LDV system allows independent measurements of the horizontal and vertical velocity

components. Table 15 shows the properties of the laser beams used and the sizes of the control volumes.

Laser colour	Beam diameter (cm) $d_{e^{-2}}$, x10^{-3}	Wavelength (cm) λ_l, x10^{-6}	Fringe distance (cm) d_f, x10^{-6}	Volume (cm^3) V_D, x10^{-3}
Green	17	51.45	53	7.66
Blue	68	48.80	50	7.26

Table 15 Laser beam properties and size of control volumes

The optical system was located outside the wave flume, with the laser beams passing through the glass side wall, and the control volume being inside the flume. The scattered light collected by the photodetectors was recorded in backscatter mode, meaning that both the sending and receiving lenses, as well as the photodetector were located in the laser head. Titanium (IV) dioxide was added to the water as seed particles to improve the data burst rate. The collected signals were processed by the TSI IFA-650 signal processor, while a fibre optic cable was used to transfer the laser light beam to the laser head. These flexible and strong cables are capable of transmitting light over long distances with little power attenuation.

The setup and location on the swash zone of the LDV measurements is described in detail in Section 4.4.6, while the derivation of the ensemble-averaged velocities is explained in Section 4.5.3.

4.2.4 Digital Pressure Transducers

To analyse how hydraulic conductivity and wave run-up influence the water table over-height in coastal barriers, six digital pressure transducers were used to measure pore-water pressures, in order to estimate the water table elevation inside the foams. These measurements were taken in experiment #2 listed in Table 13.

The pressure transducers used in these tests were *40PC Series Honeywell*, Vented Gauge (Figure 25). The power of each pressure transducer was supplied by a *Tracopower* transformers (10w, 1 output, embedded switch mode power supply). Each transformer supplied a voltage of 5V to each pressure transducer (Figure 26). The voltage output of the miniature pressure transducers ranges between 0.5 and 4.5 Volts and was fed directly to the same data translation board (DT 9800-BNC) used for the wave gauges (Figure 18) and connected to the computer. Once again, the QuickDAQ 2014 software was used to display the voltage outputs in real time.

Figure 25 40PC Series Honeywell pressure transducer and their power supplier used

Figure 26 Transformers used to supply power to the pressure transducers

As these pressure transducers and power transformers are not waterproof, they were fitted over a matrix board and placed inside individual sealed plastic boxes located outside the wave flume to prevent any water from damaging them (Figure 27 and Figure 28). Each pressure transducer was then connected with silicone tubes (2mm internal diameter) to vertical metallic needles (1.7mm internal diameters) inserted inside the permeable beaches. This technique allowed to be taken measurements on the open head or tip of the needles. Similar techniques using needle tip pressure transducers are commonly used for medical purposes to measure internal body pressures. The setup of these connections, the description of the silicone tubes and vertical metallic needles, as well as their locations are shown in detail in Section 4.4.2.

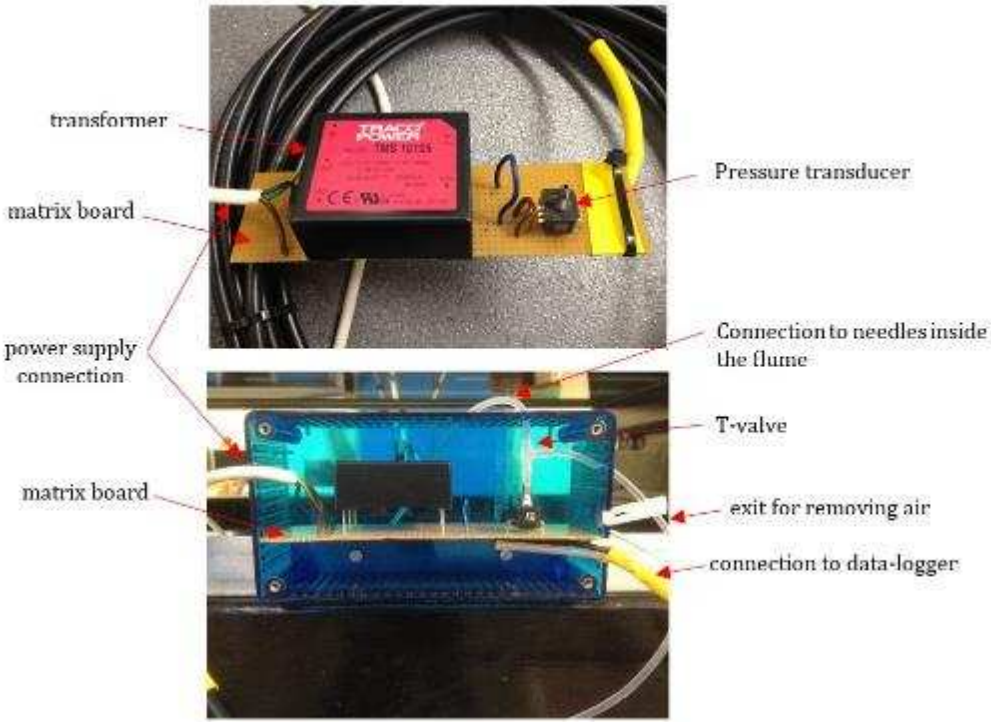

Figure 27 Installation of transformers and pressure transducers over the matrix board and inside the boxes

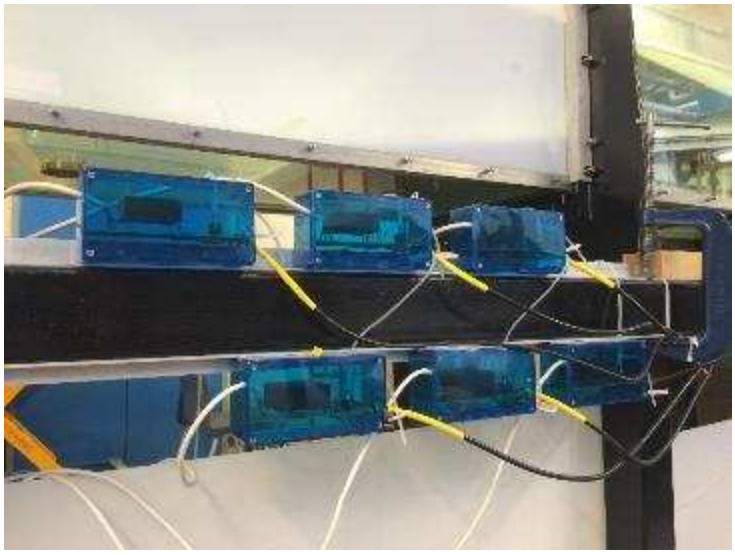

Figure 28 Boxes with the 6 pressure transducers and power suppliers

Calibration of Pressure Transducers. In hydrostatic conditions, the voltage output given by the pressure transducers has a linear relationship with the water table elevation. This is because the pressure is only affected by the weight of the water. Therefore, if the water table elevation is known, a static calibration can be performed to convert the voltage output into water table elevations.

The calibration procedure carried out at the beginning of each test to convert the outputs of the pressure transducers into metres was very similar to the one performed to convert the voltage outputs from the wave gauges into metres. However, instead of raising and

lowering the wave gauges at known heights, this time the water table elevations were raised and lowered by changing the water depths along the flume. In total, the outputs of seven water table elevations were recorded for 20 seconds: -3, -2, -1, 0, +1, +2 and +3cm relative to the SWL. The averages of the outputs of each at each water table elevation were plotted against their corresponding elevations in metres. Finally, least-squares linear regressions were performed to obtain conversion equations for each pressure transducer. As mentioned, these measurements are valid for hydrostatic water levels. However, the run-up tests are not hydrostatic. Therefore, the reduce the hydrodynamic effects, the head of the needles was located high above the bed. This is explained in detail in Section 4.3.2.

4.3 Laboratory and Scale Effects

Physical modelling and small-scale laboratory experiments can offer several advantages over prototype tests such as: easier data collection at reduced costs, controlled conditions and visual feedback. However, laboratory and scale effects can significantly affect the results obtained in small-scale experiments.

4.3.1 Scale Effects

The scale effects are the differences between prototype and model response that arise from the inability to simulate all relevant forces in the model. Wave motion is mainly a gravitational phenomenon. For this reason, most wave models scale the wave parameters and beach/coastal structure dimensions following the Froude scaling criterion. This states that the Froude number, *Fr=u/(gL)^0.5*, should be the same in the model and prototype, where u is a characteristic velocity, g is the gravitational acceleration and L is a characteristic length. Such models should not be distorted, and should be scaled down linearly (commonly known as the geometrical scale). The waves generated in the tests presented in this thesis were not site-specific so were not scaled down from a particular prototype beach. They were generic in purpose as the wave conditions and beach slopes used in these tests were carefully selected with the aim of having a wide range of breaking and non-breaking waves at the beach. Nevertheless, they could be scaled up to a prototype beach following the geometrical scale.

Most two-dimensional model studies involving beaches are carried out to study onshore/offshore sediment transport under the effects of waves or currents. Sediment can be moved along the bed (bedload), as suspended load, or by a combination of both. Therefore, an ideal movable-bed model should be able to maintain similitude for these sediment transport processes. However, if the sediment is scaled geometrically, the model sediment will result in diameters typical of clay. This can introduce a new set of problems as the non-cohesive prototype sediments may be scaled in the model to cohesive

sediments (grain diameter < 0.08mm) and the model would not be a dynamic representation of the prototype (Hughes, 1993). For this reason, to meet the some of the sediment transport similitude criteria, swash zone models generally opt to use sediment with different grain size diameter and different density than the prototype sediment. This technique as well as other commonly used techniques for scaling sediment transport in movable beds are discussed in detail by Hughes (1993). However, the tests presented in this project were carried out using fixed beds, so the sediment transport scaling effects were not a concern.

Model tests carried out on fixed permeable beds are common for modelling coastal structures such as rubble-mound breakwaters. One of the most important scale effects that can occur in models of permeable structures is the viscous forces associated with the porous flow through the structure. At prototype size, the flow within the rubble-mound will generally be fully turbulent (high Reynolds numbers), where the predominant forces are gravity and inertia. A significant scale effect can arise if the flow regime within the porous media is different in the model to that in the prototype structure, as this can lead to a wrong representation of the hydraulic resistance due to the effect of surface tension and viscosity. For this reason, models of rubble-mound structure must have turbulent flow throughout their porous materials.

However, geometric scaling of the porous material will result in less permeable materials which may lead to laminar flows (low Reynolds numbers) where the predominant forces are gravity and viscosity. Geometrically scaled porous materials can also result in a decrease in the wave transmission through the porous structure and can influence wave reflection. To overcome such problems, some studies (e.g. Jensen and Klinting, 1983; Burcharth et al. 1999) have proposed “distorted scaling methods” applied to determine the diameter of the granular material in the model and avoid viscous scale effects. These methods generally yield coarser materials in the model resulting in porous structures with large hydraulic conductivities.

The main aim of the tests carried out on fixed permeable beds was to investigate the influence of hydraulic conductivity on coarse sand to medium gravel beaches, where hydraulic conductivity plays an important role on the swash zone processes. Therefore, the hydraulic conductivities of the porous materials used in this project were within the typical range of these type of beaches. For this reason, it was decided not to apply any type of distorted scaling method to the permeable materials.

4.3.2 Laboratory Effects

The laboratory effects are the differences between prototype and model response that arise from limitations of the laboratory facilities. One of the most significant laboratory effects in a wave flume is that the hydrodynamics are constrained in two-dimensions, which do not occur in nature. However, this constraint was one of the main reasons the run-up tests from the present study were carried out in two-dimensional wave flumes, where the influence of the angle of wave attack can be neglected.

Another laboratory effect in a 2D flume are the re-reflected waves from the wave generator. In nature, the reflected waves from the slope can continue out into the ocean, whereas in a wave flume, these can be re-reflected back towards the beach. To deal this problem, the wave generators used in the experiments implement an active wave absorption technique to detect and absorb unwanted wave energy (discussed earlier in Section 4.1.2).

Two additional laboratory effects were identified for the measurements obtained using the video cameras. Both of these laboratory effects were caused by the side glass walls. The first of these effects occurred when measurements of swash depths were taken from the side of the flume through the glass walls. These measurements can be affected by the surface tension of the water when in contact to the side glass wall as surface tension can slightly increase the location of the water surface. Therefore, the measurements using this technique can show slightly larger values than measurements taken using other techniques.

The second of the laboratory effects caused by the side walls was how the walls affected the propagation of the swash flows, in particular for the uprush motion. When run-up measurements were taken from on-top of the slope, it was seen that in most cases, the wave uprush reached the maximum run-up values at the centre of the slope. However, in some cases, the maximum run-up was seen to occur at near the side walls and not in the centre of the slope. In all cases, the run-up values extracted from the top-view camera were taken at the locations where the maximum run-up was seen. This problem was avoided when the run-up measurements were recorded from one side of the flume, as it was possible to detect the maximum wave run-up, no matter if this occurred at the centre of the slope or near the side walls.

4.4 Experimental Setup and Test Conditions

This section describes the experimental setup and test conditions used for each of the six experiments listed in Table 13.

4.4.1 Preliminary Wave Run-up Experiments

A series of preliminary tests were carried out in the 20m long wave flume described in Section 4.1. The main aim of these tests was to quantify the influence of hydraulic conductivity on wave run-up from breaking and non-breaking waves. To achieve this, wave run-up tests were performed on rough-permeable slopes with different hydraulic conductivities but with the same surface roughness.

As mentioned in the literature review, most wave run-up experiments on permeable beaches have been carried out using beaches made up of coarse sands, gravel or other types of loose sediments. Most of these experiments have been aimed at measuring the beach profile evolution and sediment transport. However, if the beach face is deformed by waves breaking at the slope, its shape and angle will change and consequently the wave run-up will not be constant throughout the tests, even for regular waves. To get more reliable and constant wave run-up values throughout each test, a completely plane, non-deformable permeable beach face was adopted, similar to that shown by Kikkert et al. (2013).

Several materials were investigated and tested to construct the non-deformable permeable beaches for the run-up tests. An extensive search was done to find a bonding material that could bond sediment strongly without affecting its hydraulic conductivity. The analysis of these materials is described in Appendix B. From all the bonding materials tested, only *Elastocoast* was found to bond the aggregates strongly without affecting their permeability. Elastocoast is a bonding system used for coastal protection structures (mainly revetments) which works on the basis of mixing two polyurethane components (isocyanate and polyol).

These tests were planned to be carried out in the 20m long, 1.2m wide wave flume, which is in heavy demand by other students and researchers. Consequently, it was only possible to get access to the wave flume for short periods of time. Constructing the beach out of sediment mixed with Elastocoast and setting it up inside the wave flume would require a considerate amount of time. Furthermore, one of the objectives of the experiment was to carry out run-up tests on different slope angles and on beaches with different permeabilities. This objective would have been tough to achieve if the Elastocoast-sediment mix beach option was chosen. For these reasons, a different alternative material was considered: *reticulated open-cell foams.*

Reticulated open-cell foams are porous and permeable foams that have a homogeneous cellular structure. They are classified depending on their cell size, or their 'pores per inch'

(PPI), commonly ranging from 10 to 100PPI. Figure 29 shows close up pictures of three foams with different PPI values.

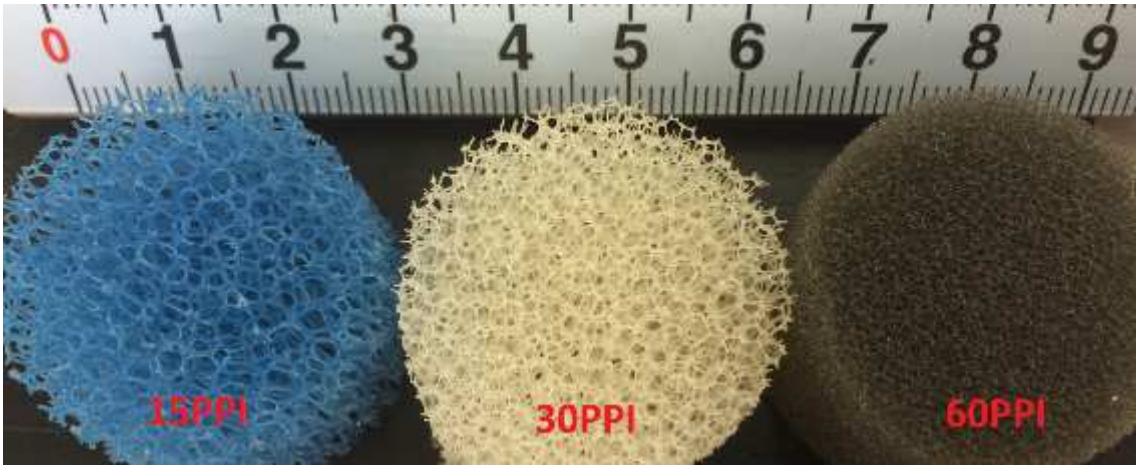

Figure 29 Example of reticulated open-cell foams with different PPI (scale in cm)

Constructing the permeable slopes using reticulated open-cell foams has several advantages over other materials such as:

- *Flat and non-deformable*: by avoiding beach profile evolution, it is possible to focus only on the swash hydrodynamics
- *Easy and quick setup and removal*: it is possible install each permeable beach inside the flume in considerably less time than if a sediment beach was constructed and there is no necessity to rebuild the beach face slope after each test
- *Easy to change the slope angle:* this allows the generation of a wider range of breaking and non-breaking waves at the slope
- *Clean*: no sediment goes into the pipes and pumps of the wave flume, and there is no necessity to clean the flume bed after each test.
- *Homogeneous porosity throughout the entire structure*: no problems with sediment compaction (generally present when using sands) which can affect the porosity and hydraulic conductivity of the material
- *More tests in less time and repeatability of tests*: all of the previous advantages allow more tests to be performed, with less time lost between tests
- *Does not scratch the glass walls of the flume*: as the foams are soft and flexible, there is no risk of scratching the glass walls of the flume. In contrast, gravel or any coarse material can scratch the glass walls, which could affect future experiments involving laser systems or video cameras.

As the aim of the tests was to analyse and include the influence of hydraulic conductivity on run-up formulae, it was necessary to know the hydraulic conductivity, K, of the reticulated open-cell foams. However, companies do not publish this information. Hence,

constant head tests were performed with the aim of estimating the *K* values of foams with different PPI values. Additional constant head tests were carried out for a range of different grain sediments (varying from coarse sands to medium gravels) to compare their *K* values with those of the foams. These results are shown in Appendix A, where the theory of the constant head tests is described as well as the procedure carried out to obtain the *K* measurements in these tests.

Experimental Setup. Four different types of slope were constructed in these experiments: a rough-impermeable beach, and three rough-permeable beaches. To isolate the influence of surface roughness on wave run-up, the slope roughness remained constant in all four types of slope. This was achieved by placing four 2m long x 1.2m wide x 1.5mm thick perforated stainless steel plates (15mm pitch and 10mm hole) on top of the all the slopes (Figure 30).

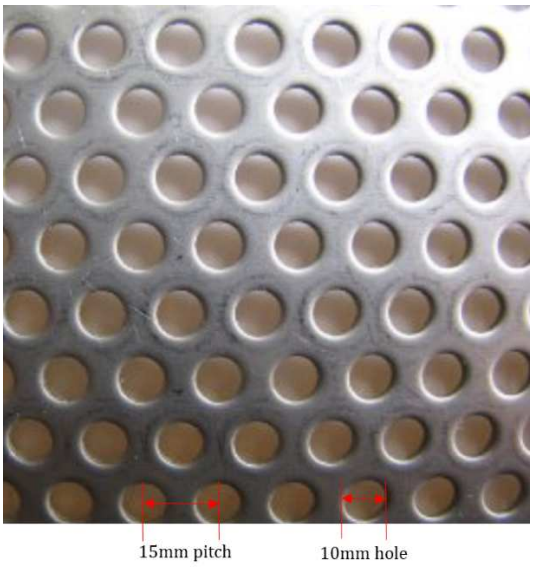

Figure 30 Perforated stainless steel plates with 15mm pitches and 10mm holes

Figure 34 shows the experimental setup for tests performed with a flat, rough-impermeable slope mounted at one end of the flume. The rough-impermeable slope was built by placing the perforated plates shown in Figure 30 on top of an impermeable slope. The impermeable slope was built by inserting 2m wide X 1.2m long smooth stainless steel plates into suspended stainless steel frames inside the wave flume. These suspended frames are held by threaded rods (two at the bottom and two at the top of each frame) which are supported by metal beams that cross the width of the flume. Once the impermeable slope was built, the perforated plates were fixed on top. This procedure is sketched in Figure 31 and pictures of the rough-impermeable slope are shown in Figure 32.

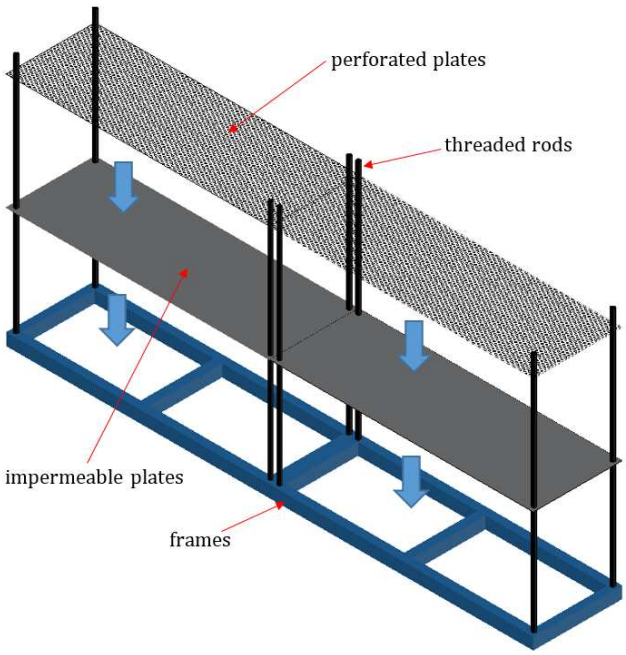

Figure 31 Installation of perforated plates on top of impermeable plates and steel frames

Figure 32 Pictures of rough-impermeable slope using the perforated plates

The threaded rods allowed the heights of the frames to be adjusted, this was used to change the angles of the slope. An inclinometer was used to measure the angle of the slope, while a level was used to make sure both sides of the plates were at the same height.

The rough-permeable structures were mounted at the same location in the flume as the rough-impermeable slope (Figure 35). The perforated stainless steel plates were also placed on top of the permeable beaches, but this time the impermeable panels were removed and the perforated plates were inserted directly into the suspended steel frames, shown in Figure 33.

Due to budget constraints, it was not possible to construct the entire permeable beaches of reticulated open-cell foam. Instead, only the beach face was of reticulated open-cell foam. Therefore, the permeable beaches consisted of a rectangular reticulated open-cell foam block placed directly below the perforated plates and steel frames. These blocks had

dimensions of 2m long, 1.2m wide and 0.4m thick. Each block had to be cut to fit the steel frame and to ensure that the foam lay directly below the perforated plates.

To support the foam block and ensure that the beds remained permeable across the beach, the rest of the beach was packed with hessian sacks filled with Expanded Polystyrene beads (EPS). The hydraulic conductivity of the hessian sacks with EPS beads (K=0.126m/s) was also estimated in the constant head tests described in Appendix A. This beach configuration was designed so that the main parameter affecting the wave run-up was the hydraulic conductivity of the foam and to ensure that the bed remained completely permeable across the swash zone. The angle of the slopes was changed the same way as with the rough-impermeable slopes. This experimental setup is shown in Figure 35.

Figure 33 Rough-permeable slope with block of foam placed below the perforated plates

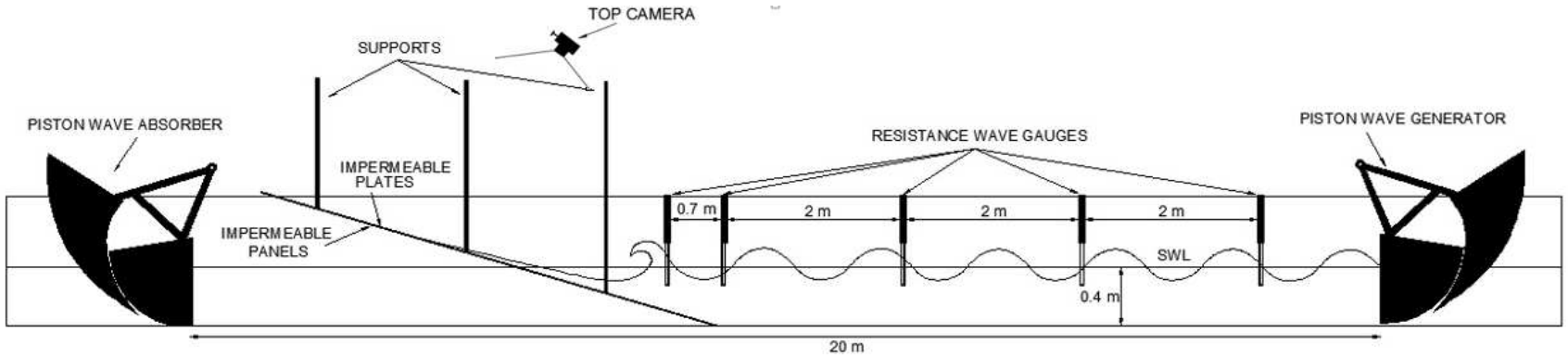

Figure 34 Experimental setup of rough-impermeable slopes using the perforated plates

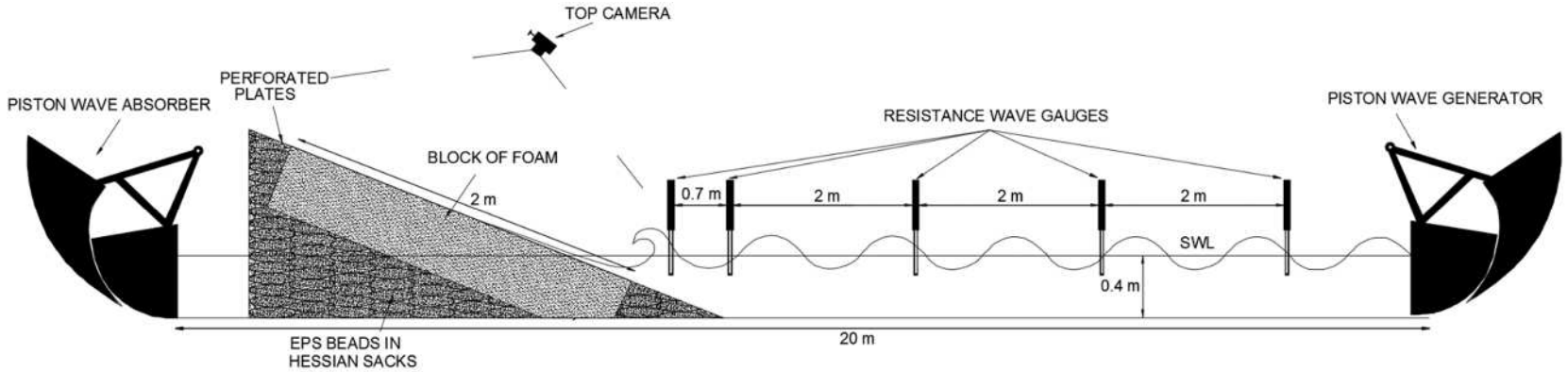

Figure 35 Experimental setup of the rough-permeable slopes using the reticulated open-cell foam blocks

Test conditions. Four different types of slope were tested in these experiments: a rough-impermeable and three rough-permeable slopes with hydraulic conductivities of: 0.0311, 0.105, and 0.401 m/s. These values were similar to the hydraulic conductivities estimated from gravel soils (Appendix A). To obtain data from breaking and non-breaking waves, each type of slope was adjusted to four different angles: 9°, 11°, 13°, and 15°. According to McLean and Kirk (1969), these slope angles are typical for coarse sand and small gravel beaches. A constant water depth of 400mm was used in all the tests and 20 different regular wave conditions were generated for each slope, combining five wave heights (0.06, 0.08, 0.1, 0.12 and 0.14m) and four wave periods (1, 1.43, 2, and 3.33s). In total, 320 tests were carried out.

Discussion. These preliminary tests were undertaken to design non-deformable permeable beaches that could be made within the experimental budget and on time. One of the objectives of these tests was to investigate the influence of hydraulic conductivity on run-up. This was achieved thanks to the design of the experimental setup that isolated the influence of surface roughness and allowed the inclination of the slopes to be changed in a short period of time.

However, two main factors might have affected the results obtained from these tests. The first one was the amount of open space and gaps that lay between the hessian bags. These gaps, which were between 10-40mm, significantly increased the hydraulic conductivity of the beaches, especially at the toe of the beach where it was difficult to pack and accommodate the hessian bags close together. This had a detrimental effect on the analysis when trying to quantify the effect of a specific hydraulic conductivity on wave run-up.

The second factor that affected the magnitude of the wave run-up over the permeable beaches was the use of the perforated plates on top of the permeable materials. The perforated plates were used to provide the same roughness on all the permeable slopes. However, they had 60% of open space (40% was impermeable) as shown in Figure 4.3, which meant that not all the water from the uprush and backwash motions reached the permeable surface of the foams and hessian sacks.

Both of these factors meant that the hydraulic conductivity of the slopes was different from the uniform value measured in the constant head tests. As one of the main aims of this thesis is to derive run-up formulae which include hydraulic conductivity, the results of these permeable tests were not considered in the analysis shown in Chapter 6. Nevertheless, the results of these tests (published in Villarroel-Lamb et al., 2014) gave a good reference point on how hydraulic conductivity influences wave run-up. These tests were also useful in testing and choosing the correct wave conditions and slope angles for subsequent tests on breaking and non-breaking waves at the slope. On the other hand, by

carrying out tests over smooth-impermeable slopes (described in Section 4.4.3), it was possible to analyse and quantify the influence of the surface roughness from the perforated plates on wave run-up.

4.4.2 Wave Run-up on Rough-Permeable Slopes

As the run-up measurements obtained from the preliminary experiments were not used in the final analysis of this study, it was necessary to carry out more tests on permeable slopes to obtain the desired data. After performing the preliminary experiments, it was decided that the best option was to build completely homogeneous permeable beaches using only the reticulated open-cell foams, without using neither the perforated steel plates nor the hessian sacks filled with EPS beads. This with the aim of having slopes with the same hydraulic conductivities of those measured in the constant head tests. Furthermore, as the preliminary experiments provided few run-up data from non-breaking waves, the next set of tests also involved steeper slopes with the aim of obtaining more data from non-breaking waves.

For this reason, a second set of run-up tests on slopes with different hydraulic conductivities were carried out in a smaller wave flume where the entire beach could be built using only foams. These second set of experiments had the aim of not only investigating the influence of hydraulic conductivity on maximum run-up, but also of investigating how this parameter influences the water table over-height, the breaking processes and the swash hydrodynamics. Therefore, the main objective of these second set of experiments was to obtain reliable run-up data on different permeable slopes for breaking and non-breaking waves.

Experimental Setup. These experiments were performed in the 13.4m wave flume described in Section 4.1. Permeable beaches 4m long were installed in the flume with a distance of 8.25m between the piston wave paddle and the toe of the beach (Figure 36).

Four different reticulated open-cell foam types were selected. These had cell sizes of 30, 45, 60, and 80 PPI and hydraulic conductivities of 0.052, 0.086, 0.192, and 0.401 m/s respectively. These hydraulic conductivities (estimated in the constant head tests) are typical for gravel beaches (McLean and Kirk, 1969). To generate a wide range of breaking and non-breaking waves, tests were carried out over three slope angles for each foam: 10°, 20°, and 30°.

The experimental setup was designed to simulate a coastal barrier dividing the ocean from a closed off lagoon system or beach aquifer. This setup is similar to the tests presented by Horn et al. (2007), Masselink and Turner (2012) and Turner et al. (2013).

One of the advantages mentioned previously of using the reticulated open-cell foams is its easy and quick setup and removal from the flume, as well as the ease to change the slope angles of the structures. The foams can be cut in specific shapes by the supplier, and it is easy to assemble and install them inside the flume.

To construct the 10° slope structures, foam blocks of each PPI type with dimensions 2m long x 0.70m high x 0.45m wide (same width as the wave flume) were bought (Figure 37). These blocks were cut into two pieces (pieces #1 and #2 in Figure 37), and arranged as shown below to build the 10° slope.

Additional blocks with dimensions of 2m long x 0.35m high x 0.45m wide were bought to construct the 20° and 30° structures. These blocks were cut in half, again with an angle of 10° between them (pieces #3 and #4). Figure 38 shows how the 20° and 30° slopes were built, by placing pieces #3 and #4 on top of piece #1 of Figure 37.

There was no necessity to add another piece of foam on top of piece #2 and behind pieces #3 and #4 as none of the run-ups tested overtopped the pieces #3 and #4 in Figure 38. Moreover, as the shoreline position with the 20° and 30° slopes moved seawards, the water table inside the foams never reached an elevation higher than 0.32m at the intersection between pieces #1 and #2. This meant that the elevation of 0.35m between these two pieces was more than enough to guarantee that the water table elevation remained inside the foams.

As the foams tend to float when placed in water, Velcro *hook* and *loop* tapes were used to stick the foam pieces into the bottom of the flume and between them. This also prevented any movement or separation of the foam blocks during the tests. Two rows of Velcro hook tapes were glued onto the glass bed of the flume and onto the top of the foam pieces #1 and #3, while two rows of Velcro loop tapes were glued onto the bottom of the pieces #1, #2, #3 and #4 in Figure 38 . The glue from the Velcro tapes was strong enough to be glued onto the glass bed of the flume. However, it was not strong enough to be glued into the foam blocks. For this reason, a synthetic resin in hydrocarbon blend (*Evo-Stick*) was used to glue the Velcro tapes onto the foams. Although the neither the Velcro tapes nor the synthetic resin are permeable, the strips of tape occupy only a small area in the surface of the foams, allowing water to go through between foams, without affecting the hydraulic conductivity of the slopes.

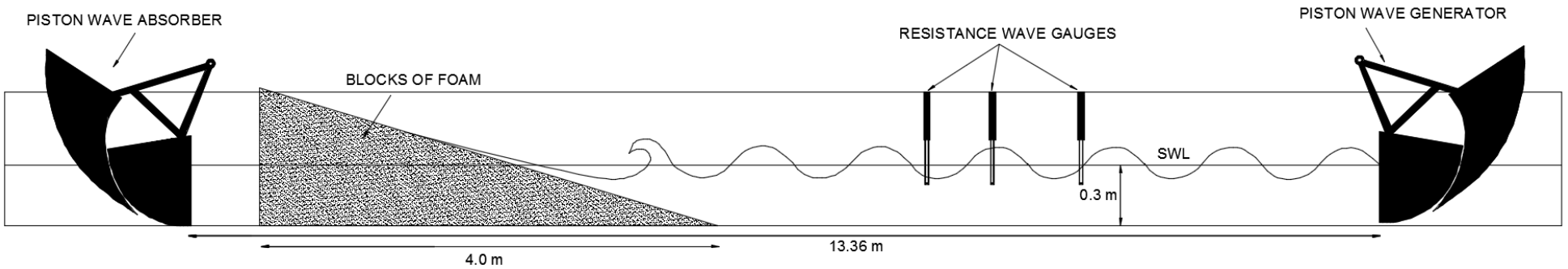

Figure 36 Sketch of permeable slopes inside the 13.4m wave flume

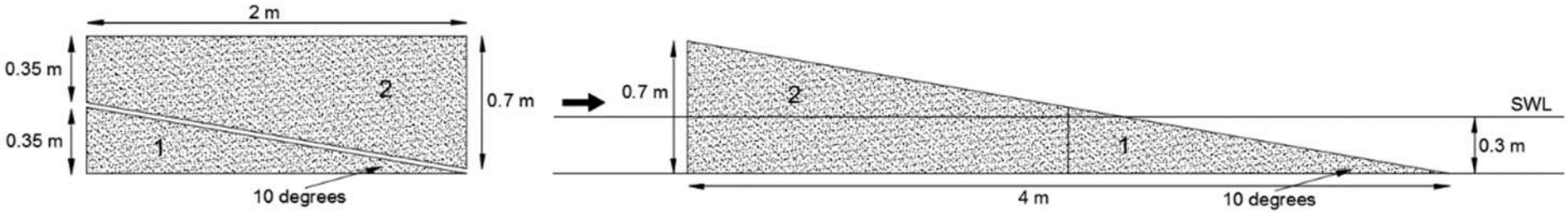

Figure 37 Foam blocks used to build the 10 degrees slope

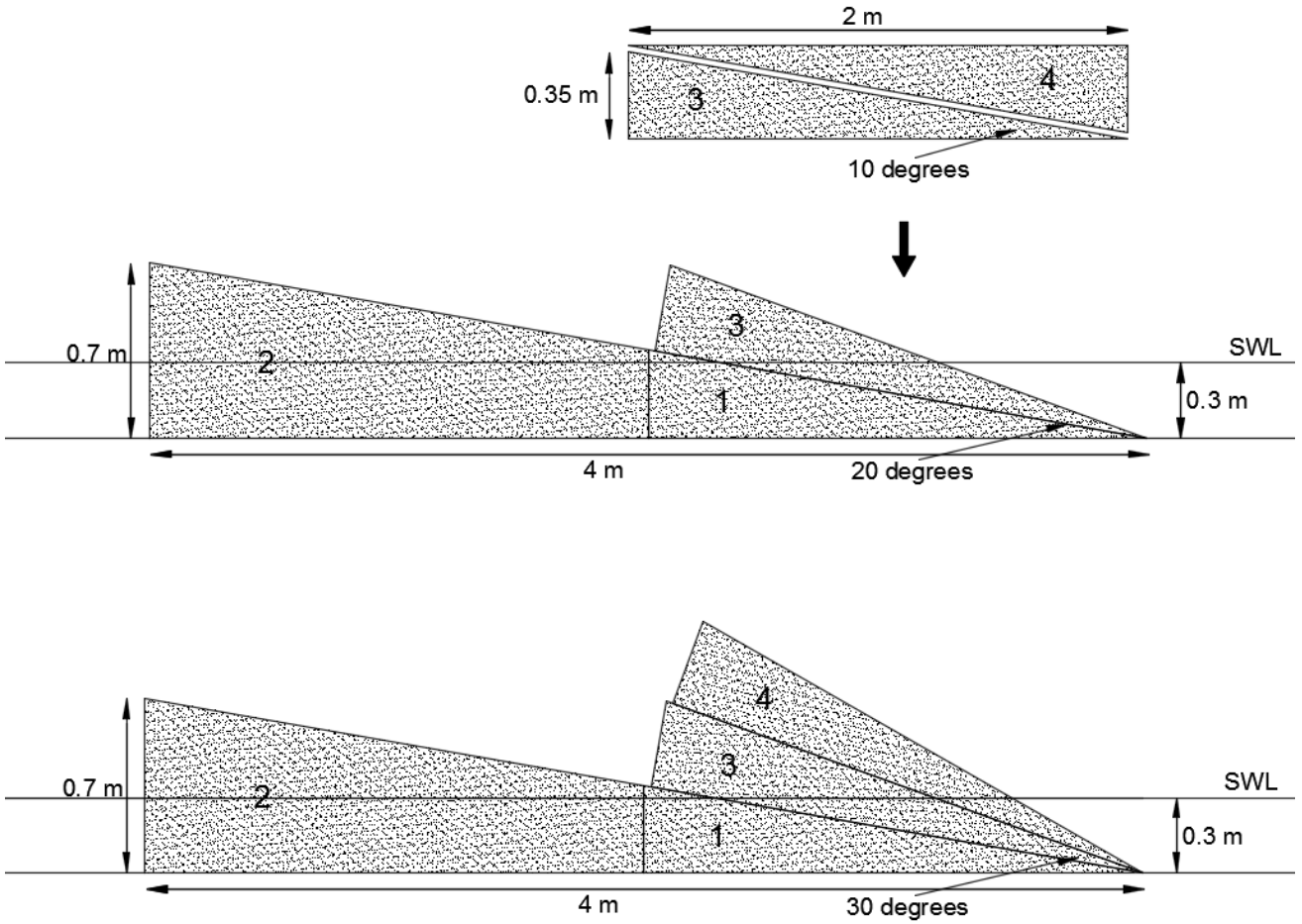

Figure 38 Foam blocks used to build the 20 and 30 degrees slopes

To record pore-water pressure measurements inside the foams, the 6 pressure transducers installed outside the wave flume were connected to vertical metallic needles inserted inside the permeable beaches. These connections (sketched in Figure 39) were made using flexible silicone tubes with an internal diameter of 2mm. Each tube was connected to the top of each pressure transducer and plastic *T-valves* were added to remove all the bubbles of air trapped inside the tubes before the start of each test (see Figure 27).

The plastic tubes were introduced inside the flume through two orifices located in the glass bed of the flume. Two special adaptors, shown in Figure 40, were built to introduce the tubes to the flume, while at the same time preventing water leaking. Each adaptor had capacity to introduce three tubes. Once inside the flume, the plastic tubes were connected to the vertical metallic needles. To prevent the foams from squeezing the tubes, a metallic conduit was built and glued to the bottom of the flume.

In hydrostatic conditions the voltage output given by the pressure transducers has a linear relationship with the water table elevation. However, in hydrodynamic conditions, changes in hydraulic potential with depth may not be linear with the pressure transducer's outputs (Horn, 2006). To reduce the hydrodynamic effects on the outputs, the measurements were taken from a position high inside the foams, and not from the bed of the flume. These measurements were taken from the top opening of the vertical needles at a height of 0.24 from the bed of the flume. This height was selected to ensure that the opening of the needles was always below the variation of the free surface induced by the waves. The vertical needles (internal diameter = 4.27mm) were supported by plastic round base structures, which were glued to the bed (Figure 41). The outlet of the needles was located at one side of the bases; this was connected through the silicone tubes to the pressure transducers. The dimensions of the structures supporting the needles is shown in Figure 41.

To make it easier to install the metallic needles into the foams and to locate the foam over the metallic conduit and orifice adaptors, it was necessary to cut holes in the bottom of the foams to avoid a gap between the foams and the bed. These cuts are shown in Figure 42.

The main objective of these measurements was to estimate the wave-induced maximum water table over-height from each test, which generally occurs near the beach face. Therefore, most of the measurements were taken at positions near the shoreline location. As the shoreline location moves seawards as the angle of the beach increases, the position where the pore-water pressure measurements were taken changed depending on the angle of the beach tested (Figure 43). Some of these locations had to be adjusted due to the

location of the orifice adaptors. The horizontal locations of the 6 metallic needles inside the foams for the 10˚, 20˚ and 30˚ slopes is shown in Figure 43.

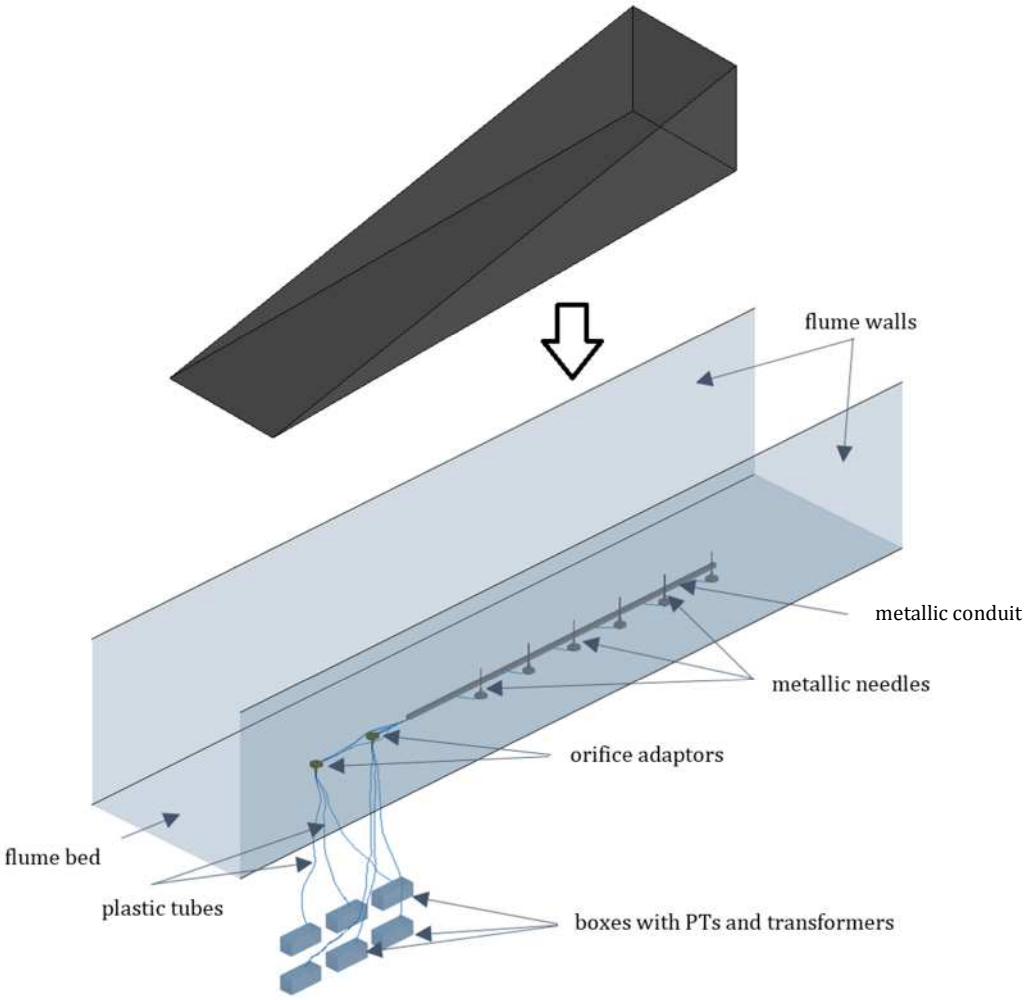

Figure 39 Set up of the pressure transducers

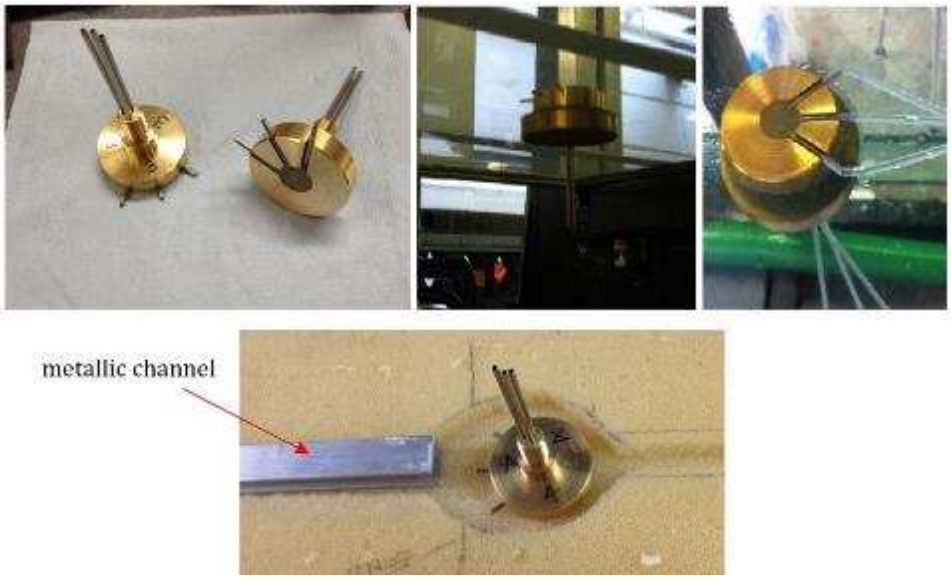

Figure 40 Different views of the adaptors placed at the orifices

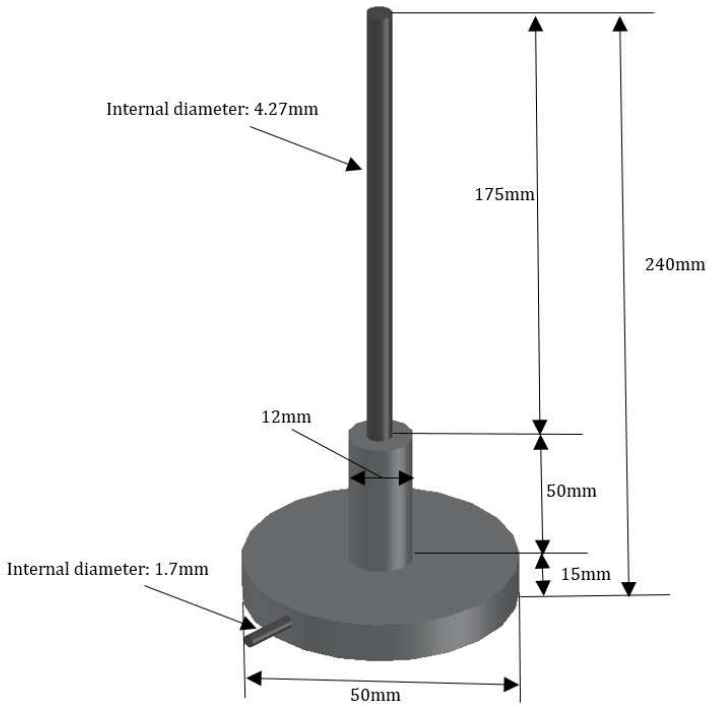

Figure 41 Vertical metallic needles (0.24m height) and base mounting

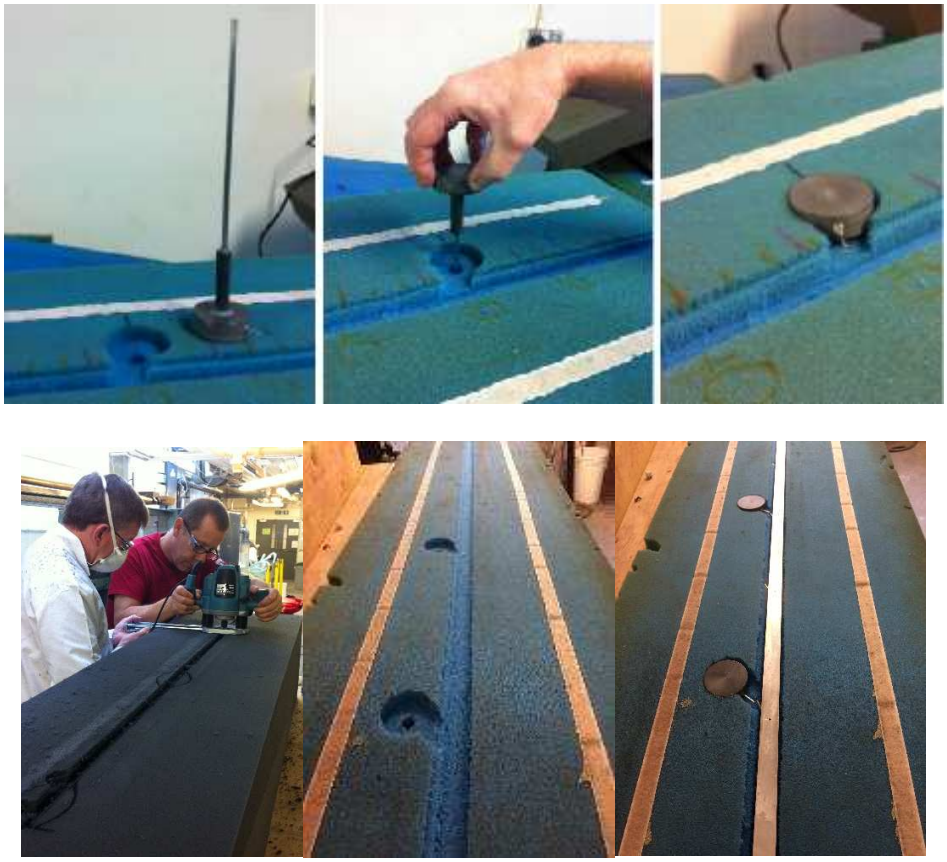

Figure 42 Bottom face of foam beach showing holes cut

Test conditions. Twenty five regular wave conditions combining 5 wave heights (0.04, 0.06, 0.08, 0.1, and 0.12m) and 5 wave periods (1, 1.43, 2, 2.86, and 3.33s) were generated with a constant water depth of 0.3m for every type of slope. Three different slopes were

used (10˚, 20˚ and 30˚) and four different beach hydraulic conductivities (0.05, 0.086, 0.192 and 0.401m/s) giving a total of 300 tests. These combination of parameters produced both breaking and non-breaking waves at the slope.

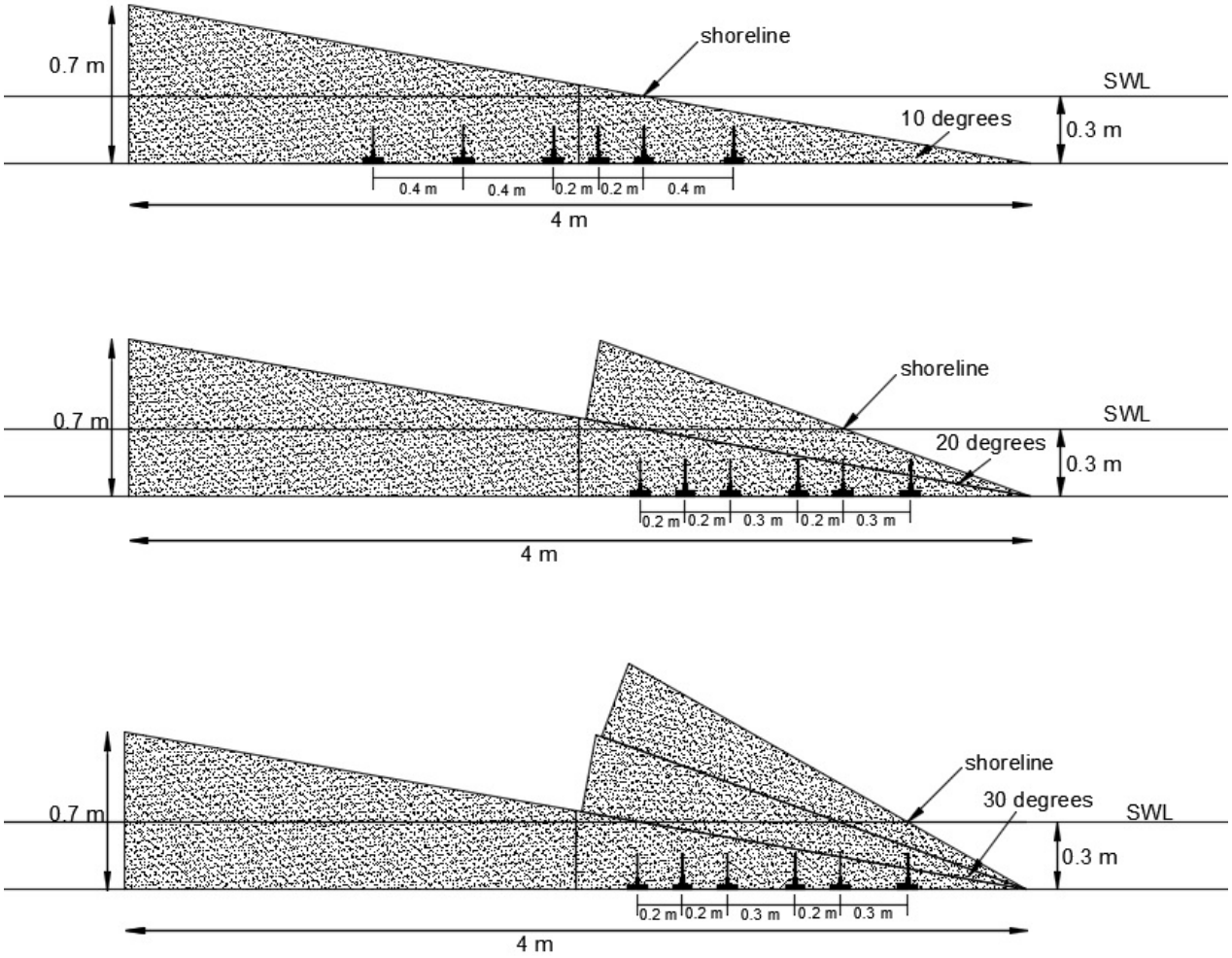

Figure 43 Location of vertical metallic needles inside the foam for the 10˚, 20˚ and 30˚ slopes

4.4.3 Wave Run-up on Smooth-Impermeable Slopes

The third set of run-up experiments were performed on smooth-impermeable slopes with the objective of obtaining run-up data from a wide range of breaking and non-breaking waves. Most of these data were obtained from tests performed in the 20m long flume. Nevertheless, as the tests performed on rough-permeable and rough-impermeable slopes were carried out in the 13.4m long wave flume, for comparison reasons an additional series of tests were carried out on a smooth-impermeable slope in this same flume. In total, 105 regular wave tests were performed on smooth-impermeable slopes in both wave flumes.

Tests performed in the 20m long wave flume

Experimental Setup. The first set of tests on smooth-impermeable slopes were carried out in the 20m long flume. The construction and setup of these slopes is detailed in Section 4.4.1, except it was made without the perforated plates on top.

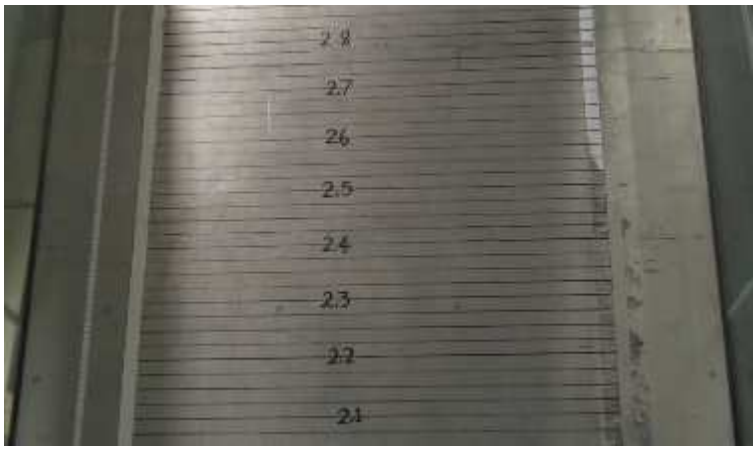

Figure 44 Smooth-impermeable metal plates

Test conditions. These tests were carried out using the same four slope angles used in the preliminary experiments: 7°, 9°, 11°, 13°, and 15°. Although this time a constant water depth of 0.3m was used for all the tests. Regular wave conditions were generated for each of the four slopes by combining wave six heights (0.04, 0.06, 0.08, 0.1, .012 and 0.14m) and wave six periods (1, 1.43, 2, 2.5, 2.86 and 3.33 s). In total, 135 tests were carried out.

Tests performed in the 13.4m long wave flume

Experimental Setup. The second set of tests were performed in the 13.4m wave flume, where a 10˚ smooth-impermeable slope was placed at the same location as the permeable beaches described in Section 4.4.2. This setup is shown in Figure 45 and sketched in Figure 46.

The slope consisted of two impermeable panels secured on top of stainless steel frames. These frames were held by six supports placed in pairs at three different locations below the frames. Once the panels and frames were placed at the desired slope angle, the sides of the panels were glued with silicon for rigidity and to avoid water from the swash motions leaving through the gaps between the walls and the slope. To allow the silicon to dry properly, it was left for twenty-four hours before filling the flume with water to perform the tests.

Figure 45 Smooth-impermeable slope (10 degrees)

Test conditions. For consistency and ease of comparisons, the same incident 25 regular wave conditions and water depth generated for the rough-permeable slopes described in Section 4.4.2 were generated on the 10˚ smooth-impermeable slope.

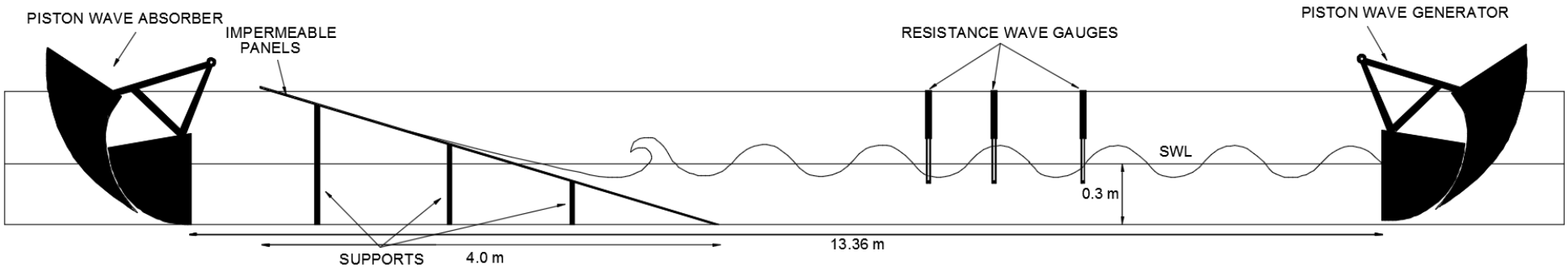

Figure 46 Sketch of the impermeable slopes inside the 13.4m wave flume

4.4.4 Wave Run-up on Rough-Impermeable Slopes

The aim of the fourth set of experiments was to investigate the influence of the different surface roughnesses of the 4 reticulated open-cell foams on run-up. For this tests, the 10˚ impermeable slope described in Section 4.4.3 was faced with the same four reticulated open-cell materials used in the permeable tests of Section 4.4.2.

Experimental Setup. The rough-impermeable slopes were constructed by gluing 3mm thick reticulated open-cell foam sheets on top of the 10° smooth-impermeable slope. Several types of adhesives were tested for gluing the foam sheets into the plates. *3M Display Mount Adhesive* spray was found to be the strongest and most water resistance of all adhesive tested.

Test conditions. For comparison with the results from the smooth-impermeable and rough-permeable tests performed in the 13.4m long flume, the same 25 incident regular wave conditions and water depth for those tests were also used for these tests.

4.4.5 Wave Run-up on Slopes with Varying Water Table Elevations

As discussed in the previous chapters, a low water table elevation favours infiltration by increasing the unsaturated area of a beach. In contrast, a high water table elevation favours exfiltration. These variations in infiltration/exfiltration rates due to water table elevations are expected to influence wave run-up. However, their influence has never been quantified. Therefore, the aim of the fifth set of experiments was to manipulate the water table elevations inside different permeable beaches and measure the wave run-up.

Experimental Setup. These tests were also performed in the 13.4m long wave flume using the same setup described in Section 4.4.2, simulating a coastal barrier dividing the ocean from a closed off lagoon system. To simulate beach groundwater level variations due to tidal drops or beach drainage systems, the water table elevations inside the barriers were manipulated by fixing the lagoon levels either higher or lower than the SWL. To analyse the influence of the water table elevations on run-up, the measurements from these tests were compared to the results from the tests described in Section 4.4.2, where the water table elevations were not manipulated.

The water levels at both sides of the coastal barrier were controlled by a 600 Watt submersible pump (Parkside PTK 600/4) (Figure 47) that recirculated water from one end of the flume to the other. Depending on the direction of the flow of the recirculated system, the pump was introduced either behind the wave generator or behind the wave absorber.

Figure 47 Submersible pump and control valve installed to regulate the recirculated flow

The recirculation system provided a closed loop, with the same amount of water pumped out from one end of the flume as was introduced at the other end. This constant outflow and inflow made it possible to generate a steady flow state through the porous beach, which also generated a head difference along the flume. This head difference depended on the flow rate of the recirculated system and on the hydraulic conductivity of the permeable slopes used. As the submersible pump used operates only at one rate, a T-valve was installed to regulate the recirculation and achieve the desired head differences.

To decrease the water table elevation, the submersible pump was placed behind the wave absorber (the coastal barrier), and through a hose attached along the top of the wave flume, the water was discharged behind the wave generator. This forced the flow in the flume to go from the open sea to the lagoon side (Figure 48). In the other case, to increase water table elevation, the submersible pump was placed behind the wave generator and the water was pumped to the back of the permeable beach (behind the wave absorber), enforcing the water to flow from the lagoon side to the open sea (Figure 49). Table 16 summarises the water depths used for these tests, as well as the recirculated flow rates. These flow rates were measured by using a graduated bucket and a stop watch. Ten measurements were taken for flow rate and the average value was recorded.

Permeable Beach Foam type	Lagoon Water Depth (mm)	Sea Side Water Depth (mm)	Flow Rate (l/s)
80 PPI k = 0.051 m/s	400	300	0.408
	200	300	0.408
45 PPI k = 0.192 m/s	400	300	1.174
	200	300	1.174

Table 16 Water depths and flow rates for tests with varied water table

Test conditions. These tests were carried out using two of the foams types in the tests described in Section 4.4.2: 45 and 80 PPI, with hydraulic conductivities of 0.105 and 0.041 m/s respectively. These foams had a beach face slope angle of 10°. The water depths at the back of the beach (barrier lagoon) were fixed at either 0.1m above or 0.1m below the SWL, while the SWL maintained a water depth of 0.3m. For each case, the same 25 incident regular wave conditions used in Sections 4.4.2 and 4.4.4 were also used for these tests.

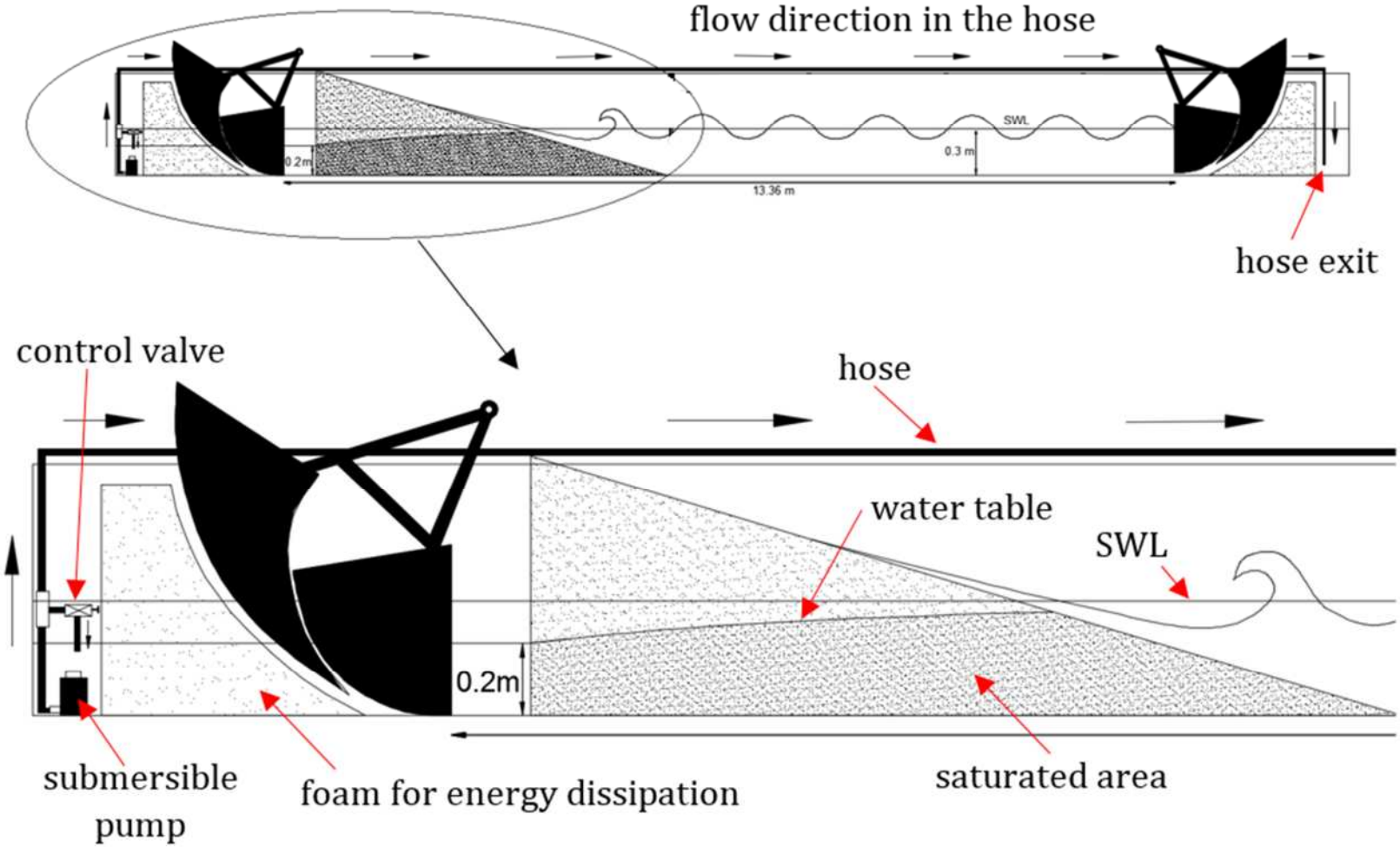

Figure 48 Experimental setup for a low water table elevation with water depths behind the beach = 0.2m; SWL in flume = 0.3m

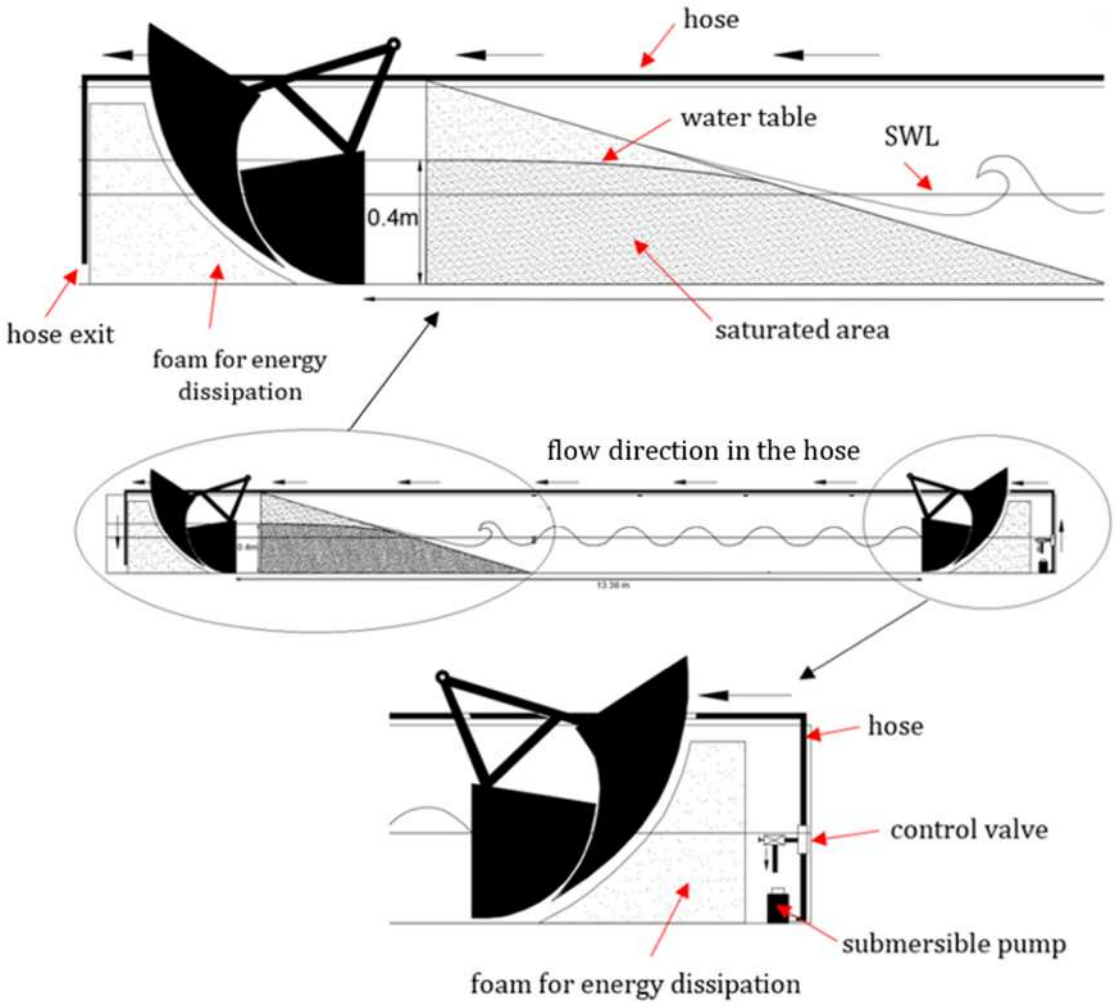

Figure 49 Experimental setup for a high water table elevation with water depths behind the beach = 0.4m; SWL in flume = 0.3m

4.4.6 Swash Flow Depths and Velocity Measurements

The sixth and final set of experiments were aimed at investigating the influence of infiltration on the swash hydrodynamics for a series of regular waves. To achieve this, swash depths and flow velocities were measured over an impermeable and a permeable slope (Figure 50), both having a slope angle of 10˚.

Synchronisation. The flow velocity and swash depth measurements taken by the LDV system and the digital video cameras respectively were synchronised using the QuickDAQ 2014 software. This software allows the specification of a trigger source that starts the acquisition on the devices. As mentioned in Section 4.2.1, the QuickDAQ 2014 software can record the voltage output signal of the wave gauges. Therefore, the voltage signal of one of the wave gauges was used as a trigger to start the acquisition on both devices. In this case, the trigger voltage from the wave gauge was set to be at 0.4 Volts.

Experimental Setup. The experimental setups performed to build these slopes are described in Sections, 4.4.2 and 4.4.3. The permeable slopes were constructed using the 30 PPI reticulated open-cell foams.

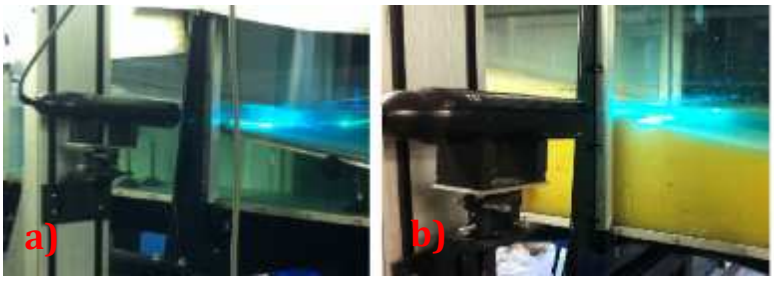

Figure 50 LDV measurements on: a) smooth-impermeable; and b) rough-permeable slopes

Test Conditions. The swash depths and flow velocities measurements were taken to derive ensemble-averaged velocities throughout a swash cycle. As breaking waves can generate a lot of turbulence and air bubbles in the swash zone, which can considerably affect the quality of the LDV measurements, the regular waves investigated were chosen to be long non-breaking waves (H=0.05m and T=4s).

The location in the slope where the velocity and depth measurements were taken was at a horizontal distance of 1.58m from the toe of the slope; this position is located slightly below the SWL (Figure 51). The setup of the LDV system to record the flow velocities at this location is described below.

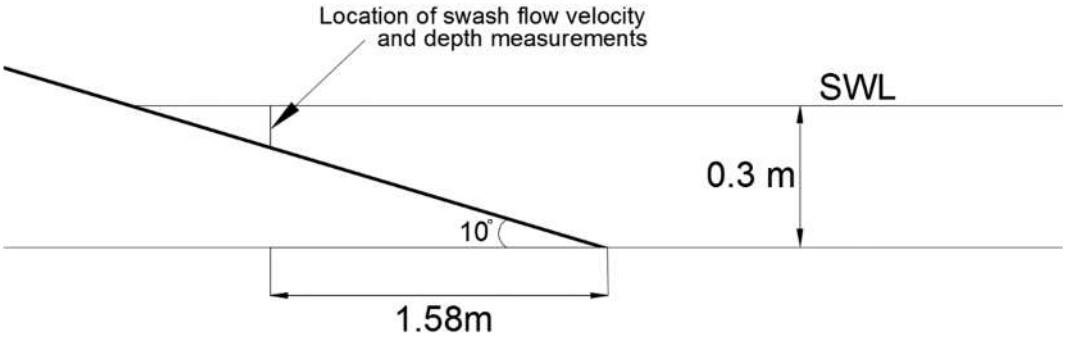

Figure 51 Location in the swash zone where the LDV measurements were taken

As the LDV system only measures flow velocities at a single point, measurements were taken at 30 vertical positions from 0 to 30mm from the bed. The measurements of 50 waves were recorded to derive ensemble-averaged velocities at each vertical position. Ensemble-average means repeating the experiment *n* times at the same spatial location and averaging values at corresponding phases in each wave cycle. Therefore, as the regular waves generated had a wave period 4 seconds, the data sampling length at each vertical position was set to be 200 seconds (50 waves x 4 seconds). After 200 seconds, the traverse was set to move automatically to the next vertical position. The sample frequency was 1000 Hz, which meant that a total of 200,000 velocity measurements were taken at each vertical position (200s x 1000 Hz). The post-processing procedure to derive the ensemble-averaged velocity profiles is explained in Section 4.5.3.

Figure 52 Picture 3-axis TSI traverse

The laser head of the LDV system was mounted on a 3-axis traverse (TSI, model T3D) (Figure 52). This traverse was supported by a mounting base which was levelled and aligned to the side glass walls of the wave flume. Once aligned, the *x* and *y* coordinates were specified to move the control volume to the location were the velocity measurements were taken. The *x*-axis coordinate was set to be at the 1.58m horizontal location from the

toe of the slope specified in Figure 51, while the *y*-axis coordinate was set to be 15cm inside the wave flume (from the inner part of the side wall of the flume). After the *x* and *y* coordinates were specified, the 0 vertical position of the *z*-axis was specified (nearest position to the bed). To do this, the wave paddles were turned on to generate uprush and backwash flows and the control volume was set slightly above the bed. The LDV software displays instantaneous readings and indicates the amount of particles passing through the control volume. Therefore, the traverse was lowered every 0.1mm until no data was displayed. This position was set to be the lowest vertical height of all the vertical positions measured to derive the velocity profiles.

The vertical origins of the velocity profiles were determined using Clauser (1956) method, in which a logarithmic velocity profile is assumed to exist in the boundary layer. Velocity profiles are plotted in a semi-logarithmic graph for various choices of origin and logarithmic regressions are applied to each velocity profile. The origin showing the best-fit is then selected.

4.5 Data Acquisition and Post-Processing Procedures

4.5.1 Wave Run-up (Time-stack method)

Time-stack images were created to visualise the leading edge of the swash as each wave moves up and down the slope in order to extract the maximum run-up values from each wave. The procedure performed to achieve this is displayed in Figure 53 and explained below.

After video recording the wave run-up tests from the side wall, individual images were extracted from the videos at a sample frequency of 10Hz using the *Burst Capture* feature in the *GOM Media* software. Then, an *image stack* with the extracted images was created with the *ImageJ* software. An image stack is a group of still images taken from a fixed viewpoint (with the same *x* and *y* coordinates), but at different regular time intervals (*z*-axis) (one on top of each other, as shown in Figure 53a). Then, the created image stack (Figure 53b) was rotated to visualise the slope of the structure in a vertical position (Figure 53c). With the slope at a vertical position, a 10 pixels wide section along the bed slope was cropped (red rectangle shown in Figure 53c). This narrow section included the front of the bore as well as the control markers drawn along the slope. Finally, the time-stack image was created by displaying the cropped sections (from all the images contained in the image stack) one next to the other (Figure 53d). As can be seen, the contrast created by the illuminated white opaque plastic sheet in the background allowed visualisation of the swash front and maximum run-up values from each wave (Figure 53d). It was not necessary to digitalise the time-stack images to achieve more contrast.

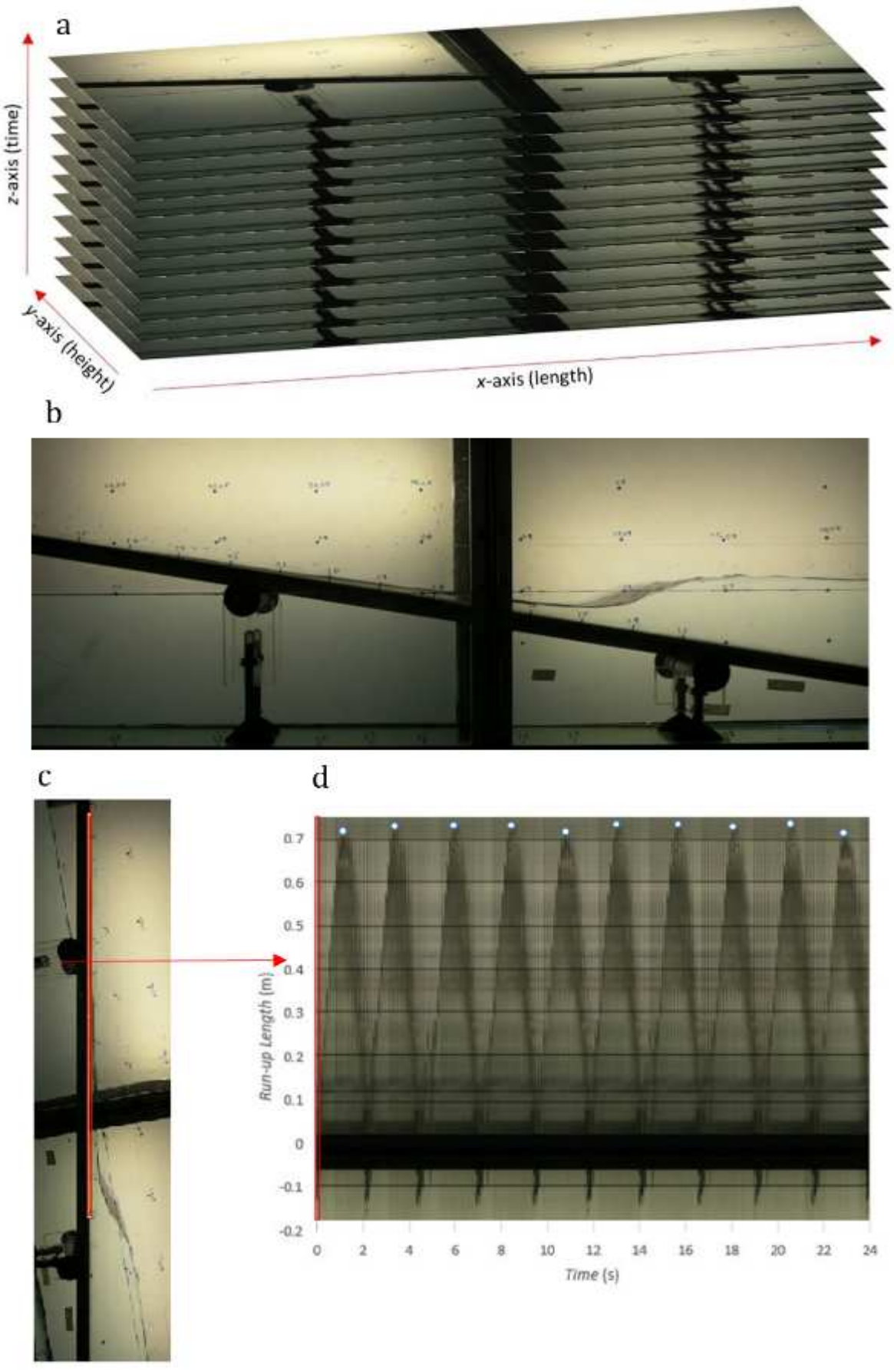

Figure 53 Procedure for extracting time-stack images of the wave run-up

The values for the run-up length were extracted manually by calibrating the dimensions of the *x and y* axes from the time-stack image using a Matlab script called *grabit.m*. The *y*-axis dimensions (representing the *wave run-up length*) were calibrated using the control lines marked on the side glass walls (shown as the horizontal lines in Figure 53d), while the *x*-axis dimensions (representing time) were calibrated knowing that each 10 pixels wide cropped section was equivalent to 0.1 seconds. The wave run-up length is defined as the maximum distance of wave uprush along the slope (Figure 54).

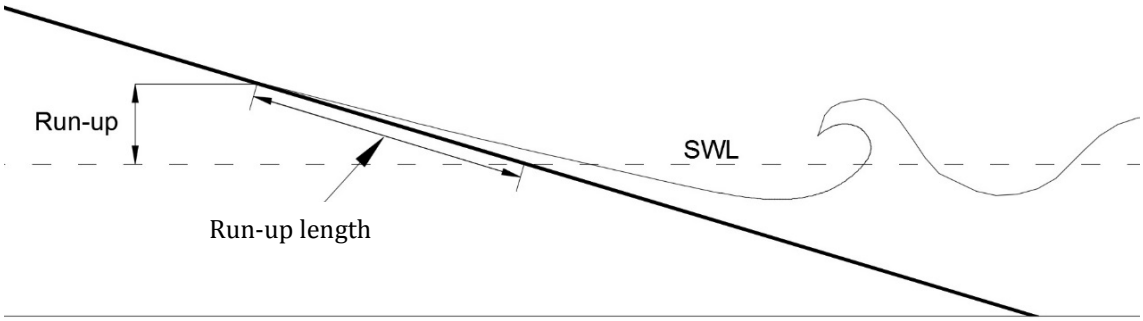

Figure 54 Definition of run-up length

Once the axes dimensions of the time-stack image were calibrated, the maximum values of the swash motion were extracted by locating the maximum run-up point of each wave (white dots shown in Figure 53d). As these dots represent the maximum extent of wave run-up along the plane of the beach, the wave run-up heights (maximum vertical distance above the SWL) were calculated by trigonometry. A similar procedure was adopted to create time-stack images from the overhead videos recorded in the tests performed in 20m long wave flume.

The maximum wave run-up in regular waves can be estimated by averaging the run-up values of several waves. In this study, the run-up values used in the analysis of each regular wave condition was estimated by averaging ten wave run-ups before the effects of re-reflection from the wave generator perturbed the values.

This post-processing technique of extracting run-up values manually from the time-stack images is practical for regular waves, as only a small number of waves need to be averaged. However, this method of manually detecting the maximum run-up values can be very time consuming for irregular waves, where a large number of waves need to be processed in order to have a reliable value of $R_{u2\%}$ (the run-up exceeded by 2% of the incoming waves). For this reason, Vousdoukas et al. (2012) developed a software in MATLAB to automatically extract and process run-up data from time-stack images.

4.5.2 Swash Flow Depth (Time-stack method)

The time-stack method was also used to extract the swash flow depth values from video recordings taken from one side of the flume. This time, a ruler (glued on the glass side wall of the flume) was used to provide control markers to calibrate the *y*-axis dimensions (Figure 55). These measurements were taken at the location where the velocity measurements were recorded with the LDV system (shown in Figure 51). Figure 55 shows the procedure to create the time-stack images, by cropping vertical sections from stack images and placing them one beside each other.

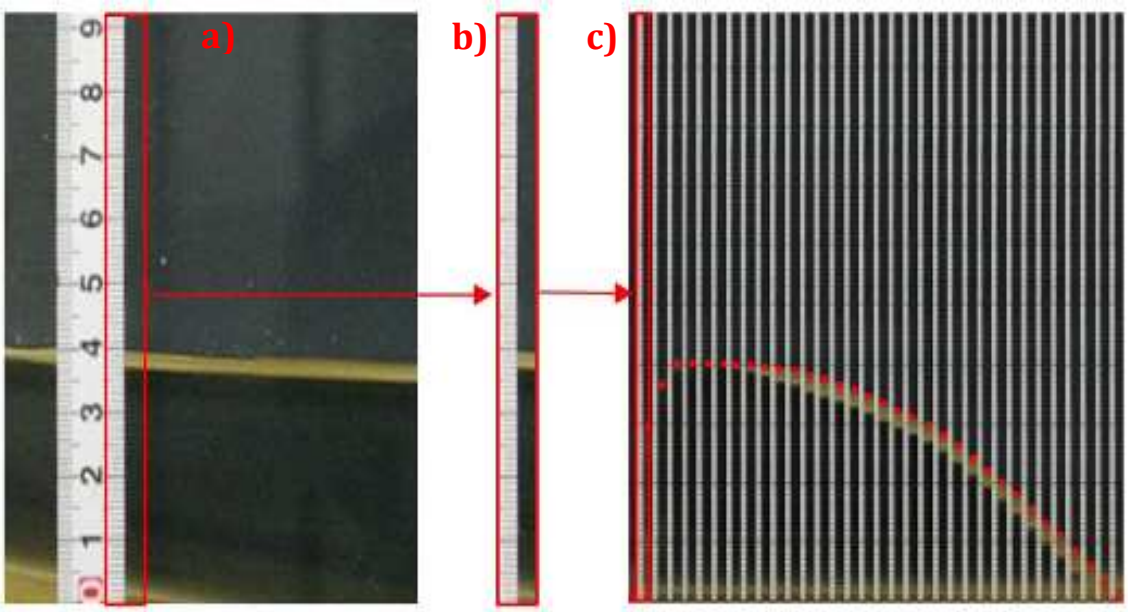

Figure 55 Procedure to extract the time-stack images to obtain the water depth measurements: a) stack image; b) cropped image and; c) time series of water depth

4.5.3 Ensemble-averaged Velocity Profiles

This section describes the procedure followed to derive ensemble-average velocity profiles of the uprush and backwash motions from a series of regular waves.

As mentioned previously, the LDV system only measures flow velocities at a single point. Therefore, to obtain detailed velocity measurements within the boundary layer and derive velocity profiles at the location specified in Figure 51, measurements were taken at 30 different vertical positions from 0 to 30mm (1000Hz at 1mm vertical spacing).

Continuous flow velocity measurements were recorded for 200s to derive *ensemble-averaged velocities* from 50 swash cycles at each vertical position. Ensemble-average means repeating the experiment *n* times at the same spatial location and then estimate the average with respect to *n* times. Therefore, as the generated regular waves had a wave period of T = 4s, continuous flow velocity measurements of 200s long (50 waves x 4s) where taken at a sample frequency of 1000Hz at each height.

Procedure to derive ensemble-averaged velocities at time-steps of 0.001s

The raw output data of the 200,000 velocity measurements (recorded for 200s at 1000Hz) at each height were displayed in a single column. This column contained the measurements of 50 waves (T = 4s) (left-hand side of Figure 56). To derive the ensemble-average values, this column was separated and arranged into 50 columns consisting of 4,000 data measurements each (middle part of Figure 56). Once the data of the 50 waves were arranged, the ensemble-average velocities were estimated by averaging the values of the 50 waves at phase, separated at 0.001s (right-hand side of Figure 56).

raw data velocities		50 WAVES							ENSEMBLE-AVERAGED	
		1	2	3	·	·	·	50	Velocities	Time Step
1		1	4001	8001	·	·	·	196001	X1	0.001
2		2	4002	8002	·	·	·	196002	X2	0.002
3	ARRANGED INTO 50 COLUMNS	3	4003	8003	·	·	·	196003	X3	0.003
4		4	4004	8004	·	·	·	196004	X4	0.004
5		5	4005	8005	·	·	·	196005	X5	0.005
6		6	4006	8006	·	·	·	196006	X6	0.006
7		7	4007	8007	·	·	·	196007	X7	0.007
·		·	·	·				·	·	·
·		·	·	·				·	·	·
·		·	·	·				·	·	·
200000		4000	8000	12000	·	·	·	200000	X4000	4

AVERAGE

Figure 56 Procedure to derive ensemble-averaged velocities with data of 50 waves at each vertical position measured

Recording velocity measurements in the swash zone meant that the control volume was not always fully submerged throughout the entire uprush and backwash motions. Hence, velocity measurements were also recorded when the control volume was outside the water. The data recorded outside the water was easy to identify when plotting the time-series of the ensemble-averaged velocities and could be removed manually (Figure 57).

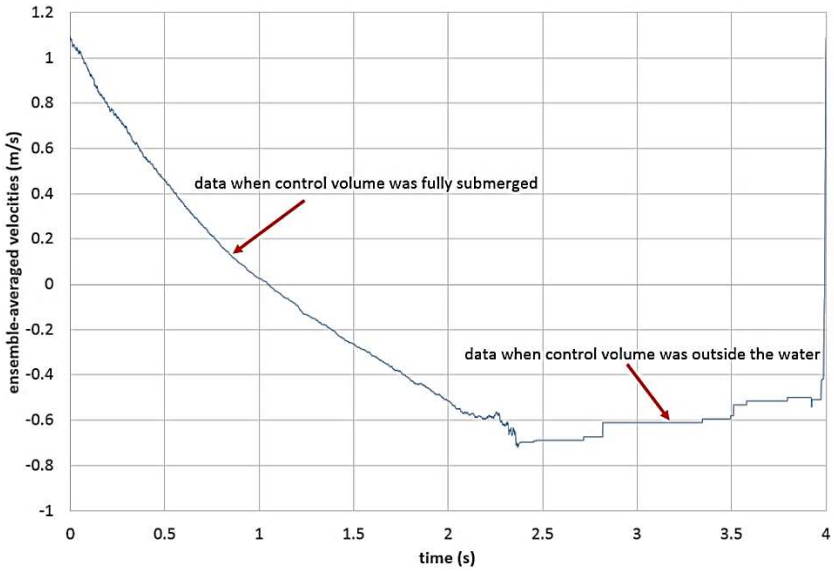

Figure 57 Example of a time-series of ensemble-averaged velocities derived at one of the vertical positions

Most of the time-series of the derived ensemble-averaged velocities contained noise and outliers. Therefore, the data were smoothened and de-spiked using the robust local regression (*rloess*) method in Matlab. This method uses a locally weighted linear least squares regression and a 2nd degree polynomial model to smooth data. The *rloess* method assigns lower weight to outliers in the regression and assigns zero weight to data outside six mean absolute deviations. An example of the raw velocity data (black line) and smoothed data (red line) using this method is shown in Figure 58. This same procedure for deriving and smoothing the ensemble-averaged velocities was performed for all 30 vertical positions.

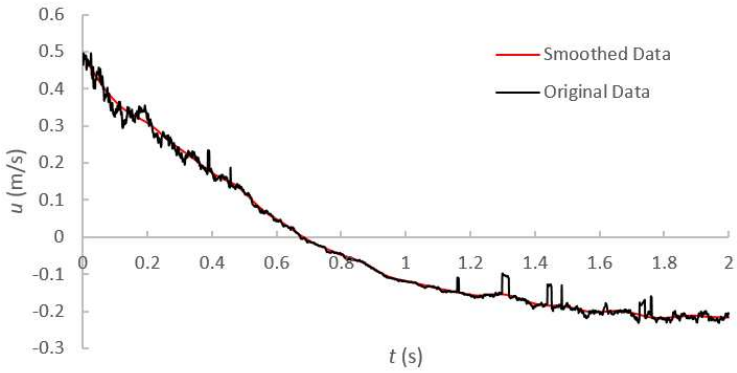

Figure 58 Example of smoothed ensemble-averaged velocity data

As seen in Figure 56, 4000 ensemble-averaged velocities were estimated at each height at time-steps of 0.001s. However, for practical reasons, it was decided to only analyse ensemble-averaged velocity profiles at time-steps of 0.1s throughout the entire swash cycle. Therefore, it was necessary to estimate ensemble-averaged velocities at every 0.1s. These were estimated by averaging the value of the 100 ensemble-averaged velocities contained in each time step of 0.1s. This was done with the purpose of including all the ensemble-averaged velocities estimated at every 0.001s in the analysis.

Once all the ensemble-averaged values at time-steps of 0.1s were estimated for each vertical position, these were arranged according to their vertical position and time-step to derive the ensemble-averaged velocity profiles.

4.5.4 Time-averaged Water Table Elevations

The analogue signal from the pressure transducers was converted into a voltage signal by the data-logger. The data collected by the data logger generated a .txt file showing the time step and the recorded voltage from each pressure transducer.

For each test, the measurements from the pressure transducers were recorded for 120 seconds at a sample frequency of 10Hz. These measurements were converted into metres using the formulae obtained from the calibrations described in Section 4.2.4.

The time-averaged water table elevation at each pressure transducer was estimated by averaging all the converted measurements throughout the 120s. However, the time-averaged water table elevation at each pressure transducer was seen to reach a stable elevation after approximately 25 seconds after the first wave arrived. Therefore, the measurements of the first 30 seconds of each test not included in the calculation of the time-averaged water table elevation. The mean water table profiles were estimated by linking the time-averaged water table elevations estimated with the six pressure transducers.

5 Numerical Simulations

Due to the highly unsteady and depth-variant flow conditions in the swash zone, one of the biggest limitations in the study of sediment transport in this region relates to the challenge of measuring the bottom boundary layer structure (Pintado-Patiño et al., 2015). As discussed in the literature review, a considerable number of field studies have investigated swash flows over permeable slopes. However, due to their uncontrolled environment, field studies cannot offer detailed and consistent measurements inside the swash. To overcome such limitations, recent studies have opted to use numerical models and laboratory experiments under controlled settings with fixed beds to study the boundary layer dynamics in the swash zone. However, most of these studies have been performed on fixed-impermeable beds, with only a few carried out on fixed-permeable slopes (e.g. Kikkert et al., 2013; Pintado-Patiño et al., 2015).

To further investigate the hydrodynamics and the effects of the hydraulic conductivity of the slope on the swash zone boundary layer, this study presents wave run-up simulations performed for impermeable and permeable slopes using a 2D Reynolds-Averaged Navier-Stokes (RANS) model called *IH-2VOF*.

The wave transformation and breaking processes simulated by RANS models have already been validated for a large number of cases (e.g. Lara et al., 2006, 2008, 2011; Torres-Freyermuth et al., 2007, 2010; Pedrozo-Acuña et al., 2010). However, due to the lack of high-resolution velocity measurements inside the swash zone, less effort has been devoted to RANS model validation inside this region. In 2013, Torres-Freyermuth et al. validated the capability of a RANS model to simulate a dam break-driven swash event over impermeable slopes against the ensemble-averaged data presented by O'Donoghue et al. (2010). The model showed reliable predictions of the swash depth, flow velocities, run-up distance and bed shear stresses when compared against the laboratory measurements. More recently, Pintado-Patiño et al. (2015) further validated the RANS model's capability of predicting a dam break-driven swash event, but this time over a permeable bed. They compared the swash depth, flow velocity, run-up distance and bed shear stress measurements presented by Kikkert et al. (2013) on fixed-permeable beds against their simulated data. Their comparisons showed good agreements.

However, the capability of the RANS models to simulate wave run-up from regular waves has not been validated against any laboratory run-up data. To fill this gap, the results from the numerical model were compared against the run-up experiments performed on the smooth-impermeable and permeable slopes presented in the previous Chapter. These

permeable slopes consisted of non-deformable, homogeneous permeable structures, so were ideal for validating the model.

This chapter is organised as follows. Section 5.1 describes the RANS model used and its governing equations used to simulate surface and porous media flow. The porous media equations include a closure model that includes two flow resistance coefficients (α and β) which values need to be defined. These coefficients depend on the porous media and flow characteristics, and thus need to be calibrated against experimental data. Section 5.2 describes the calibration procedure carried out to estimate appropriate values for these coefficients, which consisted of steady flow tests through unconfined porous dams. The setup of the numerical model is then described in Section 5.3 and the results obtained from the model are validated Section 5.4 against the data obtained from the laboratory experiments described in Chapter 4. After the validation of the model, Section 5.5 describes the run-up simulations performed to obtain additional data from regular and irregular waves on smooth-impermeable slopes. Finally, the main outcomes of the chapter are summarised in Section 5.6.

5.1 The IH-2VOF Model

The numerical simulations performed in this study were performed using a 2D numerical model (IH-2VOF). This model is capable of simulating flow through hybrid domains (outside and inside the porous media). The surface flow is modelled by solving the two-dimensional Reynolds-Averaged Navier-Stokes (RANS) equations, coupled with a turbulence closure model. The free surface in the model is tracked by a volume of fluid (VOF) method. One of the main reasons the IH-2VOF model was chosen in this project was because of its capability of simulating flow through porous media. The porous media flow in IH-2VOF is modelled by solving the Volume-Averaged Reynolds-Averaged Navier-Stokes (VARANS) equations, also coupled with a turbulence closure model. These equations include an additional closure model aimed to describe the resistance forces from the porous media.

In the IH-2VOF model, the RANS equations are solved by the finite difference two-step projection method (Chorin, 1968, 1969) and the volume of fluid method (VOF) presented by Hirt and Nichols (1981) is used to track free-surface locations. A detailed description of the governing equations for surface and porous flows and the VOF technique can be found in Lin and Liu (1998), Losada et al. (2008), Torres-Freyermuth et al. (2010) and Lara et al. (2011).

The model includes wave generation boundary conditions capable of generating waves through different methods: internal wave maker, static wave paddle and dynamic wave

paddle. A complete description of these methods can be found in Torres-Freyermuth et al. (2010) and Lara et al. (2011). The model also includes an active wave absorption boundary condition aimed to absorb incident and reflected waves on the boundaries.

As one of the aims of the study was to validate the IH-2VOF model for its use within the swash zone on permeable slopes, the model was set up to replicate the run-up experiments performed on the permeable foams described in Section 4.4.2. However, before setting up the model for the run-up simulations, it was necessary to find appropriate values for the resistance coefficients α and β needed to simulate the flow through the different types of porous foams used in the run-up tests. These values were found by performing a calibration of steady flows through unconfined porous dams which is described below.

5.2 Calibration of Porous Media Resistance Coefficients

To simulate flow through a porous medium, IH-2VOF applies a closure model to describe the resistance of frictional forces, pressures forces and added mass of the porous media. This closure model uses the extended Darcy-Forchheimer equation, which includes linear, non-linear and inertia forces to account for accelerations and is expressed as:

$$I = a\langle \overline{u_i} \rangle + b|\langle \overline{u} \rangle|\langle \overline{u_i} \rangle + c_A \frac{\partial \langle \overline{u_i} \rangle}{\partial t} \tag{67}$$

where "⟨ ⟩" denotes the intrinsic volume averaging operator, I is the hydraulic gradient, $\overline{u_i}$ is the ensemble-averaged flow velocity, a and b are resistance coefficients, while c_A is the added mass coefficient. This last parameter is also referred to as the virtual added mass coefficient or inertial acceleration coefficient proposed by Polubarinova-Kochina (1962) and is given by:

$$c_A = \gamma \frac{1-n}{n} \tag{68}$$

where the empirical coefficient γ which commonly received a value γ = 0.34. The magnitude of the mean component of the velocity in (67), $|\langle \overline{u} \rangle|$, is expressed as:

$$|\langle \overline{u} \rangle| = \sqrt{\overline{u_x}^2 + \overline{u_z}^2} \tag{69}$$

The first term in Darcy-Forchheimer (67) is the linear component and it can be seen as the laminar contribution, while the second term is the quadratic term added by Forchheimer (1901) aimed to model more turbulent flows.

Several authors have proposed formulations to determine values for the coefficients a and b for steady state flow relating them with porosity, n, and mean nominal diameter grain

diameter, d_{50}. In 1964, Ward proposed alternative expressions for a and b relating these parameters with permeability, rather than with porosity and grain diameter. A summary of some of the most common formulations developed to estimate these resistance coefficients is shown in Table 17. The main difference between all these formulations is the power values used for the porosity, n.

Authors	a	b
Ergun (1952)	$a = \alpha \frac{(1-n)^2}{n^3} \frac{v}{d_{50}^2}$	$b = \beta \frac{1-n}{n^3} \frac{1}{d_{50}}$
Engelund (1954)	$a = \alpha \frac{(1-n)^3}{n^2} \frac{v}{d_{50}^2}$	$b = \beta \frac{1-n}{n^3} \frac{1}{d_{50}}$
Ward (1964)	$a = \frac{v}{k}$	$b = \frac{0.55}{\sqrt{k}}$
den Adel (1987)	$a = \alpha \frac{(1-n)^2}{n^3} \frac{v}{d_{50}^2}$	$b = \beta \frac{1}{n^2} \frac{1}{d_{50}}$
Van Gent (1995)	$a = \alpha \frac{(1-n)^2}{n^3} \frac{v}{d_{50}^2}$	$b = \beta \left(1 + \frac{7.5}{\mathrm{KC}}\right) \frac{1-n}{n^3} \frac{1}{d_{50}}$
Burcharth and Andersen (1995)	$a = \alpha \frac{(1-n)^3}{n^2} \frac{v}{d_{50}^2}$	$b = \beta \left(1 + \frac{7.5}{\mathrm{KC}}\right) \frac{1-n}{n^3} \frac{1}{d_{50}}$
Soulsby (1997)	$a = \alpha \frac{(1-n)}{n^{4.7}} \frac{v}{d_{50}^2}$	$b = \beta \frac{1-n}{n^{4.7}} \frac{1}{d_{50}}$

Table 17 Expressions for the resistance coefficients *a* and *b*

In the IH-2VOF model, the formulations used to determine these coefficients are given by:

$$a = \alpha \frac{(1-n)^2}{n^3} \frac{v}{d_{50}^2} \tag{70}$$

$$b = \beta \frac{1-n}{n^3} \frac{1}{d_{50}} \tag{71}$$

where v the kinematic viscosity, while α and β are empirical resistance coefficients. These coefficients depend on the porous media and flow characteristics, so their values must be determined empirically.

Previous Investigations on the Resistance Coefficients α and β. Several studies have proposed values for the two resistance coefficients α and β in the Darcy-Forchheimer equation. However, the values of α and β found in literature depend on the type of porous material and flow regime in which they were calibrated. Furthermore, their values also depend on the formulation used to estimate the resistance coefficients a and b (Table 17). For example, Jensen et al. (2014) suggested values of $\alpha = 500$ and $\beta = 2$ using Van Gent's formulations. Reformulating these values into Burcharth and Andersen's formulation, these coefficients take a value of $\alpha = 2083$ and $\beta = 2$, assuming a porosity of $n = 0.4$.

Table 18 shows a summary of the most relevant studies that have proposed values for these coefficients. The table shows the original values proposed in each of these studies

and the formulation used to estimate them. As the IH-2VOF model is based on Burcharth and Andersen's formulations, this table also displays their equivalent values using these formulations, assuming a porosity of n = 0.4.

The most relevant investigations for the present study which have calibrated these parameters with laboratory experiments are: del Jesus et al. (2012), Higuera et al. (2014) and Jensen et al. (2014). These studies used VARANS models capable of simulating surface flow interacting with porous media flow. The calibration procedure for the resistance coefficients in all three studies consisted of comparing measured data against simulations with different combinations of α and β values. The values from the simulations showing the best agreement with the measured data were recommended.

del Jesus et al. (2012) and Higuera et al. (2014) calibrated the coefficients against the dam break laboratory experiments through a porous medium performed by Lin (1998). Their models were based on Burcharth and Andersen's formulations. In their calibrations, nine simulations were performed with different combinations of α and β values. The values of α were selected as $\alpha = [5000, 10000, 20000]$ and $\beta = [1, 3, 6]$. The best comparison with the experimental results was found to be $\alpha = 10000$ and $\beta = 3$.

Most studies shown in Table 18 derived their proposed α and β values for a particular type of porous media and for a particular flow regime. To overcome part of this problem, Jensen et al. (2014) found a common set of resistance coefficients that worked properly for any type of flow regime. In their study, they presented probably the most complete investigation to calibrate these parameters, using a model based on Van Gent's formulation. They performed calibrations for three different flow regimes: Forchheimer, transitional (between Forchheimer and turbulent) and fully turbulent flow regimes. For each type of flow regime, 25 simulations were performed combining 5 different values of α and β values, and the results were compared against existing experimental tests. For the Forchheimer and fully turbulent flow regimes, simulations of steady flow through a rectangular porous dam were carried out and their results were compared to the experiments presented in Billstain et al. (1999). For the transitional flow, simulations of a simple dam break through a porous media were run and their results were compared to the experiments of Liu et al. (1999). As expected, for the Forchheimer flow the coefficient α was found to be the dominant parameter, as variations of β did not show significant change in the results. The opposite was observed for the fully turbulent flows, with β being the dominant parameter. Following their three calibration cases, a common set of resistance coefficients were proposed: $\alpha = 500$ and $\beta = 2$. These values were shown to describe the flow for Forchheimer and turbulent regimes properly. As shown in Table 18,

reformulating these values into Burcharth and Andersen's formulation, these coefficients take a value of $\alpha = 2083$ and $\beta = 2$, assuming a porosity of $n = 0.4$.

Authors	Original Values		Formulation used	Burcharth and Andersen (1995) Formulation	
	α	β		α	β
Ergun (1952)	150	1.75	Ergun (1952)	625	1.75
Engelund (1954)	1500	3.6	Engelund (1953)	1500	3.6
den Adel (1987)	160	2.2	Den Adel (1987)	667	1.47
DuPlessis (1994)	207	1.88	Ergun (1952)	863	1.88
Van Gent (1995)	1000	1.1	Van Gent (1995)	4167	1.1
Soulsby (1997)	19.8	0.956	Soulsby (1998)	653	4.53
Billstain et al. (1999)	200	1.8	Ergun (1952)	833	1.8
Liu et al. (1999)	200^f 1000^t	1.1	Van Gent (1995)	833^f 4167^t	1.1
del Jesus et al. (2012)	10000	3	Burcharth and Andersen (1995)	10000	3
Higuera et al. (2014)	10000	3	Burcharth and Andersen (1995)	10000	3
Jensen et al. (2014)	500	2	Van Gent (1995)	2083	2

Table 18 Suggested values for the parameters α and β. f = Forchheimer flow and t = turbulent flow

Although Jensen's et al. (2014) calibration performed to find a common set of resistance coefficients for any type of flow regime was very complete, these parameters also depend on the physical properties of the porous medium. Therefore, for the present study, it was necessary to perform a calibration to find the best possible values for the different types of foams used in the run-up experiments.

This calibration followed a similar procedure to those presented by Del Jesus et al (2012), Higuera et al. (2014) and Jensen et al. (2014). The main difference was the materials used in the experiments to calibrate the coefficients (foams in this case). The calibration consisted of comparisons between measured and simulated water table elevations in unconfined porous dams from a series of steady flow tests. The porous dams in the laboratory experiments were set up using the same reticulated open-cell foams used for the run-up tests, while the numerical model was set up to replicate these experimental setups. Several simulations were run with different combinations of α and β values and the coefficients from the simulations showing the best agreement with the measured data were selected to use for the run-up validation cases.

5.2.1 Steady Flow through Unconfined Porous Media

The present laboratory tests performed to calibrate the resistance parameters involved a steady flow through an unconfined porous dam. In these tests, two bodies of water separated by a porous rectangular dam lay above an impermeable bed. A flow through the dam was established by imposing a head difference between the two bodies of water. Steady flow was achieved when the head difference became stable (H and h). At this

moment, the water levels of the two bodies, as well as the water table elevation or free flow surface throughout the porous dam were recorded (Figure 59).

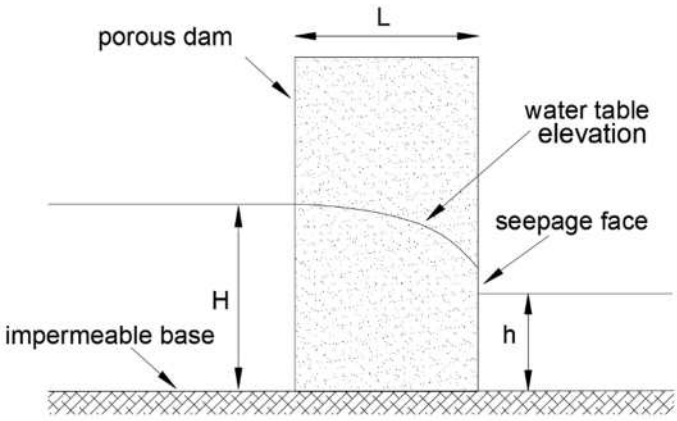

Figure 59 Sketch of steady flow through an unconfined porous dam

5.2.2 Steady Flow Laboratory Experiments

Experimental Setup. The steady flow experiments were performed in the same 13.36m long wave flume where the run-up experiments were carried out. Although this flume has a width of B = 0.45m, these experiments can be treated as two-dimensional tests.

The aim of this calibration was to find the most appropriate resistance coefficients for the four types of permeable foams used in the run-up experiments: R30, R45, R60 and R80. These same foams were used to build porous dams for the steady flow experiments. However, it was not possible to perform steady flow tests with the R60 foams because the material was slightly damaged after the run-up tests, so calibration tests were only performed for the R30, R45 and R80 foams.

As described in Chapter 4, the 10˚ permeable slopes were built from rectangular foam blocks which were cut in two pieces. For the steady flow tests, the two pieces were arranged to form the original rectangular foam block and were used as porous dams, having a base length of L = 0.7m. These were set up in the middle of the flume were supported and held together by lateral wooden plates (Figure 60). Once the porous foam dams were set in the middle of the flume, the entire flume was filled up to a water depth of 0.35m.

Figure 60 Picture of steady flow experiments through the porous foam dam

With the porous foam dam in place and the water depth at 0.35m, the head difference between the two sides of the porous foam dam was imposed through a recirculation system (Figure 61). This recirculation system, similar to the one used for the run-up tests described in Chapter 4, which guaranteed equal inflow and outflow discharges. As the pump used only worked at a single speed, the same discharge or flow rate, Q (m^3/s), was used for all three foams. This discharge was measured at the outlet of the hose with a graduated bucket and a stop watch. As the discharge rate can be affected by the head height of the outlet of the hose, these measurements were taken at the same height used in the tests. Ten time measurements were recorded to fill up a 20 litres bucket for each test. The average measurements gave a discharge value of $0.0024 m^3/s$ for all tests.

The equal inflow and outflow discharges lead to a constant head difference between the two sides of the foam, which enabled the flow to reach a steady state. As the recirculating system discharge was the same for all three foams, the head difference for each foam was only a function of their hydraulic conductivity.

Once the steady flow was achieved, the water depths at both sides of the foam were measured, as well as the water table elevation through the foam dams. This was measured using a digital video camera placed at one side of the flume. Control points were placed on the side glass wall of the flume, and the values were extracted from the images using the Matlab code *grabit.m.* The water table profiles were measured without taking the capillary rise into account.

The experimental conditions are summarised in Table 19. This table displays the water levels (H and h) at both sides of the porous dam for each type of foam, as well as measured discharges. The temperature, T, was also recorded for all tests as the viscosity is a function of the temperature.

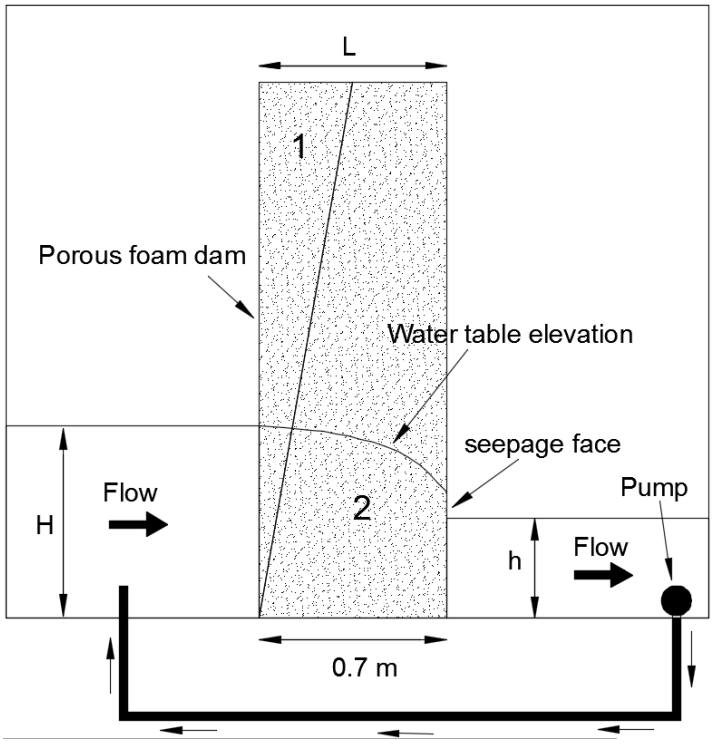

Figure 61 Sketch of recirculated system enforcing the head difference for the steady flow experiments

Foam type	K (m/s)	H (m)	h (m)	T (˚C)	L (m)	B (m)	Q (m³/s)	q_w (m²/s)
R80 PPI	0.051	0.445	0.256	20	0.7	0.45	0.0024	0.0053
R45 PPI	0.192	0.38	0.317	20	0.7	0.45	0.0024	0.0053
R30 PPI	0.401	0.364	0.335	20	0.7	0.45	0.0024	0.0053

Table 19 Experimental conditions of the steady flow tests

Estimated Discharge using Dupuit's Formula for Unconfined Aquifers. Another way of estimating the discharge passing through a section of the porous media is by using Dupuit's formula for unconfined aquifers given by:

$$q_w = K\left(\frac{H^2 - h^2}{2L}\right) \tag{72}$$

where q_w (m²/s) is the discharge per unit width. Bear (1972) showed that the Dupuit's formula is valid for a two-dimensional steady and laminar flow, through a rectangular cross-section with a constant hydraulic conductivity. The present steady flow tests through the foam dams can be seen as an unconfined aquifer. Therefore, this formula was used to validate the K estimates of the foams obtained from the constant head tests performed with the permeameter (described in Appendix A). These K estimates using both methods are shown in Table 20. As can be seen, the K estimates using Dupuit's are in close agreement with those obtained from the constant head tests. This validates both the measurements of Q obtained from the buckets and K measurements obtained from the constant head permeameter (described in Appendix A).

Foam type	K (m/s) Dupuit's Formula	K (m/s) Constant Head Tests
R80 PPI	0.056	0.051
R45 PPI	0.169	0.192
R30 PPI	0.366	0.401

Table 20 Hydraulic conductivity estimates using Dupuit's formula and constant head tests

Flow Velocity through Porous Media. The flow velocity through the porous foams was estimated to determine the flow regime of each experiment. This velocity was calculated using Darcy's Law ($Q = KAi$) and the continuity equation: $Q = Au$, where u is the velocity of the flow. If these two equations are equated, we have:

$$KAI = Au \tag{73}$$

where the hydraulic gradient, $I = \Delta h/L$. Dividing both sides by the cross-section area of flow A:

$$u = K\frac{\Delta h}{L} \tag{74}$$

where u is known as the Darcy velocity. However, the Darcy velocity is not the velocity which the fluid travelling through the pores is experiencing. The real fluid or seepage velocity, v_s, is calculated by adding the porosity, n, of the medium to (74):

$$u_s = K\frac{\Delta h}{nL} \tag{75}$$

Table 21 shows the Darcy and seepage velocities calculated for the three foams.

Foam type	K (m/s)	Δh (m)	L (m)	n	u (m/s)	u_s (m/s)
R80 PPI	0.051	0.189	0.7	0.4	0.016	0.042
R45 PPI	0.192	0.063	0.7	0.4	0.015	0.038
R30 PPI	0.401	0.029	0.7	0.4	0.014	0.034

Table 21 Darcy and seepage velocities

Flow Regimes of the Steady Flow Tests. The parameters α and β in the Darcy-Forchheimer equation depend on the porous media characteristics and flow regime. For a high Reynolds number flow the non-linear coefficient β will control flow resistance, while the linear term α will have a small influence. The opposite will occur for a low Reynolds number, where the linear term α will dominate the resistance.

The flow regimes in porous media are commonly defined by either the Reynolds number based on particle diameter, Re_d, or by the pore Reynolds number, Re_p. These are given by:

$$Re_d = \frac{ud}{\nu} \tag{76}$$

$$Re_p = \frac{ud}{n\nu} \tag{77}$$

where u is the Darcy velocity, d is the particle diameter, n is porosity and v is the kinematic viscosity. For porous media which are not particle-based, such as the reticulated open-cell foams used for the run-up tests, an alternative Reynolds number based on permeability, Re_k, can be used to estimate the flow regimes. This Reynolds number is estimated using the square root of the permeability k (m^2) as the characteristic length instead of the particle diameter, which results in:

$$Re_k = \frac{u\sqrt{k}}{\nu} v_s = K\frac{\Delta h}{nL} \tag{78}$$

Different flow regime boundaries have been proposed using Re_k for flow through a porous medium (e.g. Ward, 1964; Kececioglu and Jiang, 1994; Venkataraman and Rao, 1998; Bağcı et al., 2014). For these tests, the flow regime boundaries proposed by Bağcı et al. (2014) and shown in Table 22 were used to identify the flow regimes of the present steady flow tests. The permeability, k, of the foams was estimated using the hydraulic conductivity, K, measurements and $k = Kv/g$. The results are summarised in Table 23.

Flow Regime	Re_k
Pre-Darcy	$Re_k < 0.02$
Darcy	$0.02 < Re_k < 0.59$
Forchheimer	$1.81 < Re_k < 6.21$
Turbulent	$7.16 < Re_k$

Table 22 Flow regime boundaries using Re_k suggested by Bagci et al. (2014)

Foam type	K (m/s)	k (m^2)	u (m/s)	Re_k	Flow Regime
R80 PPI	0.051	4.09×10^{-8}	0.016	0.99	Darcy-Forchheimer
R45 PPI	0.192	1.96×10^{-8}	0.015	2.14	Forchheimer
R30 PPI	0.401	5.2×10^{-9}	0.014	3.32	Forchheimer

Table 23 Flow regimes for the steady flow tests

5.2.3 Steady Flow Numerical Simulations

The IH-2VOF program only allows the generation of waves at the inlet boundary of the numerical domain. To generate a constant flow at the inlet boundary, the IH-2VOF program has to be modified. This was done by Lopes (2012), where he used this model to analyse wave-current interaction. Another option to simulate steady flow experiments through the porous dams is to use the ihFOAM solver in the computational fluid dynamics (CFD) software OpenFOAM. This software is an open source program that allows the modification of its boundary conditions.

The ihFOAM solver, developed by Higuera et al. (2013a, 2013b), solves the exact RANS and VARANS equations for two incompressible phases, and estimates the resistance coefficients a and b using Burcharth and Andersen's formulations as in the IH-2VOF program. In both models, the free surface is tracked using the volume of fluid (VOF) method. The difference between the two models is how they solve these equations. The

IH-2VOF solves the Reynolds equations using the finite differences two-step projection method, while ihFOAM uses a finite volume discretisation. On a regular grid (squares and rectangles) both methods produce very similar results, although the differential method can be much faster.

Numerical Mesh. The numerical model in OpenFOAM was set up to mimic the laboratory experiments as a two-dimensional domain. However, to decrease the computational time, the total length of the numerical domain was reduced to 2.1m with a height of 0.8m. This numerical domain was created using the mesh generation tool *blockMesh*. The grid resolution was kept constant throughout the entire domain with a uniform cell size of 0.5cm in all directions, giving a total of 67, 200 grid cells in the entire domain. The 0.7m long rectangular porous dam was placed at the centre of the domain and its dimensions were defined using the *boxToCell* function in the *setFields* utility. This gave a length of 0.7m on the upstream and downstream sides of the porous dam (Figure 62).

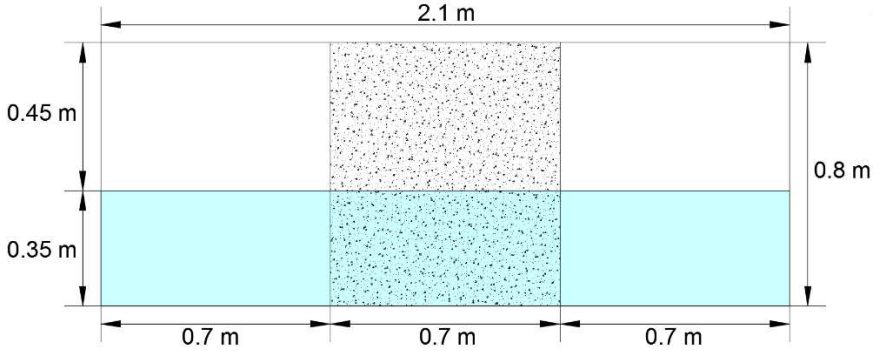

Figure 62 Dimensions of numerical domain with initial water depth and porous dam

Initial and Boundary Conditions. Once the mesh was created, the initial and boundary conditions were specified. The initial water depth of 0.35 used in the laboratory experiments was used as initial free surface elevation in all the simulations (Figure 63). This free surface elevation was defined using the same *boxToCell* used to define the dimensions of the porous dam.

In order to accurately replicate the physical behaviour of the tests, the boundary conditions had to be selected carefully. The numerical domain consisted of five boundaries: inlet, outlet, atmosphere, bottom and frontAndBack. The location of these boundaries is shown in Figure 63.

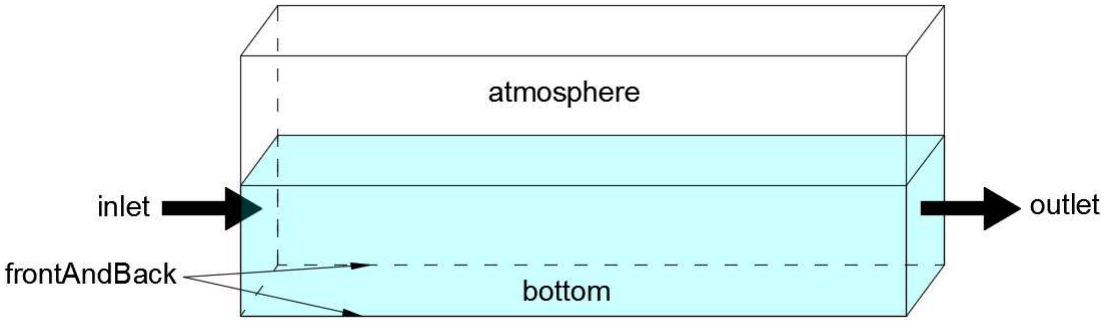

Figure 63 Name of boundary conditions of the numerical domain

The following variables that needed boundary conditions to be specified in the simulations are: *alpha1*, *U*, *p_rgh* and *porosityIndex*. *Alpha1* is the VOF function used to determine the quantity of water present in each cell, *U* is the velocity field, *p_rgh* is the dynamic pressure and *porosityIndex* is used to define the porous media. The boundary conditions used for each variable at each boundary are summarised in Table 24.

Boundary	*alpha1*	*U*	*p_rgh*	*porosityIndex*
inlet	IH_Waves_InletAlpha	IH_Waves_InletVelocity	bouyantPressure	zeroGradient
outlet	inletOutlet	zeroGradient	bouyantPressure	zeroGradient
bottom	zeroGradient	fixedValue	bouyantPressure	zeroGradient
atmosphere	inletOutlet	pressureInletOutletVelocity	totalPressure	zeroGradient
frontAndBack	empty	empty	empty	empty

Table 24 OpenFOAM boundary conditions for the steady flow simulations

The frontAndBack boundary represents both the front and back of the wave tank. In order to allow OpenFOAM to solve for two dimensions only, an "empty" boundary condition is given for all the variables in this boundary.

As the target inlet free surface elevation and flow discharge per unit width (q_w = 0.0053 m²/s) were known, it was possible to define a fixed flow velocity entering the domain for each test. These constant or fixed velocities were specified in the *IH_Waves_InletVelocity* boundary condition for the velocity variable, *U*, and are shown in Table 25.

Foam type	q_w (m²/s)	Target Inlet Height (m)	Fixed Velocity v (m/s)
R80 PPI	0.0053	0.445	0.0119
R45 PPI	0.0053	0.38	0.0139
R30 PPI	0.0053	0.364	0.0146

Table 25 Fixed inlet velocities for each test

Equivalent Mean Nominal Diameter and Porosities for the Porous Foam Dams. The first part of the calibration consisted of finding optimal mean nominal diameter, d_{50}, and porosity, *n,* values for each type of foam. As the reticulated open cell foams have no grain particles, it was necessary to find equivalent d_{50} values to use as inputs for the model. These values could have been estimated using empirical equations that relate grain size diameter and porosity with the permeability of the material (discussed in Chapter 2). However, for these simulations, the values of parameters were obtained from additional

permeameter tests performed on several very well sorted and uniformly graded granular soils. The d_{50} values of the soils having the closest hydraulic conductivity values to those obtained for the foams were selected and used as representative or equivalent values for each type of foam.

These are shown in Table 26, along with the hydraulic conductivity of the soils and of the foams obtained from the permeameter tests.

Soils Grain Size Range(mm)	d_{50} (mm)	K (m/s)	K (m/s) of Foam
Fine Gravel (4.0-5.0)	4.5	0.047	R80 = 0.051
Medium Gravel (6.0-7.0)	6.5	0.163	R45 = 0.192
Medium Gravel (9.4-13.0)	11.3	0.488	R30 = 0.401

Table 26 Equivalent grain sizes and porosities for the foams

The porosities of the reticulated open-cell foams, measured in the laboratory and shown in Table 27, are significantly more porous than granular soils with similar hydraulic conductivities. Granular soils with similar hydraulic conductivities tend to have porosities $n \approx 0.4$. The formulations of the porous media resistance coefficients a and b used in the model relate hydraulic conductivity with porosity and grain size. However, these formulations were derived from experiments carried out on granular soils (with significantly lower porosities than those of the foams). Therefore, introducing the porosity values of the foams shown in Table 27 as inputs in the model would lead to inaccurate results. For this reason, the simulated porous media of the foams were assumed to have a porosity of n = 0.4, which was the porosity measured for equivalent soils with similar hydraulic conductivities (Table 26).

Foam type	n
R80 PPI	0.7
R45 PPI	0.9
R30 PPI	0.9

Table 27 Porosity of Foams

Numerical Simulations. The properties of the porous dam were defined in the *porosityDict* file. In this file, five porous media properties had to be defined for each porous medium: mean grain size diameter d_{50}, porosity n, and the three resistance coefficients α, β and γ. The coefficient γ remained constant for all the simulations with a value of γ = 0.34, while d_{50} and n remained constant for each type of porous medium simulated. Therefore, in each simulation, only α and β were varied.

Twenty five simulations were performed for each type of porous medium by completing a simulation matrix where the two resistance coefficients were varied as $\alpha = [100, 500, 1000, 2000, 5000]$ and $\beta = [1, 1.5, 2, 2.5, 3]$. The total simulation time for each run was 80 seconds and the steady state (when the water levels at both sides of the porous structure remained constant) was seen to be achieved between 30-70 seconds. Each

simulation was performed on one processor core and was completed in approximately 1-2 hours.

Two examples of the steady flow simulations are shown in Figure 64, where the evolution of the free surface elevation is shown at times steps of 10 seconds for the R30 foam (left-hand side) and the R80 foam (right-hand side). In these examples, the steady state is achieved between 40 and 50 seconds of the simulation for the R30 foam, while for the R80 between 60 and 70 seconds.

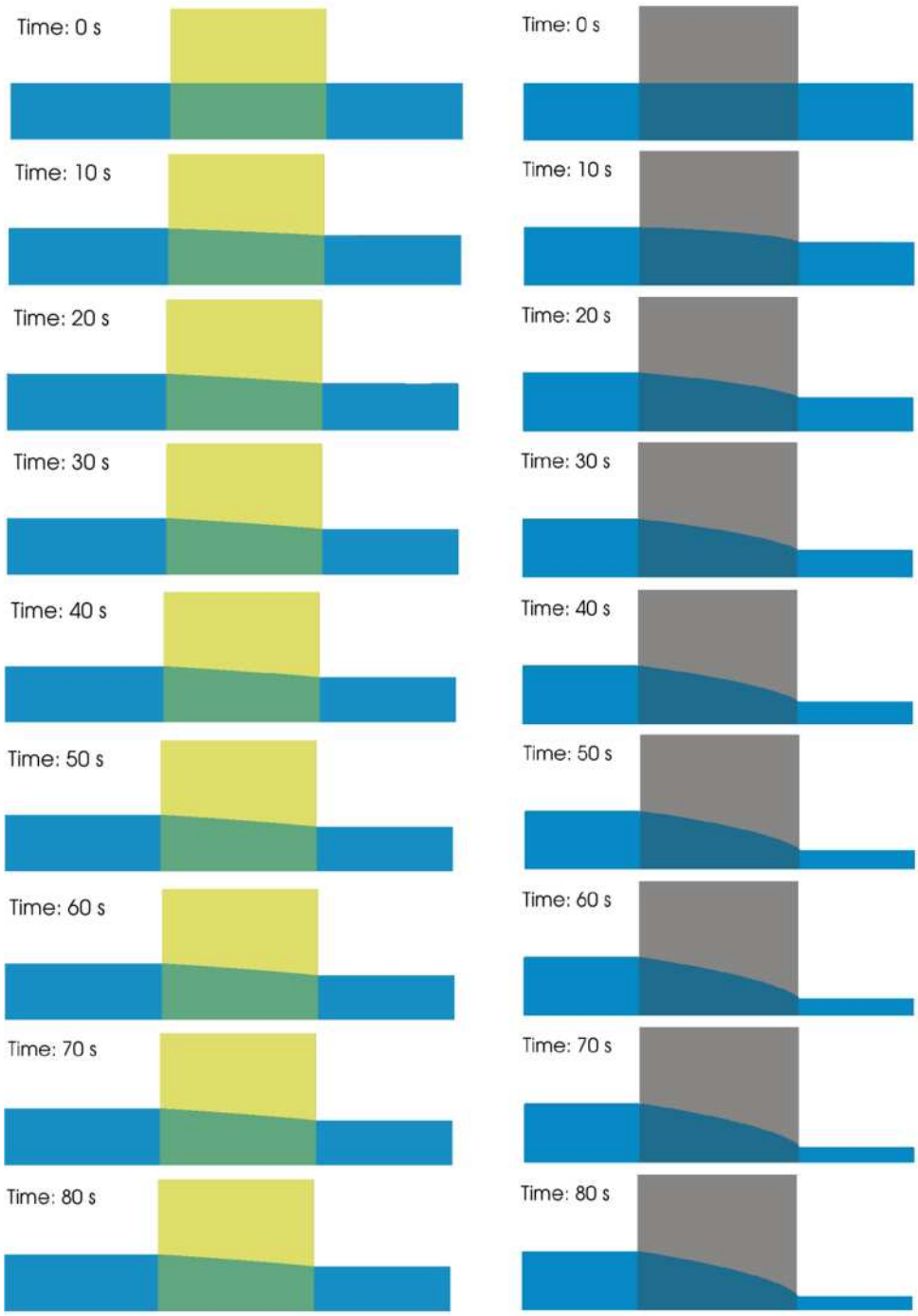

Figure 64 Two examples of steady flow simulations through a porous dam. The left-hand side shows the R30 foam, while the right-hand side the R80 foam

5.2.4 **Calibration**

The water table profiles throughout the length (L = 0.7m) of the porous structure were recorded at every 0.02m, for both the simulations and the laboratory experiments (Figure 65). This resulted in 36 readings of water surface elevation inside the porous structures.

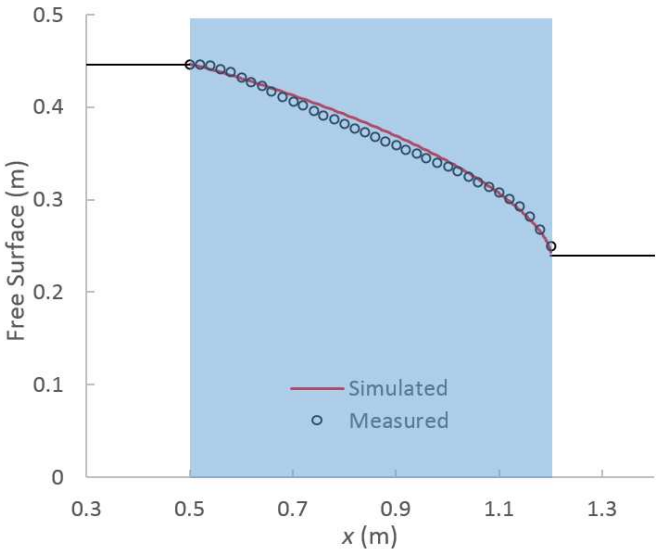

Figure 65 Example of comparison between simulated and measured water table profiles for the R80 foam, where the blue region represents the porous foam. In this example, the simulation was run with $\alpha = 2000$, $\beta = 2$ and a porosity of $n = 0.4$

The difference between the simulations and the measurements at each recorded position was computed through two statistical indicators. To quantify how close the measured and simulated values were, the Mean Absolute Error (MAE) was calculated, while to quantify the amount of dispersion the standard deviation, σ, was estimated. The MAE is calculated as:

$$\mathrm{MAE} = \frac{1}{n}\sum_{i=1}^{n}|f_i - y_i| = \frac{1}{n}\sum_{i=1}^{n}|e_i| \tag{79}$$

where f_i is the predicted value, y_i is the measured value, e_i are the absolute errors, and n is the total number of values. The standard deviation is estimated with:

$$\sigma = \sqrt{\frac{1}{n}\sum_{i=1}^{n}(e_i - MAE)^2} \tag{80}$$

Figure 66, Figure 67 and Figure 68 show the computed errors between the simulated and experimental surface elevations as contours over the parameter space, where the black dots correspond to the simulations. The purple regions in the graphs show the regions where the simulations and measurements had the best agreements.

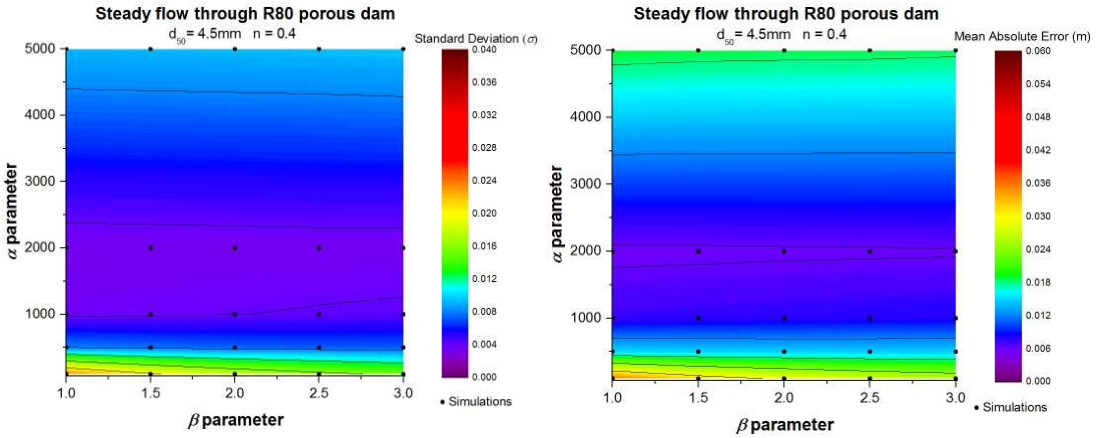

Figure 66 Contours of the error between simulated and experimental free surface elevations through the R80 porous dams with Re_k = 0.99 corresponding to a Darcy-Forchheimer flow regime. The black dots correspond to the simulations.

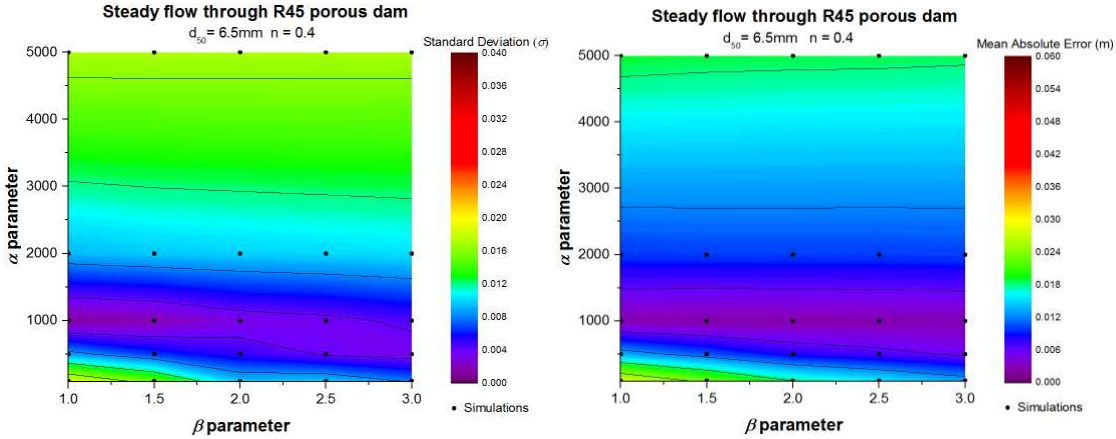

Figure 67 Contours of the error between simulated and experimental free surface elevations through the R45 porous dams with Re_k = 2.14 corresponding to a Forchheimer flow regime. The black dots correspond to the simulations.

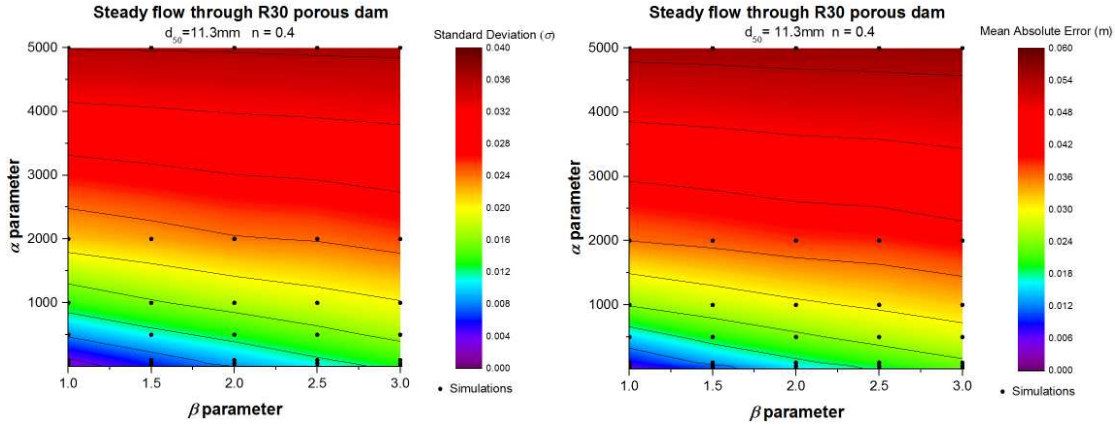

Figure 68 Contours of the error between simulated and experimental free surface elevations through the R30 porous dams with Re_k = 3.32 corresponding to a Forchheimer flow regime. The black dots correspond to the simulations.

In all graphs, the contour lines are mostly aligned with the axis representing β, meaning that there is a stronger dependency on the linear coefficient α than from the non-linear coefficient β. In the case of the Darcy-Forchheimer flow regime through the R80 dam, the non-linear coefficient β has practically no effect on the solution, as the contour lines are

almost horizontal. On the other hand, for the Forchheimer flow regimes in the R45 and R30 dams, the non-linear coefficient β has some influence, as the contour lines slightly inclined. This inclination is more evident in Figure 68 on the R30 dam. Nevertheless, in both Forchheimer flow regime cases, the linear coefficient α is still the dominant coefficient in the solution. Similar results were shown in the calibrations presented by Jensen et al. (2014), where a strong dependency on the linear coefficient α was also found on the Forchheimer flow regime calibrations.

Recommended Coefficients for Permeable Foams. Jensen et al. (2014) found a common set of coefficients α and β that gave a reliable solution for all their flow regimes tested. This was not possible for the present tests as no unique combination of α and β gave a minimum error. As can be seen, the regions showing the lowest errors (purple regions) are different in all graphs and there is no common area in the parameter space across all graphs that could provide an optimised solution for all three porous dams tested. Although it is possible to select a common value of β = 1 for all three foams, it is not possible to select a common value for the linear coefficient α. The values of the linear coefficient α showing the best agreement with the experimental tests decrease as the hydraulic conductivity of the foams increases. For the R80 tests, the optimal solution was found to be around $\alpha \approx 2000$, while for the R45 and R30 tests the best solutions were found to be around $\alpha \approx 1000$ and $\alpha \approx 100$ respectively. The combination of coefficients showing the best agreement with the experimental tests are shown in Table 28. These values are within the range of the values proposed in the literature, shown previously in Table 18.

Foam type	α	β
R80 PPI	2000	1
R45 PPI	1000	1
R30 PPI	100	1

Table 28 Recommended values for the coefficients α and β

5.3 Numerical Setup for Run-up Simulations

To validate the RANS model, the numerical model was set up to mimic the run-up laboratory experiments on impermeable and permeable slopes described in Chapter 4.

5.3.1 Numerical Mesh

The first step for setting up the model is the generation of its computational mesh. This contains all the information regarding the spatial domain, the initial condition of the free surface, as well as the geometries or structures to be included within the mesh. The computational mesh in IH-2VOF was generated using the CORAL software. This allows different geometries or structures to be created and included within the mesh, which can be either impermeable or permeable (porous). Here, the parameters defining the porous media must be introduced to define each structure created. These are: porosity, mean

nominal diameter, and the linear, non-linear and added mass resistance coefficients. The value of these parameters were obtained from the calibration described in the previous section. Once the structures are included, CORAL generates a computational grid as output in a .dat file which can be read by IH-2VOF.

In order to guarantee that the numerical model simulates the wave-structure interaction correctly, some initial considerations have to be given to the dimensions of the domain and cell size.

Dimensions of the Numerical Domain. The length of the computational domain depends on the wave conditions tested. A length before the toe of the structure of 1.2-1.5 times the wavelength is recommended. In the present case, the longest generated wave had a period of T = 3.33s, which corresponds to a deep water wavelength of L_o = 17.33m. The toe of all structures tested was set to be at 1.3 x 17.3m = 22.53m from the beginning of the domain. By considering 1.3 times the wavelength in front of the structure plus the width of the longest structure (5.7m), the total length of the domain was set to be 30m (Figure 69). As active wave absorption was used, no additional computational domain had to be considered for dissipation or relaxation zones. All structures used had a height of 1m, while the water depth at the SWL was set at 0.3m. Therefore, no overtopping events occur, so the height of the domain was also set to be 1m.

Cell-sizes and Subzones. CORAL generates orthogonal structured meshes which can consist of uniform or non-uniform cell sizes. As the finite differences scheme is first order and the numerical error due to variations in the cell dimensions can be considerable, uniform meshes (with constant cell sizes) are recommended. However, these can considerably increase the simulation time in long domains. For this reason, a variable or non-uniform mesh grid was created to decrease the number of cells in zones outside the areas of interest, while still having a good discretisation in the areas of interest.

The computational mesh was constructed from a number of subzones or submeshes defined at each coordinate direction, X and Y. The origin of the coordinate system in CORAL is at the top left hand side corner of the domain. This means that the positive Y direction goes downwards. In each subzone, a convergence point or centre point is specified, as well as the number of cells at both sides of the convergence point and the minimum cell dimension. The cell spacing is then expanded quadratically from the convergence point to the left and right edges of the subzone in accordance with the number of cells specified. To construct a uniform mesh, the number of cells specified should correspond to the number of cells (having the minimum cell dimension specified) that could fit from the convergence point to the edges of the subzone.

In the present numerical mesh, three different subzones were set to reduce the number of cells throughout the entire domain, for both the horizontal *X* and vertical *Y* directions. The maximum resolution subzone was placed in the main area of interest: around the structures, where the wave breaking, run-up and run-down processes occur (X and Y subzones 2). This region consisted of a uniform mesh grid with constant horizontal Δx and vertical Δy cell sizes. A higher resolution was also set along the free surface throughout the entire domain. For the subzones outside the main areas of interest, a variable mesh grid was used to reduce the number of cells.

Due to the VOF function convection, the *false breaking* effect can occur when various full fluid cells are adjacent to empty cells which can receive a flow that does not exist in reality. False breaking can occur when the wave steepness and the cell size aspect ratio ($\Delta x/\Delta y$) are high. To prevent this effect, it is recommended to use a number of cells per wavelength such that breaking limit wave steepness can be correctly represented. In the horizontal direction, the IH-2VOF Manual recommends to have at least 70-100 cells per wavelength for non-breaking waves and more than 100 for breaking waves. In the vertical direction at least 7-10 cells per wave height are recommended, while the suggested aspect ratio is between $1 < \Delta x/\Delta y < 5$. For the present tests, the smallest wave height used was H = 0.04m, so a vertical cell-size of Δy = 0.005m was chosen in order to have 8 cells per wave height, while for the horizontal cell-size, a value of Δx = 0.01m was selected. This resulted in an aspect ratio of $\Delta x/\Delta y = 0.01/0.005 = 2$, which lies within the recommended values. The entire domain had 1454 cells on the X-direction and 159 cells on the Y-direction, giving a total of 231,186 cells in the entire domain. The values defining the three subzones in each direction are specified in Table 29. The mesh discretization and subzones are sketched in Figure 69, while Figure 70 shows the generated mesh, as well as some of the structures tested (with various angles).

	X - Direction			**Y - Direction**		
	Subzone 1	**Subzone 2**	**Subzone 3**	**Subzone 1**	**Subzone 2**	**Subzone 3**
Centre Point	20.99	21.01	29.01	0.395	0.405	0.905
Division	0	21	29	0	0.4	0.9
# of cells left	600	1	1	40	1	1
# of cells right	1	799	50	1	99	15
Max. Separation Center	0.01	0.01	0.01	0.005	0.005	0.005

Table 29 Parameters for each subzone

Another consideration that was taken into account when constructing the variable mesh, was that the changes in the dimension of each cell were less than 5%. This was achieved by verifying that the second derivative of the coordinates of each cell satisfied:

$$\Delta^2 x < 0.05 \text{ and } \Delta^2 y < 0.05 \quad (81)$$

5.3.2 Boundary Conditions

Wave Generation Boundary Conditions. In this study, the static wave paddle method was selected for the inlet boundary in all the simulations, which is generally used to replicate the behaviour of laboratory wave piston-type paddles. To generate waves using this method, two variables for each time step and cell in the first column are specified as input at a given sampling rate. The first variable is the free surface level at the generation boundary. This forces the model to set a VOF value of 1 under the free surface and 0 otherwise. The second variable is the vertical and horizontal velocity components. These values are linearly interpolated as the simulation advances, and remained fixed in the boundary. The static wave paddle boundary condition in IH-2VOF has the capability of generating regular waves using four different wave theories: Linear theory, Stokes II, Stokes V, and Cnoidal. First and second order irregular waves following the Jonswap spectrum, can also be generated in with this boundary condition.

Wave Absorption Boundary Condition. Wave absorption is a key feature for physical and numerical experiments. In physical wave flumes, the domains are usually constrained in dimensions, while in numerical flumes the domains cannot be infinite because of computational restrictions (Higuera et al., 2013a). Therefore, wave absorption at the boundaries is needed to reduce reflections of both incoming and outgoing waves. This allows the simulations to run for longer times, avoiding the effects of re-reflected waves in the flume and avoids any unrealistic total mass increase/decrease inside the computational domain. The IH-2VOF model supports two options for wave absorption: passive and active wave absorption.

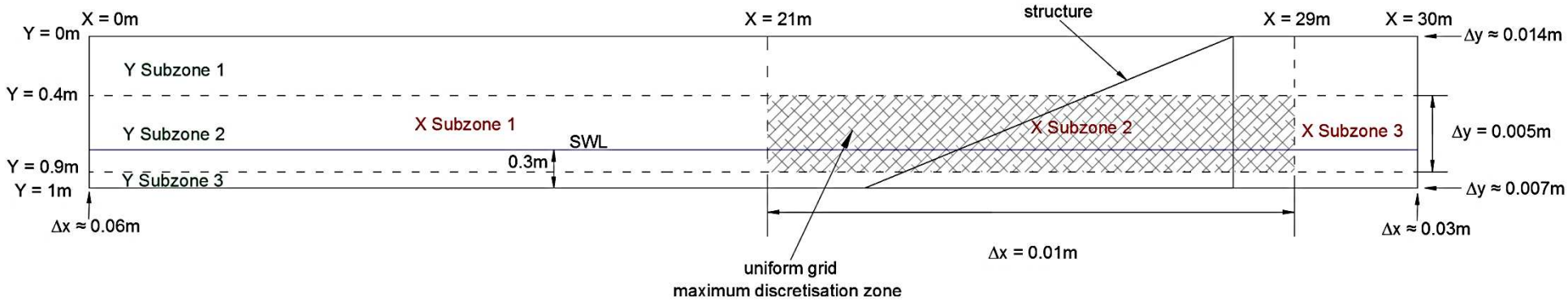

Figure 69 Mesh discretisation and subzones in X and Y directions

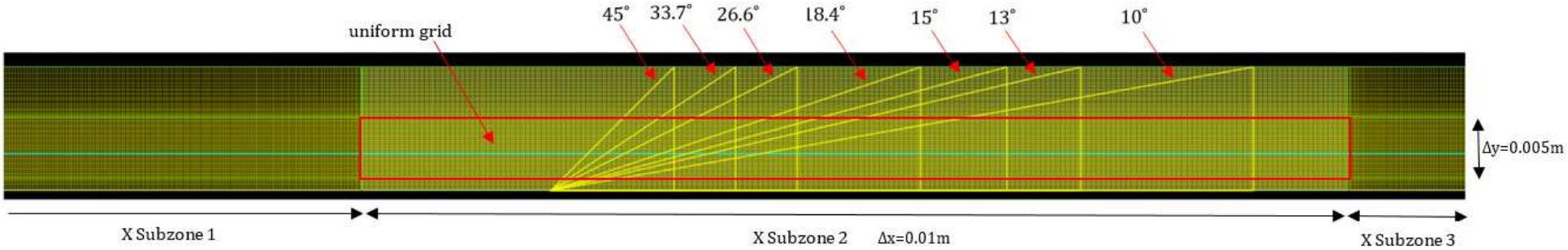

Figure 70 Mesh grid with structures of different slope angles

The first option is passive (sponge layer) wave absorption that can be used to absorb the outgoing waves. However, this requires an extension of the computational domain, as a horizontal span of about 2 wavelengths is recommended for the dissipation or relaxation zone. Hence, it can significantly increase the computational cost, especially for long wave simulations. Additionally, this method has been shown to produce an increase of the mean water level due to the added friction (Higuera et al., 2013a).

The second option is active wave absorption which follows the same technique used by the wave paddles in the physical wave flume. As described in Chapter 4, the active wave absorption adjusts the wave paddle movement based on a measured magnitude so that it continues to generate the target wave, while at the same time preventing re-reflection of waves into the flume. As the velocities at the boundaries are fixed, wave absorption is achieved by imposing the correct velocity profile on it. It identifies the waves that reach a boundary and then generates additional waves that cancel out the reflected waves. There is thus no need to extend the numerical domain as with the sponge layer. Active wave absorption in the model follows the methodology developed by Schäffer and Klopman (2000). In this project, active wave absorption was used in all the simulations performed for the left (inlet) and right (outlet) boundaries.

5.4 Validation Cases

This section presents four validation cases to analyse the capability of the model to simulate waves inside the swash zone on impermeable and permeable slopes. The first two validation cases compare measured and simulated wave run-up heights from breaking and non-breaking waves on impermeable and permeable slopes, respectively. The third and fourth validation cases compare measured and simulated swash depths, flow velocities, swash durations, bed shear stresses and roughness lengths at a cross-shore location inside the swash zone on impermeable and permeable slopes, respectively.

5.4.1 Validation of Wave Run-up

Impermeable Slopes. This validation consisted of comparing a large number of measured and simulated run-up data on impermeable slopes. Eighty-five numerical tests were run replicating the 25 experimental tests performed on the 10° slope in the 14m flume and the 60 tests performed on the 13°, and 15° slopes in the 20m flume (described in Chapter 4).

The model was set up using the mesh and numerical domain described in Section 5.3 with a water depth of 0.3m. The toe of the three impermeable structures was located at a distance of 22.53m from the beginning of the domain. The graph presented by Le Méhauté et al. (1968) was used to select the appropriate regular wave theory for each wave condition generated (Figure 71). The simulation time of each test was 120s. These were

performed on one processor core and completed in approximately 7 hours. The complete list of the simulated results is shown in Appendix D.

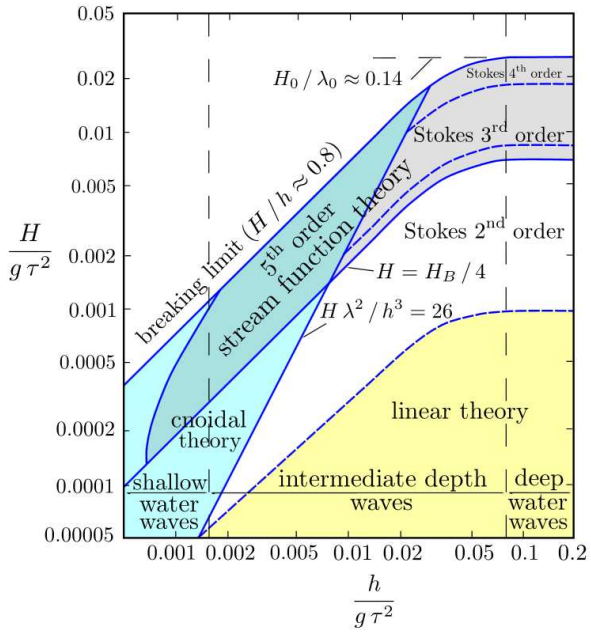

Figure 71 Wave theories range of applicability (taken from Le Méhauté, 1976)

Permeable Slopes. The numerical model was set up to replicate the laboratory experiments performed on three types of 10˚ and 20˚ permeable slopes (R30, R45 and R80 foams, described in Chapter 4). The same mesh discretization and numerical domain described in Section 5.3 was used for this simulations. The water depth was 0.3m and 10˚ and 20˚ permeable structures were included in the numerical mesh. The toe of these structures was located at the same place as the impermeable slopes, at a distance of 22.53m from the beginning of the domain. Table 30 gives the porous media parameters and resistance coefficients used as inputs to simulate flow inside each type of permeable structure (obtained from calibration described in Section 5.2).

Foam type	d_{50} (mm)	n	α	β	γ
R80 PPI	4.5	0.4	2000	1	0.34
R45 PPI	6.5	0.4	1000	1	0.34
R30 PPI	11.3	0.4	100	1	0.34

Table 30 Porous media parameters

A total of 15 regular wave conditions were generated for each slope angle using combinations of 5 wave heights (0.04, 0.06, 0.08, 0.1 and 0.12m) and 3 wave periods (1.43, 2 and 2.86s). In total, 30 simulations were performed for each type of porous structure, resulting in 90 run-up simulations. The wave theories for each wave condition generated were selected using Figure 71. The simulation time for each test was 120s. The computational time required to complete each of these simulations depended on the

hydraulic conductivity of the porous structures, with the less permeable slopes requiring more time to complete (Table 31).

Foam type	Simulation Time (s)	Computational Time (h)
R80 PPI	120	12
R45 PPI	120	11
R30 PPI	120	10

Table 31 Computational time to complete the 120s run-up simulations using one core processor

Comparisons with Measured Data. The results from the simulations on impermeable and permeable slopes are displayed in Figure 72. This graph presents the simulated non-dimensional run-up *R/H* plotted against the Iribarren number, ξ. As expected, the run-up decreases as the hydraulic conductivity of the slopes increases. This is considered in detail in Chapter 6. The comparisons between measured and simulated run-up data are shown in Figure 73, where the measured *R/H* data is plotted against the simulated *R/H* data. In these graphs, the solid black line represents the line of equivalence, where the data show perfect agreement, while the dashed blue and green lines show the ±15% error bands, respectively.

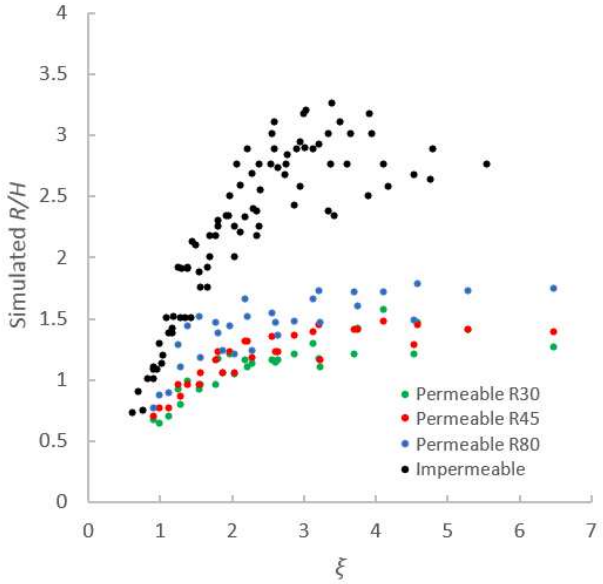

Figure 72 Simulated *R/H* data against the Iribarren number

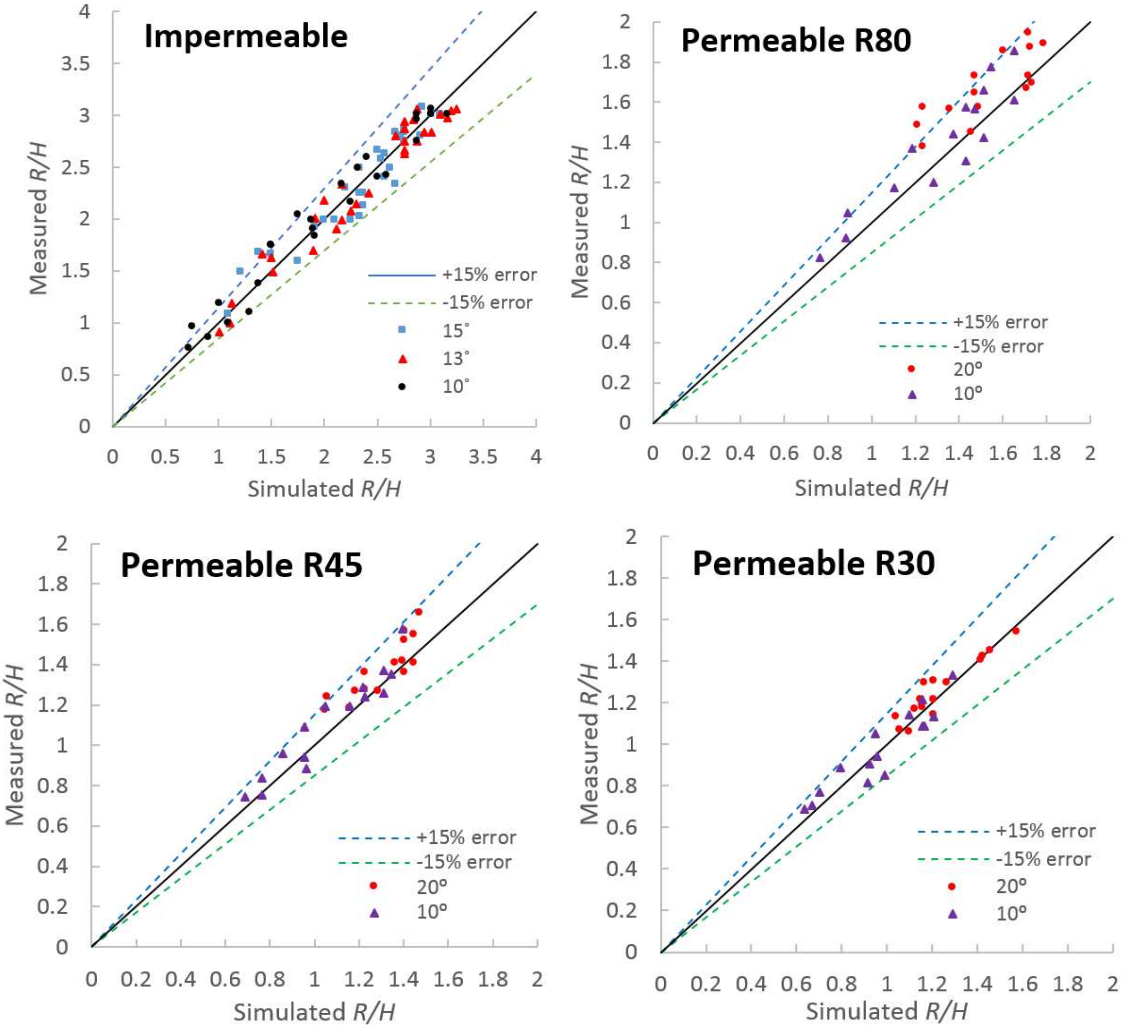

Figure 73 Comparisons between the run-up numerical predictions and the experimental measurement on impermeable and permeable slopes

The absolute average percentage error between the simulated and measured data for each type of slope is shown in Table 32.

Slope type	Absolute Average Error %
Impermeable	8.88
R80 PPI	8.83
R45 PPI	6.33
R30 PPI	5.28

Table 32 Absolute average errors between simulated and measured run-up data

As can be seen, the simulated data show an encouraging agreement with the measured run-up, as most of the data are inside the ±15% error bands in all four slopes analysed and their absolute average error is below 10%. This good agreement between measured and simulated data, confirm the model as able to reproduce wave run-up on impermeable and permeable slopes. It also validates the values used for the porous media parameters obtained from the calibration for each foam, in particular for the R30 foam, which was further used to investigate the influence of infiltration on the swash hydrodynamics.

However, in Figure 73 we can see a slight under-prediction for most of the values on the less permeable slopes R45 and R80, which suggests that the values of the porous media parameters obtained from the calibration for these foams are close, but not entirely accurate. Nevertheless, the values of these parameters can be adjusted to fit the experimental data, by making the simulated foams slightly less permeable. In order to adjust these parameters, it is necessary to know their individual influence on run-up. For this reason, a sensitivity analysis on these parameters was performed and is described below.

5.4.2 Sensitivity Analysis for the Porous Media Parameters

To investigate the influence on run-up of each of the five parameters that control the porous media flow in the model, simulations of a solitary wave (H = 0.1m) breaking over a 10° porous slope were performed. The sensitivity analysis involved performing tests where the run-up of the solitary wave was recorded. For these tests, the value of one of the porous media parameters was varied, while the values of all the other parameters remained constant. These tests were simulated using the same numerical setup described in Section 5.3.

As mentioned before, the five porous media parameters that can be modified in the model are: porosity, n, the mean nominal diameter, d_{50}, and the three resistance coefficients α, β, and Y. Previous studies have shown that the added mass coefficient, Y, does not have a significant influence on the porous media flow, and a value of 0.34 is commonly used for this coefficient (Del Jesus et al., 2012; Higuera et al., 2014). Therefore, this parameter was not investigated in the sensitivity analysis and a constant value of 0.34 was used for all the tests.

The parameters used for each test, and the run-up results are summarised in Table 33. From these tests we can see that there are four options for making the permeable slope less permeable: by decreasing the nominal grain diameter value or by increasing the porosity, α or β values. It was found that porosity is the parameter that influences run-up the most, followed by the mean nominal grain diameter. Therefore, obtaining reliable values of these two parameters is essential for having an accurate run-up prediction over a particular permeable slope. On the other hand, both resistance coefficients α and β were shown to have a similar or smaller influence on run-up, with run-up gradually increasing as the values of these parameters increased. These results can help if it is necessary to adjust the values of the calibrated parameters to fit the simulated run-up to experimental data. However, the only slope simulated in the thesis to analyse the influence of infiltration on the swash hydrodynamics was the R30 foam, which showed accurate run-up

predictions when compared to the experimental data (Figure 73). Therefore, it was not necessary to adjust the values of its porous media parameters.

Varying Porosity, *n*		***n***	***R* (m)**
CONSTANTS:	**value:**		
laminar coefficient, α	1000	0.2	0.23
turbulent coefficient, β	1	0.4	0.13
added mass coefficient, Υ	0.34	0.6	0.1
nominal grain diameter, d_{50} (m)	0.005	0.8	0.09

Varying turbulent coefficient, β		**β**	***R* (m)**
CONSTANTS:	**value:**	1	0.13
laminar coefficient, α	1000	1.5	0.13
added mass coefficient, Υ	0.34	2	0.13
nominal grain diameter, d_{50} (m)	0.005	2.5	0.15
porosity, n	0.4	3	0.16

Varying nominal grain diameter, d_{50} (m)		***d_{50}* (m)**	***R* (m)**
CONSTANTS:	**value:**	0.001	0.19
laminar coefficient, α	1000	0.005	0.13
turbulent coefficient, β	1	0.007	0.13
added mass coefficient, Υ	0.34	0.01	0.12
porosity, n	0.5	0.02	0.12

Varying laminar coefficient, α		**α**	***R* (m)**
CONSTANTS:	**value:**	100	0.12
turbulent coefficient, β	1	500	0.12
added mass coefficient, Υ	0.34	1000	0.13
nominal grain diameter, d_{50} (m)	0.005	2000	0.14
porosity, n	0.4	5000	0.15

Table 33 Parameters used for the sensitivity analysis and run-up results

5.4.3 Validation of Swash Zone Velocities and Water Depths

To further validate the RANS model inside the swash zone, the run-up laboratory experiments performed on non-deformable 10˚ impermeable and permeable (R30) slopes described in Chapter 4 were used. These experiments provided controlled and repeatable conditions which enabled the isolation of individual effects, allowing suitable flow velocity and swash depth measurements. These were ideal for validating the ability of the IH-2VOF model to simulate swash flows.

In these experiments, the flow depths and near bed velocities in the boundary layer were measured for a series of long non-breaking regular waves (H = 0.05m and T = 4s) at the

location shown in Figure 51. The fixed permeable and impermeable beds allowed detailed high-resolution flow velocities at 30 different vertical positions from 0 to 30mm (1000Hz at 1mm vertical spacing). These were obtained using the LDV system described in Chapter 4. Ensemble-averaged horizontal velocity profiles were derived from measurements of 50 waves taken at the 30 different vertical positions and the data were smoothed and de-spiked using the *robust local regression* method. The flow depths were measured at the same location using a digital video camera which was set at one side of the flume.

These experiments provided good quality data describing swash depths and flow velocities, which enabled the estimation of bed shear stresses and roughness lengths through the law-of-the-wall method.

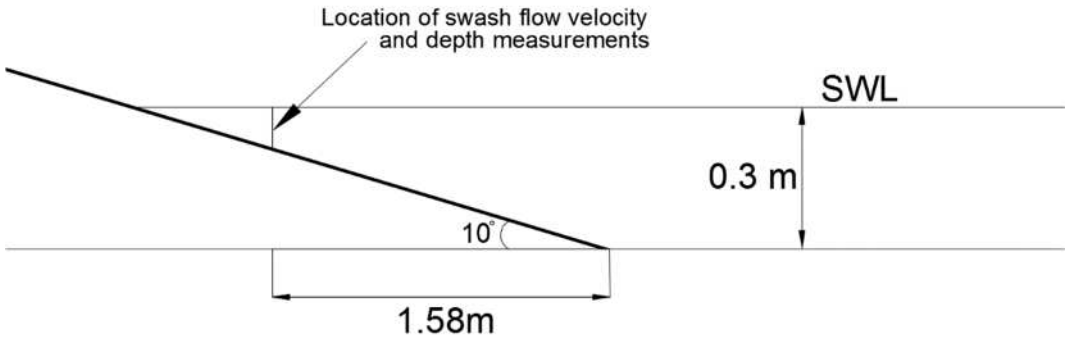

Figure 74 Swash zone location where the LDV measurements were taken

The numerical model was set up to mimic these laboratory experiments. The same mesh and numerical domain described in Section 5.3 was used for these simulations. The toe of the impermeable and permeable 10^0 structures was located at a distance of 22.53m from the beginning of the domain. Figure 73 shows that the resistance coefficients obtained from the calibration for the R30 foam are correct, as all of the predicted data are inside the 15% error bands. Therefore, there was no necessity to adjust the values of these parameters, so the same resistance coefficient values (shown in Table 30) were used for the run-up simulations.

The regular waves were generated with Cnoidal wave theory and active wave absorption was used for both the inlet and outlet boundaries. The simulations were run for 200s to derive ensemble averaged velocities from 50 waves. These were completed in approximately 9 hours for the impermeable slope, and approximately 13 hours for the permeable slope (on one processor core).

The IH-2VOF model includes a Graphical User Interface (GUI) that allows the placing of vertical gauges or sensors at desired locations along the numerical domain. These gauges can provide information of the horizontal and vertical velocities in all the cells in the vertical dimension, as well as time-series data of the free surface elevation. In this

simulation, a sensor was placed at the same location where the velocity and water depth measurements were taken in the laboratory experiments.

This information was used to compare measured and simulated swash depths, swash duration, ensemble-averaged horizontal velocities, bed-shear stresses and roughness lengths during the uprush and backwash phases. Detailed analysis of the boundary layer dynamics, its evolution throughout the entire swash event and the comparisons between the data on impermeable and permeable slopes is shown in Chapter 6.

Swash Depths. Figure 75 shows the time-series of the simulated (red line) and measured (black line with dots) water depths for the impermeable and R30 permeable foam slopes at the location indicated in Figure 51. The dashed blue and green lines indicate the ±15% error bands, respectively (with respect to the measured data). In this analysis, the arrival of the bore is considered to be the initial time (t = 0s).

As can be seen, for both the impermeable and permeable slopes, good agreement is shown through most of the swash event (between the measured and simulated water depths). The simulated values remained mostly inside the ±15% error bands.

The comparison between results for impermeable and permeable cases shows very similar results. From the arrival of the bore at t = 0s until approximately $t \approx 1.15$s for the impermeable case, and $t \approx 0.95$s for the permeable case, the measured and simulated data show almost identical results. In both measured and simulated data, the water depth rapidly increases from $0 < t < 0.4$s ($0 < t < 0.3$s for the permeable case) and remains fairly constant until $t \approx 1$s ($t \approx 0.95$s for the permeable case). The major differences are seen to occur between $1 < t < 2.4$s on the impermeable case, and between $0.9 < t < 2.2$s on the permeable case. At $t \approx 1$s ($t \approx 0.9$s for the permeable case), the simulated water depths start to decrease. In contrast, the measured water depths slightly increase and then begin to decrease at around $t \approx 1.55$s ($t \approx 1.4$s for the permeable case). This increase in the measured water depth might be attributed to the beginning of flow reversal, which was observed to start at around $t \approx 1$s for the impermeable case and at around $t \approx 0.9$s for the permeable case. However, this increase was not captured in the simulation. The measured and simulated data meet again at around $t \approx 2.4$s ($t \approx 2.2$s for the permeable case) and continue with very similar values until the end of the backwash.

The slight discrepancies shown between the measured and simulated data, on both the permeable and impermeable slopes, might be attributed to the technique used to measure the water depths. The water depths were recorded using a video camera placed at the side of the flume, where control points were used for extracting the data from the videos. As discussed in Section 4.3.2, surface tension can slightly increase the location of the water

surface projected in the side glass wall, so the measurements obtained with video cameras will generally be slightly larger.

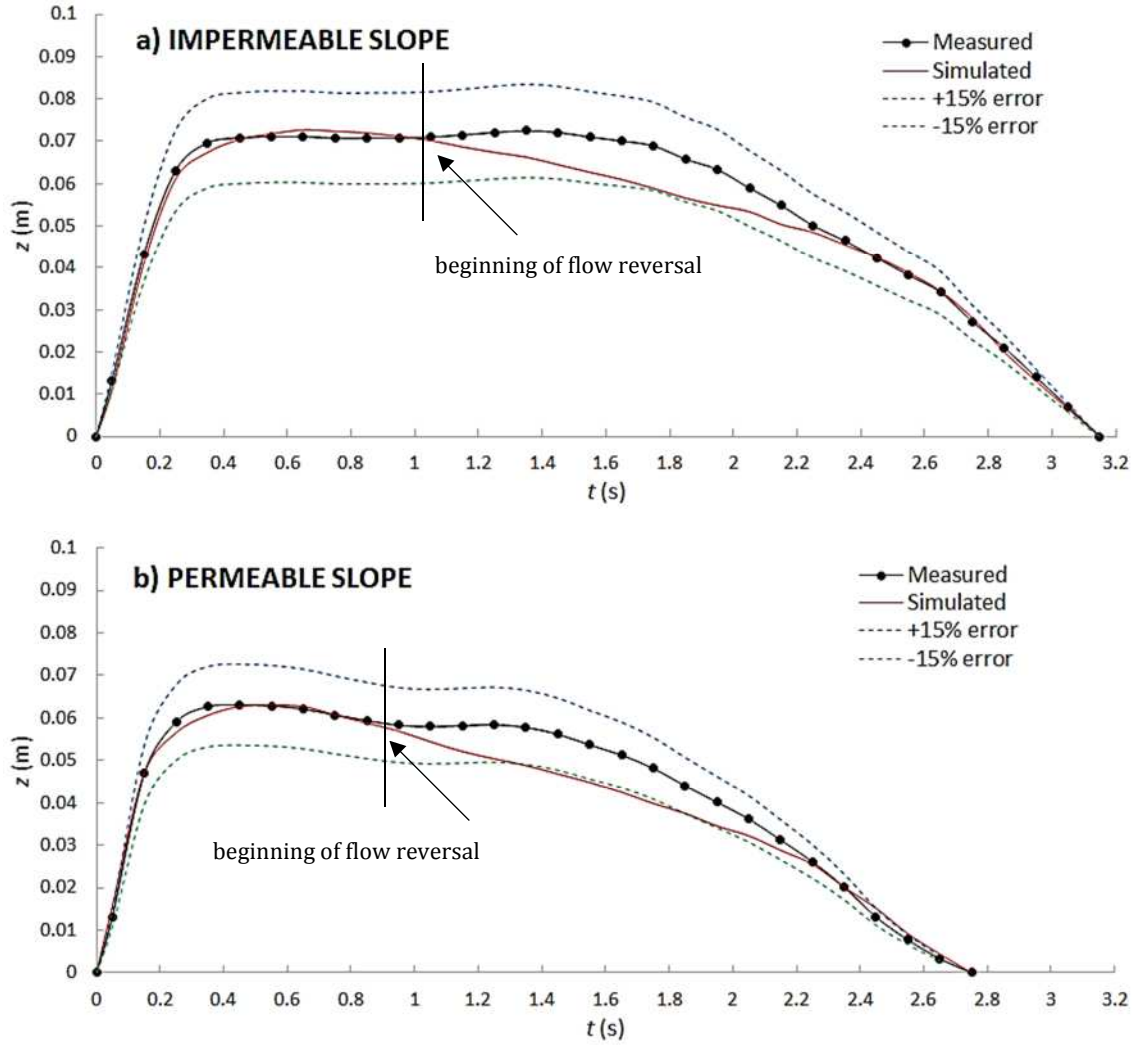

Figure 75 Comparisons between measured and simulated swash depths from a regular wave with H =0.05m and T = 4s. a) impermeable slope; b) R30 permeable slope

Swash Duration. From the graphs in Figure 75 we can see that at this location, the model predicts the duration of the swash event accurately for both impermeable and permeable cases. On the impermeable slope, the total swash event lasts approximately 3.15s from the arrival of the bore until the end of the backwash, while on the permeable slope the swash duration is seen to be shorter, lasting approximately 2.75s.

Ensemble-Averaged Horizontal Velocity Profiles. The evolution of the simulated and measured near bed ensemble-averaged horizontal velocity profiles on the impermeable and permeable slopes are shown in individual graphs in Figure 76 and Figure 77. These graphs show the recorded profiles at time steps of 0.2s and from 0-0.03m above the bed. Once again, the blue and green dashed lines in each graph indicate the ±15% error bands.

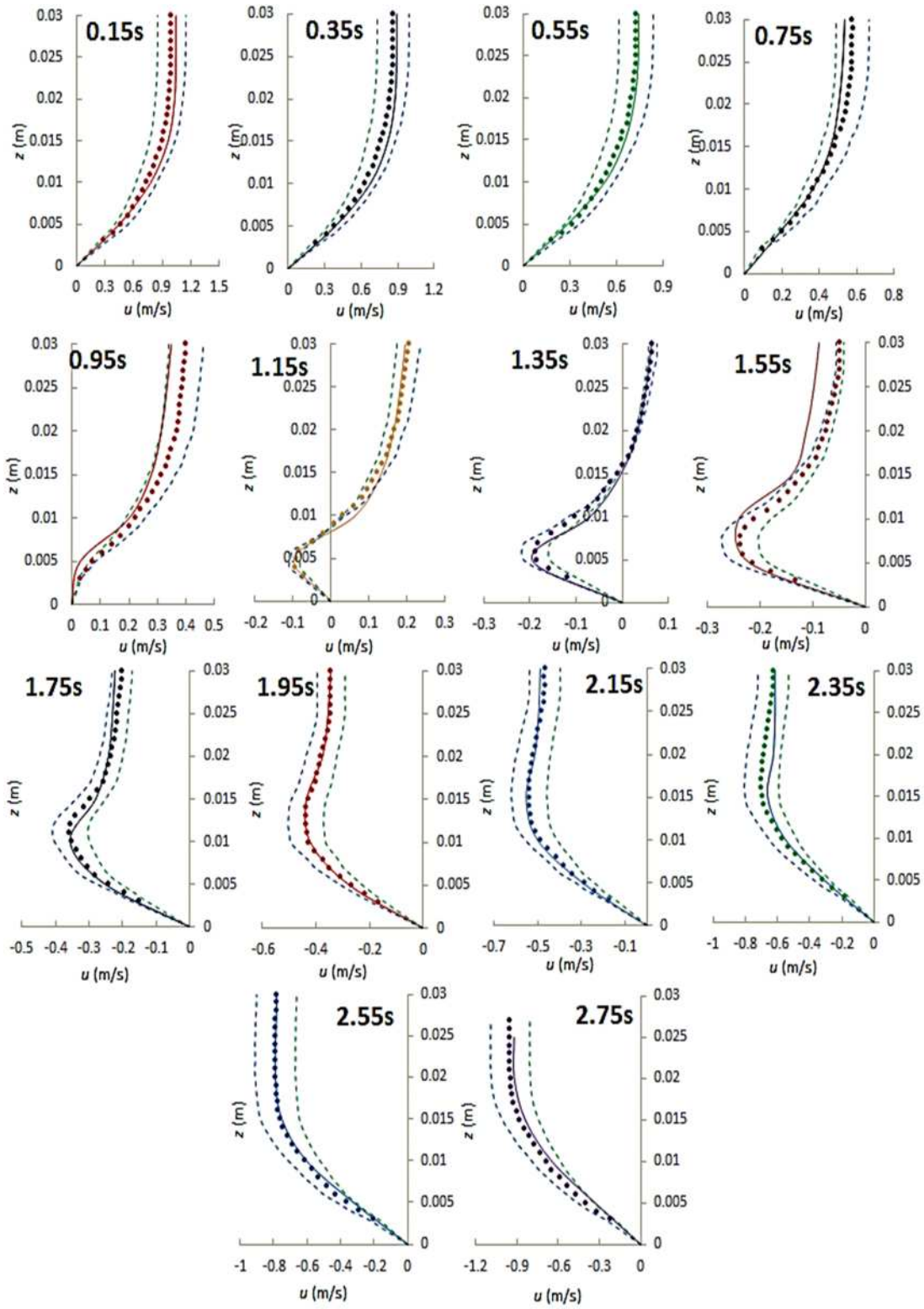

Figure 76 Comparison between measured (points) and simulated (lines) velocity profiles for a swash event on an impermeable slope at time-steps of 0.2s

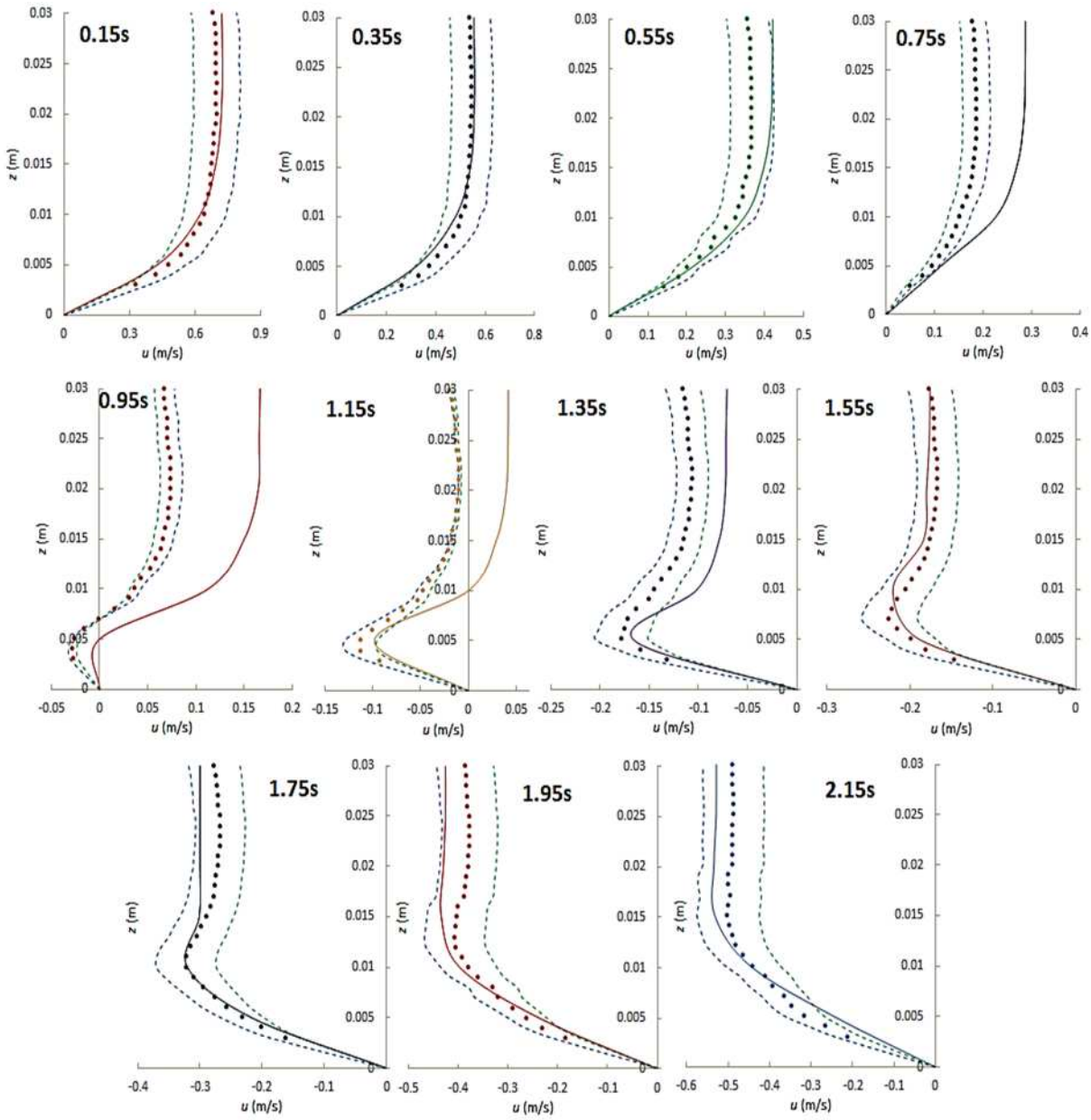

Figure 77 Comparison between measured (points) and simulated (lines) velocity profiles for a swash event on a permeable slope at time-steps of 0.2s

As can be seen, there is good agreement between the simulated data and the near-bed horizontal velocity measurements. Although some differences are seen on the flow reversal profiles on the permeable slope, between $0.75 < t < 1.55$s, most simulated data lie well inside the 15% error bands on both impermeable and permeable slopes.

A possible reason for the discrepancies shown between the simulated and measured flow velocities might be attributed to the air phase that is not resolved by the numerical model. In a 2D model, the air bubbles can significantly affect the simulated flows, as these cannot escape laterally. Therefore, air-bubbles might be trapped or might be expelled into the bore and greater turbulence is induced.

Another possible source of error between the simulated and measured flow velocities is the post-processing technique used to obtain the velocity data from the laboratory experiments. As shown in the previous images, the LDV system can provide detailed velocity measurements of shallow swash flows. However, the raw data obtained from the LDV contained significant noise and outliers, so it was necessary to apply a smoothing method to clean and de-spike the raw data. As the raw data contained significant outliers, a *robust local regression* (*rloess* in Matlab) method was selected for smoothing the data. This method was chosen because it assigns lower weight to outliers in the regression. However, there are numerous different smoothing techniques available, and each of them would have yielded slightly different results.

The refinement of the numerical mesh can also influence the results of the simulations. In these simulations, the maximum mesh resolution was placed where wave breaking and the swash processes occur (X and Y subzones 2), as well as along the free surface throughout the entire domain. These regions had a uniform mesh grid with constant horizontal Δx and vertical Δy cell sizes. It is possible that increasing the mesh resolution in these regions could have improved the results from the simulations. However, this would have considerably increased the computational time of the simulations. As the comparisons between the simulations and measured data showed good agreement in most time steps, it was decided not to modify the numerical mesh.

From Figure 76 and Figure 77, it can be seen that the velocity profiles on the impermeable and permeable slopes show a similar evolution throughout the entire swash event: the profiles gradually evolve from profiles showing a typical logarithmic boundary layer at the beginning of the uprush to profiles resembling the typical velocity profile of a wall jet at the beginning of flow reversal. Then, the wall jet-type profiles gradually evolve back to profiles showing logarithmic boundary layers at the end the backwash. This evolution of the velocity profiles and the different type of velocity distributions in the boundary layer are well captured by the numerical model throughout the swash event, on both the impermeable and permeable slopes.

The velocity measurements presented in this study on impermeable and permeable fixed beds confirm that the velocity profiles around flow reversal show opposing directions near the bed and at the surface, and thus, the log law fit is not applicable. Therefore, bed shear stresses cannot be determined from such profiles using the log law method. This can be seen in the semi-log plots in Figure 78, where log profile fitting to velocity profiles for the impermeable and permeable slopes is shown. This log law was applied in a similar way as applied in O'Donoghue et al. (2010) and Kikkert et al. (2012), by fitting only the velocity data immediately above the bed that showed a 0.95 correlation between data and fit. This

criterion eliminated the velocity profiles around the time of flow reversal where the velocities near the bed had opposing directions to those at the surface.

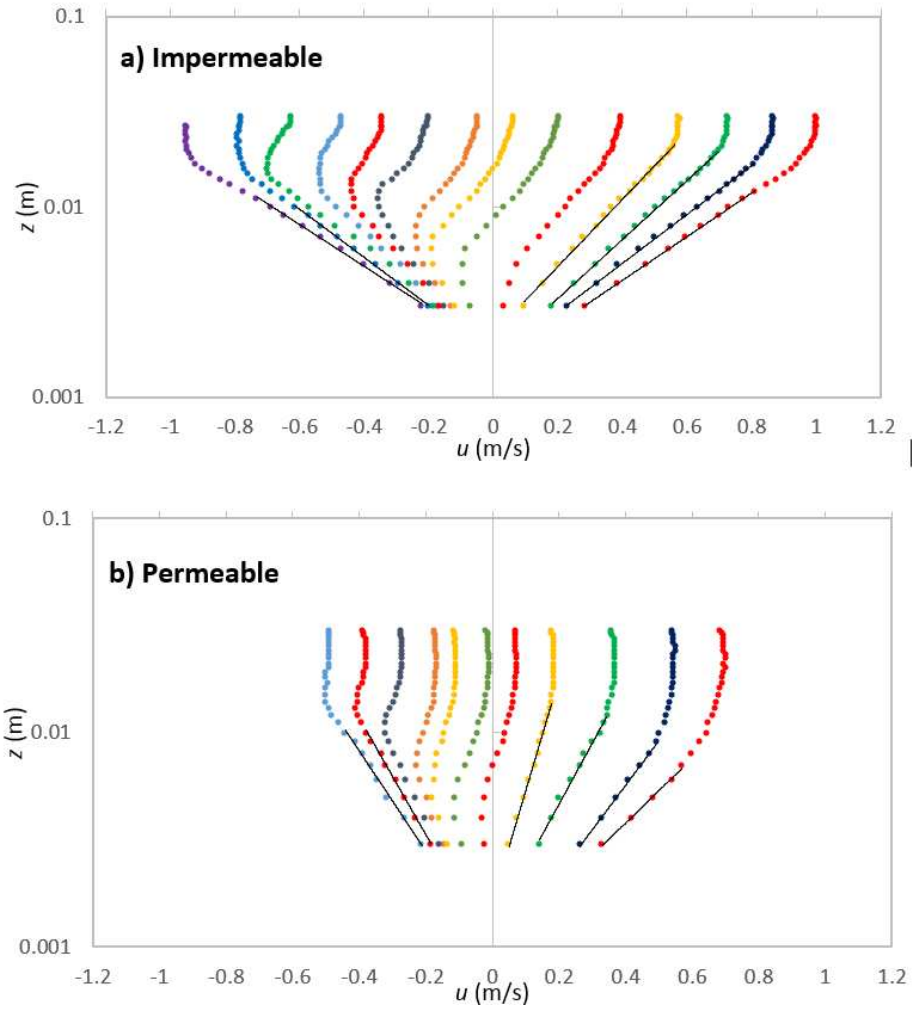

Figure 78 Semi-logarithmic velocity profiles showing were the log-law is applicable on: a) impermeable and b) permeable slopes

Bed shear stresses and Roughness Lengths. The simulated bed shear stresses and roughness lengths were compared to their measured counterparts. These parameters were obtained through the log-law method, briefly described below. The near-bed velocity in a logarithmic profile can be expressed as:

$$\bar{u}(z) = \frac{u_*}{\kappa} \ln\left(\frac{z}{z_0}\right) \tag{82}$$

where u_* is the friction velocity or shear velocity (m/s), z is the height, z_0 is the roughness length, and κ is von Karman's constant, which commonly takes a value of 0.4. The friction velocity and the roughness length can be derived from the semi-logarithmic profiles of the ensemble-averaged velocities. This procedure involves fitting straight lines by least squares regressions to the profile and calculating estimates of u_* and z_0.

Figure 79 and Figure 80 show the simulated and measured bed shear stresses and the roughness lengths obtained from the velocity profiles where the log-law was applicable both impermeable and permeable cases, respectively.

Generally good agreement was found between the simulated and measured bed shear stresses. For the impermeable case, the simulated values were around ≈ 35% larger than the measured data during the uprush phase, while during the backwash phase, values were only ≈ 15% larger. For the permeable case better agreement was seen during the uprush phase, with the simulated values around ≈ 15% larger than the measured data, while during the backwash stage the simulated values were ≈ 30% larger.

The simulated roughness lengths were also seen to be slightly larger than the measured data (around ≈ 20% larger). However, there was a good agreement in respect that z_0 remains fairly constant throughout the entire swash cycle and within the same order of magnitude. Values ranged between $0.0014 < z_0 < 0.0024$ for the impermeable case and $0.001 < z_0 < 0.0017$ for the permeable case. The influence of the hydraulic conductivity on flow velocities and bed shear stresses is analysed in the following section, where comparisons between the impermeable and permeable data are shown.

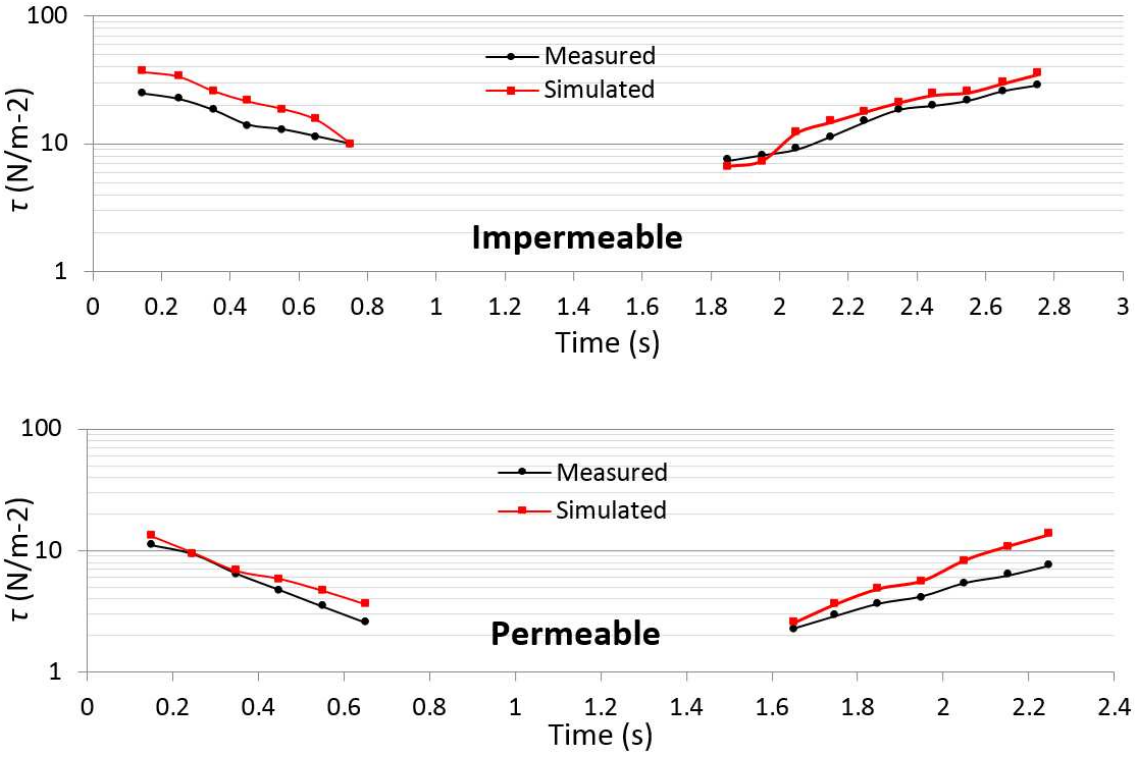

Figure 79 Comparison between simulated and measured bed-shear stresses on the impermeable and permeable cases

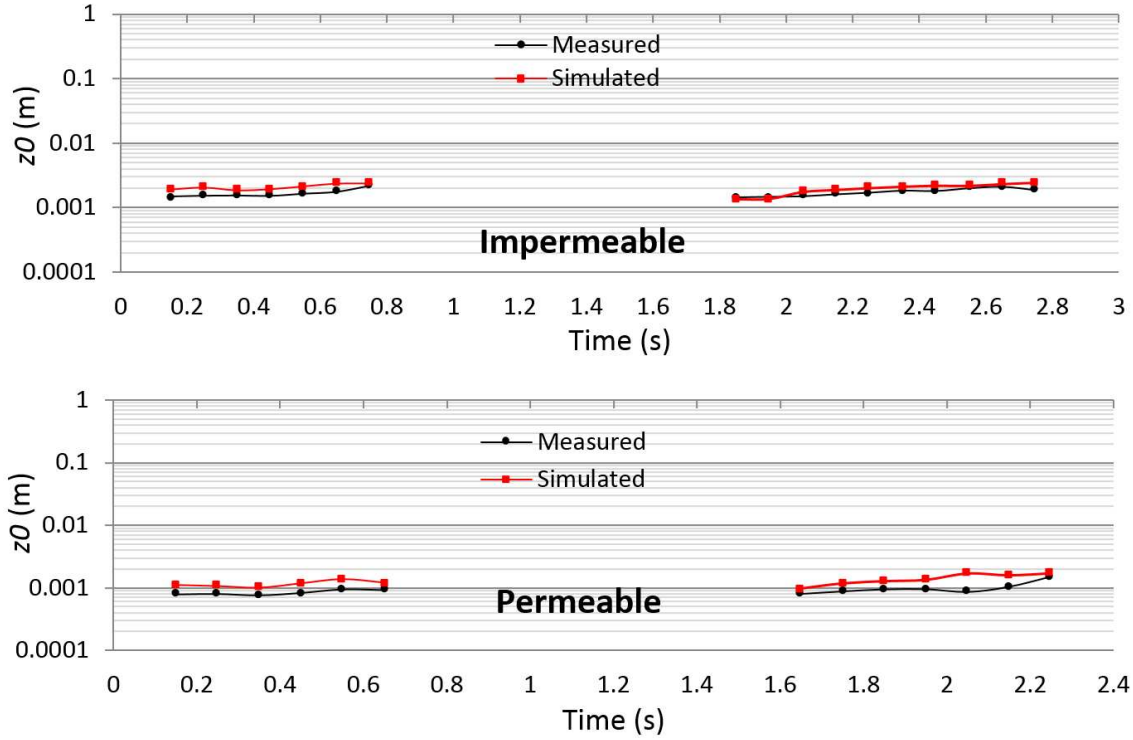

Figure 80 Comparison between simulated and measured roughness lengths on the impermeable and permeable cases

5.5 Additional Run-up Simulations on Smooth-Impermeable Slopes

After validating the capability of the model to reproduce wave run-up, two sets of simulations were carried out to obtain additional run-up data over smooth-impermeable slopes. One of the objectives of the numerical modelling was to obtain additional run-up data from regular non-breaking waves for steeper impermeable slopes. The laboratory run-up experiments on smooth-impermeable slopes were carried out with regular waves on slopes with angles varying between 7° and 15°. On these slope angles, the majority of the tests resulted in breaking waves on the slope, with only a few waves being non-breaking or surging waves. Furthermore, the model was also used to obtain run-up data from irregular waves as the run-up experiments consisted only of regular waves. These simulations were performed using the same numerical mesh and domain as described in Section 5.3.

Test conditions for regular waves. The simulations with regular waves were performed on 4 steep slope angles: 18.4°, 26.6°, 33.7° and 45°. Thirty regular wave conditions were generated for each slope combining five different wave heights (0.04, 0.06, 0.08, 0.1, and 0.12m) and six wave periods (1, 1.43, 2, 2.5, 2.86, and 3.33s), giving a total of 120 simulations. Again, Méhauté et al. (1968) was used to select the regular wave theory for each wave condition. Each simulation was run for 120 seconds and was completed in

approximately 7 hours on one processor core. Most of these simulations resulted in non-breaking or surging waves. The results are analysed in the following chapter, and the complete data set of results is shown in Appendix D.

Test conditions for regular waves. The irregular wave simulations were performed on seven different impermeable slope angles: 10˚, 13˚, 15˚, 18.4˚, 26.6˚, 33.7 ˚ and 45˚. For these tests, sixteen wave conditions following the Jonswap spectrum were generated for each slope, combining four zeroth-moment significant wave heights, H_{mo} (0.04, 0.06, 0.08 and 0.1m) and five peak wave periods, T_p (1, 1.43, 2, and 2.86s). This resulted in a total of 112 simulations. The duration of each irregular wave sequence was 300 seconds. Each simulation was performed on one processor core and was completed in approximately 16 hours. A default value of 512 frequency components and a peak enhancement factor (gamma) of 3.3 were used to create the random wave trains. Table 34 shows an approximate number of waves generated for each peak period used, while Figure 81 shows an example of the wave characteristics from a random wave train generated for 300s with T_p = 1s and H_{m0} = 0.04m. The results of these tests are discussed and analysed in Chapter 6, while the complete data set of results is shown in Appendix D.

Duration (s)	Peak Period, T_p	Number of Waves
300	1	372
300	1.43	255
300	2	193
300	2.5	151
300	2.86	130

Table 34 Approximate number of waves generated for each simulated test

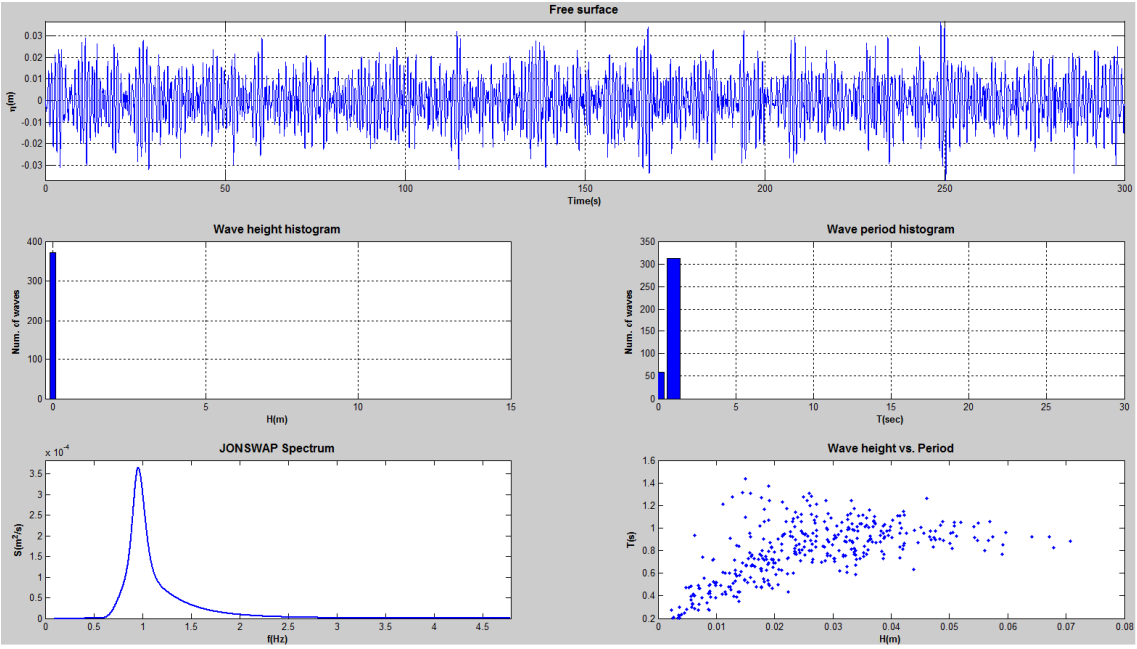

Figure 81 Example of irregular wave series characteristics

5.6 Summary and Conclusions

This chapter presented and validated a numerical model capable of simulating swash hydrodynamics on impermeable and permeable slopes. The model solves the two-dimensional Reynolds-Averaged Navier-Stokes (RANS) equations, coupled with a turbulence closure model for the clear-fluid region and the Volume-Averaged Reynolds-Averaged Navier-Stokes (VARANS) equations for the porous media flow. The porous media equations include an additional closure model which includes two resistance coefficients that need to be determined empirically. A calibration procedure consisting of steady flows through unconfined porous dams was presented and values for these resistance coefficients were proposed for each type of permeable foam used in the run-up experiments.

The model was validated by replicating the laboratory experiments presented in Chapter 4 on impermeable and permeable slopes. Comparisons between measured and simulated run-up, flow velocities, swash depths, bed-shear stresses and roughness lengths inside the swash zone were analysed. These comparisons showed that the model is capable of predicting the swash data on both impermeable and permeable slopes.

Finally, the model was set up to obtain additional run-up data from regular and irregular waves on impermeable slopes. These data are analysed in the following section alongside all the other measured run-up data.

The good agreement shown between most of the simulated and measured data validates the use of the model inside the swash zone. Therefore, the model was used to analyse in further detail the flow velocities throughout the swash events, as well as to investigate the influence of the infiltration on the swash hydrodynamics and bed shear stresses at different locations on the slope. These results are section 7.7.

6 Wave Run-up over Smooth-Impermeable Slopes

This chapter presents the analysis performed on the wave run-up data obtained from the laboratory experiments and numerical simulations carried out on smooth-impermeable slopes. The chapter is divided into three main sections.

Section 6.1 presents a dimensional and graphical analysis to investigate the influence of wave height, wave period, and slope angle on wave run-up. Here, the run-up data is plotted against wave height and wave period for each of the slopes analysed in this study.

After the dimensional analysis, Sections 6.2 and 6.3 present new formulae to estimate run-up from breaking and non-breaking waves on smooth-impermeable slopes, for regular and irregular waves respectively. Here, a new parameter is proposed as a breaking criterion to predict the transition between breaking and non-breaking waves. After comparing the present data against predictions of existing formulae, the derivation of the new formulae to predict run-up is described. This sections also presents a new dimensionless parameter aimed to describe run-up from non-breaking waves.

6.1 Influence of Wave Height, Wave period and Slope Angle on Wave Run-up

As mentioned in Chapter 3, in a 2D scenario with normally incident waves breaking on a smooth-impermeable slope, wave run-up is mainly a function of the wave height, wavelength or period and the angle of the slope. This section presents a graphical analysis to identify trends in the graphs and investigate the influence of these parameters on run-up individually. The aim of this analysis is to identify under which conditions these parameters have more influence on run-up, using the data obtained from the regular wave tests.

6.1.1 Wave Run-up Vs Wave Period

The graphs shown in Figure 82 plot the wave run-up against wave period for the eight different slopes analysed. In the graphs on the left-hand side, the data are separated by their deep-water wave steepness value (H/L_o), while the graphs on the right-hand side plot the same data but now separated according to their wave height.

From these graphs, we can see that for the shallower slopes ($\alpha \leq 13°$), the wave height, H, has a significantly larger influence on run-up on long waves with small wave steepness

(H/L_o < 0.01, red dots) than on short steeper waves (H/L_o > 0.02, black dots). This might be attributed due to the fact that steep waves breaking on shallow slopes generally produce large plunging waves which dissipate most of the wave's energy. Therefore, after the breaking process, little energy is available for the wave to travel further up the slope. On these shallow slopes, we can also see that wave period or wave length has a large influence on run-up, as its values increase as the wave period increases.

For steeper slopes ($\alpha \geq 15°$) we can see that H has a large influence on all waves, not only on those with small wave steepness. As the slope increases, the waves gradually change from breaking to non-breaking. This reduces the energy dissipated in the breaking processes and allows the waves to achieve higher run-ups. However, this run-up increment due to a slope increment has a limit or a threshold. From these graphs, the slope threshold is seen to be around the 18.43° slope. For slopes with steeper angles than 18.43°, most of the waves generated in these tests resulted in surging breakers or non-breaking waves whose run-up values are seen to gradually decrease as the slope increases. This reduction can be attributed mainly to two factors. Firstly, gravity limits the uprush motion on steeper slopes, and secondly, the backwash force from the fluid weight component $\rho g \sin \alpha$ is significantly increased, increasing the swash collision with the incoming wave.

In addition, it is interesting to note that the influence of wave period on run-up gradually decreases as the slope increases. For the steeper slopes, it can be seen that the wave run-up is mainly controlled by the wave height.

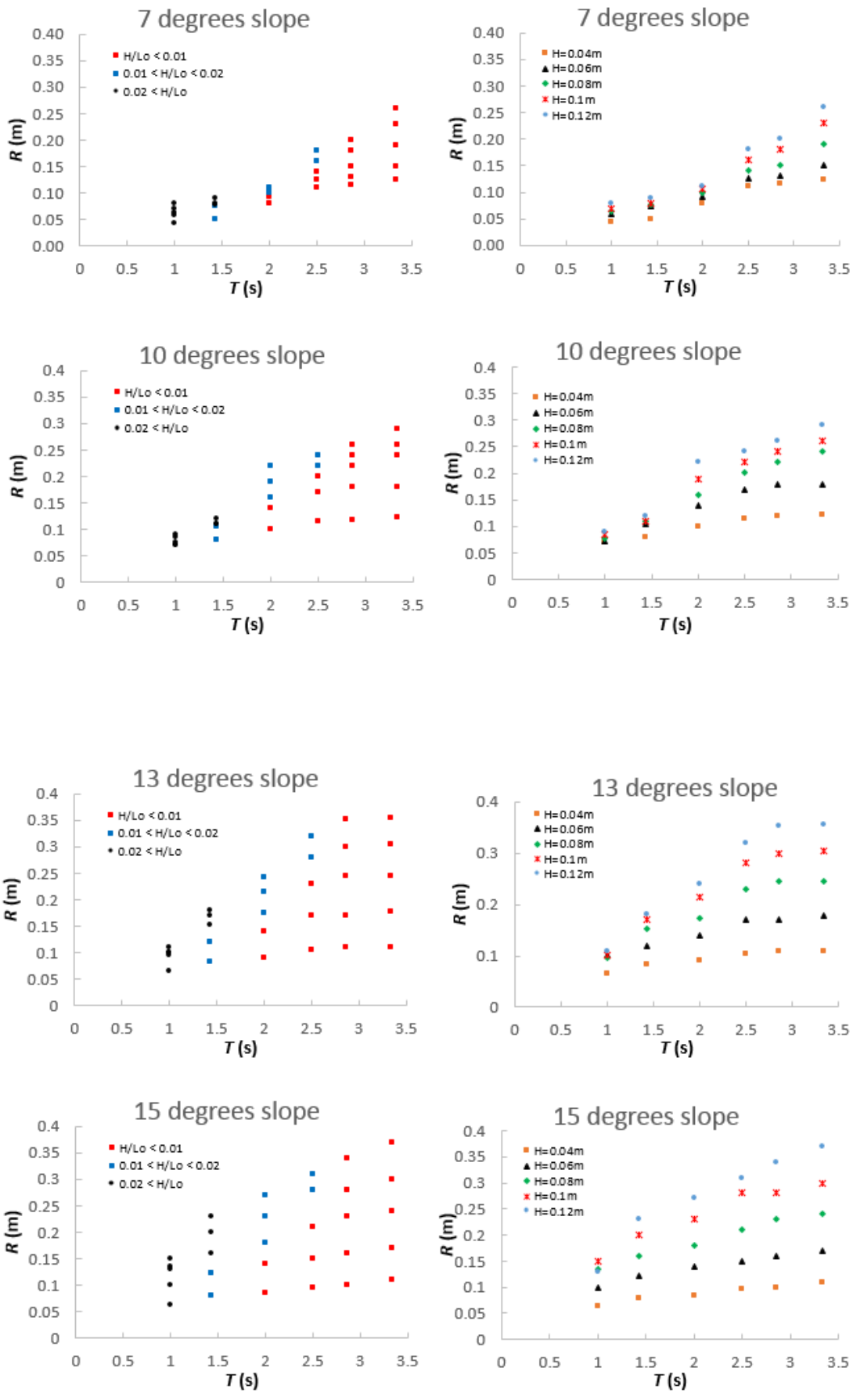

Figure 82 Wave run-up plotted against wave period for each slope.

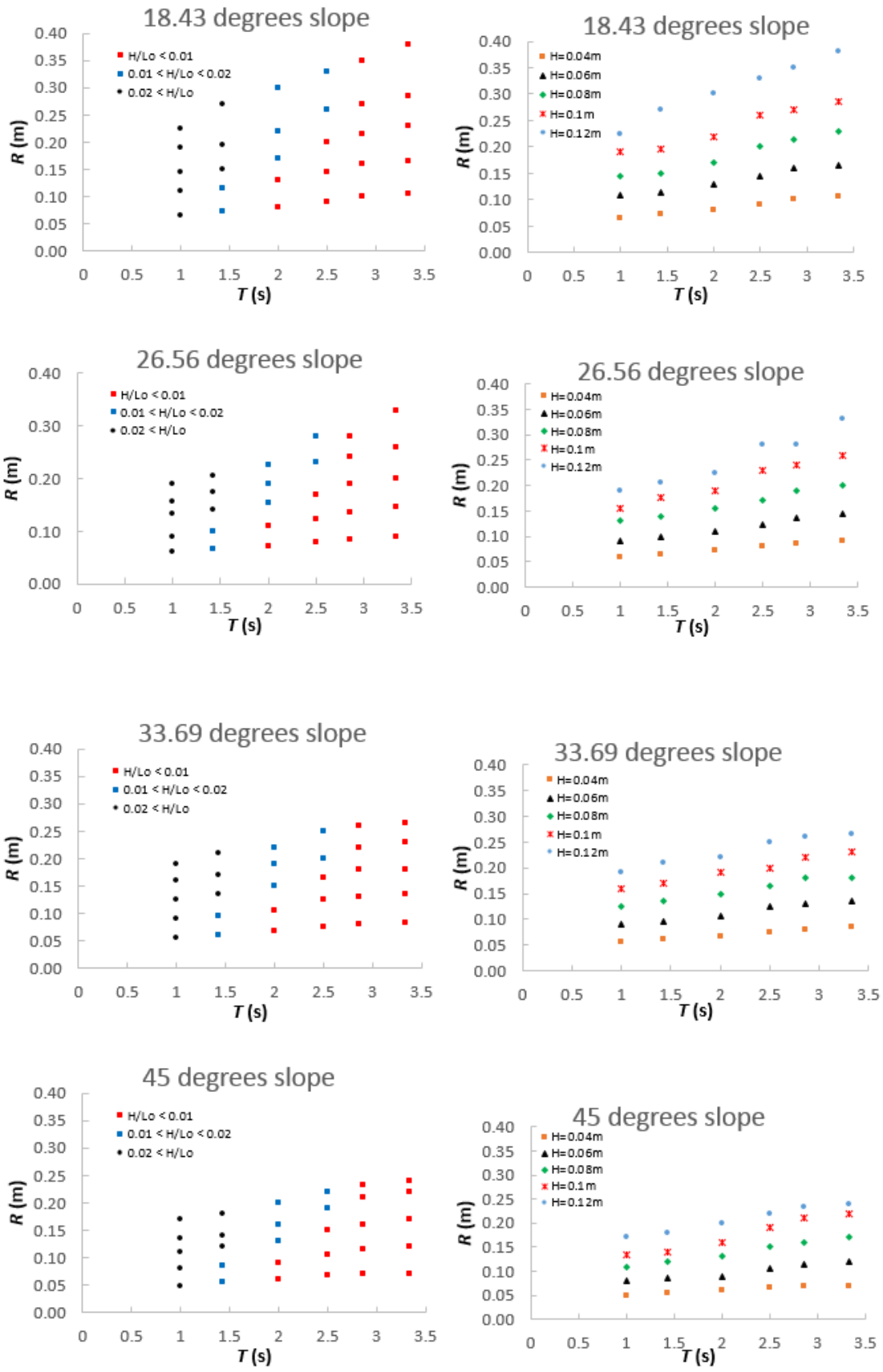

Figure 82 Continued Wave run-up plotted against wave period for each slope

6.1.2 **Wave Run-up Vs Wave Height**

Figure 83 shows graphs for the same eight slopes considered in figure 82, but this time the run-up is plotted against the wave height, *H*. Again, in the graphs on the left hand side, the data is separated by H/L_o, while the graphs on the right hand side show the same data but these are separated according to their wave period. Similar observations can be deduced from these graphs as from those observed in Figure 82. On the shallow slopes ($\alpha \leq 13°$), the wave height has a larger influence on run-up on longer waves with small wave steepness ($H/L_o < 0.01$, red dots) than on short steep waves ($H/L_o > 0.02$, black dots). From these graphs we can also appreciate how the influence of wave height increases for steep waves as the slope angle increases. After the 18.43° slope, the run-up values gradually decrease as the slope increases, and the influence of wave period decreases. This can be appreciated on the data for the steeper slopes, where most of the run-up values from different wave periods remain close together.

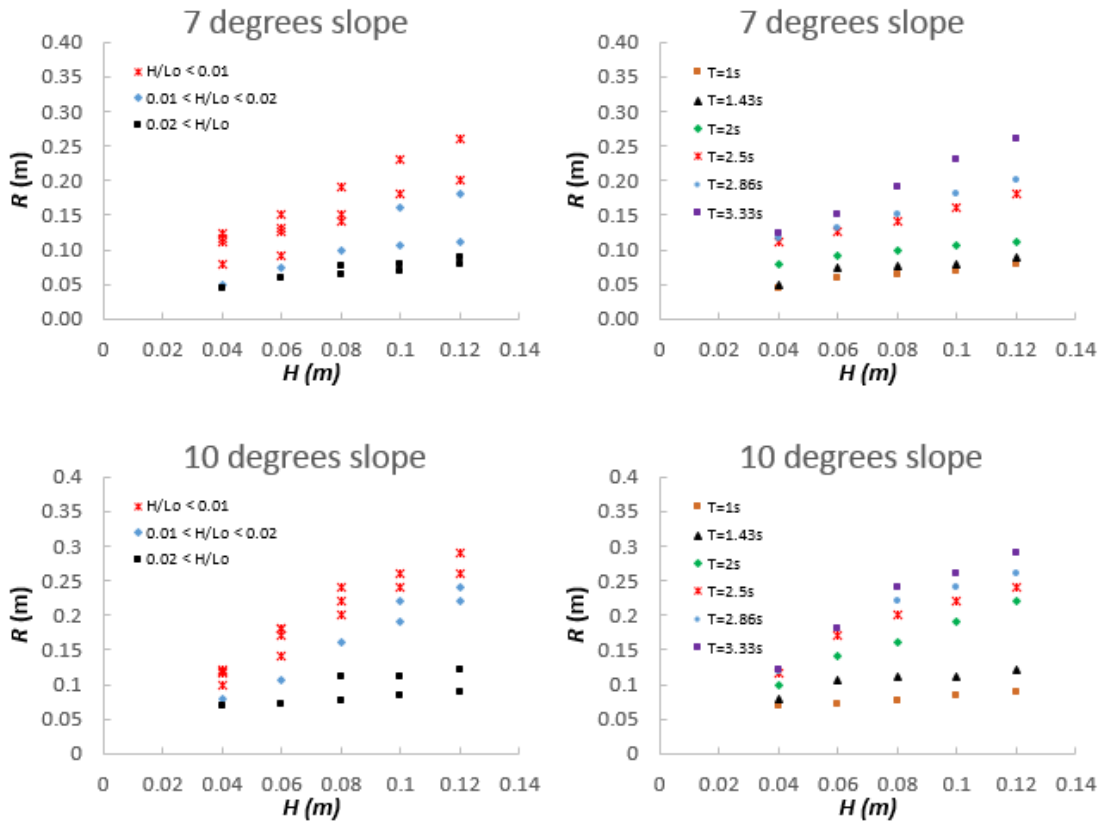

Figure 83 Wave run-up plotted against wave height for each slope

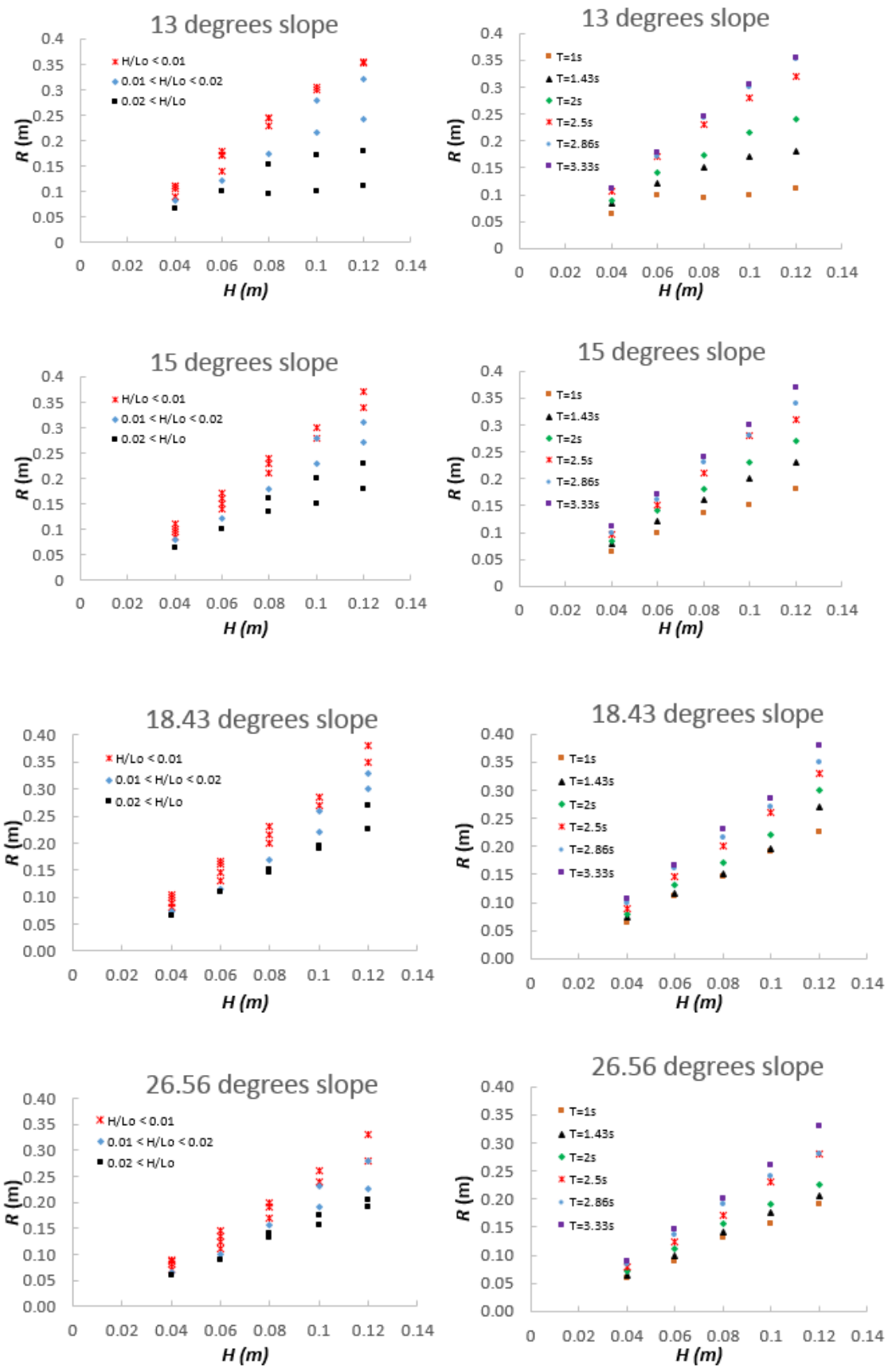

Figure 83 Continued: Wave run-up plotted against wave height for each slope

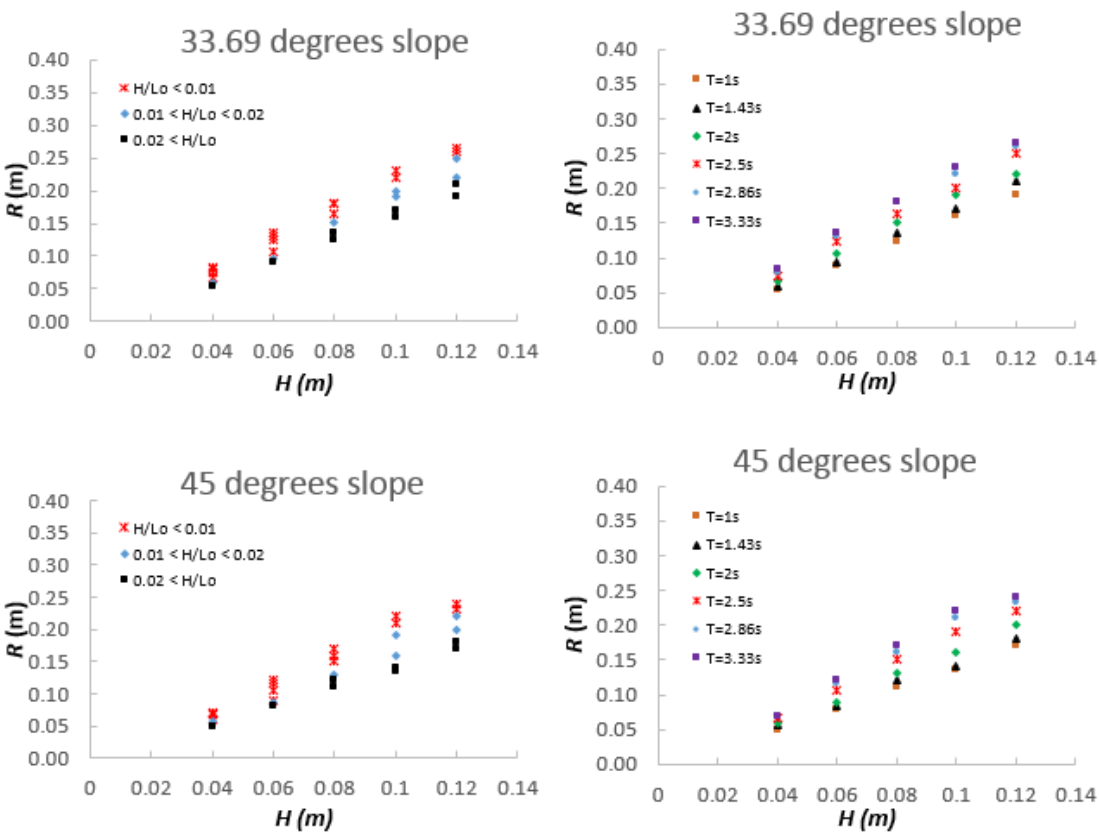

Figure 83 Continued: Wave run-up plotted against wave height for each slope

6.2 Non-Dimensional Analysis from Regular Waves

As mentioned in Chapter 2, wave run-up is commonly predicted using empirical or semi-empirical formulae based on non-dimensional parameters and empirical coefficients. Therefore, to compare the data obtained in these study to the prediction of existing run-up formulae, this section presents a non-dimensional analysis of wave run-up.

The most often used parameter to characterise wave run-up is the Iribarren number, ξ (discussed in Chapter 2.3). Figure 84 shows the run-up data obtained from the laboratory experiments (black dots) and numerical simulations (black crosses) performed with regular waves plotted against the Iribarren number. These run-up data are normalised by the wave height, R/H. For comparison, Hunt (1959) formulae $R/H = \xi$ for breaking waves and $R/H = 3$ for non-breaking waves (represented by red and black lines respectively) are also plotted in this graph. As discussed previously, most of the waves generated in the laboratory resulted in breaking waves on the slope, while most numerical simulations were performed on steep slopes resulting in non-breaking waves.

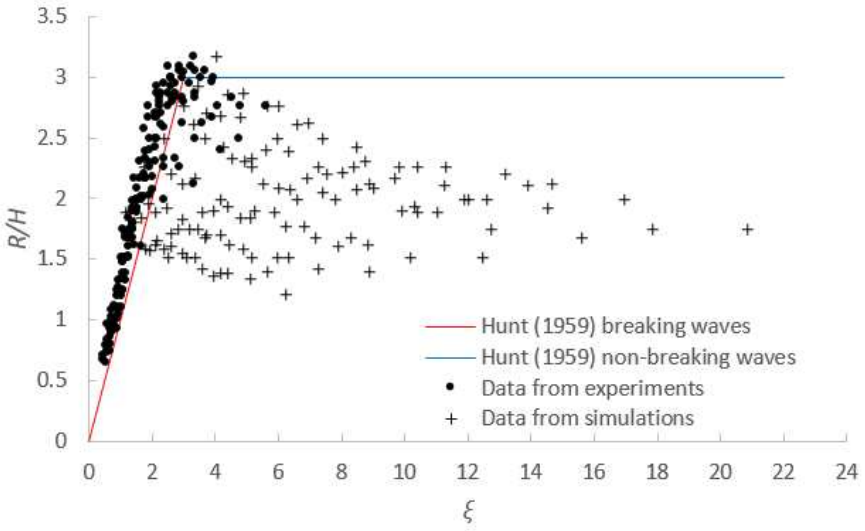

Figure 84 Run-up data from regular waves compared with Hunt (1959)

Two distinct groups of data can be observed on each side of Hunt's formula for breaking waves (red line). The first group, shown at the left-hand side, follow a similar trend as Hunt's formula, although with slightly higher values. These *R/H* data show very good correlation with ξ little scatter is seen. Most of these data correspond to the run-up from breaking waves. As discussed in the literature review chapter, this good correlation has been reported by many other authors (e.g. Hughes, 2004a; Hsu et al., 2012) and confirms previous studies suggesting the use of the Iribarren number to predict run-up from breaking waves. In contrast, the data shown on the right-hand side of Hunt's formula for breaking waves present considerable scatter. Most of these data correspond to the run-up from non-breaking waves. This significant scatter suggests that the Iribarren number might not be the ideal parameter to characterise run-up from non-breaking waves.

From this graph, it is evident why most run-up formulae have been proposed for either breaking or non-breaking waves at the slope, as these data follow completely different trends. For this reason, it is crucial to identify which run-up data correspond to breaking waves and which to non-breaking waves. This identification is necessary to compare the appropriate run-up data against previous formulae, as well for deriving new empirical formulae to predict run-up for either breaking or non-breaking waves.

6.2.1 Breaking Criteria

As discussed in the literature review, different parameters have been proposed to use as breaking criteria to determine the transition between breaking and non-breaking waves, the most common ones being H/L_o or ξ.

Hughes (2004a) suggested that the transition between breaking and non-breaking waves could be identified using the wave steepness. Using this parameter as the breaking criterion means that the slope angle of the structure does not influence whether waves

break or not on the slope. He got to this conclusion by re-analysing the run-up data presented by Ahrens (1981) and Mase (1989), where he plotted the run-up normalised by water depth at the toe of the plane slope, R/h, against the wave momentum flux parameter, ($M_F/\rho g h^2$). He noticed that the plotted R/h data exhibited two distinct trends which depended on their H/L_o values. The first trend had values of H/L_o < 0.0225. He suggested that these data corresponded to the run-up from non-breaking waves, while the data with values of H/L_o > 0.0225 corresponded to the run-up from breaking waves.

To analyse if this breaking criterion predicts correctly the transition between breaking and non-breaking waves of the present data, the R/h data were plotted against $M_F/\rho g h^2$ and divided according to their H/L_o values, as suggested by Hughes (2004a) (Figure 85). The blue dots correspond to the non-breaking waves with values of H/L_o < 0.0225, while the red dots to the breaking waves values of H/L_o > 0.0225. As can be seen, there is no clear distinction between the run-up from breaking and non-breaking waves.

When the same run-up data is normalised by the wave height, R/H, and plotted against the Iribarren number, and separated using the same criterion (H/L_o > 0.0225), two clear regions of data can be seen (Figure 86). Nonetheless, these regions do not represent the run-up from breaking and non-breaking waves, so this breaking criterion will not be used in this study. These inaccurate results of dividing breaking and non-breaking waves using wave steepness were expected as the slope angle was seen to clearly influence wave breaking throughout the tests performed.

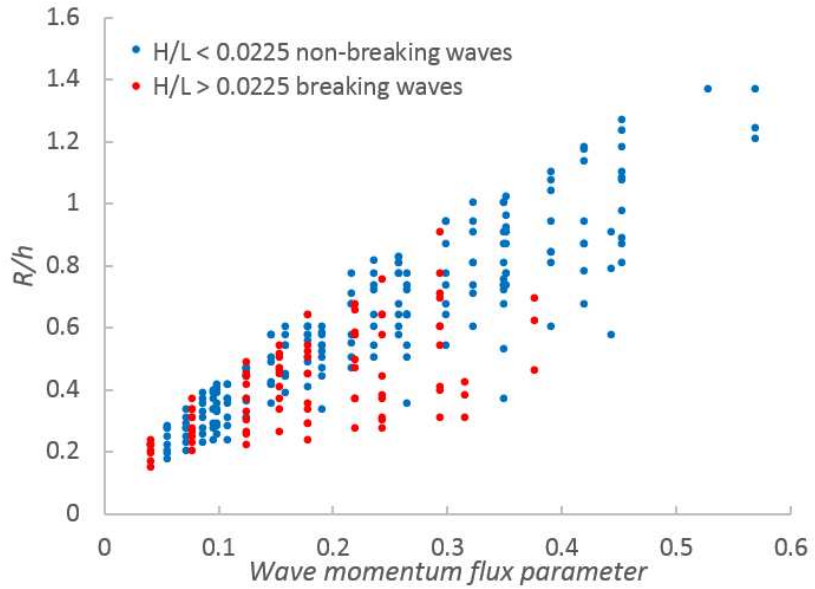

Figure 85 *R/h* separated using wave steepness as breaking criterion

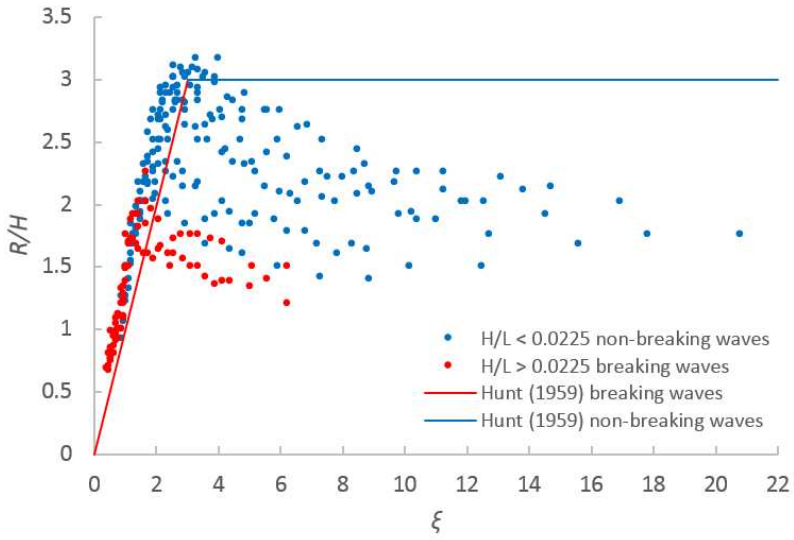

Figure 86 *R/H* separated using wave steepness as breaking criterion

The second breaking criterion analysed against the present data is the one based on the Iribarren number. This criterion is the most widely used in literature. Using this parameter as a criterion implies that the wave height, the wave length and the slope of the structure will all influence whether or not a wave will break at the slope. Several values for ξ have been proposed to indicate the transition between breaking and non-breaking waves (e.g., Burcharth and Hughes (2002) recommends a value of ξ =2.5, while the EurOtop (2007) manual suggests a value of ξ = 1.65. For the present data, a value of ξ = 3 was observed to best indicate the transition between breaking and non-breaking waves. This is shown in Figure 87, where the red dots represent the breaking waves with ξ < 3, and the blue dots represent the non-breaking waves with ξ > 3.

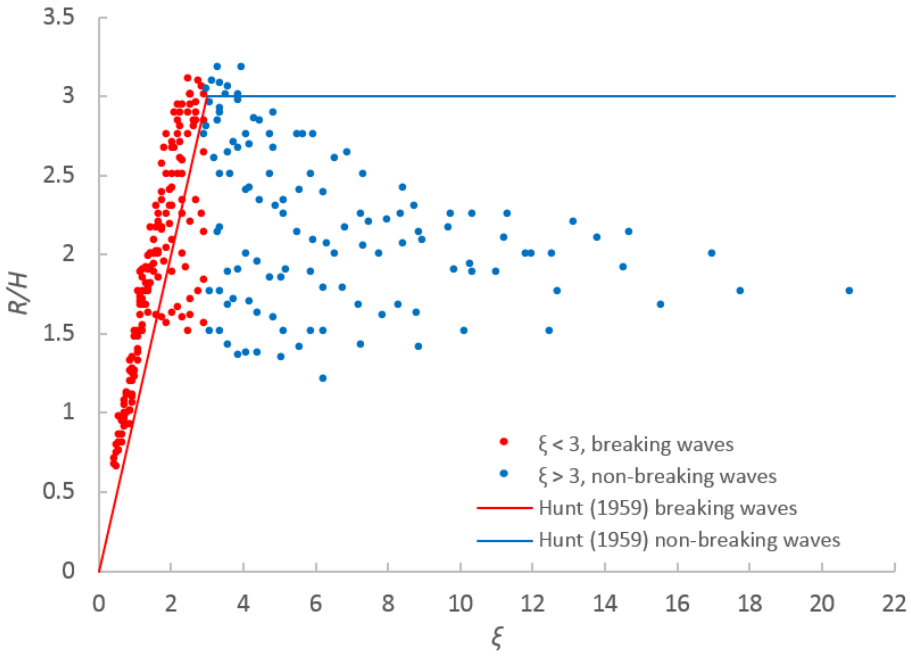

Figure 87 *R/H* separated using ξ = 3 as breaking criterion

As can be seen, ξ shows a much better division between the data representing the breaking waves and the non-breaking waves. Nevertheless, not all the data are divided properly if a single value of ξ is used to indicate the transition. In Figure 87, we can see that most of the red dots below Hunt's formula for breaking waves (red line) do not follow the same well defined trend followed by the rest of the red dots. Instead, these data follow the trends followed by the non-breaking waves (blue dots).

New Breaking Criterion. When the data were separated into groups according to their relative water depth, h/L_o, it was noticed that the data from the non-breaking waves in each group follow well-defined downward trends to the right hand side of the graph (Figure 88). The values of R/H for each case decrease as the wavelength decreases.

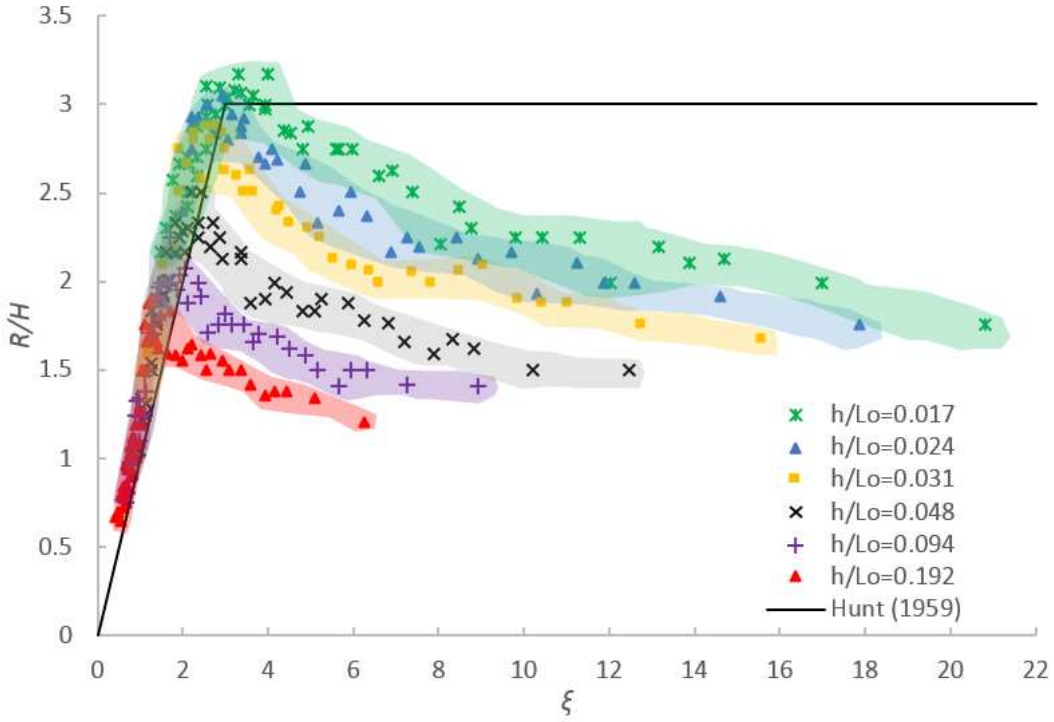

Figure 88 *R/H* data separated into groups according to their h/L_o

The data of each h/L_o group shown in Figure 88 were analysed individually and it was found that the Iribarren number predicted accurately the transition between the two trends shown in each h/L_o group. These two trends appear to represent the breaking and non-breaking waves. However, the ξ value found to indicate the transition in each h/L_o group, increased as the wavelength increased. This is shown in the graphs plotted in Figure 89 for each h/L_o group, where again the blue dots represent the non-breaking waves and the red dots represent the breaking waves. In each graph, the value of ξ indicating the transition between the two trends is displayed.

Although the Iribarren number indicates accurately the transition between both trends, the value indicating this transition changes depending on the wavelength. Therefore, it might not be the best breaking criterion for the present data. To separate the data from breaking and non-breaking waves, it is necessary to have a constant value of a parameter to indicate the transition for all the data.

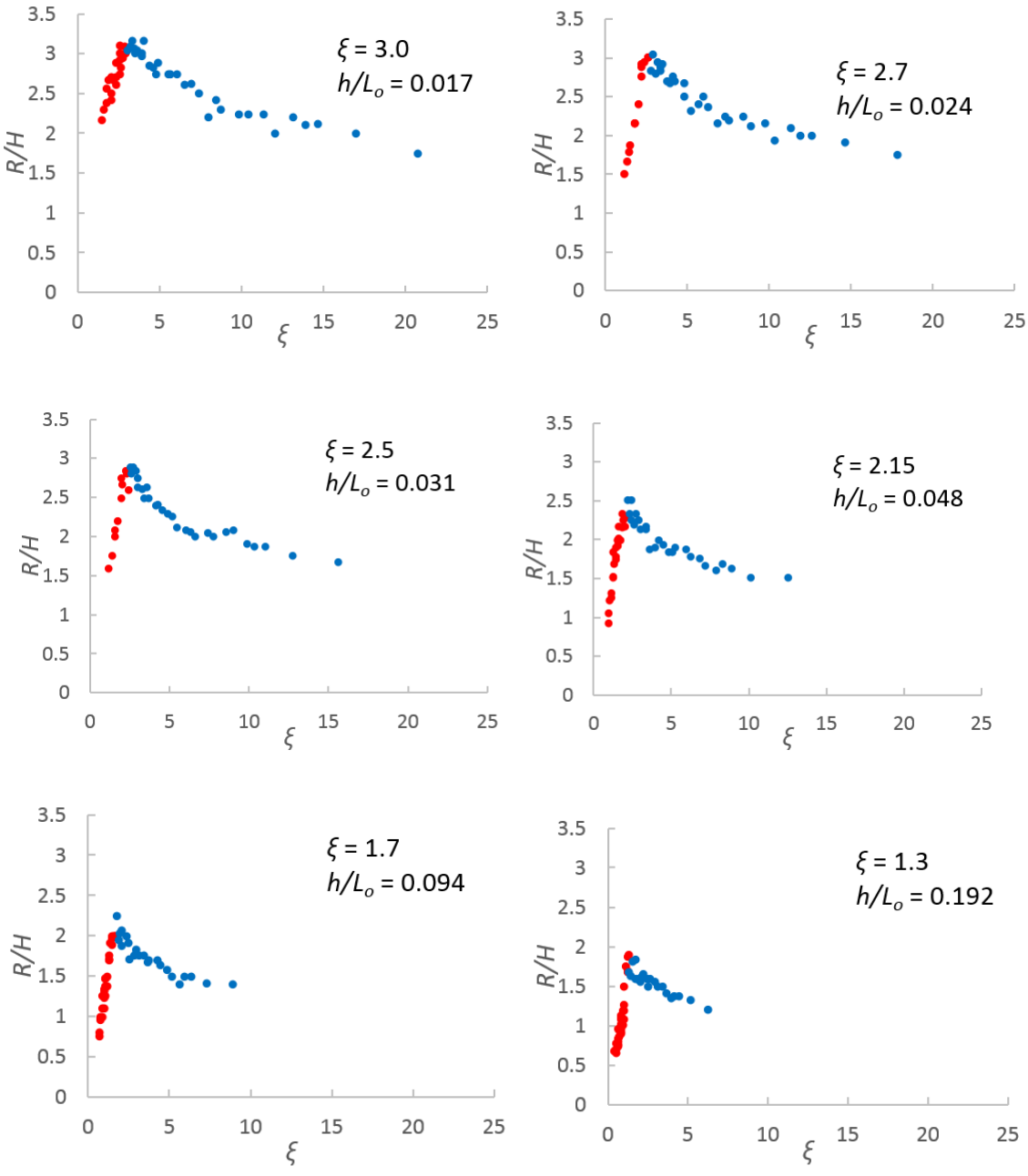

Figure 89 Individual graphs for each h/L_o group showing the value of the breaking transition using ξ; the red dots represent breaking waves while the blue dots non-breaking waves

When the data of each h/L_o group were analysed separately, it was observed that the transition between both trends depended mainly on the angle of the slope and on the wave height, and not on the wavelength. These observations led to the proposal of a new

breaking criterion. This parameter is given by the relationship between the slope of the structure, tan α, and the relative wave height, H/h:

$$\frac{\tan\alpha}{\left(H/h\right)} \tag{83}$$

The same data groups of h/L_o were used to analyse the performance of this parameter as a breaking criterion. The analysis showed that the transition between breaking and non-breaking waves occurred at a constant value of approximately $\tan\alpha/(H/h) \approx 1$ for all the h/L_o groups. This is shown in the graphs plotted in Figure 90 for each h/L_o group, where the data are divided using the following breaking criterion:

$$\tan\alpha/(H/h) < 1, \text{ for breaking waves} \tag{84}$$

$$\tan\alpha/(H/h) > 1, \text{ for non-breaking waves} \tag{85}$$

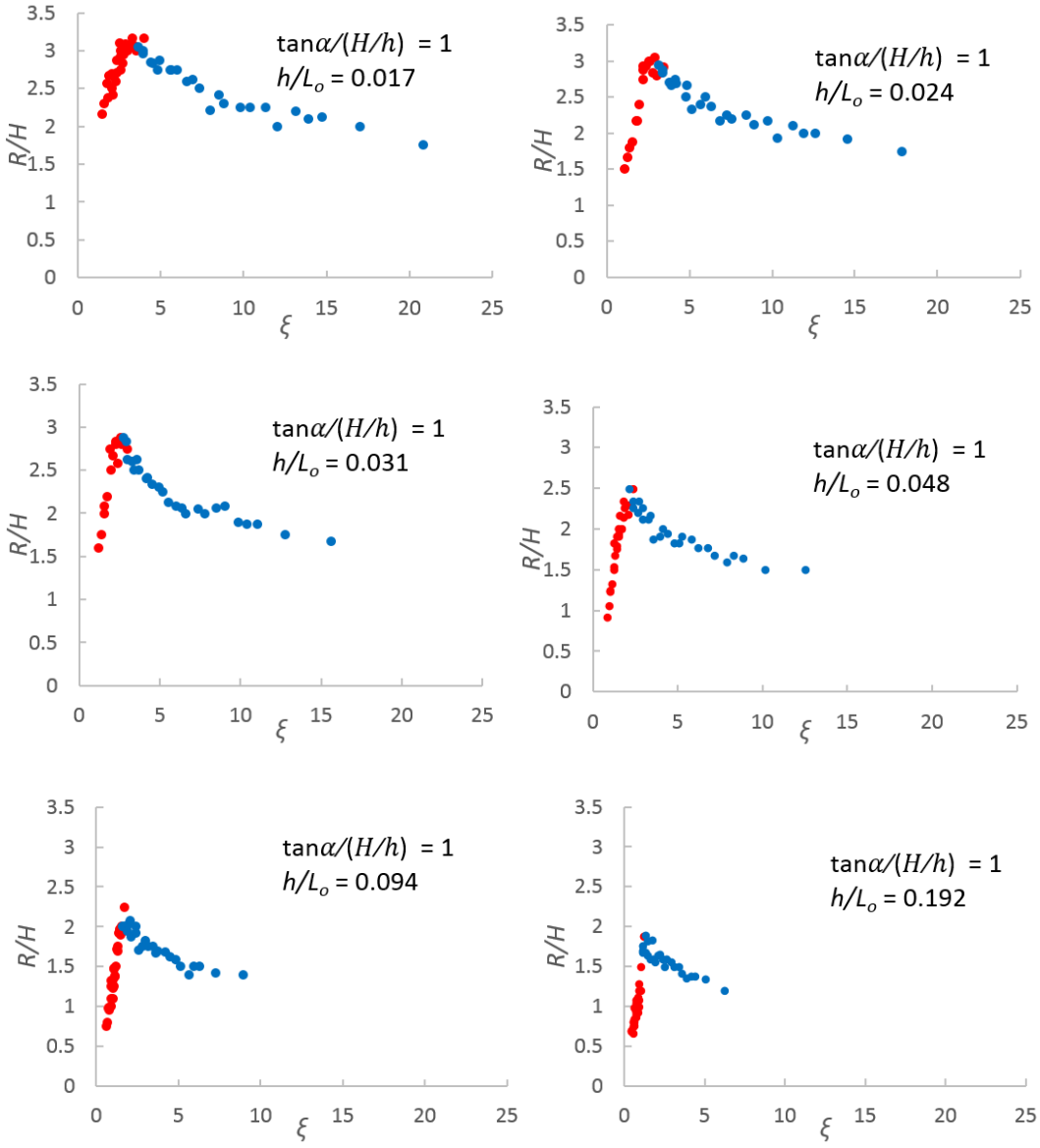

Figure 90 Individual graphs for each h/L_o group showing the value of the breaking transition using $\tan\alpha/(H/h)$

The values indicating the transition between both trends using ξ and $\tan\alpha/(H/h)$ for each h/L_o (shown in Figure 89 and Figure 90) are summarised in Table 35.

The constant transition value observed using $\tan\alpha/(H/h)$ suggests that this is the best parameter to use as breaking criterion for the present data. Therefore, it was adopted to categorize the run-up data between breaking and non-breaking waves. Figure 91 shows all the run-up data plotted together following the breaking criterion given by (84) and (85). The predictions of this breaking criterion are validated against video observations in Section 7.1.1.

h/L_o	ξ	$\tan\alpha/(H/h)$
0.192	1.3	1
0.094	1.7	1
0.048	2.15	1
0.031	2.5	1
0.024	2.7	1
0.017	3	1

Table 35 Summary of transition values using ξ and $\tan\alpha/(H/h)$

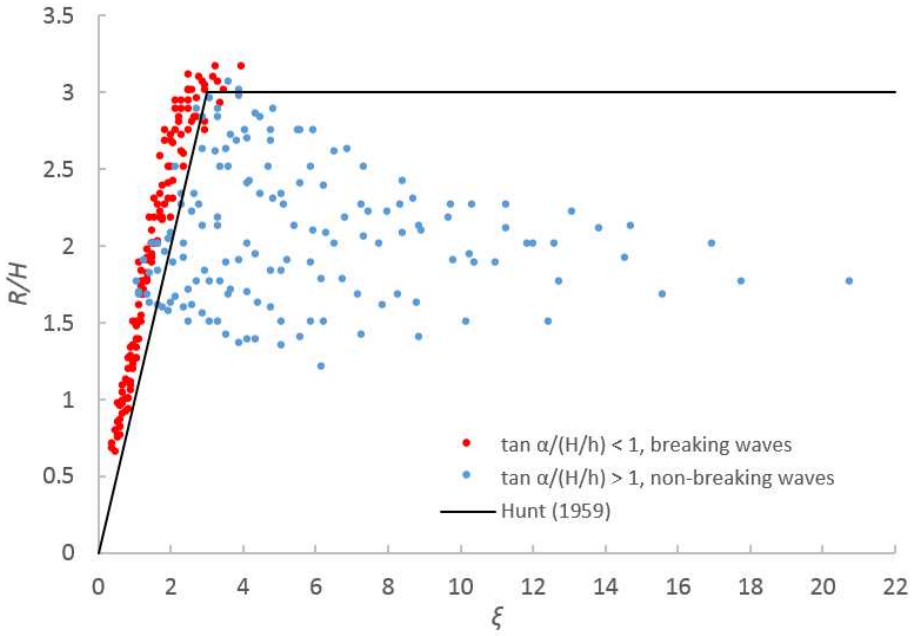

Figure 91 R/H data separated using $\tan\alpha/(H/h)$as breaking criterion

6.2.2 Breaking Waves

Previous studies have shown the efficiency of Hunt's formula in predicting wave run-up from breaking waves on smooth-impermeable slopes (e.g. Losada and Giménez-Curto, 1980; Hughes, 2004a; Hsu et al., 2012). These studies compared Hunt's formula against laboratory data sets presented by Grantham (1953), Saville (1955) and Hsu et al. (2012). However, as shown above, the present data are slightly under-predicted by Hunt's formula.

The larger run-up values obtained in this study might be explained by the technique used to measure run-up. Grantham (1953), Saville (1955) and Hsu et al. (2012) all used run-up gauges, while the run-up measurements in this study were obtained through digital video recordings. As mentioned in the literature review, previous studies (e.g. Schimmels et al, 2012; Van Broekhoven, 2011) have shown that data extracted from video cameras show slightly higher run-up values than those extracted from run-up gauges.

Figure 92 shows the R/H data from breaking waves compared with three previous formulae based on the Iribarren number: Hunt (1959), Losada and Gimenez-Curto (1980) and Schüttrumpf (2001). As can be seen, the Losada and Gimenez-Curto (1980) and Schüttrumpf (2001) formulae considerably under-predict the R/H data. The present data show two distinct trends, which are very similar to the trends followed by Hunt's formulae. The first of these trends is defined by the data with values of $\xi < 2.4$. These data follow a similar direction to the one shown by Hunt's formula $R/H = \xi$ (black line) but with slightly larger values. On the other hand, the data with values of $\xi > 2.4$ have a constant value close to the $R/H = 3$ suggested by Hunt for values of $\xi > 3$.

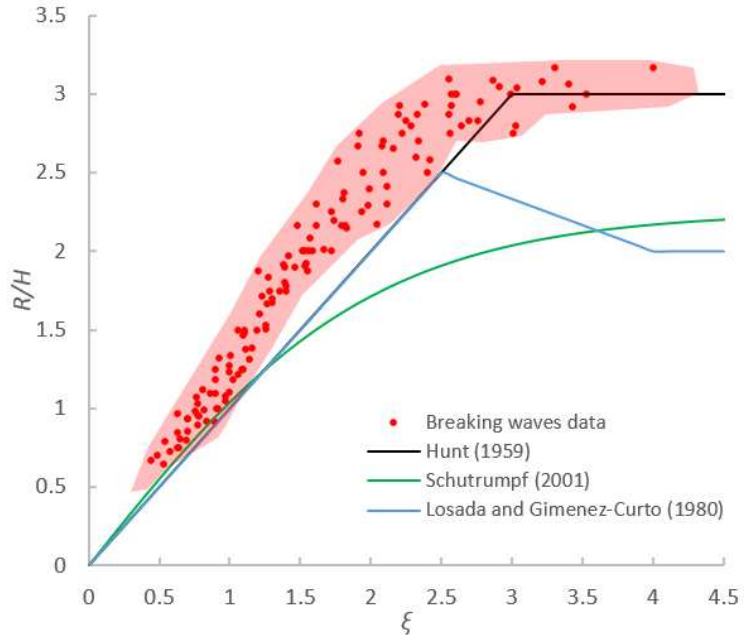

Figure 92 *R/H* data from breaking waves compared to formulae based on the Iribarren number

As Hunt's formula $R/H = \xi$ for values $\xi < 3$ under-predicts the present data, slightly modified formulae for different ranges of ξ are presented below to improve the prediction of the present run-up data from breaking waves. These are given by the following expressions:

$$\frac{R}{H} = 1.25\xi, \qquad \text{for } \xi < 2.4 \tag{86}$$

$$\frac{R}{H} = 3, \qquad \text{for } \xi > 2.4 \tag{87}$$

The run-up data from breaking waves were also shown to be very well predicted using the hyperbolic function proposed by Schüttrumpf (2001) but with modified empirical coefficients a and b:

$$\frac{R}{H} = a * \tanh(b * \xi) \tag{88}$$

Schüttrumpf (2001) suggested values of a=2.25 and b=0.5 for the empirical coefficients. However, as seen in Figure 92, these values considerably under-estimate the present data (green line). A best-fit of this equation to the run-up data yielded the following empirical coefficients: a=3.74 and b=0.38. This modified hyperbolic function describes a smoother transition between the two trends (shown in Figure 92) than equations (86) and (87).

For comparison, Figure 93 shows the R/H data from breaking waves plotted against Hunt's and Schüttrumpf (88) formulae, as well as against the new modified formulae. The solid 45° line in each graph represents the line of equivalence. As can be seen, the predictions of the two modified formulae show great agreement with the present data.

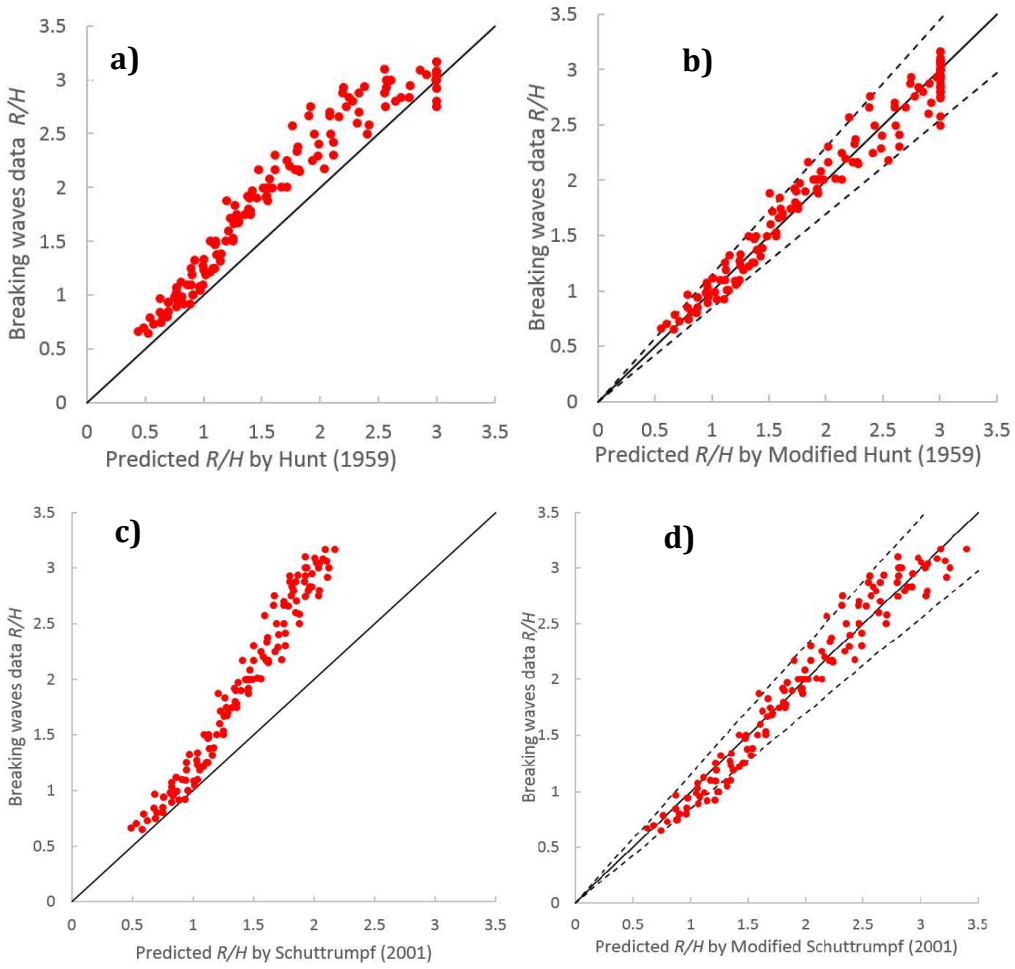

Figure 93 *R/H* data from breaking waves versus predicted values of formulae based on the Iribarren number: a) Hunt (1959); b) Modified Hunt (1959); c) Schüttrumpf (2001); and d) Modified Schüttrumpf (2001). Solid line: perfect agreement; dash line: ± 15% error bands

The well-defined trends and limited scatter shown when the *R/H* data from breaking waves is plotted against ξ is a good indicator that formulae based on this parameter will show accurate predictions.

Hughes (2004a) suggested that the success of the Iribarren number in characterising run-up from breaking waves may lie in the assumption that broken waves become self-similar during shoaling. Hughes (2004a) writes:

"Consider two waves having significantly different wave heights but the same value of wave steepness, H/L_o. Depth-limited breaking will occur at different water depths on the slope, and the magnitude of the dimensional flow kinematic parameters at breaking will be different between the two waves. However, the good correlation between run-up and the Iribarren number suggests that depth of initial wave breaking and breaking wave kinematics are not critical for breaking wave run-up because ultimately the two different waves having the same value of H/L_o become similar in the surf zone as observed by Battjes (1974)."

As mentioned in Chapter 2, another parameter that has been suggested in literature to describe wave run-up is the wave momentum flux parameter, $M_F/\rho g h^2$. However, Hughes (2004a) showed that, for breaking waves, formulae based on the Iribarren number provide better predictions than those based on the momentum flux parameter. This was also confirmed in this study when the present data were compared to Hughes (2004a) formula for breaking waves:

$$\frac{R}{h} = 3.84 \tan\alpha \left(\frac{M_F}{\rho g h^2}\right)^{1/2} \tag{89}$$

This can be seen in Figure 94a, where the run-up data from breaking waves is compared with the predictions of (89). Note that the run-up is normalised by the water depth rather than by the wave height. It can be seen that (89) also under-predicts the run-up from breaking waves. A curve-fitting of Hughes formula to the present data, yielded the following expression:

$$\frac{R}{h} = 6.25 \tan\alpha \left(\frac{M_F}{\rho g h^2}\right)^{1/2} \tag{90}$$

The predictions of this modified formulae are shown in Figure 94b. As can be seen, the data in both graphs show considerably more scatter than when the data were compared against formulae based on the Iribarren number (Figure 93). These comparisons confirm

what previous studies have suggested: the Iribarren number is the ideal parameter to use in formulae predicting run-up from breaking waves on smooth-impermeable slopes.

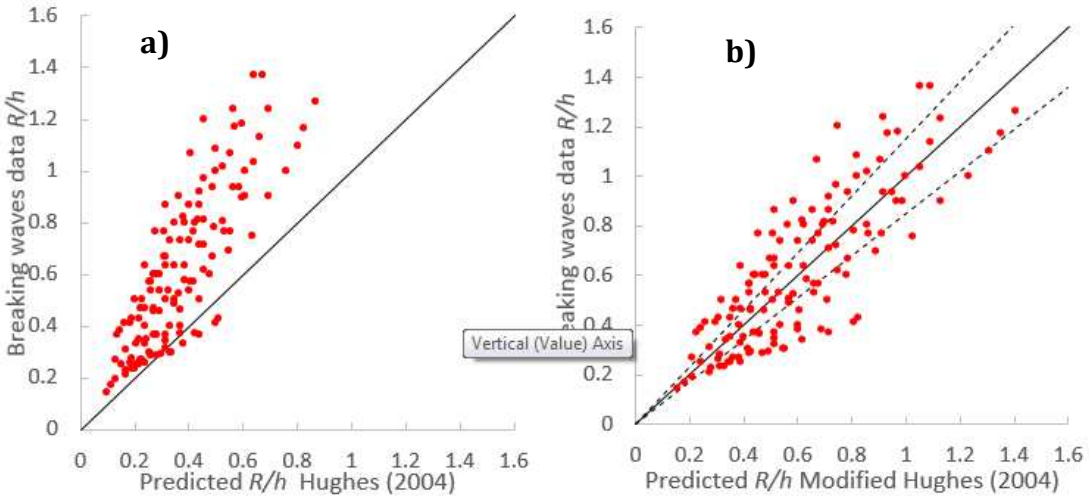

Figure 94 *R/h* data from breaking waves versus predicted values of formulae based on the wave momentum flux parameter. a) Hughes (2004) and b) Modified Hughes (2004). Solid line: perfect agreement; dash line: ± 15% error bands.

6.2.3 Non-breaking waves

Figure 95 shows the run-up data from the non-breaking waves compared to the predictions of two previous formulae based on the Iribarren number for non-breaking waves on smooth-impermeable slopes: Hunt (1959) and Losada and Gimenez-Curto (1980).

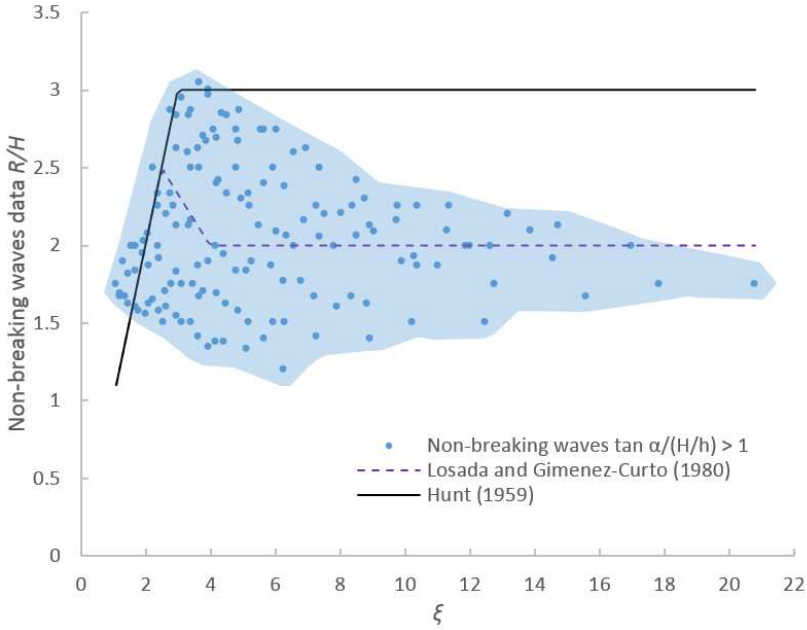

Figure 95 *R/H* data from non-breaking waves compared to formulae based on the Iribarren number

As can be seen, neither of these formulae predict accurately the present data. As discussed previously, the horizontal line representing Hunt's formula $R/H = 3$ for values $\xi > 3$

significantly over-predict the present data. This over-prediction was also reported by Hsu et al. (2012). A better prediction is shown by Losada and Gimenez-Curto's formulae, as its predictions (dotted lines) go through the middle of the data.

Run-up data separated by slope angle. Figure 96 shows the run-up data from the non-breaking waves separated according to the slope angle of the structure. The shaded coloured areas show the regions covered by the data of each data group.

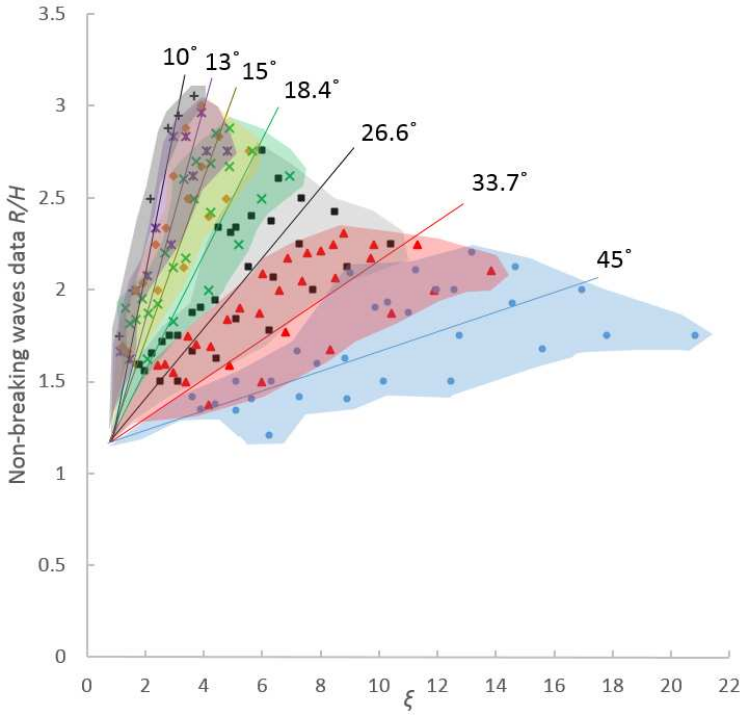

Figure 96 *R/H* data from non-breaking waves divided into groups according to their slope

From Figure 96 we can confirm that run-up from non-breaking waves is highly dependent on the slope angle of the structure as R/H decreases as the slope angle increases. Additionally, the gradient for each slope angle decreases as the angle of the structure increases. Similar observations were reported by Hsu et al. (2012), who presented results where the R/H data with values $\xi > 2$ followed well-defined trends for each slope angle tested. Similarly, the gradient of the data shown by Hsu et al. were seen to decrease as the angle of the structure increased. Hsu et al. suggested that the reduction in run-up as the slope increases can be attributed mainly to the increase in backwash force from the fluid weight component $\rho g \sin\alpha$.

Although the present data show some similarities with Hsu's results, there are also some significant differences. In Hsu et al. (2012) results, the trends corresponding to each slope angle were shown to meet around a value of $R/H = 2$ and $\xi = 2$. In contrast, the trends shown in Figure 96 meet around $R/H \approx 1.3$ and $\xi \approx 1.6$. Moreover, in Hsu et al. (2012) results, the data corresponding to each slope angle followed very well-defined trends with

little scatter. In contrast, the present data show significant scatter around each line corresponding to the different slope angles. The well-defined trends presented by Hsu et al. led them to develop an empirical formula for non-breaking waves and slopes steeper than 11.5˚ (91). This formula is based on the gradients of the data from each slope angle tested.

$$R/H = 2\left(\frac{\xi}{2}\right)^{0.04/tan^2\alpha} \tag{91}$$

However, due to the considerable scatter shown for each slope (Figure 96), the procedure shown by Hsu et al. to develop their formula is not appropriate if the present data are used to derive a new formula. For comparison, Figure 97 shows the present run-up data from non-breaking waves compared with the predictions of (91). Again, the solid line represents the line of equivalence. As can be seen, (91) also does not predict accurately the present data.

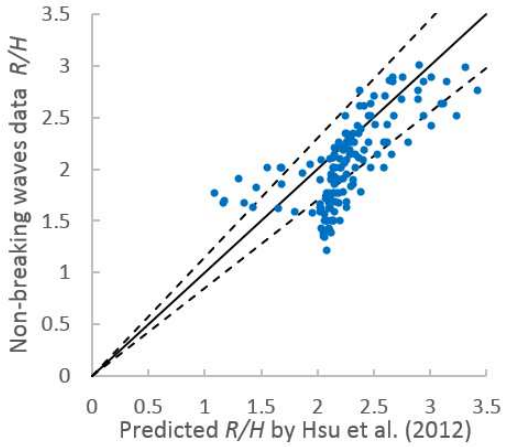

Figure 97 *R/H* data from non-breaking waves versus predicted values of (91). Solid line: perfect agreement; dash line: ±15% error bands.

Run-up data separated by wavelength. As shown in Section 6.2.1, well-defined trends were noticed when all the results were divided by the relative water depth, h/L_o. This is shown again in Figure 98, where only the data corresponding to the non-breaking waves are plotted.

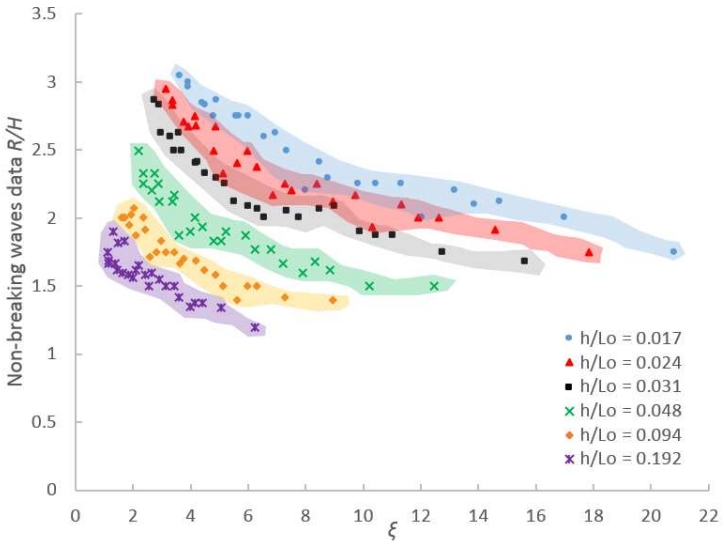

Figure 98 *R/H* data from non-breaking waves divided into groups according to their h/L_o

As can be seen, all of the groups corresponding to each h/L_o follow similar downwards well-defined trends. The *R/H* data in each group decrease as the slope angle increases and as the Iribarren number increases; also, as mentioned previously, the value of *R/H* for each group decreases as the wavelength decreases. These findings led the present study to derive a new empirical formulae for run-up of non-breaking waves based on both ξ and h/L_o. The derivation of the new formula is described below.

Each of the groups shown in Figure 98 can be seen to be well described by negative power functions of the form:

$$\frac{R}{H} = a\xi^{-b} \tag{92}$$

where a and b are empirical coefficients. Power regressions were performed to estimate the values of these coefficients for each group of h/L_o. The results are shown in Figure 99 and summarised in Table 36. Figure 99 shows the same data in a log-log graph for clearer visualisation as straight lines.

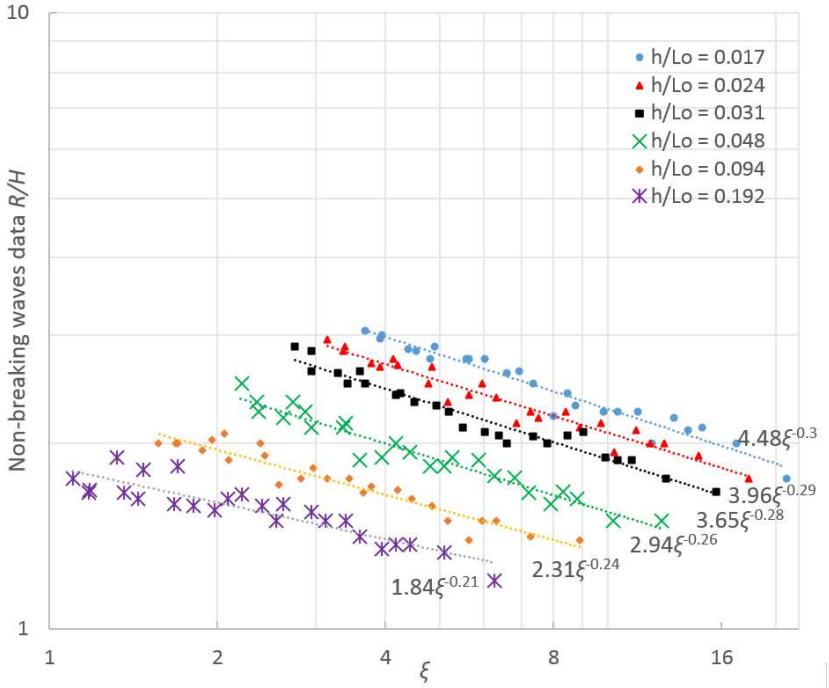

Figure 99 Log-log plot showing coefficients of power regressions performed to each h/L_o group

From Figure 99, we can see that both the values and gradient of the curves change depending on their h/L_o. The values of both coefficients increase as h/L_o increases. Therefore, we can expect both coefficients a and b to be a function of h/L_o. This is shown in Figure 100, where both parameters are plotted against their corresponding h/L_o values. The trends described by both coefficients were found to be best described by negative power formulae, which are displayed in each graph.

h/L_o	a values	b values
0.017	4.48	0.3
0.024	3.96	0.29
0.031	3.65	0.28
0.048	2.94	0.26
0.094	2.31	0.24
0.192	1.84	0.21

Table 36 Summary of a and b coefficient values for each h/L_o group

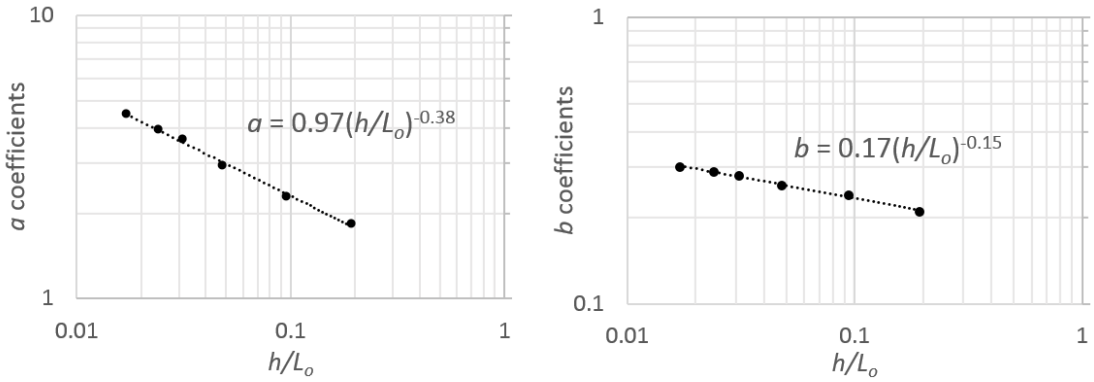

Figure 100 Log-log plot of a and b coefficient values against their corresponding h/L_o

The formulae obtained from the graphs in Figure 99 can replace the empirical coefficients in (92) resulting in:

$$\frac{R}{H} = a\xi^{-b} \tag{93}$$

where:

$$a = 0.97\left(h/L_o\right)^{-0.38} \tag{94}$$

$$b = 0.17\left(h/L_o\right)^{-0.15} \tag{95}$$

The good fit shown by the data of each h/L_o group with their corresponding negative power expressions (Figure 99), as well as the good fit shown by the empirical coefficients and their corresponding h/L_o values (Figure 100), resulted in very good agreement with the present data. This can be seen in Figure 101, where the predicted values from (93) are plotted against the present data from non-breaking waves.

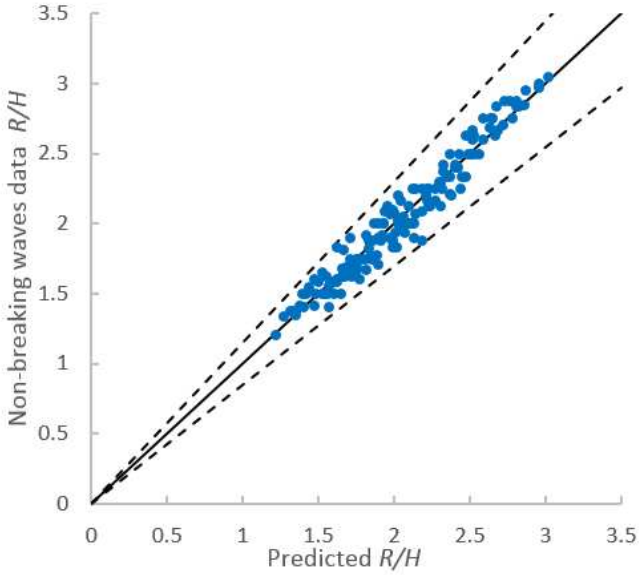

Figure 101 *R/H* data from non-breaking waves versus predicted values of equation (93). Solid line: perfect agreement; dash line: ±15% error bands.

New dimensionless parameter for non-breaking waves. The analysis shown in Section 6.1 shows that wavelength (or wave period) has a very small influence on run-up from non-breaking waves on steep slopes. However, Figure 98 shows that when the *R/H* data of non-breaking waves is plotted against the Iribarren number, the *R/H* data from each wavelength display similar downwards trends, but each with different heights. This suggests that the wavelength influence given by the Iribarren is larger than the wavelength influence observed in Section 6.1 on non-breaking waves.

Re-arranging Hunt's formula (R/H = ξ), we can see that this formula states that $R \propto \tan\alpha\sqrt{H}\sqrt{L_o}$. As discussed above, this formula allows the wavelength to play a significant

role in determining the value of wave run-up, as run-up will increase proportionally to $\sqrt{L_o}$. This has been shown to be valid for breaking waves on shallow slopes, but not for non-breaking waves on steeper slopes. For this reason, a new non-dimensional parameter is proposed in this study to replace the Iribarren number and characterise run-up from non-breaking waves. This parameter, which will be represented by the upper case Greek letter Phi, Φ, reduces the influence of wavelength and is given by:

$$\Phi = \frac{\tan\alpha \cdot h}{\sqrt{HL_0}} \tag{96}$$

The water depth, *h,* is introduced simply to make Φ a non-dimensional parameter. As *h* remained constant in all the tests presented in this study, it did not influence the calculated values of Φ. However, future studies are suggested to analyse the influence of *h* in this parameter. Plotting the *R/H* data from the non-breaking waves against Φ resulted in significantly less scatter than when plotted against ξ.

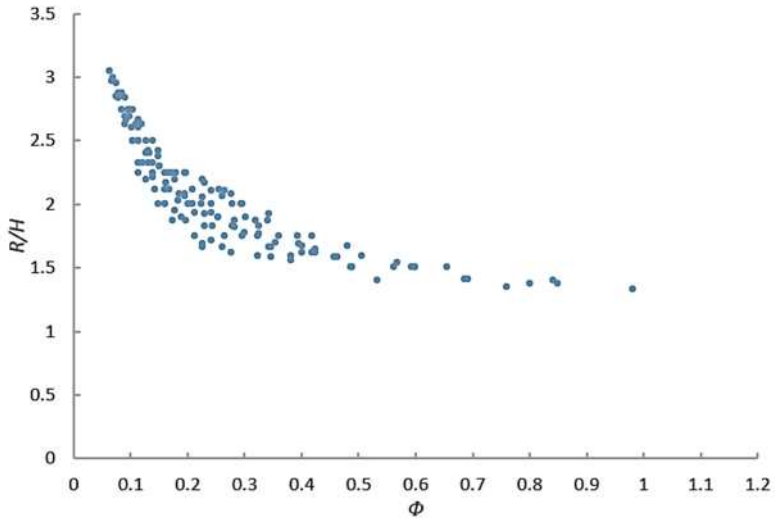

Figure 102 *R/H* data from non-breaking waves against new parameter Φ

Curve fitting of the data resulted in:

$$\frac{R}{H} = a(\Phi)^{-b} \tag{97}$$

where *a* and *b* are empirical coefficients. The curve fitting can be seen clearer on the log-log graph shown in Figure 103, where the data are seen to follow a straight line. A best-fit of this equation to the present data was obtained by performing a power regression which resulted in:

$$\frac{R}{H} = 1.25\Phi^{-0.32} \tag{98}$$

From Figure 103 we can see that this formula based on the new parameter Φ can correctly estimate run-up from non-breaking waves.

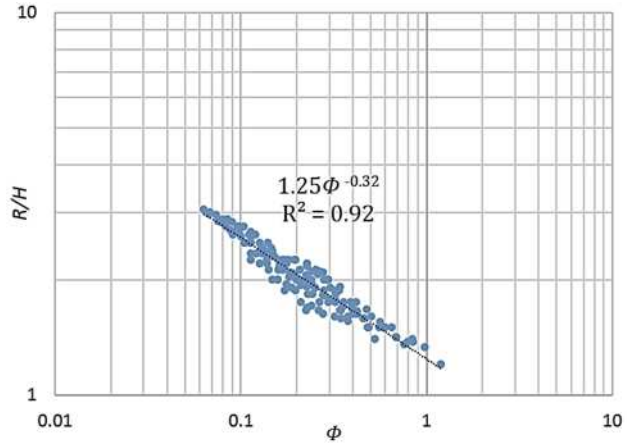

Figure 103 Log-log plot showing the coefficients *a* and *b* from the power regression

Wave momentum flux parameter. According to Hughes (2004a), the wave momentum flux parameter, $M_F/\rho g h^2$, characterises run-up from non-breaking waves better than the Iribarren number. However, none of the formulae suggested by him to predict run-up from non-breaking waves predicted the present data accurately. Nevertheless, when the present *R/h* data of each slope angle were plotted against the momentum flux parameter, a good correlation was seen (Figure 104).

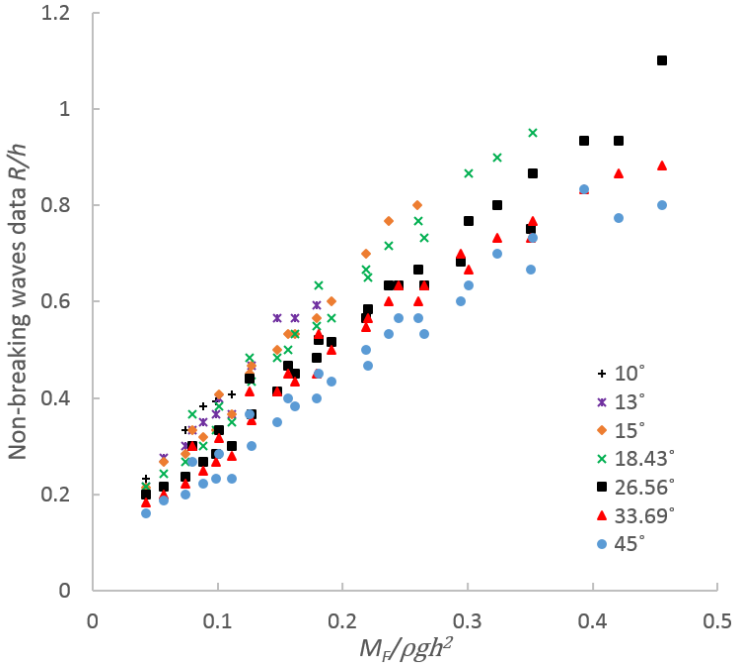

Figure 104 *R/h* data from non-breaking waves against the wave momentum flux parameter; data divided according to their slope angle

This good correlation led to the development of a new empirical formula based on this parameter. The derivation of this formula is described below.

From Figure 104 we can see that the data from each slope angle follow well-defined trends with few scattered data. These trends were found to be best described by power functions in the form of:

$$\frac{R}{h} = a\left(\frac{M_F}{\rho g h^2}\right)^b \tag{99}$$

where a and b are empirical coefficients. Power regressions were performed to the data of each slope angle to estimate values for empirical coefficients a and. These regressions are shown in the log-log graphs shown in Figure 105 and their values are summarised in Table 37. As can be seen, the data points in all the graphs show a good fit with the estimated power functions. The coefficient a in a power function serves as a scaling factor, moving the values of x^b up or down, while the coefficient b determines the function's rate of growth.

Slope Angle	cot α	a values	b values
10°	5.67	1.7	0.63
13°	4.33	2.25	0.72
15°	3.73	2.11	0.75
18.43°	3	2.04	0.74
26.56°	2	1.79	0.75
33.69°	1.5	1.65	0.73
45°	1	1.53	0.75

Table 37 Summary of a and b coefficients for each slope angle

From Table 37 we can see that the coefficient a is a function of the slope angle, as it decreases as the angle of the slope increases. Therefore, we can expect this coefficient to be a function of the cotangent of the slope. An exception is the 10° slope, where the value of the coefficient a is smaller than that on the 13° slope. In contrast, it was noticed that the power coefficients b are not a function of the slope angle, as their values remain fairly constant for all slope angles: $b \approx 0.75$ or ¾ (except on the 10° slope). On the 10° slope, only a few of the waves generated were categorised as non-breaking. Therefore, this value was derived from limited data points, making less reliable than those from the other slopes. Hence the 10° was not considered further in this analysis.

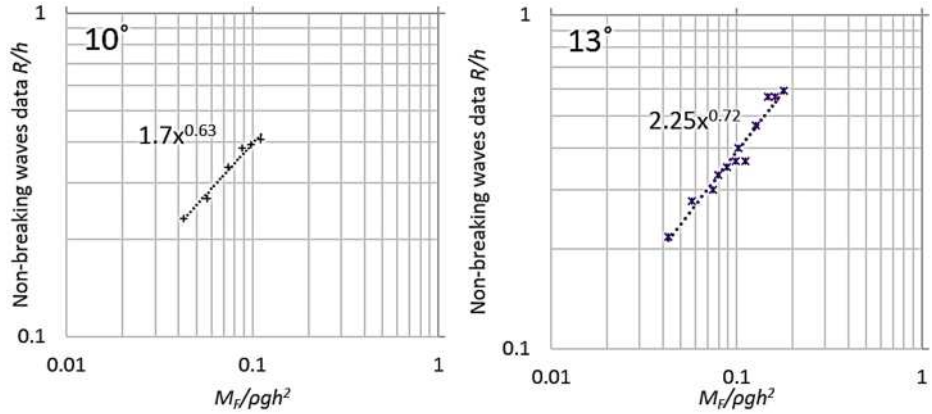

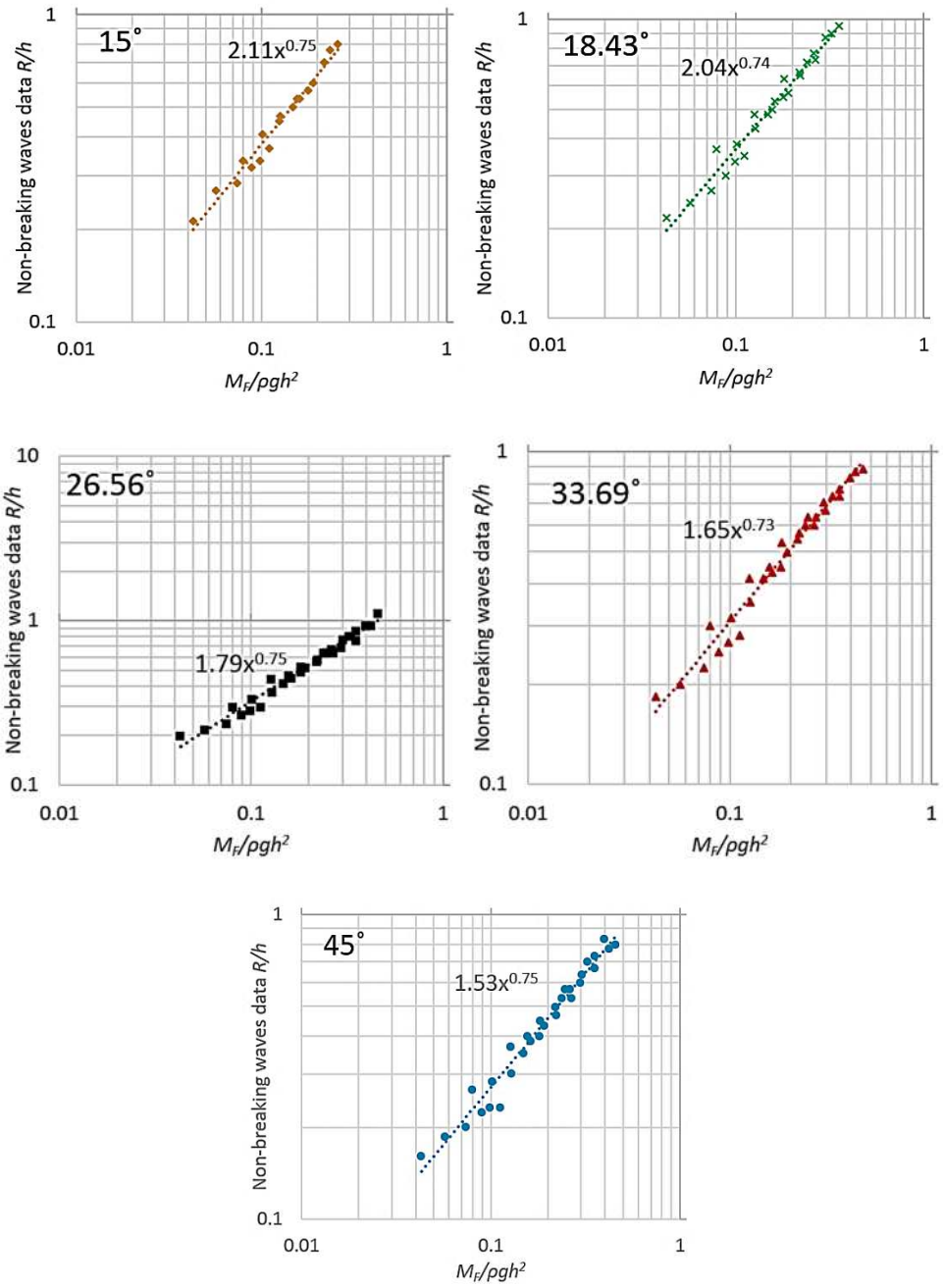

Figure 105 Individual log-log plot of data from each slope angle showing the resulting equation from the power regressions

Figure 106 plots the empirical coefficients *a* against the cotangent of the slopes (displayed in Table 37). These data points are found to be best described by an exponential function.

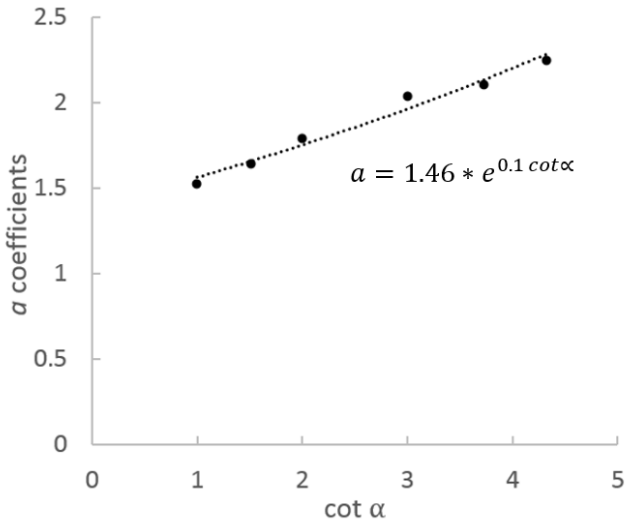

Figure 106 Coefficients *a* plotted against their corresponding cot α

The exponential function shown in Figure 106 and the coefficient value of b = 0.75 were used resulted in:

$$\frac{R}{h} = 1.46 * e^{0.1\,cot\propto}\left(\frac{M_F}{\rho g h^2}\right)^{0.75} \qquad (100)$$

Figure 107 plots the predicted values of (100) against the present data. The dashed lines indicate the ±15% error bands between the predictions and the measured data. As can be seen, a very good agreements is shown, as most data lie inside these error bands.

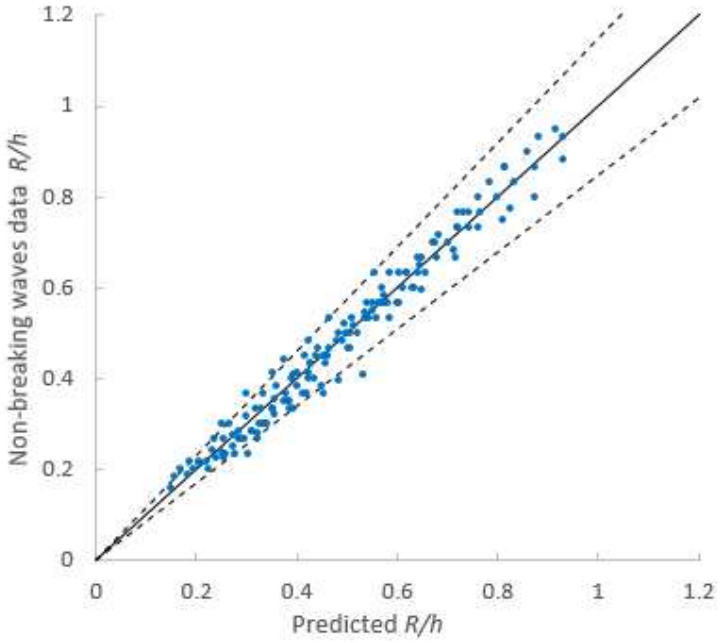

Figure 107 *R/h* data from non-breaking waves versus predicted values of (100). Solid line: perfect agreement; dash line: ±15% error bands.

Equation (100) is analogous to the general formula proposed Hughes (2004a) to predict run-up, given by:

$$\frac{R}{h} = a * F(\alpha)\left(\frac{M_F}{\rho g h^2}\right)^{0.5} \quad (101)$$

where a is an empirical coefficient and $F(\alpha)$ is a function of the slope. The power value of 0.75 in (100) obtained from the power regressions to the data is larger than the value of 0.5 suggested by Hughes (2004a). This larger power value than 0.5 was also noticed by Hughes, but he proposed a power value of 0.5 in (101) as this value was the result of a theoretical derivation based on the run-up triangular wedge (described in Chapter 2).

6.2.4 Summary

The new formulae derived in this section are summarised below:

- A new breaking criterion parameter was proposed to separate the run-up from breaking and non-breaking waves at the slope, this is given by:

$$\tan\alpha/(H/h) \quad (102)$$

- Schüttrumpf (2001) formula with modified empirical coefficients was shown to have a good agreement to the present run-up data from breaking waves. This formula is given by:

$$\frac{R}{H} = a * \tanh(b * \xi) \quad (103)$$

- The following three new formulae were derived to predict run-up from non-breaking waves from regular waves, all showing good agreement with the present data. These are given by:

$$\frac{R}{H} = a\xi^{-b} \quad (104)$$

$$\frac{R}{H} = a\Phi^{-b} \quad (105)$$

$$\frac{R}{h} = a\left(\frac{M_F}{\rho g h^2}\right)^{b} \quad (106)$$

- Values for the empirical coefficients a and b were estimated for each of these formulae by fitting them to the present data.
- The formulae were validated against the present data

6.3 Non-Dimensional Analysis from Irregular Waves

This section analyses the run-up data from irregular waves obtained from the numerical simulations described in Chapter 5. The section follows a similar analysis procedure as that in Section 6.1 for the regular waves. First, the data is separated in breaking and non-breaking waves using the new breaking criterion given by (102) . Then, the data from each

group is compared against prediction formulae from previous studies and against the new formulae for proposed for regular waves: (103), (104), (105) and (106).

Figure 108 plots $R_{u2\%}$ normalised by the significant wave height H_s and plotted against ξ_{op}. As defined previously in Chapter 3, $R_{u2\%}$ is the run-up elevation exceeded by 2% of the incoming waves at the toe of the structure, while ξ_{op} is the Iribarren number based on the deepwater wavelength, L_{op}, which is calculated with the peak spectral wave period T_p.

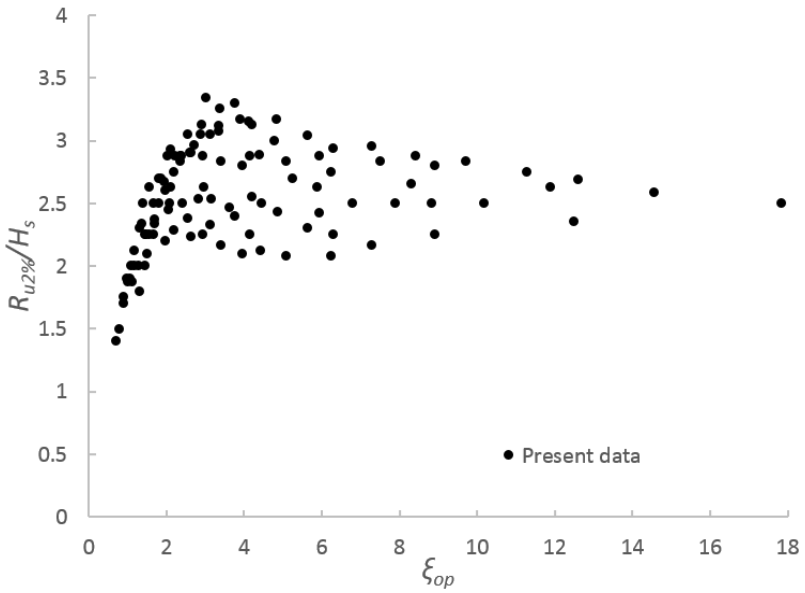

Figure 108 $R_{u2\%}/H_s$ data from irregular waves plotted against ξ_{op} and compared to previous formulae

From this figure we can see that the data shows significant scatter for values $\xi_{op} > 3$, which mainly correspond to non-breaking waves. However, before comparing these data with previous formulae proposed for either breaking or non-breaking waves, it is necessary to first separate the data using a breaking criterion.

6.3.1 Breaking Criterion

The new breaking criterion, $\tan\alpha/(H/h)$, proposed in the previous section was seen to also show a good prediction of the transition between breaking and non-breaking waves from the irregular waves. In this case, a value of 1.4 was found to show the best transition, therefore:

$$\tan\alpha/(H_s/h) < 1.4, \text{ for breaking waves} \quad (107)$$

$$\tan\alpha/(H_s/h) > 1.4, \text{ for non-breaking waves} \quad (108)$$

The predictions of this breaking criterion are shown in Figure 109 in individual graphs corresponding to the four wavelengths tested, while Figure 110 plots all the data together. In these figures the red data correspond to breaking waves, while the blue data correspond to non-breaking waves.

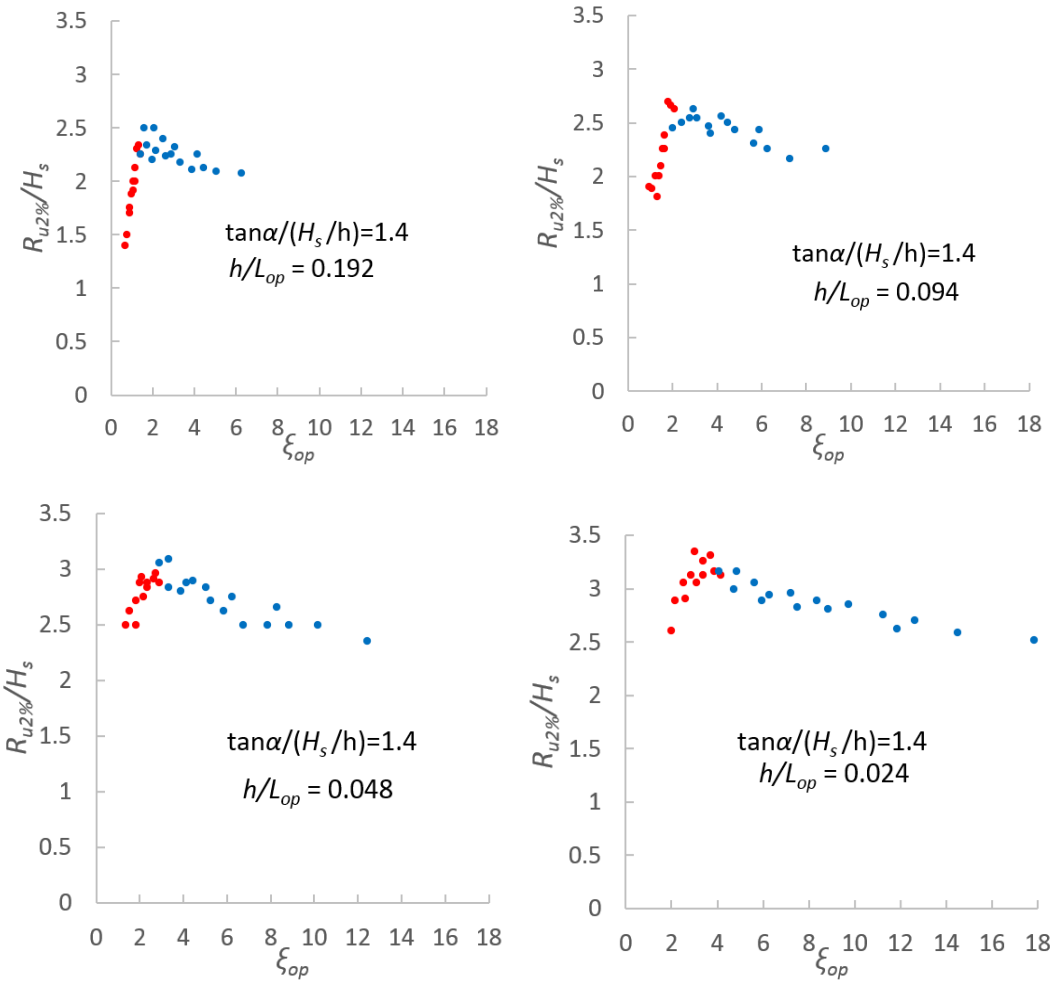

Figure 109 Individual graphs for each h/L_o group showing the value of the breaking transition using tan$\alpha/(H_s/h)$

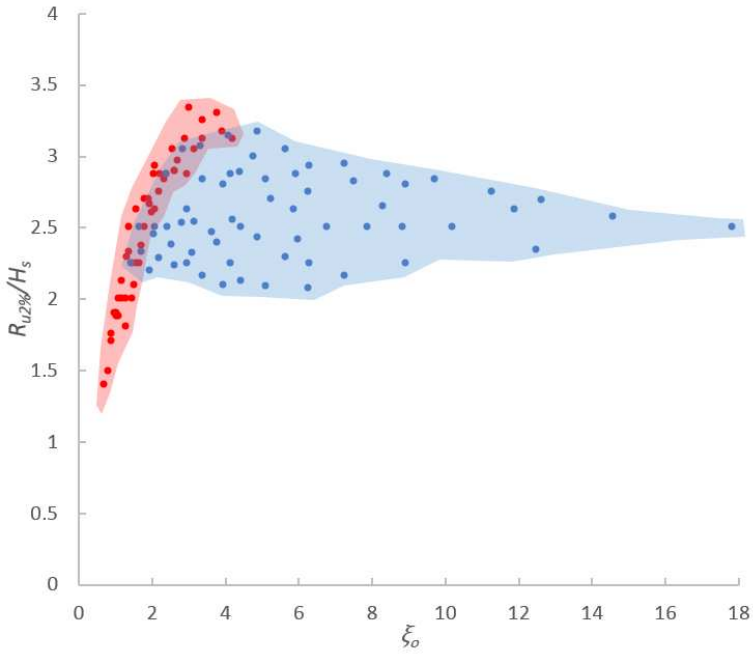

Figure 110 $R_{u2\%}/H_s$ data separated using tan$\alpha/(H_s/h)$ = 1.4 as breaking criterion

Similarly to the regular waves, when the run-up data is plotted against the Iribarren number, the data from breaking waves (red data) show little scatter. In contrast, the data from non-breaking waves show significant scatter, suggesting that formulae based on this parameter might only work to predict run-up from breaking waves.

6.3.2 Breaking waves

Figure 111 shows the present run-up data from breaking waves ($\tan\alpha/(H_s/h) < 1.4$) plotted against ξ_{op} and compared against the prediction of 7 existing formulae, all based on the ξ_{op} parameter. These formulae are shown in Chapter 3. We can see that the present data follows a smooth curved that grows as ξ_{op} increases. Most of the existing formulae suggest that two formulae are needed to describe run-up for values of ξ_o < 4.5 (e.g. Hunt, 1959; Losada and Gimenez-Curto, 1980; Van der Meer, 1995; EurOtop, 2007; Burcharth and Hughes, 2002). These formulae show a sharp transition between the formulae. On the other hand, formulae such as Schüttrumpf (2001) and Mase (1989) adopt a single curve for all values of ξ_o < 4.5.

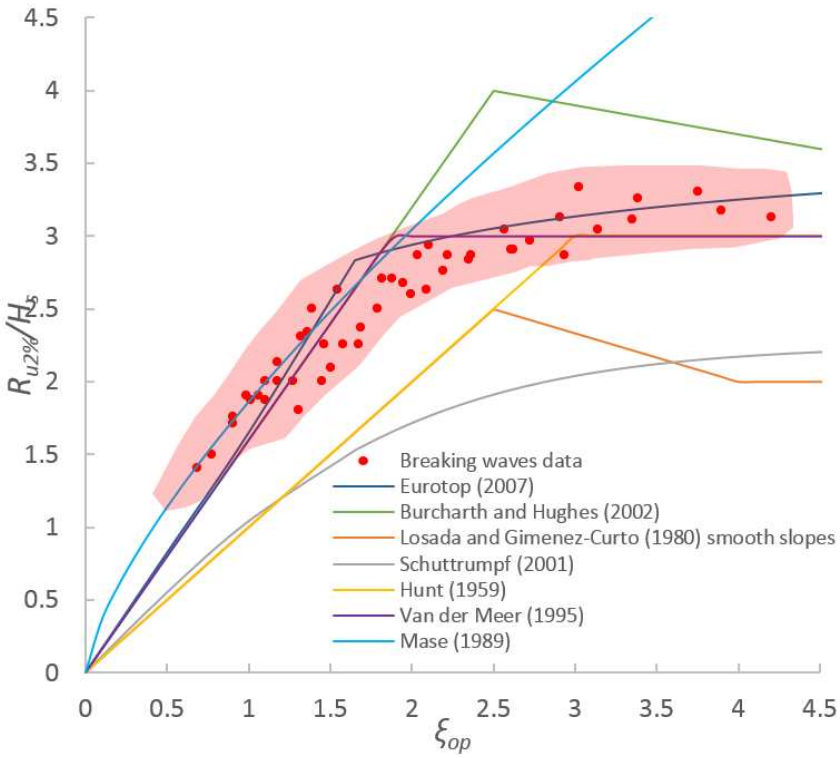

Figure 111 $R_{u2\%}/H_s$ data from breaking waves compared to previous formulae based on the Iribarren number

In Figure 111, we can see that for values of ξ_o < 1.5, Mase (1989), Van der Meer (1995), Burcharth and Hughes (2002) and EurOtop (2007) formulae, all provide a good agreement with the present data. In contrast, for values of ξ_o > 1.5, only the EurOtop formula shows a good prediction, as Mase's and Burcharth and Hughes' formulae significantly over predict the run-up, and Van der Meer's slightly under predicts it. For a better visualisation of the

predictions of these formulae against the present data, **Error! Reference source not found.** shows individual graphs corresponding to these formulae, where the present data is plotted against the predicted data. Again, the solid line represents the line of equivalence, while the dotted lines represent ±15% error bands.

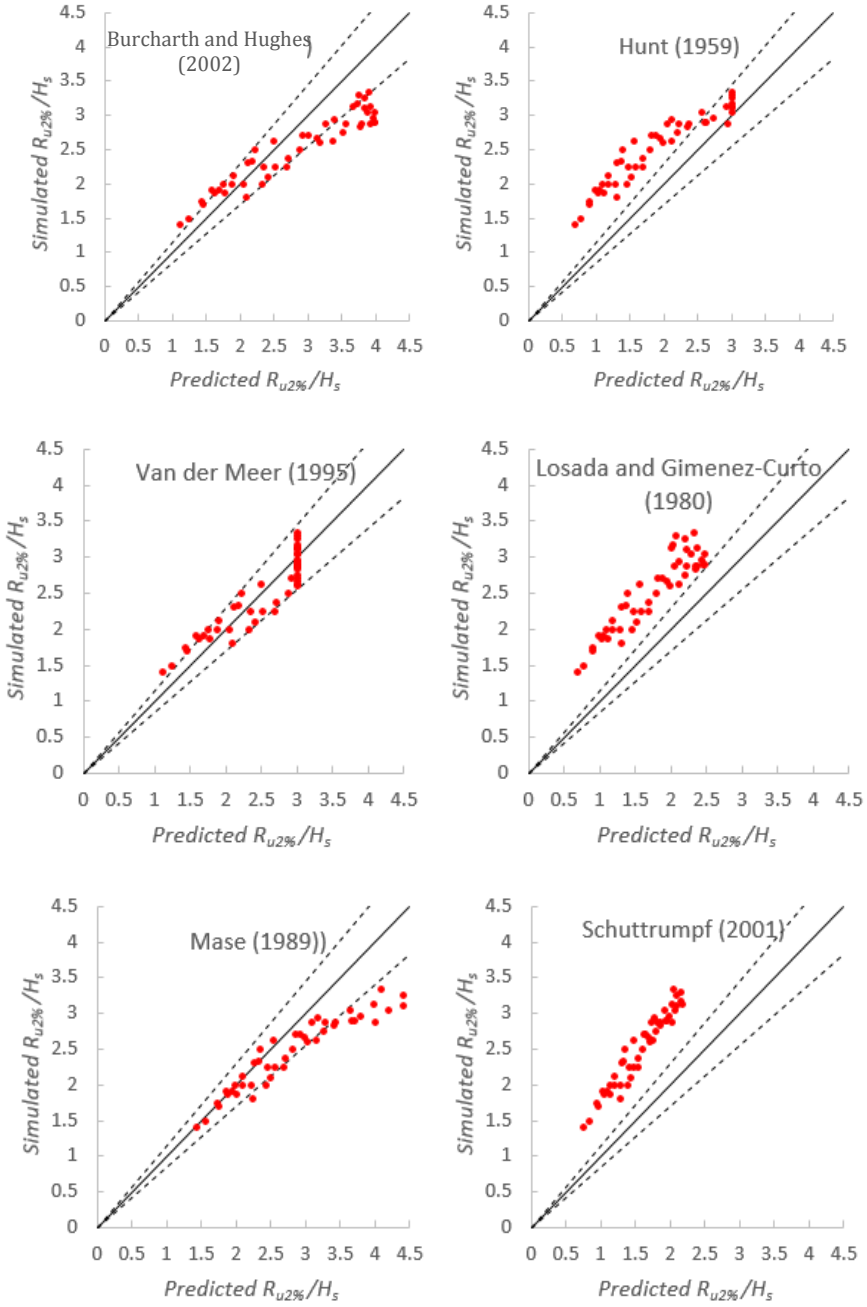

Figure 112 $R_{u2\%}/H_s$ data from breaking waves versus predicted values of formulae based on the Iribarren number. Solid line: perfect agreement; dash line: ±15% error bands.

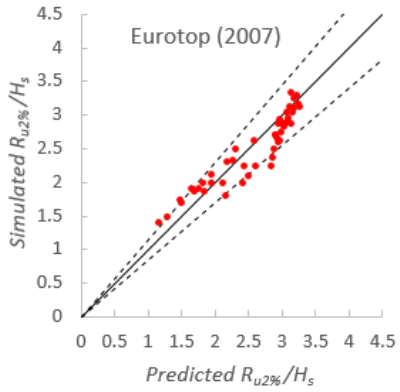

cont. Figure 110

As can be seen, the best predictions are shown by the EurOtop formula, where most of the predictions from this formula lie inside the ±15% error bands. Nevertheless, for the present data a smooth curve expression was found to show a better description of $R_{u2\%}/H_s$ from breaking waves than the EurOtop formulae. For this reason, the same as for the regular waves, this study proposes a modified best-fitted version of Schüttrumpf (2001) hyperbolic formula. This equation was best-fitted to the present data and the following values for the empirical coefficients were obtained:

$$\frac{R_{u2\%}}{Hs} = a * tanh(b * \xi_o) \qquad (109)$$

where a = 3.2 and b = 0.6.

The predictions from and (109) are shown in Figure 113. As can be seen, all the data well inside the ±15% error bands.

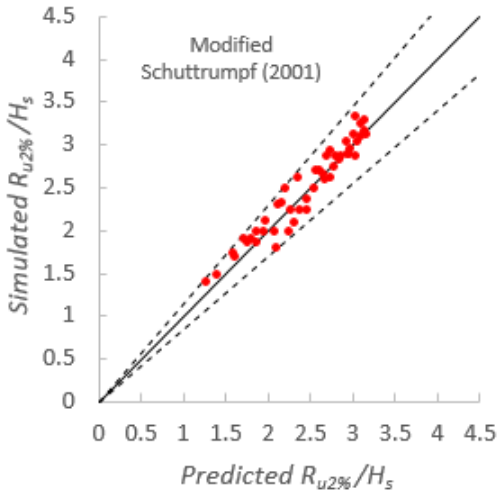

Figure 113 $R_{u2\%}/H_s$ data from breaking waves versus predicted values of the new modified formula. Solid line: perfect agreement; dash line: ±15% error bands.

6.3.3 **Non-breaking waves**

Figure 114 shows the run-up data from the non-breaking waves compared to the predictions of 5 existing formula all based on the ξ_{op} parameter. These formulae are shown in Chapter 3. As can be seen, the data lies between the predictions of some of these formulae. However, none of these predict accurately the present data.

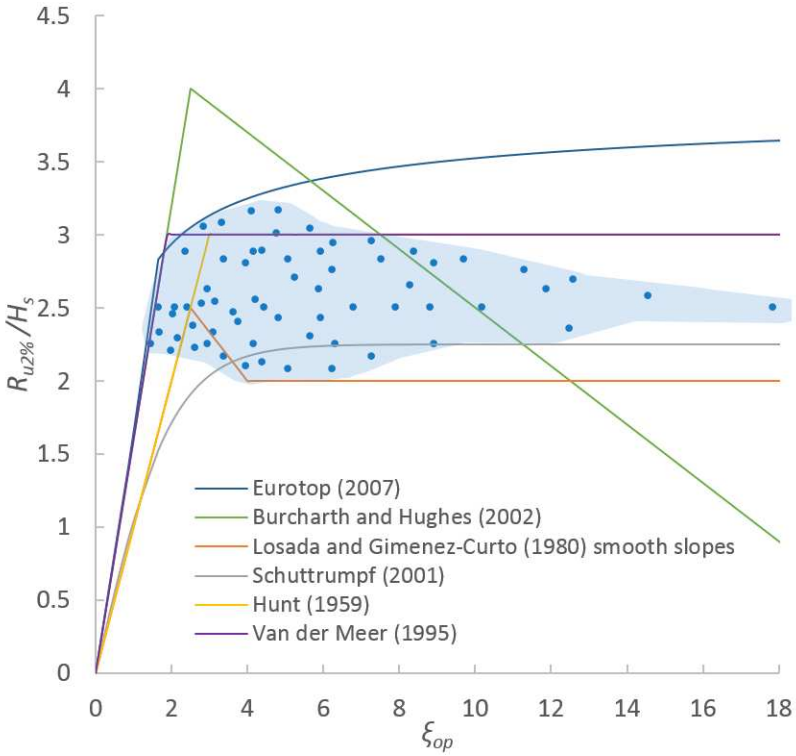

Figure 114 $R_{u2\%}/H_s$ data from non-breaking waves compared to previous formulae based on the Iribarren number

When (104), (105) and (106) proposed for non-breaking waves from regular waves were compared to the $R_{u2\%}/H_s$ data from irregular waves, it was found that these formulae (with adjusted empirical coefficients) also predicted accurately these data. Therefore, it was necessary to estimate appropriate values for the empirical coefficients. The estimation of the coefficients for each formula is described below.

Estimation of coefficients for equation (104). The same as for the data from regular waves, well-defined trends were shown when the results from irregular non-breaking waves were divided by the relative water depth, h/L_o and plotted against the Iribarren number (Figure 115). Each of these groups were also well described by negative power functions of the form:

$$\frac{R_{u2\%}}{H_s} = a{\xi_{op}}^{-b} \qquad (110)$$

where a and b are empirical coefficients that depend on h/L_o. The values of these coefficients were estimated performing power regressions to each group of h/L_o. The results are shown in the log-log graph in Figure 116 and summarised in Table 38.

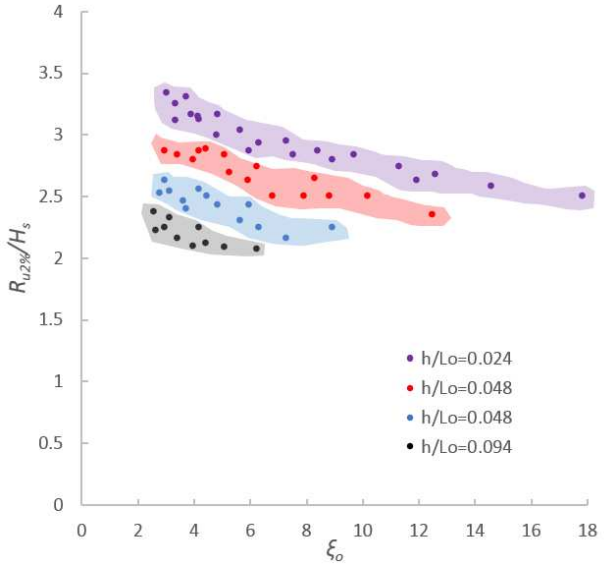

Figure 115 $R_{u2\%}/H_s$ data from non-breaking waves divided into groups according to their h/L_o

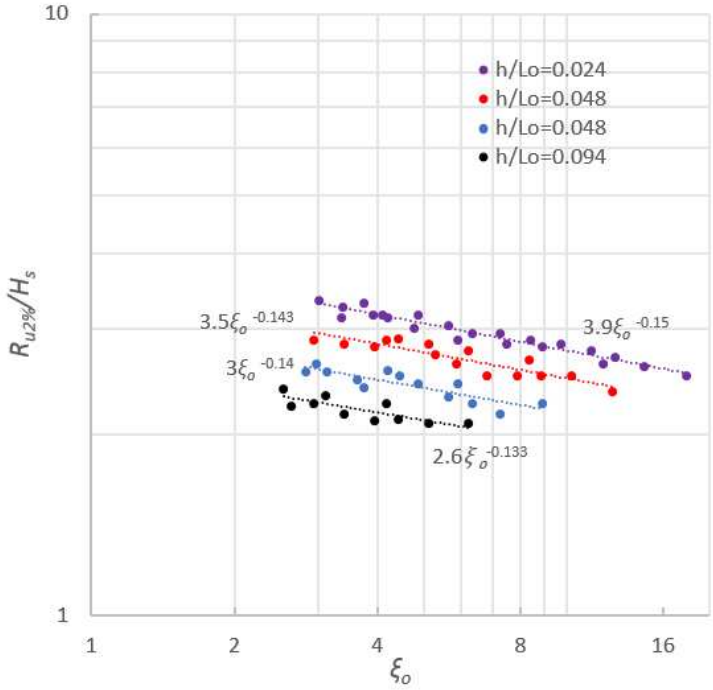

Figure 116 Log-log plot showing coefficients from power regressions performed to each h/L_o group

h/L_o	a values	b values
0.024	3.9	0.15
0.048	3.5	0.143
0.094	3	0.14
0.192	2.6	0.133

Table 38 Summary of a and b coefficients of each h/L_o group

To derive expressions for these coefficients in terms of h/L_o, these were plotted against their corresponding h/L_o values and best-fit equations were estimated (Figure 117).

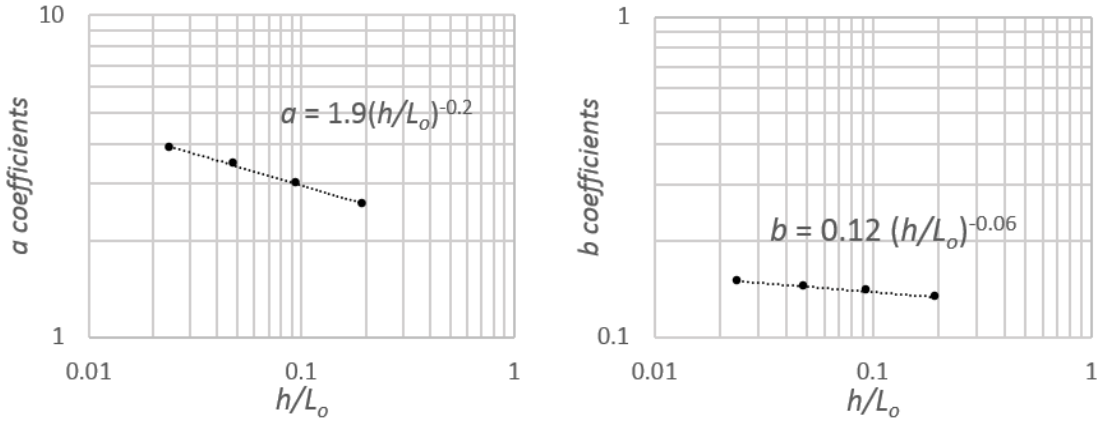

Figure 117 Log-log plots of a and b coefficients against their corresponding h/L_o

The trends described by both coefficients were also found to be best described by negative power expressions. These expressions were replaced in (110) resulting in:

$$\frac{R_{u2\%}}{H_s} = a\xi_{op}{}^{-b} \tag{111}$$

where:

$$a = 1.9\left(h/L_o\right)^{-0.2} \tag{112}$$

$$b = 0.12\left(h/L_o\right)^{-0.06} \tag{113}$$

The predictions of (111) are plotted against the present $R_{u2\%}/H_s$ data in Figure 118, where a very good agreement with the present data can be seen.

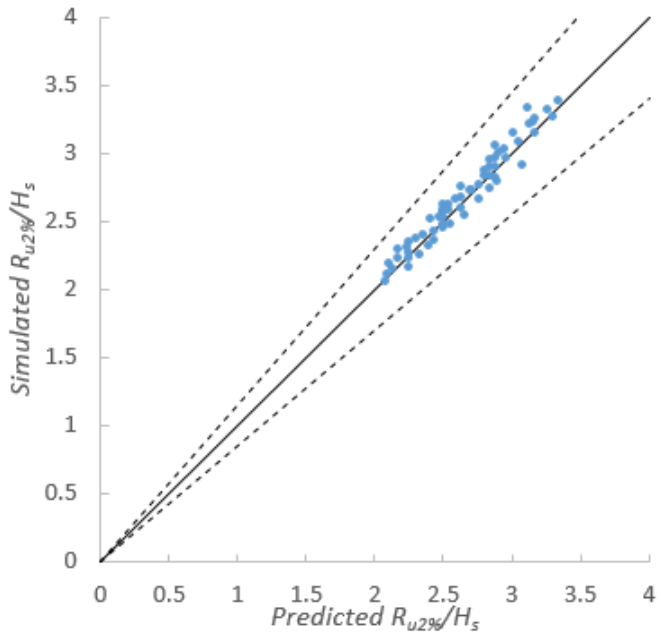

Figure 118 $R_{u2\%}/H_s$ data from non-breaking waves versus predicted values of equation (111). Solid line: perfect agreement; dash line: ±15% error bands.

Estimation of coefficients for equation (105). Figure 119 shows the same $R_{u2\%}/H_s$ data from non-breaking, irregular waves plotted against the new parameter ϕ. As can be seen, significant less scatter is seen when $R_{u2\%}/H_s$ data are plotted against this parameter than when the data are plotted against the Iribarren number (Figure 114).

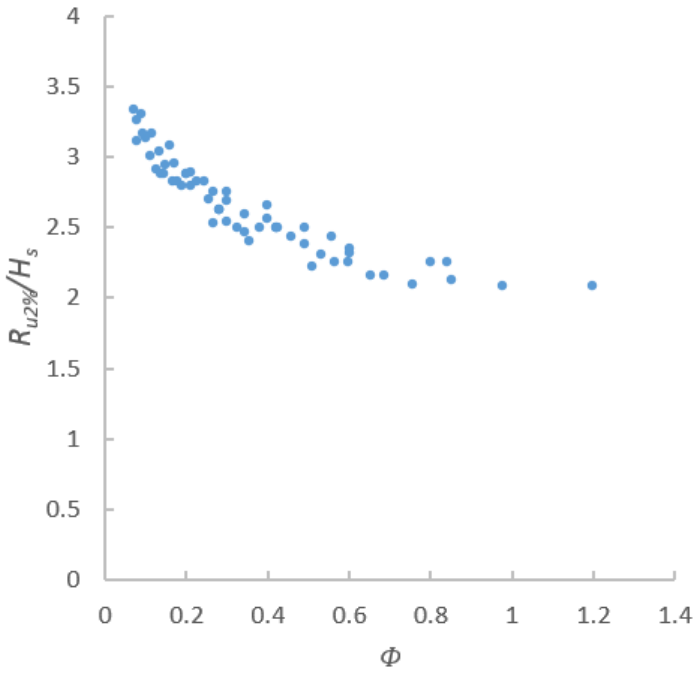

Figure 119 $R_{u2\%}/H_s$ data from non-breaking waves against new parameter ϕ

The single well-defined curve shown in Figure 119 was also well described by:

$$\frac{R_{u2\%}}{H_s} = a(\Phi)^{-b} \qquad (114)$$

where a and b are empirical coefficients. Curve-fitting of this formula to the data resulted in:

$$\frac{R_{u2\%}}{H_s} = 2.11\Phi^{-0.17} \qquad (115)$$

The predictions of (118) are plotted against the present $R_{u2\%}/H_s$ data in Figure 120, where again, a very good agreement with the present data is shown.

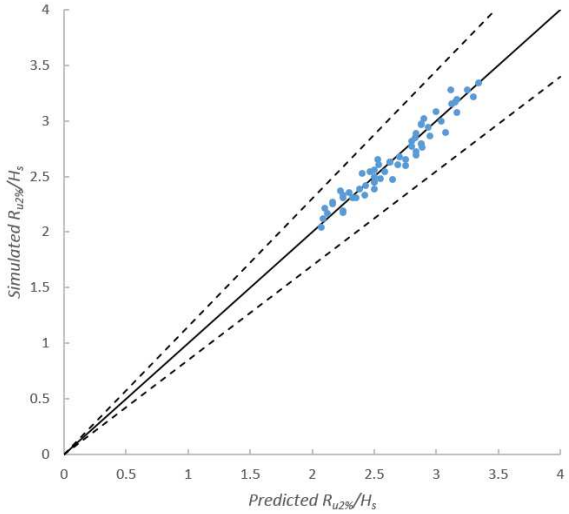

Figure 120 $R_{u2\%}/H_s$ data from non-breaking waves versus predicted values of equation (118). Solid line: perfect agreement; dash line: ±15% error bands.

Estimation of coefficients for equation (106). When the $R_{u2\%}/h$ data from each slope angle were plotted against $M_F/\rho g h^2$ (Figure 121), it was seen that the data from each slope angle were also found to be best described by power functions in the form of: $y = ax^b$. Therefore, power regressions were performed to estimate the coefficients a and b of each slope angle. The results are shown in individual log-log graphs for each slope angle in Figure 122 and the values for a and b are summarised in Table 39.

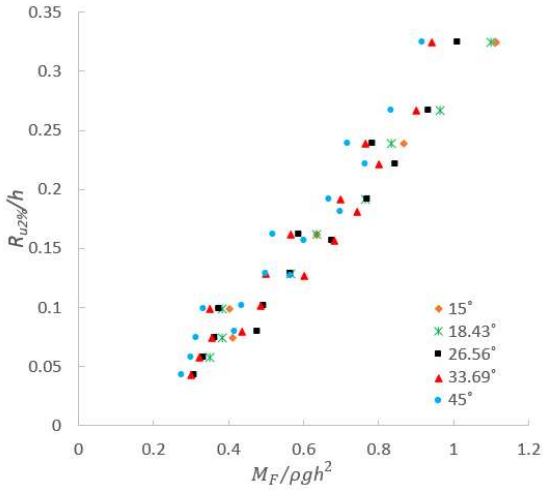

Figure 121 $R_{u2\%}/h$ data from non-breaking waves plotted against the wave momentum flux parameter

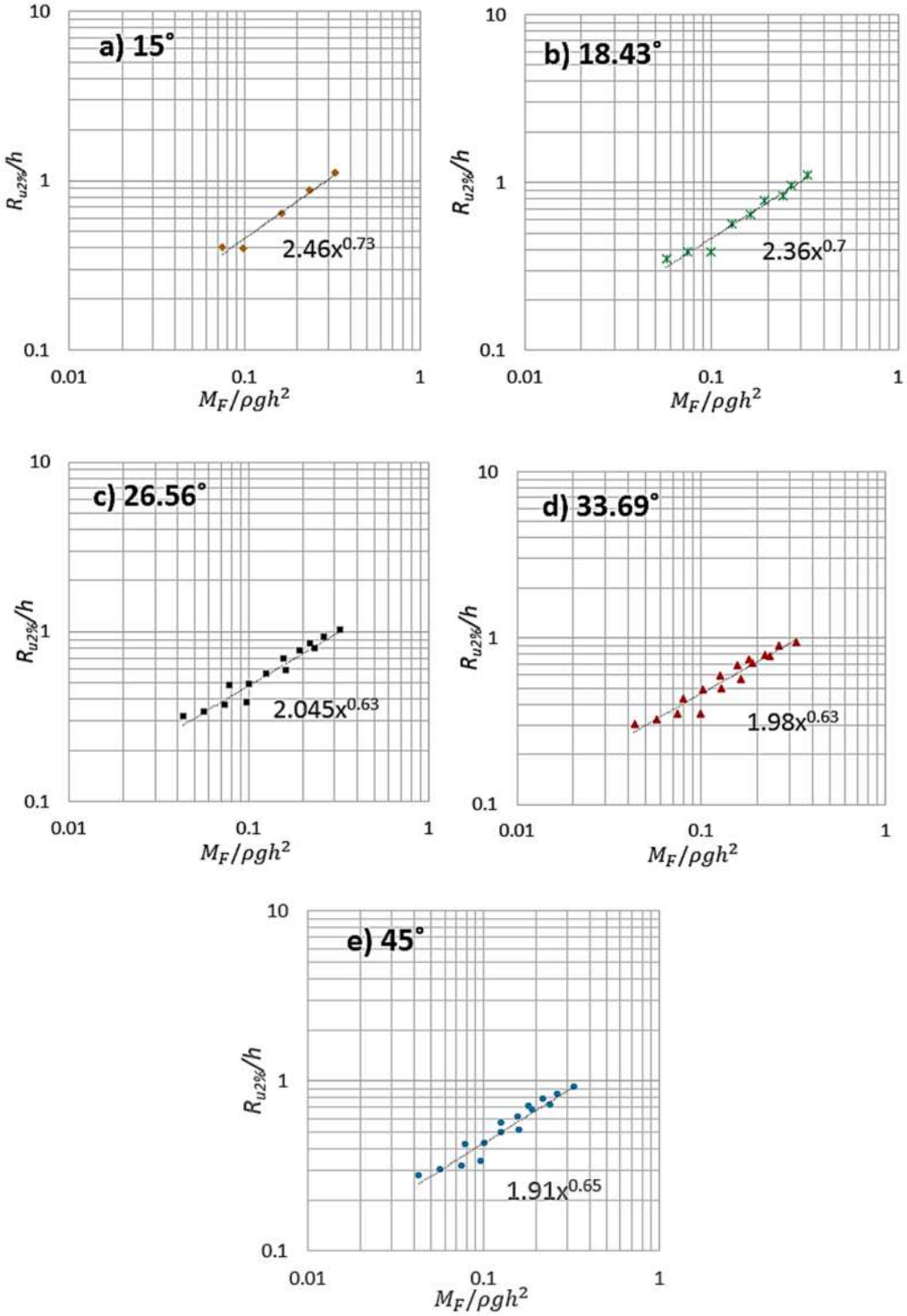

Figure 122 Individual log-log plot of data from each slope angle showing the resulting equation from the power regressions

Slope Angle	cot α	*a* values	*b* values
15°	3.73	2.46	0.73
18.43°	3	2.36	0.7
26.56°	2	2.05	0.63
33.69°	1.5	1.98	0.63
45°	1	1.91	0.65

Table 39 Summary of *a* and *b* coefficients for each slope angle

From Table 39 it can be seen that the values of the coefficients b tend to slightly increase as the slope angle decreases. Nevertheless, these values remain fairly constant, so a value of b = 0.67 is suggested to represent the b values from all slopes. This value lies between the value found for regular waves, b = 0.75, and the value suggested by Hughes (2004a), b = 0.5. On the other hand, the coefficients a decrease as the slope angle increases. Therefore, these coefficients are also expected to be a function of the cotangent of the slope. This can be seen in Figure 123, where the coefficients a are plotted against the cotangent of the slopes. Although the points in Figure 123 can be approximated by a straight line, these were also found to be best described by the exponential function shown in the graph.

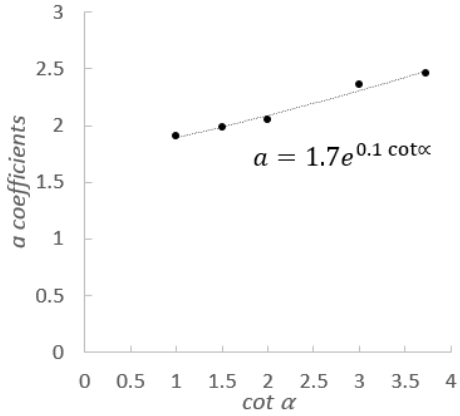

Figure 123 coefficients *a* plotted against their corresponding cot α

The function shown in Figure 123 and the coefficient value of b = 0.67 were used to replace the coefficients in (106), resulting in:

$$\frac{R_{u2\%}}{h} = 1.7 * e^{0.1\,cot\propto} * \left(\frac{M_F}{\rho g h^2}\right)^{0.67} \qquad (116)$$

The predictions of (119) are plotted against the present data. As can be seen, better results were shown from (111) and (118) than for (119). Nevertheless, the predictions of (119) are generally good, as most values lie inside the ±15% error bands.

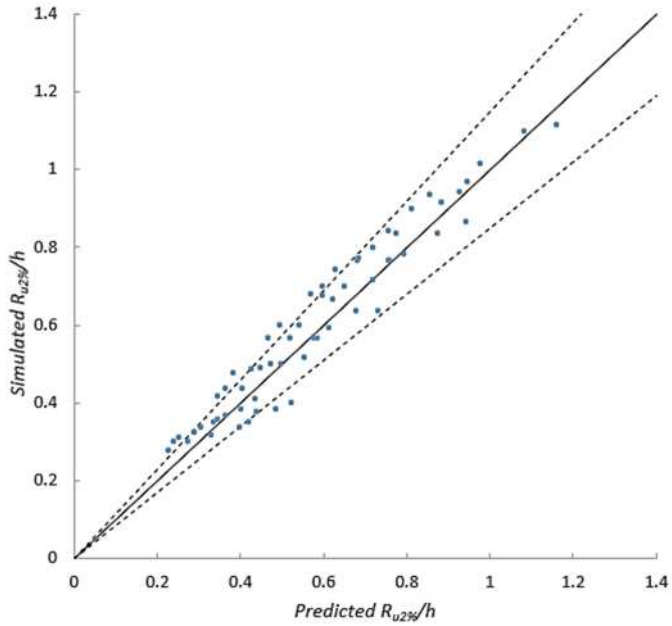

Figure 124 $R_{u2\%}/h$ data from non-breaking waves versus predicted values of (116). Solid line: perfect agreement; dash line: ±15% error bands.

6.3.4 **Summary**

- The formulae (103), (104), (105) and (106) derived from regular waves were also found to be applicable to predict run-up from irregular waves on smooth-impermeable slopes, although with modified empirical coefficients

- The new parameter $\tan\alpha/(H/h)$ proposed as breaking criterion also showed good predictions with data from irregular waves, although the transition between both types of waves was seen to occur at a higher value.

- The formulae were validated against the present data

7 Wave Run-up over Permeable Slopes

The data obtained from the laboratory experiments and numerical simulations carried out on permeable slopes are analysed in this chapter, which is divided into 7 sections.

Section 7.1 presents the results from the experimental observations of wave breaking from all the tests performed on the permeable slopes, where the breaker type and breaking point location from each test are documented. These observations are compared with the predictions of two different breaking criteria.

In Sections 7.2and 7.3, the influence of surface roughness, hydraulic conductivity and water table elevations on run-up are analysed. Here, factors to account for the influence of the slope's roughness and hydraulic conductivity for breaking and non-breaking waves are presented, and a new dimensionless hydraulic conductivity parameter is introduced.

Section 7.4 describes alternative approaches to estimate hydraulic conductivity of a beach or coastal structure from other available parameters such as porosity, grain size, pore throat size and sediment sorting.

Section 7.5 validates and shows the applicability of the new formulae by comparing their predictions against existing run-up data from previous laboratory experiments performed on impermeable and permeable slopes.

Finally, Section 7.6 presents an analysis on the influence of hydraulic conductivity on the water table over-height, while Section 7.7 discusses the influence of infiltration on the swash flows and bed shear stresses.

The main outcomes are summarised at the end of each section, while the overall conclusions of the study are summarised in Chapter 8.

7.1 Observations of Wave Breaking Processes

The wave breaking processes from all the tests performed on permeable slopes were recorded from the side of the flume using a video camera with three main objectives:

1) To identify whether the wave breaks or not at the slope and to compare these observations with the predictions of the breaking criteria based on $\tan\alpha/(H/h)$ and on the Iribarren number, ξ

2) To measure the breaking point location for all the plunging waves and to see if this location is affected by the hydraulic conductivity of the slope

3) To classify the breaker type of each run-up to investigate if hydraulic conductivity of the slope affects the wave breaking mechanism

7.1.1 **Breaking Criteria**

The breaking criterion $\tan\alpha/(H/h)$ proposed in Section 6.2.1 to predict the transition between breaking and non-breaking waves on smooth slopes was derived based on the different trends shown when the *R/H* data were plotted against ξ. Most previous breaking criteria have been derived this same way, by observing the different trends in the run-up data. They have not been derived from video observations. The present observation are intended to: 1) verify if the different trends shown by the *R/H* data actually correspond to breaking and non-breaking waves; and 2) compare the predictions of the breaking criterion $\tan\alpha/(H/h)$ and ξ with the video observations. This will allow selection of the most appropriate parameter to use as a breaking criterion for the present data on permeable slopes.

Experimental observations. Figure 125 and Figure 126 show the *R/H* data obtained from the four permeable foams carried out on three different slope angles: 10˚, 20˚ and 30˚ plotted against ξ and against Φ respectively. In these graphs, the data are separated depending on the breaker types observed from the video recordings. As can be seen, no spilling waves were observed in these tests. Most waves corresponded to either plunging or surging waves, with some few collapsing waves in between.

In Figure 125, where the data are plotted against the Iribarren number, it can be seen that most plunging waves follow a well-defined trend. However, some of the plunging wave data between $2 < \xi < 4$ are seen to be scattered between the data of the collapsing and surging waves. On the other hand, most surging or non-breaking waves show significant scatter. In the case of the collapsing waves, some data seem to behave as plunging waves, while others seem to be scattered between the data of the surging waves. From Figure 125 it is easy to identify the areas where most of the plunging and surging waves occur. All data with values of $\xi < 2$ correspond to plunging waves which are considered breaking waves. These data show well-defined non-linear trends that grow with ξ. On the other hand, all data with values of $4 < \xi$ correspond to surging or non-breaking waves, where a lot of scattering is seen.

The main problem when separating the breaking from the non-breaking waves arises in the transition zone between $2 < \xi < 4$, where all the collapsing waves occur. This area shows scatter data from all three types of breakers.

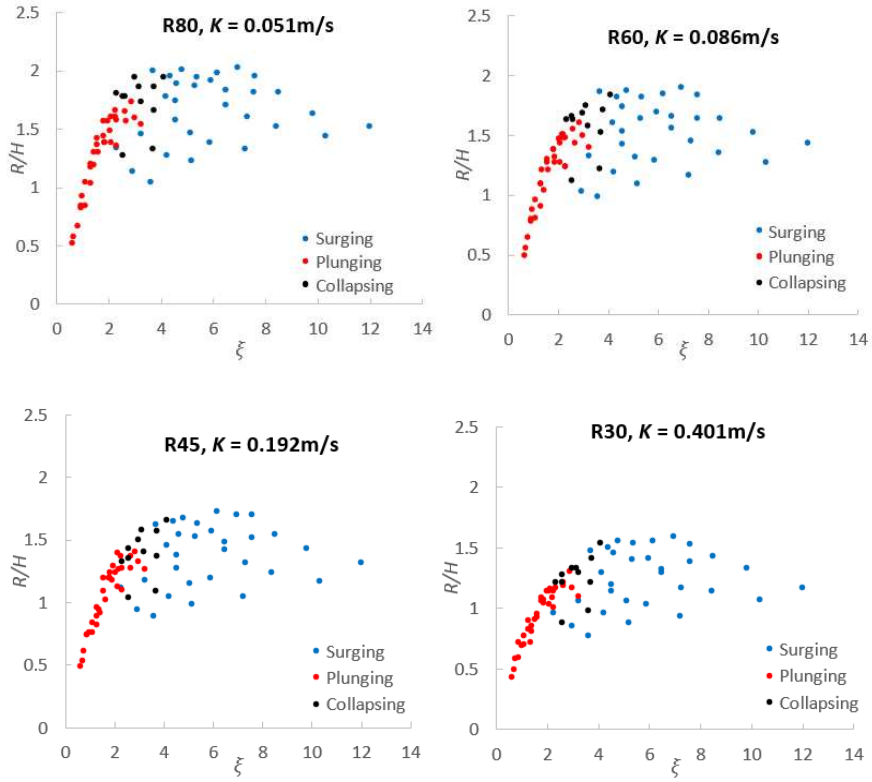

Figure 125 *R/H* data from run-up tests performed on the 4 permeable structures plotted against *ξ* and separated according to their breaker types observed

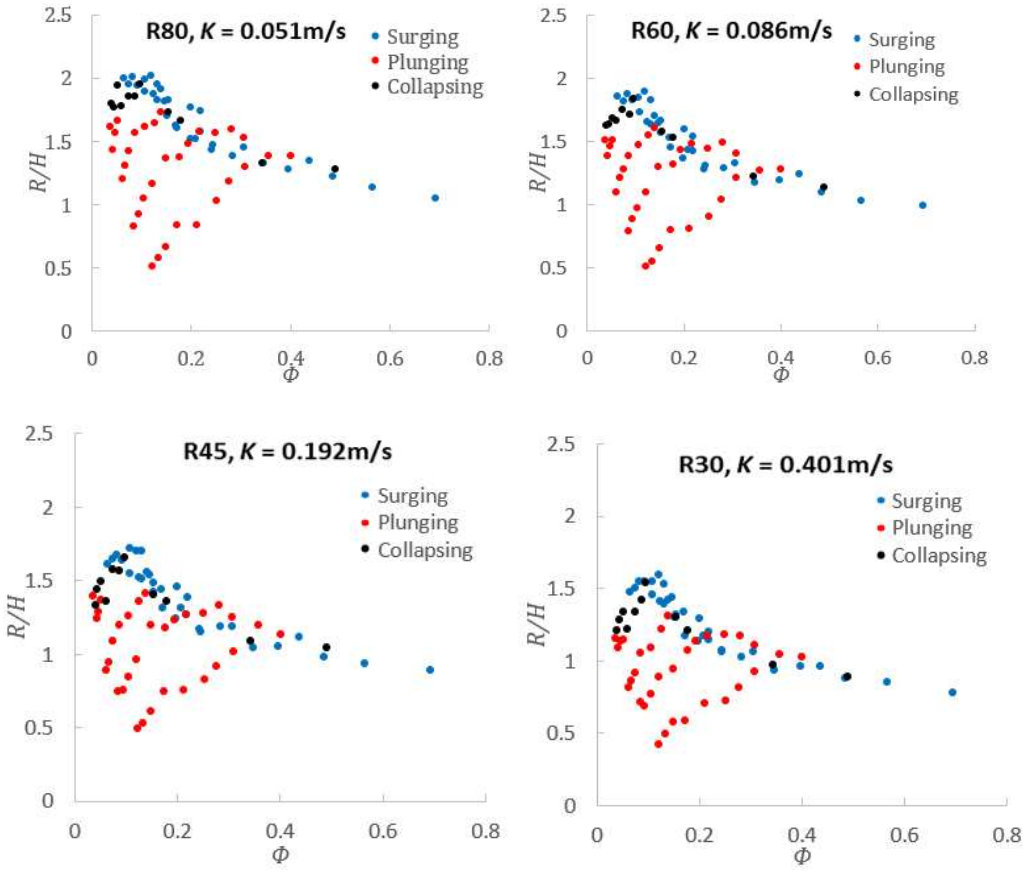

Figure 126 *R/H* data from run-up tests performed on the 4 permeable structures plotted against *Φ* and separated according to their breaker types observed

When the data is plotted against Φ (Figure 126), we can see that the data from the surging waves show a well-defined downwards trend, while the data from plunging waves are the scattered ones. Again, the collapsing waves are seen to be spread between the surging and collapsing waves. It is interesting to note that the plunging waves show several upward lines that grow until they meet the line defined by the surging waves. Each line corresponds to a different wavelength tested.

These graphs show the main reason why run-up formulae are designed either for breaking or non-breaking waves: both groups of data follow completely different patterns, and therefore need to be estimated using different expressions.

The present video observations show that not all the data from plunging and collapsing waves lie inside the well-defined trends followed by most of the plunging wave data and might be better predicted using formulae designed for non-breaking waves.

The breaker type observations were compared with the predictions using $\tan\alpha/(H/h)$ and ξ as breaking criteria. This was done firstly to validate these breaking criteria and secondly, to select the criteria that could show a clearer separation between the trends shown by the breaking and non-breaking waves of the present data. This was done by analysing both group individually and deriving influence factors for roughness and hydraulic conductivity for both of them.

A similar analysis as the one shown for the smooth slopes, where the data were separated into groups according to their h/L_o values, was performed for the permeable slopes to identify the $\tan\alpha/(H/h)$ and ξ values which could best indicate the transition between the growing trend from the breaking waves and the downwards trend from the non-breaking waves. When the Iribarren number was used to analyse the transition between both trends in each h/L_o data group, the ξ value found to best indicate the transition, increased as the wavelength increased. Nevertheless, a value of ξ = 3.2 was shown to be the most accurate one to indicate the transition for all the data. On the other hand, the transition between both trends in each h/L_o data group was seen to occur at a constant value of: $\tan\alpha/(H/h) \approx 1.4$.

Breaking criterion using the Iribarren number, ξ. The predictions using the breaking criterion of ξ = 3.2 are shown in Figure 127 and Figure 128 where again, the measurements are plotted against ξ and Φ respectively.

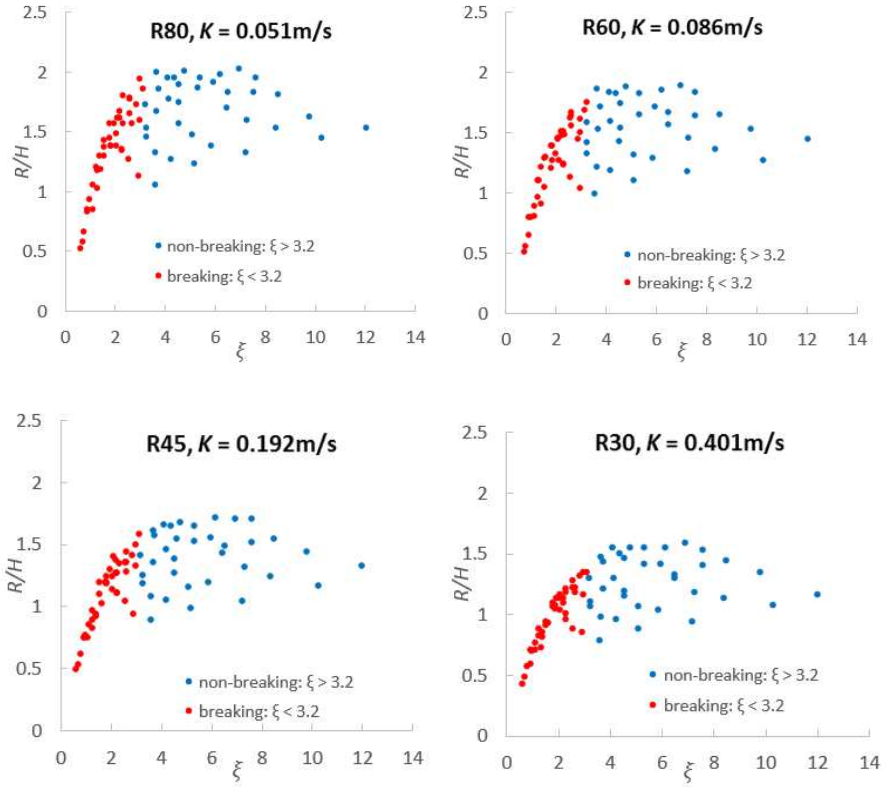

Figure 127 *R/H* data from the 4 permeable slopes plotted against *ξ* and separated using *ξ* = 3.2 as breaking criterion

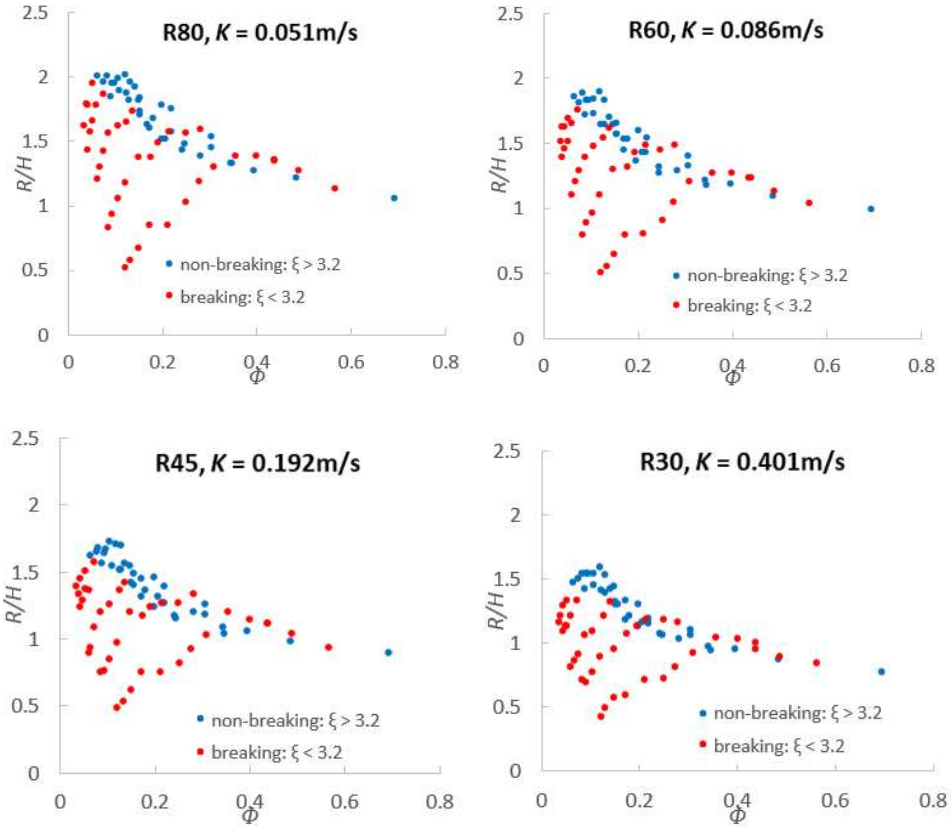

Figure 128 *R/H* data from the 4 permeable slopes plotted against *Φ* and separated using *ξ* = 3.2 as breaking criterion

As can be seen, the Iribarren number shows very good predictions when compared to the video observations, predicting most data correctly. Most of the data observed to be plunging and collapsing waves between $2 < \xi < 4$ are part of the breaking waves group. However, some of the breaking wave data seem to follow the same trends followed by the non-breaking waves. These data correspond to the shortest waves (h/L_o = 0.192) on the 20˚ and 30˚ slopes. These data might cause problems if this parameter is used to separate the data from breaking and non-breaking waves.

Breaking criterion using the new parameter: $\tan\boldsymbol{\alpha}/(\boldsymbol{H}/\boldsymbol{h})$. Figure 129 and Figure 130 show the run-up measurements plotted against ξ and Φ respectively. This time, the data are separated using the predictions of the breaking criterion of $\tan\alpha/(H/h) = 1.4$. Comparing the predictions using $\tan\alpha/(H/h)$ = 1.4 with the video observations shown in Figure 125 and Figure 126, we can see that this criterion also predicts most data correctly. The data points with values $\tan\alpha/(H/h) < 1.4$ include most of the data from the plunging and collapsing waves, while $\tan\alpha/(H/h) > 1.4$ include most of the surging waves. Some discrepancies can be noticed between $2 < \xi < 6$, where the collapsing waves and the transition between breaking and non-breaking waves occur. Nevertheless, a better separation between both groups of data can be seen than when using ξ as breaking criterion. The constant value of $\tan\alpha/(H/h)$ = 1.4 indicating the transition between both trends in each h/L_o group resulted into a clear distinction between both groups of data. With all the data points representing the breaking waves follow well-defined trends when plotted against ξ and all the data points representing the non-breaking waves follow well-defined curves when plotted against Φ.

These comparisons show that both parameters can separate accurately the breaking and non-breaking waves of the present data. Although the Iribarren number showed slightly better predictions when compared to video observations, $\tan\alpha/(H/h)$ showed a better separation between the trends of the breaking and non-breaking waves. Therefore, this parameter was chosen to separate the data from both groups, and was used in the analysis described in Sections 7.2 and 7.3.

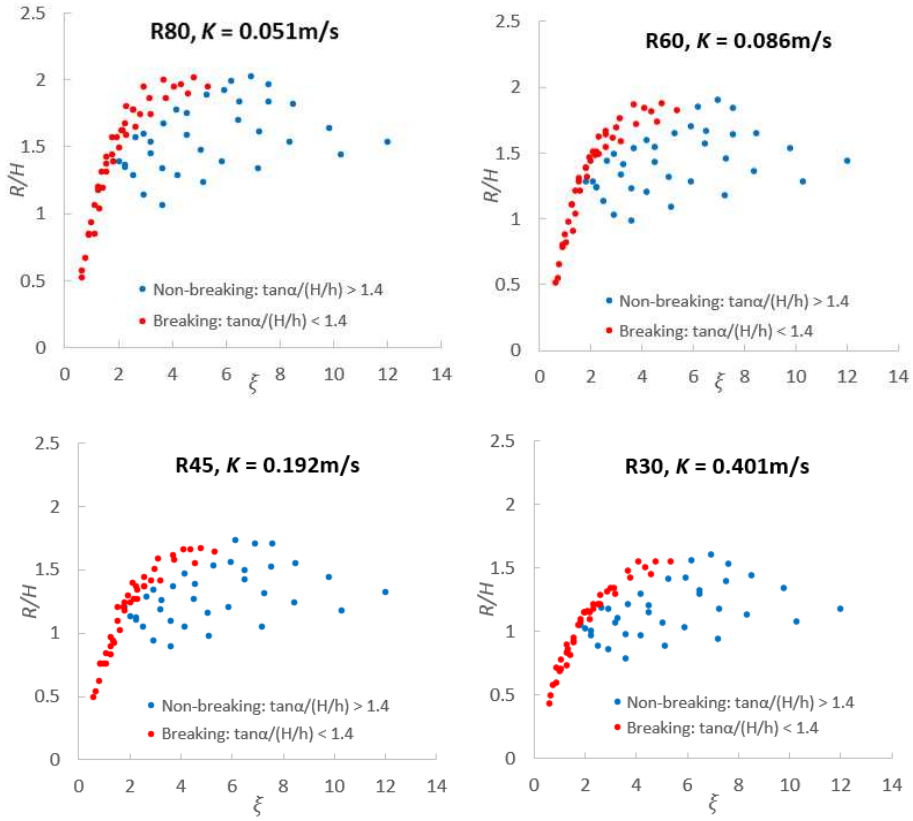

Figure 129 R/H data from the 4 permeable slopes separated using $\tan\alpha/(H/h) = 1.4$ as breaking criterion and plotted against ξ

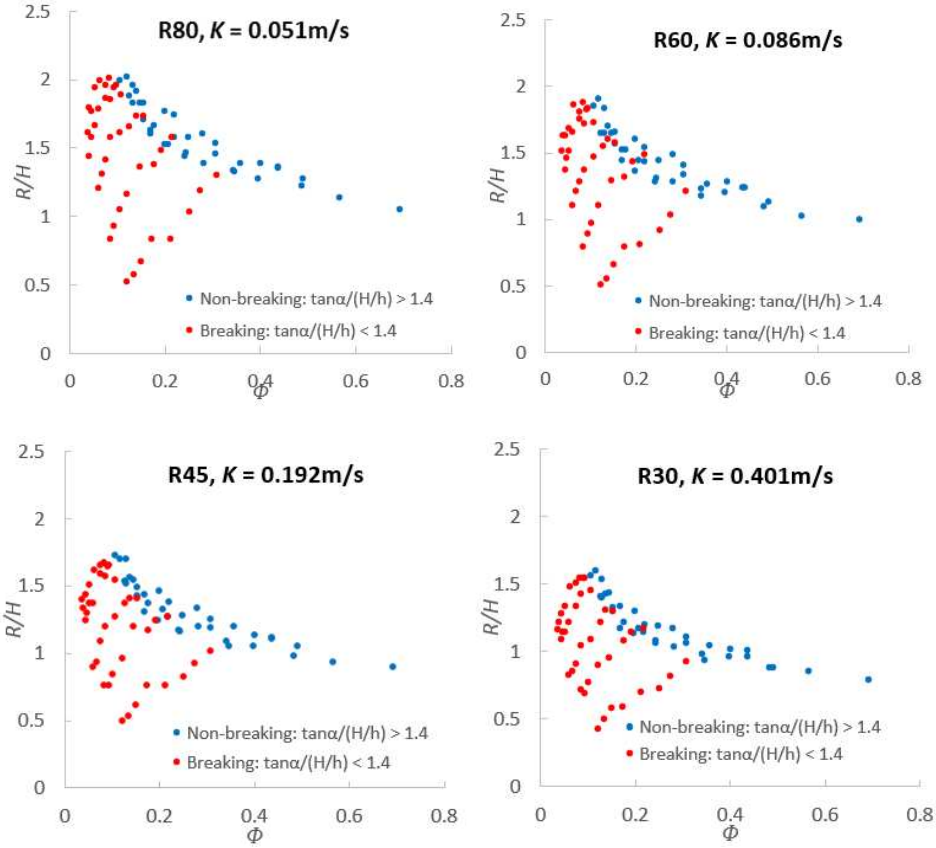

Figure 130 R/H data from the 4 permeable slopes separated using $\tan\alpha/(H/h) = 1.4$ as breaking criterion and plotted against Φ

7.1.2 Location of Breaking Point

The breaking point of the plunging breaker is the location where the front face of the breaking wave becomes nearly vertical (Bonmarin, 1989). The breaking point location in this study was recorded by measuring the horizontal distance from where the breaking point occurs to the intersection between the SWL and the slope of the structure (Figure 131).

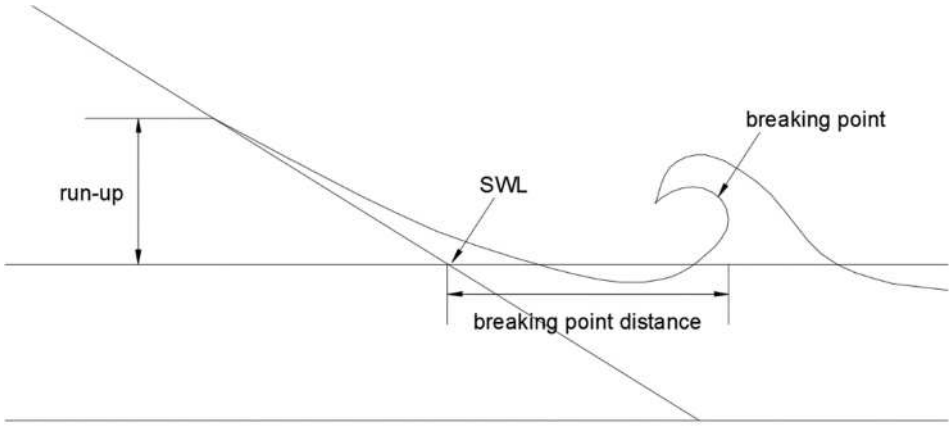

Figure 131 Breaking point distance for plunging waves

This breaking point distance was recorded for all the plunging waves generated for all four permeable slopes. These results are summarised in Appendix F. The measurements showed that, under identical wave conditions, in most cases the breaking point distance increases as the hydraulic conductivity of the slopes decreases. Similar observations were reported by Lara et al. (2006), where the breaking point location was seen to be nearer the shore on the large grain size slope than those observed on the small grain size slope. There are several processes that occur when a wave breaks over a permeable slope that can influence the location where waves break. Firstly, the additional energy dissipation caused by the permeable slope can reduce the wave height and can affect the undertow of the wave (as shown by Lara et al., 2006), and consequently can influence the breaking point location. Secondly, the uprush and backwash flows can be considerably reduced due to infiltration. These flow reductions (analysed in detail in Section 6.9) can significantly affect the swash-swash interaction processes or the swash collisions between waves. On a permeable slope, the reduced backwash flow can diminish the swash collisions, allowing the subsequent waves to travel further up the slope, and consequently to break at a location nearer the shore. Finally, the exfiltration processes that occur on the saturated part of the beach (below the mean water level) are also expected to influence the breaking processes.

No clear correlation was seen between the breaking point distance and the run-up height, which is also affected by the hydraulic conductivity. This is shown in Figure 132, where

the breaking point distance, x_b, was normalised by the wave height and plotted against R/H.

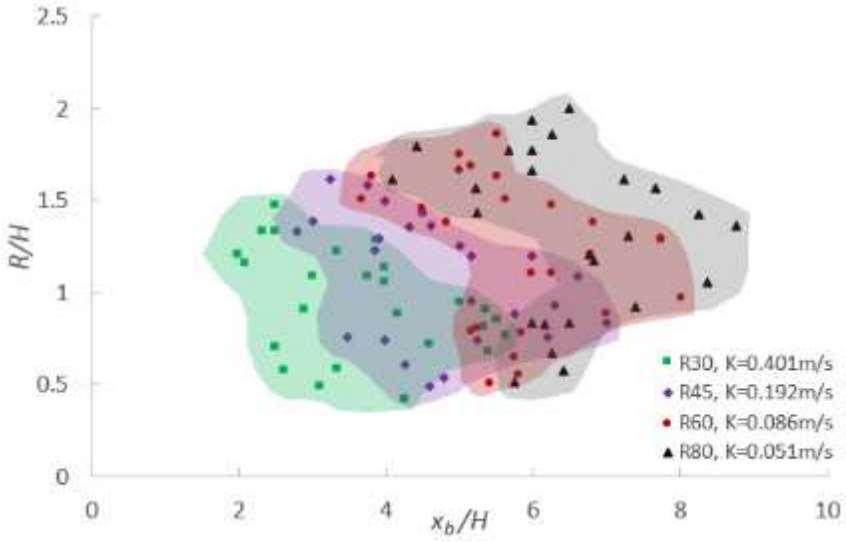

Figure 132 Correlation between run-up and breaking point distance

Furthermore, there was no obvious correlation between the breaking point location and the Iribarren number or wave steepness, although in most cases, this distance was seen to grow as H increased and as L_o decreased.

7.1.3 Breaker Type

Lara et al. (2006) reported changes from plunging to spilling or surging under identical wave conditions but with different slope permeabilities. In the present study, the different hydraulic conductivities analysed were seen to slightly modify the shape of the breaking waves, but this change in shape was not enough to modify the breaker types. However, further research would be required to compare the breaker types between the impermeable and permeable slopes as the breaker types in this study were only recorded on permeable slopes.

7.1.4 Summary

- Both the Iribarren number and $\tan\alpha/(H/h)$ were shown to accurately predict the transition between breaking and non-breaking waves on permeable slopes when compared to the experimental observations

- The breaking point distance (defined in Figure 131) was seen to increase as the hydraulic conductivity of the slopes decreases

- Hydraulic conductivity slightly modified the shape of the breaking waves, but this change was not enough to modify their breaker type

7.2 Breaking waves on Permeable Slopes

As discussed in the literature review, influence parameters have been derived by previous authors account for the effects of surface roughness, angle of wave attack, shallow water and berms on wave run-up. All of these parameters have been derived from laboratory experiments. However, no parameter has been proposed to account for the influence of hydraulic conductivity on run-up. In this study, a new influence factor for hydraulic conductivity is presented. This section shows how this parameter was derived, and discusses the influence of surface roughness and groundwater levels on run-up.

Figure 133 plots the R/H data from waves breaking on 4 foams, using the breaking criterion: $\tan\alpha/(H/h) < 1.4$. These data include the results from the three slope angles tested: 10˚, 20˚ and 30˚. The shaded areas in this figure, as well as in the rest of the graphs presented in the following sections, are shown to display the regions covered by each group of data. These regions are not error bands around a best-fit line.

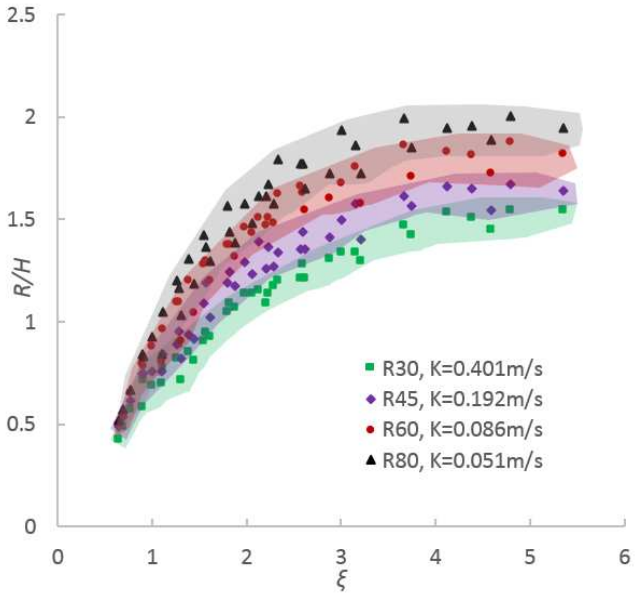

Figure 133 *R/H* data from breaking waves on the 4 permeable slopes against the Iribarren number

As can be seen, the shape of the curves from the four beach materials is very similar and the value of R/H decrease as the hydraulic conductivity of the slopes increases. At a ξ value between 3.5 and 4, the R/H values approach a maximum height, which remains constant as ξ grows.

The influence of hydraulic conductivity on run-up has traditionally been included in run-up formulae via two methods. The first method is by adding an influence factor into a formula developed for smooth impermeable slopes, while the second method is by curve-fitting expressions to run-up data obtained from specific permeable structures. The

influence factors usually include the influence of both roughness and hydraulic conductivity of the slopes and are designed for specific kinds of structure.

In this study, the curves followed by the *R/H* data for each foam are well described by the hyperbolic function suggested by Schüttrumpf (2001). As shown in the previous sections, this function also described accurately the *R/H* data on the smooth impermeable slopes, where a modified Schüttrumpf formula was presented. This suggests that it might be possible to add influence factors to the modified Schüttrumpf formula to account for the effects of roughness and hydraulic conductivity. Developing this approach, the following formula is proposed to predict run-up from breaking waves on permeable slopes:

$$\frac{R}{H} = 3.74 * \tanh(0.38 * \xi_o) * \gamma_f * \gamma_K \qquad (117)$$

where γ_f and γ_K are influence factors for surface roughness and hydraulic conductivity, respectively. To analyse and estimate values of these influence factors, run-up laboratory tests with identical wave conditions were performed on 10˚ slopes with 9 different slope configurations:

- 1 smooth-impermeable slope
- 4 rough-impermeable slopes
- 4 rough-permeable slopes

All of the waves generated resulted in breaking waves on the slope. Therefore, the individual effects of each parameter were only analysed for breaking waves. For non-breaking waves, the combined influence of roughness and hydraulic conductivity are described and estimated in Section 7.3.

7.2.1 Influence Factor for Surface Roughness

The run-up reduction in a permeable slope is produced by the energy dissipation caused by the roughness of the slope and by the infiltration into the permeable slope. Although it is possible to have roughness without permeability, it is difficult to have any permeability without some roughness. By performing tests with impermeable and permeable slopes with identical surface roughnesses, it was possible to analyse the influence of both parameters independently. This section describes the derivation of the influence factor to account for the reduction attributed only to the surface roughness of the foams.

As described in Chapter 4, run-up tests were performed over 4 different rough-impermeable 10˚ slopes. The surface roughness of each of these slopes corresponded to those of the 4 permeable foams used: R30, R45, R60 and R80. By comparing these results

with those on the 10˚ smooth-impermeable slopes, it was possible to quantify the reduction attributed to the surface roughness of the foams.

Figure 134 shows the run-up measurements on each of the four 10˚ rough-impermeable slopes plotted beside the run-up data obtained from the 10˚ smooth-impermeable slope.

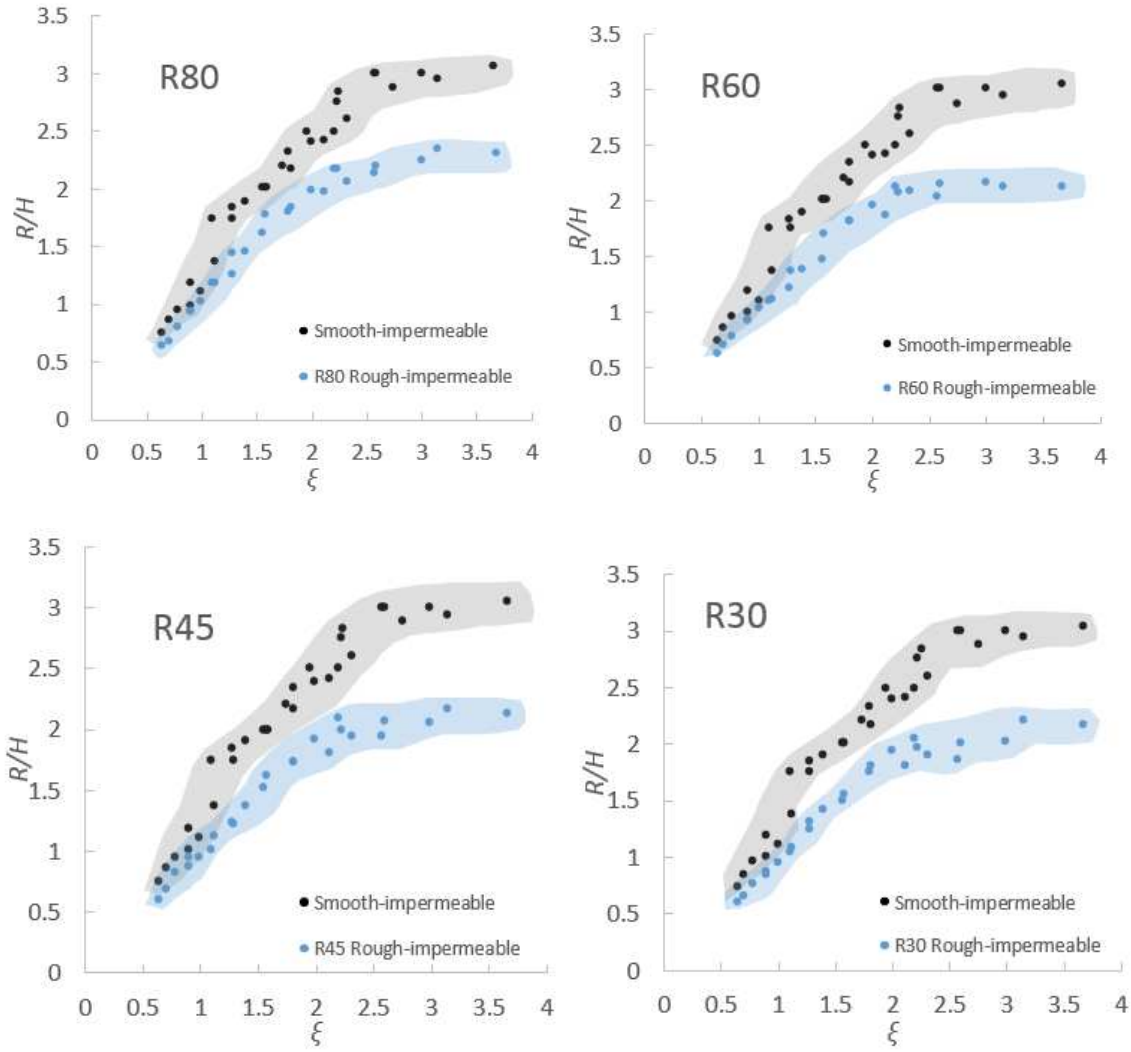

Figure 134 Comparisons between the run-up data from the 10˚ smooth-impermeable and rough-impermeable slopes

It can be seen that the roughness significantly decreases the run-up height. However, it is hard to identify the difference between the 4 graphs, as the reduction caused by the surface roughness of the 4 rough slopes was very similar. From these graphs, we can see that the reduction caused by roughness is greater for the higher Iribarren numbers. Therefore, the roughness influence factors can be expressed as functions of ξ. To estimate these functions, run-up factors were estimated. The identical wave conditions performed on the smooth and rough slopes allowed the calculation of run-up factors for each wave condition generated. These factors were obtained using the following expression:

$$r_f = \frac{R_{(\text{rough}-\text{impermeable})}}{R_{(\text{smooth}-\text{impermeable})}} \tag{118}$$

The calculated factors from the four rough slopes were plotted against ξ and are shown in Figure 135. For reference, the horizontal line in each graph represents unity value. In each graph, we can see that the value of the factors gradually decrease as ξ increases. Even though the factors seem to decrease linearly, this decrease was found to be better described through a negative power function given by:

$$\gamma_f = a\xi^{-b} \tag{119}$$

where a and b are empirical coefficients. The values of the empirical coefficients were estimated by curve-fitting this formula to the data of each rough slope. The resulting functions are displayed in each graph.

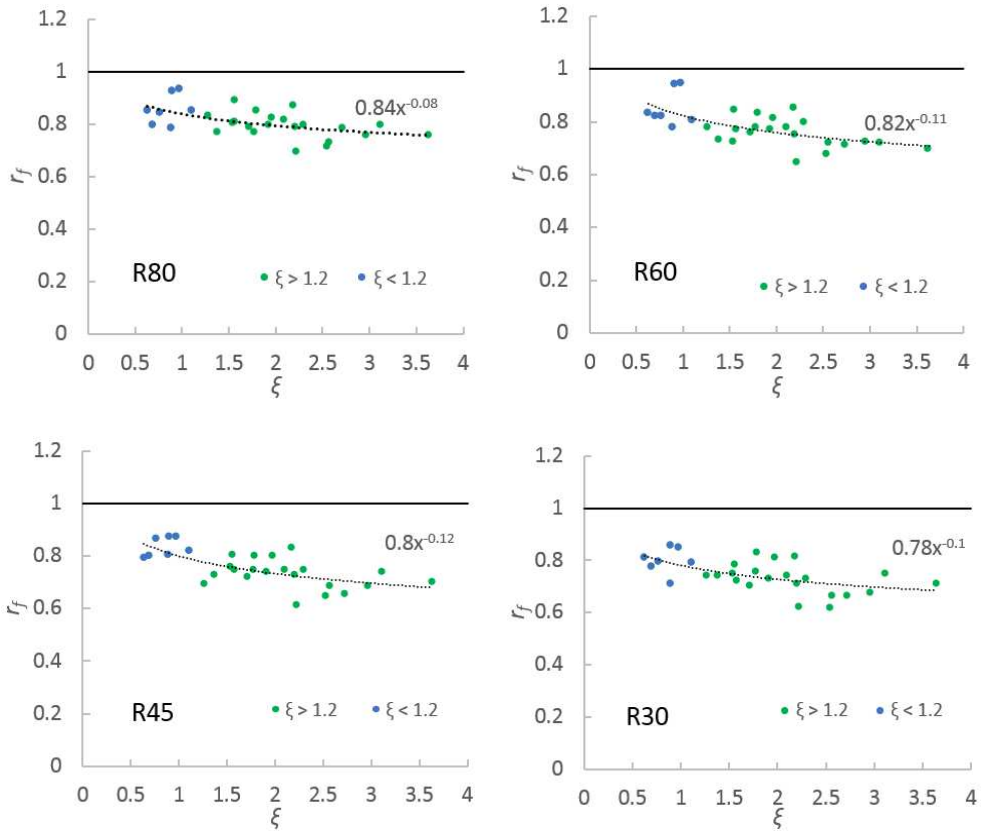

Figure 135 Reduction factors for the surface roughness of the foams

In these graphs, we can see that roughness has less influence for the data with $\xi < 1.2$ (blue dots). To quantify the reduction caused by the surface roughness of the slopes averaged reduction percentages were estimated for the data corresponding to $\xi > 1.2$, $\xi < 1.2$ and for all the data. These reduction percentages are shown in Table 40.

From this table it is evident the greater reduction is caused by roughness on waves with higher Iribarren numbers (small waves). The data with $\xi < 1.2$ correspond to large plunging waves (with larger wave steepness values, $H/L_o > 0.025$) where most of the

energy is dissipated by the breaking processes. This smaller influence of surface roughness on run-up from large wave heights is also reported in EurOtop (2007).

Although the influence of roughness slightly increases as the porosity of the slopes increases, the reduction caused by the four different surfaces is very similar. This can be seen from the similar values of the empirical coefficients obtained in each best fit function shown in Figure 135 (values summarised in Table 41).

Rough Surface Type	% Reduced $\xi < 1.2$	% Reduced $\xi > 1.2$	% Reduced All values
R30	20%	27%	26%
R45	17%	27%	25%
R60	15%	24%	22%
R80	15%	21%	19%

Table 40 *R/H* Percentage reduced by the surface roughness of the slopes

Type	***a* coefficients**	***b* coefficients**
R30	0.78	0.1
R40	0.8	0.12
R60	0.82	0.11
R80	0.83	0.08

Table 41 Summary of coefficients for each rough-impermeable slope

Therefore, the following influence factor for roughness to account for the surface roughness from all 4 slopes can be approximated by:

$$\gamma_f = 0.8\xi^{-0.1} \tag{120}$$

This roughness factor is only valid for foams within the range of porosity values tested in this study (30-80PPI).

7.2.2 Influence Factor for Hydraulic Conductivity

This section investigates how much of the run-up reduction observed in a permeable slope can be attributed only to the hydraulic conductivity of the slope. This was analysed by comparing the results from the 4 rough-permeable slopes with their impermeable counterparts with identical roughnesses.

The 4 graphs displayed in Figure 136 show the run-up measurements of the four rough-impermeable (blue dots) and the four rough-permeable (red dots) slopes. For comparison, the measurements from the smooth-impermeable slope are also displayed with black dots. As mentioned previously, all of these tests were performed under the exact same experimental conditions: same wave flume, water depth, slope angle (10°) and with the same regular wave conditions.

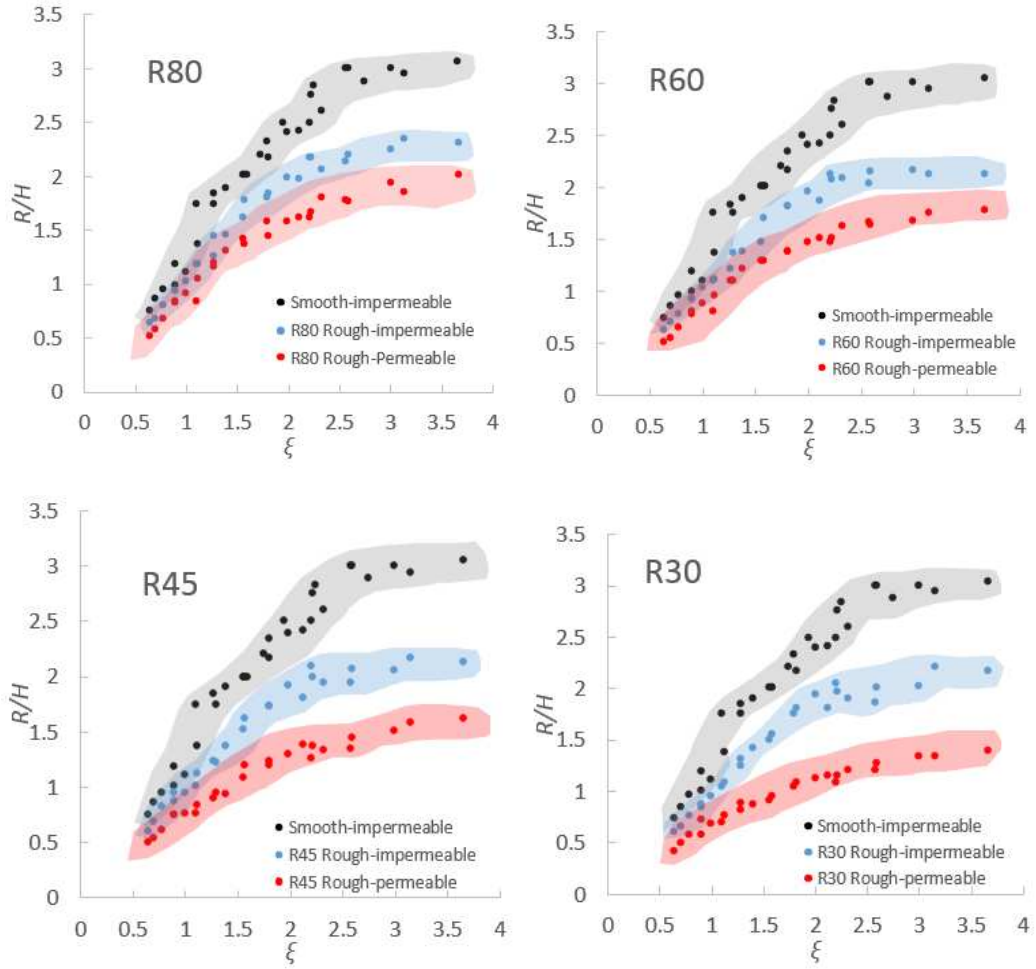

Figure 136 Comparisons between the run-up data from the 10° smooth-impermeable, rough-impermeable and rough-permeable slopes

From these graphs, it is clear that the reduction in R/H caused by the hydraulic conductivity of the slopes increases as the hydraulic conductivity of the slopes increases. We can see that the influence of hydraulic conductivity on run-up is also a function of ξ, as its reduction increases as ξ increases. To estimate expressions for the hydraulic conductivity influence factors in terms of ξ, run-up factors were again estimated. This time, the factors were obtained comparing the results from each rough permeable and impermeable slope using the following formula:

$$r_K = \frac{R_{(\text{rough}-\text{permeable})}}{R_{(\text{rough}-\text{impermeable})}} \tag{121}$$

The results obtained are displayed in Figure 137, where for reference the black horizontal line shows unity value.

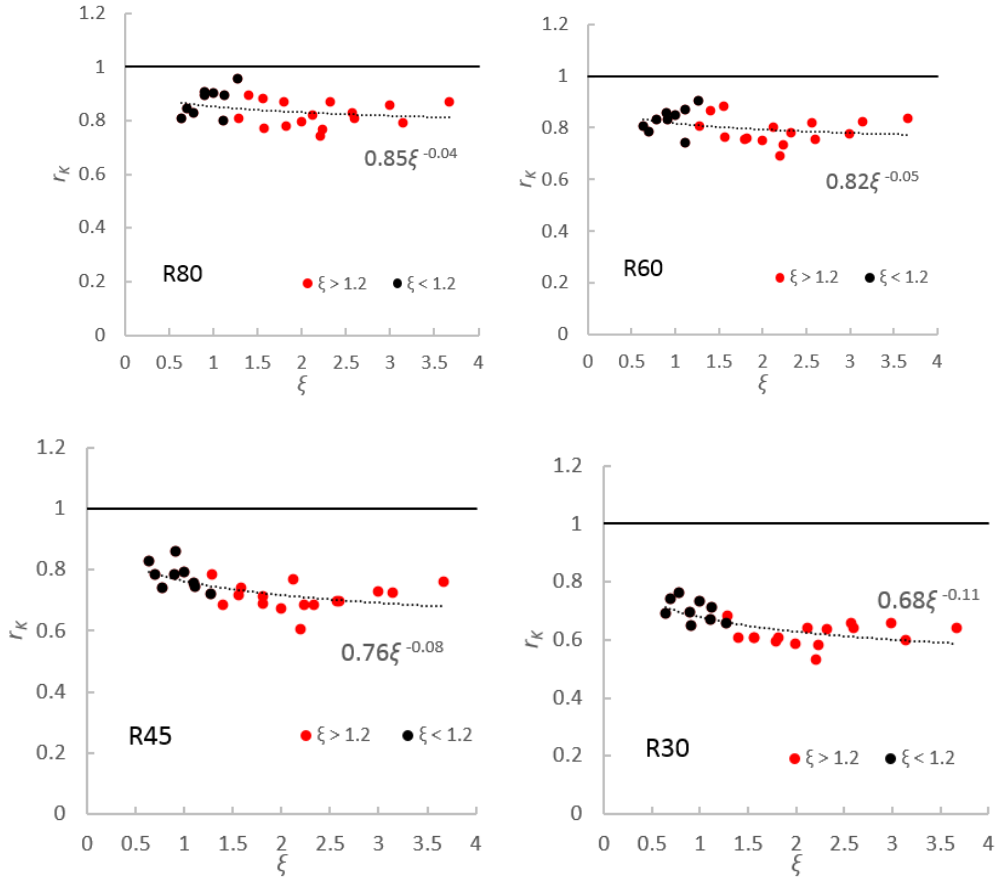

Figure 137 Reduction factors for hydraulic conductivity

From these graphs, we can see that hydraulic conductivity has less influence on run-up values $\xi < 1.2$. For run-up values $\xi > 1.2$, the value of the factors remains fairly constant as ξ grows. As mentioned previously these data with $\xi > 1.2$ correspond to waves with larger periods and smaller heights. The longer periods produce longer uprush and backwash motions, allowing more time for water to infiltrate into the slope, while the thin run-up depths from small waves also allow infiltration into the slope.

Figure 135 and Figure 137 show that both roughness and hydraulic conductivity have less influence on run-up from plunging waves with values: $\xi < 1.2$. Therefore, we can expect that their combined effects will increase the run-up reduction on larger ξ. This can be seen in Table 42 and Table 43, where the run-up reduction attributed to roughness and hydraulic conductivity, as well as their combined effects are shown. These reduction percentages are in relation to the data on the smooth slope and are shown for both ranges of ξ values analysed.

It is interesting to note that even though the surfaces of all the foams are relatively smooth, the run-up reduction on the data with $\xi > 1.2$ caused by roughness is larger than the reduction caused by the hydraulic conductivity of the slopes, except for the most permeable slope, R30. On the other hand, for the data with $\xi < 1.2$, the reduction caused by both parameters is very similar. These results suggest that on a slope consisting of

typical gravel with similar hydraulic conductivity values as those tested here (where the surface is much rougher than the foam's surface), the reduction caused by the surface roughness would be considerably larger than the reduction caused by its hydraulic conductivity.

Rough Surface Type	% Reduced *Roughness*	% Reduced *K*	% Reduced Total
R30	20%	21%	41%
R45	17%	18%	35%
R60	15%	14%	29%
R80	15%	11%	26%

Table 42 *R/H* Percentage reduced for $\xi < 1.2$

Rough Surface Type	% Reduced *Roughness*	% Reduced *K*	% Reduced Total
R30	27%	28%	55%
R45	27%	21%	48%
R60	24%	16%	40%
R80	21%	14%	35%

Table 43 *R/H* Percentage reduced for $\xi > 1.2$

The trends followed by the factors of each type of foam shown in Figure 137 are also well described by a negative power function given by:

$$\gamma_K = a\xi^{-b} \tag{122}$$

where a and b are empirical coefficients. By curve-fitting this formula to the data of each graph, the empirical coefficients were estimated and the resulting functions are shown in each of the graphs of Figure 137. As can be seen, the values of both coefficients are a function of the hydraulic conductivity of the foams. Therefore, these coefficients can be expressed terms of hydraulic conductivity, K. However, to include the hydraulic conductivity parameter in (122), this parameter has to be dimensionless. For this reason, this study presents a new non-dimensional hydraulic conductivity parameter, which will be represented by Ψ and is given by:

$$\Psi = \frac{K^3}{g\nu} \tag{123}$$

where K is the hydraulic conductivity (m/s), g is the gravitational acceleration (m/s^2) and ν is the kinematic viscosity of water (m^2/s). The K and corresponding Ψ values for the 4 permeable slopes are shown in Table 44, along with their corresponding empirical coefficients estimated in Figure 137.

Type	*K* (m/s)	$\Psi=K^3/\nu g$	*a coefficients*	*b coefficients*
R30	0.401	6546.8	0.68	0.11
R40	0.192	718.6	0.76	0.08
R60	0.086	64.6	0.82	0.05
R80	0.051	13.5	0.85	0.04

Table 44 Hydraulic conductivity, K, and dimensionless hydraulic conductivity, Ψ, values for the foams along with their corresponding a and b coefficients

Figure 138 shows the values of both coefficients a and b plotted against their corresponding Ψ values in log-log graphs. As can be seen, the coefficients a decrease as K increases, while coefficients b increase as K increases. The growth and decay rate of these coefficients were best described by power functions. These are shown in the graphs displayed in Figure 138, where the values of both coefficients are plotted against their corresponding Ψ values in log-log graphs.

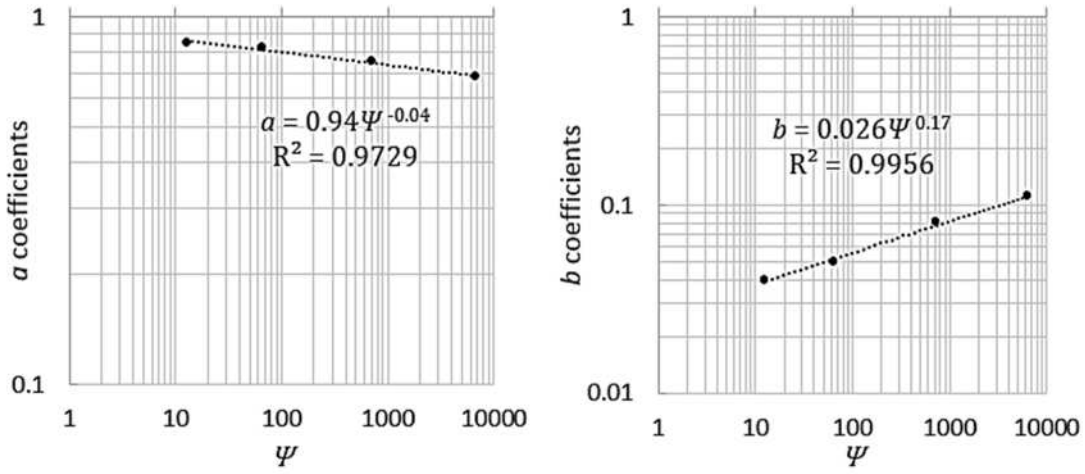

Figure 138 Empirical coefficients plotted against Ψ

Substituting the functions shown in Figure 138 in (122), the influence factor for hydraulic conductivity is:

$$\gamma_K = 0.94\Psi^{-0.04} * \xi^{-0.026\Psi^{0.17}} \tag{124}$$

7.2.3 Validation with the Present Data

The hyperbolic formula for breaking waves on permeable slopes can now be expressed as:

$$\frac{R}{H} = 3.74 * \tanh(0.38 * \xi) * \gamma_f * \gamma_K \tag{125}$$

where:

$$\gamma_f = 0.8\xi^{-0.1} \tag{126}$$

$$\gamma_K = 0.94\Psi^{-0.04} * \xi^{-0.026\Psi^{0.17}} \tag{127}$$

The predictions of this formula are compared against the R/H data from the breaking waves of the 4 foams and are shown in Figure 139. The dashed black lines indicate the ±15% error bands. As can be seen, predictions of (125) using the influence factor show excellent agreement with all the present data from the 4 permeable slopes.

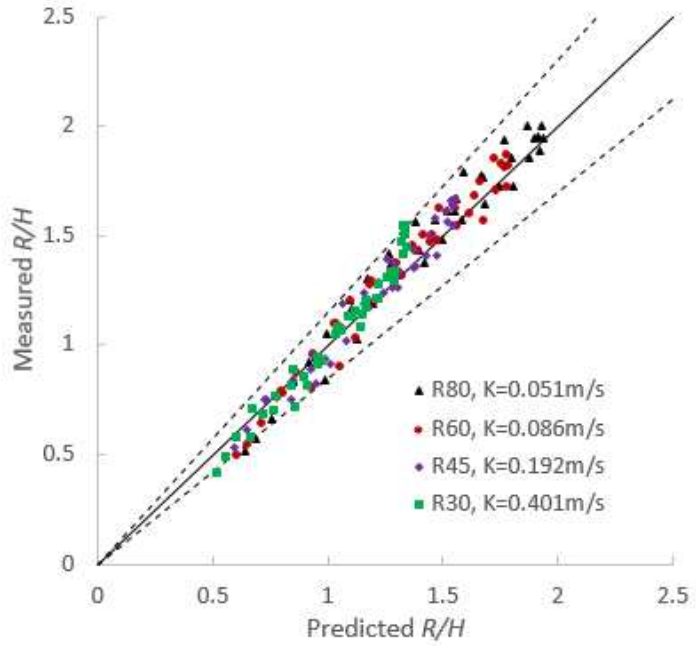

Figure 139 Measured versus predicted run-up data from breaking waves on the 4 permeable slopes. Solid line: perfect agreement; dash line: ±15% error bands.

As far as the author is concerned, this is the first time that the influence of surface roughness and hydraulic conductivity on run-up has been quantified separately and included into a run-up formula through independent influence factors.

The influence factor γ_f proposed in (126) is only valid for the roughness of the foams analysed in these experiments. As discussed in the Literature Review, the roughness influence has been extensively studied for different types of structures, where reduction values have been proposed for specific types of structures. These values can be found in tables presented in coastal manuals such as EurOtop (2007) or Van der Meer (1992) and can replace the influence factor γ_f proposed in (125).

On the other hand, the influence factor for hydraulic conductivity γ_K can be applied to any beach or structure with hydraulic conductivities between the K ranges analysed in these tests. This means that if the hydraulic conductivity of the beach or coastal structure is known, measured using permeameters or estimated through empirical formulae (discussed in 7.4), it is possible to estimate its influence on run-up.

This separation of the effects of roughness and hydraulic conductivity on run-up can be useful for many applications, for example, when estimating the influence of a permeable core in a breakwater, or a shingle beach with a course sand sublayer. Examples of the application of this formula are shown in Section 7.5.

7.2.4 Influence of Water Table Elevation on Wave Run-up

Chapter 4 described experiments where run-up measurements were taken on beaches with high and low water table elevations. These tests were aimed to analyse whether a saturated or unsaturated beach would have any significant influence on wave run-up. Beach drainage system promoters claim that by lowering the beach groundwater levels, beach erosion can be reduced. However, as discussed previously, the effectiveness of these systems has mixed results in reducing erosion. The aim of lowering the beach groundwater level is to increase the unsaturated region near the beach face and allow water from the swash motions to infiltrate into the beach. Consequently, this increase in infiltration should reduce the run-up heights and backwash volumes, reducing the amount of sediment carried away from the beach. However, the reduction of run-up caused by lowering the beach groundwater has never been analysed yet. Therefore, the aim of the tests carried out with low water table elevations was to investigate the extent to which lowering the beach groundwater levels reduces run-up.

Under the opposite scenario, a beach with a high groundwater level (which occurs when the tidal elevation drops) is expected to increase run-up heights due to two mechanisms. Firstly, a high water table elevation increases the saturated region on the beach face, decreasing the infiltration of the swash motions into the beach. Thus, the run-up heights and backwash volumes are expected to increase, and consequently, the amount of sediment carried away from the beach should also increase. And secondly, the seepage face developed between the exit point of the water table and the shoreline due to exfiltration (described in Chapter 2) could act as a smooth layer, reducing the influence of roughness. The influence of a high water table elevation on run-up has also never previously been measured or analysed. For this reason, tests were also carried out on beaches with high water table elevations.

This section analyses the run-up measurements where the water table elevation was adjusted for two different 10˚ permeable slopes (R45 and R80 foams with hydraulic conductivities of K = 0.105 and 0.051 m/s respectively). In total, tests with 4 different beach configurations were performed for this analysis:

- 2 rough-permeable slopes with high water table elevations
- 2 rough-permeable slopes with low water table elevations

These tests were carried out generating the same wave conditions and using the same water depth as for the tests described in Section 7.2.2, where the water table elevation was not manipulated. This allowed comparisons between the run-up heights with different water table elevations.

The results of these tests are shown in Figure 140 and Figure 141, where the run-up data on beaches with high water tables are plotted in blue, while the data on beaches with lower water tables in green. For comparison, the data from the smooth-impermeable (black), the rough-impermeable (purple) and the rough-permeable slopes with no water table manipulation (red) are also displayed. The shaded areas in these graphs show the region covered by each group of data, it does not have any statistical meaning.

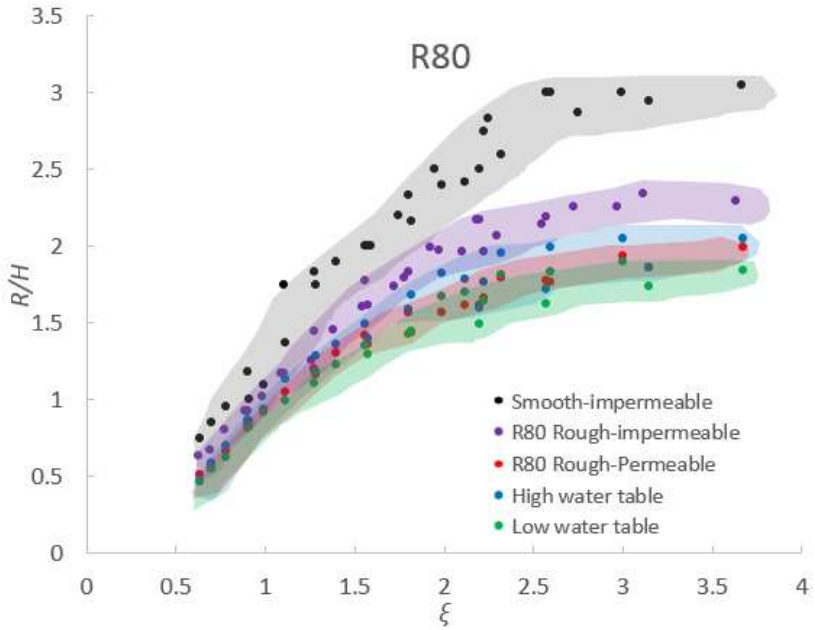

Figure 140 *R/H* data comparisons for the R80 permeable slopes with high and low water table elevations

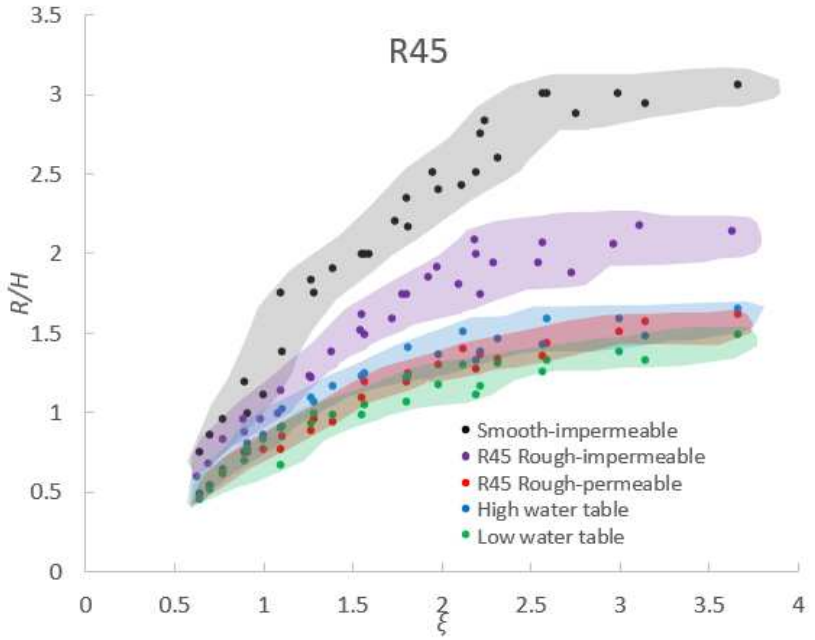

Figure 141 *R/H* data comparisons for the R45 permeable slopes with high and low water table elevations

Although it can be noticed that the water table elevations did have an effect on wave run-up, their influences are relatively small (around ±5%) so were not included in the run-up

prediction formulae (125). These influences can be better appreciated by estimating influence factors. As mentioned before, the same water depth and wave conditions enabled the estimation of influence factors for each wave condition. This were calculated using the following formulae:

$$r_{K+} = \frac{R_{(\text{rough}-\text{permeable}-\text{ high water table }\ )}}{R_{(\text{rough}-\text{permeable})}} \tag{128}$$

$$r_{K-} = \frac{R_{(\text{rough}-\text{permeable}-\text{ low water table }\ )}}{R_{(\text{rough}-\text{permeable})}} \tag{129}$$

The results obtained are displayed in Figure 142. As can be seen, these values remain fairly constant as ξ grows. Therefore, the averages of all the values from each graph were used as influence factors. These average values are summarised in Table 45.

Rough Surface Type	High Water Table Influence Factor	Low Water Table Influence Factor
R45	1.07	0.94
R80	1.05	0.96

Table 45 Influence factors for high and low water table elevations on *R/H*

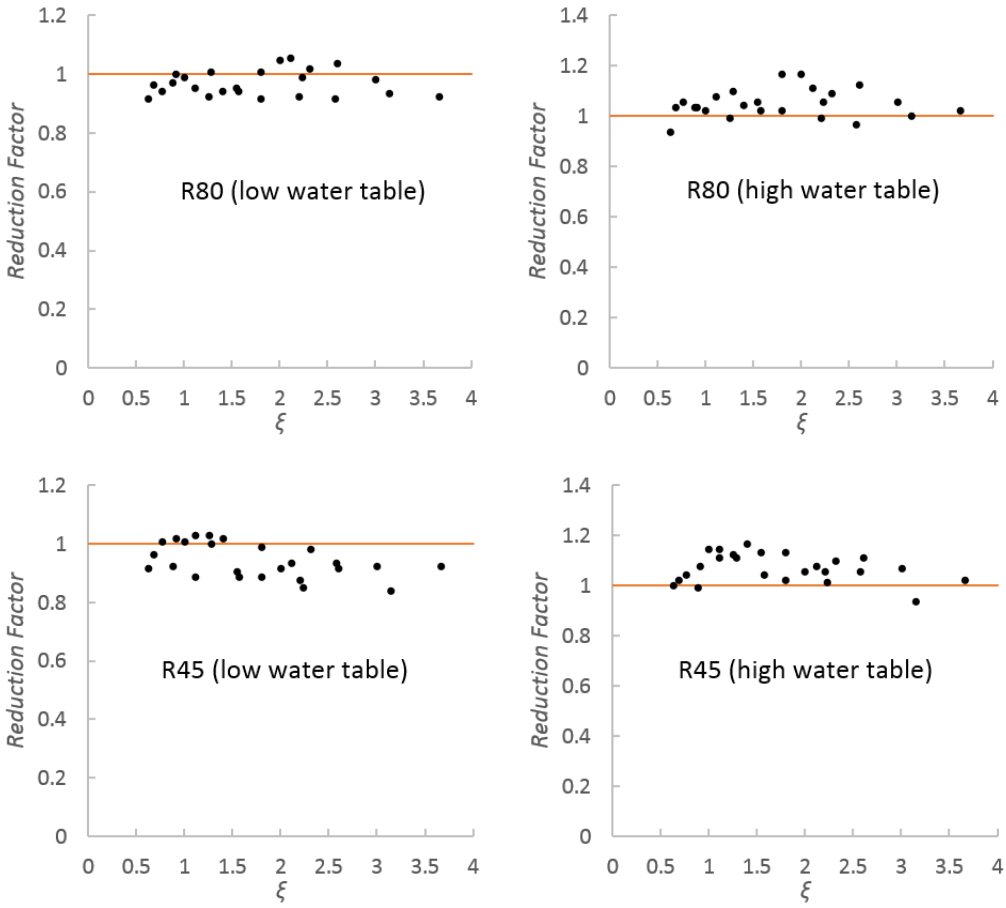

Figure 142 Reduction factors for high and low water table elevations

From Table 45 and Figure 142, we can see that the influence of water table elevations on both permeable slopes is very similar, with the run-up heights varying on average ≈ ±5%.

These small effects seen on run-up with adjusted water table elevations might be attributed to the technique used to lower or increase the water tables inside the beaches. As described in Chapter 4, the water table elevations were lowered by pumping water from the back of the beach to the other end of the flume. This is far away from the beachface. Consequently, even though the water table was lowered by 10 cm in respect to the SWL at the back of the beach, the unsaturated region at the beachface due to the low water tables was very small (Figure 143a). The same applies for the tests performed with high water table elevations.

To increase the unsaturated region at the beachface in future experiments, two options can be implemented. The first option would be to place the pump closer to the beachface (Figure 143b), while the second option would be to use a pump capable of pumping higher flow discharges. This pump should be capable of lowering the water depth at the back of the beach significantly more than the water depth used in these tests on 20cm (Figure 143c). However, none of these options were feasible in these experiments. As the beaches were made out of foams, burying a pump inside the foams would practically destroy the foams, while acquiring a more powerful pump exceeded the experimental budget of these tests.

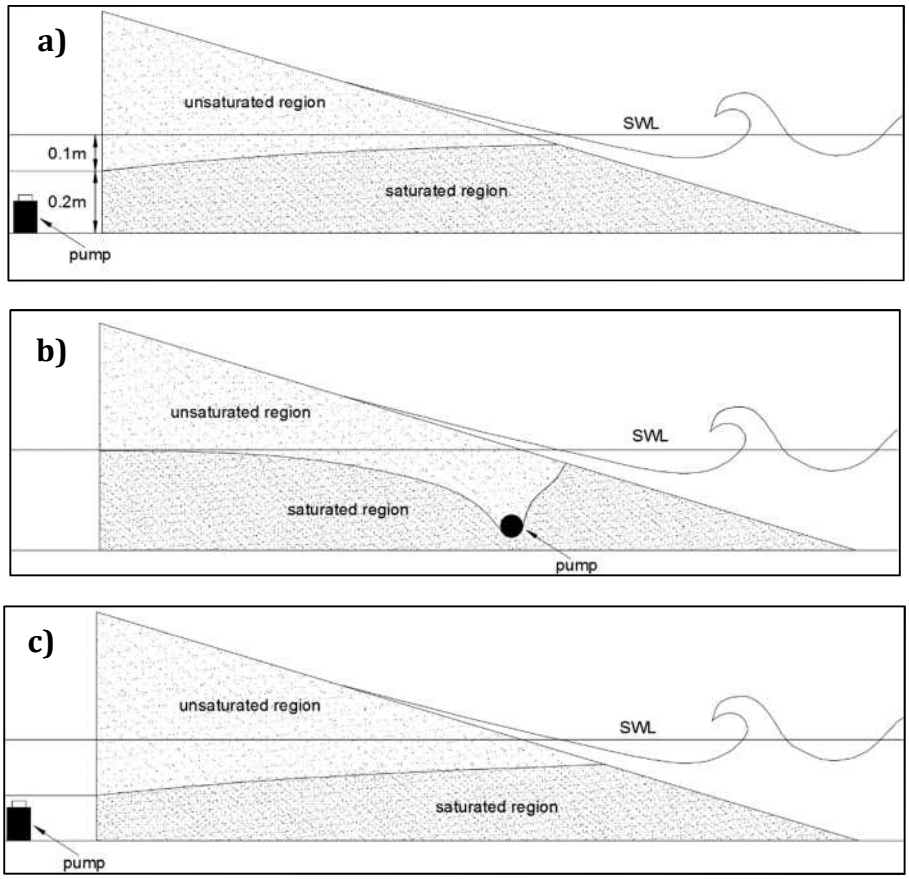

Figure 143 Alternative techniques for lowing the water table elevation in the laboratory experiments

7.2.5 Summary

- The influence of surface roughness, hydraulic conductivity and water table elevations on run-up from breaking waves were investigated

- Influence factors for roughness (126) and hydraulic conductivity (127) were derived to be included in Schüttrumpf's modified formula (125) (previously derived for smooth-impermeable slopes) to predict run-up from breaking waves on permeable slopes

- The formula with the influence factors was validated against the present data

- The hydraulic conductivity influence factor is based on a new dimensionless hydraulic conductivity parameter, Ψ

- The water table elevations were seen to slightly influence the magnitude of run-up ($\approx 5\%$)

7.3 Non-breaking waves

Previous studies have shown that the roughness of the slope only influences wave run-up from surging waves when the structure is permeable (e.g. van Broekhoven, 2011; EurOtop, 2007). For this reason, tests on steep, rough-impermeable slopes (where surging waves would occur) were not performed in this study. Only tests on steep, rough-permeable and smooth-impermeable slopes were carried out. Consequently, it was not possible to separate the influence of surface roughness and hydraulic conductivity for non-breaking waves, as was reported for the breaking waves earlier. Nevertheless, by comparing the run-up from non-breaking waves on smooth-impermeable with those on rough-permeable slopes, the combined run-up reduction caused by roughness and hydraulic conductivity in non-breaking waves was analysed.

The run-up data from non-breaking waves on smooth-impermeable slopes was obtained from different test conditions than the data obtained from the rough-permeable slopes. Most of the non-breaking wave data on smooth-impermeable slopes were obtained from 13°, 15°, 18.4 °, 26.6°, 33.7 ° and 45° slope angles, while the data on permeable slopes were obtained from 20° and 30° slopes. This meant that it was not possible to estimate run-up factors for each wave condition as performed for the breaking waves. Nonetheless, the run-up data from the non-breaking waves on permeable slopes were also shown to be well described by Φ and by the wave momentum flux parameter. This enabled the derivation of an influence factor to account for the combined influence of roughness and hydraulic conductivity on wave run-up. This section describes how this influence factor was derived.

7.3.1 **Influence Factor for Roughness and Hydraulic Conductivity**

In Section 6.2.3, the run-up from non-breaking waves was shown to be well predicted by a negative power law model given by:

$$\frac{R}{H} = a(\Phi)^{-b} \tag{130}$$

where a and b are empirical coefficients. For the smooth-impermeable slope, these coefficients had values of a = 1.25 and b = 0.32. As shown in Section 7.1.1, when the R/H data from the non-breaking waves on the permeable slopes were plotted against Φ, the data were shown to follow well-defined curves similar to those on the smooth slopes. These curves were also very well described by (130). This is shown in Figure 144, where the R/H data from each permeable slope is plotted beside R/H data from the smooth-impermeable slope. Power regressions were performed to estimate the empirical coefficients a and b for each permeable slope.

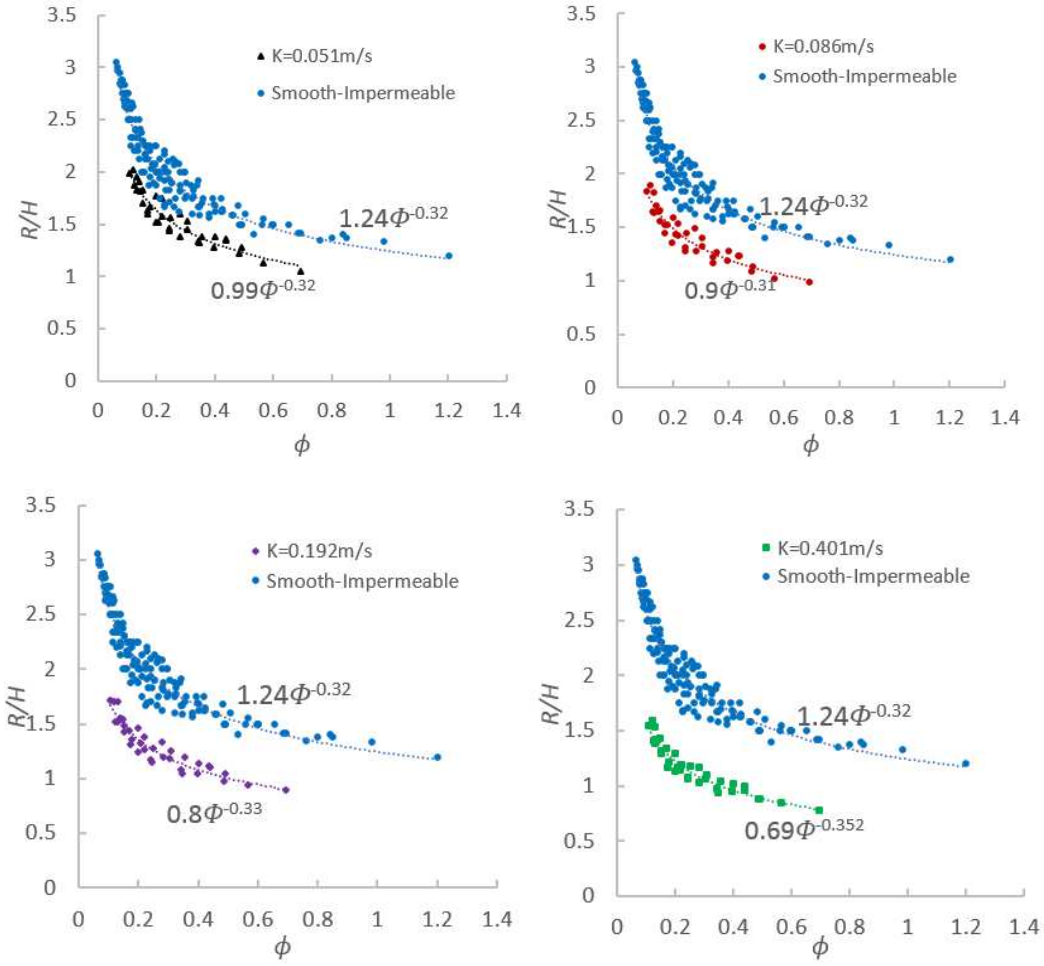

Figure 144 R/H data from the permeable slopes compared to the data from the smooth impermeable slopes plotted against Φ

As can be seen, the trends described by the data on the permeable slopes are very similar to the trend described by the data on the smooth slope. The rate of decay of these power

curves is determined by the coefficients b. From these graphs, we can see that these coefficients are not a function of hydraulic conductivity as they remain effectively constant for all permeable slopes. In contrast, the coefficients a (which determine the range of R/H for each curve) are clearly a function of hydraulic conductivity. In this case, the values of the curves decrease as the hydraulic conductivity of the slope increases.

As the rate of decay of the curves from the permeable and smooth slopes is almost identical, it was possible to quantify the reduction for each permeable slope simply by estimating factors between the coefficients a of the permeable and smooth slopes:

$$r_{f+K} = \frac{a_{(\text{rough}-\text{permeable})}}{a_{(\text{rough}-\text{impermeable})}} \tag{131}$$

where r_{f+K} is the ratio or factor accounting for both the influence of roughness and hydraulic conductivity. The factors obtained and the run-up reduction percentage attributed to both parameters are summarized in Table 46. For comparison, Table 43 is shown again as Table 47; this gives the reductions estimated for the breaking waves.

Type	K (m/s)	$\Psi=K^3/\nu g$	*a coefficients*	*Factors*	% Reduced Total
R30	0.401	6546.8	0.69	0.56	44%
R40	0.192	718.6	0.8	0.65	35%
R60	0.086	64.6	0.9	0.73	27%
R80	0.051	13.5	0.99	0.8	20%

Table 46 Summary of coefficients for non-breaking waves on each permeable slope

Type	% Reduced *Roughness*	% Reduced K	% Reduced Total
R30	27%	28%	55%
R45	27%	21%	48%
R60	24%	16%	40%
R80	21%	14%	35%

Table 47 R/H Percentages reduced for breaking waves with $\xi > 1.2$

It is interesting to see that the combined run-up reduction caused by roughness and hydraulic conductivity is larger on breaking waves than on non-breaking waves. As shown in the previous section, the surface roughness has a larger influence in reducing run-up from breaking waves than hydraulic conductivity. However, the influence of roughness on the water motion decreases as the water depth increases. The uprush from surging waves with large Iribarren numbers generally is thicker than those with small Iribarren numbers. This suggests that the combined reduction of roughness and hydraulic conductivity on run-up for surging waves might be attributed mainly to the hydraulic conductivity of the slope. This explains why the combined reduction of roughness and hydraulic conductivity observed on breaking waves is larger than those on non-breaking waves.

By plotting the factors shown in Table 46 against their corresponding non-dimensional hydraulic conductivity, Ψ, values (also shown in Table 46), a function in terms of hydraulic conductivity was derived (Figure 145). This function was found to be best described by a negative power law function with the form of $y = ax^{-b}$ and is given by:

$$\gamma_{f+K} = 0.92\Psi^{-0.056} \tag{132}$$

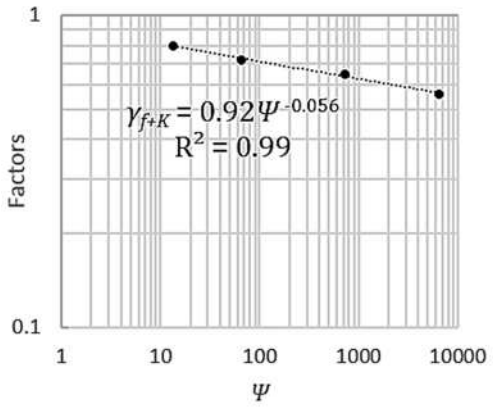

Figure 145 Hydraulic conductivity factors estimated using the Φ parameter plotted against Ψ

This function can then be applied as a factor to account for the combined influence of roughness and hydraulic conductivity in any run-up formulae originally derived for non-breaking waves on smooth-impermeable slopes.

7.3.2 Influence Factors from Wave Momentum Flux Formula

Another estimate for γ_{f+K} was obtained using formulae based on the wave momentum flux parameter. In 6.2.3, the following run-up formula was proposed for non-breaking waves on smooth slopes.

$$\frac{R}{h} = a * e^{0.1\,cot\propto}\left(\frac{M_F}{\rho g h^2}\right)^{3/4} \tag{133}$$

where the empirical coefficient a took a value of 1.46. When the data from the permeable slopes were plotted against $e^{0.1\,cot\propto} * (M_F/\rho g h^2)^{3/4}$, well-defined linear relationships were observed. This can be seen in Figure 146, where the data of each permeable foam are plotted beside the data from the smooth slope. Linear regressions were performed to estimate the coefficients a in (133) from each foam. The results are displayed in Figure 146 and summarised in Table 48. As before, the reduction caused by roughness and hydraulic conductivity was quantified by calculating the factors between the coefficients a from the permeable and smooth-impermeable slopes:

$$r_{f+K} = \frac{a_{(\text{rough}-\text{permeable})}}{a_{(\text{rough}-\text{impermeable})}} \tag{134}$$

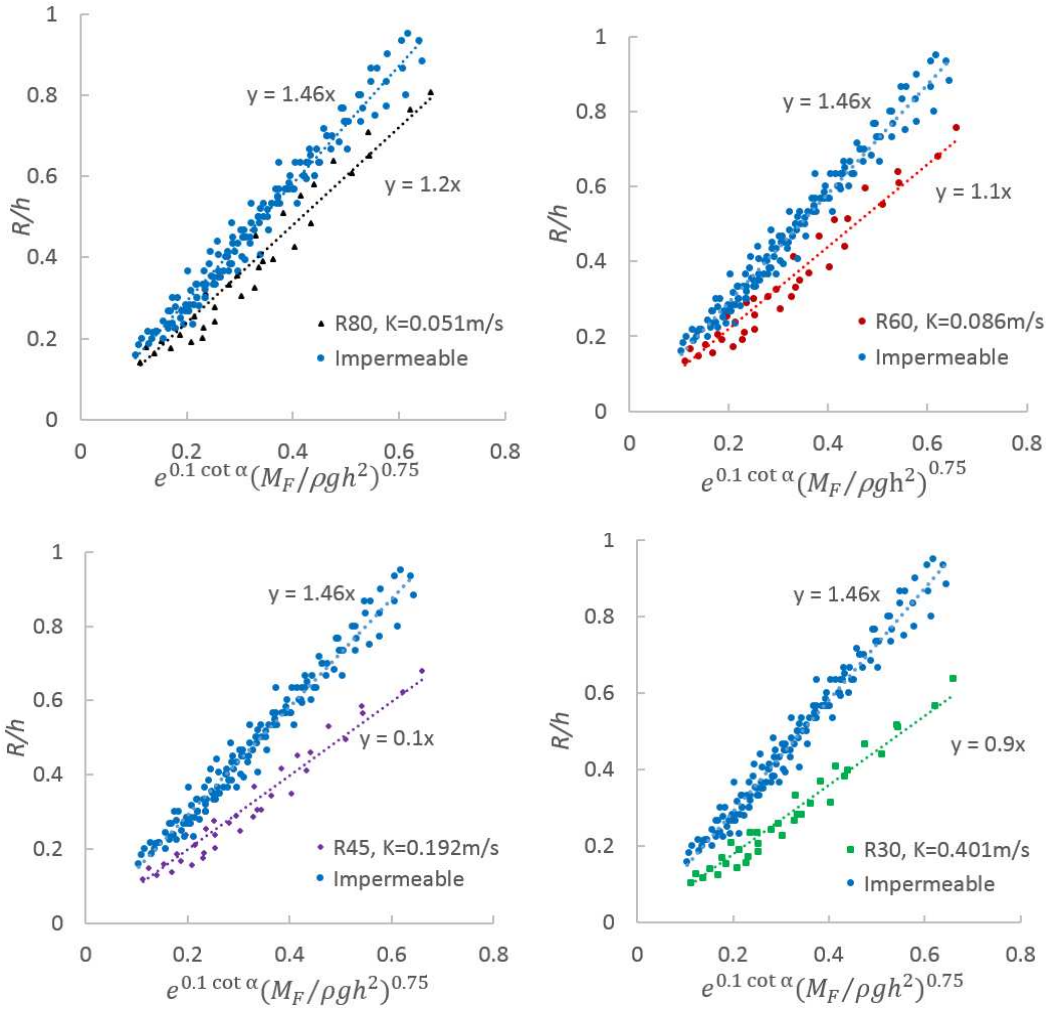

Figure 146 *R/H* data from the permeable slopes compared to the data from the smooth-impermeable slopes plotted against the wave momentum flux parameter function

Type	K (m/s)	$\Psi=K^3/\nu g$	*a coefficients*	*Factor*
R30	0.401	6546.8	0.9	0.62
R40	0.192	718.6	1	0.68
R60	0.086	64.6	1.1	0.75
R80	0.051	13.5	1.2	0.82

Table 48 Summary of coefficients for each permeable slope

The results are summarised in Table 48. These factors were plotted against their corresponding Ψ values and the following power function was obtained (Figure 147):

$$\gamma_{f+K} = 0.92\Psi^{-0.046} \quad (135)$$

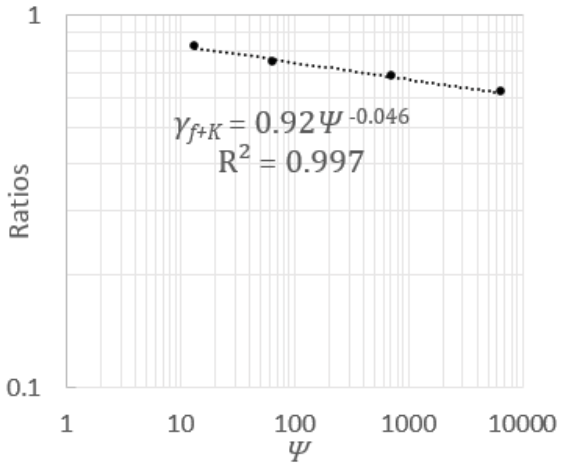

Figure 147 Hydraulic conductivity factors estimated using the wave momentum flux formula plotted against Ψ

As can be seen, the value of this influence factor γ_{f+K} is very similar to that obtained using Φ (Figure 145). The reason why both γ_{f+K} functions are not exactly same is because they were derived from prediction formulae, instead of from the data. The coefficient a in both functions is 0.92, while the power number b obtained is slightly different. For consistency, a value of b = 0.05 is proposed resulting in:

$$\gamma_{f+K} = 0.92\Psi^{-0.05} \tag{136}$$

7.3.3 Validations against Present Data

The γ_{f+K} reduction function (136) is first compared against the present data by including it in the three formulae proposed in Section 6.2.3 for non-breaking waves on smooth-impermeable slopes. Comparisons against other data are shown in Section 7.5.

$$\frac{R}{H} = 1.25(\Phi)^{-0.32} * \gamma_{f+K} \tag{137}$$

$$\frac{R}{h} = 1.46 * e^{0.1\,cot\propto}\left(\frac{M_F}{\rho g h^2}\right)^{3/4} * \gamma_{f+K} \tag{138}$$

$$\frac{R}{H} = a\xi^{-b} * \gamma_{f+K}, \quad \text{where: } a = 0.97\left({}^{h}/_{L_o}\right)^{-0.38} \text{ and } b = 0.17\left({}^{h}/_{L_o}\right)^{-0.15} \tag{139}$$

Figure 148, Figure 149 and Figure 150, show the predictions of these formulae plotted against the measured data on the 4 permeable slopes. The dashed lines indicate the ±15% error bands. As can be seen, the inclusion of γ_{f+K} into the run-up formulae derived for non-breaking waves on smooth slopes show very good agreement with the measured data on permeable slopes. This was expected as the formulae and empirical coefficients were derived from curve fits, but the lack of scatter is encouraging.

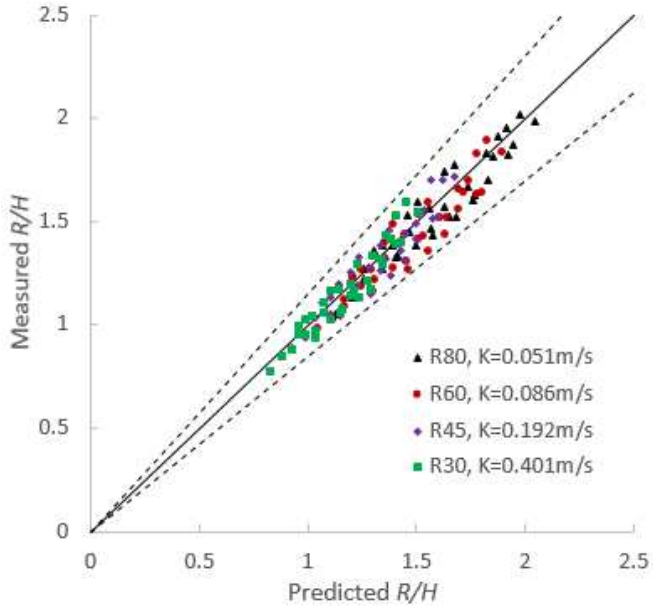

Figure 148 Measured versus predicted data using (137). Solid line: perfect agreement; dash line: ±15% error bands.

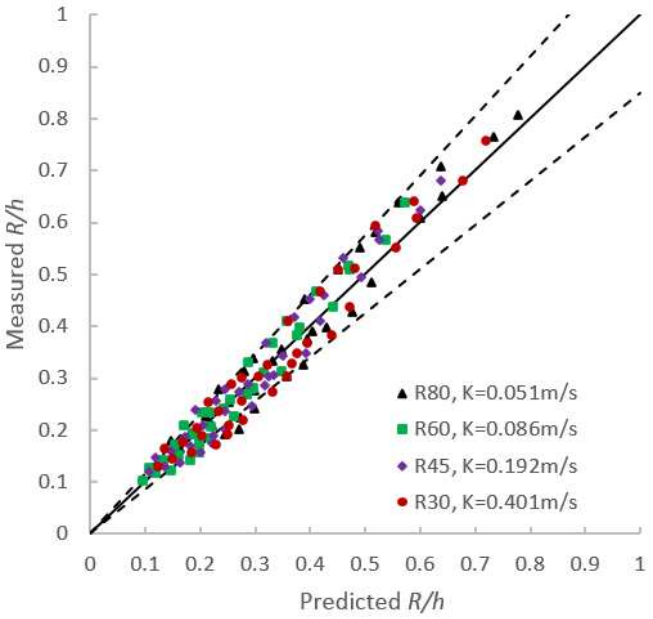

Figure 149 Measured versus predicted data using (138). Solid line: perfect agreement; dash line: ±15% error bands.

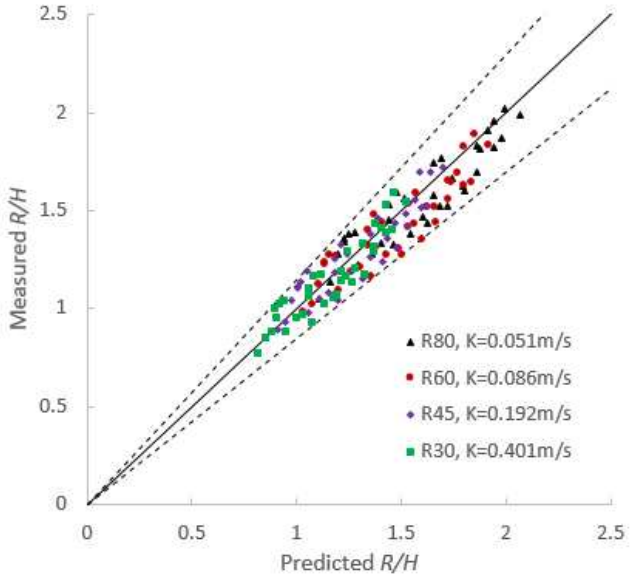

Figure 150 Measured versus predicted data using (139). Solid line: perfect agreement; dash line: ±15% error bands.

7.3.4 Summary

- The combined influence of hydraulic conductivity and roughness on run-up from non-breaking waves was investigated
- This influence was included in (103), (104), (105) and (106) through an influence factor (136) based on the non-dimensional parameter Ψ
- The formulae with the influence factor were validated against the present data

7.4 Estimation of Hydraulic Conductivity

In order to use the hydraulic conductivity influence factors proposed in Sections 7.2 and 7.3 to predict run-up on permeable slopes, it is necessary to know the hydraulic conductivity K (m/s) of the beach or coastal structure. However, measurements of K are not always available. This section describes alternative approaches to estimate K from other available parameters.

The most accurate way of estimating hydraulic conductivity on a beach is by collecting intact sediment samples across the beach and at different depths and measure their hydraulic conductivities in the laboratory using a permeameter. If a sample of the material is available, the best way to estimate its K (m/s) is by using a permeameter and performing constant head or falling head tests (as performed in this study). Otherwise, it is possible to estimate the permeability k (m^2) of the material using simple empirical formulae that relate K to other parameters such as porosity, grain size, pore throat size and sediment sorting. Once the permeability is estimated, K can then be calculated by:

$$K = kg/\nu \quad (140)$$

where k is the permeability given in m^2, g the gravitational acceleration and ν the kinematic viscosity of the fluid.

The most common formulae relating permeability to other parameters are summarised in Table 49. The usage of each of these formulae depends on the data available. In this table, the grain sizes, d, and pore throat radii, r, are expressed in microns (μm), so the coefficients may differ from the original versions.

In Table 49, σ, C, and p are sediment sorting parameters: σ is the standard deviation of grain diameter in phi units (phi=-$\log_2(d)$), p is the percentile deviation also expressed in phi units, while C is a sorting index that ranges from 0.7 for well sorted to 1 for poorly sorted sandstones. S_{wi} is the irreducible water saturation, r_h is the hydraulic radius, d_g is the geometric mean grain diameter, n is the porosity, and m is the Archie cementation exponent.

Type of Models	Parameters required	Authors	Equations
Grain size-based models	d_g and σ	Krumbein and Monk (1943)	$k = 0.76{d_g}^2 e^{-1.31\sigma}$
	d, n and p	Berg (1970)	$k = 80.8d^2\phi^{5.1}e^{-1.385p}$
	d, n and C	Van Baaren (1979)	$k = 10d^2\phi^{3.64+m}C^{-3.64}$
Surface-area models	S_{wi} and n	Timur (1968)	$k = 8{,}581{S_{wi}}^{-2}\phi^{4.4}$
Pore-size models	r_h, m and n	Carman (1956)	$k = 400{r_h}^2\phi^m$

Table 49 Equations relating permeability to porosity, grain sizes, sorting and pore throat radii

Studies have shown significant differences between measured and calculated hydraulic conductivities using these equations, so their use should be treated with caution (e.g. Baird et al., 1998). Moreover, these empirical formulae are best applicable to fine (sand-sized) sediments, where the intergranular flow is laminar and is governed by Darcy's Law:

$$V_B = KI \quad (141)$$

where V_B is the bulk velocity or discharge of water per unit area of bed normal to the flow direction, and I is the hydraulic gradient. For coarser sediments with grains larger than 1 mm, the intergranular flow may become turbulent and the force exerted on the grains becomes a combination of laminar and turbulent forces. For these cases, the flow is best described using Forchheimer's equation:

$$I = aV_B + b{V_B}^2 \quad (142)$$

where $a = 1/K$. The dimensional coefficients a and b are often referred as the laminar and turbulent resistance coefficients respectively. These coefficients are functions of porosity, grain size, grain shape, packing, orientation and grading. Several expressions have been

proposed to express them in terms of porosity and grain diameter. These are reviewed in Van Gent (1993) and Soulsby (1997). As discussed in Chapter 5, the most widely used expressions for *a* and *b* are those proposed by Eugelund (1953) given by:

$$a = \alpha \frac{\nu}{gd^2} \frac{(1-n)^3}{n^2} \tag{143}$$

$$b = \beta \frac{1}{gd} \frac{(1-n)}{n^3} \tag{144}$$

where for uniform rounded sand grains α = 1000 and β = 2.8. However, these values were derived for materials with nominal grain diameters less than 10mm. For coarser materials, Shih (1991) modified Eugelund's expressions and proposed empirical formulae to estimate these parameters for single size and wide graded materials. For wide graded materials, these parameters are given by:

$$a = \left(\alpha_{1+}\alpha_2 \left(\frac{g}{\nu^2}\right)^{2/3} {d_*}^2\right) \frac{(1-n)^3}{n^2} \frac{\nu}{g{d_*}^2} \tag{145}$$

$$b = \left(\beta_{1+}\beta_2 e^{\left(\beta_3 \left(\frac{g}{\nu^2}\right)^{1/3} d_*\right)}\right) \frac{(1-n)}{n^3} \frac{1}{gd_*} \tag{146}$$

where α_1= 1683.71, α_2= 3.12 x 10^{-3}, β_1= 1.72, β_2= 1.57 and β_3= -5.1 x 10^{-3} and $d_*$is a characteristic grain size to account for the wide grading and is given by:

$$d_* = d_{15} \left(\frac{d_{15}}{d_{50}}\right)^{-1.11} \left(\frac{d_{50}}{d_{85}}\right)^{0.52} \tag{147}$$

7.5 Applicability of Present Formulae and Influence Factors

To validate the applicability of the present formulae to predict run-up from breaking and non-breaking waves on permeable and impermeable slopes, predictions were compared to run-up data from previous laboratory experiments. Table 50 summarises the studies from where the data was obtained, a description of the structures used in each of these studies, and the formulae used to predict the data from each experiment. All of these experiments were performed with regular waves.

Data	Description	Formulae
Grantham (1953) Saville (1955) Hsu et al. (2012)	Breaking waves on smooth-impermeable slopes	$\frac{R}{H} = 3.74 \tanh(0.38\xi)$
Grantham (1953)	Non-breaking waves on smooth-impermeable slopes	$\frac{R}{H} = 1.25\Phi^{-0.32}$ $\frac{R}{H} = a\xi^{-b}$ $\frac{R}{h} = 1.46 * e^{0.1\,cot\propto}\left(\frac{M_F}{\rho g h^2}\right)^{3/4}$
Oumeraci et al. (2010)	Non-breaking waves on rough-impermeable slopes	$\frac{R}{H} = 1.25\Phi^{-0.32}$ $\frac{R}{H} = a\xi^{-b}$ $\frac{R}{h} = 1.46 * e^{0.1\,cot\propto}\left(\frac{M_F}{\rho g h^2}\right)^{3/4}$
Van Broekhoven (2011)	Breaking waves on rough-permeable slopes	$\frac{R}{H} = 3.74 \tanh(0.38\xi)\,\gamma_f\gamma_K$
Van Broekhoven (2011)	Non-breaking waves on rough-permeable slopes	$\frac{R}{H} = 1.25(\Phi)^{-0.32}\gamma_{f+K}$ $\frac{R}{H} = a\xi^{-b}\gamma_{f+K}$ $\frac{R}{h} = 1.46 * e^{0.1\,cot\propto}\left(\frac{M_F}{\rho g h^2}\right)^{3/4}\gamma_{f+K}$

Table 50 Run-up data sets used to validate the present formulae

7.5.1 Breaking Waves on Smooth-impermeable Slopes

Granthem (1953), Saville (1955) and Hsu et al. (2012) published run-up data for breaking waves on smooth slopes. Their measurements are shown in Figure 151, where the *R/H* data are plotted against the Iribarren number. This graph also shows the predictions of the formula (88) developed in Section 6.2.2 to predict breaking waves on smooth slopes:

$$\frac{R}{H} = 3.74 \tanh(0.38\xi) \qquad (148)$$

It can be seen that the data from the three studies follow a similar trend to the predictions of (148), although with slightly smaller run-up values than predicted. As discussed at the beginning of this chapter, this might be attributed to the measuring technique used. Although the differences between measurements obtained using video cameras and run-up gauges were not investigated in this project, several previous studies have shown that run-up measurements obtained from video cameras are generally slightly larger than those obtained using run-up gauges (e.g. Schimmels et al, 2012; Van Broekhoven, 2011). Granthem (1953), Saville (1955) and Hsu's et al. (2012) all used run-up gauges, while (148) was derived from measurements taken with video cameras.

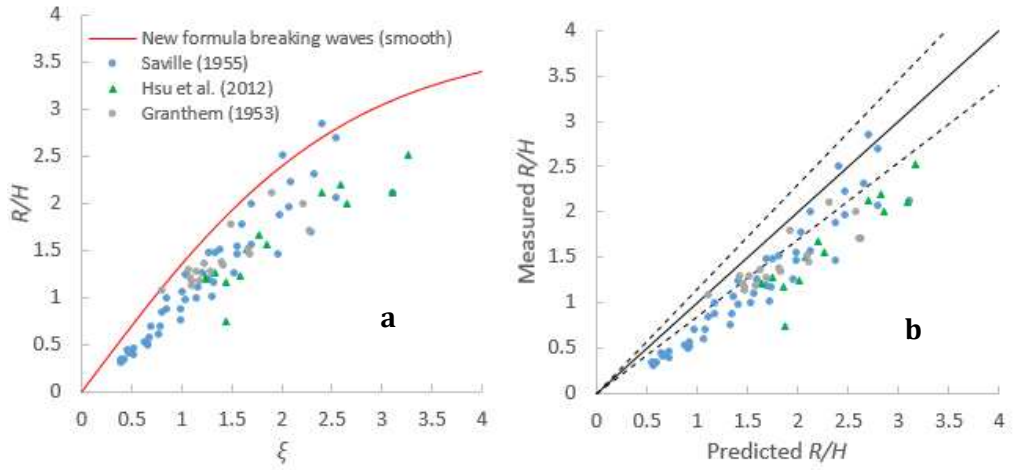

Figure 151 Run-up data from breaking waves from previous studies compared the predictions of (148). Solid line: perfect agreement; dash line: ±15% error bands.

7.5.2 Non-breaking Waves on Smooth-impermeable Slopes

Granthem (1953) also published run-up data from non-breaking waves on steep smooth slopes. These data were compared against the predictions of the three formulae derived for surging waves shown in Section 6.2.3. Figure 152a plots Granthem's data against the Iribarren number, also showing the predictions of Hunt's Formula. It is evident that Hunt's formula R/H = 3 proposed for non-breaking waves overestimates Granthem's data. Moreover, significant scatter can be seen when plotting the data against the Iribarren number. In Figure 152b, these same data are plotted against Φ also showing the formula $R/H = 1.25\Phi^{-0.32}$. It can be seen that the data are slightly less scattered and (137) shows very good predictions to most of the data. Five data points were under-predicted by (137). These values correspond to waves with large wave steepness: H/L_o > 0.05, which might be better predicted using formulae for breaking waves.

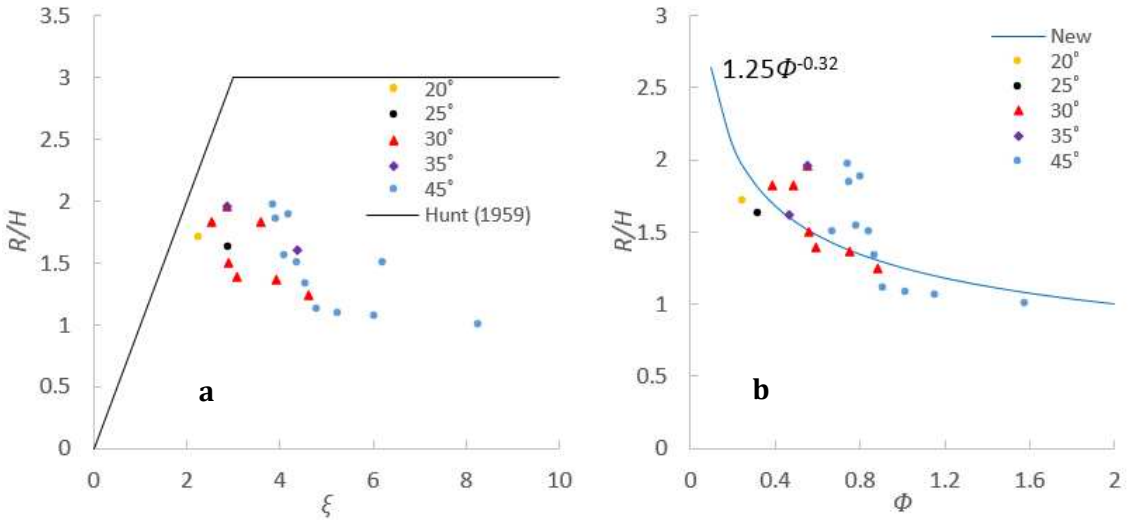

Figure 152 Run-up data for non-breaking waves from Granthem (1953) plotted against: a) ξ and b) Φ

The predictions of (138) and (139) based on the wave momentum flux parameter and on the relative water depth, respectively, were also compared with Granthem's data in Figure 153. Again, both formulae give good agreement with most run-up data, except for those waves with H/L_o > 0.05, where their run-up is underestimated.

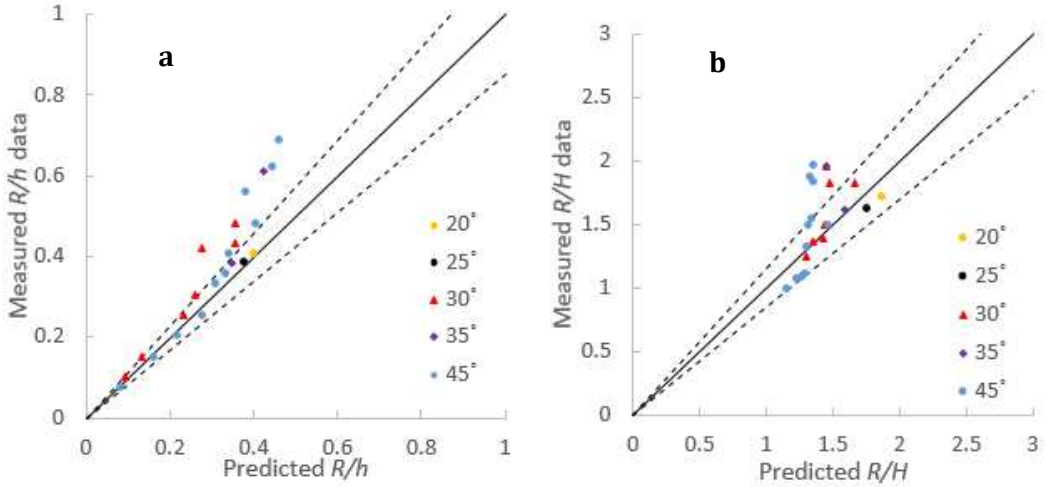

Figure 153 Granthem (1953) measured data from non-breaking waves versus the predictions of (138) and (139). Solid line: perfect agreement; dash line: ±15% error bands.

7.5.3 Non-breaking Waves on Rough-impermeable Slopes

Oumeraci (2010) performed large-scale laboratory experiments, where run-up was measured on three different revetments with impermeable cores and slopes of 1:3 (18.43˚). Each revetment contained three layers: an armour layer, a filter layer and a sand core. The top layer consisted of a 15cm bonded permeable armour placed over an unbonded filter layer, itself laid over a compacted sand core (d_{50} = 0.34mm). The difference between the three revetments was the thickness of the unbonded filter layer. The fine sand core used was practically impermeable. Previous studies have shown that surface roughness has almost no influence on run-up from surging waves on armoured structures with impermeable cores (e.g. van Broekhoven, 2011; and EurOtop, 2007). This is because all the water from the uprush and backwash motions of the surging waves stays in the armour layer, which creates a "smooth layer" on top of the armour layer. When this happens, the surging waves do not feel the roughness of the structure and the run-up acts as a wave on a smooth slope (EurOtop, 2007). This suggests that the formulae developed for non-breaking waves on smooth slopes could give a good approximation in predicting Oumeraci 's run-up measurements from surging waves.

Figure 154 plots Oumeraci's data from non-breaking waves on the three different structures against the Iribarren number. For comparison, the Hunt formula for smooth slopes is also shown. Again, it is evident that the Iribarren number is not the ideal

parameter to characterise run-up from non-breaking waves and the Hunt formula over-predicts the data.

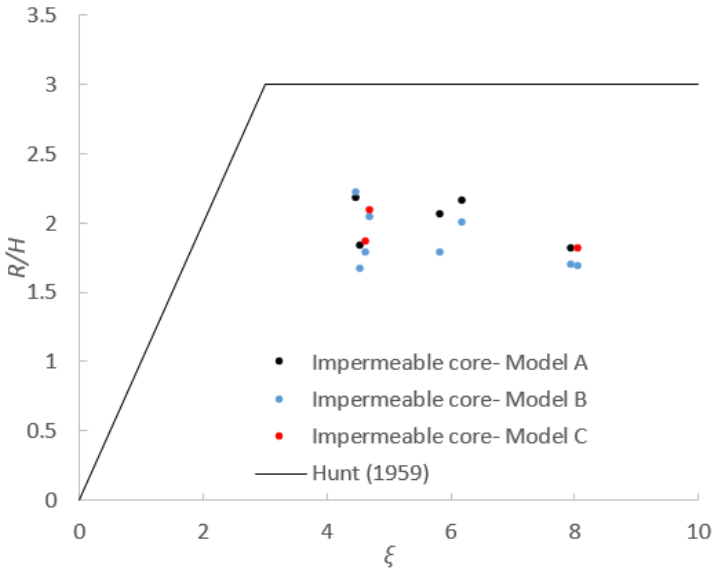

Figure 154 Oumeraci (2010) run-up data from non-breaking waves plotted against ξ

The same data is shown in Figure 155, this time with R/H plotted against the parameter Φ. This figure also shows the predictions of the formula (98): $R/H = 1.25\Phi^{-0.32}$ for smooth impermeable slopes. As we can see, the data is still slightly scattered. Nevertheless, these data seem to follow the same curve described by the negative power function and are ins. The negligible influence of roughness on run-up from surging waves can be seen in this graph, as no clear difference can be distinguished between the data from the three different rough revetments and the data have good agreement with the formulae developed in this study for smooth impermeable slopes.

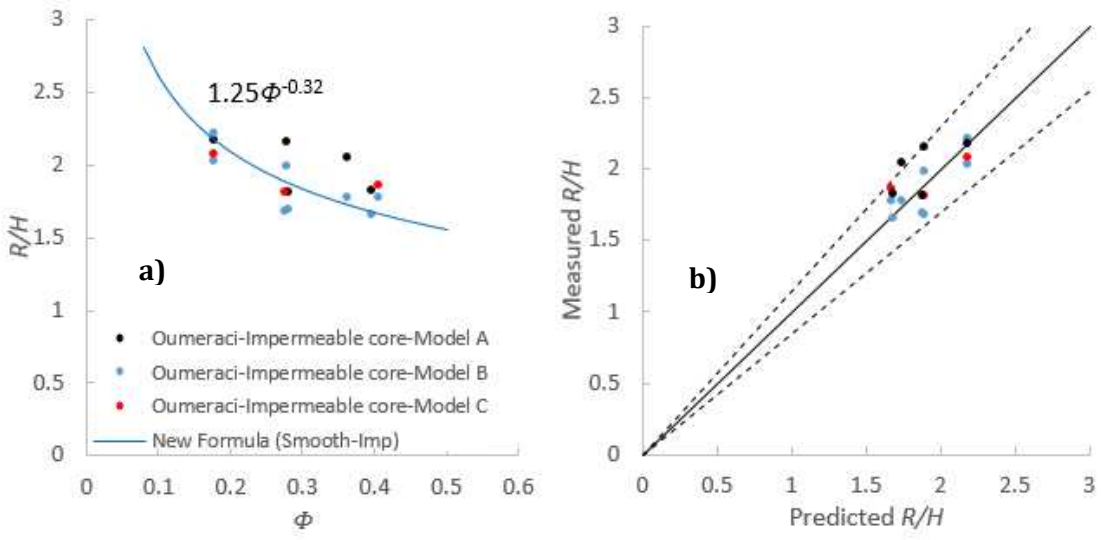

Figure 155 Oumeraci (2010) run-up data for non-breaking waves plotted against Φ and beside the predictions of (137). Solid line: perfect agreement; dash line: ±15% error bands.

Equations (138) and (139) for smooth slopes also showed good agreement with Oumeraci's data (Figure 156).

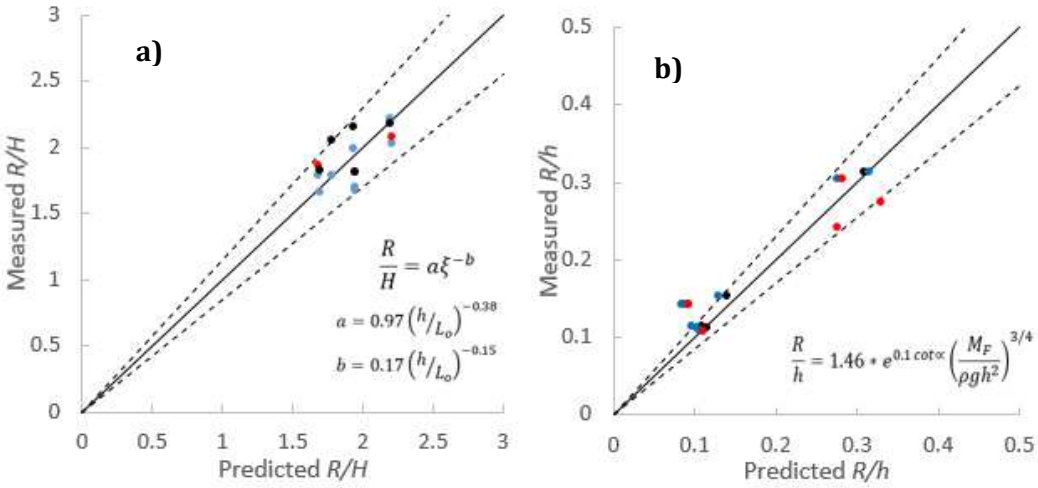

Figure 156 Oumeraci (2010) run-up data from non-breaking compared to the predictions of (138) and (139). Solid line: perfect agreement; dash line: ±15% error bands.

7.5.4 Breaking Waves on Rough-permeable Slopes

Van Broekhoven (2011) performed laboratory experiments on a 1:2 slope (26.56°) with an armour layer on a permeable core (d_{50} = 33mm). His measurements were used to show the applicability of the roughness and hydraulic conductivity factors (γ_f and γ_K) on breaking waves and the influence factor γ_{f+K} for non-breaking waves.

Figure 157 plots Van Broekhoven's *R/H* data plotted against the Iribarren number. The blue dots represent the non-breaking waves and the red dots the breaking waves. Significant scatter can be seen, especially for data from non-breaking waves.

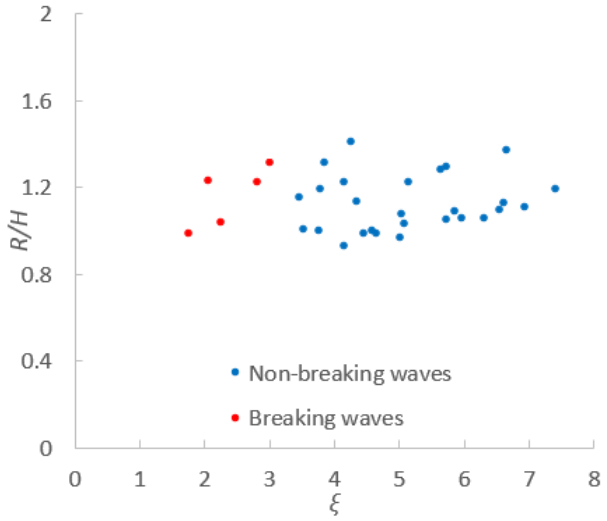

Figure 157 Van Broekhoven (2011) run-up data on permeable slopes plotted against ξ

Van Broekhoven (2011) did not report measurements of the hydraulic conductivity of the material used to construct the permeable core. Nevertheless, he showed measurements of

its porosity and grain size distribution, so these parameters were used to estimate K of the material. The permeable coarse core material used in van Broekhoven's tests had a porosity of ϕ = 0.40 with the following grain sizes and gradings:

d_{15}	d_{50}	d_{85}	d_{50}/d_{15}	d_{85}/d_{50}	d_{85}/d_{15}	d_*
0.02	0.04	0.08	2	2	4	0.03

Table 51 Grain sizes (m) and gradings used in van Broekhoven's tests

According to Shih (1991), these grading values fall into the category of wide graded materials. Therefore, (145) and (147) were used to estimate the hydraulic conductivity of the permeable core. Substituting the values shown in Table 51 in (145) and (147) resulted in: d_*= 0.03m and a = 1.96. As a = 1/K, the hydraulic conductivity of the permeable core results in K = 0.509 m/s. Table 52 shows the non-dimensional hydraulic conductivity Ψ and influence factors obtained for breaking and non-breaking waves using the hydraulic conductivity calculated using Shih's equations.

K (m/s)	$\Psi=K^3/\nu g$	Breaking Waves $\gamma_K = 0.94\Psi^{-0.04}\xi^{-0.026\Psi^{0.17}}$	Non-breaking Waves $\gamma_{f+K} = 0.92\Psi^{-0.05}$
0.509	13,407	$0.64\xi^{-0.13}$	0.57

Table 52 Influence factors for the permeable core's hydraulic conductivity from Van Broekhoven's (2011) tests

The run-up data from breaking waves were compared against the predictions of the hyperbolic formula (125) proposed for breaking with the influence factors for roughness and hydraulic conductivity:

$$\frac{R}{H} = 3.74 \tanh(0.38\xi)\,\gamma_f \gamma_K \tag{149}$$

where:

$$\gamma_f = 0.8\xi^{-0.1} \tag{150}$$

$$\gamma_K = 0.64\xi^{-0.13} \tag{151}$$

As Van Broekhoven did not report information to account for the influence of surface roughness of the armour layer, the reduction function for roughness $\gamma_f = 0.8\xi^{-0.1}$ derived in Section 7.2.1 was also used here. These predictions and the measured data are shown in Figure 158, where for comparison the predictions for a smooth slope are also shown.

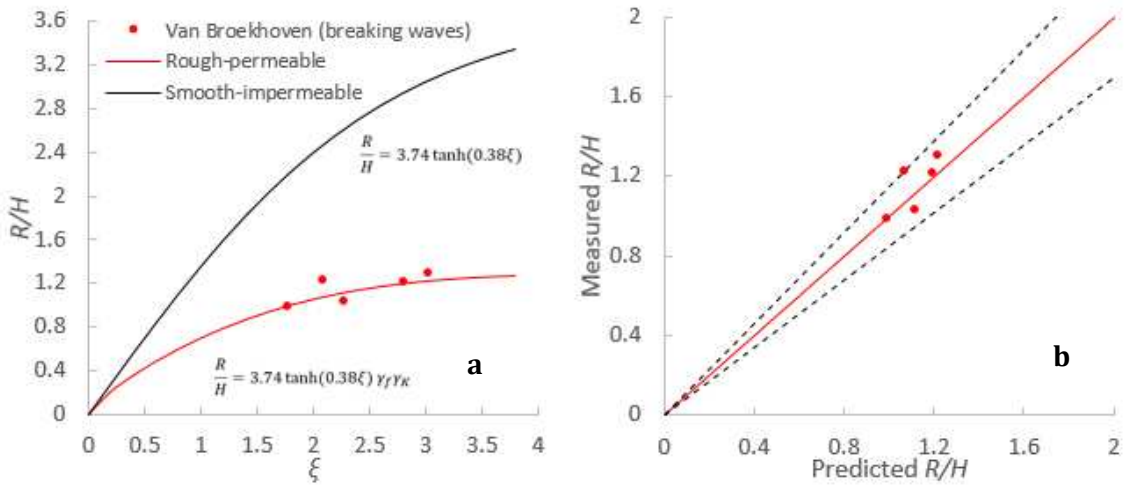

Figure 158 Van Broekhoven (2011) run-up data from breaking waves compared to the predictions of (149). Solid line: perfect agreement; dash line: ±15% error bands.

As can be seen, the new formula with the influence factors shows good agreement with the measured data from breaking waves. These encouraging results were also shown for non-breaking waves.

7.5.5 Non-breaking Waves on Rough-permeable Slopes

If we compare Oumeraci's data from non-breaking waves on a rough-impermeable slope shown in Figure 154 to Van Broekhoven's data from non-breaking waves on rough-permeable slope (Figure 157), it is evident that a permeable core considerably reduced run-up heights. Both sets of data have similar ξ values. With an impermeable core most of the data ranged between $1.5 < R/H < 2.5$, while with a permeable core the data ranges between $0.8 < R/H < 1.6$. Therefore, it is necessary to include the reduction caused by the hydraulic conductivity of the structure.

When Van Broekhoven's data from non-breaking waves were plotted against Φ, a well-defined curve was observed. This trend is similar to those observed for the data from non-breaking waves presented in this study. This suggests that the negative power function $R/H = 1.25\Phi^{-0.32}$ proposed for non-breaking waves could give good predictions to Van Broekhoven's data. The influence factor $\gamma_{f+K} = 0.57$ estimated to account for the effects of the permeable core was included to (137) and its predictions are compared to Van Broekhoven's data in Figure 159. For comparison, the predictions for a smooth slope are also shown in this figure.

$$\frac{R}{H} = 1.25(\Phi)^{-0.32} * (0.57) \qquad (152)$$

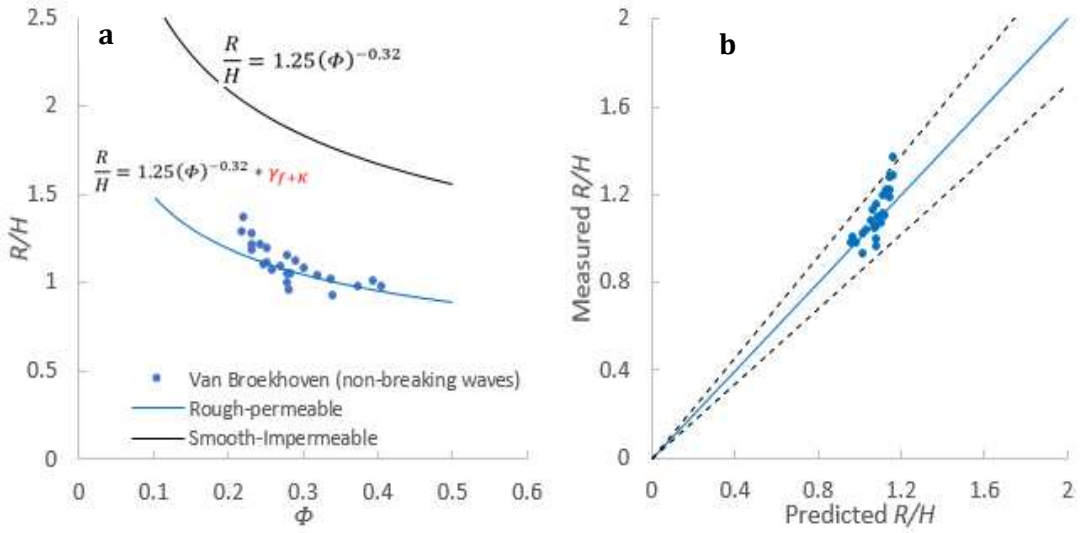

Figure 159 Van Broekhoven (2011) run-up data from non-breaking waves plotted against Φ and compared to the predictions of (152). Solid line: perfect agreement; dash line: ±15% error bands.

As can be seen, the trend is well predicted by (152), while its height reduction is well predicted by the influence factor $\gamma_{f+K} = 0.57$. Van Broekhoven's data was also compared to (138) and (139) (Figure 160). Again, a very good agreement was shown, in particular with the formula based on the wave momentum flux parameter, where most of the data followed the same trend as the predicted values.

$$\frac{R}{h} = 1.46 * e^{0.1\,cot\propto}\left(\frac{M_F}{\rho g h^2}\right)^{\frac{3}{4}} * (0.57) \tag{153}$$

$$\frac{R}{H} = a\xi^{-b} * (0.57), \quad \text{where:} \quad a = 0.97\left({}^{h}/_{L_o}\right)^{-0.38} \quad \text{and } b = 0.17\left({}^{h}/_{L_o}\right)^{-0.15} \tag{154}$$

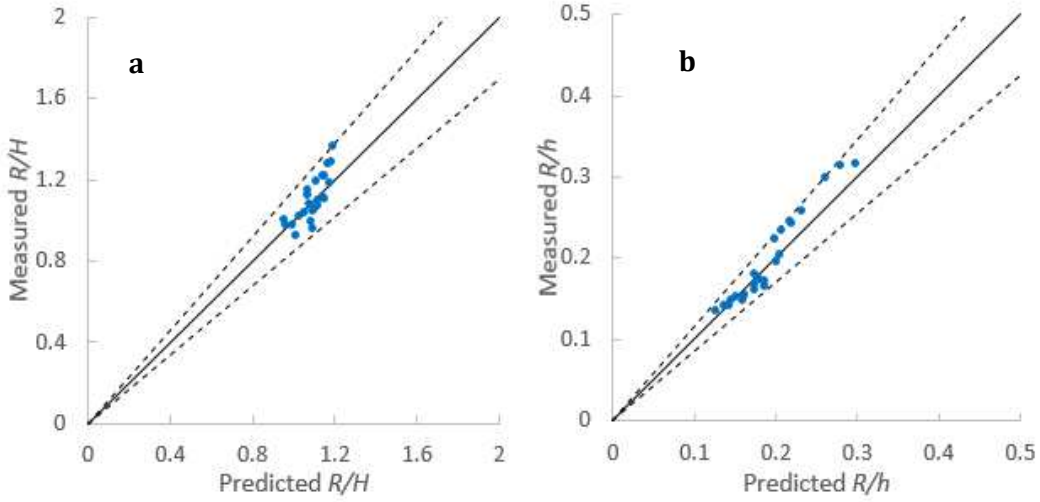

Figure 160 Van Broekhoven (2011) run-up data from non-breaking waves compared to the predictions of (153) and (154). Solid line: perfect agreement; dash line: ±15% error bands.

7.5.6 Summary

As can be seen, there is an encouraging agreement between the measured data from previous studies and the predictions from the formulae and influence factors proposed in this study. Several remarks can be made from these comparisons:

- The limited scatter and well-defined trends demonstrate that the new parameter Φ and the wave momentum flux parameter can correctly describe run-up from non-breaking waves

- The proposed empirical functions based on these parameters were shown to accurately predict the trends followed by the data from previous works

- The empirical hydraulic conductivity factors: $\gamma_K = 0.94\Psi^{-0.04}\xi^{-0.026\Psi^{0.17}}$ and $\gamma_{f+K} = 0.92\Psi^{-0.05}$ for breaking and non-breaking waves respectively were shown to correctly account for the reduction caused by the hydraulic conductivity of the slopes

- The good agreement between the measured and predicted data shows that even when measurements of hydraulic conductivity are not available, empirical equations can be used to estimate a reliable *K* value.

7.6 Wave-induced Maximum Water Table Over-height

As mentioned in the Literature Review, the current formula to estimate the wave induced maximum water table over-height, η_w^+, from regular waves was proposed by Kang (1995) and is given by:

$$\eta_w^+ = 0.62\xi \qquad (155)$$

It should be noted that this formula takes no account of grain size or hydraulic conductivity dependence in (155). This formula was derived from a series of laboratory experiments on two sand beaches. In these experiments, Kang noticed that η_w^+ was a function of wave run-up as the ratio between them remained constant ($\eta_w^+/R \approx 0.62$) regardless of the sediment size and hence of the hydraulic conductivity. Equation (155) is based on Hunt's formula to estimate run-up. However, as discussed earlier in this chapter, Hunt's formula only shows good results for breaking waves on smooth-impermeable slopes (in fact it slightly underestimates the run-up of these waves). More recent studies (e.g. Turner and Masselink, 2012; and Turner et al., 2013), where η_w^+ was measured inside gravel and sand coastal barriers, showed that hydraulic conductivity does influence the magnitude of η_w^+ and cannot be ignored when attempting to predict it.

This section investigates the influence of hydraulic conductivity on η_w^+ and analyses the relationship between η_w^+ and *R*. This analysis enabled the derivation of new formulae to

predict η_w^+ on permeable beaches or coastal barriers. These were derived from the present laboratory experiments where η_w^+ and R were measured in four permeable foams.

7.6.1 Influence of Hydraulic Conductivity on η_w^+

Figure 161 shows the measurements of η_w^+ normalised by the wave height for the four permeable foams. As mentioned before, tests in each permeable foam were carried out for three different slope angles: 10˚, 20˚ and 30˚. Figure 161a plots the measurements from breaking waves plotted against ξ, while Figure 161b shows the measurements from non-breaking waves plotted against Φ. In a similar way as for the run-up, the two parameters give a good description of η_w^+ for breaking and non-breaking waves respectively. The separation between these groups of data was based on the breaking criterion $\tan\alpha/(H/h) = 1.4$.

From Figure 161 it is evident that, as the hydraulic conductivity of the beach increases, the magnitude of η_w^+ decreases. Therefore, this parameter needs to be considered when predicting η_w^+.

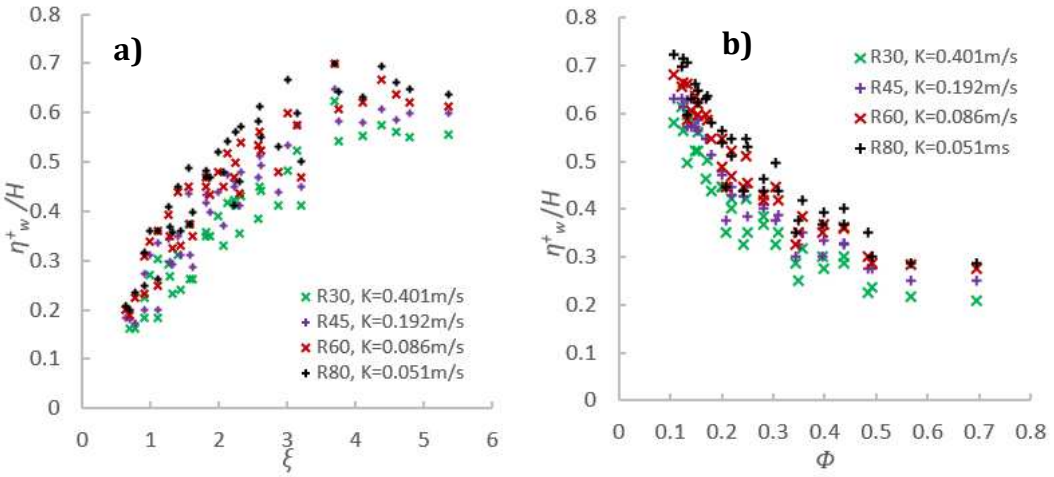

Figure 161 Measurements of the maximum wave-induced water table over-height, η_w^+

7.6.2 Influence of Run-up on η_w^+

Figure 162 shows η_w^+ measurements plotted against their corresponding wave run-up heights, R. As can be seen, there is a very good linear relationship between the parameters and their factors remain fairly constant for all permeable foams. Therefore, Kang's (1995) observations on η_w^+ having a linear relationship with run-up are validated here. Although the factors slightly increased as the hydraulic conductivity increased, this increase is so small it can be neglected. Therefore, the following relationship is proposed for permeable slopes within the range of hydraulic conductivities tested ($0.051 < K < 0.401$m/s):

$$\eta_w^+/R = 0.34 \qquad (156)$$

From these observations, it can be deduced that an accurate prediction of run-up will lead to a better prediction of η_w^+. However, Kang's formula to predict run-up and, thus η_w^+, is designed for breaking waves on relatively impermeable slopes. To have a more accurate prediction, the formulae derived for breaking and non-breaking waves on permeable slopes are also proposed to predict η_w^+. In this case, (125) and (137) will be used to predict this parameter. This results in:

For breaking waves:

$$\frac{R}{H} = (0.34) * 3.74 \tanh(0.38\xi)\, \gamma_f \gamma_K \tag{157}$$

For non-breaking waves:

$$\frac{R}{H} = (0.34) * 1.25(\Phi)^{-0.32} \gamma_f \gamma_K \tag{158}$$

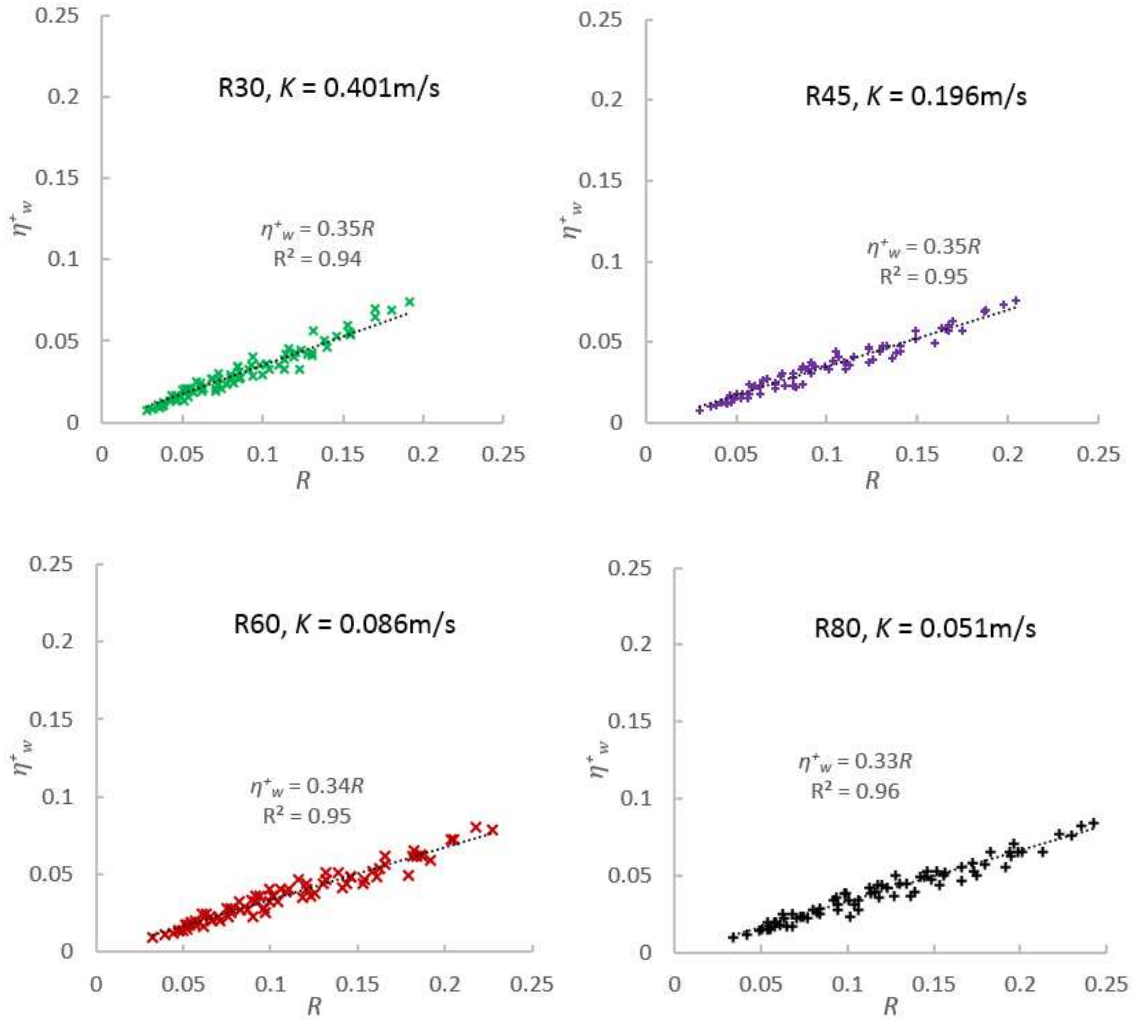

Figure 162 Maximum water table over-height plotted against run-up

Predictions using (157) and (158) are compared against the measurements in Figure 163, while Table 53 shows the absolute average percentage errors between the predicted and measured values for each permeable slope. Although some scatter can be seen in Figure

163, most data from all 4 permeable slopes lie inside the ±15% error bands. Therefore, it can be said that a good estimate of η_w^+ can be obtained using run-up formulae as suggested by Kang (1995). However, these formulae need to consider the influence of hydraulic conductivity.

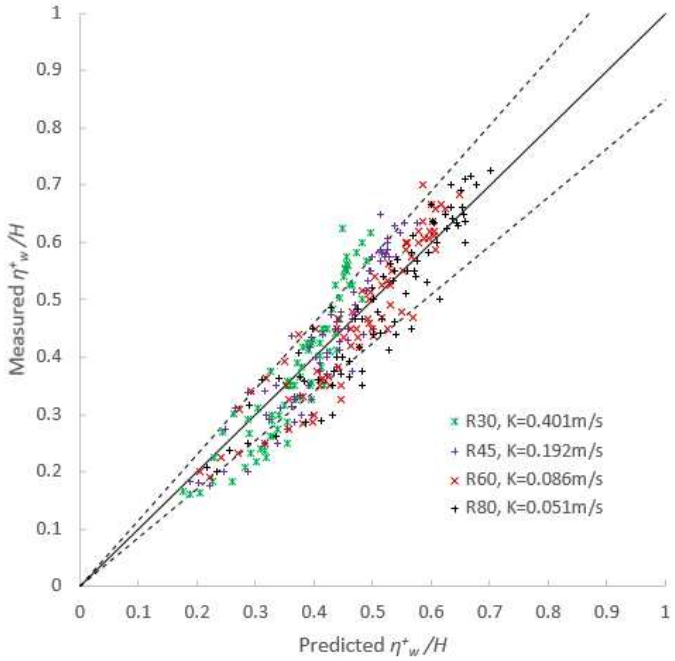

Figure 163 Predicted versus measured water table over-heights. Solid line: perfect agreement; dash line: ±15% error bands.

Type	*K* (m/s)	*% error*
R30	0.401	13.5
R40	0.192	11.43
R60	0.086	9.5
R80	0.051	9.33

Table 53 Absolute average percentage errors between simulated and measured data for each permeable slope

7.6.3 Summary

- The measurements presented in this study showed that hydraulic conductivity significantly influences the magnitude of η_w^+
- η_w^+ was seen to be a function of wave run-up
- A reduction factor was included to the formulae previously proposed to predict run-up from breaking and non-breaking waves over permeable slopes to predict η_w^+

7.7 Influence of Infiltration on the Swash Flows and Boundary Layer Dynamics

Accretion and erosion in the swash zone are known to be influenced by infiltration into the beach and exfiltration from the water table (Figure 164). However, the way infiltration/exfiltration influence the sediment transport is still not fully understood as these processes can influence sediment mobility through different mechanisms with opposing effects. Improving our understanding of how infiltration/exfiltration affect these mechanisms will lead to better modelling of the swash zone hydrodynamics and prediction of sediment transport.

It is well known that infiltration influences sediment transport in the swash zone by increasing the flow asymmetry. This increase in swash asymmetry is expected to promote accretion because the energy available to carry sediment onto the beach by the uprush flow will be larger than the energy available to carry sediment away from the beach by the backwash flow. Therefore, an increase in the swash infiltration rates will tend to decrease the offshore sediment transport.

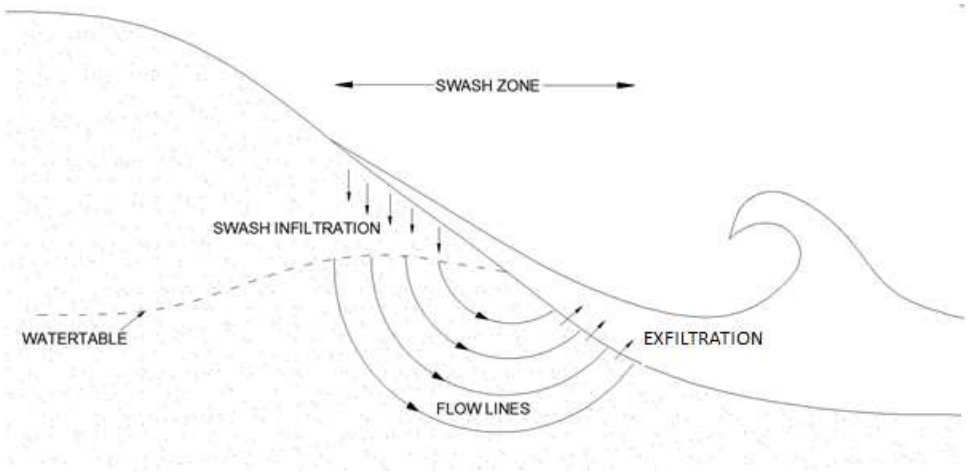

Figure 164 Infiltration and exfiltration in the swash zone and beach groundwater system (Masselink and Turner, 2012)

There are two main ways for increasing the infiltration rates into a beach: by increasing its hydraulic conductivity or by increasing its unsaturated area. This second option has become a common soft engineering practice (beach dewatering) which aims to reduce erosion by lowering the water table elevation in a beach. Beach dewatering schemes usually consist of a system of buried drains and pumps, although other methods for lowering the water table have also been proposed (some of these techniques are summarised in Table 9, presented in Section 3.3.5). However, beach dewatering schemes have led to mixed results in mitigating local erosion problems as their efficiency can depend on numerous factors whose effects are still not clearly understood. Some of these

factors include the location of the drains, wave climate, tidal range, sediment size and sorting, beach slope and frequency of storm events. Until the effects of these factors are understood and quantified, it will not be possible to predict the performance or success of a beach dewatering scheme (Horn, 2002). In addition, previous studies have reported contradictory results concerning the effects of infiltration/exfiltration on the swash zone sediment transport (e.g. Watters and Rao, 1971; Willets and Drossos, 1975; Conley and Inman, 1992; and Rao et al., 1994). Horn (2002) suggested that these contradictory results might be due to the opposing effects on the potential for sediment mobility of two additional mechanisms caused by infiltration/exfiltration: the alteration of the effective weight of the surface sediment and the modified bed shear stresses exerted on the bed due to an alteration of the boundary layer thickness.

The flow through a permeable boundary exerts a force within the bed called the seepage force, which acts in the direction of the flow. During infiltration, the seepage force will tend to increase the weight of the sediment, stabilizing the bed and reducing the potential for sediment mobility. These forces will also tend to reduce the thickness of the boundary layer (thinning), which will increase the bed shear stresses, and as a consequence the potential for sediment mobility will be increased. The opposite will occur during exfiltration. According to Nielsen et al. (2001), the relative importance of these opposing effects depends on the hydraulic conductivity of the bed and the density of the sediment. However, these two mechanisms do not always have opposing effects on the potential for sediment mobility, because infiltration does more than just increase the bed shear stress by thinning the boundary layer. Infiltration can also indirectly decrease the bed shear stress by reducing the volume of water in the surface flows. Baldock and Nielsen (2009) called this mechanism the '*continuity effect*'. The opposing effects of these mechanisms on the potential for swash zone sediment mobility during infiltration and exfiltration are summarized in Table 54 and are sketched in Figure 165.

Type of flow	Process	Mechanism	Consequence	Potential for sediment transport
Infiltration	seepage force	increase the effective weight of sediment	bed stabilisation	reduced
		boundary layer thinning	increase of bed shear stresses	increased
	flow reduction	continuity effect	decrease of bed shear stresses	reduced
Exfiltration	seepage force	decrease the effective weight of sediment	bed destabilisation	increased
		boundary layer thickening	decrease of bed shear stresses	reduced
	flow increase	continuity effect	increase of bed shear stresses	increased

Table 54 Mechanisms caused by infiltration and exfiltration which can influence the potential for sediment transport in the swash zone

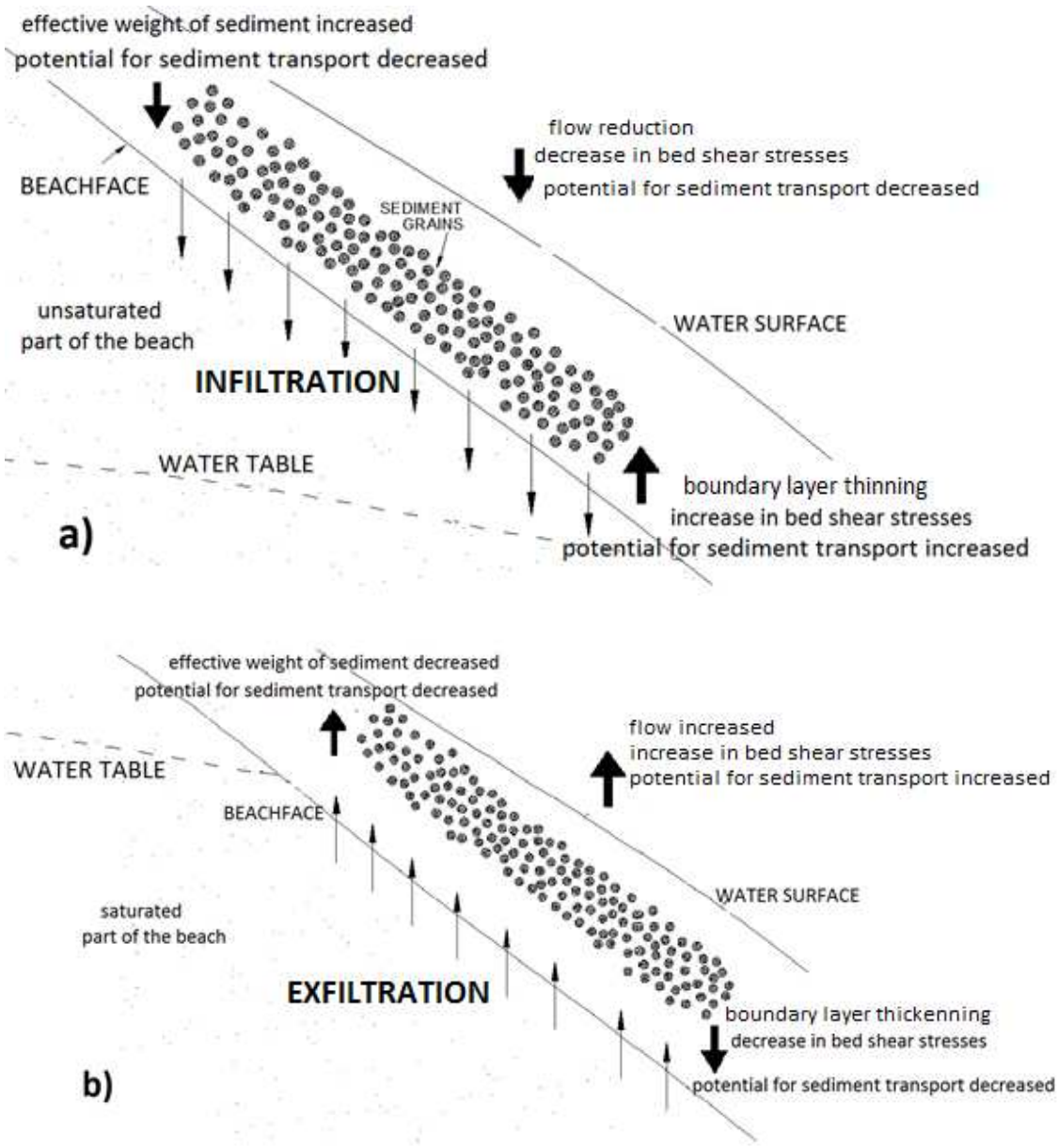

Figure 165 Sketch of the processes and mechanisms influenced by: a) infiltration and b) exfiltration in the swash zone (adopted from Butt et al. 2001; and Horn, 2006)

The relative importance of the two opposing effects of infiltration on the bed shear stresses depends on the particular flow conditions. For steady, uniform flows, infiltration has been shown to increase the bed shear stresses (Chen and Chiew, 2004; Conley and Inman, 1992; Willets and Drossos, 1975). Therefore, in steady flow conditions, the direct effect will be much larger than the continuity effect. However, it is difficult to assess which effects are dominant under the highly unsteady and depth-variant flow conditions in the swash zone, as it is challenging to measure the bottom boundary layer structure under such conditions. Although a considerable number of field studies have investigated swash flows over permeable slopes, field studies cannot offer detailed and consistent measurements inside the swash due to the uncontrolled environment.

To overcome such limitations, recent studies have opted to use numerical models and laboratory experiments under controlled settings using non-deformable slopes to study the boundary layer dynamics in the swash zone. Most of these studies have been performed on fixed, impermeable beds, with only a few carried out on fixed, permeable slopes (e.g. Kikkert et al., 2013; Pintado-Patiño et al., 2015). These latter studies analysed a solitary wave generated by a dam-break flow and showed that the significant reduction in backwash flows due to infiltration decreased the bed shear stresses when compared to their impermeable counterpart. This means that the continuity effect was shown to be larger than the direct effect on the backwash flows and, as a consequence, infiltration decreased the overall bed shear stresses.

Both Kikkert et al. (2013) and Pintado-Patiño et al. (2015) focused their research on a solitary wave generated by a dam-break. However, the influence of infiltration on the mechanisms that influence sediment transport requires further study for periodic waves, where infiltration can also play an important role in the swash-swash interaction. In this study, the numerical model described in Chapter 5 is used to investigate how infiltration affects the swash hydrodynamics for a series of non-breaking regular waves, and, consequently, how it affects the bed shear stresses.

The simulations were restricted to regular non-breaking waves (H = 0.05m and T = 4s) over non-deformable permeable and impermeable 10° slopes, where wash flow velocity and water depth data recorded at three different locations on both slopes (Figure 166). The regular waves were generated using *Cnoidal* wave theory and active wave absorption was used for both the inlet and outlet boundaries. The simulations were run for 200s to derive ensemble-averaged velocities from 50 waves and were completed in approximately 9 hours for the impermeable slope, and approximately 13 hours for the permeable slope (on one processor core).

The permeable slope used for these tests is the same permeable slope used to validate the model in section 5.4.3. It simulates the R30 foam with a hydraulic conductivity of K =0 .401 m/s. The resistance porous media parameters used to simulate the flow through these porous structure are summarised in Table 55.

Foam type	d_{50} (mm)	n	α	β	γ
R30 PPI	11.3	0.4	100	1	0.34

Table 55 Porous media parameters used to simulate flow through the R30 Foam (K=0.401m/s)

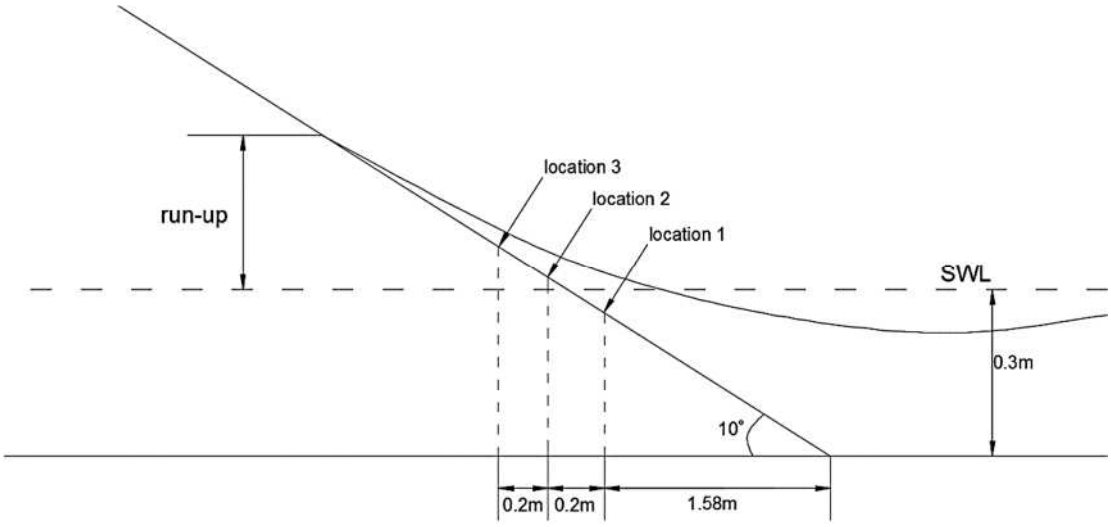

Figure 166 Swash zone locations where the velocity and water depth data were obtained

To enable comparisons between the impermeable and permeable slopes and between locations, normalized time, space and velocity coordinates are introduced in this analysis. The time dimension is normalised as:

$$t' = \frac{t}{t_{swash}} \tag{159}$$

where t_{swash} is the total duration of the swash cycle of each case, hence t' ranges from 0 to 1. The vertical space coordinates are normalised by the maximum water depth, h_{max}, of each case:

$$h' = \frac{h}{h_{max}} \tag{160}$$

Finally, the velocity coordinates are normalised by the maximum uprush depth-averaged ensemble-averaged horizontal velocities, u_u, of each case:

$$u' = \frac{u}{u_u} \tag{161}$$

In all the graphs shown in this analysis, the arrival of the bore is considered to be the initial time, $t = 0$.

7.7.1 Water Depths and Swash Duration

The influence of the location at the slope on water depth, h, and swash duration, t_{swash}, on both the impermeable and permeable slopes is first analysed. The time series of the water depths at locations 1, 2 and 3 are shown in Figure 167. The water depth profiles on the impermeable slope are shown in solid lines (Figure 167a), while the profiles on the permeable slope are displayed with dashed lines (Figure 167b). As expected, we can

clearly notice that on both slopes, the water depth and swash duration decrease with distance up the slope.

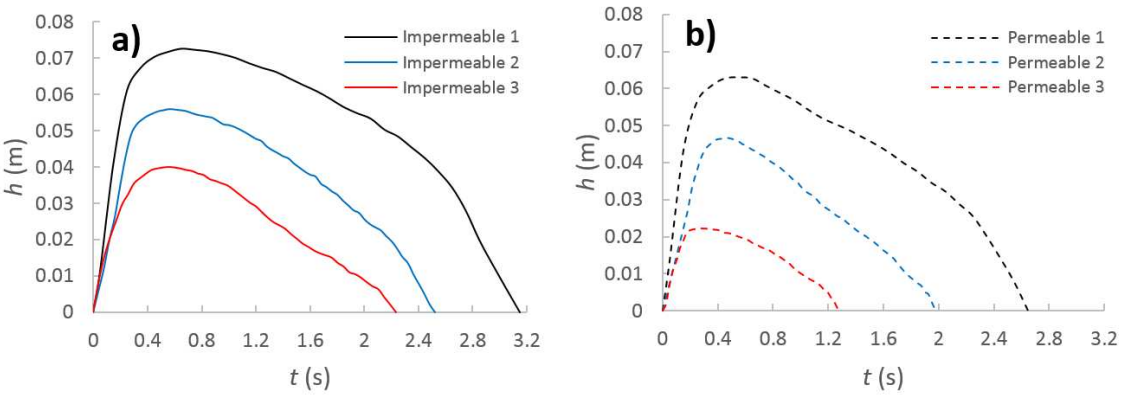

Figure 167 Time series of water depth at different locations in the swash zone for: a) impermeable and b) permeable slopes

It is interesting to notice that the shape of the water depth profiles is not significantly affected by the hydraulic conductivity nor the location at the slope. This can be better visualised when the *X* and *Y* axes are normalised with *t'* and *h'*, respectively (Figure 168). From this figure, we can see that in all profiles the water depths rapidly increasing soon after bore arrival. Then, they gradually decrease until the final stages of the backwash phase ($t' \approx 0.85$), where the water depths start to decrease at a faster rate. The major differences are noticed from around $0.5 < t' < 0.9$, which might be attributed to the different times when flow reversal occurs in each location and slope.

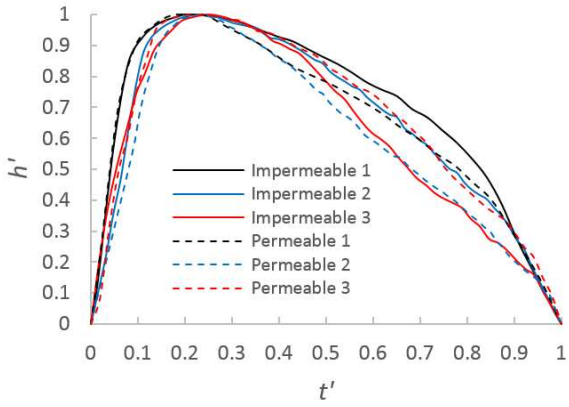

Figure 168 Time series of water depths at locations 1, 2 and 3 on: a) impermeable (solid lines) and b) permeable (dashed lines) slopes; c) and d) show the same water depth profiles against the non-dimensional time t/t_{swash}

To analyse the influence of infiltration on the water depths and swash durations, Figure 169 compares water depth profiles on the impermeable and permeable slopes at locations 1, 2 and 3. To visualise the influence of infiltration on the swash durations, Figure 169 (a, b and c) plot the normalised water depths, *h'*, against time, *t*. Similarly, the influence of infiltration on the water depths is shown in Figure 169 (d, e and f), where the water depths, *h*, are plotted against the normalised time, *t'*. It can be seen that infiltration

reduces both parameters and these reductions are more evident further up the slope. The reductions in swash duration are mainly attributed to the significant decrease of the backwash periods caused by infiltration. The effects of infiltration on water depth are observed just before the bores reach their maximum water depth. These reductions remain fairly constant until the end of the backwash periods

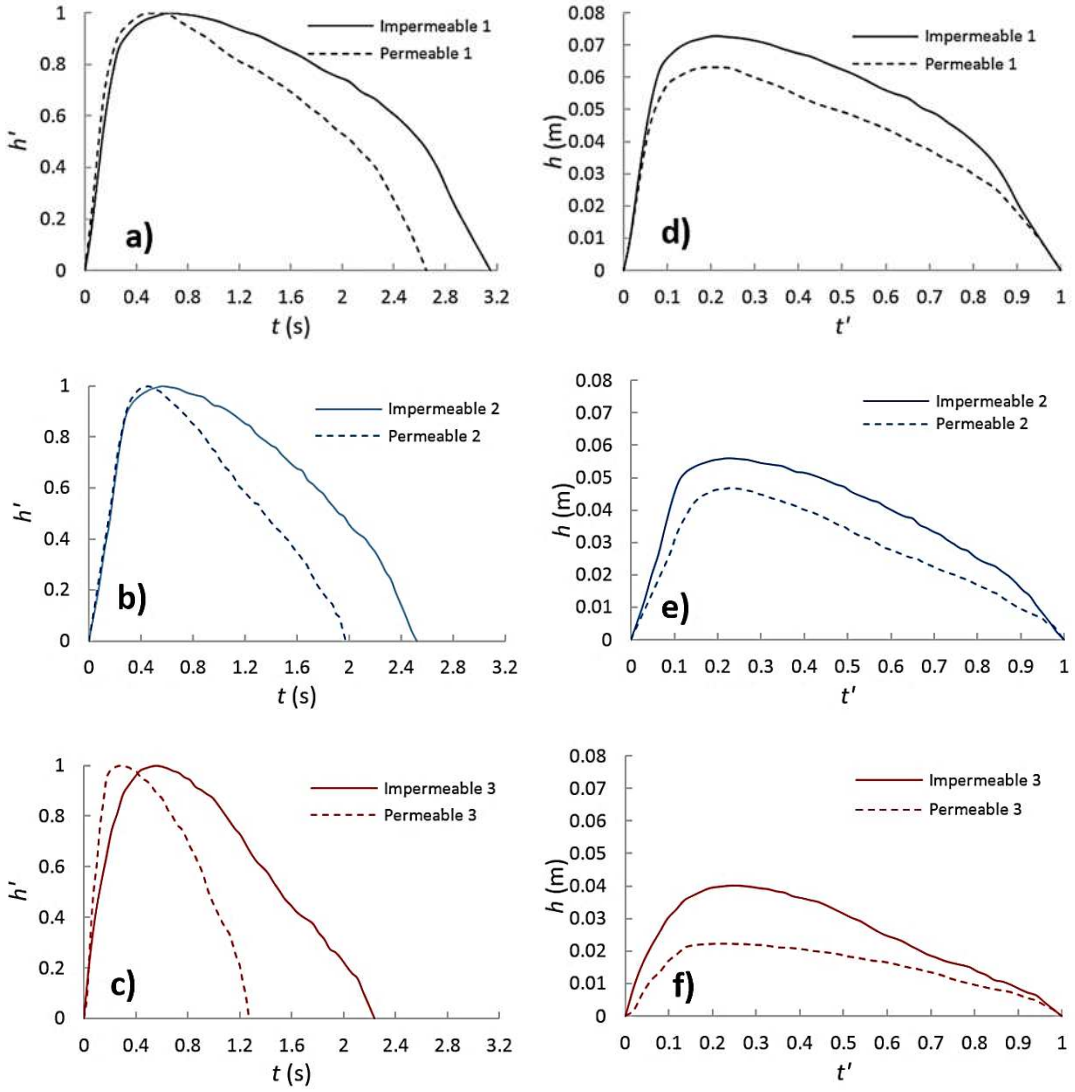

Figure 169 Comparisons of water depth profiles for impermeable (solid lines) and permeable (dashed lines) slopes at locations 1, 2 and 3. Graphs a, b and c show the normalized depth, *h'*, against time, while graphs d, e and f show the depth against the normalized time, *t'*.

7.7.2 Horizontal Velocities

Figure 170 shows time series of depth-averaged ensemble-averaged horizontal velocities, u, on the impermeable (solid lines) and permeable (dashed lines) slopes at locations 1, 2 and 3. Although all the velocity profiles show different gradients, they all decelerate and accelerate at fairly constant rates. Just after bore arrival, the velocities rapidly increase reaching a maximum magnitude, shown on the first time step recorded at t = 0.15s. The velocities then gradually decrease through the entire uprush phase and after flow reversal,

the negative velocities start to accelerate at a similar rate, reaching a maximum magnitude just before the end of the backwash. Towards the end of the backwash, the velocities on the impermeable slope are seen to reach a constant magnitude. As expected, the flow velocities on the permeable slope at the three locations remain smaller than on the impermeable slope.

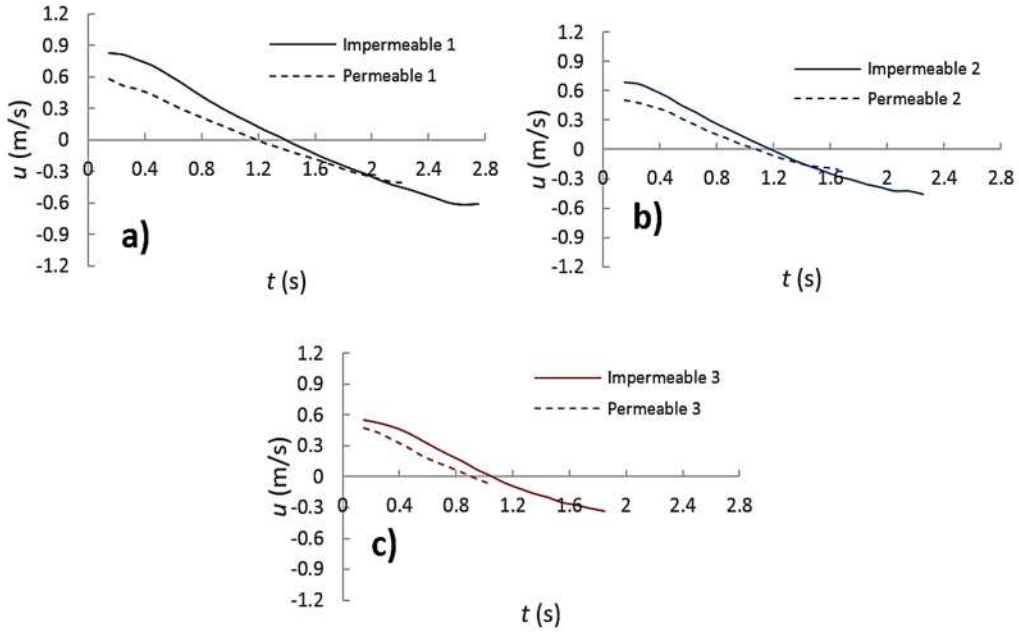

Figure 170 Time series of depth-averaged ensemble-averaged horizontal velocities at locations 1, 2 and 3. Solid lines: impermeable slope; dashed lines: permeable slope

To visualise the influence infiltration on the start of flow reversal at each location, Figure 171 shows the velocities plotted against the normalised time, *t'*, which ranges from 0 to 1. From this figure, it can be seen that the reduction on the backwash time caused by infiltration, is significantly increased on the onshore direction.

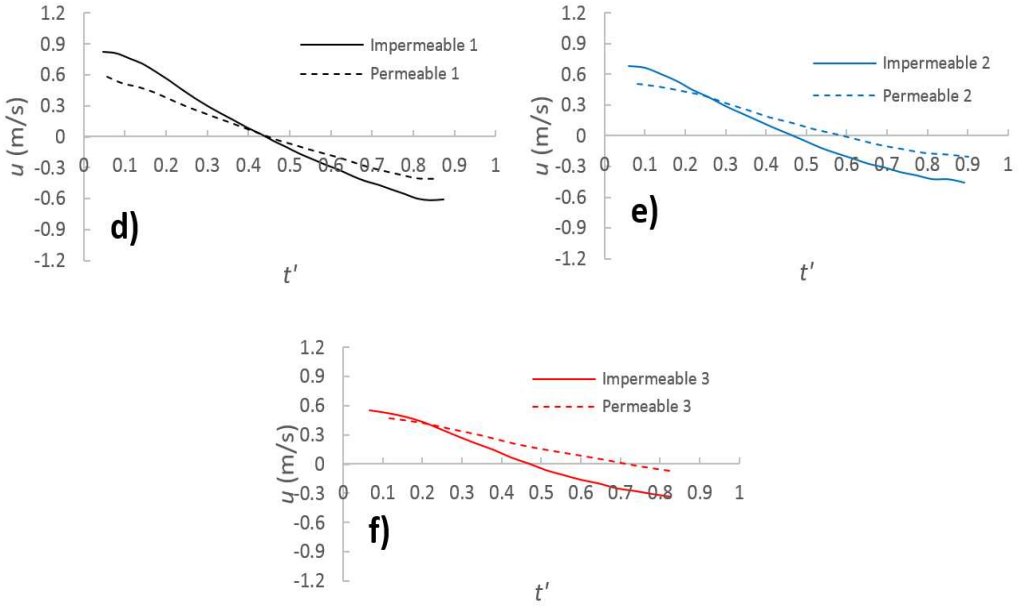

Figure 171 Normalized time series of depth-averaged ensemble-averaged horizontal velocities at locations 1, 2 and 3

Time and Velocity Asymmetries. The influence of slope infiltration on the swash hydrodynamics becomes clearer when the time and velocity asymmetries (T_u/T_b and u_u/u_b, respectively) are analyzed. These flow asymmetries on the permeable (dotted black line) and impermeable (solid black line) slopes are plotted in Figure 172 against the horizontal locations, x. The horizontal locations were previously shown in Figure 166 (x = 1.58m being the toe of the beach). As a reference, the red solid line indicates the value of unity for the asymmetry (where the uprush flow is equal to the backwash flow). These graphs show that infiltration enhances onshore time and velocity asymmetry. This increase in flow asymmetry, mainly attributed to the significant reduction of the backwash period, is expected to promote onshore sediment transport.

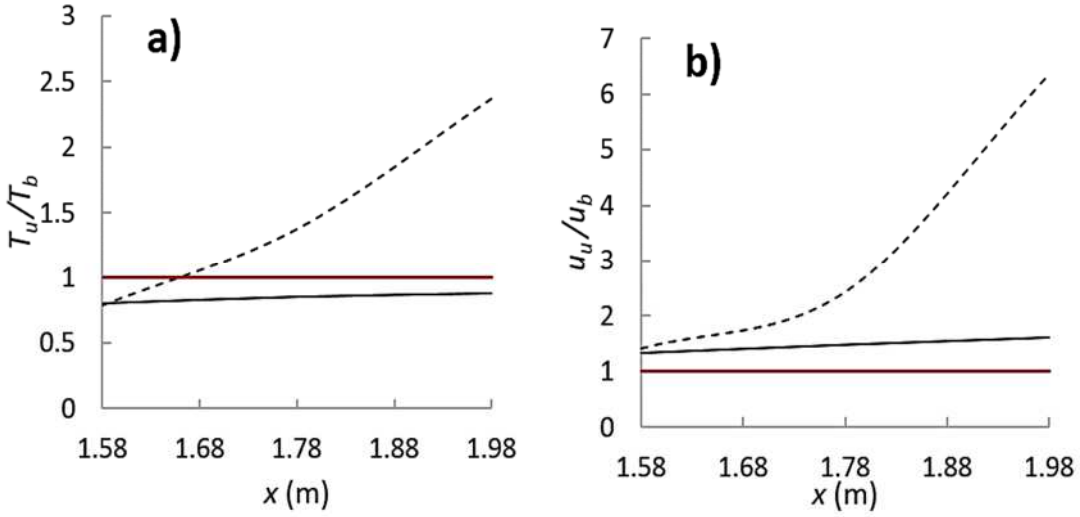

Figure 172 Swash asymmetries on permeable (dotted black lines) and impermeable (solid black line): a) Time asymmetry and b) velocity asymmetry

Table 56 summarises the periods of uprush, T_u, and backwash, T_b, and their corresponding time asymmetry, T_u/T_b, while Table 57 displays the maximum uprush, u_u, and backwash, u_b, depth-averaged ensemble-averaged velocities and their corresponding velocity asymmetry u_u/u_b. These are shown for both slopes at the three different locations. For ease of comparison between locations, Table 56 gives the uprush and backwash periods in terms of the non-dimensional scale t'.

On the impermeable slope, the uprush and backwash periods and maximum velocities have similar magnitudes at the three locations analysed, hence, T_u/T_b and u_u/u_b remain close to 1 (solid black lines in Figure 172). The uprush periods are always slightly shorter than the backwash periods, and therefore, T_u/T_b remains smaller than unity. Nevertheless, T_u/T_b gradually increases with distance up the slope: from 0.79 at location 1, to 0.85 at location 2, and finally to 0.88 at location 3. Similar results were shown by Masselink and Li

(2001), who observed that T_u/T_b increases progressively from 0.5 to 1 in the landward direction. Table 4 shows that the uprush velocities are always slightly larger than the backwash velocities, hence, u_u/u_b remains larger than 1 (Figure 172b), and the velocity asymmetry also slightly increases with distance up the slope.

	Swash duration T_s	**Uprush duration T_u**	**Backwash duration T_b**	**Time asymmetry T_u/T_b**
Location 1				
Impermeable 1	t = 3.15 t' = 1	t = 1.4 t' = 0.44	t = 1.75 t' = 0.56	0.79
Permeable 1	t = 2.65 t' = 1	1.17 t' = 0.44	1.48 t' = 0.56	0.79
Location 2				
Impermeable 2	t = 2.52 t' = 1	t = 1.16 t' = 0.46	t = 1.36 t' = 0.54	0.85
Permeable 2	1.83 t' = 1	1.06 t' = 0.58	0.77 t' = 0.42	1.38
Location 3				
Impermeable 3	t = 2.24 t' = 1	t = 1.04 t' = 0.47	t = 1.18 t' = 0.53	0.88
Permeable 3	1.28 t' = 1	0.9 t' = 0.7	0.38 t' = 0.3	2.33

Table 56 Uprush and backwash durations on impermeable and permeable slopes at locations 1, 2 and 3

	Maximum uprush velocity u^+ (m/s)	**Maximum backwash velocity u^- (m/s)**	**Maximum velocity asymmetry u^+/u^-**
Location 1			
Impermeable 1	0.82	-0.62	1.32
Permeable 1	0.58	-0.41	1.42
Location 2			
Impermeable 2	0.68	-0.46	1.48
Permeable 2	0.51	-0.21	2.47
Location 3			
Impermeable 3	0.55	-0.34	1.61
Permeable 3	0.47	-0.074	6.36

Table 57 Uprush and backwash velocities on impermeable and permeable slopes at locations 1, 2 and 3

Although infiltration reduces the periods and velocities of both the uprush and backwash phases, the major differences occur on the backwash phase. The reduction in backwash flow increases with distance up the slope, and as a consequence, both T_u/T_b and u_u/u_b also increase significantly in the landward direction (dashed lines in Figure 172). This increase in onshore flow and time asymmetry is expected to promote onshore sediment transport, as the amount of sediment carried away from the beach is reduced. This supports the claim from beach dewatering promoters that beach erosion can be reduced by lowering the beach groundwater levels, and thus increasing the infiltration rates.

7.7.3 Evolution of Horizontal Velocity Profiles

The above comparisons show that infiltration decreases the swash depth, swash duration and flow velocity, especially at locations further up the slope. As mentioned in Kikkert et al., (2013), these bulk effects complicate the comparison of the velocity profiles on

impermeable and permeable slopes at different time steps. Nevertheless, the velocity profiles of the ensemble-averaged horizontal velocities on the impermeable (solid lines) and permeable slopes (dashed lines) at time-steps of 0.2s are presented in Figure 173, Figure 174 and Figure 175, for locations 1, 2 and 3 respectively. For reference, the time series of the water depth profiles are also displayed at the top of these figures showing the location in time corresponding to each velocity profile. The colour of each point inside the water depth profiles corresponds to the colour of each velocity profile.

These figures show that the velocity profiles on the impermeable and permeable show a similar evolution throughout the entire swash cycle. These profiles gradually evolve from profiles showing a typical logarithmic boundary layer at the beginning of the uprush stage to profiles resembling the typical velocity profile of a wall jet at the beginning of flow reversal. Then, the wall jet profiles gradually evolve back to profiles showing logarithmic boundary layers at the end the backwash.

These transitions are shown in Figure 176 for the impermeable slope and Figure 177 for the permeable slope at location 1. In these figures, the velocity profiles at every 0.1s are separated in 5 stages: a) uniform uprush – logarithmic profile; b) first transition; c) flow reversal – wall jet, d) second transition and e) uniform backwash – logarithmic profile. As the swash cycle on the permeable slope is shorter, the stages on the permeable slope occur at different times than on the impermeable slope. These stages at location 1 are briefly described below.

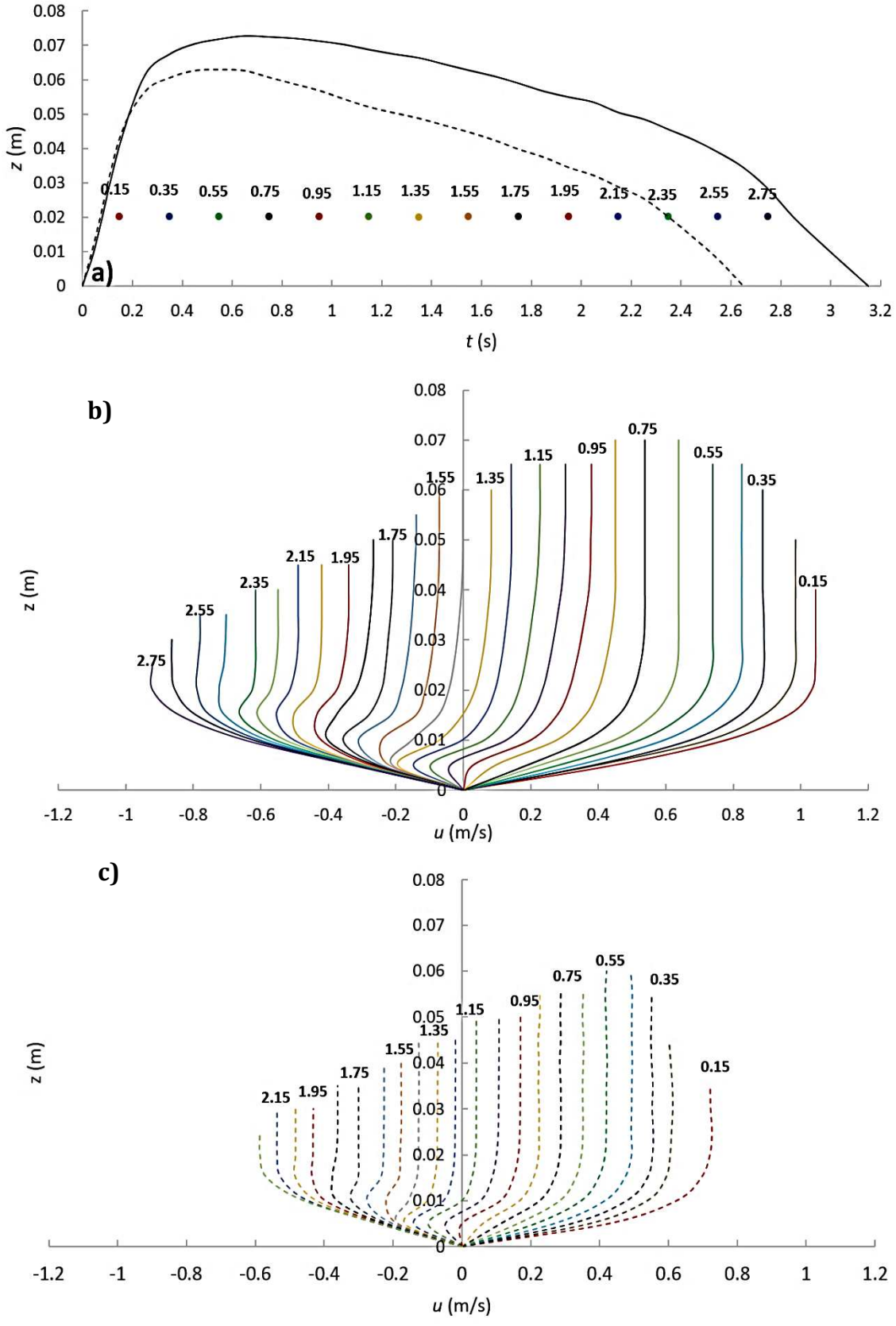

Figure 173 Evolution of horizontal velocity profiles at location 1 at every 0.1s: a) Water depth profiles; b) impermeable slope and c) permeable slope

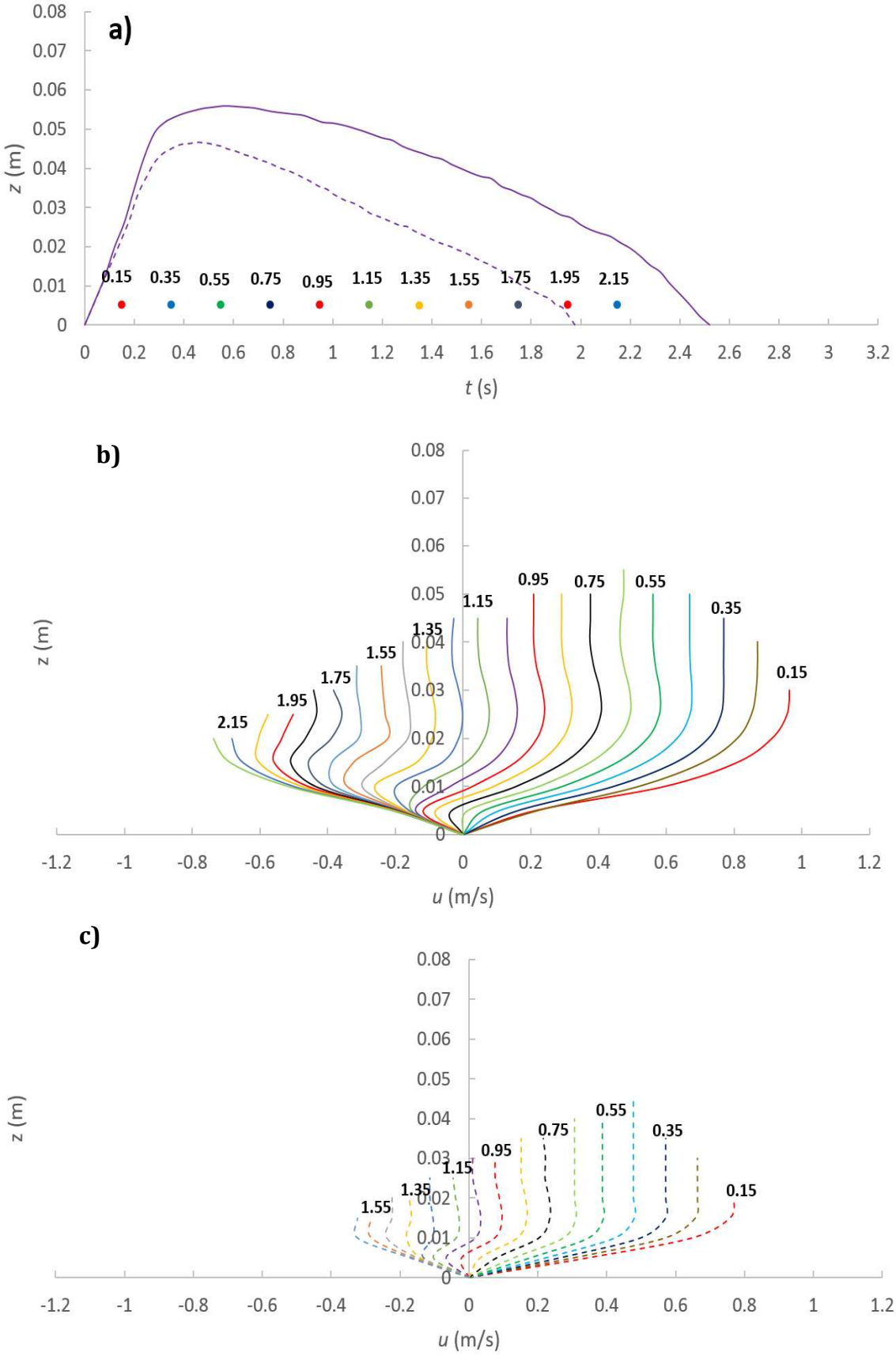

Figure 174 Evolution of horizontal velocity profiles at location 2 at every 0.1s: a) Water depth profiles; b) impermeable slope and c) permeable slope

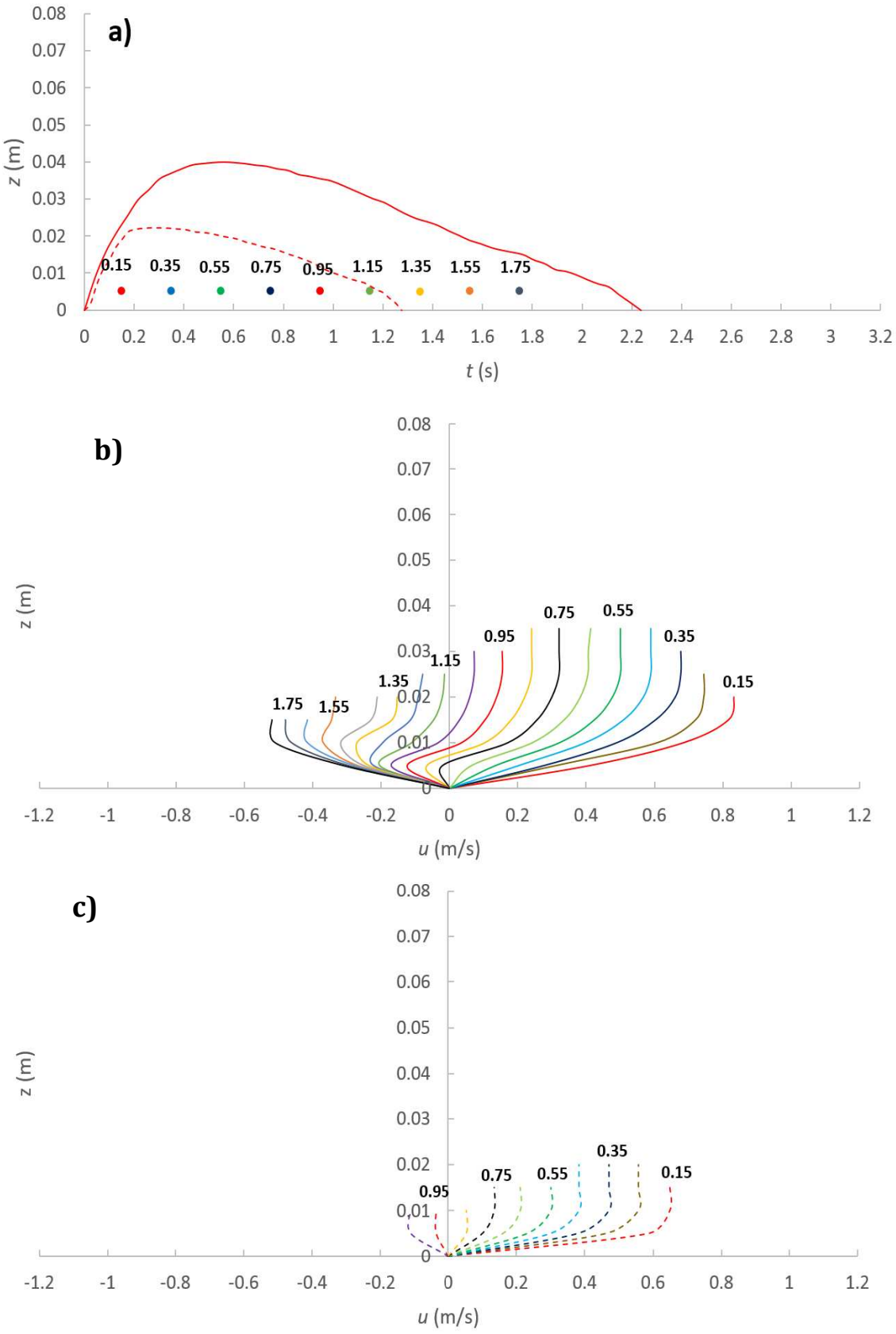

Figure 175 Evolution of horizontal velocity profiles at location 3 at every 0.1s: a) Water depth profiles; b) impermeable slope and c) permeable slope

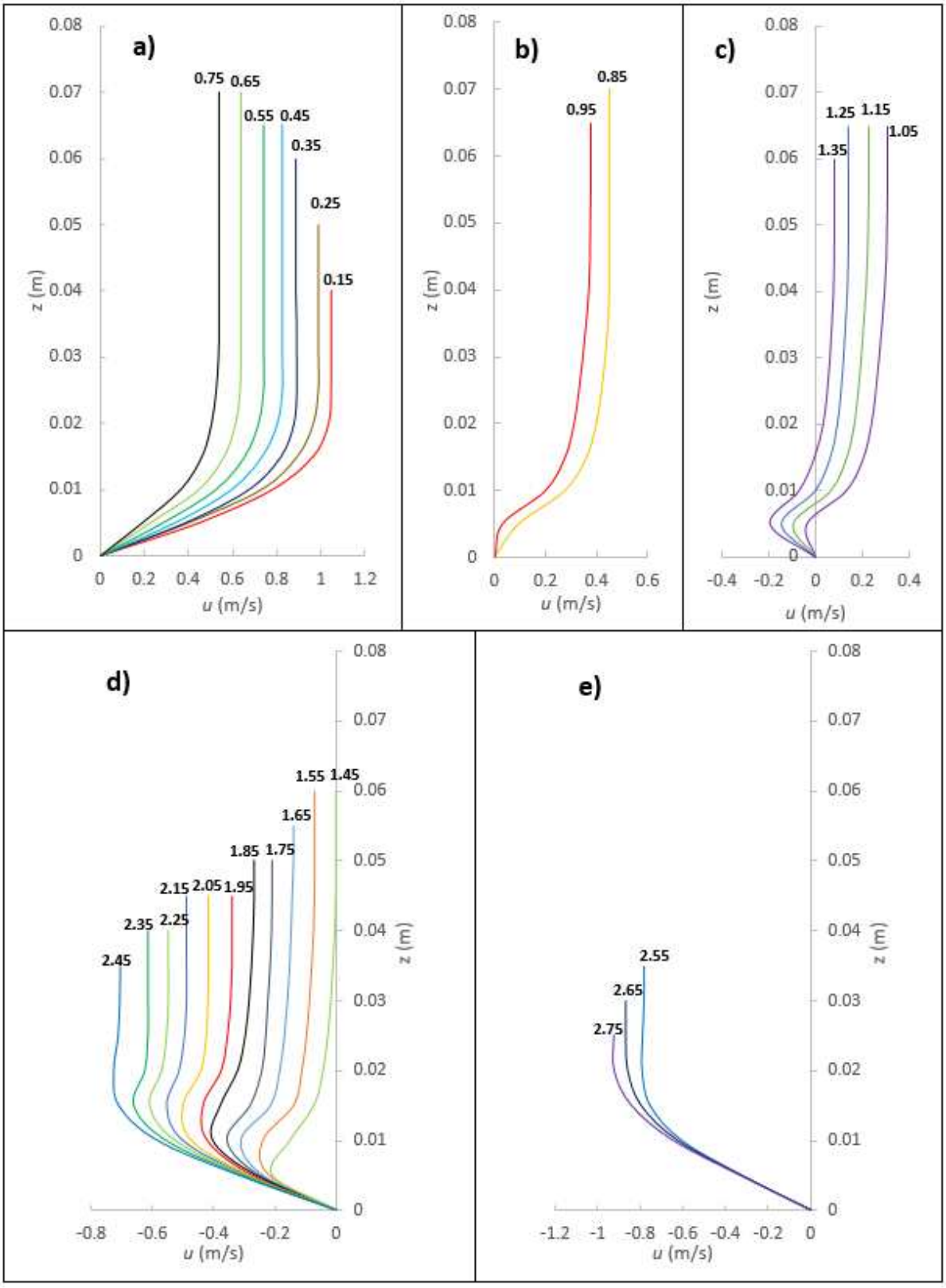

Figure 176 Evolution of velocity profiles on an impermeable slope a) uniform uprush – logarithmic profile; b) first transition; c) flow reversal – wall jet, d) second transition and e) uniform backwash – logarithmic profile.

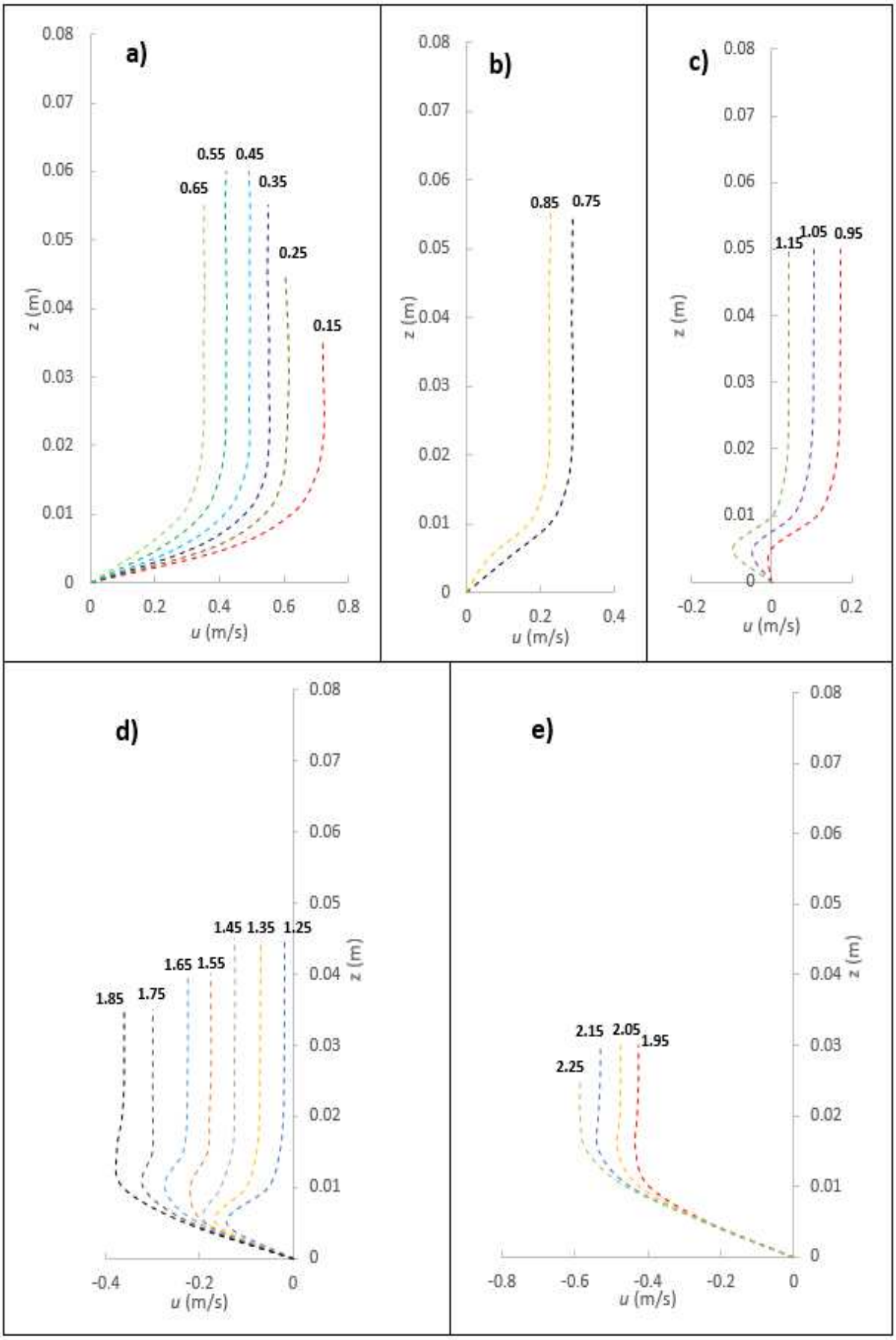

Figure 177 Evolution of velocity profiles on an impermeable slope a) uniform uprush – logarithmic profile; b) first transition; c) flow reversal – wall jet, d) second transition and e) uniform backwash – logarithmic profile.

a) Uniform uprush – logarithmic profile

During the uniform uprush stage, when flow in the entire vertical column is positive (0.15 < t < 0.75s on the impermeable slope and 0.15 < t < 0.65s on permeable slope), the velocity profiles show a logarithmic growth in the boundary layer. Figure 178 shows a typical velocity profile with a logarithmic boundary layer. In such velocity profiles, the magnitude of the horizontal velocity $u(t)$ begins at zero and gradually increases as the distance to the bed increases until reaching a free-stream velocity $u_\infty(t)$ at the edge of the boundary layer. The boundary layer thickness, δ, is considered to be the height where the horizontal velocities reach 99% of the free-stream velocity, $Y = 0.99u_\infty(t)$.

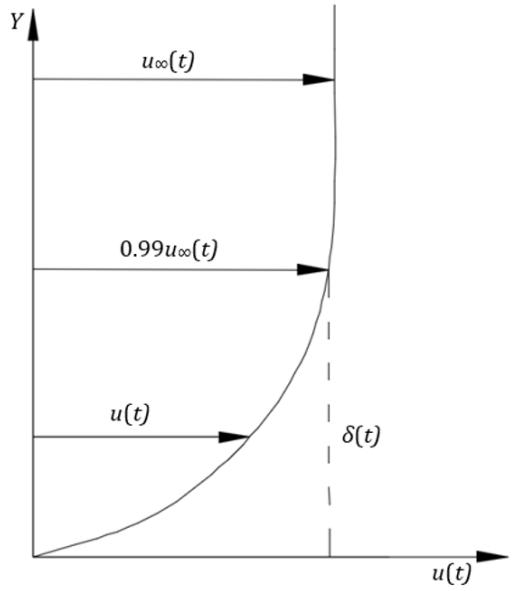

Figure 178 Velocity profile with a logarithmic boundary layer

b) First transition

A brief transition stage occurs between 0.85 < t < 0.95s on the impermeable slope and 0.75 < t < 0.85s on the permeable slope. In these stage, the velocity profiles start to show the effect of flow reversal in the near bed region and the profiles gradually evolve from logarithmic profiles to flow reversal profiles.

c) Flow reversal – wall jet profiles

The first changes in flow direction occur near the bed, where the velocities are lowest, while the rest of the profile remains positive. These flow reversal profiles can be seen in the approximate interval 1.05 < t < 1.35s on the impermeable slope and between 0.95 < t < 1.15s on permeable slope. The velocity distribution of these profiles resembles the typical velocity profile of a wall jet. These are characterised by a wall jet region with negative velocities in the area close to the sloping bed, whereas the velocities above the wall jet region remain positive and asymptotically reach the free-stream velocity. A typical flow

reversal velocity profile resembling a wall jet profile is sketched in Figure 179. The thickness of half-width, b_h, and the height were the maximum negative velocity, U_m (t), in the wall jet region occurs, b_m, continue to increase as time, t, increases, while the free-stream velocity gradually decreases and becomes negative due of the effect of gravitational force. The maximum negative velocity reaches a maximum when the free-stream velocities decrease to zero.

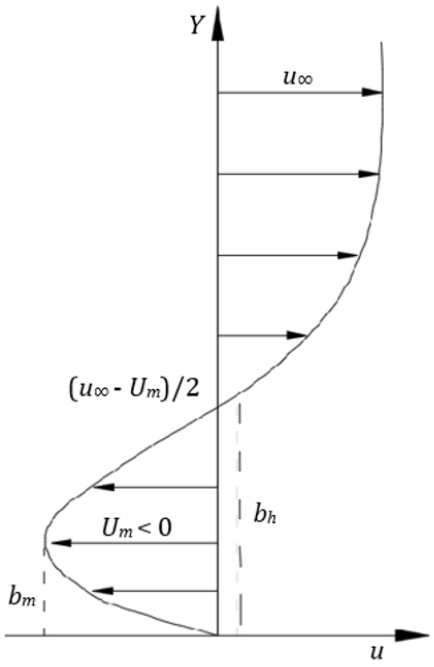

Figure 179 Typical flow reversal velocity profile

d) Second transition

After the beginning of flow reversal, the wall jet type profiles slowly evolve back to logarithmic profiles at the end of the backwash. These transitions are seen to occur between the intervals 1.45 < t < 2.45s on the impermeable slope and between 1.25 < t < 1.85s on the permeable slope. These transitions start when the velocity profiles in the entire field become negative and move in the offshore direction. The velocity profiles in these intervals also show a wall jet region which continues to increase in magnitude and layer thickness as time increases. These profiles are also characterised by some overshooting (e.g. Pedersen et al.,2013; Lin et al., 2014), which gradually diminishes until the velocity profiles return a uniform negative logarithmic boundary layer.

e) Uniform backwash – logarithmic profile

The velocity profiles at the end of the backwash (between 2.55 < t < 2.75s on the impermeable slope and between 1.95 < t < 2.25s on the permeable slope) are similar to those present at the beginning of the uprush, but in the opposite direction. These profiles also present the logarithmic growth in the boundary layer sketched in Figure 178. Due to

the increase of the free-stream velocity in the offshore (negative) direction due to the gravitational force, the maximum offshore velocity occurs at the end of the backwash phase.

7.7.4 Boundary Layer Thickness

In this analysis, the boundary layer thickness, δ, is defined as the elevation from the bed where the velocity reaches 99% of the free stream velocity. Values of δ were obtained only from the velocity profiles that showed a logarithmic region. Figure 180 shows the evolution of δ at the three locations along both slopes during the uprush and backwash flows, where δ is plotted against the normalized time, t'. At the three locations on both slopes, δ gradually increases from soon after the bore arrives until the beginning of flow reversal. After flow reversal, these gradually start to grow again until the end of the backwash phase. As discussed above, infiltration is expected to decrease δ, which is seen in all three graphs. The reduction of δ caused by infiltration is similar for both the uprush and backwash flows and the scale of these changes increases further up the slope. Such changes are expected to increase the bed shear stresses exerted on the slope. However, as mentioned previously, the continuity effect of infiltration can also indirectly increase the bed shear stresses due to a loss in surface flows. This is analysed in the following section

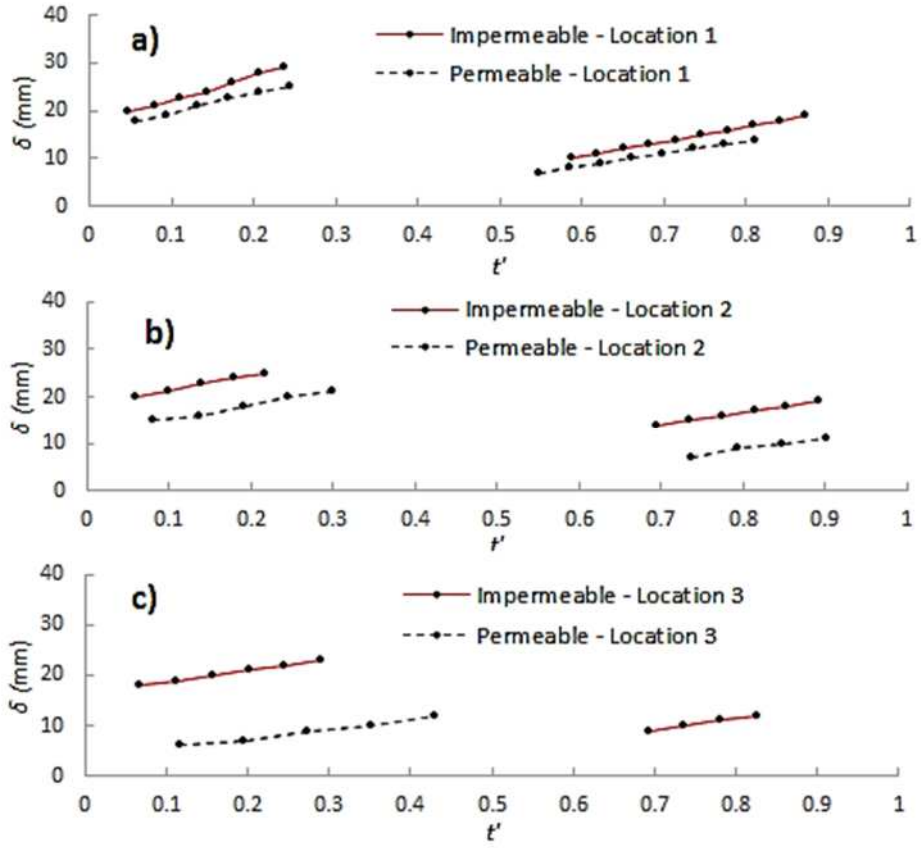

Figure 180 Boundary layer thickness on the impermeable and permeable slopes at: a) location 1; b) location 2; and c) location 3

7.7.5 **Bed Shear Stresses**

The bed shear stresses can be estimated indirectly using the near-bed velocity measurements through a number of different methods such as application of momentum balance to a control volume, logarithmic profile fitting to the measured velocity profiles (log-law method), and relating the shear velocity to the turbulent kinetic energy dissipation rate.

Kikkert et al. (2009) evaluated the practicality of applying these methods in unsteady swash flows and showed that bed shear stress estimates based on the turbulent kinetic energy dissipation rate could only be determined when the bed shear stress values are very low (e.g. during flow reversal). Furthermore, only the momentum balance method is strictly applicable to unsteady and non-uniform swash flows. However, Kikkert et al. (2009) showed that the log-law method could also give accurate estimates of bed shear stresses in the swash zone. Their study compared estimates obtained from both the log-law and momentum balance method to estimate bed shear stresses from swash flow velocity measurements. Their estimates using the log-law showed good agreement with those obtained from the momentum balance. For this reason, the log-law method was selected in this study to estimate the bed shear stresses.

The bed shear stresses, τ_0, on the impermeable bed were obtained using the law-of-the-wall or log law described in Chapter 2. This method involves fitting logarithmic profiles to the near bed horizontal velocity profiles. Therefore, the accuracy of this method depends on the accuracy of the velocity data. However, it cannot be applied on permeable slopes as it does not include infiltration velocities, which are known to influence the shear stresses. For permeable slopes, Chen and Chiew (2004) proposed a modified log-law method which considers infiltration velocities and uses a similar fitting approach to the traditional log-law method, given by:

$$\frac{u-u_0}{u_*}=\frac{1}{\kappa}\ln\left(\frac{z+z_0}{z_0}\right)+\frac{v_0}{4u_*}\left(\frac{1}{\kappa}\ln\left(\frac{z+z_0}{z_0}\right)\right)^2 \qquad (162)$$

where u_* is the shear velocity defined as $u_*=\sqrt{\tau_0/\rho}$ (τ_0= bed shear stress, ρ = fluid density), u_0 is the horizontal velocity at the surface, v_0 is the vertical velocity at the surface (infiltration velocity), z_0 is the vertical displacement of the origin of the mean velocity profile (also called roughness length) and κ is the von Karman constant = 0.4. As there are several unknown values in (162), Chen and Chiew (2004) rewrote (162) as (163) in order to fit the data to the modified log law and obtain the shear velocity, u_*.

$$u=ax^2+bx+c \qquad (163)$$

where:

$$x = \frac{1}{\kappa}\ln\left(\frac{z + d'}{z_0}\right) \tag{164}$$

$$a = \frac{v_0}{4} \tag{165}$$

$$b = u_* \tag{166}$$

$$c = u_0 \tag{167}$$

The values of *d'*, u_* and u_o are obtained by fitting (163) to the data using a trial-and-error routine to find best fitted values. This routine consists of assigning arbitrary values to *d'* and comparing the computed v_o to those obtained from simulations or measurements until the error is minimized. By comparing estimates of shear velocities for sand and gravel beaches using both methods, Kikkert et al. (2013) showed that when infiltration rates are significant (e.g. gravel beach), the modified log-law gives significantly higher values than the traditional log law. As the permeable slope used in this study has a comparable hydraulic conductivity to a gravel beach, the modified log-law method was used in this analysis to compare the bed shear stresses of the impermeable and permeable slopes. These comparisons are shown in Figure 181, where the bed shear stress estimates for both slopes at locations 1, 2 and 3 are plotted against the normalized time, *t'*. The bed shear stresses corresponding to the flow reversal velocity profiles are not shown due to the unsuitability of the log-law on this type of profile. At location 3 of the permeable slope, none of the profiles during the backwash phase had a logarithmic region, so bed shear stresses could not be estimated for this phase

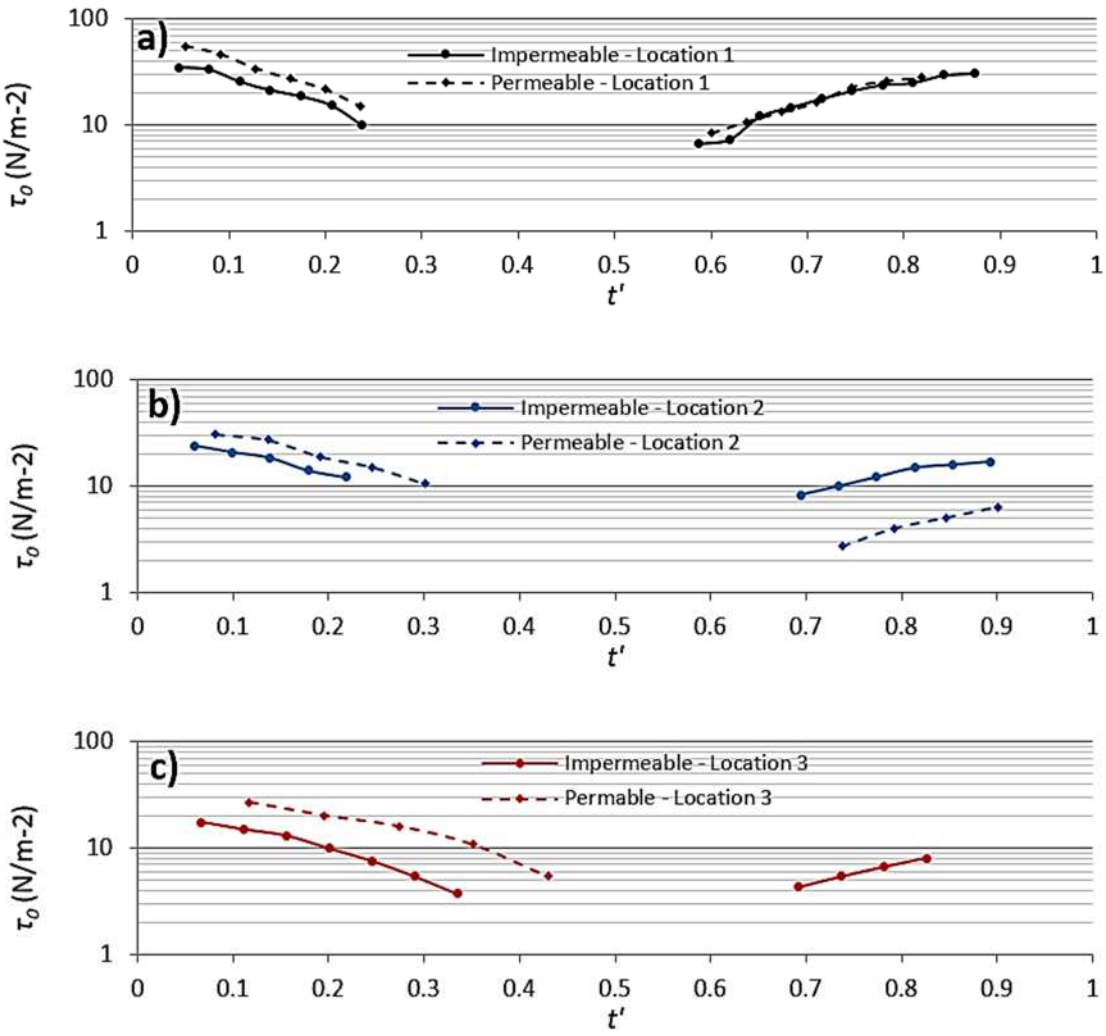

Figure 181 Bed shear stresses on impermeable and permeable slopes at: a) location 1; b) location 2; and c) location 3

The three graphs show similar results and are consistent with the results presented in Kikkert et al. (2012 and 2013) on solitary waves. On both permeable and impermeable slopes, the magnitude of the bed shear stresses is clearly seen to be related to the flow velocities. The maximum shear stresses occur at the beginning of the uprush, where the maximum velocities also occur and gradually decrease until the beginning of flow reversal. As the backwash flow starts to increase after flow reversal, the shear stresses also start to increase.

The bed shear stresses are commonly related to the depth-averaged velocities, $\bar{u}$, through the drag coefficient, $C_{D,}$ (also known as friction factor) by the quadratic friction law given by:

$$\tau_0 = C_D \bar{u}^2 \rho \qquad (168)$$

The clear dependence of the bed shear stresses on the depth-averaged velocities can be seen in Figure 182, where τ_0 is plotted against $\bar{u}^2\rho$. This figure shows the results of the linear regressions performed to get an estimate of the drag coefficients for each slope.

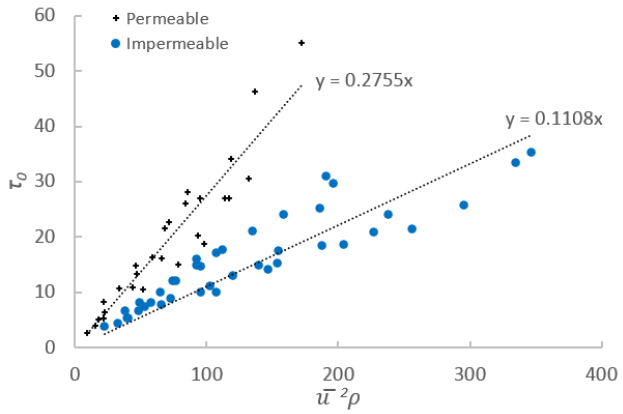

Figure 182 Bed shear stresses on impermeable and permeable slopes

Figure 181 shows that on a slope with a hydraulic conductivity of K = 0.401 m/s, infiltration can have opposing effects on the bed shear stresses. These opposing effects depend on the particular flow condition. During the uprush stages (when the flow velocities and water depths on the impermeable and permeable slopes are comparable) infiltration directly increases the bed shear stresses by thinning the boundary layer. As discussed before, this has been shown in previous studies for steady flows (e.g. Maclean, 1991; Chen and Chiew, 2004) and for oscillatory flows with suction (e.g. Conley and Inman, 1994). In contrast, the significant loss of water in the surface flow during the backwash phase results in considerably smaller flow velocities when compared to those on the impermeable slope, and consequently, the bed shear stresses are also reduced (the continuity effect). As the reductions of flow velocities and depth caused by infiltration during the backwash phase increase with distance up the slope, the reduction of bed shear stress also increases. This can be seen in the backwash phases of Locations 1 and 2. In the backwash phase of Location 1, the decrease in flow depths and velocities reduce the difference between the bed shear stresses of the impermeable and permeable slopes when compared to the uprush phase. This reduction of bed shear stresses due to loss of water in the surface flow is increased in the backwash phase of Location 3, where the bed shear stresses are even smaller than those of the impermeable slope.

These results suggest that for a beach with a K = 0.401 m/s (typical in coarse sand to medium gravel beaches), the effective weight of sediment and the bed shear stresses will have opposite effects on sediment mobility during the uprush flows, while for the backwash flows, these mechanisms will work together to decrease the potential for sediment mobility.

7.7.6 **Drag Coefficient**

Figure 183 shows the time series of the estimated drag coefficients for both slopes at locations 1, 2 and 3 estimated using the quadratic friction law (168). As also shown in

Figure 182, the drag coefficients on the permeable slope are higher those observed on the impermeable slope throughout both the uprush and backwash phases. On both slopes the values remain fairly constant in the uprush and backwash phases, with similar values as the values obtained from the regressions shown in Figure 182.

On the uprush phase at locations 2 and 3 on the impermeable slope there is a slight increase in the drag coefficient as flow reversal is approach. This is consistent with drag coefficient behaviour in uniform, steady flow, were C_D increases with decelerating and shallower flows, hence, with decreasing Reynolds number. This increase of C_D on impermeable slopes before flow reversal was also observed in Kikkert et al. (2012). Furthermore, on the impermeable slopes, C_D is consistently slightly higher on the backwash phases than those observed on the uprush phases. This might be attributed to the increase of flow acceleration on the backwash phase after flow reversal.

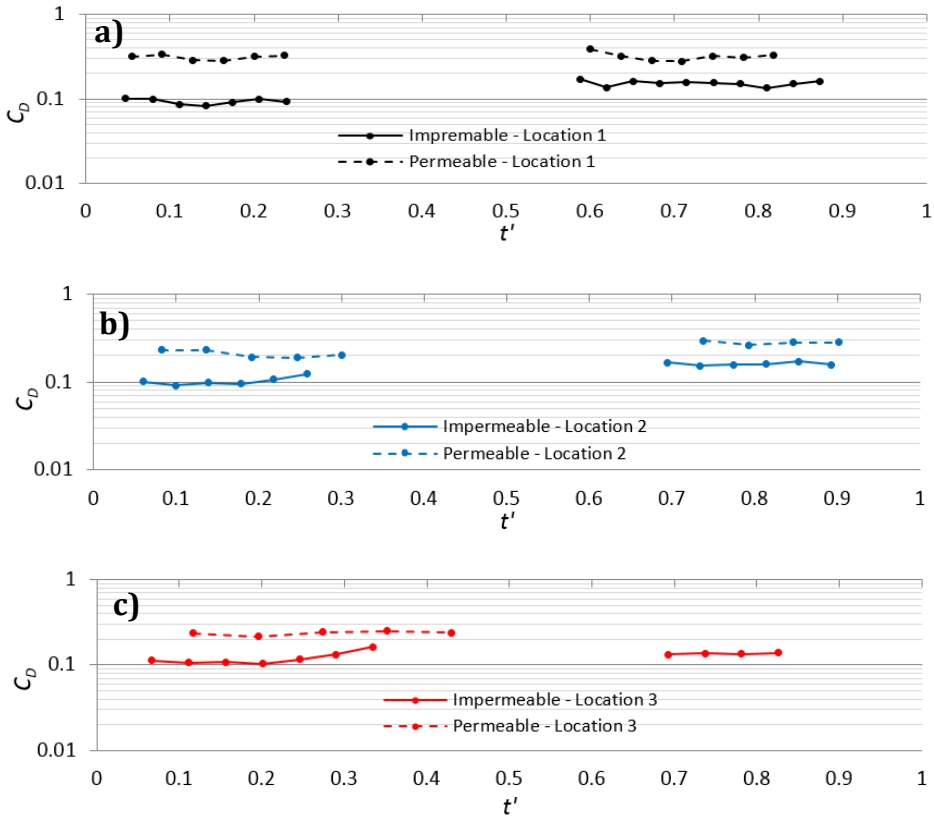

Figure 183 Normalised time series of drag coefficients on impermeable and permeable slopes at: a) location 1; b) location2; and c) location 3

7.7.7 Summary

- Infiltration was seen to decrease the water depths, flow velocities and swash durations, and increase the drag coefficients
- These reductions increase with distance up the slope and during the backwash phases, increasing onshore time and flow asymmetry. These decrease in backwash

flow is expected to reduce the sediment carried away from the beach, promoting onshore sediment transport.

- The velocity profiles on the impermeable and permeable were shown to have similar evolution throughout the entire swash cycle. These velocity profiles showed a logarithmic distribution at the beginning of the uprush phase, then gradually evolved to a wall jet type profile during flow reversal, and finally evolving back to a logarithmic profile at the end of the backwash phase.
- The log-law method was used to obtain bed shear stresses from the velocity profiles showing logarithmic distributions.
- Infiltration directly increases the bed shear stresses at the uprush phases by thinning the boundary layer. In contrast, the substantial reduction in backwash flows caused by infiltration indirectly reduces the overall bed shear stresses when compared to the impermeable slope. This shows that modified bed shear stresses due to infiltration can have opposing effects on the potential for sediment mobility.
- The drag coefficients were seen to remain fairly constant on both the permeable and impermeable slopes; as expected these were seen to be larger on the permeable slope

8 Conclusions

The research project described within this dissertation has sought to investigate the swash zone processes. One of the main motivations of the present study was to improve the prediction of wave run-up from both breaking and non-breaking waves on impermeable and permeable slopes. Given the absence of run-up data over permeable slopes with different hydraulic conductivities, an extensive laboratory and numerical study was undertaken. These involved innovative wave flume laboratory experiments and simulations on a RANS model. The laboratory experiments were carried out with non-deformable permeable structures consisting of reticulated open-cell foams with known hydraulic conductivities. These foams were found to have several advantages over other permeable materials (e.g. easy and quick removal, clean, homogeneous hydraulic conductivity, flat and non-deformable). The results obtained from the laboratory experiments were used to validate the RANS model used. These comparisons showed that the model is well capable of simulating run-up on both permeable and impermeable slopes.

Using the data obtained from both the laboratory and numerical model, new run-up formulae were derived for impermeable and permeable slopes, for both breaking and non-breaking waves. These formulae, which were validated against the present and against existing published data, included the influence of surface roughness and hydraulic conductivity through influence factors. As far as the author is concerned, these formulae are the first to include the influence of hydraulic conductivity through a non-dimensional parameter. These formulae were also shown to correctly predict the wave-induced maximum water table over-height in coastal barriers.

The influence factor of hydraulic conductivity derived assumes that the hydraulic conductivity of the beach or coastal structure is homogeneous and does not vary, as these were derived from completely homogeneous structures. The permeable cores of coastal structures are generally also homogeneous, so its hydraulic conductivity remains fairly constant throughout the entire structure. This is one of the reasons why the proposed formulae and influence factors were successful in predicting the data from Van Broekhoven (2011) on permeable structures. However, the use of these influence factors should be treated with caution on beaches as sediment size across a beach may not be constant, and hydraulic conductivity may vary. Therefore, assuming a constant hydraulic conductivity throughout the entire beach could lead to inaccurate results. For this reason, these influence factors may have better results in estimating run-up heights on coastal structures than on permeable beaches.

To improve our current predictions of the swash zone sediment transport and consequently our predictions on beach profile evolution, it is necessary to improve our understanding of the influence of infiltration/exfiltration on the swash zone sediment transport. This study showed that infiltration can have opposing effects on the bed shear stresses, and as a consequence, on sediment transport in the swash zone. However, further research is still needed to understand and quantify how hydraulic conductivity and water table elevations affect the infiltration/exfiltration processes. Improving our understanding of the influence of these processes on sediment transport is crucial for soft engineering projects such as beach nourishments (where it is possible to select the type of sediment to recharge a beach) and beach drainage schemes (who claim that infiltration can promote onshore sediment transport). Possible future research studies that could enhance our knowledge on the swash processes and sediment transport predictions are suggested in Section 8.4.

8.1 Scientific Findings and Contributions:

The scientific findings described below are separated according to the four main topics analysed in this study: wave run-up, water table over-height, wave breaking processes and swash hydrodynamics. The following findings are valid for the slope angles, wave conditions and hydraulic conductivities tested in this project.

1.) WAVE RUN-UP

Wave Run-up from Regular and Irregular Waves on Smooth-Impermeable Slopes

- **Breaking waves:**
    - On shallow slopes ($\alpha < 13°$) it was shown that wavelength or wave period has a large influence on run-up from breaking waves, while wave height only had a large influence on long waves with small wave steepness ($H/L_o < 0.01$)
    - For slopes $\alpha < 18°$ run-up was seen to increases as the angle of the slope increases, while for steeper slopes ($\alpha > 18°$) run-up decreases as the slope increases.
    - The Iribarren number was proven to correctly describe run-up from breaking waves
    - A slight under-prediction was seen of most existing formulae for breaking waves when compared to the present data, which might be attributed to the measuring technique (measurements taken with video cameras generally show larger values than those obtained from run-up gauges)

- Schüttrumpf's (2001) hyperbolic formula with fitted empirical coefficients was shown to have the best agreement to the present run-up data (this formula is based on the Iribarren number)

- **Non-breaking waves:**
  - Wavelength or wave period was shown to have less influence than wave height on run-up from non-breaking waves on steep slopes ($\alpha > 18°$)
  - The Iribarren number was shown not to be the ideal parameter to describe run-up from non-breaking waves.
  - These waves were shown to be better characterised by a new parameter proposed in this study, Φ, and by the wave momentum flux parameter proposed by Hughes (2004b)
  - The run-up data from the present study was used to derive new formulae to predict run-up from non-breaking waves based on these two parameters

Wave Run-up from Regular on Rough-Permeable Slopes

- **Breaking waves:**
  - The influence of surface roughness, hydraulic conductivity and water table elevations on wave run-up was investigated separately
  - The roughness and hydraulic conductivity of the slopes were seen to have less influence on values $\xi < 1.2$; the combined run-up reduction of these parameters on data with $\xi < 1.2$ was between 26-41%, while for data $\xi > 1.2$ these reductions were between 35-55%, when compared to the smooth-impermeable slopes
  - On plunging waves, the surface roughness of the foams was seen to cause a larger reduction than the reduction caused by their hydraulic conductivity
  - The variations in water table elevations were seen to influence run-up by around 5%, so were not included in the prediction formulae
  - The run-up from breaking waves on permeable slopes were also shown to be well described by Schüttrumpf's (2001) hyperbolic formula
  - The influence of the surface roughness and hydraulic conductivity were included in this formula through two influence factors: γ_f and γ_K
  - The influence factor for hydraulic conductivity, γ_K, is based on a new dimensionless hydraulic conductivity parameter, Ψ, proposed in this study given by: K^3/gv
- **Non-breaking waves:**

- The combined run-up reduction caused by roughness and hydraulic conductivity was observed to be larger on breaking waves than on non-breaking waves; on non-breaking waves these reductions were seen to be between 20-44% when compared to the data from the smooth-impermeable slopes
- The run-up data from non-breaking waves were also shown to be well predicted by the formulae derived for smooth-impermeable slopes
- A roughness and hydraulic conductivity factor was derived and included in these formulae; this factor is also based on Ψ

2.) WAVE-INDUCED WATER TABLE OVER-HEIGHT

- The hydraulic conductivity of a coastal barrier has a significant influence on η_w^+
- As expected, η_w^+ was proven to be a function of wave run-up and the ratio between these parameters was found to remain constant regardless of the hydraulic conductivity of the beach
- Therefore, the formulae proposed to predict run-up on permeable slopes were also used to predict η_w^+; these formulae included a reduction factor
- When compared against the measurements, the predictions of these formula showed some scatter; nevertheless, most predictions were inside the ±15% error bands

3.) WAVE BREAKING PROCESSES

- The hydraulic conductivity of the slopes was seen to decrease the breaking point distance of plunging waves
- This parameter was also observed to slightly alter the shape of the breaking waves; however, this change was too small to modify their breaker type
- The Iribarren number was shown to correctly predict the transition between breaking and non-breaking waves; however, the value predicting this transition changed depending on the wavelength of the waves
- For this reason, a new breaking criterion was proposed given by: $\tan\alpha/(H/h)$; this parameter was shown to correctly predict the transition between breaking and non-breaking waves on both impermeable and permeable slopes
- Both the Iribarren number and $\tan\alpha/(H/h)$ were shown to show good predictions when compared to the experiments observations

4.) SWASH HYDRODYNAMICS

- Hydraulic conductivity of the slope was seen to decrease the water depths, flow velocities and swash durations.
- These reductions were seen to be further increased with distance up the slope
- T_u/T_b and u_u/u_b were seen to remain close to the unity value on the impermeable slope at the three locations analysed
- In contrast, T_u/T_b and u_u/u_b on the permeable slope were seen to significantly increase with distance up the slope; this was mainly attributed to the increased reductions in backwash periods and velocities caused by infiltration
- The velocity profiles on the impermeable and permeable show a similar evolution throughout the entire swash cycle, gradually evolving from logarithmic at the start of the uprush to wall jet type profiles at flow reversal and back to logarithmic profiles at the end of the backwash.
- Infiltration was seen to directly increase the bed shear stresses at the uprush phases, mainly due to the change in the boundary layer thickness
- However, infiltration indirectly reduced the bed shear stresses at the backwash phases by significantly reducing the backwash flows (continuity effect)
- The drag coefficients were seen to remain fairly constant on both the permeable and impermeable slopes; as expected these were seen to be larger on the permeable slope

8.2 Numerical Contributions:

- The resistance coefficients α and β for porous flow simulation in the VARANS model used were calibrated against steady flow tests through three porous dams, and recommended values for each porous material were given
- The capability of the RANS model (*IH-2VOF*) used to simulate run-up over permeable and impermeable slopes was validated through comparisons against the present experimental data. The following results were obtained from these comparisons:
    - **Wave run-up.** Most of the simulated wave run-up data on the impermeable slope and the three permeable slopes were inside the ±15% error bands when compared to the measured data. Although some under-prediction was seen for the R45 and R80 foams, the absolute average errors for all slopes remained lower than 10%.
    - **Swash depths.** A good agreement was seen on both impermeable and permeable slopes, although in both cases some under-predictions were seen after flow reversal. Nevertheless, the simulated data remained mostly inside the ±15% error bands through most of the swash events.

- **Swash duration.** The model was seen to predict accurately the duration of the swash for both impermeable and permeable cases.
- **Ensemble-averaged horizontal velocity profiles.** A good agreement was seen between the simulated and measured velocity profiles in both cases. Most of the simulated data were inside the ±15% error bands, although some differences were seen on the flow reversal profiles on the permeable slope. The model was also shown to correctly simulate the evolution of the velocity profiles from logarithmic profiles at the beginning of the uprush to wall jet-type profiles at flow reversal and back to logarithmic profiles at the end of the backwash.
- **Bed shear stresses.** Mostly good predictions of the bed shear stresses were seen in both cases as these remained in the same order of magnitude as the measured data, although in both cases these were over-estimated. On the impermeable slope, the simulated values were seen to be around 35% and 15% larger than the measured data on the uprush and backwash phases respectively, while for the permeable slope, the simulated data were around 15% and 30% larger on the uprush and backwash phases, respectively.
- **Roughness lengths.** In both cases an over-prediction of around 20% was seen on the simulated roughness lengths when compared to the measured data. Nonetheless, these values remained fairly constant throughout the entire swash cycle and within the same order of magnitude.

8.3 Technical Contributions:

- Novel laboratory experiments were designed on smooth-impermeable, rough-impermeable and fixed rough-permeable slopes with known hydraulic conductivities
- A recirculating water system was designed to maintain the water levels at the back of the permeable structures either higher or lower than the sea-side water level, while keeping the sea-side water level constant
- An experiment was set up to enable measurements of water table elevations at different locations inside the permeable slopes using pressure transducers
- A series of tests were carried out for steady flow through different permeable structures to measure seepage elevations and head differences for the calibration of the resistance coefficients used in the numerical model
- Measurements were made of the hydraulic conductivity of open-cell foams commonly used in industry as filters (previously unknown)

8.4 Suggestions for Further Research

- The run-up data collected during the laboratory tests on permeable and impermeable slopes could be used to develop, refine and validate models capable of simulating the swash hydrodynamics.
- By following a similar analysis approach as the one presented in this study, the reticulated open-cell foams could be used to investigate the influence of hydraulic conductivity on the overtopping discharge with the aim of including its influence on prediction formulae.
- As the reticulated open-cell foams can be cut into specific shapes, these foam could also be used to investigate the influence of hydraulic conductivity on run-up on slopes with different types of berms, as well as on concave-shaped slopes.
- The influence of hydraulic conductivity, surface roughness and water table elevations on run-up was only investigated for regular waves. Further research is suggested to investigate the influence of these parameters on run-up from irregular and solitary waves.
- The new parameter, Φ, proposed in this study was shown to have a good correlation with the run-up from all the non-breaking waves presented in this study. This parameter includes the influence of water depth, h. However, as all the tests presented in this study were carried out using a constant water depth, the influence of h on run-up was not investigated. Future research is suggested to investigate the performance of the parameter, Φ, in predicting run-up for waves in different water depths.
- The breaking point locations and breaker types were only recorded on the run-up tests performed on permeable slopes. Therefore, the influence of hydraulic conductivity on both parameters was only analysed for the range of hydraulic conductivities used. The results showed that the shapes of some of the waves breaking on the different permeable slopes were slightly different, but their different shapes were not enough to classify them as different breaker types. Further research is suggested to record the wave breaking processes on both impermeable and permeable slopes to investigate whether or not hydraulic conductivity on permeable slopes can change the breaker types, and under which conditions.
- This study presented flow velocity and water depth data from three different locations inside the swash zone. These data were used to investigate how the influence of infiltration on the swash flows and boundary layer dynamics varied at different locations along the swash zone. However, these three locations do not represent the entire extent of the swash zone. Further research is still required to

investigate data from the entire swash zone (from the run-down location to the run-up location).

- The swash flow velocity measurements presented in this study were only obtained from one fixed permeable slope and from one fixed impermeable slope. The comparisons of the data obtained from these tests showed that the infiltration on the permeable slope had a significant effect on the flow asymmetries and bed shear stresses inside the swash zone. Both these mechanisms are expected to influence the swash zone sediment transport and, thus, the beach profile evolution. However, a much better understanding of how hydraulic conductivity affects the infiltration/exfiltration processes (and consequently the flow asymmetries and bed shear stresses) is still required in order to improve our predictions of the swash zone sediment transport. The tests presented in this study were only performed on one permeable slope, so it was not possible to quantify its influence. Therefore, a possible next step would be to quantify this influence. This could be done by performing a similar analysis procedure as the one presented in this study, where the influence of K on run-up was quantified on several fixed permeable slopes with different hydraulic conductivities. A similar study could be carried out to quantify the influence of K on the infiltration/exfiltration rates, and thus on the flow asymmetries and bed shear stresses.
- The infiltration/exfiltration rates on a beach do not depend only on its hydraulic conductivity; the water table elevation inside the beach can also influence these processes. However, its influence on the infiltration/exfiltration rates has also never been quantified. The influence of the water table elevation on the infiltration/exfiltration processes will depend on the hydraulic conductivity of the beach. Therefore, in order to quantify its influence, it would be necessary to carry out similar tests as the ones presented in this study (where the water table elevation was manipulated), on different permeable slopes with known hydraulic conductivities. In the present study, the water table elevation on two different permeable slopes was manipulated to investigate its influence on run-up, but a similar procedure could be carried out to investigate its influence on the infiltration/exfiltration processes.
- Fixed permeable slopes with completely homogeneous hydraulic conductivities (such as the reticulated open-cell foams used in this study) can be extremely useful for quantifying the influence of hydraulic conductivity and water table elevations on the infiltration/exfiltration processes. However, permeable beaches in nature, such as coarse sand or gravel beaches, are generally composed of mixed sediments with varying hydraulic conductivities. Therefore, further research is still needed

firstly to improve the hydraulic conductivity estimates of different mixed sediment beaches, where small grain particles are expected to control the K of the beach; and secondly to investigate how beaches with mixed sediments influence the infiltration/exfiltration processes. Possible future laboratory studies on this topic could use fixed slopes composed of a top layer of bonded sediment using *Elastocoast*, with the remaining part of the beach consisting of different combinations of mixed sediments. These tests should also include hydraulic conductivity tests using permeameters.

- The run-up in this study was only measured using video cameras. The data obtained from the video observations were not compared with measurements taken using other techniques such as run-up gauges as these have only been proven to show good results in large-scale experiments. However, run-up in small-scale experiments could also be measured using other techniques such laser beams to detect run-up. This could simplify the post-processing of the data. Nevertheless, as far as the author knows, run-up data obtained from laser techniques have not been compared to run-up measurements obtained using video cameras, so further research is needed to validate this technique.
- Predicting run-up is particularly important in extreme waves. However, extreme waves, which are often reproduced in laboratory and numerical studies through focused waves, were not investigated in this study. A focused wave is created when all the components in a transient wave group come in phase. Recent studies have successfully developed iterative methodologies that can focus waves of any height at a predetermined temporal and spatial location along the wave flume (e.g. Stagonas et al., 2014). These studies can be used to investigate run-up from focused waves and analyse how the temporal and spatial location of focused wave influences run-up.
- The hydraulic conductivity of a beach or coastal structure can also significantly influence the hydraulic responses, in particular wave reflection and wave transmission. A similar analysis procedure as the one presented in this project to analyse the influence of K on run-up could be applied to analyse the influence of K on both these hydraulic responses (which are expected to influence wave run-up). Wave transmission could be analysed by measuring the pore water pressures inside the permeable beaches using pressure transducers, as well as measuring the free surface elevation behind the permeable beaches.
- Most of the run-up data from non-breaking waves on the smooth-impermeable slopes were obtained from the numerical model. Therefore, further laboratory experiments are recommended to verify and validate the findings presented here.

9 References

Ahmadian, A. (2013). *Wave field around submerged breakwaters.* (Ph.D.), University College London.

Ahrens, J. (1981). Ireggular wave run-up on smooth slopes *Coastal Engineering Research Centre* (Vol. CETA 81-17)

Ahrens, J., & Heimbaugh, M. (1988a). *Approximate upper limit of irregular wave runup on riprap*. U.S. Army Engineer Waterways Experiment Station.

Ahrens, J., & Heimbaugh, M. (1988b). Irregular Wave Runup on Riprap Revetments. *Journal of Waterway, Port, Coastal, and Ocean Engineering, 114*(4), 524-530. doi:10.1061/(ASCE)0733-950X(1988)114:4(524)

Ahrens, J., Seelig, W., Ward, D., & Allsop, W. (1993). *Wave runup on and wave reflection from coastal structures.* Proceedings of Ocean Wave Measurement and Analysis (Waves '93) Conference, ASCE, 489-502

Ahrens, J., & Titus, M. (1985). Wave Runup Formulas for Smooth Slopes. *Journal of Waterway, Port, Coastal, and Ocean Engineering, 111*(1), 128-133. doi:doi:10.1061/(ASCE)0733-950X(1985)111:1(128)

Allsop, W. (1983). *Low-crested breakwaters, studies in random waves.* Proceedings of Coastal Structures.

Allsop, W., Franco, L., & Hawkes, P. (1985). *Wave run-up on steep slopes - a literature review*. Hydraulics Research Wallingford

Allsop, W., Hawkes, P., Jackson, F., & Franco, L. (1985). *Wave run-up on steep slopes - model tests under random waves*. Hydraulics Research Wallingford

Ang, L., Sum, H.-Y., Baldock, T., Li, L., & Nielsen, P. (2004). *Measurement and modelling of controlled beach groundwater levels under wave action.* Proceedings of the 15th Australiasian Fluid Mechanics Conference, 1-4.

Archetti, R., & Brocchini, M. (2002). An integral swash zone model with friction: an experimental and numerical investigation. *Coastal Engineering, 45*(2), 89-110. doi:http://dx.doi.org/10.1016/S0378-3839(02)00038-8

Austin, M., & Masselink, G. (2006). Observations of morphological change and sediment transport on a steep gravel beach. *Marine Geology, 229*(1–2), 59-77. doi:http://dx.doi.org/10.1016/j.margeo.2006.02.003

Bağcı, Ö., Dukhan, N., & Özdemir, M. (2014). Flow Regimes in Packed Beds of Spheres from Pre-Darcy to Turbulent. *Transport in porous media, 104*(3), 501-520.

Baird, A., Mason, T., & Horn, D. (1998). Validation of a Boussinesq model of beach ground water behaviour. *Marine Geology, 148*(1–2), 55-69. doi:http://dx.doi.org/10.1016/S0025-3227(98)00026-7

Bakhtyar, R., Barry, D., Li, L., Jeng, D., & Yeganeh-Bakhtiary, A. (2009). Modeling sediment transport in the swash zone: A review. *Ocean Engineering, 36*(9–10), 767-783. doi:http://dx.doi.org/10.1016/j.oceaneng.2009.03.003

Baldock, T., & Hughes, M. (2006). Field observations of instantaneous water slopes and horizontal pressure gradients in the swash-zone. *Continental Shelf Research, 26*(5), 574-588. doi:http://dx.doi.org/10.1016/j.csr.2006.02.003

Baldock, T., & Nielsen, P. (2009). Discussion of "Effect of Seepage-Induced Nonhydrostatic Pressure Distribution on Bed-Load Transport and Bed Morphodynamics" by Simona Francalanci, Gary Parker, and Luca Solari. *Journal of Hydraulic Engineering, 136*(1), 77-79. doi:10.1061/(ASCE)HY.1943-7900.0000015

Barnes, M., & Baldock, T. (2007). Direct bed shear stress measurements in laboratory swash. *Journal of Coastal Research, SI 50*, 641-645.

Barnes, M., & Baldock, T. (2010). A Lagrangian model for boundary layer growth and bed shear stress in the swash zone. *Coastal Engineering, 57*(4), 385-396. doi:http://dx.doi.org/10.1016/j.coastaleng.2009.11.009

Barnes, M., O'Donoghue, T., Alsina, J., & Baldock, T. (2009). Direct bed shear stress measurements in bore-driven swash. *Coastal Engineering, 56*(8), 853-867. doi:http://dx.doi.org/10.1016/j.coastaleng.2009.04.004

Battjes, J. (1974). Surf Similarity. Proceedings of the 14th Coastal Engineering Conference, ASCE, 466-480.

Bear, J. (1972). *Dynamics of fluids in porous media*. New York.

Berg, R. (1970). Method for Determining Permeability from Reservoir Rock Properties. *Gulf Coast Association of Geological Societies Transactions, 20*, 303-317.

Billstain, M., Svensson, U., & Johansson, N. (1999). Development and validation of a numerical model of flow through embankment dams comparisons with experimental data and analytical solutions. *Transport in Porous Media, 35*(3), 395-406.

Blenkinsopp, C., Turner, I., Masselink, G., & Russell, P. (2011). Swash zone sediment fluxes: Field observations. *Coastal Engineering, 58*(1), 28-44. doi:http://dx.doi.org/10.1016/j.coastaleng.2010.08.002

Beach Erosion Board (1954). *Shore Protection Planning and Design*. US Army Corps of Engineers (Vol. 4).

Bonmarin, P. (1989). Geometric properties of deep-water breaking waves. *Journal of Fluid Mechanics, 209*, 405-433. doi:10.1017/S0022112089003162

Briganti, R., Dodd, N., Pokrajac, D., & O'Donoghue, T. (2011). Non linear shallow water modelling of bore-driven swash: Description of the bottom boundary layer. *Coastal Engineering, 58*(6), 463-477. doi:http://dx.doi.org/10.1016/j.coastaleng.2011.01.004

Burcharth, H., & Andersen, O. (1995). On the one-dimensional steady and unsteady porous flow equations. *Coastal Engineering, 24*, 233-257.

Burcharth, H., Lui, Z & Troch, P. *Scaling of core material in rubble mound breakwater model tests*. Proceedings of the 5th COPEDEC. Cape Town, South Africa, 1518-1528.

Burcharth, H., & Hughes, S. (2002). Funtamentals of Design *Coastal Engineering Manual*. Washington D.C.: US Army Corps of Engineers.

Butt, T., Russell, P., Puleo, J., Miles, J., & Masselink, G. (2004). The influence of bore turbulence on sediment transport in the swash and inner surf zones. *Continental Shelf Research, 24*(7–8), 757-771. doi:http://dx.doi.org/10.1016/j.csr.2004.02.002

Calabrese, M., Buccino, M., Ciardulli, F., Di Pace, P., Tomasicchio, R., & Vicinanza, D. (2010, 01/29/). *Wave run-up and reflection at rubble mound breakwaters with ecopode armor layer.* Proceedings of 32nd Conference on Coastal Engineering, Shanghai, China, 2010, 45

Capel, A. (2015). Wave run-up and overtopping reduction by block revetments with enhanced roughness. *Coastal Engineering, 104*, 76-92. doi:http://dx.doi.org/10.1016/j.coastaleng.2015.06.007

Carman, P. (1956). *Flow of gases through porous media*. New York: Academic Press.

Cartwright, N. (2004). *Groundwater Dynamics and the Salinity Structure in Sandy Beaches.* (Doctor of Philosophy), University of Queensland.

Cartwright, N., Baldock, T., Nielsen, P., Jeng, D., & Tao, L. (2005). Swash-aquifer interaction in sandy beaches. *Coastal Living; Australasian Conference*.

Channell, A., Stevenson, T., & Brown, R. (1985). *Run-up on shingle beaches*. Hydraulics Research Wallingford, SR 72

Chappell, J., Eliot, I., Bradshaw, M., & Lonsdale, E. (1979). Experimental control of beach face dynamics by watertable pumping. *Engineering Geology, 14*(1), 29-41. doi:http://dx.doi.org/10.1016/0013-7952(79)90061-9

Chen, X., & Chiew, Y. (2004). Velocity Distribution of Turbulent Open-Channel Flow with Bed Suction. *Journal of Hydraulic Engineering, 130*(2), 140-148. doi:10.1061/(ASCE)0733-9429(2004)130:2(140)

Chiaia, G., Damiani, L., & Ranieri, G. (2005). *Experimental analysis of the water table of a beach equipped with a drainage system.* Proceeding of the 31th IAHR congress Seoul, 44-54.

Chorin, A. (1968). Numerical solution of the Navier–Stokes equations. *Mathematics of Computation, 22*, 745-762.

Chorin, A. (1969). On the Convergence of Discrete Approximations to the Navier-Stokes Equations. *Mathematics of Computation, 23*(106), 341-353. doi:10.2307/2004428

Chue, S. (1980). Technical Note. Wave Run-up formula of Universal Applicability. *Proceedings of the Institution of Civil Engineers, 69*(4), 1035-1041. doi:doi:10.1680/iicep.1980.2185

Ciavola, P., Vicinanza, D., Aristodemo, F., & Constestabile, P. (2011). Large-scale morphodynamic experiments on a beach drainage system. *Journal of Hydraulic Research, 49*(4), 523-528.

Clauser, F. (1956). The turbulent boundary layer. *Advances in Applied Mechanics, 4*, 1-51.

Conley, D., & Griffin, J. (2004). Direct measurements of bed stress under swash in the field. *Journal of Geophysical Research: Oceans, 109*(C3), n/a-n/a. doi:10.1029/2003JC001899

Conley, D., & Inman, D. (1994). Ventilated Oscillatory Boundary Layers. *Journal of Fluid Mechanics, 273*, 261-284.

Contestabile, P., Aristodemo, F., Vicinanza, D., & Ciavola, P. (2012). Laboratory study on a beach drainage system. *Coastal Engineering, 66*(0), 50-64. doi:http://dx.doi.org/10.1016/j.coastaleng.2012.03.012

Cox, D., & Kobayashi, N. (2000). Identification of intense, intermittent coherent motions under shoaling and breaking waves. *Journal of Geophysical Research: Oceans, 105*(C6), 14223-14236. doi:10.1029/2000JC900048

Cox, R., & Tajziehchi, M. (2006). 2D experimental modelling of hydrodynamic effects of submerged breakwaters. *Coastal Dynamics, 1-12*.

Damiani, L., Petrillo, A., & Saponieri, A. (2009). *Beach dewatering systems: modelling coastal ground-water flow.* Proceeding of the 33th IAHR Congress Vancouver. 1-8.

Davis, G., Hanslow, D., Hibbert, K., & Nielsen, P. (1992). Gravity drainage: A new method of beach stabilisation through drainage of the water table. *International Conference on Coastal and Ocean Engineering*(23), 1129-1141.

De Rouck, J., Van de Walle, B., Troch, P., Van der Meer, J., Van Damme, L., Medina, J., . . . Frigaard, P. (2007). Wave Run-Up on the Zeebrugge Rubble Mound Breakwater: Full-Scale Measurement Results. *Journal of Coastal Research, 23*, 577-583.

de Waal, J., & van der Meer, J. (2012). *Wave run-up and overtopping on coastal structures.* Proceedings of 23rd Conference on Coastal Engineering, Venice, Italy. 1758-1771.

del Jesus, M., Lara, J., & Losada, I. (2012). Three-dimensional interaction of waves and porous coastal structures: Part I: Numerical model formulation. *Coastal Engineering, 64*, 57-72. doi:http://dx.doi.org/10.1016/j.coastaleng.2012.01.008

den Adel, H. (1987). *Cyclic permeability of granular material*. Delft Soil Mechanics (in Dutch) Report number CO-272550/35.

Drei, E., & Lamberti, A. (1999). *Wave pumping effect of a submerged barrier.* Proceedings of the Coastal Structures Conference, Santander. 667-673.

Durst, F., Melling, A., & Witelaw, J. (1981). *Principles and practice of laser-Doppler anemometry* (2nd ed.). Academic Press.

Edinburgh Desings Ltd. (2010). *Proposal for a recirculating coastal flume and ocean towing tank for University College London*

Engelund, F. (1954). *On the laminar and turbulent flows of ground water through homogeneous sand*. Trans. Danish Academy of Technical Studies. Bull, 4.

Ergun, S. (1952). Fluid flow through packed columns. *Chemical Engineering Progress, 48*(89-94).

EurOtop. (2007). *European Overtopping Manual*.

Foote, M., & Horn, D. (2002). Swash zone morphodynamics and uprush/backwash asymmetry. *Proceedings of the 28th International Conference on Coastal Engineering*(World Scientific), 980-992.

Forchheimer, P. (1901). Wasserbewegung durch Boden. *VDIZ*, 1782-1788.

Gourlay, M. (1992). Wave set-up, wave run-up and beach water table: Interaction between surf zone hydraulics and groundwater hydraulics. *Coastal Engineering*, 93-144.

Goda, Y., & Suzuki, T. (1976). *Estimation of incident and reflected waves in random wave experiments.* Proceedings of the 15th International Conference on Coastal Engineering, Honolulu. 828-845.

Grantham, K. (1953). *Wave run-up on sloping structures*. Trans. Am. Geophysics Union, Vol. 34, No. 5.

Gunbak, A. (1979). *Wave mechanics principles on the design of rubble mound breakwaters*. Norwegian Institute of Technology, POAC-79.

Herrington, T. (1993). *Laboratory Study of the Stabeach Erosion Control System*. Stevens Institute of Technology, New Jersey, 30p.

Higuera, P., Lara, J., & Losada, I. (2013a). Realistic wave generation and active wave absorption for Navier–Stokes models: Application to OpenFOAM®. *Coastal Engineering, 71*, 102-118. doi:http://dx.doi.org/10.1016/j.coastaleng.2012.07.002

Higuera, P., Lara, J., & Losada, I. (2013b). Simulating coastal engineering processes with OpenFOAM®. *Coastal Engineering, 71*, 119-134. doi:http://dx.doi.org/10.1016/j.coastaleng.2012.06.002

Higuera, P., Lara, J., & Losada, I. (2014). Three-dimensional interaction of waves and porous coastal structures using OpenFOAM®. Part I: Formulation and validation. *Coastal Engineering, 83*, 243-258. doi:http://dx.doi.org/10.1016/j.coastaleng.2013.08.010

Hirt, C., & Nichols, B. (1981). Volume of fluid (VOF) method for the dynamics of free boundaries. *Journal of Computational Physics, 39*(1), 201-225. doi:http://dx.doi.org/10.1016/0021-9991(81)90145-5

Holland, K., & Puleo, J. (2001). Variable swash motions associated with foreshore profile change. *Journal of Geophysical Research: Oceans, 106*(C3), 4613-4623. doi:10.1029/1999JC000172

Holman, R. (1986). Extreme value statistics for wave run-up on a natural beach. *Coastal Engineering, 9*(6), 527-544. doi:http://dx.doi.org/10.1016/0378-3839(86)90002-5

Horn, D. (2002). Beach groundwater dynamics. *Geomorphology, 48*(1–3), 121-146. doi:http://dx.doi.org/10.1016/S0169-555X(02)00178-2

Horn, D. (2006). Measurements and modelling of beach groundwater flow in the swash-zone: a review. *Continental Shelf Research, 26*, 622-652.

Horn, D., Baldock, T., & Ling, L. (2007). The influence of groundwater on profile evolution of fine and coarse sand beaches. In Kraus, N.C. and Rosati, J.D. (eds) Proceedings of the International Conference on Coastal Sediments 2007. Reston, Virginia: American Society of Civil Engineers, 506-519

Hsu, T., Liang, S., Young, B., & Ou, S. (2012). Nonlinear run-ups of regular waves on sloping structures. *Natural Hazards and Earth System Sciences, 12*(12), 3811-3820. doi:10.5194/nhess-12-3811-2012

Hudson, R. (1958). *Design of quarrystone cover layers of rubble-mound breakwater - hydraulic laboratory investigation*. WES Vicksburg, Report No.2-2.

Hughes, M., & Baldock, T. (2004). Eulerian flow velocities in the swash zone: Field data and model predictions. *Journal of Geophysical Research: Oceans, 109*, 1-11.

Hughes, M., Masselink, G., & Brander, R. (1997). Flow velocity and sediment transport in the swash zone of a steep beach. *Marine Geology, 138*(1), 91-103. doi:http://dx.doi.org/10.1016/S0025-3227(97)00014-5

Hughes, S. (2004a). Estimation of wave run-up on smooth, impermeable slopes using the wave momentum flux parameter. *Coastal Engineering, 11-12*, 1085-1104.

Hughes, S. (2004b). Wave momentum flux parameter: a descriptor for nearshore waves. *Coastal Engineering, 51*(11–12), 1067-1084. doi:http://dx.doi.org/10.1016/j.coastaleng.2004.07.025

Hughes, S. (2005). *Estimating Irregular Wave Run-up on Rough, Impermeable Slopes*. US Army Corps of Engineers, ERDC/CHL CHETN-III-70

Hunt, I. (1959). *Design of seawalls and breakwaters*. Journal of the Waterways and Harbors Division, Vol. 85, Issure 3, 123-152.

Technical Advisory Committee on Protection against Inundation (1974). *Wave Run-up and Overtopping*. Government Publishing Office, The Hague, 1974, 3.

Iribarren, C., & Nogales, C. (1949). *Protection des Ports.* XVII International Navigation Congress, Lisbon, SII-4. 31-80.

Isaacson, E. (1950). Water waves over a sloping bottom. *Communications on Pure and Applied Mathematics, 3*(1), 11-31. doi:10.1002/cpa.3160030103

Jensen, B., Jacobsen, N., & Christensen, E. (2014). Investigations on the porous media equations and resistance coefficients for coastal structures. *Coastal Engineering, 84*, 56-72.

Jensen, O.J. and Klinting P. (1983). *Evaluation of scale effects in hydraulic models by analysis of laminar and turbulent flows*. Coastal Engineering, 7, 319-329.

Kanazawa, H., Matsukawa, F., Katoh, K., & Hasegawa, I. (1996). *Experimental study on the effect of gravity drainage system on beach stabilization.* Coastal Engineering. 2640-2653.

Kang, H.-Y. (1995). *Watertable dynamics foced by waves.* (PhD), University of Queensland.

Kang, H.-Y., & Nielsen, P. (1996). Watertable dynamics in coastal areas. *Proceedings of the 25th International Conference on Coastal Engineering*, 4601-4612.

Kang, H.-Y., Nielsen, P., & Hanslow, D. (1994). *Watertable overheight due to wave runup on a sandy beach.* Proceedings of the 24th International Conference of Coastal Engineering. 2115-2124.

Katoh, K., & Yanagishima, S. (1996). *Field experiment of the effect of gravity drainage system on beach stabilization.* Coastal Engineering Conference, 2645-2665.

Kawata, Y., & Tsuchiya, Y. (1986). *Applicability of sub-sand system to beach erosion control.* Proceedings of the 20th International Conference on Coastal Engineering. 1255-1267.

Kececioglu, I., & Jiang, Y. (1994). Flow Through Porous Media of Packed Spheres Saturated With Water. *Journal of Fluids Engineering, 116*(1), 164-170. doi:10.1115/1.2910229

Keller, J., & Keller, H. (1964). *Water wave run-up on a beach*: Service Bureau Corp.

Kikkert, G., T., Pokrajac, D., O'Donoghue, T. (2009). Bed-shear stress in bore-generated swash on steep beaches. *Proceeding of the 6th International Conference on Coastal Dynamics,* 1,25.

Kikkert, G., O'Donoghue, T., Pokrajac, D., & Dodd, N. (2012). Experimental study of bore-driven swash hydrodynamics on impermeable rough slopes. *Coastal Engineering, 60*, 149-166. doi:http://dx.doi.org/10.1016/j.coastaleng.2011.09.006

Kikkert, G., Pokrajac, D., O'Donoghue, T., & Steenhauer, K. (2013). Experimental study of bore-driven swash hydrodynamics on permeable rough slopes. *Coastal Engineering, 79*, 42-56. doi:http://dx.doi.org/10.1016/j.coastaleng.2013.04.008

Kingston, K., & Murphy, J. (1996). *Wave run-up/run-down*. *MAST II*, Cork, Ireland. Report, 1996.

Kobayashi, N., Cox, D., & Wurjanto, A. (1990). Irregular Wave Reflection and Run-Up on Rough Impermeable Slopes. *Journal of Waterway, Port, Coastal, and Ocean Engineering, 116*(6), 708-726. doi:doi:10.1061/(ASCE)0733-950X(1990)116:6(708)

Kriezi, E., & Karambas, T. (2010). *Modelling wave deformation due to submerged breakwaters.* Proceedings of the ICE-Maritime Engineering. 19-29.

Krumbein, W., & Monk, G. (1943). Permeability as a Function of the Size Parameters of Unconsolidated Sand. doi:10.2118/943153-G

Lanckriet, T., Puleo, J., Masselink, G., Turner, I., Conley, D., Blenkinsopp, C., & Russell, P. (2013). Comprehensive Field Study of Swash-Zone Processes. II: Sheet Flow Sediment Concentrations during Quasi-Steady Backwash. *Journal of Waterway, Port, Coastal, and Ocean Engineering, 140*(1), 29-42. doi:10.1061/(ASCE)WW.1943-5460.0000209

Lara, J., Cowen, E., & Sou, I. (2002). A depth-of-field limited particle image velocimetry technique applied to oscillatory boundary layer flow over a porous bed. *Experiments in Fluids, 33*(1), 47-53. doi:10.1007/s00348-002-0461-4

Lara, J., Losada, I., & Guanche, R. (2008). Wave interaction with low-mound breakwaters using a RANS model. *Ocean Engineering, 35*(13), 1388-1400. doi:http://dx.doi.org/10.1016/j.oceaneng.2008.05.006

Lara, J., Losada, I., & Liu, P. (2006). Breaking waves over a mild gravel slope: Experimental and numerical analysis. *Journal of Geophysical Research: Oceans, 111*(C11), 2156-2202

Lara, J., Losada, I., Maza, M., & Guanche, R. (2011). Breaking solitary wave evolution over a porous underwater step. *Coastal Engineering, 58*, 837-850.

Lee, K., Mizutani, N., Hur, D., & Kamiya, A. (2007). The effect of groundwater on topographic changes in a gravel beach. *Ocean Engineering, 34*(3–4), 605-615. doi:http://dx.doi.org/10.1016/j.oceaneng.2005.10.026

Lin. (1998). *Numerical Modeling of Breaking Waves.* (Ph.D. thesis), Cornell University.

Lin, C., & Huang, C. (2004). Decomposition of incident and reflected higher harmonic waves using four wave gauges. *Coastal Engineering, 51*(5–6), 395-406. doi:http://dx.doi.org/10.1016/j.coastaleng.2004.04.004

Lin, C., Yeh, P., Kao, M., Yu, M., Hsieh, S., Chang, S., . . . Tsai, C. (2014). Velocity Fields in Near-Bottom and Boundary Layer Flows in Prebreaking Zone of a Solitary Wave Propagating over a 1:10 Slope. *Journal of Waterway, Port, Coastal, and Ocean Engineering, 141*(3), 04014038. doi:10.1061/(ASCE)WW.1943-5460.0000269

Lin, P., & Liu, P. (1998). A numerical study of breaking waves in the surf zone. *Journal of Fluid Mechanics, 359*, 239-264. doi:10.1017/S002211209700846X

Liu, P., Lin, P., Chang, K., & Sakakiyama, T. (1999). Numerical Modeling of Wave Interaction with Porous Structures. *Journal of Waterway, Port, Coastal, and Ocean Engineering, 125*(6), 322-330. doi:10.1061/(ASCE)0733-950X(1999)125:6(322)

Longo, S., Petti, M., & Losada, I. (2002). Turbulence in the swash and surf zones: a review. *Coastal Engineering, 45*(3–4), 129-147. doi:http://dx.doi.org/10.1016/S0378-3839(02)00031-5

Longuet-Higgins, M., & Stewart, R. (1964). Radiation stresses in water waves; a physical discussion, with applications. *Deep Sea Research and Oceanographic Abstracts, 11*(4), 529-562. doi:http://dx.doi.org/10.1016/0011-7471(64)90001-4

Lopes, J. (2012). Study of the flow of waves and currents *Instituto Superior Técnico*. Universidad de Lisboa.

Losada, I., Lara, J., Guanche, R., & Gonzalez-Ondina, J. (2008). Numerical analysis of wave overtopping of rubble mound breakwaters. *Coastal Engineering, 55*(1), 47-62. doi:http://dx.doi.org/10.1016/j.coastaleng.2007.06.003

Losada, M., & Giménez-Curto, L. (1980). Flow characteristics on rough, permeable slopes under wave action. *Coastal Engineering, 4*, 187-206. doi:http://dx.doi.org/10.1016/0378-3839(80)90019-8

Machemehl, J. L., French, T. J., & Huang, N. E. (1975). *New method for beach erosion control.* Proceeding: Engineering in the Oceans, American Society of civil Engineers Specialty Conference. 142-160.

Maclean, A. (1991). Open channel velocity profiles over a zone of rapid infiltration. *Journal of Hydraulic Research, 29*(1), 15-27. doi:10.1080/00221689109498990

Shore Protection Manual (1984). (4th Edition ed.). Washington, DC.

Mansard, E., & Funke, E. (1980). *The measurement of incident and reflected spectra using a least squares method.* Proceedings of the 17th International Conference on Coastal Engineering, Sydney. 154-172.

Mase, H. (1989). Random Wave Runup Height on Gentle Slope. *Journal of Waterway, Port, Coastal, and Ocean Engineering, 115*(5), 649-661. doi:doi:10.1061/(ASCE)0733-950X(1989)115:5(649)

Masselink, G., Evans, D., Hughes, M., & Russell, P. (2005). Suspended sediment transport in the swash zone of a dissipative beach. *Marine Geology, 216*(3), 169-189. doi:http://dx.doi.org/10.1016/j.margeo.2005.02.017

Masselink, G., & Hughes, M. (1998). Field investigation of sediment transport in the swash zone. *Continental Shelf Research, 18*(10), 1179-1199. doi:http://dx.doi.org/10.1016/S0278-4343(98)00027-2

Masselink, G., & Li, L. (2001). The role of swash infiltration in determining the beachface gradient: a numerical study. *Marine Geology, 176*(1–4), 139-156. doi:http://dx.doi.org/10.1016/S0025-3227(01)00161-X

Masselink, G., Ruju, A., Conley, D., Turner, I., Ruessink, G., Matias, A., . . . Wolters, G. (2016). Large-scale Barrier Dynamics Experiment II (BARDEX II): Experimental design, instrumentation, test program, and data set. *Coastal Engineering, 113*, 3-18. doi:http://dx.doi.org/10.1016/j.coastaleng.2015.07.009

Masselink, G., & Russell, P. (2006). Flow velocities, sediment transport and morphological change in the swash zone of two contrasting beaches. *Marine Geology, 227*(3–4), 227-240. doi:http://dx.doi.org/10.1016/j.margeo.2005.11.005

Masselink, G., Russell, P., Blenkinsopp, C., & Turner, I. (2010). Swash zone sediment transport, step dynamics and morphological response on a gravel beach. *Marine Geology, 274*(1–4), 50-68. doi:http://dx.doi.org/10.1016/j.margeo.2010.03.005

Masselink, G., & Turner, I. (2012). Large-scale laboratory investigation into the effect of varying back-barrier lagoon water levels on gravel beach morphology and swash zone sediment transport. *Coastal Engineering, 63*(0), 23-38. doi:http://dx.doi.org/10.1016/j.coastaleng.2011.12.007

Mayer, R., & Kriebel, D. (1994). *Wave run-up on composite-slope an concave beaches.* Proceedings of the 24th Coastal Engineering Conference, Kobe, Japan. 2325-2339.

McLean, R. F., & Kirk, R. M. (1969). Relationships between grain size, size-sorting, and foreshore slope on mixed sand - shingle beaches. *New Zealand Journal of Geology and Geophysics, 12*(1), 138-155. doi:10.1080/00288306.1969.10420231

Méhauté, L., Koh, R., & Hwang, L. (1968). A Synthesis on Wave Run-up. *Journal of the Waterways and Harbors Division, 94*(1), 77-92.

Melito, I., & Melby, J. (2002). *Wave runup ,transmission, and reflection for structures armored with CORE-LOC*. U.S. Army Engineer Research and Development Center, Coastal and Hydraulics laboratory, 3909 Halls Ferry Road

Miche, R. (1944). Mouvements ondulatoires de la mer en profondeur constante ou décroissante *Annales des Ponte et Chaussees*. Paris.

Mizuguchi, M. (1986). *Experimental study on kinematics and dynamics of wave breaking.* Proceedings of the 20th International Conference on Coastal Engineering, Reston, Va.

Muttray, M., Oumeraci, H., & ten Over, E. (2006). *Wave reflection and wave run-up at rubble mound breakwaters.* Proceedings of 30th International Conference on Coastal Engineering, San Diego, California, USA.

Nielsen, P. (1988). Wave setup: A field study. *Journal of Geophysical Research: Oceans, 93*(C12), 15643-15652. doi:10.1029/JC093iC12p15643

Nielsen, P. (1990). Tidal dynamics of the water table in beaches. *Water Resources Research, 26*(9), 2127-2134. doi:10.1029/WR026i009p02127

Nielsen, P. (1999). Groundwater Dynamics and Salinity in Coastal Barriers. *Journal of Coastal Research, 15*(3), 732-740. doi:10.2307/4298987

Nielsen, P, Robert, S., Moller-Christiansen, B., Olivia, P., (2001). Infiltration effects on sediment mobility under waves. Coastal Engineering 42, 1005-114.

Nielsen, P. (2009). *Coastal and Estuarine Processes*, World Scientific, Volume 29 of Advanced series on ocean engineering. ISSN 1793-074X.

O'Donoghue, T., Pokrajac, D., & Hondebrink, L. (2010). Laboratory and numerical study of dambreak-generated swash on impermeable slopes. *Coastal Engineering, 57*(5), 513-530. doi:http://dx.doi.org/10.1016/j.coastaleng.2009.12.007

UN Atlas of the Oceans (2010). *Percentage of total population living in coastal areas*. Report for the United Nations. http://www.un.org/esa/sustdev/natlinfo/indicators/methodology_sheets/oceans_seas_coasts/pop_coastal_areas.pdf

Ogden, M., & Weisman, R. (1991). Beach stabilization using drains - an experimental model study. *Coastal Sediments*. 1955-1969.

Oh, T., & Dean, R. (1992). *Beach Face Dynamics as Affected by Groundwater Table Elevations*. Tech Report UFL/COEL-92/004, Dept. of Coastal and Oceanographical Engineering, University of Florida, 35.

Oh, T., & Dean, R. (1994). *Effects of controlled water table on beach profile dynamics.* Proceedings of the 24th International Conference on Coastal Engineering. 2449-2460.

Oumeraci, H., Staal, T., Pförtner, S., & Ludwigs, G. (2010). Hydraulic performance, wave loading and response of PBA revetments and their foundations. *European Journal of Environmental and Civil Engineering, 16*(8), 953-980.

Pedersen, C., Deigaard, R., & Sutherland, J. (1993). *Turbulent measurements under breaking waves*. University of Denmark (pp. 91–97): Prog. Rep. ISVA 74.

Pedersen, G., Lindstrøm, E., Bertelsen, A., Jensen, A., Laskovski, D., & Sælevik, G. (2013). Runup and boundary layers on sloping beaches. *Physics of Fluids 25*(1), 012102.

Pedrozo-Acuña, A., Simmonds, D., Otta, A., & Chadwick, A. (2006). On the cross-shore profile change of gravel beaches. *Coastal Engineering, 53*(4), 335-347. doi:http://dx.doi.org/10.1016/j.coastaleng.2005.10.019

Pedrozo-Acuña, A., Torres-Freyermuth, A., Zou, Q., Hsu, T., & Reeve, D. (2010). Diagnostic investigation of impulsive pressures induced by plunging breakers impinging on gravel beaches. *Coastal Engineering, 57*(3), 252-266. doi:http://dx.doi.org/10.1016/j.coastaleng.2009.09.010

Petti, M., & Longo, S. (2001). Turbulence experiments in the swash zone. *Coastal Engineering, 43*(1), 1-24. doi:http://dx.doi.org/10.1016/S0378-3839(00)00068-5

Pintado-Patiño, J., Torres-Freyermuth, A., Puleo, J., & Pokrajac, D. (2015). On the role of infiltration and exfiltration in swash zone boundary layer dynamics. *Journal of Geophysical Research: Oceans, 120*(9), 6329-6350. doi:10.1002/2015JC010806

Pocklington, H. (1921). *Standing waves parallel to a plane beach.* Proceedings of the Cambridge Phil. Soc., 308-310.

Polubarinova-Kochina, P. (1962). *Theory of Ground Water Movement*. Princeton, USA.

Puleo, J., Beach, R., Holman, R., & Allen, J. (2000). Swash zone sediment suspension and transport and the importance of bore-generated turbulence. *Journal of Geophysical Research: Oceans, 105*(C7), 17021-17044. doi:10.1029/2000JC900024

Puleo, J., Blenkinsopp, C., Conley, D., Masselink, G., Turner, I., Russell, P., . . . Poate, T. (2013). Comprehensive Field Study of Swash-Zone Processes. I: Experimental Design with Examples of Hydrodynamic and Sediment Transport Measurements. *Journal of Waterway, Port, Coastal, and Ocean Engineering, 140*(1), 14-28. doi:10.1061/(ASCE)WW.1943-5460.0000210

Rao, A.R., Subrahmannyam, V, Thayumanavan, S., Namboodiripad, D., (1994). Seepage effects on sand-bed channels.. *Journal of Irrigation and Drainage Engineering, 120*(1), 60-79.

Raubenheimer, B. (2002). Observations and predictions of fluid velocities in the surf and swash zones. *Journal of Geophysical Research: Oceans, 107*(C11), 11-11-11-17. doi:10.1029/2001JC001264

Raubenheimer, B., Elgar, S., & Guza, R. (2004). Observations of swash zone velocities: A note on friction coefficients. *Journal of Geophysical Research: Oceans, 109*(C1), C01027. doi:10.1029/2003JC001877

World Ocean Review (2016). Living with the oceans. – A report on the state of the world's oceans, http://worldoceanreview.com/en/wor-1/coasts/living-in-coastal-areas/

Ruggiero, P., Komar, P., McDougal, W., Marra, J., & Beach, R. (2001). Wave runup, extreme water levels and the erosion of properties backing beaches. *Journal of Coastal Research, 2*, 407-419.

Rundgren, L. (1958). *Water Wave Forces: A theoretical and laboratory study*. Bulletin of the Division of Hydraulics at the Royal Institute of Technology, Stockholm, Sweden.

Sato, M. (1990). *Underground water table and beach face erosion.* Proceedings of the 22nd International Conference on Coastal Engineering, 2644-2657.

Savage, R. (1958). Wave run-up on roughned and permeable slopes. *Journal of the Waterways and Harbors Division*, American Society of Civil Engineers, 852-870.

Saville, T. (1955). *Laboratory data on wave run-up and overtopping on shore structures*. No. TM64, Coastal Engineering Research Center, Vicksburg, US.

Saville, T. (1957). *Wave run-up on composite slopes.* Proceedings of 6th Conference on Coastal Engineering, Gainesville, Florida. 1 (6) 41.

Sawaragi, T., Iwata, K., & Kobayashi, M. (1982). Conditon and probability of occurrence of resonance on steep slopes of coastal structures. *Coastal engineering in Japan, 25*.

Schäffer, H., & Klopman, G. (2000). Review of Multidirectional Active Wave Absorption Methods. *Journal of Waterway, Port, Coastal, and Ocean Engineering, 126*(2), 88-97. doi:10.1061/(ASCE)0733-950X(2000)126:2(88)

Schimmels, S., Vousdoukas, M., Wziatek, D., Becker, K., Gier, F., & Oumeraci, H. (2012). *Wave run-up observations on revetments with different porosities.* Coastal Engineering Proceedings. 1 (33) 73.

Schüttrumpf, H. (2001). *Wellenüberlaufsromung bei See-deichen.* (Ph.D. Thesis), Technical University Braunschweig.

Shankar, N., & Jayaratne, M. (2003). Wave run-up and overtopping on smooth and rough slopes of coastal structures. *Ocean Engineering, 30*(2), 221-238. doi:10.1016/S0029-8018(02)00016-1

Shin, S., & Cox, D. (2006). Laboratory observations of inner surf and swash-zone hydrodynamics on a steep slope. *Continental Shelf Research, 26*(5), 561-573. doi:http://dx.doi.org/10.1016/j.csr.2005.10.005

Sou, I., & Yeh, H. (2011). Laboratory study of the cross-shore flow structure in the surf and swash zones. *Journal of Geophysical Research: Oceans, 116*(C3).

Soulsby, R. (1997). *Dynamics of Marine Sands*: *A manual for practical aplications.* ICE Publishing. Thomas Telford.

Stagonas, D., Buldakov, E. & Simons, RR. (2014). Focusing unidirectional wave groups on finite water depth with and without currents. Proceedings of the 34Th Conference of Coastal Engineering. Seoul, South Korea. 31-37.

Stive, M. (1980). Velocity and Pressure Field of Spilling Breakers. *Coastal Engineering Proceedings*(17). doi:10.9753/icce.v17.%p

Stoa, N. (1978). *Reanalysis of wave runup on structures and beaches*. No. CERC-TP-78-2. Coastal Engineering Research Center, Fort Belvoir, USA.

Stockdon, H., Sallenger Jr, A., Holman, R., & Howd, P. (2006). A simple model for the spatially-variable coastal response to hurricanes. *Marine Geology, 238*(1–4), 1-20. doi:http://dx.doi.org/10.1016/j.margeo.2006.11.004

Szmytkiewicz, M., Zeidler, R., & Pilarczyk, K. (1994). *Irregular wave run-up on composite rough slopes.* Coastal Dynamics, ASCE, 599-613..

Takada, A. (1970). On relation among wave run-up, overtopping and reflection. *Proceedings of the Japan Society of Civil Engineers, 1970*(182), 19-30. doi:10.2208/jscej1969.1970.182_19

Tautenhain, E., Kohlhase, S., & Partenscky, H. (1982). *Wave run-up at sea dikes under oblique wave approach.* Proceedings of the 18th Coastal Engineering Conference, 804-810.

Timur, A. (1968). An Investigation Of Permeability, Porosity and Residual Water Saturation Relationships For Sandstone Reservoirs, *SPWLA 9th annual logging symposium,* Society of Petrophysicists and Well-Log Analysts.

Ting, F., & Kirby, J. (1996). Dynamics of surf-zone turbulence in a spilling breaker. *Coastal Engineering, 27*(3), 131-160. doi:http://dx.doi.org/10.1016/0378-3839(95)00037-2

Torres-Freyermuth, A., Lara, J., & Losada, I. (2010). Numerical modelling of short- and long-wave transformation on a barred beach. *Coastal Engineering, 57*(3), 317-330. doi:http://dx.doi.org/10.1016/j.coastaleng.2009.10.013

Torres-Freyermuth, A., Losada, I., & Lara, J. (2007). Modeling of surf zone processes on a natural beach using Reynolds-Averaged Navier-Stokes equations. *Journal of Geophysical Research: Oceans, 112*(C9), 2156-2202

Torres-Freyermuth, A., Puleo, J., & Pokrajac, D. (2013). Modeling swash-zone hydrodynamics and shear stresses on planar slopes using Reynolds-Averaged Navier-Stokes equations. *Journal of Geophysical Research: Oceans, 118*(2), 1019-1033. doi:10.1002/jgrc.20074

Turner, I., Coates, B., & Acworth, R. (1997). Tides, Waves and the Super-elevation of Groundwater at the Coast. *Journal of Coastal Research, 13*(1), 46-60. doi:10.2307/4298589

Turner, I., & Masselink, G. (2012). Coastal gravel barrier hydrology — Observations from a prototype-scale laboratory experiment (BARDEX). *Coastal Engineering, 63*(0), 13-22. doi:http://dx.doi.org/10.1016/j.coastaleng.2011.12.008

Turner, I., Rau, G., Andersen, M., Austin, M., Puleo, J., & Masselink, G. (2013). Coastal sand barrier hydrology – observations from the BARDEX II prototype-scale laboratory experiment. *Journal of Coastal Research*, 1886-1891. doi:10.2112/SI65-319.1

Van Baaren, J. (1979). *Quick-Look Permeability Estimates Using Sidewall Samples and Porosity Logs.* Trans., 6th Annual European Logging Symposium.

Van Broekhoven, P. (2011). *The influence of armour layer and core permeability on the wave run-up.* (Masters Master Thesis), Delft University of Technology.

Van der Meer, J. (1988). *Rock slopes and gravel beaches under wave attack.* (Ph.D), Faculty of Civil Engineering, Delft University of Technology.

Van der Meer, J. (1992). Conceptual Design of Rubble Mound Breakwaters *Design and Reliability of Coastal Structures, short course during the 23rd ICCE in Venice*.

Van Gent, M. (1993). *Stationary and oscillatory flow through coarse porous media*. Faculty of Civil Engineering. Delft University of Technology,

Van Gent, M. (1995). Porous Flow through Rubble-Mound Material. *Journal of Waterway, Port, Coastal, and Ocean Engineering, 121*(3), 176-181. doi:10.1061/(ASCE)0733-950X(1995)121:3(176)

Venkataraman, P., & Rao, P. (1998). Darcian, Transitional, and Turbulent Flow through Porous Media. *Journal of Hydraulic Engineering, 124*(8), 840-846. doi:10.1061/(ASCE)0733-9429(1998)124:8(840)

Villarroel-Lamb, D., Hammeken, A., & Simons, R. (2014, 10/02/). *Quantifying the effect of bed permeability on maximum wave run-up.* Proceedings of 34th Conference on Coastal Engineering, Seoul, Korea, 2014. 1 (34) p 45.

Vousdoukas, M., Dagmara, W., & Almeida, L. (2012). Coastal vulnerability assessment based on video wave run-up observations at a mesotidal, steep-sloped beach *Ocean Dynamics* (Vol. 62, pp. 123-137).

Ward, J. (1964). Turbulent Flow in Porous Media. *Journal of the Hydraulics Division, 90*(5), 1-12.

Watters, G.Z., & Rao, P. (1971). Hydrodynamic effects of seepage on bed particles. *Journal of the Hydraulic Division*, 421-439.

Wassing, F. (1957). *Model investigations of wave run-up on dikes carried out in the Netherlands in the last 20 years.* Proceedings of the 6th Coastal Engineering Conference, Florida, USA. (6) 42.

Weisman, R., Seidel, G., & Ogden, M. (1995). Effect of Water-Table Manipulation on Beach Profiles. *Journal of Waterway, Port, Coastal and Ocean Engineering*. 134-142.

Willets,B.B. & Drossos, M.E. (1975). Local erosion caused by rapid infiltration. *Journal of the Hydraulic Division,* 1477-1488*.*

Williams, J., Buscombe, D., Masselink, G., Turner, I., & Swinkels, C. (2012). Barrier dynamics experiment (BARDEX): Aims, design and procedures. *Coastal Engineering, 63*(0), 3-12. doi:http://dx.doi.org/10.1016/j.coastaleng.2011.12.009

Williams, J., Masselink, G., Buscombe, D., Turner, I., Matias, A., Ferreria, O., . . . Pan, S. (2010). BARDEX (barrier dynamics experiment): A laboratory study of gravel barrier response to waves and tides. *Proceedings of the HYDRALAB III Joint User Meeting, Hannover*.

Yeh, H. (1991). Vorticity-Generation Mechanisms in Bores. *Proceedings of the Royal Society of London. Series A: Mathematical and Physical Sciences, 432*(1885), 215.

Zhang, Q., & Liu, P. (2008). A numerical study of swash flows generated by bores. *Coastal Engineering, 55*(12), 1113-1134.

Appendix A

Hydraulic Conductivity Measurements

One of the main aims of this study was to consider the influence of hydraulic conductivity on run-up formulae by including a non-dimensional hydraulic conductivity parameter into these formulae. To do this, it was necessary to know the hydraulic conductivity, K, of the reticulated open-cell foams used in the laboratory experiments. However, companies do not have information about the K values of the reticulated open-cell foams. For this reason, a series of constant head tests were carried out using a *permeameter* to estimate the K values of eight foams with different PPI values. Additional tests were also carried out to a range of different grain soils (varying from coarse sands to medium gravels). This was performed to select the foams which could be equivalent or similar hydraulic conductivity to a coarse sand or a medium gravel beach.

Two types of tests are commonly performed with a permeameter to measure the hydraulic conductivity of soils: the *constant head* test and the *falling head* test. The constant head test is commonly recommended for more permeable materials such as coarse-grained soils, while for less permeable materials the falling head test is recommended. In this case, as all the foams and soils tested were more permeable than a fine-grain soil, the constant head test was chosen. The constant head test involves the flow of water through a permeable material contained in a test cylinder under a constant hydraulic head. The cylinder is connected to a water reservoir (constant head tank) for which the hydraulic head is held constant. This procedure allows water to move through the permeable material under a steady state head condition while the volume of water flowing out of the test cylinder is measured over a period of time.

Theory of tests. The hydraulic conductivity is equal to the rate of flow of water through a unit cross section area under a unit hydraulic gradient. In the constant head test, the flow through the specimen remains constant so the hydraulic conductivity can be obtained using Darcy's law: $k = qL/Ah$, where q is the discharge, L is the length of the specimen, h is the head causing the flow and A is the cross-sectional area of the specimen.

Two sets of experiments were carried out in this study using two cylindrical permeameters with different diameters. The permeameter used in the first set of tests had an internal diameter of d = 2.96cm (Figure 184), while the permeameter used in the second set of tests had an internal diameter of d = 7.5cm (Figure 185).

Tests Procedure. Before starting the tests, it was necessary to cut each foam into a cylindrical shape with the same diameter as the internal diameter of the test cylinder.

Each foam was then introduced into the test cylinder, making sure it fitted correctly (without compressing the foam, as this could affect its hydraulic conductivity), and all the tubes in the system were connected. Figure 186 shows the cylindrical shaped foams introduced inside the 7.5cm permeameter. When the head at the tank was constant, the valve was opened to allow water flow into the sample. Before measuring the flow rate, water was let to flow through the sample for a few minutes to make sure any trapped air or bubbles were removed. Once the sample was fully saturated, a graduated jar was used to measure the volume of water Q and a stop-watch were used to measure time t required for the selected volume to be filled. This flow rate measurement (Q/t) was repeated five times, and the average was estimated.

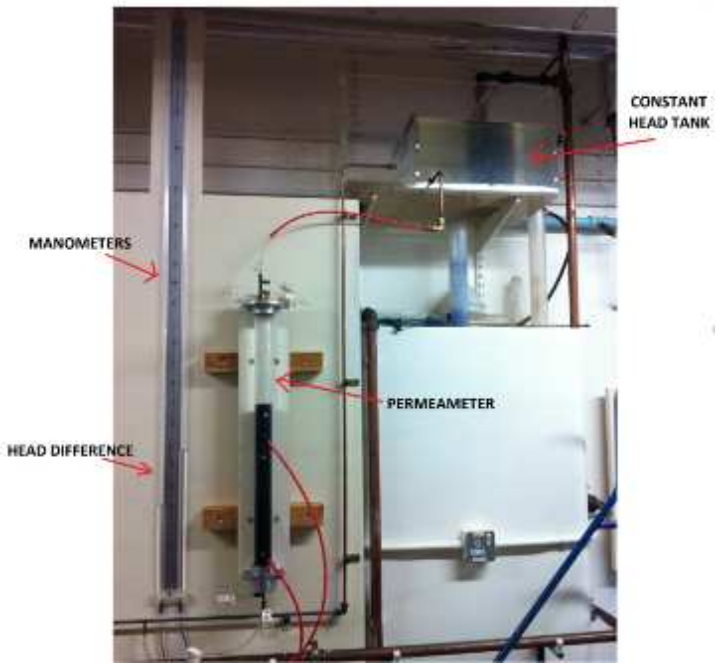

Figure 184 Setup of constant head tests with the d = 2.96cm permeameter

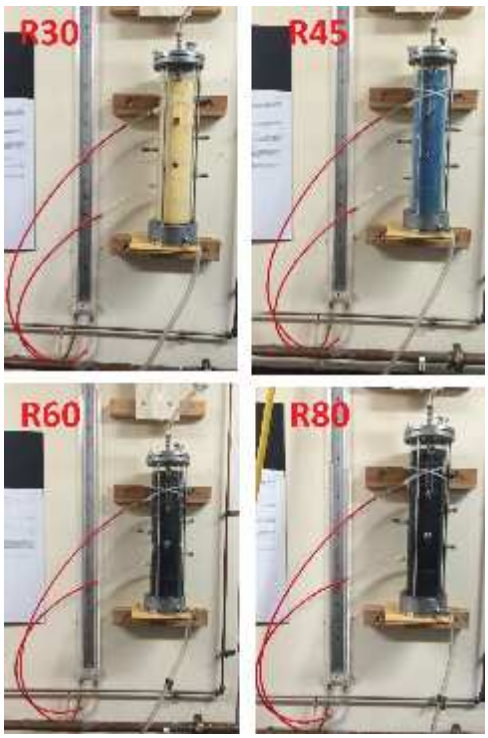

Figure 185 Second set of tests with the *d* = 7.5cm permeameter

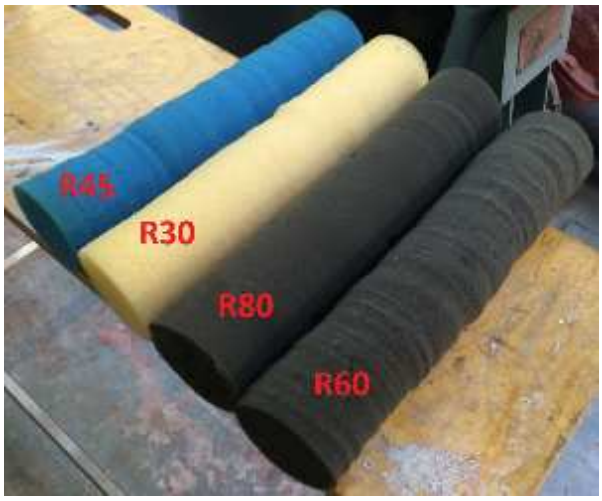

Figure 186 Cylindrical foams used for constant head tests

The results from the first set of tests are summarised in Table 58. As can be seen, the 85 PPI (0.0311m/s) foam had similar hydraulic conductivity values as a fine gravel soil with a size range between 2.4 – 4.0mm (0.0289m/s); the 45 PPI (0.105m/s) foam was similar to the hydraulic conductivity of a medium gravel soil 6.0-9.4mm (0.1182m/s); while the 30 PPI foam's hydraulic conductivity value (0.401m/s) lied between the values of the 6.0-9.4mm and the 9.4-13mm medium gravels. These three foams 85, 45, and 30 PPI were selected to be used on the preliminary run-up experiments.

The results from the second set of tests using the larger permeameter are shown in Table 59. These tests were carried out with the aim of measuring the 4 reticulated open-cell foams used for the experiments described in Section 4.3.2 and validate the results

obtained from the smaller permeameter. As can be seen, the hydraulic conductivities obtained for the R30, R60 and R80 foams are very similar to those obtained in the smaller permeameter. The main difference between both tests was seen on the R45 foam. The results from this second set of tests were used in the analysis shown in Chapter 6.

As mentioned in Section 4.3.1, the rest of the beach permeable beach on the preliminary tests consisted of hessian sacks filled with 4 mm diameter EPS (expanded polystyrene) beads. These hessian sacks and EPS beads were also tested in the permeameter.

MATERIAL	K (m/s)
Foams:	
85 PPI	0.0311
80 PPI	0.041
60 PPI	0.091
45 PPI	0.105
30 PPI	0.401
20 PPI	0.433
15 PPI	0.450
10 PPI	0.878
Polystyrene Beads (D_{50}=5 mm)	0.0156
Polystyrene Beads with Hessian Layers	0.0126
Soils (size range):	
Coarse Sand (1.7 - 2.5 mm)	0.0126
Fine Gravel (2.4 - 4.0 mm)	0.0289
Fine Gravel (4.0 – 6.0 mm)	0.0478
Medium Gravel (6.0 – 9.4 mm)	0.1182
Medium Gravel (9.4 – 13.0 mm)	1.262

Table 58 Hydraulic conductivities estimated using a d = 2.96cm permeameter

MATERIAL	K (m/s)
80 PPI	0.052
60 PPI	0.086
45 PPI	0.192
30 PPI	0.401

Table 59 Hydraulic conductivities estimated using a d = 7.5cm permeameter

Appendix B

Bonding materials tested to construct a non-deformable beach

To construct a non-deformable beach, it is not necessary to bond the entire beach, only the upper layer of the beach would need to be bonded to prevent beach deformation. This was demonstrated by Kikkert et al. (2012) where the upper layer of their non-deformable permeable slopes was bonded using a cement-water mix, while the sediments inside of the beach remained without any bonding material. Kikkert's experiments were performed testing solitary surging (non-breaking) waves which did not cause much damage in deforming the beach profile. However, these tests were planned to involve periodic plunging waves breaking at the slope, which are likely to cause significant beach deformation. Therefore, several bonding materials and options were investigated for constructing the non-deformable permeable beaches. Sample test were performed aimed to find a bonding material that could strongly bond the sediments without affecting the hydraulic conductivity of the beach. The bonding materials analysed were tested to bond three different sizes of aggregates: 2, 5 and 10mm. These are summarised in Table 60, where their main advantages and disadvantages are shown. Figure 187 shows some of the tested samples of aggregates mixed with the bonding materials shown in Table 60.

Bonding Material	Advantages	Disadvantages
Cement-water mix	- It has been used before in similar experiments with positive results - Does not have a significant effect on hydraulic conductivity - Cheap - Could work better for coarser sediments	- Hard to find the mix right ratio for each sediment size - Takes a lot of time to cure - Might erode as water runs through the sediments - Not strong enough and sediments can detach
Varnish (polyurethane)	- Easy to mix - Bonds sediments well - Could work better for coarser sediments	- Affects hydraulic conductivity - Not very resistant to water
Silicone	- Easy to mix	- Affects hydraulic conductivity - Not strong enough
Resin bound aggregate (aliphatic polymer resin)	- Strong and durable - Dries quickly - Water resistant - Could work better for coarser sediments	- Affects the hydraulic conductivity
Lacquer Spray	- Easy to mix	- Not strong enough - Affects hydraulic conductivity
Wood adhesive	- Dries almost immediately - Easy to mix	- Not strong enough, very flexible - Not water resistant - Affects hydraulic conductivity
Elastocoast (mix of isocyanate and polyol)	- Specially design for bonding revetments - Strong - Does not affect hydraulic cond.	- Expensive

Table 60 Bonding materials tested for constructing a non-deformable permeable beach

Figure 187 Samples of bonding materials

From all the tested bonding materials, only Elastocoast was found to strongly bond the aggregates without having affecting its hydraulic conductivity. The cement-water mixed also did not affect the hydraulic conductivity of the aggregates, but was its bonding was not strong enough to resist the impact of breaking waves at the slope. Elastocoast is a bonding system that works on the basis of mixing two polyurethane components (isocyanate and polyol) and has been used in coastal protection structures (mainly revetments). A sample of gravel bonded with Elastocoast is shown in Figure 188.

Figure 188 Sample of gravel bonded with Elastocoast

However, the constructing a permeable structure using sediment mixed with Elastocoast has two main disadvantages. The first one being its construction cost. The amount of material required to construct the slopes using sediment mixed with Elastocoast inside the 20m long, 1.2wide wave flume exceeded the tests' budget. The second disadvantage was the amount of time required to construct it. The wave flumes are constantly used by other students and researchers, so there are many time constraints when performing tests in the flumes. This means that if an Elastocoast beach was chosen, it would be possible to carry out only a small amount of tests, with probably only one slope angle.

These tests were planned to be carried out in the 20m long, 1.2m wide wave flume, which is also commonly used by other students and researchers. Consequently, it was only possible to book the wave flume for one month. Constructing the beaches out of sediment mixed with Elastocoast and setting it up inside the wave flume would require a considerate amount of time and sediment material. Furthermore, as one of the objectives of the experiments was to carry out tests over different beach slope angles, with an Elastocoast-sediment mix beach, it would have been tough and time consuming to change the setup to increase the angle of each permeable beach. So if this setup was followed, only a small amount of test would have been able to carry out. For this reason a different alternative material to construct the beaches was considered. It was decided that the best option to construct a permeable beach would be using *reticulated polyether open-cell foams.*

Appendix C

Wave Reflection. Waves generated in the wave flume are reflected by the beaches. To analyse the reflection coefficients from each test, it is necessary to separate the measured wave into its incident and reflected wave components.

To correctly estimate the reflection coefficients, three parameters need to be defined before recording the surface elevations with the wave gauges: 1) the number of wave gauges used and the distance between them; 2) the recording sample frequency; and 3) the sampling duration.

Number of wave gauges and distances between them. The wave gauges used were denoted WG1, WG2, WG3 and WG4 respectively, while Δx_1 is the distance between WG1 and WG2, Δx_2 the distance between WG1 and WG3, and Δx_3 the distance between WG1 and WG4, as illustrated in Figure 189.

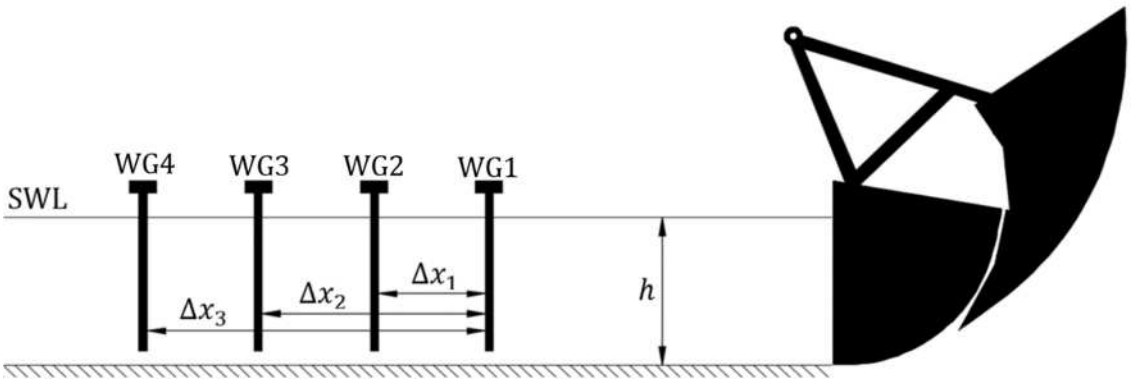

Figure 189 Distance between resistance wave gauges

The number of wave gauges used and the distance between them depends on the method chosen to decompose the incident and reflected wave components. Several methods have been proposed, the most popular ones being Goda and Susuki (1976), Mansard and Funke (1980) and Lin and Huang (2004). In the present study, the reflection analysis was carried out using both Mansard and Funke (1980) and Lin and Huang (2004) methods.

The Lin and Huang (2004) method was used for all the tests carried out in the 20m long wave flume. This method requires the use of four wave gauges to decompose the higher harmonics into their free and bound modes. To avoid the singularity condition, the distances between the four wave gauges were set at: Δx_1=2m, Δx_2=4m, and Δx_3=6m (Figure 189). The reflection analysis was performed using a Matlab script.

The second method used is the least squares fit method of Mansard and Funke (1980). This method was used in all the tests performed in the 13.4m long wave flume and

requires the use of three wave gauges. The recommended distance for Δx_1 is $L/10$, while the distance for Δx_2 can be estimated fulfilling the following conditions:

- $L/6 < \Delta x_2 < L/3$
- $\Delta x_2 \neq L/5$
- $\Delta x_2 \neq 3L/10$

To fulfil these conditions, $L/4$ was chosen for Δx_2. Table 61 shows the distances used for Δx_1 and Δx_2 corresponding to each wave period and wave length. The wave lengths were determined using Linear Wave Theory. To set these distances, WG1 was always placed at 3.6m from the wave generator, while WG2 and WG3 were adjusted along the flume depending on the wave period used.

T (s)	***L (m)***	Δx_1 ***(m)***	Δx_2 ***(m)***
3.33	5.61	0.56	1.40
2.86	4.78	0.48	1.20
2	3.26	0.32	0.82
1.43	2.21	0.22	0.55
1	1.37	0.14	0.34

Table 61 Distances between wave gauges for the tests performed in the 13.4m long wave flume

This analysis was performed using the *WS Reflection Analysis* tool in *MIKE WSWAT*. The complete instructions and procedures for using this module can be found in the User Guide of the WS Wave Analysis Tools of MIKE by DHI (2011).

Sample frequency of wave gauges. The output voltage data from the wave gauges is recorded in time domain at a specific sample frequency, f_s. To view the amplitude of each frequency component contained within the wave, these data have to be transformed into frequency domain using a Fast Fourier Transform (FFT) algorithm.

The frequency chosen to sample a continuous time-series influences the quality of the spectrum calculated by the Fast Fourier Transform (FFT). One common problem that could occur if the wrong sample frequency is chosen is *aliasing.* An example of this is illustrated in Figure 190, where a sine wave with signal frequency of f =3.5Hz (orange line) is being recorded at a sampling frequency of f_s=4Hz (black dots).

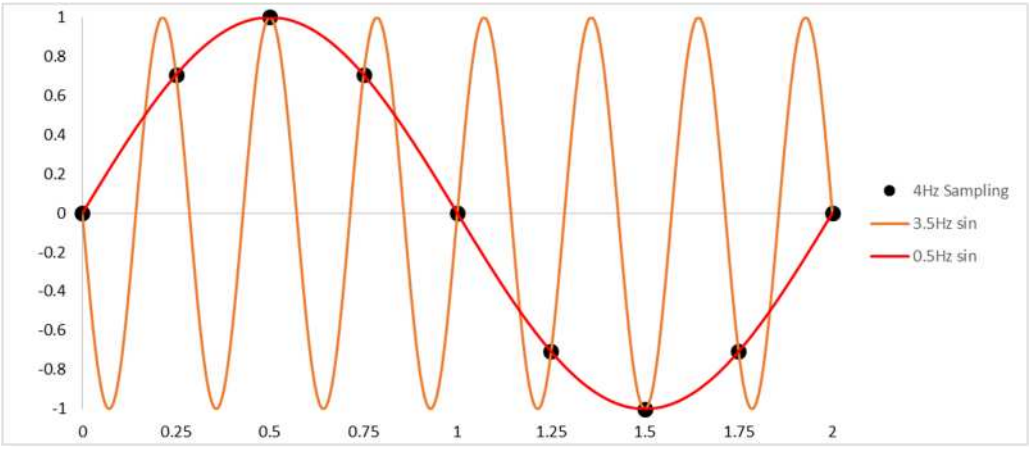

Figure 190 Example of aliasing problem

The maximum frequency that can be analysed correctly must be smaller than the Nyquist frequency, defined as $f_s/2$. In this case the Nyquist frequency is equal to 2Hz. As can be seen, the recorded 3.5Hz signal is larger than 2Hz and as a consequence, it is being recorded as a 0.5Hz signal (red line). To avoid this problem, the frequency of the signal being measured has to be inside the frequency bandwidth delimited by: $0 < f < f_s/2$.

Sampling duration. The sampling duration must be set such that an integer number of signal periods can be recorded, if not errors will arise in the FFT analysis. The sampling duration, T_s, defines the frequency resolution, f_R, which is defined as:

$$f_R = {}^{1}/_{T_s}$$

The fundamental frequency of the incident wave, should be an integer multiple of the frequency resolution so that it fits exactly within a frequency band. An error known as 'spilling' occurs in the FFT if the frequency component of a signal being measured is not an integer multiple of the frequency resolution. If this happens, the amplitude of the real component will be spread over the nearest frequency bands in the FFT.

In this study, the fundamental frequencies of the generated waves were: 0.3, 0.35, 0.5, 0.7 and 1Hz. To fulfil the sampling frequency and sampling duration requirements, and avoid the aliasing problem, a sample frequency of $f_s = 10Hz$ and a sampling duration of $T_s = 120s$ were chosen for all tests. This meant that a total of 1200 data points were required to analyse each wave. Table 62 shows the number of waves that fitted within the selected sampling duration of 120s, for each of the wave frequencies analysed.

Frequency (Hz)	Period (s)	Number of Waves
0.3	3.333	36
0.35	2.857	42
0.5	2	60
0.7	1.429	84
1	1	120

Table 62 Table showing the number of waves within a sampling duration of 120s

Appendix D

This appendix shows all the parameters and run-up measurements from the experiments described in Section 4.3.

Run-up measurements on rough-permeable slopes (Section 4.3.2.)

Parameters	Variables
Wave flume dimensions	13.4m long and 0.45m width
Slope angle	10˚, 20˚ and 30˚
Hydraulic conductivities	0.051, 0.086, 0.192 and 0.401 m/s
Types of waves	Regular Waves
Water depth	0.3m
Wave heights	0.04, 0.06, 0.08, 0.1, and 0.12m
Wave periods	1, 1.43, 2, 2.86, and 3.33s
Iribarren number	Between 0.63 and 12
Wave steepness (H/L)	Between 0.002 and 0.08
Number of tests	300

Table 63 Summary of parameters used for the rough-permeable slopes

#	α (˚)	tanα	cotα	h (m)	T (s)	H (m)	fr (htz)	Lo (m)	h/Lo	H/L	H/h	ξ	ϕ	tanα/(H/h)	R	R/H	R/h
1	10	0.18	5.67	0.3	1	0.04	1	1.56	0.19	0.0256	0.13	1.1	0.21	1.32	0.03	0.70	0.09
2	10	0.18	5.67	0.3	1	0.06	1	1.56	0.19	0.0385	0.20	0.9	0.17	0.88	0.04	0.58	0.12
3	10	0.18	5.67	0.3	1	0.08	1	1.56	0.19	0.0513	0.27	0.78	0.15	0.66	0.05	0.58	0.15
4	10	0.18	5.67	0.3	1	0.1	1	1.56	0.19	0.0641	0.33	0.7	0.13	0.53	0.05	0.49	0.16
5	10	0.18	5.67	0.3	1	0.12	1	1.56	0.19	0.0769	0.40	0.64	0.12	0.44	0.05	0.42	0.17
6	10	0.18	5.67	0.3	1.43	0.04	0.7	3.18	0.09	0.0126	0.13	1.57	0.15	1.32	0.04	0.95	0.13
7	10	0.18	5.67	0.3	1.43	0.06	0.7	3.18	0.09	0.0188	0.20	1.28	0.12	0.88	0.05	0.89	0.18
8	10	0.18	5.67	0.3	1.43	0.08	0.7	3.18	0.09	0.0251	0.27	1.11	0.10	0.66	0.06	0.77	0.21
9	10	0.18	5.67	0.3	1.43	0.1	0.7	3.18	0.09	0.0314	0.33	0.99	0.09	0.53	0.07	0.69	0.23
10	10	0.18	5.67	0.3	1.43	0.12	0.7	3.18	0.09	0.0377	0.40	0.91	0.09	0.44	0.09	0.71	0.29
11	10	0.18	5.67	0.3	2	0.04	0.5	6.24	0.05	0.0064	0.13	2.2	0.11	1.32	0.04	1.09	0.14
12	10	0.18	5.67	0.3	2	0.06	0.5	6.24	0.05	0.0096	0.20	1.8	0.09	0.88	0.06	1.05	0.21
13	10	0.18	5.67	0.3	2	0.08	0.5	6.24	0.05	0.0128	0.27	1.56	0.07	0.66	0.07	0.91	0.24
14	10	0.18	5.67	0.3	2	0.1	0.5	6.24	0.05	0.0160	0.33	1.39	0.07	0.53	0.09	0.86	0.29
15	10	0.18	5.67	0.3	2	0.12	0.5	6.24	0.05	0.0192	0.40	1.27	0.06	0.44	0.10	0.82	0.33
16	10	0.18	5.67	0.3	2.86	0.04	0.35	12.7	0.02	0.0031	0.13	3.15	0.07	1.32	0.05	1.33	0.18
17	10	0.18	5.67	0.3	2.86	0.06	0.35	12.7	0.02	0.0047	0.20	2.57	0.06	0.88	0.07	1.22	0.24
18	10	0.18	5.67	0.3	2.86	0.08	0.35	12.7	0.02	0.0063	0.27	2.22	0.05	0.66	0.09	1.14	0.30
19	10	0.18	5.67	0.3	2.86	0.1	0.35	12.7	0.02	0.0079	0.33	1.99	0.05	0.53	0.11	1.14	0.38
20	10	0.18	5.67	0.3	2.86	0.12	0.35	12.7	0.02	0.0094	0.40	1.82	0.04	0.44	0.13	1.09	0.43
21	10	0.18	5.67	0.3	3.33	0.04	0.3	17.3	0.02	0.0023	0.13	3.67	0.06	1.32	0.06	1.47	0.20
22	10	0.18	5.67	0.3	3.33	0.06	0.3	17.3	0.02	0.0035	0.20	3	0.05	0.88	0.08	1.33	0.27
23	10	0.18	5.67	0.3	3.33	0.08	0.3	17.3	0.02	0.0046	0.27	2.6	0.04	0.66	0.10	1.28	0.34
24	10	0.18	5.67	0.3	3.33	0.1	0.3	17.3	0.02	0.0058	0.33	2.32	0.04	0.53	0.12	1.21	0.40
25	10	0.18	5.67	0.3	3.33	0.12	0.3	17.3	0.02	0.0069	0.40	2.12	0.04	0.44	0.14	1.16	0.46
26	20	0.36	2.75	0.3	1	0.04	1	1.56	0.19	0.0256	0.13	2.27	0.44	2.73	0.04	0.96	0.13
27	20	0.36	2.75	0.3	1	0.06	1	1.56	0.19	0.0385	0.20	1.86	0.36	1.82	0.06	1.04	0.21
28	20	0.36	2.75	0.3	1	0.08	1	1.56	0.19	0.0513	0.27	1.61	0.31	1.36	0.07	0.93	0.25
29	20	0.36	2.75	0.3	1	0.1	1	1.56	0.19	0.0641	0.33	1.44	0.28	1.09	0.08	0.82	0.27
30	20	0.36	2.75	0.3	1	0.12	1	1.56	0.19	0.0769	0.40	1.31	0.25	0.91	0.09	0.72	0.29
31	20	0.36	2.75	0.3	1.43	0.04	0.7	3.18	0.09	0.0126	0.13	3.25	0.31	2.73	0.04	1.06	0.14
32	20	0.36	2.75	0.3	1.43	0.06	0.7	3.18	0.09	0.0188	0.20	2.65	0.25	1.82	0.07	1.18	0.24
33	20	0.36	2.75	0.3	1.43	0.08	0.7	3.18	0.09	0.0251	0.27	2.3	0.22	1.36	0.09	1.17	0.31
34	20	0.36	2.75	0.3	1.43	0.1	0.7	3.18	0.09	0.0314	0.33	2.05	0.19	1.09	0.11	1.14	0.38
35	20	0.36	2.75	0.3	1.43	0.12	0.7	3.18	0.09	0.0377	0.40	1.87	0.18	0.91	0.13	1.07	0.43
36	20	0.36	2.75	0.3	2	0.04	0.5	6.24	0.05	0.0064	0.13	4.55	0.22	2.73	0.05	1.14	0.15
37	20	0.36	2.75	0.3	2	0.06	0.5	6.24	0.05	0.0096	0.20	3.71	0.18	1.82	0.07	1.21	0.24
38	20	0.36	2.75	0.3	2	0.08	0.5	6.24	0.05	0.0128	0.27	3.21	0.15	1.36	0.10	1.30	0.35
39	20	0.36	2.75	0.3	2	0.1	0.5	6.24	0.05	0.0160	0.33	2.88	0.14	1.09	0.13	1.31	0.44
40	20	0.36	2.75	0.3	2	0.12	0.5	6.24	0.05	0.0192	0.40	2.62	0.13	0.91	0.15	1.21	0.49
41	20	0.36	2.75	0.3	2.86	0.04	0.35	12.7	0.02	0.0031	0.13	6.49	0.15	2.73	0.05	1.30	0.17
42	20	0.36	2.75	0.3	2.86	0.06	0.35	12.7	0.02	0.0047	0.20	5.3	0.12	1.82	0.08	1.41	0.28
43	20	0.36	2.75	0.3	2.86	0.08	0.35	12.7	0.02	0.0063	0.27	4.59	0.11	1.36	0.12	1.45	0.39
44	20	0.36	2.75	0.3	2.86	0.1	0.35	12.7	0.02	0.0079	0.33	4.11	0.10	1.09	0.15	1.54	0.51
45	20	0.36	2.75	0.3	2.86	0.12	0.35	12.7	0.02	0.0094	0.40	3.75	0.09	0.91	0.17	1.42	0.57
46	20	0.36	2.75	0.3	3.33	0.04	0.3	17.3	0.02	0.0023	0.13	7.58	0.13	2.73	0.06	1.39	0.19
47	20	0.36	2.75	0.3	3.33	0.06	0.3	17.3	0.02	0.0035	0.20	6.19	0.11	1.82	0.09	1.55	0.31
48	20	0.36	2.75	0.3	3.33	0.08	0.3	17.3	0.02	0.0046	0.27	5.36	0.09	1.36	0.12	1.54	0.41

49	20	0.36	2.75	0.3	3.33	0.1	0.3	17.3	0.02	0.0058	0.33	4.79	0.08	1.09	0.15	1.55	0.52
50	20	0.36	2.75	0.3	3.33	0.12	0.3	17.3	0.02	0.0069	0.40	4.37	0.08	0.91	0.18	1.50	0.60
51	30	0.58	1.73	0.3	1	0.04	1	1.56	0.19	0.0256	0.13	3.61	0.69	4.33	0.03	0.78	0.10
52	30	0.58	1.73	0.3	1	0.06	1	1.56	0.19	0.0385	0.20	2.94	0.57	2.89	0.05	0.85	0.17
53	30	0.58	1.73	0.3	1	0.08	1	1.56	0.19	0.0513	0.27	2.55	0.49	2.17	0.07	0.89	0.24
54	30	0.58	1.73	0.3	1	0.1	1	1.56	0.19	0.0641	0.33	2.28	0.44	1.73	0.10	1.00	0.33
55	30	0.58	1.73	0.3	1	0.12	1	1.56	0.19	0.0769	0.40	2.08	0.40	1.44	0.12	1.02	0.41
56	30	0.58	1.73	0.3	1.43	0.04	0.7	3.18	0.09	0.0126	0.13	5.15	0.49	4.33	0.04	0.88	0.12
57	30	0.58	1.73	0.3	1.43	0.06	0.7	3.18	0.09	0.0188	0.20	4.21	0.40	2.89	0.06	0.96	0.19
58	30	0.58	1.73	0.3	1.43	0.08	0.7	3.18	0.09	0.0251	0.27	3.64	0.34	2.17	0.08	0.97	0.26
59	30	0.58	1.73	0.3	1.43	0.1	0.7	3.18	0.09	0.0314	0.33	3.26	0.31	1.73	0.11	1.11	0.37
60	30	0.58	1.73	0.3	1.43	0.12	0.7	3.18	0.09	0.0377	0.40	2.97	0.28	1.44	0.14	1.17	0.47
61	30	0.58	1.73	0.3	2	0.04	0.5	6.24	0.05	0.0064	0.13	7.21	0.35	4.33	0.04	0.94	0.12
62	30	0.58	1.73	0.3	2	0.06	0.5	6.24	0.05	0.0096	0.20	5.89	0.28	2.89	0.06	1.03	0.21
63	30	0.58	1.73	0.3	2	0.08	0.5	6.24	0.05	0.0128	0.27	5.1	0.25	2.17	0.08	1.06	0.28
64	30	0.58	1.73	0.3	2	0.1	0.5	6.24	0.05	0.0160	0.33	4.56	0.22	1.73	0.12	1.19	0.40
65	30	0.58	1.73	0.3	2	0.12	0.5	6.24	0.05	0.0192	0.40	4.16	0.20	1.44	0.16	1.29	0.52
66	30	0.58	1.73	0.3	2.86	0.04	0.35	12.7	0.02	0.0031	0.13	10.3	0.24	4.33	0.04	1.07	0.14
67	30	0.58	1.73	0.3	2.86	0.06	0.35	12.7	0.02	0.0047	0.20	8.41	0.20	2.89	0.07	1.13	0.23
68	30	0.58	1.73	0.3	2.86	0.08	0.35	12.7	0.02	0.0063	0.27	7.28	0.17	2.17	0.09	1.17	0.31
69	30	0.58	1.73	0.3	2.86	0.1	0.35	12.7	0.02	0.0079	0.33	6.52	0.15	1.73	0.13	1.32	0.44
70	30	0.58	1.73	0.3	2.86	0.12	0.35	12.7	0.02	0.0094	0.40	5.95	0.14	1.44	0.17	1.42	0.57
71	30	0.58	1.73	0.3	3.33	0.04	0.3	17.3	0.02	0.0023	0.13	12	0.21	4.33	0.05	1.17	0.16
72	30	0.58	1.73	0.3	3.33	0.06	0.3	17.3	0.02	0.0035	0.20	9.81	0.17	2.89	0.08	1.34	0.27
73	30	0.58	1.73	0.3	3.33	0.08	0.3	17.3	0.02	0.0046	0.27	8.5	0.15	2.17	0.11	1.43	0.38
74	30	0.58	1.73	0.3	3.33	0.1	0.3	17.3	0.02	0.0058	0.33	7.6	0.13	1.73	0.15	1.53	0.51
75	30	0.58	1.73	0.3	3.33	0.12	0.3	17.3	0.02	0.0069	0.40	6.94	0.12	1.44	0.19	1.59	0.64

Table 64 List of parameters and run-up results for the R30 permeable slopes

#	α (°)	tanα	cotα	h (m)	T (s)	H (m)	fr (htz)	Lo (m)	h/Lo	H/L	H/h	ξ	ϕ	tanα/(H/h)	R	R/H	R/h
1	30	0.58	1.73	0.3	3.33	0.04	0.3	17.3	0.02	0.002	0.1	12	0.21	4.33	0.05	1.3	0.18
2	30	0.58	1.73	0.3	2.86	0.04	0.35	12.7	0.02	0.003	0.1	10.3	0.24	4.33	0.05	1.2	0.16
3	30	0.58	1.73	0.3	2	0.04	0.5	6.24	0.05	0.006	0.1	7.21	0.35	4.33	0.04	1	0.14
4	30	0.58	1.73	0.3	1.43	0.04	0.7	3.18	0.09	0.013	0.1	5.15	0.49	4.33	0.04	1	0.13
5	30	0.58	1.73	0.3	1	0.04	1	1.56	0.19	0.026	0.1	3.61	0.69	4.33	0.04	0.9	0.12
6	30	0.58	1.73	0.3	3.33	0.06	0.3	17.3	0.02	0.003	0.2	9.81	0.17	2.89	0.09	1.4	0.29
7	30	0.58	1.73	0.3	2.86	0.06	0.35	12.7	0.02	0.005	0.2	8.41	0.20	2.89	0.07	1.2	0.25
8	30	0.58	1.73	0.3	2	0.06	0.5	6.24	0.05	0.01	0.2	5.89	0.28	2.89	0.07	1.2	0.24
9	30	0.58	1.73	0.3	1.43	0.06	0.7	3.18	0.09	0.019	0.2	4.21	0.40	2.89	0.06	1	0.21
10	30	0.58	1.73	0.3	1	0.06	1	1.56	0.19	0.038	0.2	2.94	0.57	2.89	0.06	0.9	0.19
11	30	0.58	1.73	0.3	3.33	0.08	0.3	17.3	0.02	0.005	0.3	8.5	0.15	2.17	0.12	1.5	0.41
12	30	0.58	1.73	0.3	2.86	0.08	0.35	12.7	0.02	0.006	0.3	7.28	0.17	2.17	0.1	1.3	0.35
13	30	0.58	1.73	0.3	2	0.08	0.5	6.24	0.05	0.013	0.3	5.1	0.25	2.17	0.09	1.2	0.31
14	30	0.58	1.73	0.3	1.43	0.08	0.7	3.18	0.09	0.025	0.3	3.64	0.34	2.17	0.09	1.1	0.29
15	30	0.58	1.73	0.3	1	0.08	1	1.56	0.19	0.051	0.3	2.55	0.49	2.17	0.08	1	0.28
16	30	0.58	1.73	0.3	3.33	0.1	0.3	17.3	0.02	0.006	0.3	7.6	0.13	1.73	0.17	1.7	0.57
17	30	0.58	1.73	0.3	2.86	0.1	0.35	12.7	0.02	0.008	0.3	6.52	0.15	1.73	0.15	1.5	0.5
18	30	0.58	1.73	0.3	2	0.1	0.5	6.24	0.05	0.016	0.3	4.56	0.22	1.73	0.14	1.4	0.46
19	30	0.58	1.73	0.3	1.43	0.1	0.7	3.18	0.09	0.031	0.3	3.26	0.31	1.73	0.13	1.3	0.42
20	30	0.58	1.73	0.3	1	0.1	1	1.56	0.19	0.064	0.3	2.28	0.44	1.73	0.11	1.1	0.37
21	30	0.58	1.73	0.3	3.33	0.12	0.3	17.3	0.02	0.007	0.4	6.94	0.12	1.44	0.2	1.7	0.68
22	30	0.58	1.73	0.3	2.86	0.12	0.35	12.7	0.02	0.009	0.4	5.95	0.14	1.44	0.19	1.6	0.62
23	30	0.58	1.73	0.3	2	0.12	0.5	6.24	0.05	0.019	0.4	4.16	0.20	1.44	0.18	1.5	0.58
24	30	0.58	1.73	0.3	1.43	0.12	0.7	3.18	0.09	0.038	0.4	2.97	0.28	1.44	0.16	1.3	0.53
25	30	0.58	1.73	0.3	1	0.12	1	1.56	0.19	0.077	0.4	2.08	0.40	1.44	0.14	1.1	0.45
26	20	0.36	2.75	0.3	3.33	0.04	0.3	17.3	0.02	0.002	0.1	7.58	0.13	2.73	0.06	1.5	0.2
27	20	0.36	2.75	0.3	2.86	0.04	0.35	12.7	0.02	0.003	0.1	6.49	0.15	2.73	0.06	1.4	0.19
28	20	0.36	2.75	0.3	2	0.04	0.5	6.24	0.05	0.006	0.1	4.55	0.22	2.73	0.05	1.3	0.17
29	20	0.36	2.75	0.3	1.43	0.04	0.7	3.18	0.09	0.013	0.1	3.25	0.31	2.73	0.05	1.2	0.16
30	20	0.36	2.75	0.3	1	0.04	1	1.56	0.19	0.026	0.1	2.27	0.44	2.73	0.04	1.1	0.15
31	20	0.36	2.75	0.3	3.33	0.06	0.3	17.3	0.02	0.003	0.2	6.19	0.11	1.82	0.1	1.7	0.34
32	20	0.36	2.75	0.3	2.86	0.06	0.35	12.7	0.02	0.005	0.2	5.3	0.12	1.82	0.09	1.5	0.3
33	20	0.36	2.75	0.3	2	0.06	0.5	6.24	0.05	0.01	0.2	3.71	0.18	1.82	0.08	1.4	0.27
34	20	0.36	2.75	0.3	1.43	0.06	0.7	3.18	0.09	0.019	0.2	2.65	0.25	1.82	0.08	1.3	0.26
35	20	0.36	2.75	0.3	1	0.06	1	1.56	0.19	0.038	0.2	1.86	0.36	1.82	0.07	1.2	0.24
36	20	0.36	2.75	0.3	3.33	0.08	0.3	17.3	0.02	0.005	0.3	5.36	0.09	1.36	0.13	1.6	0.44
37	20	0.36	2.75	0.3	2.86	0.08	0.35	12.7	0.02	0.006	0.3	4.59	0.11	1.36	0.12	1.5	0.41
38	20	0.36	2.75	0.3	2	0.08	0.5	6.24	0.05	0.013	0.3	3.21	0.15	1.36	0.11	1.4	0.37
39	20	0.36	2.75	0.3	1.43	0.08	0.7	3.18	0.09	0.025	0.3	2.3	0.22	1.36	0.1	1.3	0.34
40	20	0.36	2.75	0.3	1	0.08	1	1.56	0.19	0.051	0.3	1.61	0.31	1.36	0.08	1	0.27
41	10	0.18	5.67	0.3	3.33	0.04	0.3	17.3	0.02	0.002	0.1	3.67	0.06	1.32	0.06	1.6	0.22
42	10	0.18	5.67	0.3	2.86	0.04	0.35	12.7	0.02	0.003	0.1	3.15	0.07	1.32	0.06	1.6	0.21
43	10	0.18	5.67	0.3	2	0.04	0.5	6.24	0.05	0.006	0.1	2.2	0.11	1.32	0.05	1.3	0.17
44	10	0.18	5.67	0.3	1.43	0.04	0.7	3.18	0.09	0.013	0.1	1.57	0.15	1.32	0.05	1.2	0.16
45	10	0.18	5.67	0.3	1	0.04	1	1.56	0.19	0.026	0.1	1.1	0.21	1.32	0.03	0.8	0.1
46	20	0.36	2.75	0.3	3.33	0.1	0.3	17.3	0.02	0.006	0.3	4.79	0.08	1.09	0.17	1.7	0.56
47	20	0.36	2.75	0.3	2.86	0.1	0.35	12.7	0.02	0.008	0.3	4.11	0.10	1.09	0.17	1.7	0.55
48	20	0.36	2.75	0.3	2	0.1	0.5	6.24	0.05	0.016	0.3	2.88	0.14	1.09	0.14	1.4	0.47
49	20	0.36	2.75	0.3	1.43	0.1	0.7	3.18	0.09	0.031	0.3	2.05	0.19	1.09	0.12	1.2	0.41
50	20	0.36	2.75	0.3	1	0.1	1	1.56	0.19	0.064	0.3	1.44	0.28	1.09	0.09	0.9	0.3
51	20	0.36	2.75	0.3	3.33	0.12	0.3	17.3	0.02	0.007	0.4	4.37	0.08	0.91	0.2	1.6	0.66

52	20	0.36	2.75	0.3	2.86	0.12	0.35	12.7	0.02	0.009	0.4	3.75	0.09	0.91	0.19	1.6	0.63
53	20	0.36	2.75	0.3	2	0.12	0.5	6.24	0.05	0.019	0.4	2.62	0.13	0.91	0.16	1.4	0.54
54	20	0.36	2.75	0.3	1.43	0.12	0.7	3.18	0.09	0.038	0.4	1.87	0.18	0.91	0.14	1.2	0.47
55	20	0.36	2.75	0.3	1	0.12	1	1.56	0.19	0.077	0.4	1.31	0.25	0.91	0.1	0.8	0.33
56	10	0.18	5.67	0.3	3.33	0.06	0.3	17.3	0.02	0.003	0.2	3	0.05	0.88	0.09	1.5	0.3
57	10	0.18	5.67	0.3	2.86	0.06	0.35	12.7	0.02	0.005	0.2	2.57	0.06	0.88	0.08	1.4	0.27
58	10	0.18	5.67	0.3	2	0.06	0.5	6.24	0.05	0.01	0.2	1.8	0.09	0.88	0.07	1.2	0.24
59	10	0.18	5.67	0.3	1.43	0.06	0.7	3.18	0.09	0.019	0.2	1.28	0.12	0.88	0.06	1	0.19
60	10	0.18	5.67	0.3	1	0.06	1	1.56	0.19	0.038	0.2	0.9	0.17	0.88	0.04	0.7	0.15
61	10	0.18	5.67	0.3	3.33	0.08	0.3	17.3	0.02	0.005	0.3	2.6	0.04	0.66	0.11	1.4	0.38
62	10	0.18	5.67	0.3	2.86	0.08	0.35	12.7	0.02	0.006	0.3	2.22	0.05	0.66	0.11	1.4	0.36
63	10	0.18	5.67	0.3	2	0.08	0.5	6.24	0.05	0.013	0.3	1.56	0.07	0.66	0.09	1.1	0.29
64	10	0.18	5.67	0.3	1.43	0.08	0.7	3.18	0.09	0.025	0.3	1.11	0.10	0.66	0.07	0.8	0.22
65	10	0.18	5.67	0.3	1	0.08	1	1.56	0.19	0.051	0.3	0.78	0.15	0.66	0.05	0.6	0.16
66	10	0.18	5.67	0.3	3.33	0.1	0.3	17.3	0.02	0.006	0.3	2.32	0.04	0.53	0.13	1.3	0.44
67	10	0.18	5.67	0.3	2.86	0.1	0.35	12.7	0.02	0.008	0.3	1.99	0.05	0.53	0.13	1.3	0.43
68	10	0.18	5.67	0.3	2	0.1	0.5	6.24	0.05	0.016	0.3	1.39	0.07	0.53	0.09	0.9	0.31
69	10	0.18	5.67	0.3	1.43	0.1	0.7	3.18	0.09	0.031	0.3	0.99	0.09	0.53	0.08	0.8	0.25
70	10	0.18	5.67	0.3	1	0.1	1	1.56	0.19	0.064	0.3	0.7	0.13	0.53	0.05	0.5	0.18
71	10	0.18	5.67	0.3	3.33	0.12	0.3	17.3	0.02	0.007	0.4	2.12	0.04	0.44	0.17	1.4	0.56
72	10	0.18	5.67	0.3	2.86	0.12	0.35	12.7	0.02	0.009	0.4	1.82	0.04	0.44	0.15	1.2	0.5
73	10	0.18	5.67	0.3	2	0.12	0.5	6.24	0.05	0.019	0.4	1.27	0.06	0.44	0.11	0.9	0.36
74	10	0.18	5.67	0.3	1.43	0.12	0.7	3.18	0.09	0.038	0.4	0.91	0.09	0.44	0.09	0.7	0.3
75	10	0.18	5.67	0.3	1	0.12	1	1.56	0.19	0.077	0.4	0.64	0.12	0.44	0.06	0.5	0.2

Table 65 List of parameters and run-up results for the R45 permeable slopes

#	α (˚)	tanα	cotα	h (m)	T (s)	H (m)	fr (htz)	Lo (m)	h/Lo	H/L	H/h	ξ	ϕ	tanα/(H/h)	R	R/H	R/h
1	30	0.58	1.73	0.3	3.33	0.04	0.3	17.3	0.02	0.002	0.1	12	0.21	4.33	0.06	1.4	0.19
2	30	0.58	1.73	0.3	2.86	0.04	0.35	12.7	0.02	0.003	0.1	10.3	0.24	4.33	0.05	1.3	0.17
3	30	0.58	1.73	0.3	2	0.04	0.5	6.24	0.05	0.006	0.1	7.21	0.35	4.33	0.05	1.2	0.16
4	30	0.58	1.73	0.3	1.43	0.04	0.7	3.18	0.09	0.013	0.1	5.15	0.49	4.33	0.04	1.1	0.15
5	30	0.58	1.73	0.3	1	0.04	1	1.56	0.19	0.026	0.1	3.61	0.69	4.33	0.04	1	0.13
6	30	0.58	1.73	0.3	3.33	0.06	0.3	17.3	0.02	0.003	0.2	9.81	0.17	2.89	0.09	1.5	0.3
7	30	0.58	1.73	0.3	2.86	0.06	0.35	12.7	0.02	0.005	0.2	8.41	0.20	2.89	0.08	1.4	0.27
8	30	0.58	1.73	0.3	2	0.06	0.5	6.24	0.05	0.01	0.2	5.89	0.28	2.89	0.08	1.3	0.26
9	30	0.58	1.73	0.3	1.43	0.06	0.7	3.18	0.09	0.019	0.2	4.21	0.40	2.89	0.07	1.2	0.24
10	30	0.58	1.73	0.3	1	0.06	1	1.56	0.19	0.038	0.2	2.94	0.57	2.89	0.06	1	0.2
11	30	0.58	1.73	0.3	3.33	0.08	0.3	17.3	0.02	0.005	0.3	8.5	0.15	2.17	0.13	1.6	0.44
12	30	0.58	1.73	0.3	2.86	0.08	0.35	12.7	0.02	0.006	0.3	7.28	0.17	2.17	0.12	1.4	0.39
13	30	0.58	1.73	0.3	2	0.08	0.5	6.24	0.05	0.013	0.3	5.1	0.25	2.17	0.1	1.3	0.35
14	30	0.58	1.73	0.3	1.43	0.08	0.7	3.18	0.09	0.025	0.3	3.64	0.34	2.17	0.1	1.2	0.33
15	30	0.58	1.73	0.3	1	0.08	1	1.56	0.19	0.051	0.3	2.55	0.49	2.17	0.09	1.1	0.3
16	30	0.58	1.73	0.3	3.33	0.1	0.3	17.3	0.02	0.006	0.3	7.6	0.13	1.73	0.18	1.8	0.61
17	30	0.58	1.73	0.3	2.86	0.1	0.35	12.7	0.02	0.008	0.3	6.52	0.15	1.73	0.17	1.7	0.55
18	30	0.58	1.73	0.3	2	0.1	0.5	6.24	0.05	0.016	0.3	4.56	0.22	1.73	0.15	1.5	0.51
19	30	0.58	1.73	0.3	1.43	0.1	0.7	3.18	0.09	0.031	0.3	3.26	0.31	1.73	0.14	1.4	0.47
20	30	0.58	1.73	0.3	1	0.1	1	1.56	0.19	0.064	0.3	2.28	0.44	1.73	0.12	1.2	0.41
21	30	0.58	1.73	0.3	3.33	0.12	0.3	17.3	0.02	0.007	0.4	6.94	0.12	1.44	0.23	1.9	0.76
22	30	0.58	1.73	0.3	2.86	0.12	0.35	12.7	0.02	0.009	0.4	5.95	0.14	1.44	0.2	1.7	0.68
23	30	0.58	1.73	0.3	2	0.12	0.5	6.24	0.05	0.019	0.4	4.16	0.20	1.44	0.19	1.6	0.64
24	30	0.58	1.73	0.3	1.43	0.12	0.7	3.18	0.09	0.038	0.4	2.97	0.28	1.44	0.18	1.5	0.6
25	30	0.58	1.73	0.3	1	0.12	1	1.56	0.19	0.077	0.4	2.08	0.40	1.44	0.15	1.3	0.51
26	20	0.36	2.75	0.3	3.33	0.04	0.3	17.3	0.02	0.002	0.1	7.58	0.13	2.73	0.07	1.6	0.22
27	20	0.36	2.75	0.3	2.86	0.04	0.35	12.7	0.02	0.003	0.1	6.49	0.15	2.73	0.06	1.6	0.21
28	20	0.36	2.75	0.3	2	0.04	0.5	6.24	0.05	0.006	0.1	4.55	0.22	2.73	0.06	1.4	0.19
29	20	0.36	2.75	0.3	1.43	0.04	0.7	3.18	0.09	0.013	0.1	3.25	0.31	2.73	0.05	1.3	0.18
30	20	0.36	2.75	0.3	1	0.04	1	1.56	0.19	0.026	0.1	2.27	0.44	2.73	0.05	1.2	0.16
31	20	0.36	2.75	0.3	3.33	0.06	0.3	17.3	0.02	0.003	0.2	6.19	0.11	1.82	0.11	1.8	0.37
32	20	0.36	2.75	0.3	2.86	0.06	0.35	12.7	0.02	0.005	0.2	5.3	0.12	1.82	0.1	1.6	0.33
33	20	0.36	2.75	0.3	2	0.06	0.5	6.24	0.05	0.01	0.2	3.71	0.18	1.82	0.09	1.5	0.3
34	20	0.36	2.75	0.3	1.43	0.06	0.7	3.18	0.09	0.019	0.2	2.65	0.25	1.82	0.09	1.4	0.29
35	20	0.36	2.75	0.3	1	0.06	1	1.56	0.19	0.038	0.2	1.86	0.36	1.82	0.08	1.3	0.25
36	20	0.36	2.75	0.3	3.33	0.08	0.3	17.3	0.02	0.005	0.3	5.36	0.09	1.36	0.15	1.8	0.49
37	20	0.36	2.75	0.3	2.86	0.08	0.35	12.7	0.02	0.006	0.3	4.59	0.11	1.36	0.14	1.7	0.46
38	20	0.36	2.75	0.3	2	0.08	0.5	6.24	0.05	0.013	0.3	3.21	0.15	1.36	0.13	1.6	0.42
39	20	0.36	2.75	0.3	1.43	0.08	0.7	3.18	0.09	0.025	0.3	2.3	0.22	1.36	0.12	1.5	0.4
40	20	0.36	2.75	0.3	1	0.08	1	1.56	0.19	0.051	0.3	1.61	0.31	1.36	0.1	1.2	0.32
41	10	0.18	5.67	0.3	3.33	0.04	0.3	17.3	0.02	0.002	0.1	3.67	0.06	1.32	0.07	1.9	0.25
42	10	0.18	5.67	0.3	2.86	0.04	0.35	12.7	0.02	0.003	0.1	3.15	0.07	1.32	0.07	1.8	0.23
43	10	0.18	5.67	0.3	2	0.04	0.5	6.24	0.05	0.006	0.1	2.2	0.11	1.32	0.06	1.5	0.2
44	10	0.18	5.67	0.3	1.43	0.04	0.7	3.18	0.09	0.013	0.1	1.57	0.15	1.32	0.05	1.3	0.17
45	10	0.18	5.67	0.3	1	0.04	1	1.56	0.19	0.026	0.1	1.1	0.21	1.32	0.03	0.8	0.11
46	20	0.36	2.75	0.3	3.33	0.1	0.3	17.3	0.02	0.006	0.3	4.79	0.08	1.09	0.19	1.9	0.63
47	20	0.36	2.75	0.3	2.86	0.1	0.35	12.7	0.02	0.008	0.3	4.11	0.10	1.09	0.18	1.8	0.61
48	20	0.36	2.75	0.3	2	0.1	0.5	6.24	0.05	0.016	0.3	2.88	0.14	1.09	0.16	1.6	0.54
49	20	0.36	2.75	0.3	1.43	0.1	0.7	3.18	0.09	0.031	0.3	2.05	0.19	1.09	0.14	1.4	0.48
50	20	0.36	2.75	0.3	1	0.1	1	1.56	0.19	0.064	0.3	1.44	0.28	1.09	0.1	1	0.35
51	20	0.36	2.75	0.3	3.33	0.12	0.3	17.3	0.02	0.007	0.4	4.37	0.08	0.91	0.22	1.8	0.72
52	20	0.36	2.75	0.3	2.86	0.12	0.35	12.7	0.02	0.009	0.4	3.75	0.09	0.91	0.21	1.7	0.68
53	20	0.36	2.75	0.3	2	0.12	0.5	6.24	0.05	0.019	0.4	2.62	0.13	0.91	0.19	1.5	0.62
54	20	0.36	2.75	0.3	1.43	0.12	0.7	3.18	0.09	0.038	0.4	1.87	0.18	0.91	0.16	1.3	0.53

55	20	0.36	2.75	0.3	1	0.12	1	1.56	0.19	0.077	0.4	1.31	0.25	0.91	0.11	0.9	0.36
56	10	0.18	5.67	0.3	3.33	0.06	0.3	17.3	0.02	0.003	0.2	3	0.05	0.88	0.1	1.7	0.34
57	10	0.18	5.67	0.3	2.86	0.06	0.35	12.7	0.02	0.005	0.2	2.57	0.06	0.88	0.1	1.7	0.33
58	10	0.18	5.67	0.3	2	0.06	0.5	6.24	0.05	0.01	0.2	1.8	0.09	0.88	0.08	1.4	0.28
59	10	0.18	5.67	0.3	1.43	0.06	0.7	3.18	0.09	0.019	0.2	1.28	0.12	0.88	0.07	1.1	0.22
60	10	0.18	5.67	0.3	1	0.06	1	1.56	0.19	0.038	0.2	0.9	0.17	0.88	0.05	0.8	0.16
61	10	0.18	5.67	0.3	3.33	0.08	0.3	17.3	0.02	0.005	0.3	2.6	0.04	0.66	0.13	1.6	0.43
62	10	0.18	5.67	0.3	2.86	0.08	0.35	12.7	0.02	0.006	0.3	2.22	0.05	0.66	0.12	1.5	0.4
63	10	0.18	5.67	0.3	2	0.08	0.5	6.24	0.05	0.013	0.3	1.56	0.07	0.66	0.1	1.3	0.34
64	10	0.18	5.67	0.3	1.43	0.08	0.7	3.18	0.09	0.025	0.3	1.11	0.10	0.66	0.08	1	0.26
65	10	0.18	5.67	0.3	1	0.08	1	1.56	0.19	0.051	0.3	0.78	0.15	0.66	0.05	0.6	0.17
66	10	0.18	5.67	0.3	3.33	0.1	0.3	17.3	0.02	0.006	0.3	2.32	0.04	0.53	0.16	1.6	0.54
67	10	0.18	5.67	0.3	2.86	0.1	0.35	12.7	0.02	0.008	0.3	1.99	0.05	0.53	0.15	1.5	0.49
68	10	0.18	5.67	0.3	2	0.1	0.5	6.24	0.05	0.016	0.3	1.39	0.07	0.53	0.12	1.2	0.4
69	10	0.18	5.67	0.3	1.43	0.1	0.7	3.18	0.09	0.031	0.3	0.99	0.09	0.53	0.09	0.9	0.29
70	10	0.18	5.67	0.3	1	0.1	1	1.56	0.19	0.064	0.3	0.7	0.13	0.53	0.05	0.5	0.18
71	10	0.18	5.67	0.3	3.33	0.12	0.3	17.3	0.02	0.007	0.4	2.12	0.04	0.44	0.18	1.5	0.6
72	10	0.18	5.67	0.3	2.86	0.12	0.35	12.7	0.02	0.009	0.4	1.82	0.04	0.44	0.17	1.4	0.55
73	10	0.18	5.67	0.3	2	0.12	0.5	6.24	0.05	0.019	0.4	1.27	0.06	0.44	0.13	1.1	0.44
74	10	0.18	5.67	0.3	1.43	0.12	0.7	3.18	0.09	0.038	0.4	0.91	0.09	0.44	0.09	0.8	0.31
75	10	0.18	5.67	0.3	1	0.12	1	1.56	0.19	0.077	0.4	0.64	0.12	0.44	0.06	0.5	0.2

Table 66 List of parameters and run-up results for the R60 permeable slopes

#	α (°)	tanα	cotα	h (m)	T (s)	H (m)	fr (htz)	Lo (m)	h/Lo	H/L	H/h	ξ	ϕ	tanα/(H/h)	R	R/H	R/h
1	30	0.58	1.73	0.3	3.33	0.04	0.3	17.3	0.02	0.002	0.1	12	0.21	4.33	0.06	1.5	0.2
2	30	0.58	1.73	0.3	2.86	0.04	0.35	12.7	0.02	0.003	0.1	10.3	0.24	4.33	0.06	1.4	0.19
3	30	0.58	1.73	0.3	2	0.04	0.5	6.24	0.05	0.006	0.1	7.21	0.35	4.33	0.05	1.3	0.18
4	30	0.58	1.73	0.3	1.43	0.04	0.7	3.18	0.09	0.013	0.1	5.15	0.49	4.33	0.05	1.2	0.16
5	30	0.58	1.73	0.3	1	0.04	1	1.56	0.19	0.026	0.1	3.61	0.69	4.33	0.04	1.1	0.14
6	30	0.58	1.73	0.3	3.33	0.06	0.3	17.3	0.02	0.003	0.2	9.81	0.17	2.89	0.1	1.6	0.33
7	30	0.58	1.73	0.3	2.86	0.06	0.35	12.7	0.02	0.005	0.2	8.41	0.20	2.89	0.09	1.5	0.3
8	30	0.58	1.73	0.3	2	0.06	0.5	6.24	0.05	0.01	0.2	5.89	0.28	2.89	0.08	1.4	0.28
9	30	0.58	1.73	0.3	1.43	0.06	0.7	3.18	0.09	0.019	0.2	4.21	0.40	2.89	0.08	1.3	0.26
10	30	0.58	1.73	0.3	1	0.06	1	1.56	0.19	0.038	0.2	2.94	0.57	2.89	0.07	1.1	0.23
11	30	0.58	1.73	0.3	3.33	0.08	0.3	17.3	0.02	0.005	0.3	8.5	0.15	2.17	0.15	1.8	0.48
12	30	0.58	1.73	0.3	2.86	0.08	0.35	12.7	0.02	0.006	0.3	7.28	0.17	2.17	0.13	1.6	0.43
13	30	0.58	1.73	0.3	2	0.08	0.5	6.24	0.05	0.013	0.3	5.1	0.25	2.17	0.12	1.5	0.39
14	30	0.58	1.73	0.3	1.43	0.08	0.7	3.18	0.09	0.025	0.3	3.64	0.34	2.17	0.11	1.3	0.36
15	30	0.58	1.73	0.3	1	0.08	1	1.56	0.19	0.051	0.3	2.55	0.49	2.17	0.1	1.3	0.34
16	30	0.58	1.73	0.3	3.33	0.1	0.3	17.3	0.02	0.006	0.3	7.6	0.13	1.73	0.2	2	0.65
17	30	0.58	1.73	0.3	2.86	0.1	0.35	12.7	0.02	0.008	0.3	6.52	0.15	1.73	0.18	1.8	0.61
18	30	0.58	1.73	0.3	2	0.1	0.5	6.24	0.05	0.016	0.3	4.56	0.22	1.73	0.17	1.7	0.58
19	30	0.58	1.73	0.3	1.43	0.1	0.7	3.18	0.09	0.031	0.3	3.26	0.31	1.73	0.15	1.5	0.51
20	30	0.58	1.73	0.3	1	0.1	1	1.56	0.19	0.064	0.3	2.28	0.44	1.73	0.14	1.4	0.45
21	30	0.58	1.73	0.3	3.33	0.12	0.3	17.3	0.02	0.007	0.4	6.94	0.12	1.44	0.24	2	0.81
22	30	0.58	1.73	0.3	2.86	0.12	0.35	12.7	0.02	0.009	0.4	5.95	0.14	1.44	0.23	1.9	0.77
23	30	0.58	1.73	0.3	2	0.12	0.5	6.24	0.05	0.019	0.4	4.16	0.20	1.44	0.21	1.8	0.71
24	30	0.58	1.73	0.3	1.43	0.12	0.7	3.18	0.09	0.038	0.4	2.97	0.28	1.44	0.19	1.6	0.64
25	30	0.58	1.73	0.3	1	0.12	1	1.56	0.19	0.077	0.4	2.08	0.40	1.44	0.17	1.4	0.55
26	20	0.36	2.75	0.3	3.33	0.04	0.3	17.3	0.02	0.002	0.1	7.58	0.13	2.73	0.07	1.8	0.24
27	20	0.36	2.75	0.3	2.86	0.04	0.35	12.7	0.02	0.003	0.1	6.49	0.15	2.73	0.07	1.7	0.23
28	20	0.36	2.75	0.3	2	0.04	0.5	6.24	0.05	0.006	0.1	4.55	0.22	2.73	0.06	1.6	0.21
29	20	0.36	2.75	0.3	1.43	0.04	0.7	3.18	0.09	0.013	0.1	3.25	0.31	2.73	0.06	1.5	0.19
30	20	0.36	2.75	0.3	1	0.04	1	1.56	0.19	0.026	0.1	2.27	0.44	2.73	0.05	1.3	0.18
31	20	0.36	2.75	0.3	3.33	0.06	0.3	17.3	0.02	0.003	0.2	6.19	0.11	1.82	0.12	2	0.4
32	20	0.36	2.75	0.3	2.86	0.06	0.35	12.7	0.02	0.005	0.2	5.3	0.12	1.82	0.11	1.9	0.37
33	20	0.36	2.75	0.3	2	0.06	0.5	6.24	0.05	0.01	0.2	3.71	0.18	1.82	0.1	1.7	0.33
34	20	0.36	2.75	0.3	1.43	0.06	0.7	3.18	0.09	0.019	0.2	2.65	0.25	1.82	0.09	1.6	0.31
35	20	0.36	2.75	0.3	1	0.06	1	1.56	0.19	0.038	0.2	1.86	0.36	1.82	0.08	1.4	0.28
36	20	0.36	2.75	0.3	3.33	0.08	0.3	17.3	0.02	0.005	0.3	5.36	0.09	1.36	0.16	1.9	0.52
37	20	0.36	2.75	0.3	2.86	0.08	0.35	12.7	0.02	0.006	0.3	4.59	0.11	1.36	0.15	1.9	0.5
38	20	0.36	2.75	0.3	2	0.08	0.5	6.24	0.05	0.013	0.3	3.21	0.15	1.36	0.14	1.7	0.46
39	20	0.36	2.75	0.3	1.43	0.08	0.7	3.18	0.09	0.025	0.3	2.3	0.22	1.36	0.13	1.6	0.42
40	20	0.36	2.75	0.3	1	0.08	1	1.56	0.19	0.051	0.3	1.61	0.31	1.36	0.1	1.3	0.35
41	10	0.18	5.67	0.3	3.33	0.04	0.3	17.3	0.02	0.002	0.1	3.67	0.06	1.32	0.08	2	0.27
42	10	0.18	5.67	0.3	2.86	0.04	0.35	12.7	0.02	0.003	0.1	3.15	0.07	1.32	0.07	1.9	0.25
43	10	0.18	5.67	0.3	2	0.04	0.5	6.24	0.05	0.006	0.1	2.2	0.11	1.32	0.06	1.6	0.22
44	10	0.18	5.67	0.3	1.43	0.04	0.7	3.18	0.09	0.013	0.1	1.57	0.15	1.32	0.05	1.4	0.18
45	10	0.18	5.67	0.3	1	0.04	1	1.56	0.19	0.026	0.1	1.1	0.21	1.32	0.03	0.8	0.11
46	20	0.36	2.75	0.3	3.33	0.1	0.3	17.3	0.02	0.006	0.3	4.79	0.08	1.09	0.2	2	0.67
47	20	0.36	2.75	0.3	2.86	0.1	0.35	12.7	0.02	0.008	0.3	4.11	0.10	1.09	0.19	1.9	0.65
48	20	0.36	2.75	0.3	2	0.1	0.5	6.24	0.05	0.016	0.3	2.88	0.14	1.09	0.17	1.7	0.58
49	20	0.36	2.75	0.3	1.43	0.1	0.7	3.18	0.09	0.031	0.3	2.05	0.19	1.09	0.15	1.5	0.49
50	20	0.36	2.75	0.3	1	0.1	1	1.56	0.19	0.064	0.3	1.44	0.28	1.09	0.12	1.2	0.4
51	20	0.36	2.75	0.3	3.33	0.12	0.3	17.3	0.02	0.007	0.4	4.37	0.08	0.91	0.23	2	0.78
52	20	0.36	2.75	0.3	2.86	0.12	0.35	12.7	0.02	0.009	0.4	3.75	0.09	0.91	0.22	1.9	0.74
53	20	0.36	2.75	0.3	2	0.12	0.5	6.24	0.05	0.019	0.4	2.62	0.13	0.91	0.2	1.6	0.66
54	20	0.36	2.75	0.3	1.43	0.12	0.7	3.18	0.09	0.038	0.4	1.87	0.18	0.91	0.17	1.4	0.55
55	20	0.36	2.75	0.3	1	0.12	1	1.56	0.19	0.077	0.4	1.31	0.25	0.91	0.12	1	0.41
56	10	0.18	5.67	0.3	3.33	0.06	0.3	17.3	0.02	0.003	0.2	3	0.05	0.88	0.12	1.9	0.39
57	10	0.18	5.67	0.3	2.86	0.06	0.35	12.7	0.02	0.005	0.2	2.57	0.06	0.88	0.11	1.8	0.36

58	10	0.18	5.67	0.3	2	0.06	0.5	6.24	0.05	0.01	0.2	1.8	0.09	0.88	0.09	1.6	0.31
59	10	0.18	5.67	0.3	1.43	0.06	0.7	3.18	0.09	0.019	0.2	1.28	0.12	0.88	0.07	1.2	0.23
60	10	0.18	5.67	0.3	1	0.06	1	1.56	0.19	0.038	0.2	0.9	0.17	0.88	0.05	0.8	0.17
61	10	0.18	5.67	0.3	3.33	0.08	0.3	17.3	0.02	0.005	0.3	2.6	0.04	0.66	0.14	1.8	0.47
62	10	0.18	5.67	0.3	2.86	0.08	0.35	12.7	0.02	0.006	0.3	2.22	0.05	0.66	0.13	1.7	0.44
63	10	0.18	5.67	0.3	2	0.08	0.5	6.24	0.05	0.013	0.3	1.56	0.07	0.66	0.11	1.4	0.38
64	10	0.18	5.67	0.3	1.43	0.08	0.7	3.18	0.09	0.025	0.3	1.11	0.10	0.66	0.08	1.1	0.28
65	10	0.18	5.67	0.3	1	0.08	1	1.56	0.19	0.051	0.3	0.78	0.15	0.66	0.05	0.7	0.18
66	10	0.18	5.67	0.3	3.33	0.1	0.3	17.3	0.02	0.006	0.3	2.32	0.04	0.53	0.18	1.8	0.6
67	10	0.18	5.67	0.3	2.86	0.1	0.35	12.7	0.02	0.008	0.3	1.99	0.05	0.53	0.16	1.6	0.52
68	10	0.18	5.67	0.3	2	0.1	0.5	6.24	0.05	0.016	0.3	1.39	0.07	0.53	0.13	1.3	0.43
69	10	0.18	5.67	0.3	1.43	0.1	0.7	3.18	0.09	0.031	0.3	0.99	0.09	0.53	0.09	0.9	0.31
70	10	0.18	5.67	0.3	1	0.1	1	1.56	0.19	0.064	0.3	0.7	0.13	0.53	0.06	0.6	0.19
71	10	0.18	5.67	0.3	3.33	0.12	0.3	17.3	0.02	0.007	0.4	2.12	0.04	0.44	0.19	1.6	0.65
72	10	0.18	5.67	0.3	2.86	0.12	0.35	12.7	0.02	0.009	0.4	1.82	0.04	0.44	0.17	1.4	0.57
73	10	0.18	5.67	0.3	2	0.12	0.5	6.24	0.05	0.019	0.4	1.27	0.06	0.44	0.14	1.2	0.48
74	10	0.18	5.67	0.3	1.43	0.12	0.7	3.18	0.09	0.038	0.4	0.91	0.09	0.44	0.1	0.8	0.33
75	10	0.18	5.67	0.3	1	0.12	1	1.56	0.19	0.077	0.4	0.64	0.12	0.44	0.06	0.5	0.21

Table 67 List of parameters and run-up results for the R80 permeable slopes

Run-up measurements on smooth-impermeable slopes (13.4m flume) (Section 4.3.3)

Parameters	Variables
Wave flume dimensions	13.4m long and 0.45m width
Slope angle	10˚
Slope type	Plane, smooth and impermeable
Types of waves	Regular Waves
Water depth	0.3m
Wave heights	0.04, 0.06, 0.08, 0.1, and 0.12m
Wave periods	1, 1.43, 2, 2.86, and 3.33s
Iribarren number	Between 0.63 and 3.63
Wave steepness (H/L)	Between 0.002 and 0.077
Number of tests	25

Table 68 Summary of parameters used in the 13.4m long flume with smooth-impermeable slopes

#	α (˚)	tanα	cotα	h (m)	T (s)	H (m)	fr (htz)	Lo (m)	h/Lo	H/L	H/h	ξ	ϕ	tanα/(H/h)	R	R/H	R/h
1	10	0.18	5.67	0.3	1	0.04	1	1.56	0.19	0.026	0.1	1.1	0.21	1.32	**0.1**	1.8	0.23
2	10	0.18	5.67	0.3	1.43	0.04	0.7	3.18	0.09	0.013	0.1	1.57	0.15	1.32	**0.1**	2	0.27
3	10	0.18	5.67	0.3	2	0.04	0.5	6.24	0.05	0.006	0.1	2.2	0.11	1.32	**0.1**	2.5	0.33
4	10	0.18	5.67	0.3	2.86	0.04	0.35	12.7	0.02	0.003	0.1	3.15	0.07	1.32	**0.1**	3	0.39
5	10	0.18	5.67	0.3	3.33	0.04	0.3	17.3	0.02	0.002	0.1	3.67	0.06	1.32	**0.1**	3.1	0.41
6	10	0.18	5.67	0.3	1	0.06	1	1.56	0.19	0.038	0.2	0.9	0.17	0.88	**0.1**	1.2	0.24
7	10	0.18	5.67	0.3	1.43	0.06	0.7	3.18	0.09	0.019	0.2	1.28	0.12	0.88	**0.1**	1.8	0.35
8	10	0.18	5.67	0.3	2	0.06	0.5	6.24	0.05	0.01	0.2	1.8	0.09	0.88	**0.1**	2.3	0.47
9	10	0.18	5.67	0.3	2.86	0.06	0.35	12.7	0.02	0.005	0.2	2.57	0.06	0.88	**0.2**	3	0.6
10	10	0.18	5.67	0.3	3.33	0.06	0.3	17.3	0.02	0.003	0.2	2.99	0.05	0.88	**0.2**	3	0.6
11	10	0.18	5.67	0.3	1	0.08	1	1.56	0.19	0.051	0.3	0.78	0.15	0.66	**0.1**	1	0.25
12	10	0.18	5.67	0.3	1.43	0.08	0.7	3.18	0.09	0.025	0.3	1.11	0.1	0.66	**0.1**	1.4	0.37
13	10	0.18	5.67	0.3	2	0.08	0.5	6.24	0.05	0.013	0.3	1.56	0.07	0.66	**0.2**	2	0.53
14	10	0.18	5.67	0.3	2.86	0.08	0.35	12.7	0.02	0.006	0.3	2.22	0.05	0.66	**0.2**	2.8	0.73
15	10	0.18	5.67	0.3	3.33	0.08	0.3	17.3	0.02	0.005	0.3	2.59	0.04	0.66	**0.2**	3	0.8
16	10	0.18	5.67	0.3	1	0.1	1	1.56	0.19	0.064	0.3	0.7	0.13	0.53	**0.1**	0.9	0.28
17	10	0.18	5.67	0.3	1.43	0.1	0.7	3.18	0.09	0.031	0.3	0.99	0.09	0.53	**0.1**	1.1	0.37
18	10	0.18	5.67	0.3	2	0.1	0.5	6.24	0.05	0.016	0.3	1.39	0.07	0.53	**0.2**	1.9	0.63
19	10	0.18	5.67	0.3	2.86	0.1	0.35	12.7	0.02	0.008	0.3	1.99	0.05	0.53	**0.2**	2.4	0.8
20	10	0.18	5.67	0.3	3.33	0.1	0.3	17.3	0.02	0.006	0.3	2.32	0.04	0.53	**0.3**	2.6	0.87
21	10	0.18	5.67	0.3	1	0.12	1	1.56	0.19	0.077	0.4	0.64	0.12	0.44	**0.1**	0.8	0.3
22	10	0.18	5.67	0.3	1.43	0.12	0.7	3.18	0.09	0.038	0.4	0.91	0.09	0.44	**0.1**	1	0.4
23	10	0.18	5.67	0.3	2	0.12	0.5	6.24	0.05	0.019	0.4	1.27	0.06	0.44	**0.2**	1.8	0.73
24	10	0.18	5.67	0.3	2.86	0.12	0.35	12.7	0.02	0.009	0.4	1.82	0.04	0.44	**0.3**	2.2	0.87
25	10	0.18	5.67	0.3	3.33	0.12	0.3	17.3	0.02	0.007	0.4	2.12	0.04	0.44	**0.3**	2.4	0.97

Table 69 List of parameters and run-up results for the smooth-impermeable slopes on the 13.4m long wave flume

Run-up measurements on smooth-impermeable slopes (20m flume) (Section 4.3.3)

Parameters	Variables
Wave flume dimensions	20m long and 1.2m width
Slopes angles	7˚,9˚, 11˚, 13 ˚, and 15˚
Slope type	Plane, smooth and impermeable
Types of waves	Regular Waves
Water depth	0.3m
Wave heights	0.04, 0.06, 0.08, 0.1, 0.12 and 0.14m
Wave periods	1, 1.43, 2, 2.5, 2.86 and 3.33 seconds
Iribarren number	Between 0.44 and 5.57
Wave steepness (H/L)	Between 0.002 and 0.077
Number of tests	135

Table 70 Summary of parameters used in the 20m long flume with smooth-impermeable slopes

#	α (˚)	tanα	cotα	h (m)	T (s)	H (m)	fr (htz)	Lo (m)	h/Lo	H/L	H/h	ξ	ϕ	tanα/(H/h)	R	R/H	R/h
1	7	0.12	8.14	0.3	1	0.04	1	1.56	0.19	0.026	0.1	0.77	0.15	0.92	**0.04**	1.08	0.14
2	7	0.12	8.14	0.3	1.43	0.04	0.7	3.18	0.09	0.013	0.1	1.1	0.10	0.92	**0.05**	1.25	0.17
3	7	0.12	8.14	0.3	2	0.04	0.5	6.24	0.05	0.006	0.1	1.53	0.07	0.92	**0.08**	2.00	0.27
4	7	0.12	8.14	0.3	2.5	0.04	0.4	9.75	0.03	0.004	0.1	1.92	0.06	0.92	**0.11**	2.75	0.37
5	7	0.12	8.14	0.3	2.86	0.04	0.35	12.7	0.02	0.003	0.1	2.19	0.05	0.92	**0.12**	2.88	0.38
6	7	0.12	8.14	0.3	3.33	0.04	0.3	17.3	0.02	0.002	0.1	2.56	0.04	0.92	**0.12**	3.10	0.41
7	7	0.12	8.14	0.3	1	0.06	1	1.56	0.19	0.038	0.2	0.63	0.12	0.61	**0.06**	0.97	0.19
8	7	0.12	8.14	0.3	1.43	0.06	0.7	3.18	0.09	0.019	0.2	0.89	0.08	0.61	**0.08**	1.25	0.25
9	7	0.12	8.14	0.3	2	0.06	0.5	6.24	0.05	0.01	0.2	1.25	0.06	0.61	**0.09**	1.53	0.31
10	7	0.12	8.14	0.3	2.5	0.06	0.4	9.75	0.03	0.006	0.2	1.57	0.05	0.61	**0.13**	2.08	0.42
11	7	0.12	8.14	0.3	2.86	0.06	0.35	12.7	0.02	0.005	0.2	1.79	0.04	0.61	**0.13**	2.17	0.43
12	7	0.12	8.14	0.3	3.33	0.06	0.3	17.3	0.02	0.003	0.2	2.09	0.04	0.61	**0.15**	2.50	0.50
13	7	0.12	8.14	0.3	1	0.08	1	1.56	0.19	0.051	0.3	0.54	0.10	0.46	**0.06**	0.79	0.21
14	7	0.12	8.14	0.3	1.43	0.08	0.7	3.18	0.09	0.025	0.3	0.77	0.07	0.46	**0.08**	0.96	0.26
15	7	0.12	8.14	0.3	2	0.08	0.5	6.24	0.05	0.013	0.3	1.08	0.05	0.46	**0.10**	1.25	0.33
16	7	0.12	8.14	0.3	2.5	0.08	0.4	9.75	0.03	0.008	0.3	1.36	0.04	0.46	**0.14**	1.75	0.47
17	7	0.12	8.14	0.3	2.86	0.08	0.35	12.7	0.02	0.006	0.3	1.55	0.04	0.46	**0.15**	1.88	0.50
18	7	0.12	8.14	0.3	3.33	0.08	0.3	17.3	0.02	0.005	0.3	1.81	0.03	0.46	**0.19**	2.38	0.63
19	7	0.12	8.14	0.3	1	0.1	1	1.56	0.19	0.064	0.3	0.48	0.09	0.37	**0.07**	0.70	0.23
20	7	0.12	8.14	0.3	1.43	0.1	0.7	3.18	0.09	0.031	0.3	0.69	0.07	0.37	**0.08**	0.80	0.27
21	7	0.12	8.14	0.3	2	0.1	0.5	6.24	0.05	0.016	0.3	0.97	0.05	0.37	**0.11**	1.05	0.35
22	7	0.12	8.14	0.3	2.5	0.1	0.4	9.75	0.03	0.01	0.3	1.21	0.04	0.37	**0.16**	1.60	0.53
23	7	0.12	8.14	0.3	2.86	0.1	0.35	12.7	0.02	0.008	0.3	1.39	0.03	0.37	**0.18**	1.80	0.60
24	7	0.12	8.14	0.3	3.33	0.1	0.3	17.3	0.02	0.006	0.3	1.62	0.03	0.37	**0.23**	2.30	0.77
25	7	0.12	8.14	0.3	1	0.12	1	1.56	0.19	0.077	0.4	0.44	0.09	0.31	**0.08**	0.67	0.27
26	7	0.12	8.14	0.3	1.43	0.12	0.7	3.18	0.09	0.038	0.4	0.63	0.06	0.31	**0.09**	0.75	0.30
27	7	0.12	8.14	0.3	2	0.12	0.5	6.24	0.05	0.019	0.4	0.89	0.04	0.31	**0.11**	0.92	0.37
28	7	0.12	8.14	0.3	2.5	0.12	0.4	9.75	0.03	0.012	0.4	1.11	0.03	0.31	**0.18**	1.50	0.60
29	7	0.12	8.14	0.3	2.86	0.12	0.35	12.7	0.02	0.009	0.4	1.26	0.03	0.31	**0.20**	1.67	0.67
30	7	0.12	8.14	0.3	3.33	0.12	0.3	17.3	0.02	0.007	0.4	1.48	0.03	0.31	**0.26**	2.17	0.87
31	9	0.16	6.31	0.3	1	0.06	1	1.56	0.19	0.038	0.2	0.81	0.16	0.79	**0.07**	1.12	0.22
32	9	0.16	6.31	0.3	1.43	0.06	0.7	3.18	0.09	0.019	0.2	1.15	0.11	0.79	**0.08**	1.38	0.28
33	9	0.16	6.31	0.3	2	0.06	0.5	6.24	0.05	0.01	0.2	1.62	0.08	0.79	**0.13**	2.17	0.43
34	9	0.16	6.31	0.3	3.33	0.06	0.3	17.3	0.02	0.003	0.2	2.69	0.05	0.79	**0.17**	2.83	0.57
35	9	0.16	6.31	0.3	1	0.08	1	1.56	0.19	0.051	0.3	0.7	0.13	0.59	**0.08**	0.94	0.25
36	9	0.16	6.31	0.3	1.43	0.08	0.7	3.18	0.09	0.025	0.3	1	0.09	0.59	**0.10**	1.23	0.33
37	9	0.16	6.31	0.3	2	0.08	0.5	6.24	0.05	0.013	0.3	1.4	0.07	0.59	**0.14**	1.75	0.47
38	9	0.16	6.31	0.3	3.33	0.08	0.3	17.3	0.02	0.005	0.3	2.33	0.04	0.59	**0.23**	2.88	0.77
39	9	0.16	6.31	0.3	1	0.1	1	1.56	0.19	0.064	0.3	0.63	0.12	0.48	**0.08**	0.84	0.28
40	9	0.16	6.31	0.3	1.43	0.1	0.7	3.18	0.09	0.031	0.3	0.89	0.08	0.48	**0.11**	1.10	0.37
41	9	0.16	6.31	0.3	2	0.1	0.5	6.24	0.05	0.016	0.3	1.25	0.06	0.48	**0.15**	1.50	0.50
42	9	0.16	6.31	0.3	3.33	0.1	0.3	17.3	0.02	0.006	0.3	2.09	0.04	0.48	**0.27**	2.70	0.90
43	9	0.16	6.31	0.3	1	0.12	1	1.56	0.19	0.077	0.4	0.57	0.11	0.40	**0.09**	0.73	0.29
44	9	0.16	6.31	0.3	1.43	0.12	0.7	3.18	0.09	0.038	0.4	0.82	0.08	0.40	**0.12**	0.99	0.40
45	9	0.16	6.31	0.3	2	0.12	0.5	6.24	0.05	0.019	0.4	1.14	0.05	0.40	**0.16**	1.32	0.53
46	9	0.16	6.31	0.3	3.33	0.12	0.3	17.3	0.02	0.007	0.4	1.9	0.03	0.40	**0.32**	2.67	1.07
47	9	0.16	6.31	0.3	1	0.14	1	1.56	0.19	0.09	0.5	0.53	0.10	0.34	**0.09**	0.65	0.30
48	9	0.16	6.31	0.3	1.43	0.14	0.7	3.18	0.09	0.044	0.5	0.76	0.07	0.34	**0.14**	0.98	0.46
49	9	0.16	6.31	0.3	2	0.14	0.5	6.24	0.05	0.022	0.5	1.06	0.05	0.34	**0.17**	1.22	0.57
50	9	0.16	6.31	0.3	3.33	0.14	0.3	17.3	0.02	0.008	0.5	1.76	0.03	0.34	**0.36**	2.57	1.20
51	11	0.19	5.14	0.3	1	0.06	1	1.56	0.19	0.038	0.2	0.99	0.19	0.97	**0.08**	1.27	0.25
52	11	0.19	5.14	0.3	1.43	0.06	0.7	3.18	0.09	0.019	0.2	1.42	0.13	0.97	**0.12**	1.97	0.39
53	11	0.19	5.14	0.3	2	0.06	0.5	6.24	0.05	0.01	0.2	1.98	0.10	0.97	**0.14**	2.29	0.46
54	11	0.19	5.14	0.3	3.33	0.06	0.3	17.3	0.02	0.003	0.2	3.3	0.06	0.97	**0.19**	3.17	0.63
55	11	0.19	5.14	0.3	1	0.08	1	1.56	0.19	0.051	0.3	0.86	0.17	0.73	**0.09**	1.10	0.29
56	11	0.19	5.14	0.3	1.43	0.08	0.7	3.18	0.09	0.025	0.3	1.23	0.12	0.73	**0.14**	1.72	0.46

57	11	0.19	5.14	0.3	2	0.08	0.5	6.24	0.05	0.013	0.3	1.72	0.08	0.73	**0.16**	2.00	0.53
58	11	0.19	5.14	0.3	3.33	0.08	0.3	17.3	0.02	0.005	0.3	2.86	0.05	0.73	**0.25**	3.09	0.82
59	11	0.19	5.14	0.3	1	0.1	1	1.56	0.19	0.064	0.3	0.77	0.15	0.58	**0.10**	1.03	0.34
60	11	0.19	5.14	0.3	1.43	0.1	0.7	3.18	0.09	0.031	0.3	1.1	0.10	0.58	**0.15**	1.47	0.49
61	11	0.19	5.14	0.3	2	0.1	0.5	6.24	0.05	0.016	0.3	1.54	0.07	0.58	**0.19**	1.91	0.64
62	11	0.19	5.14	0.3	3.33	0.1	0.3	17.3	0.02	0.006	0.3	2.56	0.04	0.58	**0.27**	2.75	0.92
63	11	0.19	5.14	0.3	1	0.12	1	1.56	0.19	0.077	0.4	0.7	0.13	0.49	**0.11**	0.94	0.38
64	11	0.19	5.14	0.3	1.43	0.12	0.7	3.18	0.09	0.038	0.4	1	0.09	0.49	**0.16**	1.34	0.53
65	11	0.19	5.14	0.3	2	0.12	0.5	6.24	0.05	0.019	0.4	1.4	0.07	0.49	**0.21**	1.78	0.71
66	11	0.19	5.14	0.3	3.33	0.12	0.3	17.3	0.02	0.007	0.4	2.34	0.04	0.49	**0.32**	2.70	1.08
67	11	0.19	5.14	0.3	1	0.14	1	1.56	0.19	0.09	0.5	0.65	0.12	0.42	**0.11**	0.80	0.38
68	11	0.19	5.14	0.3	1.43	0.14	0.7	3.18	0.09	0.044	0.5	0.93	0.09	0.42	**0.19**	1.32	0.62
69	11	0.19	5.14	0.3	2	0.14	0.5	6.24	0.05	0.022	0.5	1.3	0.06	0.42	**0.23**	1.68	0.78
70	11	0.19	5.14	0.3	3.33	0.14	0.3	17.3	0.02	0.008	0.5	2.16	0.04	0.42	**0.37**	2.66	1.24
71	13	0.23	4.33	0.3	1	0.04	1	1.56	0.19	0.026	0.1	1.44	0.28	1.73	**0.07**	1.63	0.22
72	13	0.23	4.33	0.3	1.43	0.04	0.7	3.18	0.09	0.013	0.1	2.06	0.19	1.73	**0.08**	2.08	0.28
73	13	0.23	4.33	0.3	2	0.04	0.5	6.24	0.05	0.006	0.1	2.88	0.14	1.73	**0.09**	2.25	0.30
74	13	0.23	4.33	0.3	2.5	0.04	0.4	9.75	0.03	0.004	0.1	3.6	0.11	1.73	**0.11**	2.63	0.35
75	13	0.23	4.33	0.3	2.86	0.04	0.35	12.7	0.02	0.003	0.1	4.12	0.10	1.73	**0.11**	2.75	0.37
76	13	0.23	4.33	0.3	3.33	0.04	0.3	17.3	0.02	0.002	0.1	4.81	0.08	1.73	**0.11**	2.75	0.37
77	13	0.23	4.33	0.3	1	0.06	1	1.56	0.19	0.038	0.2	1.18	0.23	1.15	**0.10**	1.67	0.33
78	13	0.23	4.33	0.3	1.43	0.06	0.7	3.18	0.09	0.019	0.2	1.68	0.16	1.15	**0.12**	2.00	0.40
79	13	0.23	4.33	0.3	2	0.06	0.5	6.24	0.05	0.01	0.2	2.35	0.11	1.15	**0.14**	2.33	0.47
80	13	0.23	4.33	0.3	2.5	0.06	0.4	9.75	0.03	0.006	0.2	2.94	0.09	1.15	**0.17**	2.83	0.57
81	13	0.23	4.33	0.3	2.86	0.06	0.35	12.7	0.02	0.005	0.2	3.36	0.08	1.15	**0.17**	2.83	0.57
82	13	0.23	4.33	0.3	3.33	0.06	0.3	17.3	0.02	0.003	0.2	3.92	0.07	1.15	**0.18**	2.97	0.59
83	13	0.23	4.33	0.3	1	0.08	1	1.56	0.19	0.051	0.3	1.02	0.20	0.87	**0.10**	1.19	0.32
84	13	0.23	4.33	0.3	1.43	0.08	0.7	3.18	0.09	0.025	0.3	1.46	0.14	0.87	**0.15**	1.90	0.51
85	13	0.23	4.33	0.3	2	0.08	0.5	6.24	0.05	0.013	0.3	2.04	0.10	0.87	**0.17**	2.18	0.58
86	13	0.23	4.33	0.3	2.5	0.08	0.4	9.75	0.03	0.008	0.3	2.55	0.08	0.87	**0.23**	2.88	0.77
87	13	0.23	4.33	0.3	2.86	0.08	0.35	12.7	0.02	0.006	0.3	2.91	0.07	0.87	**0.24**	3.05	0.81
88	13	0.23	4.33	0.3	3.33	0.08	0.3	17.3	0.02	0.005	0.3	3.4	0.06	0.87	**0.25**	3.06	0.82
89	13	0.23	4.33	0.3	1	0.1	1	1.56	0.19	0.064	0.3	0.91	0.18	0.69	**0.10**	1.00	0.33
90	13	0.23	4.33	0.3	1.43	0.1	0.7	3.18	0.09	0.031	0.3	1.3	0.12	0.69	**0.17**	1.70	0.57
91	13	0.23	4.33	0.3	2	0.1	0.5	6.24	0.05	0.016	0.3	1.82	0.09	0.69	**0.22**	2.15	0.72
92	13	0.23	4.33	0.3	2.5	0.1	0.4	9.75	0.03	0.01	0.3	2.28	0.07	0.69	**0.28**	2.80	0.93
93	13	0.23	4.33	0.3	2.86	0.1	0.35	12.7	0.02	0.008	0.3	2.61	0.06	0.69	**0.30**	3.00	1.00
94	13	0.23	4.33	0.3	3.33	0.1	0.3	17.3	0.02	0.006	0.3	3.04	0.05	0.69	**0.30**	3.04	1.01
95	13	0.23	4.33	0.3	1	0.12	1	1.56	0.19	0.077	0.4	0.83	0.16	0.58	**0.11**	0.92	0.37
96	13	0.23	4.33	0.3	1.43	0.12	0.7	3.18	0.09	0.038	0.4	1.19	0.11	0.58	**0.18**	1.50	0.60
97	13	0.23	4.33	0.3	2	0.12	0.5	6.24	0.05	0.019	0.4	1.66	0.08	0.58	**0.24**	2.01	0.80
98	13	0.23	4.33	0.3	2.5	0.12	0.4	9.75	0.03	0.012	0.4	2.08	0.06	0.58	**0.32**	2.67	1.07
99	13	0.23	4.33	0.3	2.86	0.12	0.35	12.7	0.02	0.009	0.4	2.38	0.06	0.58	**0.35**	2.93	1.17
100	13	0.23	4.33	0.3	3.33	0.12	0.3	17.3	0.02	0.007	0.4	2.77	0.05	0.58	**0.35**	2.95	1.18
101	13	0.23	4.33	0.3	1	0.14	1	1.56	0.19	0.09	0.5	0.77	0.15	0.49	**0.13**	0.89	0.42
102	13	0.23	4.33	0.3	1.43	0.14	0.7	3.18	0.09	0.044	0.5	1.1	0.10	0.49	**0.21**	1.48	0.69
103	13	0.23	4.33	0.3	2	0.14	0.5	6.24	0.05	0.022	0.5	1.54	0.07	0.49	**0.27**	1.92	0.90
104	13	0.23	4.33	0.3	2.86	0.14	0.35	12.7	0.02	0.011	0.5	2.2	0.05	0.49	**0.41**	2.93	1.37
105	13	0.23	4.33	0.3	3.33	0.14	0.3	17.3	0.02	0.008	0.5	2.57	0.04	0.49	**0.41**	2.93	1.37
106	15	0.27	3.73	0.3	1	0.04	1	1.56	0.19	0.026	0.1	1.67	0.32	2.01	**0.06**	1.60	0.21
107	15	0.27	3.73	0.3	1.43	0.04	0.7	3.18	0.09	0.013	0.1	2.39	0.23	2.01	**0.08**	2.00	0.27
108	15	0.27	3.73	0.3	2	0.04	0.5	6.24	0.05	0.006	0.1	3.35	0.16	2.01	**0.09**	2.13	0.28
109	15	0.27	3.73	0.3	2.5	0.04	0.4	9.75	0.03	0.004	0.1	4.18	0.13	2.01	**0.10**	2.40	0.32
110	15	0.27	3.73	0.3	2.86	0.04	0.35	12.7	0.02	0.003	0.1	4.78	0.11	2.01	**0.10**	2.50	0.33
111	15	0.27	3.73	0.3	3.33	0.04	0.3	17.3	0.02	0.002	0.1	5.57	0.10	2.01	**0.11**	2.75	0.37
112	15	0.27	3.73	0.3	1	0.06	1	1.56	0.19	0.038	0.2	1.37	0.26	1.34	**0.10**	1.67	0.33
113	15	0.27	3.73	0.3	1.43	0.06	0.7	3.18	0.09	0.019	0.2	1.95	0.18	1.34	**0.12**	2.03	0.41
114	15	0.27	3.73	0.3	2	0.06	0.5	6.24	0.05	0.01	0.2	2.73	0.13	1.34	**0.14**	2.33	0.47
115	15	0.27	3.73	0.3	2.5	0.06	0.4	9.75	0.03	0.006	0.2	3.42	0.11	1.34	**0.15**	2.50	0.50
116	15	0.27	3.73	0.3	2.86	0.06	0.35	12.7	0.02	0.005	0.2	3.9	0.09	1.34	**0.16**	2.67	0.53
117	15	0.27	3.73	0.3	3.33	0.06	0.3	17.3	0.02	0.003	0.2	4.55	0.08	1.34	**0.17**	2.83	0.57
118	15	0.27	3.73	0.3	1	0.08	1	1.56	0.19	0.051	0.3	1.18	0.23	1.00	**0.14**	1.69	0.45
119	15	0.27	3.73	0.3	1.43	0.08	0.7	3.18	0.09	0.025	0.3	1.69	0.16	1.00	**0.16**	2.00	0.53
120	15	0.27	3.73	0.3	2	0.08	0.5	6.24	0.05	0.013	0.3	2.37	0.11	1.00	**0.18**	2.25	0.60
121	15	0.27	3.73	0.3	2.5	0.08	0.4	9.75	0.03	0.008	0.3	2.96	0.09	1.00	**0.21**	2.63	0.70
122	15	0.27	3.73	0.3	2.86	0.08	0.35	12.7	0.02	0.006	0.3	3.38	0.08	1.00	**0.23**	2.88	0.77
123	15	0.27	3.73	0.3	3.33	0.08	0.3	17.3	0.02	0.005	0.3	3.94	0.07	1.00	**0.24**	3.00	0.80
124	15	0.27	3.73	0.3	1	0.1	1	1.56	0.19	0.064	0.3	1.06	0.20	0.80	**0.15**	1.50	0.50
125	15	0.27	3.73	0.3	1.43	0.1	0.7	3.18	0.09	0.031	0.3	1.51	0.14	0.80	**0.20**	2.00	0.67
126	15	0.27	3.73	0.3	2	0.1	0.5	6.24	0.05	0.016	0.3	2.12	0.10	0.80	**0.23**	2.30	0.77
127	15	0.27	3.73	0.3	2.5	0.1	0.4	9.75	0.03	0.01	0.3	2.65	0.08	0.80	**0.28**	2.80	0.93
128	15	0.27	3.73	0.3	2.86	0.1	0.35	12.7	0.02	0.008	0.3	3.02	0.07	0.80	**0.28**	2.80	0.93
129	15	0.27	3.73	0.3	3.33	0.1	0.3	17.3	0.02	0.006	0.3	3.52	0.06	0.80	**0.30**	3.00	1.00
130	15	0.27	3.73	0.3	1	0.12	1	1.56	0.19	0.077	0.4	0.97	0.19	0.67	**0.13**	1.08	0.43
131	15	0.27	3.73	0.3	1.43	0.12	0.7	3.18	0.09	0.038	0.4	1.38	0.13	0.67	**0.23**	1.92	0.77
132	15	0.27	3.73	0.3	2	0.12	0.5	6.24	0.05	0.019	0.4	1.93	0.09	0.67	**0.27**	2.25	0.90
133	15	0.27	3.73	0.3	2.5	0.12	0.4	9.75	0.03	0.012	0.4	2.42	0.07	0.67	**0.31**	2.58	1.03
134	15	0.27	3.73	0.3	2.86	0.12	0.35	12.7	0.02	0.009	0.4	2.76	0.07	0.67	**0.34**	2.83	1.13
135	15	0.27	3.73	0.3	3.33	0.12	0.3	17.3	0.02	0.007	0.4	3.22	0.06	0.67	**0.37**	3.08	1.23

Table 71 List of parameters and run-up results for the smooth-impermeable slopes on the 20m long wave flume

Run-up measurements on rough-impermeable slopes (Section 4.3.4)

Parameters	Variables
Wave flume dimensions	13.4m long and 0.45m width
Slope angle	10˚
Surface Roughness Types	3mm sheets of 30, 45, 60 and 80 PPI foams
Types of waves	Regular Waves
Water depth	0.3m
Wave heights	0.04, 0.06, 0.08, 0.1, and 0.12m
Wave periods	1, 1.43, 2, 2.86, and 3.33s
Iribarren number	Between 0.63 and 3.63
Wave steepness (H/L)	Between 0.002 and 0.08
Number of tests	100

Table 72 Summary of parameters used in the 13.4m long flume with rough-impermeable slopes

#	α (˚)	tanα	cotα	h (m)	T (s)	H (m)	fr (htz)	Lo (m)	h/Lo	H/L	H/h	ξ	ϕ	tanα/(H/h)	R	R/H	R/h
1	10	0.18	5.67	0.3	3.33	0.04	0.3	17.3	0.02	0.002	0.1	3.67	0.06	1.32	0.09	2.2	0.29
2	10	0.18	5.67	0.3	2.86	0.04	0.35	12.7	0.02	0.003	0.1	3.15	0.07	1.32	0.09	2.2	0.3
3	10	0.18	5.67	0.3	3.33	0.06	0.3	17.3	0.02	0.003	0.2	3	0.05	0.88	0.12	2	0.41
4	10	0.18	5.67	0.3	3.33	0.08	0.3	17.3	0.02	0.005	0.3	2.6	0.04	0.66	0.16	2	0.53
5	10	0.18	5.67	0.3	2.86	0.06	0.35	12.7	0.02	0.005	0.2	2.57	0.06	0.88	0.11	1.9	0.37
6	10	0.18	5.67	0.3	3.33	0.1	0.3	17.3	0.02	0.006	0.3	2.32	0.04	0.53	0.19	1.9	0.63
7	10	0.18	5.67	0.3	2.86	0.08	0.35	12.7	0.02	0.006	0.3	2.22	0.05	0.66	0.16	2	0.52
8	10	0.18	5.67	0.3	2	0.04	0.5	6.24	0.05	0.006	0.1	2.2	0.11	1.32	0.08	2	0.27
9	10	0.18	5.67	0.3	3.33	0.12	0.3	17.3	0.02	0.007	0.4	2.12	0.04	0.44	0.22	1.8	0.72
10	10	0.18	5.67	0.3	2.86	0.1	0.35	12.7	0.02	0.008	0.3	1.99	0.05	0.53	0.19	1.9	0.65
11	10	0.18	5.67	0.3	2.86	0.12	0.35	12.7	0.02	0.009	0.4	1.82	0.04	0.44	0.22	1.8	0.72
12	10	0.18	5.67	0.3	2	0.06	0.5	6.24	0.05	0.01	0.2	1.8	0.09	0.88	0.11	1.8	0.35
13	10	0.18	5.67	0.3	1.43	0.04	0.7	3.18	0.09	0.013	0.1	1.57	0.15	1.32	0.06	1.6	0.21
14	10	0.18	5.67	0.3	2	0.08	0.5	6.24	0.05	0.013	0.3	1.56	0.07	0.66	0.12	1.5	0.4
15	10	0.18	5.67	0.3	2	0.1	0.5	6.24	0.05	0.016	0.3	1.39	0.07	0.53	0.14	1.4	0.47
16	10	0.18	5.67	0.3	1.43	0.06	0.7	3.18	0.09	0.019	0.2	1.28	0.12	0.88	0.08	1.3	0.26
17	10	0.18	5.67	0.3	2	0.12	0.5	6.24	0.05	0.019	0.4	1.27	0.06	0.44	0.15	1.2	0.5
18	10	0.18	5.67	0.3	1.43	0.08	0.7	3.18	0.09	0.025	0.3	1.11	0.10	0.66	0.09	1.1	0.29
19	10	0.18	5.67	0.3	1	0.04	1	1.56	0.19	0.026	0.1	1.1	0.21	1.32	0.04	1	0.14
20	10	0.18	5.67	0.3	1.43	0.1	0.7	3.18	0.09	0.031	0.3	0.99	0.09	0.53	0.09	0.9	0.31
21	10	0.18	5.67	0.3	1.43	0.12	0.7	3.18	0.09	0.038	0.4	0.91	0.09	0.44	0.1	0.9	0.34
22	10	0.18	5.67	0.3	1	0.06	1	1.56	0.19	0.038	0.2	0.9	0.17	0.88	0.05	0.8	0.17
23	10	0.18	5.67	0.3	1	0.08	1	1.56	0.19	0.051	0.3	0.78	0.15	0.66	0.06	0.8	0.2
24	10	0.18	5.67	0.3	1	0.1	1	1.56	0.19	0.064	0.3	0.7	0.13	0.53	0.07	0.7	0.22
25	10	0.18	5.67	0.3	1	0.12	1	1.56	0.19	0.077	0.4	0.64	0.12	0.44	0.07	0.6	0.24

Table 73 List of parameters and run-up results for the rough-impermeable R30 slope

#	α (˚)	tanα	cotα	h (m)	T (s)	H (m)	fr (htz)	Lo (m)	h/Lo	H/L	H/h	ξ	ϕ	tanα/(H/h)	R	R/H	R/h
1	10	0.18	5.67	0.3	3.33	0.04	0.3	17.3	0.02	0.002	0.1	3.67	0.06	1.32	0.09	2.1	0.28
2	10	0.18	5.67	0.3	2.86	0.04	0.35	12.7	0.02	0.003	0.1	3.15	0.07	1.32	0.09	2.2	0.29
3	10	0.18	5.67	0.3	3.33	0.06	0.3	17.3	0.02	0.003	0.2	3	0.05	0.88	0.12	2.1	0.41
4	10	0.18	5.67	0.3	3.33	0.08	0.3	17.3	0.02	0.005	0.3	2.6	0.04	0.66	0.16	2.1	0.55
5	10	0.18	5.67	0.3	2.86	0.06	0.35	12.7	0.02	0.005	0.2	2.57	0.06	0.88	0.12	1.9	0.39
6	10	0.18	5.67	0.3	3.33	0.1	0.3	17.3	0.02	0.006	0.3	2.32	0.04	0.53	0.19	1.9	0.65
7	10	0.18	5.67	0.3	2.86	0.08	0.35	12.7	0.02	0.006	0.3	2.22	0.05	0.66	0.16	2	0.53
8	10	0.18	5.67	0.3	2	0.04	0.5	6.24	0.05	0.006	0.1	2.2	0.11	1.32	0.08	2.1	0.28
9	10	0.18	5.67	0.3	3.33	0.12	0.3	17.3	0.02	0.007	0.4	2.12	0.04	0.44	0.22	1.8	0.72
10	10	0.18	5.67	0.3	2.86	0.1	0.35	12.7	0.02	0.008	0.3	1.99	0.05	0.53	0.19	1.9	0.64
11	10	0.18	5.67	0.3	2.86	0.12	0.35	12.7	0.02	0.009	0.4	1.82	0.04	0.44	0.21	1.7	0.69
12	10	0.18	5.67	0.3	2	0.06	0.5	6.24	0.05	0.01	0.2	1.8	0.09	0.88	0.1	1.7	0.35
13	10	0.18	5.67	0.3	1.43	0.04	0.7	3.18	0.09	0.013	0.1	1.57	0.15	1.32	0.06	1.6	0.21
14	10	0.18	5.67	0.3	2	0.08	0.5	6.24	0.05	0.013	0.3	1.56	0.07	0.66	0.12	1.5	0.41
15	10	0.18	5.67	0.3	2	0.1	0.5	6.24	0.05	0.016	0.3	1.39	0.07	0.53	0.14	1.4	0.46
16	10	0.18	5.67	0.3	1.43	0.06	0.7	3.18	0.09	0.019	0.2	1.28	0.12	0.88	0.07	1.2	0.24
17	10	0.18	5.67	0.3	2	0.12	0.5	6.24	0.05	0.019	0.4	1.27	0.06	0.44	0.15	1.2	0.49
18	10	0.18	5.67	0.3	1.43	0.08	0.7	3.18	0.09	0.025	0.3	1.11	0.10	0.66	0.09	1.1	0.3
19	10	0.18	5.67	0.3	1	0.04	1	1.56	0.19	0.026	0.1	1.1	0.21	1.32	0.04	1	0.13
20	10	0.18	5.67	0.3	1.43	0.1	0.7	3.18	0.09	0.031	0.3	0.99	0.09	0.53	0.1	1	0.32
21	10	0.18	5.67	0.3	1.43	0.12	0.7	3.18	0.09	0.038	0.4	0.91	0.09	0.44	0.1	0.9	0.35
22	10	0.18	5.67	0.3	1	0.06	1	1.56	0.19	0.038	0.2	0.9	0.17	0.88	0.06	1	0.19
23	10	0.18	5.67	0.3	1	0.08	1	1.56	0.19	0.051	0.3	0.78	0.15	0.66	0.07	0.8	0.22
24	10	0.18	5.67	0.3	1	0.1	1	1.56	0.19	0.064	0.3	0.7	0.13	0.53	0.07	0.7	0.23
25	10	0.18	5.67	0.3	1	0.12	1	1.56	0.19	0.077	0.4	0.64	0.12	0.44	0.07	0.6	0.24

Table 74 List of parameters and run-up results for the rough-impermeable R45 slope

#	α (˚)	tanα	cotα	h (m)	T (s)	H (m)	fr (htz)	Lo (m)	h/Lo	H/L	H/h	ξ	ϕ	tanα/(H/h)	R	R/H	R/h
1	10	0.18	5.67	0.3	3.33	0.04	0.3	17.3	0.02	0.002	0.1	3.67	0.06	1.32	0.09	2.1	0.28
2	10	0.18	5.67	0.3	2.86	0.04	0.35	12.7	0.02	0.003	0.1	3.15	0.07	1.32	0.09	2.1	0.28
3	10	0.18	5.67	0.3	3.33	0.06	0.3	17.3	0.02	0.003	0.2	3	0.05	0.88	0.13	2.2	0.43
4	10	0.18	5.67	0.3	3.33	0.08	0.3	17.3	0.02	0.005	0.3	2.6	0.04	0.66	0.17	2.1	0.57
5	10	0.18	5.67	0.3	2.86	0.06	0.35	12.7	0.02	0.005	0.2	2.57	0.06	0.88	0.12	2	0.41
6	10	0.18	5.67	0.3	3.33	0.1	0.3	17.3	0.02	0.006	0.3	2.32	0.04	0.53	0.21	2.1	0.69
7	10	0.18	5.67	0.3	2.86	0.08	0.35	12.7	0.02	0.006	0.3	2.22	0.05	0.66	0.16	2.1	0.55
8	10	0.18	5.67	0.3	2	0.04	0.5	6.24	0.05	0.006	0.1	2.2	0.11	1.32	0.09	2.1	0.28
9	10	0.18	5.67	0.3	3.33	0.12	0.3	17.3	0.02	0.007	0.4	2.12	0.04	0.44	0.23	1.9	0.75
10	10	0.18	5.67	0.3	2.86	0.1	0.35	12.7	0.02	0.008	0.3	1.99	0.05	0.53	0.19	1.9	0.65
11	10	0.18	5.67	0.3	2.86	0.12	0.35	12.7	0.02	0.009	0.4	1.82	0.04	0.44	0.22	1.8	0.72
12	10	0.18	5.67	0.3	2	0.06	0.5	6.24	0.05	0.01	0.2	1.8	0.09	0.88	0.11	1.8	0.36
13	10	0.18	5.67	0.3	1.43	0.04	0.7	3.18	0.09	0.013	0.1	1.57	0.15	1.32	0.07	1.7	0.23
14	10	0.18	5.67	0.3	2	0.08	0.5	6.24	0.05	0.013	0.3	1.56	0.07	0.66	0.12	1.5	0.39
15	10	0.18	5.67	0.3	2	0.1	0.5	6.24	0.05	0.016	0.3	1.39	0.07	0.53	0.14	1.4	0.46
16	10	0.18	5.67	0.3	1.43	0.06	0.7	3.18	0.09	0.019	0.2	1.28	0.12	0.88	0.08	1.4	0.27
17	10	0.18	5.67	0.3	2	0.12	0.5	6.24	0.05	0.019	0.4	1.27	0.06	0.44	0.15	1.2	0.49
18	10	0.18	5.67	0.3	1.43	0.08	0.7	3.18	0.09	0.025	0.3	1.11	0.10	0.66	0.09	1.1	0.3
19	10	0.18	5.67	0.3	1	0.04	1	1.56	0.19	0.026	0.1	1.1	0.21	1.32	0.04	1.1	0.14
20	10	0.18	5.67	0.3	1.43	0.1	0.7	3.18	0.09	0.031	0.3	0.99	0.09	0.53	0.1	1	0.35
21	10	0.18	5.67	0.3	1.43	0.12	0.7	3.18	0.09	0.038	0.4	0.91	0.09	0.44	0.11	0.9	0.38
22	10	0.18	5.67	0.3	1	0.06	1	1.56	0.19	0.038	0.2	0.9	0.17	0.88	0.06	0.9	0.19
23	10	0.18	5.67	0.3	1	0.08	1	1.56	0.19	0.051	0.3	0.78	0.15	0.66	0.06	0.8	0.21
24	10	0.18	5.67	0.3	1	0.1	1	1.56	0.19	0.064	0.3	0.7	0.13	0.53	0.07	0.7	0.23
25	10	0.18	5.67	0.3	1	0.12	1	1.56	0.19	0.077	0.4	0.64	0.12	0.44	0.07	0.6	0.25

Table 75 List of parameters and run-up results for the rough-impermeable R60 slope

#	α (˚)	tanα	cotα	h (m)	T (s)	H (m)	fr (htz)	Lo (m)	h/Lo	H/L	H/h	ξ	ϕ	tanα/(H/h)	R	R/H	R/h
1	10	0.18	5.67	0.3	3.33	0.04	0.3	17.3	0.02	0.002	0.1	3.67	0.06	1.32	0.09	2.3	0.31
2	10	0.18	5.67	0.3	2.86	0.04	0.35	12.7	0.02	0.003	0.1	3.15	0.07	1.32	0.09	2.3	0.31
3	10	0.18	5.67	0.3	3.33	0.06	0.3	17.3	0.02	0.003	0.2	3	0.05	0.88	0.14	2.3	0.45
4	10	0.18	5.67	0.3	3.33	0.08	0.3	17.3	0.02	0.005	0.3	2.6	0.04	0.66	0.18	2.2	0.58
5	10	0.18	5.67	0.3	2.86	0.06	0.35	12.7	0.02	0.005	0.2	2.57	0.06	0.88	0.13	2.1	0.43
6	10	0.18	5.67	0.3	3.33	0.1	0.3	17.3	0.02	0.006	0.3	2.32	0.04	0.53	0.21	2.1	0.69
7	10	0.18	5.67	0.3	2.86	0.08	0.35	12.7	0.02	0.006	0.3	2.22	0.05	0.66	0.17	2.2	0.58
8	10	0.18	5.67	0.3	2	0.04	0.5	6.24	0.05	0.006	0.1	2.2	0.11	1.32	0.09	2.2	0.29
9	10	0.18	5.67	0.3	3.33	0.12	0.3	17.3	0.02	0.007	0.4	2.12	0.04	0.44	0.24	2	0.79
10	10	0.18	5.67	0.3	2.86	0.1	0.35	12.7	0.02	0.008	0.3	1.99	0.05	0.53	0.2	2	0.66
11	10	0.18	5.67	0.3	2.86	0.12	0.35	12.7	0.02	0.009	0.4	1.82	0.04	0.44	0.22	1.8	0.74
12	10	0.18	5.67	0.3	2	0.06	0.5	6.24	0.05	0.01	0.2	1.8	0.09	0.88	0.11	1.8	0.36
13	10	0.18	5.67	0.3	1.43	0.04	0.7	3.18	0.09	0.013	0.1	1.57	0.15	1.32	0.07	1.8	0.24
14	10	0.18	5.67	0.3	2	0.08	0.5	6.24	0.05	0.013	0.3	1.56	0.07	0.66	0.13	1.6	0.43
15	10	0.18	5.67	0.3	2	0.1	0.5	6.24	0.05	0.016	0.3	1.39	0.07	0.53	0.15	1.5	0.49
16	10	0.18	5.67	0.3	1.43	0.06	0.7	3.18	0.09	0.019	0.2	1.28	0.12	0.88	0.09	1.4	0.29
17	10	0.18	5.67	0.3	2	0.12	0.5	6.24	0.05	0.019	0.4	1.27	0.06	0.44	0.15	1.3	0.5
18	10	0.18	5.67	0.3	1.43	0.08	0.7	3.18	0.09	0.025	0.3	1.11	0.10	0.66	0.09	1.2	0.31
19	10	0.18	5.67	0.3	1	0.04	1	1.56	0.19	0.026	0.1	1.1	0.21	1.32	0.05	1.2	0.16
20	10	0.18	5.67	0.3	1.43	0.1	0.7	3.18	0.09	0.031	0.3	0.99	0.09	0.53	0.1	1	0.34
21	10	0.18	5.67	0.3	1.43	0.12	0.7	3.18	0.09	0.038	0.4	0.91	0.09	0.44	0.11	0.9	0.37
22	10	0.18	5.67	0.3	1	0.06	1	1.56	0.19	0.038	0.2	0.9	0.17	0.88	0.06	0.9	0.19
23	10	0.18	5.67	0.3	1	0.08	1	1.56	0.19	0.051	0.3	0.78	0.15	0.66	0.06	0.8	0.21
24	10	0.18	5.67	0.3	1	0.1	1	1.56	0.19	0.064	0.3	0.7	0.13	0.53	0.07	0.7	0.23
25	10	0.18	5.67	0.3	1	0.12	1	1.56	0.19	0.077	0.4	0.64	0.12	0.44	0.08	0.6	0.25

Table 76 List of parameters and run-up results for the rough-impermeable R80 slope

Run-up measurements on permeable slopes with adjusted water table elevations (Section 4.3.5)

Parameters	Variables
Wave flume dimensions	13.4m long and 0.45m width
Slope angle	10˚
Hydraulic conductivities	0.052 and 0.105 m/s
Types of waves	Regular Waves
SWL water depth	0.3m
Lagoon water depths	0.4 and 0.2m
Wave heights	0.04, 0.06, 0.08, 0.1, and 0.12m
Wave periods	1, 1.43, 2, 2.86, and 3.33s
Iribarren number	Between 0.63 and 12
Wave steepness (H/L)	Between 0.002 and 0.08
Number of tests	100

Table 77 Summary of parameters on permeable slopes with adjusted water table elevations

#	α (˚)	tanα	cotα	h (m)	T (s)	H (m)	fr (htz)	Lo (m)	h/Lo	H/L	H/h	ξ	ϕ	tanα/(H/h)	R	R/H	R/h
1	10	0.18	5.67	0.3	3.33	0.04	0.3	17.3	0.02	0.002	0.1	3.67	0.06	1.32	0.09	2.2	0.29
2	10	0.18	5.67	0.3	2.86	0.04	0.35	12.7	0.02	0.003	0.1	3.15	0.07	1.32	0.08	2	0.27
3	10	0.18	5.67	0.3	3.33	0.06	0.3	17.3	0.02	0.003	0.2	3	0.05	0.88	0.13	2.2	0.45
4	10	0.18	5.67	0.3	3.33	0.08	0.3	17.3	0.02	0.005	0.3	2.6	0.04	0.66	0.17	2.1	0.57
5	10	0.18	5.67	0.3	2.86	0.06	0.35	12.7	0.02	0.005	0.2	2.57	0.06	0.88	0.11	1.9	0.38
6	10	0.18	5.67	0.3	3.33	0.1	0.3	17.3	0.02	0.006	0.3	2.32	0.04	0.53	0.21	2.1	0.71
7	10	0.18	5.67	0.3	2.86	0.08	0.35	12.7	0.02	0.006	0.3	2.22	0.05	0.66	0.15	1.9	0.52
8	10	0.18	5.67	0.3	2	0.04	0.5	6.24	0.05	0.006	0.1	2.2	0.11	1.32	0.07	1.8	0.23
9	10	0.18	5.67	0.3	3.33	0.12	0.3	17.3	0.02	0.007	0.4	2.12	0.04	0.44	0.24	2	0.8
10	10	0.18	5.67	0.3	2.86	0.1	0.35	12.7	0.02	0.008	0.3	1.99	0.05	0.53	0.2	2	0.65
11	10	0.18	5.67	0.3	2.86	0.12	0.35	12.7	0.02	0.009	0.4	1.82	0.04	0.44	0.23	1.9	0.75
12	10	0.18	5.67	0.3	2	0.06	0.5	6.24	0.05	0.01	0.2	1.8	0.09	0.88	0.1	1.7	0.34
13	10	0.18	5.67	0.3	1.43	0.04	0.7	3.18	0.09	0.013	0.1	1.57	0.15	1.32	0.06	1.5	0.2
14	10	0.18	5.67	0.3	2	0.08	0.5	6.24	0.05	0.013	0.3	1.56	0.07	0.66	0.13	1.6	0.42
15	10	0.18	5.67	0.3	2	0.1	0.5	6.24	0.05	0.016	0.3	1.39	0.07	0.53	0.14	1.4	0.48
16	10	0.18	5.67	0.3	1.43	0.06	0.7	3.18	0.09	0.019	0.2	1.28	0.12	0.88	0.08	1.4	0.28
17	10	0.18	5.67	0.3	2	0.12	0.5	6.24	0.05	0.019	0.4	1.27	0.06	0.44	0.16	1.3	0.52
18	10	0.18	5.67	0.3	1.43	0.08	0.7	3.18	0.09	0.025	0.3	1.11	0.10	0.66	0.09	1.2	0.31
19	10	0.18	5.67	0.3	1	0.04	1	1.56	0.19	0.026	0.1	1.1	0.21	1.32	0.04	0.9	0.12
20	10	0.18	5.67	0.3	1.43	0.1	0.7	3.18	0.09	0.031	0.3	0.99	0.09	0.53	0.11	1.1	0.36
21	10	0.18	5.67	0.3	1.43	0.12	0.7	3.18	0.09	0.038	0.4	0.91	0.09	0.44	0.12	1	0.39
22	10	0.18	5.67	0.3	1	0.06	1	1.56	0.19	0.038	0.2	0.9	0.17	0.88	0.04	0.7	0.14
23	10	0.18	5.67	0.3	1	0.08	1	1.56	0.19	0.051	0.3	0.78	0.15	0.66	0.06	0.7	0.2
24	10	0.18	5.67	0.3	1	0.1	1	1.56	0.19	0.064	0.3	0.7	0.13	0.53	0.07	0.7	0.24
25	10	0.18	5.67	0.3	1	0.12	1	1.56	0.19	0.077	0.4	0.64	0.12	0.44	0.07	0.5	0.22

Table 78 List of parameters and run-up results for the R80 slope with a low water table

#	α (˚)	tanα	cotα	h (m)	T (s)	H (m)	fr (htz)	Lo (m)	h/Lo	H/L	H/h	ξ	ϕ	tanα/(H/h)	R	R/H	R/h
1	10	0.18	5.67	0.3	3.33	0.04	0.3	17.3	0.02	0.002	0.1	3.67	0.06	1.32	0.09	2.3	0.31
2	10	0.18	5.67	0.3	2.86	0.04	0.35	12.7	0.02	0.003	0.1	3.15	0.07	1.32	0.09	2.1	0.28
3	10	0.18	5.67	0.3	3.33	0.06	0.3	17.3	0.02	0.003	0.2	3	0.05	0.88	0.14	2.3	0.47
4	10	0.18	5.67	0.3	3.33	0.08	0.3	17.3	0.02	0.005	0.3	2.6	0.04	0.66	0.18	2.3	0.61
5	10	0.18	5.67	0.3	2.86	0.06	0.35	12.7	0.02	0.005	0.2	2.57	0.06	0.88	0.12	2	0.39
6	10	0.18	5.67	0.3	3.33	0.1	0.3	17.3	0.02	0.006	0.3	2.32	0.04	0.53	0.22	2.2	0.75
7	10	0.18	5.67	0.3	2.86	0.08	0.35	12.7	0.02	0.006	0.3	2.22	0.05	0.66	0.16	2	0.54
8	10	0.18	5.67	0.3	2	0.04	0.5	6.24	0.05	0.006	0.1	2.2	0.11	1.32	0.07	1.8	0.24
9	10	0.18	5.67	0.3	3.33	0.12	0.3	17.3	0.02	0.007	0.4	2.12	0.04	0.44	0.24	2	0.82
10	10	0.18	5.67	0.3	2.86	0.1	0.35	12.7	0.02	0.008	0.3	1.99	0.05	0.53	0.21	2.1	0.69
11	10	0.18	5.67	0.3	2.86	0.12	0.35	12.7	0.02	0.009	0.4	1.82	0.04	0.44	0.23	1.9	0.77
12	10	0.18	5.67	0.3	2	0.06	0.5	6.24	0.05	0.01	0.2	1.8	0.09	0.88	0.11	1.8	0.36
13	10	0.18	5.67	0.3	1.43	0.04	0.7	3.18	0.09	0.013	0.1	1.57	0.15	1.32	0.06	1.6	0.21
14	10	0.18	5.67	0.3	2	0.08	0.5	6.24	0.05	0.013	0.3	1.56	0.07	0.66	0.14	1.7	0.46
15	10	0.18	5.67	0.3	2	0.1	0.5	6.24	0.05	0.016	0.3	1.39	0.07	0.53	0.16	1.6	0.52
16	10	0.18	5.67	0.3	1.43	0.06	0.7	3.18	0.09	0.019	0.2	1.28	0.12	0.88	0.09	1.5	0.3
17	10	0.18	5.67	0.3	2	0.12	0.5	6.24	0.05	0.019	0.4	1.27	0.06	0.44	0.16	1.4	0.54
18	10	0.18	5.67	0.3	1.43	0.08	0.7	3.18	0.09	0.025	0.3	1.11	0.10	0.66	0.1	1.3	0.35
19	10	0.18	5.67	0.3	1	0.04	1	1.56	0.19	0.026	0.1	1.1	0.21	1.32	0.04	0.9	0.12
20	10	0.18	5.67	0.3	1.43	0.1	0.7	3.18	0.09	0.031	0.3	0.99	0.09	0.53	0.11	1.1	0.36
21	10	0.18	5.67	0.3	1.43	0.12	0.7	3.18	0.09	0.038	0.4	0.91	0.09	0.44	0.12	1	0.39
22	10	0.18	5.67	0.3	1	0.06	1	1.56	0.19	0.038	0.2	0.9	0.17	0.88	0.05	0.8	0.15
23	10	0.18	5.67	0.3	1	0.08	1	1.56	0.19	0.051	0.3	0.78	0.15	0.66	0.06	0.8	0.21
24	10	0.18	5.67	0.3	1	0.1	1	1.56	0.19	0.064	0.3	0.7	0.13	0.53	0.07	0.7	0.23
25	10	0.18	5.67	0.3	1	0.12	1	1.56	0.19	0.077	0.4	0.64	0.12	0.44	0.07	0.5	0.22

Table 79 List of parameters and run-up results for the R80 slope with high water table

#	α (°)	tanα	cotα	h (m)	T (s)	H (m)	fr (htz)	Lo (m)	h/Lo	H/L	H/h	ξ	ϕ	tanα/(H/h)	R	R/H	R/h
1	10	0.18	5.67	0.3	3.33	0.04	0.3	17.3	0.02	0.002	0.1	3.67	0.06	1.32	0.07	1.8	0.24
2	10	0.18	5.67	0.3	2.86	0.04	0.35	12.7	0.02	0.003	0.1	3.15	0.07	1.32	0.06	1.6	0.21
3	10	0.18	5.67	0.3	3.33	0.06	0.3	17.3	0.02	0.003	0.2	3	0.05	0.88	0.1	1.6	0.33
4	10	0.18	5.67	0.3	3.33	0.08	0.3	17.3	0.02	0.005	0.3	2.6	0.04	0.66	0.13	1.6	0.42
5	10	0.18	5.67	0.3	2.86	0.06	0.35	12.7	0.02	0.005	0.2	2.57	0.06	0.88	0.09	1.5	0.3
6	10	0.18	5.67	0.3	3.33	0.1	0.3	17.3	0.02	0.006	0.3	2.32	0.04	0.53	0.16	1.6	0.52
7	10	0.18	5.67	0.3	2.86	0.08	0.35	12.7	0.02	0.006	0.3	2.22	0.05	0.66	0.11	1.4	0.37
8	10	0.18	5.67	0.3	2	0.04	0.5	6.24	0.05	0.006	0.1	2.2	0.11	1.32	0.05	1.3	0.18
9	10	0.18	5.67	0.3	3.33	0.12	0.3	17.3	0.02	0.007	0.4	2.12	0.04	0.44	0.19	1.5	0.62
10	10	0.18	5.67	0.3	2.86	0.1	0.35	12.7	0.02	0.008	0.3	1.99	0.05	0.53	0.14	1.4	0.47
11	10	0.18	5.67	0.3	2.86	0.12	0.35	12.7	0.02	0.009	0.4	1.82	0.04	0.44	0.18	1.5	0.58
12	10	0.18	5.67	0.3	2	0.06	0.5	6.24	0.05	0.01	0.2	1.8	0.09	0.88	0.07	1.2	0.24
13	10	0.18	5.67	0.3	1.43	0.04	0.7	3.18	0.09	0.013	0.1	1.57	0.15	1.32	0.05	1.3	0.17
14	10	0.18	5.67	0.3	2	0.08	0.5	6.24	0.05	0.013	0.3	1.56	0.07	0.66	0.09	1.2	0.31
15	10	0.18	5.67	0.3	2	0.1	0.5	6.24	0.05	0.016	0.3	1.39	0.07	0.53	0.11	1.1	0.38
16	10	0.18	5.67	0.3	1.43	0.06	0.7	3.18	0.09	0.019	0.2	1.28	0.12	0.88	0.07	1.2	0.24
17	10	0.18	5.67	0.3	2	0.12	0.5	6.24	0.05	0.019	0.4	1.27	0.06	0.44	0.13	1.1	0.44
18	10	0.18	5.67	0.3	1.43	0.08	0.7	3.18	0.09	0.025	0.3	1.11	0.10	0.66	0.09	1.1	0.29
19	10	0.18	5.67	0.3	1	0.04	1	1.56	0.19	0.026	0.1	1.1	0.21	1.32	0.03	0.8	0.11
20	10	0.18	5.67	0.3	1.43	0.1	0.7	3.18	0.09	0.031	0.3	0.99	0.09	0.53	0.1	1	0.33
21	10	0.18	5.67	0.3	1.43	0.12	0.7	3.18	0.09	0.038	0.4	0.91	0.09	0.44	0.11	0.9	0.36
22	10	0.18	5.67	0.3	1	0.06	1	1.56	0.19	0.038	0.2	0.9	0.17	0.88	0.05	0.8	0.15
23	10	0.18	5.67	0.3	1	0.08	1	1.56	0.19	0.051	0.3	0.78	0.15	0.66	0.05	0.7	0.18
24	10	0.18	5.67	0.3	1	0.1	1	1.56	0.19	0.064	0.3	0.7	0.13	0.53	0.06	0.6	0.19
25	10	0.18	5.67	0.3	1	0.12	1	1.56	0.19	0.077	0.4	0.64	0.12	0.44	0.06	0.5	0.19

Table 80 List of parameters and run-up results for the R45 slope with low water table

#	α (°)	tanα	cotα	h (m)	T (s)	H (m)	fr (htz)	Lo (m)	h/Lo	H/L	H/h	ξ	ϕ	tanα/(H/h)	R	R/H	R/h
1	10	0.18	5.67	0.3	3.33	0.04	0.3	17.3	0.02	0.002	0.1	3.67	0.06	1.32	0.08	1.9	0.25
2	10	0.18	5.67	0.3	2.86	0.04	0.35	12.7	0.02	0.003	0.1	3.15	0.07	1.32	0.07	1.7	0.23
3	10	0.18	5.67	0.3	3.33	0.06	0.3	17.3	0.02	0.003	0.2	3	0.05	0.88	0.11	1.8	0.36
4	10	0.18	5.67	0.3	3.33	0.08	0.3	17.3	0.02	0.005	0.3	2.6	0.04	0.66	0.15	1.8	0.49
5	10	0.18	5.67	0.3	2.86	0.06	0.35	12.7	0.02	0.005	0.2	2.57	0.06	0.88	0.1	1.6	0.33
6	10	0.18	5.67	0.3	3.33	0.1	0.3	17.3	0.02	0.006	0.3	2.32	0.04	0.53	0.17	1.7	0.56
7	10	0.18	5.67	0.3	2.86	0.08	0.35	12.7	0.02	0.006	0.3	2.22	0.05	0.66	0.13	1.6	0.42
8	10	0.18	5.67	0.3	2	0.04	0.5	6.24	0.05	0.006	0.1	2.2	0.11	1.32	0.06	1.5	0.2
9	10	0.18	5.67	0.3	3.33	0.12	0.3	17.3	0.02	0.007	0.4	2.12	0.04	0.44	0.21	1.7	0.69
10	10	0.18	5.67	0.3	2.86	0.1	0.35	12.7	0.02	0.008	0.3	1.99	0.05	0.53	0.16	1.6	0.52
11	10	0.18	5.67	0.3	2.86	0.12	0.35	12.7	0.02	0.009	0.4	1.82	0.04	0.44	0.19	1.6	0.64
12	10	0.18	5.67	0.3	2	0.06	0.5	6.24	0.05	0.01	0.2	1.8	0.09	0.88	0.08	1.3	0.27
13	10	0.18	5.67	0.3	1.43	0.04	0.7	3.18	0.09	0.013	0.1	1.57	0.15	1.32	0.05	1.2	0.16
14	10	0.18	5.67	0.3	2	0.08	0.5	6.24	0.05	0.013	0.3	1.56	0.07	0.66	0.11	1.4	0.38
15	10	0.18	5.67	0.3	2	0.1	0.5	6.24	0.05	0.016	0.3	1.39	0.07	0.53	0.13	1.3	0.45
16	10	0.18	5.67	0.3	1.43	0.06	0.7	3.18	0.09	0.019	0.2	1.28	0.12	0.88	0.07	1.2	0.24
17	10	0.18	5.67	0.3	2	0.12	0.5	6.24	0.05	0.019	0.4	1.27	0.06	0.44	0.15	1.2	0.5
18	10	0.18	5.67	0.3	1.43	0.08	0.7	3.18	0.09	0.025	0.3	1.11	0.10	0.66	0.09	1.2	0.31
19	10	0.18	5.67	0.3	1	0.04	1	1.56	0.19	0.026	0.1	1.1	0.21	1.32	0.04	1	0.14
20	10	0.18	5.67	0.3	1.43	0.1	0.7	3.18	0.09	0.031	0.3	0.99	0.09	0.53	0.1	1	0.33
21	10	0.18	5.67	0.3	1.43	0.12	0.7	3.18	0.09	0.038	0.4	0.91	0.09	0.44	0.1	0.9	0.34
22	10	0.18	5.67	0.3	1	0.06	1	1.56	0.19	0.038	0.2	0.9	0.17	0.88	0.05	0.8	0.16
23	10	0.18	5.67	0.3	1	0.08	1	1.56	0.19	0.051	0.3	0.78	0.15	0.66	0.05	0.7	0.18
24	10	0.18	5.67	0.3	1	0.1	1	1.56	0.19	0.064	0.3	0.7	0.13	0.53	0.06	0.6	0.19
25	10	0.18	5.67	0.3	1	0.12	1	1.56	0.19	0.077	0.4	0.64	0.12	0.44	0.06	0.5	0.19

Table 81 List of parameters and run-up results for the R45 slope with high water table

Appendix E

This appendix shows all the run-up results obtained from the simulations described in Sections 5.4 and 5.5.

Run-up simulations on impermeable slopes for model validation (Section 5.4.1)

Parameters	Variables
Numerical wave flume dimensions	30m long
Slope angles	10˚, 13˚, and 15˚
Slope type	Plane, smooth and impermeable
Types of waves	Regular Waves
Water depth	0.3m
Wave heights	0.04, 0.06, 0.08, 0.1, and 0.12m
Wave periods	1, 1.43, 2, 2.5, 2.86 and 3.33 seconds
Number of tests	85

Table 82 Summary of parameters for simulations on impermeable slopes for model validation

#	α (˚)	tanα	cotα	h (m)	T (s)	H (m)	fr (htz)	Lo (m)	h/Lo	H/L	H/h	ξ	ϕ	tanα/(H/h)	R	R/H	R/h
1	10	0.18	5.67	0.3	3.33	0.04	0.3	17.3	0.02	0.002	0.1	3.67	0.06	1.32	0.12	3	0.4
2	10	0.18	5.67	0.3	3.33	0.06	0.3	17.3	0.02	0.003	0.2	2.99	0.05	0.88	0.19	3.2	0.63
3	10	0.18	5.67	0.3	3.33	0.08	0.3	17.3	0.02	0.005	0.3	2.59	0.04	0.66	0.23	2.9	0.77
4	10	0.18	5.67	0.3	3.33	0.1	0.3	17.3	0.02	0.006	0.3	2.32	0.04	0.53	0.24	2.4	0.8
5	10	0.18	5.67	0.3	3.33	0.12	0.3	17.3	0.02	0.007	0.4	2.12	0.04	0.44	0.31	2.6	1.03
6	10	0.18	5.67	0.3	2.86	0.04	0.35	12.7	0.02	0.003	0.1	3.15	0.07	1.32	0.12	2.9	0.38
7	10	0.18	5.67	0.3	2.86	0.06	0.35	12.7	0.02	0.005	0.2	2.57	0.06	0.88	0.18	3	0.6
8	10	0.18	5.67	0.3	2.86	0.08	0.35	12.7	0.02	0.006	0.3	2.22	0.05	0.66	0.23	2.9	0.77
9	10	0.18	5.67	0.3	2.86	0.1	0.35	12.7	0.02	0.008	0.3	1.99	0.05	0.53	0.25	2.5	0.83
10	10	0.18	5.67	0.3	2.86	0.12	0.35	12.7	0.02	0.009	0.4	1.82	0.04	0.44	0.27	2.3	0.9
11	10	0.18	5.67	0.3	2	0.04	0.5	6.24	0.05	0.006	0.1	2.20	0.11	1.32	0.09	2.3	0.31
12	10	0.18	5.67	0.3	2	0.06	0.5	6.24	0.05	0.01	0.2	1.80	0.09	0.88	0.13	2.2	0.43
13	10	0.18	5.67	0.3	2	0.08	0.5	6.24	0.05	0.013	0.3	1.56	0.07	0.66	0.15	1.9	0.5
14	10	0.18	5.67	0.3	2	0.1	0.5	6.24	0.05	0.016	0.3	1.39	0.07	0.53	0.19	1.9	0.63
15	10	0.18	5.67	0.3	2	0.12	0.5	6.24	0.05	0.019	0.4	1.27	0.06	0.44	0.23	1.9	0.77
16	10	0.18	5.67	0.3	1.43	0.04	0.7	3.18	0.09	0.013	0.1	1.57	0.15	1.32	0.07	1.8	0.23
17	10	0.18	5.67	0.3	1.43	0.06	0.7	3.18	0.09	0.019	0.2	1.28	0.12	0.88	0.09	1.5	0.3
18	10	0.18	5.67	0.3	1.43	0.08	0.7	3.18	0.09	0.025	0.3	1.11	0.10	0.66	0.11	1.4	0.37
19	10	0.18	5.67	0.3	1.43	0.1	0.7	3.18	0.09	0.031	0.3	0.99	0.09	0.53	0.13	1.3	0.43
20	10	0.18	5.67	0.3	1.43	0.12	0.7	3.18	0.09	0.038	0.4	0.91	0.09	0.44	0.13	1.1	0.43
21	10	0.18	5.67	0.3	1	0.04	1	1.56	0.19	0.026	0.1	1.10	0.21	1.32	0.06	1.5	0.2
22	10	0.18	5.67	0.3	1	0.06	1	1.56	0.19	0.038	0.2	0.90	0.17	0.88	0.06	1	0.2
23	10	0.18	5.67	0.3	1	0.08	1	1.56	0.19	0.051	0.3	0.78	0.15	0.66	0.06	0.8	0.2
24	10	0.18	5.67	0.3	1	0.1	1	1.56	0.19	0.064	0.3	0.70	0.13	0.53	0.09	0.9	0.3
25	10	0.18	5.67	0.3	1	0.12	1	1.56	0.19	0.077	0.4	0.64	0.12	0.44	0.09	0.7	0.29
26	13	0.23	4.33	0.3	1	0.04	1	1.56	0.19	0.026	0.1	1.44	0.28	1.73	0.06	1.5	0.2
27	13	0.23	4.33	0.3	1	0.06	1	1.56	0.19	0.038	0.2	1.18	0.23	1.15	0.09	1.4	0.28
28	13	0.23	4.33	0.3	1	0.08	1	1.56	0.19	0.051	0.3	1.02	0.20	0.87	0.09	1.1	0.3
29	13	0.23	4.33	0.3	1	0.1	1	1.56	0.19	0.064	0.3	0.91	0.18	0.69	0.11	1.1	0.37
30	13	0.23	4.33	0.3	1	0.12	1	1.56	0.19	0.077	0.4	0.83	0.16	0.58	0.12	1	0.4
31	13	0.23	4.33	0.3	1.43	0.04	0.7	3.18	0.09	0.013	0.1	2.06	0.19	1.73	0.09	2.3	0.3
32	13	0.23	4.33	0.3	1.43	0.06	0.7	3.18	0.09	0.019	0.2	1.68	0.16	1.15	0.13	2.2	0.43
33	13	0.23	4.33	0.3	1.43	0.08	0.7	3.18	0.09	0.025	0.3	1.46	0.14	0.87	0.17	2.1	0.57
34	13	0.23	4.33	0.3	1.43	0.1	0.7	3.18	0.09	0.031	0.3	1.3	0.12	0.69	0.19	1.9	0.63
35	13	0.23	4.33	0.3	1.43	0.12	0.7	3.18	0.09	0.038	0.4	1.19	0.11	0.58	0.18	1.5	0.61
36	13	0.23	4.33	0.3	2	0.04	0.5	6.24	0.05	0.006	0.1	2.88	0.14	1.73	0.1	2.4	0.32
37	13	0.23	4.33	0.3	2	0.06	0.5	6.24	0.05	0.01	0.2	2.35	0.11	1.15	0.13	2.2	0.43
38	13	0.23	4.33	0.3	2	0.08	0.5	6.24	0.05	0.013	0.3	2.04	0.10	0.87	0.16	2	0.53
39	13	0.23	4.33	0.3	2	0.1	0.5	6.24	0.05	0.016	0.3	1.82	0.09	0.69	0.23	2.3	0.77
40	13	0.23	4.33	0.3	2	0.12	0.5	6.24	0.05	0.019	0.4	1.66	0.08	0.58	0.23	1.9	0.77
41	13	0.23	4.33	0.3	2.5	0.04	0.4	9.75	0.03	0.004	0.1	3.6	0.11	1.73	0.11	2.8	0.37
42	13	0.23	4.33	0.3	2.5	0.06	0.4	9.75	0.03	0.006	0.2	2.94	0.09	1.15	0.18	2.9	0.59
43	13	0.23	4.33	0.3	2.5	0.08	0.4	9.75	0.03	0.008	0.3	2.55	0.08	0.87	0.22	2.8	0.73
44	13	0.23	4.33	0.3	2.5	0.1	0.4	9.75	0.03	0.01	0.3	2.28	0.07	0.69	0.27	2.7	0.89
45	13	0.23	4.33	0.3	2.5	0.12	0.4	9.75	0.03	0.012	0.4	2.08	0.06	0.58	0.33	2.8	1.1
46	13	0.23	4.33	0.3	2.86	0.04	0.35	12.7	0.02	0.003	0.1	4.12	0.10	1.73	0.11	2.8	0.37
47	13	0.23	4.33	0.3	2.86	0.06	0.35	12.7	0.02	0.005	0.2	3.36	0.08	1.15	0.18	3	0.6
48	13	0.23	4.33	0.3	2.86	0.08	0.35	12.7	0.02	0.006	0.3	2.91	0.07	0.87	0.23	2.9	0.77
49	13	0.23	4.33	0.3	2.86	0.1	0.35	12.7	0.02	0.008	0.3	2.61	0.06	0.69	0.31	3.1	1.03
50	13	0.23	4.33	0.3	2.86	0.12	0.35	12.7	0.02	0.009	0.4	2.38	0.06	0.58	0.33	2.8	1.1

51	13	0.23	4.33	0.3	3.33	0.04	0.3	17.3	0.02	0.002	0.1	4.81	0.08	1.73	0.12	2.9	0.38
52	13	0.23	4.33	0.3	3.33	0.06	0.3	17.3	0.02	0.003	0.2	3.92	0.07	1.15	0.19	3.2	0.63
53	13	0.23	4.33	0.3	3.33	0.08	0.3	17.3	0.02	0.005	0.3	3.4	0.06	0.87	0.26	3.3	0.87
54	13	0.23	4.33	0.3	3.33	0.1	0.3	17.3	0.02	0.006	0.3	3.04	0.05	0.69	0.32	3.2	1.07
55	13	0.23	4.33	0.3	3.33	0.12	0.3	17.3	0.02	0.007	0.4	2.77	0.05	0.58	0.34	2.8	1.13
56	15	0.27	3.73	0.3	1	0.04	1	1.56	0.19	0.026	0.1	1.67	0.32	2.01	0.07	1.8	0.23
57	15	0.27	3.73	0.3	1	0.06	1	1.56	0.19	0.038	0.2	1.37	0.26	1.34	0.09	1.5	0.3
58	15	0.27	3.73	0.3	1	0.08	1	1.56	0.19	0.051	0.3	1.18	0.23	1.00	0.11	1.4	0.37
59	15	0.27	3.73	0.3	1	0.1	1	1.56	0.19	0.064	0.3	1.06	0.20	0.80	0.12	1.2	0.4
60	15	0.27	3.73	0.3	1	0.12	1	1.56	0.19	0.077	0.4	0.97	0.19	0.67	0.13	1.1	0.43
61	15	0.27	3.73	0.3	1.43	0.04	0.7	3.18	0.09	0.013	0.1	2.39	0.23	2.01	0.09	2.3	0.3
62	15	0.27	3.73	0.3	1.43	0.06	0.7	3.18	0.09	0.019	0.2	1.95	0.18	1.34	0.14	2.3	0.47
63	15	0.27	3.73	0.3	1.43	0.08	0.7	3.18	0.09	0.025	0.3	1.69	0.16	1.00	0.16	2	0.53
64	15	0.27	3.73	0.3	1.43	0.1	0.7	3.18	0.09	0.031	0.3	1.51	0.14	0.80	0.21	2.1	0.7
65	15	0.27	3.73	0.3	1.43	0.12	0.7	3.18	0.09	0.038	0.4	1.38	0.13	0.67	0.23	1.9	0.77
66	15	0.27	3.73	0.3	2	0.04	0.5	6.24	0.05	0.006	0.1	3.35	0.16	2.01	0.1	2.4	0.32
67	15	0.27	3.73	0.3	2	0.06	0.5	6.24	0.05	0.01	0.2	2.73	0.13	1.34	0.16	2.7	0.53
68	15	0.27	3.73	0.3	2	0.08	0.5	6.24	0.05	0.013	0.3	2.37	0.11	1.00	0.19	2.4	0.63
69	15	0.27	3.73	0.3	2	0.1	0.5	6.24	0.05	0.016	0.3	2.12	0.10	0.80	0.22	2.2	0.73
70	15	0.27	3.73	0.3	2	0.12	0.5	6.24	0.05	0.019	0.4	1.93	0.09	0.67	0.28	2.3	0.93
71	15	0.27	3.73	0.3	2.5	0.04	0.4	9.75	0.03	0.004	0.1	4.18	0.13	2.01	0.1	2.6	0.34
72	15	0.27	3.73	0.3	2.5	0.06	0.4	9.75	0.03	0.006	0.2	3.42	0.11	1.34	0.14	2.3	0.47
73	15	0.27	3.73	0.3	2.5	0.08	0.4	9.75	0.03	0.008	0.3	2.96	0.09	1.00	0.21	2.6	0.69
74	15	0.27	3.73	0.3	2.5	0.1	0.4	9.75	0.03	0.01	0.3	2.65	0.08	0.80	0.27	2.7	0.91
75	15	0.27	3.73	0.3	2.5	0.12	0.4	9.75	0.03	0.012	0.4	2.42	0.07	0.67	0.31	2.5	1.02
76	15	0.27	3.73	0.3	2.86	0.04	0.35	12.7	0.02	0.003	0.1	4.78	0.11	2.01	0.11	2.6	0.35
77	15	0.27	3.73	0.3	2.86	0.06	0.35	12.7	0.02	0.005	0.2	3.9	0.09	1.34	0.15	2.5	0.5
78	15	0.27	3.73	0.3	2.86	0.08	0.35	12.7	0.02	0.006	0.3	3.38	0.08	1.00	0.22	2.8	0.73
79	15	0.27	3.73	0.3	2.86	0.1	0.35	12.7	0.02	0.008	0.3	3.02	0.07	0.80	0.29	2.9	0.97
80	15	0.27	3.73	0.3	2.86	0.12	0.35	12.7	0.02	0.009	0.4	2.76	0.07	0.67	0.33	2.8	1.1
81	15	0.27	3.73	0.3	3.33	0.04	0.3	17.3	0.02	0.002	0.1	5.57	0.10	2.01	0.11	2.8	0.37
82	15	0.27	3.73	0.3	3.33	0.06	0.3	17.3	0.02	0.003	0.2	4.55	0.08	1.34	0.16	2.7	0.53
83	15	0.27	3.73	0.3	3.33	0.08	0.3	17.3	0.02	0.005	0.3	3.94	0.07	1.00	0.24	3	0.8
84	15	0.27	3.73	0.3	3.33	0.1	0.3	17.3	0.02	0.006	0.3	3.52	0.06	0.80	0.31	3.1	1.03
85	15	0.27	3.73	0.3	3.33	0.12	0.3	17.3	0.02	0.007	0.4	3.22	0.06	0.67	0.35	2.9	1.17

Table 83 List of parameters and run-up results for the simulations ran on impermeable slopes for model validation

Run-up simulations on permeable slopes for model validation (Section 5.4.1)

Parameters	Variables
Numerical wave flume dimensions	30m long
Slope angles	10˚ and 20˚
Slope type	Permeable R30, R45 and R80
Types of waves	Regular Waves
Water depth	0.3m
Wave heights	0.04, 0.06, 0.08, 0.1, and 0.12m
Wave periods	1.43, 2 and 2.86 seconds
Number of simulations	90

Table 84 Summary of numerical parameters for simulations on permeable slopes for model validation

#	α (˚)	tanα	cotα	h (m)	T (s)	H (m)	fr (htz)	Lo (m)	h/Lo	H/L	H/h	ξ	ϕ	tanα/(H/h)	R	R/H	R/h
1	20	0.36	2.75	0.3	1.43	0.12	0.7	3.18	0.09	0.038	0.4	1.87	0.18	0.91	1.05	8.8	3.51
2	20	0.36	2.75	0.3	1.43	0.1	0.7	3.18	0.09	0.031	0.3	2.05	0.19	1.09	1.05	10	3.48
3	20	0.36	2.75	0.3	1.43	0.08	0.7	3.18	0.09	0.025	0.3	2.3	0.22	1.36	1.13	14	3.76
4	20	0.36	2.75	0.3	1.43	0.06	0.7	3.18	0.09	0.019	0.2	2.65	0.25	1.82	1.16	19	3.85
5	20	0.36	2.75	0.3	1.43	0.04	0.7	3.18	0.09	0.013	0.1	3.25	0.31	2.73	1.1	28	3.67
6	20	0.36	2.75	0.3	2	0.12	0.5	6.24	0.05	0.019	0.4	2.62	0.13	0.91	1.15	9.5	3.82
7	20	0.36	2.75	0.3	2	0.1	0.5	6.24	0.05	0.016	0.3	2.88	0.14	1.09	1.21	12	4.03
8	20	0.36	2.75	0.3	2	0.08	0.5	6.24	0.05	0.013	0.3	3.21	0.15	1.36	1.17	15	3.9
9	20	0.36	2.75	0.3	2	0.06	0.5	6.24	0.05	0.01	0.2	3.71	0.18	1.82	1.21	20	4.03
10	20	0.36	2.75	0.3	2	0.04	0.5	6.24	0.05	0.006	0.1	4.55	0.22	2.73	1.21	30	4.03
11	20	0.36	2.75	0.3	2.86	0.12	0.35	12.7	0.02	0.009	0.4	3.75	0.09	0.91	1.42	12	4.74
12	20	0.36	2.75	0.3	2.86	0.1	0.35	12.7	0.02	0.008	0.3	4.11	0.10	1.09	1.57	16	5.24
13	20	0.36	2.75	0.3	2.86	0.08	0.35	12.7	0.02	0.006	0.3	4.59	0.11	1.36	1.46	18	4.86
14	20	0.36	2.75	0.3	2.86	0.06	0.35	12.7	0.02	0.005	0.2	5.3	0.12	1.82	1.41	24	4.71
15	20	0.36	2.75	0.3	2.86	0.04	0.35	12.7	0.02	0.003	0.1	6.49	0.15	2.73	1.27	32	4.22
16	10	0.18	5.67	0.3	1.43	0.12	0.7	3.18	0.09	0.038	0.4	0.91	0.09	0.44	0.67	5.6	2.23
17	10	0.18	5.67	0.3	1.43	0.1	0.7	3.18	0.09	0.031	0.3	0.99	0.09	0.53	0.64	6.4	2.13
18	10	0.18	5.67	0.3	1.43	0.08	0.7	3.18	0.09	0.025	0.3	1.11	0.10	0.66	0.7	8.8	2.34
19	10	0.18	5.67	0.3	1.43	0.06	0.7	3.18	0.09	0.019	0.2	1.28	0.12	0.88	0.79	13	2.63
20	10	0.18	5.67	0.3	1.43	0.04	0.7	3.18	0.09	0.013	0.1	1.57	0.15	1.32	0.96	24	3.21
21	10	0.18	5.67	0.3	2	0.12	0.5	6.24	0.05	0.019	0.4	1.27	0.06	0.44	0.92	7.6	3.06
22	10	0.18	5.67	0.3	2	0.1	0.5	6.24	0.05	0.016	0.3	1.39	0.07	0.53	0.99	9.9	3.3
23	10	0.18	5.67	0.3	2	0.08	0.5	6.24	0.05	0.013	0.3	1.56	0.07	0.66	0.92	12	3.07
24	10	0.18	5.67	0.3	2	0.06	0.5	6.24	0.05	0.01	0.2	1.8	0.09	0.88	0.95	16	3.18
25	10	0.18	5.67	0.3	2	0.04	0.5	6.24	0.05	0.006	0.1	2.2	0.11	1.32	1.16	29	3.85
26	10	0.18	5.67	0.3	2.86	0.12	0.35	12.7	0.02	0.009	0.4	1.82	0.04	0.44	1.16	9.7	3.88
27	10	0.18	5.67	0.3	2.86	0.1	0.35	12.7	0.02	0.008	0.3	1.99	0.05	0.53	1.21	12	4.03
28	10	0.18	5.67	0.3	2.86	0.08	0.35	12.7	0.02	0.006	0.3	2.22	0.05	0.66	1.1	14	3.67
29	10	0.18	5.67	0.3	2.86	0.06	0.35	12.7	0.02	0.005	0.2	2.57	0.06	0.88	1.16	19	3.85
30	10	0.18	5.67	0.3	2.86	0.04	0.35	12.7	0.02	0.003	0.1	3.15	0.07	1.32	1.29	32	4.31

Table 85 List of parameters and run-up results for the simulations ran on the R30 permeable slopes for model validation

#	α (˚)	tanα	cotα	h (m)	T (s)	H (m)	fr (htz)	Lo (m)	h/Lo	H/L	H/h	ξ	ϕ	tanα/(H/h)	R	R/H	R/h
1	20	0.36	2.75	0.3	1.43	0.12	0.7	3.18	0.09	0.038	0.4	1.87	0.18	0.91	1.05	8.8	3.5
2	20	0.36	2.75	0.3	1.43	0.1	0.7	3.18	0.09	0.031	0.3	2.05	0.19	1.09	1.06	11	3.54
3	20	0.36	2.75	0.3	1.43	0.08	0.7	3.18	0.09	0.025	0.3	2.3	0.22	1.36	1.18	15	3.94
4	20	0.36	2.75	0.3	1.43	0.06	0.7	3.18	0.09	0.019	0.2	2.65	0.25	1.82	1.23	20	4.08
5	20	0.36	2.75	0.3	1.43	0.04	0.7	3.18	0.09	0.013	0.1	3.25	0.31	2.73	1.16	29	3.85
6	20	0.36	2.75	0.3	2	0.12	0.5	6.24	0.05	0.019	0.4	2.62	0.13	0.91	1.23	10	4.08
7	20	0.36	2.75	0.3	2	0.1	0.5	6.24	0.05	0.016	0.3	2.88	0.14	1.09	1.37	14	4.55
8	20	0.36	2.75	0.3	2	0.08	0.5	6.24	0.05	0.013	0.3	3.21	0.15	1.36	1.44	18	4.81
9	20	0.36	2.75	0.3	2	0.06	0.5	6.24	0.05	0.01	0.2	3.71	0.18	1.82	1.4	23	4.67
10	20	0.36	2.75	0.3	2	0.04	0.5	6.24	0.05	0.006	0.1	4.55	0.22	2.73	1.29	32	4.29
11	20	0.36	2.75	0.3	2.86	0.12	0.35	12.7	0.02	0.009	0.4	3.75	0.09	0.91	1.4	12	4.67
12	20	0.36	2.75	0.3	2.86	0.1	0.35	12.7	0.02	0.008	0.3	4.11	0.10	1.09	1.47	15	4.9
13	20	0.36	2.75	0.3	2.86	0.08	0.35	12.7	0.02	0.006	0.3	4.59	0.11	1.36	1.44	18	4.81
14	20	0.36	2.75	0.3	2.86	0.06	0.35	12.7	0.02	0.005	0.2	5.3	0.12	1.82	1.4	23	4.67
15	20	0.36	2.75	0.3	2.86	0.04	0.35	12.7	0.02	0.003	0.1	6.49	0.15	2.73	1.39	35	4.64
16	10	0.18	5.67	0.3	1.43	0.12	0.7	3.18	0.09	0.038	0.4	0.91	0.09	0.44	0.69	5.8	2.3
17	10	0.18	5.67	0.3	1.43	0.1	0.7	3.18	0.09	0.031	0.3	0.99	0.09	0.53	0.77	7.7	2.56
18	10	0.18	5.67	0.3	1.43	0.08	0.7	3.18	0.09	0.025	0.3	1.11	0.10	0.66	0.76	9.5	2.54
19	10	0.18	5.67	0.3	1.43	0.06	0.7	3.18	0.09	0.019	0.2	1.28	0.12	0.88	0.86	14	2.86
20	10	0.18	5.67	0.3	1.43	0.04	0.7	3.18	0.09	0.013	0.1	1.57	0.15	1.32	1.05	26	3.5
21	10	0.18	5.67	0.3	2	0.12	0.5	6.24	0.05	0.019	0.4	1.27	0.06	0.44	0.96	8	3.21
22	10	0.18	5.67	0.3	2	0.1	0.5	6.24	0.05	0.016	0.3	1.39	0.07	0.53	0.96	9.6	3.19
23	10	0.18	5.67	0.3	2	0.08	0.5	6.24	0.05	0.013	0.3	1.56	0.07	0.66	0.96	12	3.19

24	10	0.18	5.67	0.3	2	0.06	0.5	6.24	0.05	0.01	0.2	1.8	0.09	0.88	1.16	19	3.85
25	10	0.18	5.67	0.3	2	0.04	0.5	6.24	0.05	0.006	0.1	2.2	0.11	1.32	1.31	33	4.38
26	10	0.18	5.67	0.3	2.86	0.12	0.35	12.7	0.02	0.009	0.4	1.82	0.04	0.44	1.23	10	4.08
27	10	0.18	5.67	0.3	2.86	0.1	0.35	12.7	0.02	0.008	0.3	1.99	0.05	0.53	1.22	12	4.06
28	10	0.18	5.67	0.3	2.86	0.08	0.35	12.7	0.02	0.006	0.3	2.22	0.05	0.66	1.31	16	4.38
29	10	0.18	5.67	0.3	2.86	0.06	0.35	12.7	0.02	0.005	0.2	2.57	0.06	0.88	1.35	22	4.49
30	10	0.18	5.67	0.3	2.86	0.04	0.35	12.7	0.02	0.003	0.1	3.15	0.07	1.32	1.39	35	4.64

Table 86 List of parameters and run-up results for the simulations ran on the R45 permeable slopes for model validation

#	α (°)	tanα	cotα	h (m)	T (s)	H (m)	fr (htz)	Lo (m)	h/Lo	H/L	H/h	ξ	ϕ	tanα/(H/h)	R	R/H	R/h
1	20	0.36	2.75	0.3	1.43	0.12	0.7	3.18	0.09	0.038	0.4	1.87	0.18	0.91	1.24	10	4.13
2	20	0.36	2.75	0.3	1.43	0.1	0.7	3.18	0.09	0.031	0.3	2.05	0.19	1.09	1.21	12	4.03
3	20	0.36	2.75	0.3	1.43	0.08	0.7	3.18	0.09	0.025	0.3	2.3	0.22	1.36	1.24	15	4.13
4	20	0.36	2.75	0.3	1.43	0.06	0.7	3.18	0.09	0.019	0.2	2.65	0.25	1.82	1.36	23	4.52
5	20	0.36	2.75	0.3	1.43	0.04	0.7	3.18	0.09	0.013	0.1	3.25	0.31	2.73	1.46	36	4.86
6	20	0.36	2.75	0.3	2	0.12	0.5	6.24	0.05	0.019	0.4	2.62	0.13	0.91	1.47	12	4.89
7	20	0.36	2.75	0.3	2	0.1	0.5	6.24	0.05	0.016	0.3	2.88	0.14	1.09	1.47	15	4.91
8	20	0.36	2.75	0.3	2	0.08	0.5	6.24	0.05	0.013	0.3	3.21	0.15	1.36	1.72	21	5.73
9	20	0.36	2.75	0.3	2	0.06	0.5	6.24	0.05	0.01	0.2	3.71	0.18	1.82	1.71	28	5.68
10	20	0.36	2.75	0.3	2	0.04	0.5	6.24	0.05	0.006	0.1	4.55	0.22	2.73	1.49	37	4.95
11	20	0.36	2.75	0.3	2.86	0.12	0.35	12.7	0.02	0.009	0.4	3.75	0.09	0.91	1.6	13	5.35
12	20	0.36	2.75	0.3	2.86	0.1	0.35	12.7	0.02	0.008	0.3	4.11	0.10	1.09	1.72	17	5.72
13	20	0.36	2.75	0.3	2.86	0.08	0.35	12.7	0.02	0.006	0.3	4.59	0.11	1.36	1.79	22	5.96
14	20	0.36	2.75	0.3	2.86	0.06	0.35	12.7	0.02	0.005	0.2	5.3	0.12	1.82	1.72	29	5.74
15	20	0.36	2.75	0.3	2.86	0.04	0.35	12.7	0.02	0.003	0.1	6.49	0.15	2.73	1.73	43	5.78
16	10	0.18	5.67	0.3	1.43	0.12	0.7	3.18	0.09	0.038	0.4	0.91	0.09	0.44	0.76	6.3	2.54
17	10	0.18	5.67	0.3	1.43	0.1	0.7	3.18	0.09	0.031	0.3	0.99	0.09	0.53	0.88	8.8	2.93
18	10	0.18	5.67	0.3	1.43	0.08	0.7	3.18	0.09	0.025	0.3	1.11	0.10	0.66	0.89	11	2.98
19	10	0.18	5.67	0.3	1.43	0.06	0.7	3.18	0.09	0.019	0.2	1.28	0.12	0.88	1.1	18	3.67
20	10	0.18	5.67	0.3	1.43	0.04	0.7	3.18	0.09	0.013	0.1	1.57	0.15	1.32	1.18	30	3.94
21	10	0.18	5.67	0.3	2	0.12	0.5	6.24	0.05	0.019	0.4	1.27	0.06	0.44	1.28	11	4.28
22	10	0.18	5.67	0.3	2	0.1	0.5	6.24	0.05	0.016	0.3	1.39	0.07	0.53	1.43	14	4.77
23	10	0.18	5.67	0.3	2	0.08	0.5	6.24	0.05	0.013	0.3	1.56	0.07	0.66	1.51	19	5.04
24	10	0.18	5.67	0.3	2	0.06	0.5	6.24	0.05	0.01	0.2	1.8	0.09	0.88	1.47	24	4.89
25	10	0.18	5.67	0.3	2	0.04	0.5	6.24	0.05	0.006	0.1	2.2	0.11	1.32	1.65	41	5.5
26	10	0.18	5.67	0.3	2.86	0.12	0.35	12.7	0.02	0.009	0.4	1.82	0.04	0.44	1.38	11	4.58
27	10	0.18	5.67	0.3	2.86	0.1	0.35	12.7	0.02	0.008	0.3	1.99	0.05	0.53	1.43	14	4.77
28	10	0.18	5.67	0.3	2.86	0.08	0.35	12.7	0.02	0.006	0.3	2.22	0.05	0.66	1.51	19	5.04
29	10	0.18	5.67	0.3	2.86	0.06	0.35	12.7	0.02	0.005	0.2	2.57	0.06	0.88	1.54	26	5.13
30	10	0.18	5.67	0.3	2.86	0.04	0.35	12.7	0.02	0.003	0.1	3.15	0.07	1.32	1.65	41	5.5

Table 87 List of parameters and run-up results for the simulations ran on the R80 permeable slopes for model validation

Run-up simulations on steep impermeable slopes (regular waves) (Section 5.5)

Parameters	Variables
Numerical wave flume dimensions	30m long
Slope angles	18.4˚, 26.6˚, 33.7 ˚ and 45˚
Slope type	Plane, smooth and impermeable
Types of waves	Regular Waves
Water depth	0.3m
Wave heights	0.04, 0.06, 0.08, 0.1, and 0.12m
Wave periods	1, 1.43, 2, 2.5, 2.86, and 3.33s
Number of tests	120

Table 88 Summary of numerical parameters used for the simulations of regular waves

#	α (˚)	tanα	cotα	h (m)	T (s)	H (m)	fr (htz)	Lo (m)	h/Lo	H/L	H/h	ξ	ϕ	tanα/(H/h)	R	R/H	R/h
1	18.43	0.33	3	0.3	1	0.04	1	1.56	0.19	0.026	0.1	2.08	0.4	2.50	**0.1**	1.6	0.22
2	18.43	0.33	3	0.3	1.43	0.04	0.7	3.18	0.09	0.013	0.1	2.97	0.28	2.50	**0.1**	1.8	0.24
3	18.43	0.33	3	0.3	2	0.04	0.5	6.24	0.05	0.006	0.1	4.16	0.2	2.50	**0.1**	2	0.27
4	18.43	0.33	3	0.3	2.5	0.04	0.4	9.75	0.03	0.004	0.1	5.2	0.16	2.50	**0.1**	2.3	0.3
5	18.43	0.33	3	0.3	2.86	0.04	0.35	12.7	0.02	0.003	0.1	5.95	0.14	2.50	**0.1**	2.5	0.33
6	18.43	0.33	3	0.3	3.33	0.04	0.3	17.3	0.02	0.002	0.1	6.94	0.12	2.50	**0.1**	2.6	0.35
7	18.43	0.33	3	0.3	1	0.06	1	1.56	0.19	0.038	0.2	1.7	0.33	1.67	**0.1**	1.8	0.37
8	18.43	0.33	3	0.3	1.43	0.06	0.7	3.18	0.09	0.019	0.2	2.43	0.23	1.67	**0.1**	1.9	0.38
9	18.43	0.33	3	0.3	2	0.06	0.5	6.24	0.05	0.01	0.2	3.4	0.16	1.67	**0.1**	2.2	0.43
10	18.43	0.33	3	0.3	2.5	0.06	0.4	9.75	0.03	0.006	0.2	4.25	0.13	1.67	**0.1**	2.4	0.48
11	18.43	0.33	3	0.3	2.86	0.06	0.35	12.7	0.02	0.005	0.2	4.85	0.11	1.67	**0.2**	2.7	0.53
12	18.43	0.33	3	0.3	3.33	0.06	0.3	17.3	0.02	0.003	0.2	5.66	0.1	1.67	**0.2**	2.8	0.55
13	18.43	0.33	3	0.3	1	0.08	1	1.56	0.19	0.051	0.3	1.47	0.28	1.25	**0.1**	1.8	0.48
14	18.43	0.33	3	0.3	1.43	0.08	0.7	3.18	0.09	0.025	0.3	2.1	0.2	1.25	**0.2**	1.9	0.5
15	18.43	0.33	3	0.3	2	0.08	0.5	6.24	0.05	0.013	0.3	2.94	0.14	1.25	**0.2**	2.1	0.57
16	18.43	0.33	3	0.3	2.5	0.08	0.4	9.75	0.03	0.008	0.3	3.68	0.11	1.25	**0.2**	2.5	0.67
17	18.43	0.33	3	0.3	2.86	0.08	0.35	12.7	0.02	0.006	0.3	4.2	0.1	1.25	**0.2**	2.7	0.72
18	18.43	0.33	3	0.3	3.33	0.08	0.3	17.3	0.02	0.005	0.3	4.91	0.08	1.25	**0.2**	2.9	0.77
19	18.43	0.33	3	0.3	1	0.1	1	1.56	0.19	0.064	0.3	1.32	0.25	1.00	**0.2**	1.9	0.63
20	18.43	0.33	3	0.3	1.43	0.1	0.7	3.18	0.09	0.031	0.3	1.88	0.18	1.00	**0.2**	2	0.65
21	18.43	0.33	3	0.3	2	0.1	0.5	6.24	0.05	0.016	0.3	2.63	0.13	1.00	**0.2**	2.2	0.73
22	18.43	0.33	3	0.3	2.5	0.1	0.4	9.75	0.03	0.01	0.3	3.29	0.1	1.00	**0.3**	2.6	0.87
23	18.43	0.33	3	0.3	2.86	0.1	0.35	12.7	0.02	0.008	0.3	3.76	0.09	1.00	**0.3**	2.7	0.9
24	18.43	0.33	3	0.3	3.33	0.1	0.3	17.3	0.02	0.006	0.3	4.39	0.08	1.00	**0.3**	2.9	0.95
25	18.43	0.33	3	0.3	1	0.12	1	1.56	0.19	0.077	0.4	1.2	0.23	0.83	**0.2**	1.9	0.75
26	18.43	0.33	3	0.3	1.43	0.12	0.7	3.18	0.09	0.038	0.4	1.72	0.16	0.83	**0.3**	2.3	0.9
27	18.43	0.33	3	0.3	2	0.12	0.5	6.24	0.05	0.019	0.4	2.4	0.12	0.83	**0.3**	2.5	1
28	18.43	0.33	3	0.3	2.5	0.12	0.4	9.75	0.03	0.012	0.4	3	0.09	0.83	**0.3**	2.8	1.1
29	18.43	0.33	3	0.3	2.86	0.12	0.35	12.7	0.02	0.009	0.4	3.43	0.08	0.83	**0.4**	2.9	1.17
30	18.43	0.33	3	0.3	3.33	0.12	0.3	17.3	0.02	0.007	0.4	4.01	0.07	0.83	**0.4**	3.2	1.27
31	26.56	0.5	2	0.3	1	0.04	1	1.56	0.19	0.026	0.1	3.12	0.6	3.75	**0.1**	1.5	0.2
32	26.56	0.5	2	0.3	1.43	0.04	0.7	3.18	0.09	0.013	0.1	4.46	0.42	3.75	**0.1**	1.6	0.22
33	26.56	0.5	2	0.3	2	0.04	0.5	6.24	0.05	0.006	0.1	6.24	0.3	3.75	**0.1**	1.8	0.24
34	26.56	0.5	2	0.3	2.5	0.04	0.4	9.75	0.03	0.004	0.1	7.8	0.24	3.75	**0.1**	2	0.27
35	26.56	0.5	2	0.3	2.86	0.04	0.35	12.7	0.02	0.003	0.1	8.92	0.21	3.75	**0.1**	2.1	0.28
36	26.56	0.5	2	0.3	3.33	0.04	0.3	17.3	0.02	0.002	0.1	10.4	0.18	3.75	**0.1**	2.3	0.3
37	26.56	0.5	2	0.3	1	0.06	1	1.56	0.19	0.038	0.2	2.55	0.49	2.50	**0.1**	1.5	0.3
38	26.56	0.5	2	0.3	1.43	0.06	0.7	3.18	0.09	0.019	0.2	3.64	0.34	2.50	**0.1**	1.7	0.33
39	26.56	0.5	2	0.3	2	0.06	0.5	6.24	0.05	0.01	0.2	5.1	0.25	2.50	**0.1**	1.8	0.37
40	26.56	0.5	2	0.3	2.5	0.06	0.4	9.75	0.03	0.006	0.2	6.37	0.2	2.50	**0.1**	2.1	0.41
41	26.56	0.5	2	0.3	2.86	0.06	0.35	12.7	0.02	0.005	0.2	7.28	0.17	2.50	**0.1**	2.3	0.45
42	26.56	0.5	2	0.3	3.33	0.06	0.3	17.3	0.02	0.003	0.2	8.5	0.15	2.50	**0.1**	2.4	0.48
43	26.56	0.5	2	0.3	1	0.08	1	1.56	0.19	0.051	0.3	2.21	0.42	1.87	**0.1**	1.7	0.44
44	26.56	0.5	2	0.3	1.43	0.08	0.7	3.18	0.09	0.025	0.3	3.15	0.3	1.87	**0.1**	1.8	0.47
45	26.56	0.5	2	0.3	2	0.08	0.5	6.24	0.05	0.013	0.3	4.41	0.21	1.87	**0.2**	1.9	0.52
46	26.56	0.5	2	0.3	2.5	0.08	0.4	9.75	0.03	0.008	0.3	5.52	0.17	1.87	**0.2**	2.1	0.57
47	26.56	0.5	2	0.3	2.86	0.08	0.35	12.7	0.02	0.006	0.3	6.31	0.15	1.87	**0.2**	2.4	0.63
48	26.56	0.5	2	0.3	3.33	0.08	0.3	17.3	0.02	0.005	0.3	7.36	0.13	1.87	**0.2**	2.5	0.67
49	26.56	0.5	2	0.3	1	0.1	1	1.56	0.19	0.064	0.3	1.97	0.38	1.50	**0.2**	1.6	0.52
50	26.56	0.5	2	0.3	1.43	0.1	0.7	3.18	0.09	0.031	0.3	2.82	0.27	1.50	**0.2**	1.8	0.58
51	26.56	0.5	2	0.3	2	0.1	0.5	6.24	0.05	0.016	0.3	3.95	0.19	1.50	**0.2**	1.9	0.63
52	26.56	0.5	2	0.3	2.5	0.1	0.4	9.75	0.03	0.01	0.3	4.94	0.15	1.50	**0.2**	2.3	0.77
53	26.56	0.5	2	0.3	2.86	0.1	0.35	12.7	0.02	0.008	0.3	5.64	0.13	1.50	**0.2**	2.4	0.8
54	26.56	0.5	2	0.3	3.33	0.1	0.3	17.3	0.02	0.006	0.3	6.58	0.11	1.50	**0.3**	2.6	0.87
55	26.56	0.5	2	0.3	1	0.12	1	1.56	0.19	0.077	0.4	1.8	0.35	1.25	**0.2**	1.6	0.63
56	26.56	0.5	2	0.3	1.43	0.12	0.7	3.18	0.09	0.038	0.4	2.57	0.24	1.25	**0.2**	1.7	0.68
57	26.56	0.5	2	0.3	2	0.12	0.5	6.24	0.05	0.019	0.4	3.6	0.17	1.25	**0.2**	1.9	0.75
58	26.56	0.5	2	0.3	2.5	0.12	0.4	9.75	0.03	0.012	0.4	4.51	0.14	1.25	**0.3**	2.3	0.93
59	26.56	0.5	2	0.3	2.86	0.12	0.35	12.7	0.02	0.009	0.4	5.15	0.12	1.25	**0.3**	2.3	0.93
60	26.56	0.5	2	0.3	3.33	0.12	0.3	17.3	0.02	0.007	0.4	6.01	0.1	1.25	**0.3**	2.8	1.1

61	33.69	0.67	1.5	0.3	1	0.04	1	1.56	0.19	0.026	0.1	4.16	0.8	5.00	**0.1**	1.4	0.18
62	33.69	0.67	1.5	0.3	1.43	0.04	0.7	3.18	0.09	0.013	0.1	5.95	0.56	5.00	**0.1**	1.5	0.2
63	33.69	0.67	1.5	0.3	2	0.04	0.5	6.24	0.05	0.006	0.1	8.33	0.4	5.00	**0.1**	1.7	0.22
64	33.69	0.67	1.5	0.3	2.5	0.04	0.4	9.75	0.03	0.004	0.1	10.4	0.32	5.00	**0.1**	1.9	0.25
65	33.69	0.67	1.5	0.3	2.86	0.04	0.35	12.7	0.02	0.003	0.1	11.9	0.28	5.00	**0.1**	2	0.27
66	33.69	0.67	1.5	0.3	3.33	0.04	0.3	17.3	0.02	0.002	0.1	13.9	0.24	5.00	**0.1**	2.1	0.28
67	33.69	0.67	1.5	0.3	1	0.06	1	1.56	0.19	0.038	0.2	3.4	0.65	3.33	**0.1**	1.5	0.3
68	33.69	0.67	1.5	0.3	1.43	0.06	0.7	3.18	0.09	0.019	0.2	4.86	0.46	3.33	**0.1**	1.6	0.32
69	33.69	0.67	1.5	0.3	2	0.06	0.5	6.24	0.05	0.01	0.2	6.8	0.33	3.33	**0.1**	1.8	0.35
70	33.69	0.67	1.5	0.3	2.5	0.06	0.4	9.75	0.03	0.006	0.2	8.5	0.26	3.33	**0.1**	2.1	0.41
71	33.69	0.67	1.5	0.3	2.86	0.06	0.35	12.7	0.02	0.005	0.2	9.71	0.23	3.33	**0.1**	2.2	0.43
72	33.69	0.67	1.5	0.3	3.33	0.06	0.3	17.3	0.02	0.003	0.2	11.3	0.2	3.33	**0.1**	2.3	0.45
73	33.69	0.67	1.5	0.3	1	0.08	1	1.56	0.19	0.051	0.3	2.94	0.57	2.50	**0.1**	1.6	0.41
74	33.69	0.67	1.5	0.3	1.43	0.08	0.7	3.18	0.09	0.025	0.3	4.21	0.4	2.50	**0.1**	1.7	0.45
75	33.69	0.67	1.5	0.3	2	0.08	0.5	6.24	0.05	0.013	0.3	5.89	0.28	2.50	**0.2**	1.9	0.5
76	33.69	0.67	1.5	0.3	2.5	0.08	0.4	9.75	0.03	0.008	0.3	7.36	0.23	2.50	**0.2**	2.1	0.55
77	33.69	0.67	1.5	0.3	2.86	0.08	0.35	12.7	0.02	0.006	0.3	8.41	0.2	2.50	**0.2**	2.3	0.6
78	33.69	0.67	1.5	0.3	3.33	0.08	0.3	17.3	0.02	0.005	0.3	9.81	0.17	2.50	**0.2**	2.3	0.6
79	33.69	0.67	1.5	0.3	1	0.1	1	1.56	0.19	0.064	0.3	2.63	0.51	2.00	**0.2**	1.6	0.53
80	33.69	0.67	1.5	0.3	1.43	0.1	0.7	3.18	0.09	0.031	0.3	3.76	0.35	2.00	**0.2**	1.7	0.57
81	33.69	0.67	1.5	0.3	2	0.1	0.5	6.24	0.05	0.016	0.3	5.27	0.25	2.00	**0.2**	1.9	0.63
82	33.69	0.67	1.5	0.3	2.5	0.1	0.4	9.75	0.03	0.01	0.3	6.58	0.2	2.00	**0.2**	2	0.67
83	33.69	0.67	1.5	0.3	2.86	0.1	0.35	12.7	0.02	0.008	0.3	7.52	0.18	2.00	**0.2**	2.2	0.73
84	33.69	0.67	1.5	0.3	3.33	0.1	0.3	17.3	0.02	0.006	0.3	8.78	0.15	2.00	**0.2**	2.3	0.77
85	33.69	0.67	1.5	0.3	1	0.12	1	1.56	0.19	0.077	0.4	2.4	0.46	1.67	**0.2**	1.6	0.63
86	33.69	0.67	1.5	0.3	1.43	0.12	0.7	3.18	0.09	0.038	0.4	3.43	0.32	1.67	**0.2**	1.8	0.7
87	33.69	0.67	1.5	0.3	2	0.12	0.5	6.24	0.05	0.019	0.4	4.81	0.23	1.67	**0.2**	1.8	0.73
88	33.69	0.67	1.5	0.3	2.5	0.12	0.4	9.75	0.03	0.012	0.4	6.01	0.18	1.67	**0.3**	2.1	0.83
89	33.69	0.67	1.5	0.3	2.86	0.12	0.35	12.7	0.02	0.009	0.4	6.87	0.16	1.67	**0.3**	2.2	0.87
90	33.69	0.67	1.5	0.3	3.33	0.12	0.3	17.3	0.02	0.007	0.4	8.01	0.14	1.67	**0.3**	2.2	0.88
91	45	1	1	0.3	1	0.04	1	1.56	0.19	0.026	0.1	6.24	1.2	7.50	**0**	1.2	0.16
92	45	1	1	0.3	1.43	0.04	0.7	3.18	0.09	0.013	0.1	8.92	0.84	7.50	**0.1**	1.4	0.19
93	45	1	1	0.3	2	0.04	0.5	6.24	0.05	0.006	0.1	12.5	0.6	7.50	**0.1**	1.5	0.2
94	45	1	1	0.3	2.5	0.04	0.4	9.75	0.03	0.004	0.1	15.6	0.48	7.50	**0.1**	1.7	0.22
95	45	1	1	0.3	2.86	0.04	0.35	12.7	0.02	0.003	0.1	17.8	0.42	7.50	**0.1**	1.8	0.23
96	45	1	1	0.3	3.33	0.04	0.3	17.3	0.02	0.002	0.1	20.8	0.36	7.50	**0.1**	1.8	0.23
97	45	1	1	0.3	1	0.06	1	1.56	0.19	0.038	0.2	5.1	0.98	5.00	**0.1**	1.3	0.27
98	45	1	1	0.3	1.43	0.06	0.7	3.18	0.09	0.019	0.2	7.28	0.69	5.00	**0.1**	1.4	0.28
99	45	1	1	0.3	2	0.06	0.5	6.24	0.05	0.01	0.2	10.2	0.49	5.00	**0.1**	1.5	0.3
100	45	1	1	0.3	2.5	0.06	0.4	9.75	0.03	0.006	0.2	12.7	0.39	5.00	**0.1**	1.8	0.35
101	45	1	1	0.3	2.86	0.06	0.35	12.7	0.02	0.005	0.2	14.6	0.34	5.00	**0.1**	1.9	0.38
102	45	1	1	0.3	3.33	0.06	0.3	17.3	0.02	0.003	0.2	17	0.29	5.00	**0.1**	2	0.4
103	45	1	1	0.3	1	0.08	1	1.56	0.19	0.051	0.3	4.42	0.85	3.75	**0.1**	1.4	0.37
104	45	1	1	0.3	1.43	0.08	0.7	3.18	0.09	0.025	0.3	6.31	0.59	3.75	**0.1**	1.5	0.4
105	45	1	1	0.3	2	0.08	0.5	6.24	0.05	0.013	0.3	8.83	0.42	3.75	**0.1**	1.6	0.43
106	45	1	1	0.3	2.5	0.08	0.4	9.75	0.03	0.008	0.3	11	0.34	3.75	**0.2**	1.9	0.5
107	45	1	1	0.3	2.86	0.08	0.35	12.7	0.02	0.006	0.3	12.6	0.3	3.75	**0.2**	2	0.53
108	45	1	1	0.3	3.33	0.08	0.3	17.3	0.02	0.005	0.3	14.7	0.25	3.75	**0.2**	2.1	0.57
109	45	1	1	0.3	1	0.1	1	1.56	0.19	0.064	0.3	3.95	0.76	3.00	**0.1**	1.4	0.45
110	45	1	1	0.3	1.43	0.1	0.7	3.18	0.09	0.031	0.3	5.64	0.53	3.00	**0.1**	1.4	0.47
111	45	1	1	0.3	2	0.1	0.5	6.24	0.05	0.016	0.3	7.9	0.38	3.00	**0.2**	1.6	0.53
112	45	1	1	0.3	2.5	0.1	0.4	9.75	0.03	0.01	0.3	9.87	0.3	3.00	**0.2**	1.9	0.63
113	45	1	1	0.3	2.86	0.1	0.35	12.7	0.02	0.008	0.3	11.3	0.27	3.00	**0.2**	2.1	0.7
114	45	1	1	0.3	3.33	0.1	0.3	17.3	0.02	0.006	0.3	13.2	0.23	3.00	**0.2**	2.2	0.73
115	45	1	1	0.3	1	0.12	1	1.56	0.19	0.077	0.4	3.61	0.69	2.50	**0.2**	1.4	0.57
116	45	1	1	0.3	1.43	0.12	0.7	3.18	0.09	0.038	0.4	5.15	0.49	2.50	**0.2**	1.5	0.6
117	45	1	1	0.3	2	0.12	0.5	6.24	0.05	0.019	0.4	7.21	0.35	2.50	**0.2**	1.7	0.67
118	45	1	1	0.3	2.5	0.12	0.4	9.75	0.03	0.012	0.4	9.01	0.28	2.50	**0.3**	2.1	0.83
119	45	1	1	0.3	2.86	0.12	0.35	12.7	0.02	0.009	0.4	10.3	0.24	2.50	**0.2**	1.9	0.77
120	45	1	1	0.3	3.33	0.12	0.3	17.3	0.02	0.007	0.4	12	0.21	2.50	**0.2**	2	0.8

Table 89 List of parameters and run-up results for the simulations ran with regular waves on steep impermeable slopes

Run-up simulations on impermeable slopes (irregular waves) (Section 5.5)

Parameters	Variables
Numerical wave flume dimensions	30m long
Slope angles	10˚, 13˚, 15˚, 18.4˚, 26.6˚, 33.7 ˚ and 45˚
Slope type	Plane, smooth and impermeable
Types of waves	Irregular Waves (Jonswap spectrum)
Water depth	0.3m
Zeroth-moment significan wave heights, H_{mo}	0.04, 0.06, 0.08 and 0.1m
Wave peak periods, T_p	1, 1.43, 2 and 2.86s
Number of tests	112

Table 90 Numerical parameters used for the irregular wave tests

#	α (˚)	tanα	cotα	h (m)	T (s)	H (m)	fr (htz)	Lo (m)	h/Lo	H/L	H/h	ξ	ϕ	tanα/(H/h)	R	R/H	R/h
1	10	0.18	5.67	0.3	1	0.04	1	1.56	0.19	0.026	0.1	1.1	0.21	1.32	0.08	2	0.27
2	10	0.18	5.67	0.3	1.43	0.04	0.7	3.18	0.09	0.013	0.1	1.57	0.15	1.32	0.09	2.3	0.3
3	10	0.18	5.67	0.3	2	0.04	0.5	6.24	0.05	0.006	0.1	2.2	0.11	1.32	0.11	2.8	0.37
4	10	0.18	5.67	0.3	2.86	0.04	0.35	12.7	0.02	0.003	0.1	3.15	0.07	1.32	0.12	3.1	0.41
5	10	0.18	5.67	0.3	1	0.06	1	1.56	0.19	0.038	0.2	0.9	0.17	0.88	0.11	1.8	0.35
6	10	0.18	5.67	0.3	1.43	0.06	0.7	3.18	0.09	0.019	0.2	1.28	0.12	0.88	0.12	2	0.4
7	10	0.18	5.67	0.3	2	0.06	0.5	6.24	0.05	0.01	0.2	1.8	0.09	0.88	0.15	2.5	0.5
8	10	0.18	5.67	0.3	2.86	0.06	0.35	12.7	0.02	0.005	0.2	2.57	0.06	0.88	0.18	3.1	0.61
9	10	0.18	5.67	0.3	1	0.08	1	1.56	0.19	0.051	0.3	0.78	0.15	0.66	0.12	1.5	0.4
10	10	0.18	5.67	0.3	1.43	0.08	0.7	3.18	0.09	0.025	0.3	1.11	0.10	0.66	0.15	1.9	0.5
11	10	0.18	5.67	0.3	2	0.08	0.5	6.24	0.05	0.013	0.3	1.56	0.07	0.66	0.21	2.6	0.7
12	10	0.18	5.67	0.3	2.86	0.08	0.35	12.7	0.02	0.006	0.3	2.22	0.05	0.66	0.23	2.9	0.77
13	10	0.18	5.67	0.3	1	0.1	1	1.56	0.19	0.064	0.3	0.7	0.13	0.53	0.14	1.4	0.47
14	10	0.18	5.67	0.3	1.43	0.1	0.7	3.18	0.09	0.031	0.3	0.99	0.09	0.53	0.19	1.9	0.63
15	10	0.18	5.67	0.3	2	0.1	0.5	6.24	0.05	0.016	0.3	1.39	0.07	0.53	0.25	2.5	0.83
16	10	0.18	5.67	0.3	2.86	0.1	0.35	12.7	0.02	0.008	0.3	1.99	0.05	0.53	0.26	2.6	0.87
17	13	0.23	4.33	0.3	1	0.04	1	1.56	0.19	0.026	0.1	1.44	0.28	1.73	0.09	2.3	0.3
18	13	0.23	4.33	0.3	1.43	0.04	0.7	3.18	0.09	0.013	0.1	2.06	0.19	1.73	0.1	2.5	0.33
19	13	0.23	4.33	0.3	2	0.04	0.5	6.24	0.05	0.006	0.1	2.88	0.14	1.73	0.12	3.1	0.41
20	13	0.23	4.33	0.3	2.86	0.04	0.35	12.7	0.02	0.003	0.1	4.12	0.10	1.73	0.13	3.2	0.42
21	13	0.23	4.33	0.3	1	0.06	1	1.56	0.19	0.038	0.2	1.18	0.23	1.15	0.12	2	0.4
22	13	0.23	4.33	0.3	1.43	0.06	0.7	3.18	0.09	0.019	0.2	1.68	0.16	1.15	0.14	2.3	0.45
23	13	0.23	4.33	0.3	2	0.06	0.5	6.24	0.05	0.01	0.2	2.35	0.11	1.15	0.17	2.8	0.57
24	13	0.23	4.33	0.3	2.86	0.06	0.35	12.7	0.02	0.005	0.2	3.36	0.08	1.15	0.19	3.1	0.62
25	13	0.23	4.33	0.3	1	0.08	1	1.56	0.19	0.051	0.3	1.02	0.20	0.87	0.15	1.9	0.5
26	13	0.23	4.33	0.3	1.43	0.08	0.7	3.18	0.09	0.025	0.3	1.46	0.14	0.87	0.16	2	0.53
27	13	0.23	4.33	0.3	2	0.08	0.5	6.24	0.05	0.013	0.3	2.04	0.10	0.87	0.23	2.9	0.77
28	13	0.23	4.33	0.3	2.86	0.08	0.35	12.7	0.02	0.006	0.3	2.91	0.07	0.87	0.25	3.1	0.83
29	13	0.23	4.33	0.3	1	0.1	1	1.56	0.19	0.064	0.3	0.91	0.18	0.69	0.17	1.7	0.57
30	13	0.23	4.33	0.3	1.43	0.1	0.7	3.18	0.09	0.031	0.3	1.3	0.12	0.69	0.18	1.8	0.6
31	13	0.23	4.33	0.3	2	0.1	0.5	6.24	0.05	0.016	0.3	1.82	0.09	0.69	0.27	2.7	0.9
32	13	0.23	4.33	0.3	2.86	0.1	0.35	12.7	0.02	0.008	0.3	2.61	0.06	0.69	0.29	2.9	0.97
33	15	0.27	3.73	0.3	1	0.04	1	1.56	0.19	0.026	0.1	1.67	0.32	2.01	0.1	2.5	0.33
34	15	0.27	3.73	0.3	1.43	0.04	0.7	3.18	0.09	0.013	0.1	2.39	0.23	2.01	0.12	2.9	0.38
35	15	0.27	3.73	0.3	2	0.04	0.5	6.24	0.05	0.006	0.1	3.35	0.16	2.01	0.12	3.1	0.41
36	15	0.27	3.73	0.3	2.86	0.04	0.35	12.7	0.02	0.003	0.1	4.78	0.11	2.01	0.12	3	0.4
37	15	0.27	3.73	0.3	1	0.06	1	1.56	0.19	0.038	0.2	1.37	0.26	1.34	0.14	2.3	0.47
38	15	0.27	3.73	0.3	1.43	0.06	0.7	3.18	0.09	0.019	0.2	1.95	0.18	1.34	0.16	2.7	0.53
39	15	0.27	3.73	0.3	2	0.06	0.5	6.24	0.05	0.01	0.2	2.73	0.13	1.34	0.18	3	0.59
40	15	0.27	3.73	0.3	2.86	0.06	0.35	12.7	0.02	0.005	0.2	3.9	0.09	1.34	0.19	3.2	0.63
41	15	0.27	3.73	0.3	1	0.08	1	1.56	0.19	0.051	0.3	1.18	0.23	1.00	0.17	2.1	0.57
42	15	0.27	3.73	0.3	1.43	0.08	0.7	3.18	0.09	0.025	0.3	1.69	0.16	1.00	0.19	2.4	0.63
43	15	0.27	3.73	0.3	2	0.08	0.5	6.24	0.05	0.013	0.3	2.37	0.11	1.00	0.23	2.9	0.77
44	15	0.27	3.73	0.3	2.86	0.08	0.35	12.7	0.02	0.006	0.3	3.38	0.08	1.00	0.26	3.3	0.87
45	15	0.27	3.73	0.3	1	0.1	1	1.56	0.19	0.064	0.3	1.06	0.20	0.80	0.19	1.9	0.63
46	15	0.27	3.73	0.3	1.43	0.1	0.7	3.18	0.09	0.031	0.3	1.51	0.14	0.80	0.21	2.1	0.7
47	15	0.27	3.73	0.3	2	0.1	0.5	6.24	0.05	0.016	0.3	2.12	0.10	0.80	0.29	2.9	0.98
48	15	0.27	3.73	0.3	2.86	0.1	0.35	12.7	0.02	0.008	0.3	3.02	0.07	0.80	0.33	3.3	1.11
49	18.43	0.33	3	0.3	1	0.04	1	1.56	0.19	0.026	0.1	2.08	0.40	2.50	0.1	2.5	0.33
50	18.43	0.33	3	0.3	1.43	0.04	0.7	3.18	0.09	0.013	0.1	2.97	0.28	2.50	0.11	2.6	0.35
51	18.43	0.33	3	0.3	2	0.04	0.5	6.24	0.05	0.006	0.1	4.16	0.20	2.50	0.12	2.9	0.38
52	18.43	0.33	3	0.3	2.86	0.04	0.35	12.7	0.02	0.003	0.1	5.95	0.14	2.50	0.12	2.9	0.38
53	18.43	0.33	3	0.3	1	0.06	1	1.56	0.19	0.038	0.2	1.7	0.33	1.67	0.14	2.3	0.47
54	18.43	0.33	3	0.3	1.43	0.06	0.7	3.18	0.09	0.019	0.2	2.43	0.23	1.67	0.15	2.5	0.5
55	18.43	0.33	3	0.3	2	0.06	0.5	6.24	0.05	0.01	0.2	3.4	0.16	1.67	0.17	2.8	0.57
56	18.43	0.33	3	0.3	2.86	0.06	0.35	12.7	0.02	0.005	0.2	4.85	0.11	1.67	0.19	3.2	0.63
57	18.43	0.33	3	0.3	1	0.08	1	1.56	0.19	0.051	0.3	1.47	0.28	1.25	0.18	2.3	0.6
58	18.43	0.33	3	0.3	1.43	0.08	0.7	3.18	0.09	0.025	0.3	2.1	0.20	1.25	0.21	2.6	0.7
59	18.43	0.33	3	0.3	2	0.08	0.5	6.24	0.05	0.013	0.3	2.94	0.14	1.25	0.23	2.9	0.77
60	18.43	0.33	3	0.3	2.86	0.08	0.35	12.7	0.02	0.006	0.3	4.2	0.10	1.25	0.25	3.1	0.83

61	18.43	0.33	3	0.3	1	0.1	1	1.56	0.19	0.064	0.3	1.32	0.25	1.00	0.23	2.3	0.77
62	18.43	0.33	3	0.3	1.43	0.1	0.7	3.18	0.09	0.031	0.3	1.88	0.18	1.00	0.27	2.7	0.9
63	18.43	0.33	3	0.3	2	0.1	0.5	6.24	0.05	0.016	0.3	2.63	0.13	1.00	0.29	2.9	0.97
64	18.43	0.33	3	0.3	2.86	0.1	0.35	12.7	0.02	0.008	0.3	3.76	0.09	1.00	0.33	3.3	1.1
65	26.56	0.5	2	0.3	1	0.04	1	1.56	0.19	0.026	0.1	3.12	0.60	3.75	0.09	2.3	0.31
66	26.56	0.5	2	0.3	1.43	0.04	0.7	3.18	0.09	0.013	0.1	4.46	0.42	3.75	0.1	2.5	0.33
67	26.56	0.5	2	0.3	2	0.04	0.5	6.24	0.05	0.006	0.1	6.24	0.30	3.75	0.11	2.8	0.37
68	26.56	0.5	2	0.3	2.86	0.04	0.35	12.7	0.02	0.003	0.1	8.92	0.21	3.75	0.11	2.8	0.37
69	26.56	0.5	2	0.3	1	0.06	1	1.56	0.19	0.038	0.2	2.55	0.49	2.50	0.14	2.4	0.48
70	26.56	0.5	2	0.3	1.43	0.06	0.7	3.18	0.09	0.019	0.2	3.64	0.34	2.50	0.15	2.5	0.49
71	26.56	0.5	2	0.3	2	0.06	0.5	6.24	0.05	0.01	0.2	5.1	0.25	2.50	0.17	2.8	0.57
72	26.56	0.5	2	0.3	2.86	0.06	0.35	12.7	0.02	0.005	0.2	7.28	0.17	2.50	0.18	3	0.59
73	26.56	0.5	2	0.3	1	0.08	1	1.56	0.19	0.051	0.3	2.21	0.42	1.87	0.18	2.3	0.61
74	26.56	0.5	2	0.3	1.43	0.08	0.7	3.18	0.09	0.025	0.3	3.15	0.30	1.87	0.2	2.5	0.68
75	26.56	0.5	2	0.3	2	0.08	0.5	6.24	0.05	0.013	0.3	4.41	0.21	1.87	0.23	2.9	0.77
76	26.56	0.5	2	0.3	2.86	0.08	0.35	12.7	0.02	0.006	0.3	6.31	0.15	1.87	0.24	2.9	0.78
77	26.56	0.5	2	0.3	1	0.1	1	1.56	0.19	0.064	0.3	1.97	0.38	1.50	0.22	2.2	0.73
78	26.56	0.5	2	0.3	1.43	0.1	0.7	3.18	0.09	0.031	0.3	2.82	0.27	1.50	0.25	2.5	0.84
79	26.56	0.5	2	0.3	2	0.1	0.5	6.24	0.05	0.016	0.3	3.95	0.19	1.50	0.28	2.8	0.93
80	26.56	0.5	2	0.3	2.86	0.1	0.35	12.7	0.02	0.008	0.3	5.64	0.13	1.50	0.3	3	1.01
81	33.69	0.67	1.5	0.3	1	0.04	1	1.56	0.19	0.026	0.1	4.16	0.80	5.00	0.09	2.3	0.3
82	33.69	0.67	1.5	0.3	1.43	0.04	0.7	3.18	0.09	0.013	0.1	5.95	0.56	5.00	0.1	2.4	0.32
83	33.69	0.67	1.5	0.3	2	0.04	0.5	6.24	0.05	0.006	0.1	8.33	0.40	5.00	0.11	2.7	0.35
84	33.69	0.67	1.5	0.3	2.86	0.04	0.35	12.7	0.02	0.003	0.1	11.9	0.28	5.00	0.11	2.6	0.35
85	33.69	0.67	1.5	0.3	1	0.06	1	1.56	0.19	0.038	0.2	3.4	0.65	3.33	0.13	2.2	0.43
86	33.69	0.67	1.5	0.3	1.43	0.06	0.7	3.18	0.09	0.019	0.2	4.86	0.46	3.33	0.15	2.4	0.49
87	33.69	0.67	1.5	0.3	2	0.06	0.5	6.24	0.05	0.01	0.2	6.8	0.33	3.33	0.15	2.5	0.5
88	33.69	0.67	1.5	0.3	2.86	0.06	0.35	12.7	0.02	0.005	0.2	9.71	0.23	3.33	0.17	2.8	0.57
89	33.69	0.67	1.5	0.3	1	0.08	1	1.56	0.19	0.051	0.3	2.94	0.57	2.50	0.18	2.3	0.6
90	33.69	0.67	1.5	0.3	1.43	0.08	0.7	3.18	0.09	0.025	0.3	4.21	0.40	2.50	0.2	2.6	0.68
91	33.69	0.67	1.5	0.3	2	0.08	0.5	6.24	0.05	0.013	0.3	5.89	0.28	2.50	0.21	2.6	0.7
92	33.69	0.67	1.5	0.3	2.86	0.08	0.35	12.7	0.02	0.006	0.3	8.41	0.20	2.50	0.23	2.9	0.77
93	33.69	0.67	1.5	0.3	1	0.1	1	1.56	0.19	0.064	0.3	2.63	0.51	2.00	0.22	2.2	0.74
94	33.69	0.67	1.5	0.3	1.43	0.1	0.7	3.18	0.09	0.031	0.3	3.76	0.35	2.00	0.24	2.4	0.8
95	33.69	0.67	1.5	0.3	2	0.1	0.5	6.24	0.05	0.016	0.3	5.27	0.25	2.00	0.27	2.7	0.9
96	33.69	0.67	1.5	0.3	2.86	0.1	0.35	12.7	0.02	0.008	0.3	7.52	0.18	2.00	0.28	2.8	0.94
97	45	1	1	0.3	1	0.04	1	1.56	0.19	0.026	0.1	6.24	1.20	7.50	0.08	2.1	0.28
98	45	1	1	0.3	1.43	0.04	0.7	3.18	0.09	0.013	0.1	8.92	0.84	7.50	0.09	2.3	0.3
99	45	1	1	0.3	2	0.04	0.5	6.24	0.05	0.006	0.1	12.5	0.60	7.50	0.09	2.4	0.31
100	45	1	1	0.3	2.86	0.04	0.35	12.7	0.02	0.003	0.1	17.8	0.42	7.50	0.1	2.5	0.33
101	45	1	1	0.3	1	0.06	1	1.56	0.19	0.038	0.2	5.1	0.98	5.00	0.13	2.1	0.42
102	45	1	1	0.3	1.43	0.06	0.7	3.18	0.09	0.019	0.2	7.28	0.69	5.00	0.13	2.2	0.43
103	45	1	1	0.3	2	0.06	0.5	6.24	0.05	0.01	0.2	10.2	0.49	5.00	0.15	2.5	0.5
104	45	1	1	0.3	2.86	0.06	0.35	12.7	0.02	0.005	0.2	14.6	0.34	5.00	0.16	2.6	0.52
105	45	1	1	0.3	1	0.08	1	1.56	0.19	0.051	0.3	4.42	0.85	3.75	0.17	2.1	0.57
106	45	1	1	0.3	1.43	0.08	0.7	3.18	0.09	0.025	0.3	6.31	0.59	3.75	0.18	2.3	0.6
107	45	1	1	0.3	2	0.08	0.5	6.24	0.05	0.013	0.3	8.83	0.42	3.75	0.2	2.5	0.67
108	45	1	1	0.3	2.86	0.08	0.35	12.7	0.02	0.006	0.3	12.6	0.30	3.75	0.22	2.7	0.72
109	45	1	1	0.3	1	0.1	1	1.56	0.19	0.064	0.3	3.95	0.76	3.00	0.21	2.1	0.7
110	45	1	1	0.3	1.43	0.1	0.7	3.18	0.09	0.031	0.3	5.64	0.53	3.00	0.23	2.3	0.77
111	45	1	1	0.3	2	0.1	0.5	6.24	0.05	0.016	0.3	7.9	0.38	3.00	0.25	2.5	0.83
112	45	1	1	0.3	2.86	0.1	0.35	12.7	0.02	0.008	0.3	11.3	0.27	3.00	0.28	2.8	0.92

Table 91 List of parameters and run-up results for the simulations ran with irregular waves on steep impermeable slopes

Appendix F

Breaking Point Location

Table 92 shows the breaking point distance observed for the plunging waves on the four permeable slopes: R30, R45, R60 and R 80. These tests are discussed in Section 6.3.2.

														Breaking Point Distance			
#	α (°)	tanα	cotα	h (m)	T (s)	H (m)	fr (htz)	Lo (m)	h/Lo	H/L	H/h	ξ	ϕ	R30	R45	R60	R80
1	10	0.18	5.67	0.3	3.33	0.04	0.3	17.3	0.02	0.002	0.1	3.67	0.06	0.1	0.13	0.2	0.26
2	10	0.18	5.67	0.3	2.86	0.04	0.35	12.7	0.02	0.003	0.1	3.15	0.07	0.1	0.15	0.2	0.25
3	10	0.18	5.67	0.3	2	0.04	0.5	6.24	0.05	0.006	0.1	2.2	0.11	0.15	0.2	0.3	0.29
4	10	0.18	5.67	0.3	1.43	0.04	0.7	3.18	0.09	0.013	0.1	1.57	0.15	0.2	0.24	0.3	0.35
5	10	0.18	5.67	0.3	1	0.04	1	1.56	0.19	0.026	0.1	1.1	0.21	0.1	0.14	0.2	0.24
6	10	0.18	5.67	0.3	3.33	0.06	0.3	17.3	0.02	0.003	0.2	3	0.05	0.14	0.24	0.3	0.36
7	10	0.18	5.67	0.3	2.86	0.06	0.35	12.7	0.02	0.005	0.2	2.57	0.06	0.2	0.26	0.3	0.34
8	10	0.18	5.67	0.3	2	0.06	0.5	6.24	0.05	0.01	0.2	1.8	0.09	0.24	0.31	0.4	0.46
9	10	0.18	5.67	0.3	1.43	0.06	0.7	3.18	0.09	0.019	0.2	1.28	0.12	0.25	0.31	0.4	0.41
10	10	0.18	5.67	0.3	1	0.06	1	1.56	0.19	0.038	0.2	0.9	0.17	0.2	0.24	0.3	0.39
11	10	0.18	5.67	0.3	3.33	0.08	0.3	17.3	0.02	0.005	0.3	2.6	0.04	0.31	0.36	0.4	0.48
12	10	0.18	5.67	0.3	2.86	0.08	0.35	12.7	0.02	0.006	0.3	2.22	0.05	0.32	0.37	0.5	0.48
13	10	0.18	5.67	0.3	2	0.08	0.5	6.24	0.05	0.013	0.3	1.56	0.07	0.43	0.53	0.6	0.66
14	10	0.18	5.67	0.3	1.43	0.08	0.7	3.18	0.09	0.025	0.3	1.11	0.10	0.45	0.56	0.6	0.67
15	10	0.18	5.67	0.3	1	0.08	1	1.56	0.19	0.051	0.3	0.78	0.15	0.21	0.34	0.5	0.5
16	10	0.18	5.67	0.3	3.33	0.1	0.3	17.3	0.02	0.006	0.3	2.32	0.04	0.2	0.28	0.4	0.44
17	10	0.18	5.67	0.3	2.86	0.1	0.35	12.7	0.02	0.008	0.3	1.99	0.05	0.29	0.39	0.5	0.52
18	10	0.18	5.67	0.3	2	0.1	0.5	6.24	0.05	0.016	0.3	1.39	0.07	0.55	0.63	0.7	0.73
19	10	0.18	5.67	0.3	1.43	0.1	0.7	3.18	0.09	0.031	0.3	0.99	0.09	0.54	0.62	0.7	0.74
20	10	0.18	5.67	0.3	1	0.1	1	1.56	0.19	0.064	0.3	0.7	0.13	0.31	0.48	0.6	0.64
21	10	0.18	5.67	0.3	3.33	0.12	0.3	17.3	0.02	0.007	0.4	2.12	0.04	0.25	0.36	0.4	0.49
22	10	0.18	5.67	0.3	2.86	0.12	0.35	12.7	0.02	0.009	0.4	1.82	0.04	0.36	0.46	0.6	0.63
23	10	0.18	5.67	0.3	2	0.12	0.5	6.24	0.05	0.019	0.4	1.27	0.06	0.64	0.69	0.8	0.81
24	10	0.18	5.67	0.3	1.43	0.12	0.7	3.18	0.09	0.038	0.4	0.91	0.09	0.55	0.63	0.7	0.74
25	10	0.18	5.67	0.3	1	0.12	1	1.56	0.19	0.077	0.4	0.64	0.12	0.51	0.55	0.7	0.69
26	20	0.36	2.75	0.3	1.43	0.06	0.7	3.18	0.09	0.019	0.2	2.65	0.25	0.16	0.19	0.3	0.28
27	20	0.36	2.75	0.3	1.43	0.08	0.7	3.18	0.09	0.025	0.3	2.3	0.22	0.26	0.29	0.3	0.34
28	20	0.36	2.75	0.3	1	0.04	1	1.56	0.19	0.026	0.1	2.27	0.44	0.07	0.13	0.2	0.17
29	20	0.36	2.75	0.3	1.43	0.12	0.7	3.18	0.09	0.038	0.4	1.87	0.18	0.31	0.36	0.4	0.45

Table 92 Breaking point for plunging waves on permeable slopes